



Advanced Photon Source Upgrade

Advanced Photon Source Upgrade Project

Preliminary Design Report

September, 2017

Chapter 4: Accelerator Upgrade

Document Number : APSU-2.01-RPT-002
ICMS Content ID : APSU_1705610

Table of Contents

4	Accelerator Upgrades	1
4-1	Introduction	1
4-1.1	Performance Goals	1
4-1.2	Brightness Goals	1
4-1.3	Choice of Beam Energy	2
4-1.4	Choice of Beam Current	2
4-1.5	Choice of RF Frequency	3
4-1.6	Beam Stability	3
4-1.7	Insertion Device Sources	4
4-1.8	Swap-Out Injection	4
4-2	Beam Physics	6
4-2.1	Lattice Design	7
4-2.1.1	Beam Energy	8
4-2.1.2	Constraints on the Lattice	8
4-2.1.3	Insertion Device Straights	9
4-2.1.4	Optimization of Nonlinear Dynamics	10
4-2.1.5	Characterization of Nonlinear Dynamics	12
4-2.1.6	Summary of Lattice and Magnet Properties	14
4-2.2	Tolerances and Correction Schemes	20
4-2.2.1	Static Random Errors	20
4-2.2.2	Static Systematic Errors	25
4-2.2.3	Variable Errors	26

4-2.2.4	Simulation of Orbit and Lattice Correction	37
4-2.2.5	Simulation of Beam Size Stability	39
4-2.3	Lattice Evaluation	42
4-2.3.1	Magnet Multipole Errors	42
4-2.3.2	Beam Dynamics Effects from Undulators	43
4-2.3.3	Effect of Errors on Dynamic and Momentum Acceptance	45
4-2.4	Impedance and Single-Bunch Stability	53
4-2.4.1	Impedance Model	54
4-2.4.2	Predictions of collective beam dynamics from tracking	55
4-2.4.3	Longitudinal Impedance and Rf Heating	60
4-2.4.3.1	BPM-bellows assembly	61
4-2.4.3.2	Injection/extraction kickers	65
4-2.4.3.3	In-line photon absorbers	67
4-2.4.4	Rf measurements and the impedance test stand	68
4-2.4.5	Future Directions of Collective Effects R&D	69
4-2.5	Multi-bunch Stability	72
4-2.5.1	Damping Effects	72
4-2.5.2	Cavity Impedance	76
4-2.5.3	Monte Carlo Calculation of Growth Rates	77
4-2.5.4	Conclusion for Instability from Cavity Impedance	82
4-2.6	Ion Trapping and Instabilities	84
4-2.6.1	Trapping Criteria	84
4-2.6.2	Instability Simulations	85
4-2.6.3	Train Gaps	86
4-2.6.4	Commissioning and Early Operation	88

4-2.6.5	Emittance Growth from Ion Effects	89
4-2.7	Intrabeam Scattering	91
4-2.8	Beam Lifetime	94
4-2.8.1	Touschek Lifetime including Harmonic Cavity	94
4-2.8.2	Gas Scattering Lifetime Based on Species-Specific Pressure Profiles	96
4-2.8.3	Total Lifetime and Beam Parameters	97
4-2.9	Beam Dynamics with Bunch-Lengthening Cavity	100
4-2.9.1	Theoretical Expectations	100
4-2.9.2	Simulation Methods	102
4-2.9.3	Choice of Loaded Q and Detuning	102
4-2.9.4	Effects of Bunch Population Variation	104
4-2.9.5	Multibunch Instabilities	105
4-2.9.6	Effects of Bunch Train Gaps	108
4-2.10	Swap-out Injection Design and Performance	111
4-2.10.1	Injection Line Design	111
4-2.10.2	Swap-out Extraction Section	115
4-2.10.3	Injection Performance	118
4-2.10.3.1	Optical mismatch.	118
4-2.10.3.2	Longitudinal mismatch.	118
4-2.10.3.3	Trajectory error.	119
4-2.10.3.4	Summary and results.	120
4-2.10.4	Perturbations to Stored Beam	121
4-2.11	Beam Dumps and Collimation	125
4-2.11.1	Collimation of Touschek Losses	126
4-2.11.2	Swap-out Beam Dump	127

4-2.11.3	Energy Deposition Simulations	129
4-2.11.3.1	Geometry	129
4-2.11.4	Whole-beam dump	132
4-2.12	Ray Tracing Guidelines	139
4-3	Implementation	146
4-3.1	Introduction	146
4-3.1.1	Key Design Drivers	148
4-3.2	Magnets	150
4-3.2.1	Quadrupole Magnets	152
4-3.2.2	Sextupole Magnets	155
4-3.2.3	Longitudinal-Gradient Dipoles	156
4-3.2.4	Transverse-Gradient Dipoles	157
4-3.2.5	Reverse-Bends	159
4-3.2.6	Magnet Trims and Fast Correctors	159
4-3.2.7	Magnet Modules	160
4-3.2.8	Magnetic Measurements	160
4-3.2.8.1	Rotating Coil Measurements of Multipole Magnets	160
4-3.2.8.2	Wire-Based Measurements	161
4-3.2.8.3	Hall Probe Measurements	162
4-3.3	Vacuum System	164
4-3.3.1	Requirements and Constraints	164
4-3.3.2	System Design	164
4-3.3.3	System Design Analysis	166
4-3.3.3.1	Computer Simulations for a Precise Understanding of Syn- chrotron Radiation Loads and Residual Gas Pressures	166

4-3.3.3.2	Numerical Ray Tracing to Understand Bending Magnet Radiation under Off-Normal Steering Conditions	167
4-3.3.4	Component Design	168
4-3.3.4.1	Doublet and Multiplet Section Vacuum Chambers	168
4-3.3.4.2	L-bend Section Vacuum Chambers	169
4-3.3.4.3	FODO Section Vacuum Chambers	170
4-3.3.4.4	Photon Absorbers	170
4-3.3.4.5	Integrated Beam Position Monitor with Bellows Assemblies	171
4-3.3.4.6	Mechanical Supports	173
4-3.3.5	Zone F Straight Sections	174
4-3.4	Magnet Support and Alignment System	178
4-3.4.1	Support Concept	178
4-3.4.2	Support System Vibration and Stability	182
4-3.4.3	Magnet and Plinth Transport and Assembly	185
4-3.4.3.1	Transport Test	186
4-3.4.4	Alignment Strategy	187
4-3.5	Power Supply System	191
4-3.5.1	Overview	191
4-3.5.2	Stand-alone Unipolar Power Supplies for M1 and M2 Dipole Strings	193
4-3.5.3	Unipolar DC-DC Power Converter System	193
4-3.5.4	Bipolar DC-DC Converter System for Trims, Slow Correctors, and Skew Quads	194
4-3.5.5	Bipolar Power Supply System for Fast Correctors	194
4-3.5.6	Power Supply Controllers	195
4-3.5.7	External Current Measurement and Calibration System	197
4-3.5.8	Power Supply Communication Structure	198

4-3.5.9	Double Sector Configuration and Layout	199
4-3.6	Beam Injection and Extraction Systems	205
4-3.6.1	Overview	205
4-3.6.2	Lambertson DC Septum	206
4-3.6.3	Stripline rf Design	208
4-3.6.4	High-Voltage Feedthrough	211
4-3.6.5	Stripline Mechanical Design	211
4-3.6.6	End-to-end Simulations	214
4-3.6.7	Fast High-Voltage Pulser	215
4-3.6.8	Pulser Timing	216
4-3.6.9	Prototype Kicker Tests	217
4-3.7	Orbit Positioning and Stabilization	220
4-3.7.1	Introduction	220
4-3.7.2	Beam Stability Tolerances	220
4-3.7.3	Sources of Orbit Motion	221
4-3.7.3.1	Vibration	221
4-3.7.3.2	Temperature Stability	222
4-3.7.4	Orbit Feedback System	222
4-3.7.5	APS-Upgrade Fast Orbit Feedback System	224
4-3.7.6	Long-Term Orbit Drift	225
4-3.7.7	Unified Feedback Algorithm	226
4-3.7.8	Fast Corrector Magnets	227
4-3.7.9	Prototype Development and Testing - ‘4x4’ tests	228
4-3.7.10	Prototype Development and Testing - ‘16x8’ Integrated Tests	229
4-3.7.10.1	Unified feedback algorithm at 22.6 kHz correction rate	230

4-3.7.10.2	Fast corrector latency and response time	230
4-3.7.10.3	Closed-loop orbit correction bandwidth	231
4-3.7.10.4	Feedback controller processor comparisons	231
4-3.7.10.5	Summary	232
4-3.8	Diagnostics	235
4-3.8.1	Diagnostic Systems Overview	235
4-3.8.2	RF Beam Position Monitors	236
4-3.8.3	X-ray Beam Position Monitors	238
4-3.8.4	Beam Size Monitor (BSM)	239
4-3.8.4.1	Relative Beam Size Monitor and X-ray Beam Position Mon- itor	241
4-3.8.4.1.1	Relative Beam Size Monitors: Aperture No. 3 & 4	241
4-3.8.4.1.2	Source Position and Beam Angle Monitors: Aper- tures No. 1 and 2	242
4-3.8.4.2	Absolute Beam Size Monitors	243
4-3.8.4.2.1	X-ray Pinhole Camera: Aperture No. 5	243
4-3.8.4.2.2	Fresnel Diffractometer: Aperture No. 6	243
4-3.8.4.2.3	Young’s Double-Slit Inteferometer: Aperture No. 7	244
4-3.8.5	Mechanical Motion Monitoring	244
4-3.8.6	Bunch Length and Bunch Purity Monitoring	246
4-3.8.7	Current and Loss Monitoring	248
4-3.8.8	Longitudinal Feedback System	248
4-3.8.8.1	System Layout	250
4-3.8.8.2	Longitudinal Feedback Kicker	251
4-3.8.8.3	Advanced feedback topology	252
4-3.9	Accelerator Control System	255

4-3.9.1	Overview	255
4-3.9.2	Control System Infrastructure	256
4-3.9.2.1	Hardware Infrastructure - Timing and Event System	256
4-3.9.2.2	Infrastructure - Double-sector Configuration	257
4-3.9.2.3	Infrastructure - EPICS IOC Software & Development Environment	258
4-3.9.2.4	Infrastructure - Data Acquisition (DAQ) System	258
4-3.9.2.5	Infrastructure - Network	258
4-3.9.3	High-Level Engineering and Database Applications	260
4-3.9.3.1	Database Applications - Component Database (CDB)	260
4-3.9.3.2	Control System Engineering Applications	260
4-3.9.4	Controls for Technical Systems	261
4-3.9.4.1	Technical Systems Interfaces	261
4-3.9.4.2	Simulation of Technical Systems	262
4-3.9.4.3	Integration Tests and Startup Tools/Applications	262
4-3.9.5	Pre-Installation Phase	262
4-3.9.6	Controls Support for Machine Testing and Commissioning	263
4-3.10	Main Ring Rf System	266
4-3.10.1	High-Level Rf System	266
4-3.10.1.1	High-Power Coupler	268
4-3.10.1.2	HOM Damping	268
4-3.10.2	Low Level Rf System	269
4-3.11	Bunch Lengthening System	271
4-3.11.1	High Harmonic Cavity and Cryomodule	271
4-3.11.2	High-level System Parameters	271
4-3.11.3	Cavity Design, Fabrication, and Testing	272

4-3.11.4	Fundamental RF power couplers	274
4-3.11.5	Higher Order Mode Dampers	277
4-3.11.6	Cavity Slow Mechanical Tuner	278
4-3.11.7	Bunch Lengthening System Cryomodule	281
4-3.11.8	Cryogenic Plant	282
4-3.11.9	Bunch-Lengthening RF System	283
4-3.12	Engineered Safety Systems	286
4-3.12.1	Access Control and Interlock System	286
4-3.12.2	Personnel Safety System	287
4-3.12.3	Radiation and Shielding Assessment	287
4-3.12.3.1	Introduction	287
4-3.12.3.2	APS-U Limits for Annual Dose	288
4-3.12.3.3	APS-U Shielding Policy	289
4-3.12.3.4	Tracking Simulations	293
4-3.12.3.5	Radiation Physics Analysis	294
4-3.12.3.6	Beam Lifetime Requirements	295
4-3.12.3.7	Results of Beam Loss Studies	297
4-3.12.3.8	Activated Materials	297
4-3.12.4	Machine Protection Systems	298
4-3.13	Injector Modifications	301
4-3.13.1	Injector Timing	302
4-3.13.1.1	1-Hz Timing Operation	302
4-3.13.1.2	Booster-Storage Ring Synchronization	303
4-3.13.2	PAR Performance	306
4-3.13.3	PAR Improvements	308

4-3.13.4	Booster Performance	310
4-3.13.5	Booster Improvements	314
4-3.14	Magnet Module Assembly and Testing	320
4-3.14.1	Module Assembly	320
4-3.14.2	Module Testing	323
4-3.14.3	Facilities to Support Module Assembly and Testing	323

List of Figures

Figure 4.1:	Brightness Envelope	3
Figure 4.2:	Hybrid 7BA lattice with reverse bends for the APS. The natural emittance is 42 pm. Blue blocks represent normal-direction dipoles, orange blocks represent reverse-direction dipoles, red blocks represent quadrupoles, and green blocks represent sextupoles.	8
Figure 4.3:	Dynamic acceptance with errors for selected Pareto-optimal solution from MOGA.	13
Figure 4.4:	Local momentum acceptance with errors for selected Pareto-optimal solution from MOGA.	13
Figure 4.5:	Chromatic tune dependence for nominal lattice. Black: horizontal, red: vertical.	13
Figure 4.6:	Transverse (x, y) FMA for nominal lattice	13
Figure 4.7:	Transverse (nux, nuy) for nominal lattice	14
Figure 4.8:	(x, δ) FMA for nominal lattice	14
Figure 4.9:	Distribution of the equilibrium beam energy errors due to dipole errors for two different orbit correction configurations (black – all correctors, red – six correctors per sector) and without orbit correction (blue).	22
Figure 4.10:	Comparison of energy errors for the cases when M1 and M2 dipoles powered in series or separately.	22
Figure 4.11:	Processes affecting a noise component before its effect reaches the user sample. .	28
Figure 4.12:	AC magnetic field attenuation due to losses in both the solid iron yoke of the quadrupole magnet and the copper wall of the vacuum chamber. The field attenuation is approximated as $1/f^{1/4}$ between 1 Hz and 100 Hz and as $1/f^{1/2}$ above 100 Hz (black lines).	30
Figure 4.13:	From left to right: Power spectral density of electrical (blue) and vibrational noise (black) with power amplitudes D_e and D_v ; electrical noise attenuation due to solid iron core and vacuum chamber with bandwidths f_{SIA1} and f_{SIA2} ; lattice amplification factors: blue – for electric noise, black – for vibrational noise; beam motion attenuation due to orbit correction with bandwidth f_{bw}	31
Figure 4.14:	Lattice amplification factor dependence on the ground motion correlation length. An amplification of 1 means that everything moves together, so no relative motion is detected.	31

Figure 4.15: Final orbit errors.	39
Figure 4.16: Probability distribution of the required maximum skew quadrupole integrated strength.	39
Figure 4.17: (Left): Final beta function errors. (Right): Final dispersion errors. Vertical dispersion distribution is the result of adjusting coupling from the minimum number to the requested 10%.	40
Figure 4.18: Distribution of horizontal (left) and vertical (right) emittance after lattice correction but before adjusting coupling.	40
Figure 4.19: Distribution of standard deviation of beam sizes at IDs, normalized to the average beam size at IDs, assuming 5×10^{-3} rms variation in tune separation.	41
Figure 4.20: Distribution of rms tilt angles at IDs, assuming 5×10^{-3} rms variation in tune separation.	41
Figure 4.21: 10^{th} -percentile dynamic acceptance contours for five cases. See text for details.	49
Figure 4.22: Cumulative distributions of approximate Touschek lifetime for several cases	50
Figure 4.23: Beta function-weighted transverse dipole impedance for the APS-U ring.	56
Figure 4.24: Longitudinal collective effects from tracking.	57
Figure 4.25: Transverse collective effects during injection.	59
Figure 4.26: Model of the BPM-bellows and a BPM button.	62
Figure 4.27: BPM button longitudinal impedance and wakepotential analysis.	63
Figure 4.28: Bellows longitudinal impedance and wakepotential analysis.	64
Figure 4.29: Electric field distribution for injection/extraction kicker.	66
Figure 4.30: Impedance calculations for injection/extraction kickers.	66
Figure 4.31: Impedance considerations for in-line absorbers.	67
Figure 4.32: Measured S_{21} transmission coefficient for a NEG-coated copper chamber.	68
Figure 4.33: Proposed Goubau-line-based impedance measurement stand.	70
Figure 4.34: Coherent damping demonstrated in multi-bunch instability simulations	74
Figure 4.35: Shunt Impedances of damped cavity	77
Figure 4.36: Measured HOM frequencies	79

Figure 4.37: Distribution of growth rates of instability	80
Figure 4.38: Effect of temperature tuning of cavities	82
Figure 4.39: Left: lattice functions for one sector of the APS-U lattice. Right: critical mass for different emittance ratios, compared with the mass numbers of common gasses.	85
Figure 4.40: Pressure profiles for one sector of the APS-U storage ring, calculated by MolFlow+.	86
Figure 4.41: Simulated ion density for 324 bunches, 200 mA.	87
Figure 4.42: Ion instability amplitude (in units of vertical beam size) for 324 bunches, 200 mA.	87
Figure 4.43: Bunch population with ion clearing gaps.	87
Figure 4.44: Simulated ion density for 324 bunches, round beams, 1000 A-hrs, and 2-bunch gaps.	88
Figure 4.45: Vertical ion instability amplitude for 324 bunches, round beams, 1000 A-hrs, and 2-bunch gaps.	88
Figure 4.46: Simulated ion density for 324 bunches, round beams, 100 A-hrs, and 2-bunch gaps.	88
Figure 4.47: Vertical ion instability amplitude for 324 bunches, round beams, 100 A-hrs, and 2-bunch gaps.	88
Figure 4.48: Vertical ion instability with 25 mA and 5 A-hr beam conditioning, as a function of number of bunches.	89
Figure 4.49: Vertical ion instability with 200 mA and 100 A-hr beam conditioning, as a function of number of bunches.	89
Figure 4.50: Effect of IBS on emittances, energy spread, and bunch length for 48-bunch and 324-bunch fills at 200 mA as a function of the assumed emittance ratio $\kappa = \epsilon_y/\epsilon_x$.	91
Figure 4.51: Ratio of electron beam brightness with IBS to that without IBS as a function of the emittance ratio, for various numbers of bunches in a 200 mA fill. The nominal rms bunch length is 15.6 mm.	93
Figure 4.52: Touschek lifetime results over 100 ensembles for 48-bunch mode at 200 mA, as a function of HHC detuning.	95
Figure 4.53: Touschek lifetime results over 100 ensembles for 324-bunch mode at 200 mA, as a function of HHC detuning.	95
Figure 4.54: Variation in Touschek lifetime as a function of energy loss from IDs, assuming optimized HHC settings.	96

Figure 4.55: Variation in emittance as a function of energy loss from IDs, assuming optimized HHC settings.	96
Figure 4.56: Local gas scattering rates computed using data from MOLFLOW/SYNRAD and <i>elegant</i> . This example shows results using PSD data from Mathewson, assuming $5 A \cdot h$ dose and 25 mA operating current.	99
Figure 4.57: Rf voltages for a maximally flat total voltage using a 4 th harmonic cavity for bunch lengthening.	101
Figure 4.58: Instantaneous current for 48-bunch fill with 200 mA beam current, 4.1 MV main rf voltage, and $n=4$, for various bunch-lengthening conditions.	101
Figure 4.59: Rms bunch duration for 48- and 324-bunch modes as a function of the harmonic cavity detuning Δf_h	104
Figure 4.60: Rms energy spread for 48- and 324-bunch modes as a function of the harmonic cavity detuning Δf_h	104
Figure 4.61: Samples of the longitudinal bunch density normalized to unit area for 48-bunch mode for various values of Δf_h	104
Figure 4.62: Samples of the longitudinal bunch density normalized to unit area for 324-bunch mode for various values of Δf_h	104
Figure 4.63: Rms bunch duration and rms energy spread as a function of total current for a 48-bunch fill, with fixed $\Delta f_h = 9.0$ kHz and $Q_L = 6 \times 10^5$	105
Figure 4.64: Distribution of rms bunch duration when the charge per bunch varies by 10% due to nonuniformity of the fill.	106
Figure 4.65: Net growth rates of multi-bunch instabilities for 48-bunch, 200-mA beam for various randomized HOM frequencies, labeled by the expected percentile of the growth rate.	106
Figure 4.66: Maximum LFB driver output in steady-state conditions for 48-bunch, 200-mA beam for various randomized HOM frequencies, labeled by the expected percentile of the growth rate.	107
Figure 4.67: Equilibrium bunch centroids for 48-bunch fill after kicking out of bunch 0.	107
Figure 4.68: Equilibrium rms bunch durations for 48-bunch fill after (black) kicking out bunch 0, compared to values with all bunches present (red).	108
Figure 4.69: Equilibrium bunch shapes for bunch 1 (red) through 47 (magenta) after bunch 0 is lost.	108

Figure 4.70: Touschek lifetime for unique bunches when various numbers of simple two-bunch gaps are used in the nominally 324-bunch fill.	109
Figure 4.71: Touschek lifetime for unique bunches when various numbers of compensated two-bunch gaps are used in the nominally 324-bunch fill.	109
Figure 4.72: Loss rate due to Touschek scattering for two gap schemes as a function of the number of two-bunch gaps, along with a modified guard-bunch scheme.	110
Figure 4.73: Schematic layout of extraction-injection region. Red line shows the current BTS line configuration. Blue box shows the section requiring modification for APSU.	111
Figure 4.74: Layout of the on-axis injection section and the projected injected beam orbit.	112
Figure 4.75: Schematic layout of APS injection region.	114
Figure 4.76: BTS line layout, upper plot – horizontal plane, lower plot – vertical plane. Black line – SR; red – APS-U BTS line; blue – APS BTS line.	114
Figure 4.77: Optical functions of the BTS transfer line. The last optical and geometry matching section has two weak skew quads to correct the vertical dispersion to zero at the injection point.	115
Figure 4.78: Layout of swap-out extraction section and dumping beam trajectory at different scenario.	117
Figure 4.79: Bunch 0 transverse distribution at swap-out dump if extracted without (left) and with (right) a pre-kick. The two plots are on a fixed x-y scale and illustrate the large reduction in particle density with the pre-kick.	118
Figure 4.80: Cumulative distribution of fraction of injected particles that are lost, for various assumptions of horizontal and vertical emittance of the injected beam.	121
Figure 4.81: Locations of injection losses for the nominal 60nm by 16nm injected beam emittances.	121
Figure 4.82: Maximum stored-beam perturbation amplitude A_y vs. stripline kicker error levels (in percentage of full kick strength.	122
Figure 4.83: Cumulative distribution of fraction of stored particles for the three maximum perturbation cases.	123
Figure 4.84: The BSC aperture over a sector. The horizontal aperture is limited by the smallest ID aperture; The vertical aperture is limited by the vertical collimator aperture.	126
Figure 4.85: Locations of Touschek losses (minimum lifetime case): linear scale (upper); log scale (bottom).	128

Figure 4.86: Normal-incidence x-y block geometry for the central section.	129
Figure 4.87: Normal-incidence x-z block geometry, showing the densely-gridded central section as a dark band.	129
Figure 4.88: Transverse total dose distribution in the upstream collimator segment.	130
Figure 4.89: Integrated swap-out bunch x-profiles at turn 0 and turn 250.	131
Figure 4.90: Integrated swap-out bunch y-profiles at turn 0 and turn 250.	131
Figure 4.91: Longitudinal peak ΔT distributions for a single decohered bunch.	132
Figure 4.92: Fractional momentum offset of bunch 0 vs. pass, where the rf is muted at pass 2.	133
Figure 4.93: Fractional momentum spread of bunch 0 at the end of sector 40 vs. pass, where the rf is muted at pass 2.	133
Figure 4.94: Charge in bunch 0 vs. pass, where the rf is muted at pass 2.	133
Figure 4.95: Horizontal and vertical beam size of bunch 0 at the end of sector 40 vs. pass, where the rf is muted at pass 2.	133
Figure 4.96: X-Z view of beam dump geometry.	134
Figure 4.97: Peak dose (Gray) versus z for various materials during a beam dump.	134
Figure 4.98: Electron-positron fluence from a whole beam dump in Al (10^{15}cm^{-2}).	134
Figure 4.99: Total dose in Al (MGy). Note, the dose is integrated across the region shown in Fig. 4.86.	134
Figure 4.100: Total dose (MGy) in the transverse plane near peak in Al.	135
Figure 4.101: FLE 5 cm downstream from an aluminum beam dump.	136
Figure 4.102: Total dose (kGy) in the beam chamber wall and adjoining magnet iron, for an aluminum beam dump.	136
Figure 4.103: Downstream electron-positron spectra for different dump metals.	137
Figure 4.104: Downstream neutron spectra for different dump metals.	137
Figure 4.105: Possible closed orbits generated by two orthogonal correctors. Different colors correspond to different orbit amplitudes A	140
Figure 4.106: Possible closed orbits at the middle of consecutive ID straight sections.	141

Figure 4.107:Orbit phase space at the entrance to seven non-reverse bending dipoles. Betatron ellipses encompassing the orbit phase space are also shown.	143
Figure 4.108:Orbit phase space at the entrance to reverse bending dipoles. Betatron ellipses encompassing the orbit phase space are also shown.	144
Figure 4.109:Orbit phase at entrance (left) and exit (right) of the dipole A:M2. Red symbols on the left plot outline the boundary of the phase space and are obtained by simple analysis of all the points on the plot. Red symbols on the right are obtained by applying expression (4.46) to the red symbols on the left plot. . . .	145
Figure 4.110:Block diagram showing major components and practical implementation for one sector of the APS-U storage ring lattice.	146
Figure 4.111:Crosstalk between the dipole and sextupole components	151
Figure 4.112:Design guideline for operating magnet	152
Figure 4.113:Flux density, B , in a cross-sectional view of the first quadrant of a Q1 quadrupole magnet at maximum current. This cross-section is taken at the axial center of the magnet (in the beam direction). The highest value of $ B $ is 2.1 T, at the corners of the pole tip.	154
Figure 4.114:Q1 quadrupole 3-D calculation for the flux density. The values of $ B $ shown here are for the surface of the magnet. The highest value, 3.7 T, occurs at the upstream and downstream ends of the pole tips.	154
Figure 4.115:Flux density $ B $ in a cross-sectional view of the sextupole magnet at maximum current. The cross-section is taken at the axial center of the magnet.	156
Figure 4.116:(a) Prototype M1 L-bend magnet with uniform gap and (b) M1 yoke.	157
Figure 4.117:Cross-section of the M4 Q-bend magnet. A) Whole magnet. B) Close up of pole tips with 10 mm radius.	158
Figure 4.118:Layout for the vacuum system in a typical storage ring arc.	164
Figure 4.119:Synchrotron radiation power distribution in a typical storage ring sector.	165
Figure 4.120:The difference in photon flux distribution in the storage ring at 200 mA operation when reflections are accounted for.	166
Figure 4.121:Vacuum pressure distribution in a typical storage ring sector at 200 mA operation after 1000 Ah conditioning.	167
Figure 4.122:Reduction in pressure with beam conditioning.	168
Figure 4.123:Residual gas composition at 200 mA operation after 1000 Ah conditioning. . . .	169

Figure 4.124:Minimum heights of photon absorbers required to protect sensitive components under all conceivable mis-steered beam scenarios.	170
Figure 4.125:Standard aluminum doublet and multiplet section vacuum chamber.	171
Figure 4.126:Aluminum L-bend section vacuum chamber.	172
Figure 4.127:Copper FODO section vacuum chamber with independently-cooled inline photon absorber.	173
Figure 4.128:Typical end absorber with examples of CFD and thermal FEM simulation data.	174
Figure 4.129:CAD models of crotch absorbers for x-ray beam extraction to ID beamlines (left) and BM beamlines (right).	174
Figure 4.130:Concept for a beam position monitor assembly with GlidCop bellows liner. . . .	175
Figure 4.131:Render of an adjustable flexure-based chamber support.	176
Figure 4.132:CAD model of the sector 37 straight section used to develop integrated design.	177
Figure 4.133:Plan and elevation views of the APS Upgrade lattice. The different magnet groups include (1) curved FODO, (2) DLM modules, and (3) M2 L-bend dipoles. The quad-doublet, M1 L-bend dipoles, multiplet, and curved FODO magnets are all supported on unique plinths, while the M2 L-bend dipoles are supported from the ends of these plinths.	178
Figure 4.134:Preliminary FODO module assembly consists of (1) epoxy grout, (2) concrete/steel plinth, (3) cast iron support girder, (4) individual magnets and vacuum system, and (5) quick attach plate for the air caster system tug.	179
Figure 4.135:Plinth and alignment mechanisms without the magnet assembly. The alignment mechanism components are (1) three-point vertical supports with spherical bearings and slip plates to decouple translation and rotation from the vertical motion, (2) lateral pushers to provide lateral and yaw constraint and alignment while decoupling vertical motion, (3) longitudinal pusher to provide longitudinal constraint and alignment while decoupling vertical motion, and (4) support outriggers (three total) to provide six degrees of freedom for plinth alignment. . .	180
Figure 4.136:Preliminary DLM module A assembly. All of the magnet modules have similar designs with standardized support and alignment system components.	181
Figure 4.137:Preliminary M2 L-bend dipole magnet assembly resting on the semi-kinematic support and alignment system.	181
Figure 4.138:Images comparing the a) DMM experimentally measured first mode of 64 Hz, and the b) DMM FE calculated first mode of 67 Hz. The simulation differed from the experiment by 5%.	182

Figure 4.139:APS storage ring tunnel sector 28 integrated floor motion on a 1-100 Hz bandwidth showing the transverse (X), vertical (Y), and longitudinal (Z) components.	183
Figure 4.140:Simulated first mode of the DLM module, 42 Hz.	183
Figure 4.141:The FE-calculated DLM response. The floor motion (blue), quadrupole motion (red), and the integrated quadrupole motion (black) are shown. The quadrupole motion can be taken to be the same as the girder motion.	184
Figure 4.142:The measured quadrupole-to-quadrupole motion on the DMM.	184
Figure 4.143:Chart showing the square root of the absolute and relative motion PSDs of the APS storage ring floor at a 9 m separation for both the transverse (X) and vertical (Y) directions. Curves fit to the region between 0.1 and 1 Hz are also shown. Both absolute motions and the X direction relative motion follow $1/f^2$, whereas the Y direction relative motion grows at a slightly lower rate, following $1/f^{1.5}$.	185
Figure 4.144:Prototype FODO module being moved into the test area using an air caster system after it was unloaded from a flatbed truck using two Versa-Lifts in tandem.	186
Figure 4.145:DMM magnet alignment before and after the transport tests.	187
Figure 4.146:DMM magnet alignment before and after the transport tests.	187
Figure 4.147:APS Storage Ring floor settlement 1993-2015.	189
Figure 4.148:Magnet power supply generic block diagram	191
Figure 4.149:Block diagram of the unipolar power supply system.	193
Figure 4.150:Prototype fast corrector power supply.	194
Figure 4.151:Block diagram of an H-bridge switching circuit for fast corrector power supplies.	195
Figure 4.152:Fast Corrector Power Supply Current Regulation Loop.	195
Figure 4.153:Power Supply Controller function diagram and external DCCT interface.	196
Figure 4.154:Precision current measurement system in-situ calibration diagram.	198
Figure 4.155:Double sector power supply communication structure.	199
Figure 4.156:Double sector power supply layout.	200
Figure 4.157:Layouts for Extraction and Injection sections.	205
Figure 4.158:The septum magnet viewed from the stored beam chamber at DS (a) and US (b)ends.	207

Figure 4.159: Calculated magnetic flux density distribution over the septum magnet calculated with an Opera-2D model, with the different colors representing different flux densities. The injection beam-pipe aperture is located immediately below the center pole of the magnet.	208
Figure 4.160: Septum magnet top view (a) of the injected and stored electron beam trajectories in the storage ring coordinate system (all other parts except the bottom pole are hidden); (b) Plots of injected and stored electron beam trajectories in the magnet coordinate system. The ideal trajectory (in)board and (out)board show the allowed range of the injected beam in the XZ-plane using an ideal field.	208
Figure 4.161: Kicker pulse shape requirements: (a) intra-bunch spacing, (b) pulse shape.	209
Figure 4.162: Upper half of the stripline kicker model; geometric-parameters for optimization.	210
Figure 4.163: E-Field distribution of the 2-D stripline kicker mode	211
Figure 4.164: Differential mode S-parameters for stripline kicker	211
Figure 4.165: Cross-sectional view of prototype feedthrough design.	212
Figure 4.166: Finished prototype feedthrough.	212
Figure 4.167: Body (Left) and tapered transition (Right) parts for the vertical kicker.	213
Figure 4.168: Photograph of the stripline blades manufactured for the prototype kicker.	213
Figure 4.169: Prototype kicker assembly prior to beam testing (Left). The kicker copper stripline blades and a view down the bore of the kicker beam aperture (Right).	214
Figure 4.170: Model of kicker assembly for end-to-end TDR simulations.	215
Figure 4.171: Comparison of differential-mode and common-mode TDR measurements with simulations.	215
Figure 4.172: Extraction/Injection block diagram, showing timing.	217
Figure 4.173: Beam spot deflection for kicker amplitudes from 0 kV to 15 kV.	217
Figure 4.174: Measured y-centroid position as a function of kicker amplitude for 7 GeV beam. The maximum deflection corresponds to a kick angle of 0.66 mrad at ± 15 kV	218
Figure 4.175: Measurement of kick strength at several voltages vs pulser trigger delay. Note that the right-side edge of the pulse is the leading (upstream) edge	218
Figure 4.176: Architecture for the present APS RTFB that is the basis of the preliminary design for the APS Upgrade.	223
Figure 4.177: Partitioning the inverse-response matrix computations to the local controllers.	224

Figure 4.178:FOFB controller	224
Figure 4.179:orbit feedback spatial requirements	226
Figure 4.180:Unified orbit feedback step reponse comparison	227
Figure 4.181:Prototype fast corrector magnet frequency response	228
Figure 4.182:Fast orbit feedback signal flow diagram	228
Figure 4.183:Feedback controller algorithm implementation	229
Figure 4.184:4x4 step-response comparison	229
Figure 4.185:Response of correctors to a $50\mu\text{m}$ angle bump for unified mode. Both ‘fast’ and ‘slow’ correctors receive their setpoints at 22.6 kHz.	230
Figure 4.186:Prototype fast power supply step response	231
Figure 4.187:Execution time measurements for the ‘16x8’ test using new prototype power supplies.	231
Figure 4.188:RMS beam motion at S27 in unified mode	232
Figure 4.189:Hardware configuration for the S27 ‘16x8’ integrated beam stability tests.	233
Figure 4.190:MBA BPM assembly cross-section.	237
Figure 4.191:MBA BPM electrodes.	238
Figure 4.192:MBA BPM button assembly TDR data.	239
Figure 4.193:Commercial BPM processing electronics	240
Figure 4.194:Ratio of x-ray Flux Through Pinhole Collimators	242
Figure 4.195:Pinhole Camera X-ray Profiles	243
Figure 4.196:Fresnel Diffraction Pattern	244
Figure 4.197:Youngs Interference Pattern	245
Figure 4.198:Capacitive and hydrostatic level mechanical motion monitoring.	245
Figure 4.199:Bunch length and purity monitor system layout.	247
Figure 4.200:Bunch purity histogram.	247
Figure 4.201:Aliased HOM impedance spectrum of the beam modes	249

Figure 4.202:Block diagram of the longitudinal feedback system.	250
Figure 4.203:3-d rendering of a conceptual design for the APS-U longitudinal-feedback kicker. Length of this model is 30 cm. Two of these kickers will be used in the APS-U storage ring.	251
Figure 4.204:Controls Scope (yellow background).	256
Figure 4.205:R&D DAQ use-case: simultaneous capture and time-correlation of waveforms from multiple sources during storage ring injection.	259
Figure 4.206:Controls networks topology.	264
Figure 4.207:CDB catalog item.	265
Figure 4.208:352-MHz HLRF system configuration for MBA upgrade.	267
Figure 4.209:Exploded view of the CERN-ANL high-power rf coupler. The structure on the left side is a mounting car and not part of the coupler structure. (Figure courtesy of E. Montesinos, CERN.)	269
Figure 4.210:The APS HOM damper. Four of these dampers are installed in the Sec. 36 cavities.	270
Figure 4.211:1.4 GHz higher-harmonic cavity. Left: bare cavity weldment. Center: Cavity encapsulated within helium vessel. Right: View along cavity bore.	273
Figure 4.212:APS-U higher-harmonic cavity assembly during electropolishing.	273
Figure 4.213:Cavity cold test configuration.	274
Figure 4.214:Cavity cold test configuration.	275
Figure 4.215:ANSYS mechanical model (top) and thermal simulation (bottom) showing the equilibrium temperature distribution for 20 kW cw operation of the fundamental power coupler in travelling wave mode.	275
Figure 4.216:RF power coupler R&D test assembly.	276
Figure 4.217:Measured rf heating in the power coupler for 18 kW of transmitted power at 1.3 GHz.	277
Figure 4.218:(a) RF model for impedance simulations and (b) simulation results by CST Wakefield and Eigenmode Solvers. Z_{0L} represents the longitudinal impedance of the monopole modes and Z_{1T} represents the transverse impedances of the dipole modes. Resolution in three impedance spectra calculated by the Wakefield Solver is 200 kHz and it is fine enough to resolve every high impedance peak.	279

Figure 4.219:Details of the large HOM absorber assembly. (a): mechanical model, (b): von-Mises stress due to interference in diameter simulated by ANSYS, (c): finished assembly of the large HOM absorber.	279
Figure 4.220:Mechanical model of the slow frequency tuner (a) and the prototype tuner assembled with the cavity (b). Detailed slow frequency tuner parts are as follows; (1), (2): cold (2 K) and warm (80 K) retaining rings, (3), (6): pressure plates, (4), (5) outer and inner bellows for the pressure plates, (7): cavity beam port flange clamp ring, (8): single-convolution bellow in helium jacket. On pressurizing the bellows (4,5), the pressure plate (6) and the clamp ring (7) move right relative to the cylindrical part of the helium jacket and this leads to longitudinal compression of the niobium cavity.	280
Figure 4.221:Measured cavity resonant frequency change with slow tuner helium gas pressure. Red dots were measured when the pressure was increasing, blue dots (partially obscured by the red dots) were measured when the pressure was decreasing. . . .	281
Figure 4.222:Vacuum vessel, thermal and magnetic shields (left) and half section of the full cryomodule (right).	282
Figure 4.223:Schematic of the BLS cryogenic system.	283
Figure 4.224:Block diagram for the bunch lengthening rf system.	284
Figure 4.225:Minimum beam lifetime and injection efficiency for an annual dose of 100 mrem outside the APS-U storage ring bulk shielding.	296
Figure 4.226:Present APS Injector Complex.	301
Figure 4.227:PAR accumulation cycle in 1-Hz timing.	303
Figure 4.228:Booster dipole current ramp in 1-Hz timing. The short ramp is the default. . . .	303
Figure 4.229:Evolution of the beam size during the acceleration cycle of the Booster. The $6\text{-}\sigma$ values shown are meant to give an indication of the aperture required. The blue curve is for on-momentum operation, the green curve, for -0.6% momentum offset.	304
Figure 4.230:Booster rf program for injection into storage-ring, for the uncorrected ramp and two extreme corrections of ramp time (negative=faster). The uncorrected ramp is $7.275\ \mu\text{s}$ faster than the unramped $\Delta f_{rf} = 0$ case.	305
Figure 4.231:PAR bunch length as a function of charge, measured near extraction.	306
Figure 4.232:PAR charge-dependent horizontal (left) and vertical (right) rms beam size after extraction.	307
Figure 4.233:Best measured charge performance in Booster.	311

Figure 4.234:Booster charge-dependent efficiency compared to simulation. The 85% goal is marked.	311
Figure 4.235:Comparison of measured and simulated booster vertical tune shift with charge. .	312
Figure 4.236:Simulated booster injection efficiency at 20 nC vs bunch length, ignoring collective effects.	312
Figure 4.237:Simulated booster injection efficiency at 20 nC vs momentum offset, for fixed 330 ps PAR bunch length.	312
Figure 4.238:Horizontal booster orbit before and after correction. Note that the corrected orbit follows the dispersion function, since the booster is run off-momentum. . .	313
Figure 4.239:Vertical booster orbit before and after correction.	313
Figure 4.240:Simulated booster transmission at 20 nC with and without beam-loading. . . .	314
Figure 4.241:High intensity Robinson stability limit at injection voltage of 600kV as a function of detuning.	315
Figure 4.242:High intensity Robinson stability limit across the Booster ramp. The actual beam-loading factor is the blue curve.	315
Figure 4.243:Integrated Assembly and Test Workflow.	321
Figure 4.244:Component delivery driven magnet module assembly schedule.	322
Figure 4.245:Exploded view of FODO magnet module assembly.	322
Figure 4.246:Preliminary design of M2 L-bend magnet module assembly.	323
Figure 4.247:Preliminary layout of typical assembly and testing building.	325

Acronyms and Abbreviations

2D	two dimensional
3D	three dimensional
3PW	three-pole wiggler
7BA	seven-bend achromat
ABSM	absolute beam size monitor
AC	alternating current
ACIS	APS Access Control and Interlock System
ADC	analog-to-digital converter
AGC	automatic gain control
ALARA	as low as reasonably achievable
APD	avalanche photodiodes
APS	Advanced Photon Source
APS-U	Advanced Photon Source Upgrade
BM	bending magnet
BNL	Brookhaven National Laboratory
BPLD	beam position limit detector
BPM	beam position monitor
BSC	beam stay clear
BSM	beam size monitor
BTS	booster-to-storage ring
BTX	booster extraction test line
CAD	computer-aided design
CDB	component database
CDF	cumulative distribution function
CFD	computational fluid dynamics
CMM	coordinate measuring machine
CUFE	canted undulator front end
CW	continuous wave

DA	dynamic acceptance
DAQ	data acquisition
DC	direct current
DCCT	direct-current current transformer
DLM	doublet-L-bend-multiplet
DMM	Demonstration Modular Multiplet
DOF	degree of freedom
DS	downstream
DSC	double-sector controller
DSP	digital signal processor
EAA	Early Assembly Area
EDM	electrical discharge machining
EPICS	Experimental Physics and Industrial Control System
ERL	Energy Recovery Linac
ESRF	European Synchrotron Radiation Facility
FB	feedback
FBC	feedback controller
FDS	fast data stream
FEA	finite element analysis
FEM	finite element method
FID	fast ionization dynistor
FIR	finite impulse response
FLE	electron-positron fluence
FODO	focusing-drift-defocusing-drift
FOFB	fast orbit feedback
FPBC	feedback controller
FPGA	field programmable gate array
FSE	fractional-strength-error
FWHM	full width half maximum

G-line	Goubau-line
GDX	gigabyte data exchange
GRID	grazing-incidence insertion-device
H7BA	hybrid seven-bend achromat
HGSCU	horizontal-gap superconducting undulator
HHC	higher-harmonic cavity
HHC	high harmonic cavity
HHLFE	high heat load front end
HLRF	high level radio-frequency
HLS	hydrostatic leveling system
HMBA	hybrid multi-bend achromat
HOM	higher order mode
HSCU	helical superconducting undulator
HV	high voltage
I/O	input/output
IBS	intra-beam scattering
ID	insertion device
IOC	input-output controllers
LEA	linac extension area
LFB	longitudinal feedback
LLRF	low level radio-frequency
LMA	local momentum acceptance
LO	local oscillator
MBA	multi-bend achromat
MCI	maximum credible incident
MCR	Main Control Room
MLI	multi-layer insulation
MMS	Mechanical Motion System
MOGA	multi-objective genetic algorithm

MOSFET	metal-oxide semiconductor field-effect transistor
MPS	machine protection system
MRF	MicroResearch Finland
MTBF	mean time between failure
MWS	Microwave Studio
NEG	non-evaporable getter
NMR	nuclear magnetic resonance
NLS-II	National Synchrotron Light Source II
ODH	oxygen deficiency hazard
PAR	Particle Accumulator Ring
PCG	photoinjector rf gun
PEP	Positron-Electron Project
PLC	programmable logic controller
PSD	power spectral density
PSD	photon-stimulated desorption
PSS	Personnel safety system
PTB	PAR-to-Booster
PV	process variable
QA	quality assurance
QR	quick response
RBSM	relative beam size monitor
rf	radio-frequency
RGA	residual gas analyzer
RM	response-matrix
rms	root mean square
RTFB	real-time fast orbit feedback
SCU	superconducting undulator
SD	defocusing sextupole
SF	focusing sextupole

SiC	silicon carbide
SLM	synchrotron light monitor
SoC	system on chip
SPI	serial peripheral interface
SR	storage ring
SRF	superconducting radio-frequency
ST	low carbon steel
SV	singular value
TBT	turn-by-turn
TCSPC	time-correlated single-photon counting
TDR	Time Domain Reflectometer
TIM	timing module
US	upstream
VLAN	virtual local area network
VP	Vanadium Permendur
XBPM	x-ray beam position monitor

4 Accelerator Upgrades

4-1 Introduction

The Advanced Photon Source (APS) storage ring will be upgraded by using a multibend achromat (MBA) lattice to provide dramatically enhanced hard x-ray brightness and coherent flux to beam-line experiments in comparison to the present machine. To accomplish this, a hybrid multi-bend achromat magnetic lattice has been developed. It includes seven bending magnets in each of the 40 sectors, in comparison to the present two per sector, and in addition will use an additional 6 horizontally offset quadrupole magnets as weak reverse bends.

This new machine has a number of novel features, including nearly round beams in contrast to the present relatively wide beam. The present suite of insertion device beamlines (including canted lines) and bending magnet (BM) beamlines will be supported. Relatively high single-bunch current operation will be preserved, with 4.2 mA per bunch in a uniformly-spaced 48-bunch fill pattern. New particle- and x-ray beam position monitors and feedback systems will be used to provide ultra-stable operation commensurate with the significantly smaller transverse particle beam dimensions. To accommodate very strong linear and non-linear magnetic focussing elements, a new injection scheme which does not require large horizontal vacuum chamber apertures, has been developed. This “swap-out” technique involves wholesale replacement of individual bunches in contrast to the present incremental top-up method.

4-1.1 Performance Goals

The proposed design parameters shown in Table 4.1 have been chosen to increase x-ray brightness by 2 to 3 orders of magnitude in comparison to the present APS machine, over a broad range of hard x-ray energies. The source size and divergence correspond to insertion device source points. The parameters shown are nominal, and do not include known physics such as intrabeam scattering, impedance, and harmonic cavity effects.

Note that the emittance ratio is variable and can be adjusted to suit x-ray experimental requirements. In particular, a ratio of 0.1 shown in Table 4.1 for the 324-bunch brightness mode was selected to maximize overall brightness. In addition, round beams are also straight forward to produce.

4-1.2 Brightness Goals

Shown in Figure 4.1 is a comparison of the average beam brightness for the present APS storage ring to various possible insertion device sources installed on the APS-U storage ring. Over a wide range of hard x-ray energies extending up to and beyond 100 keV, an improvement by a factor of 100 to 1000 is seen.

Table 4.1. Beam parameter comparison.

Quantity	APS Now	APS MBA		Units
		Timing Mode	Brightness Mode	
Beam Energy	7	6	6	GeV
Beam Current	100	200	200	mA
Number of Bunches	24	48	324	
Bunch Duration (rms)	34	104	88	ps
Energy Spread (rms)	0.095	0.156	0.130	%
Bunch Spacing	153	77	11	ns
Emittance Ratio	0.013	1	0.1	
Horizontal Emittance	3100	31.9	42.2	pm-rad
Horizontal Beam Size (rms)	275	12.6	14.5	μm
Horizontal Divergence (rms)	11	2.5	2.9	μrad
Vertical Emittance	40	31.7	4.2	pm-rad
Vertical Beam Size (rms)	10	7.7	2.8	μm
Vertical Divergence (rms)	3.5	4.1	1.5	μrad

Table 4.2. Undulator parameters for comparison of APS and APS-U

Type	Gap mm	Period mm	Length m
APS			
HPM	10.75	33	4.8
HPM	10.75	27	4.8
APS-U			
HPM	8.5	28	4.6
HPM	8.5	25	4.6
SCU	8.0	20.5	3.5
SCU	8.0	15.5	3.5

4-1.3 Choice of Beam Energy

For the present stage of the design, a nominal energy of 6 GeV vs. the present 7 GeV has been chosen to balance competing effects. Emittance scales quadratically with beam energy, yielding a 36% increase in brightness by lowering the energy. However, lower energy makes the beam more susceptible to wakefield-induced instabilities, intrabeam scattering effects, and Touschek lifetime reduction. Additionally, extremely high magnetic field gradients (>80 T/m) that scale linearly with energy argue for a lower energy to allow feasible magnet designs. Finally, the total energy loss per turn from the electron beam due to emission of synchrotron radiation scales as the fourth power of energy, allowing the possibility of storing a larger total beam current at 6 GeV vs. 7 GeV while relaxing the power and voltage requirements from the radio-frequency (rf) systems.

4-1.4 Choice of Beam Current

For the present design, considerable effort has gone into preserving high single-bunch charge, which is important for many x-ray timing experiments. This involves a tradeoff between the vacuum chamber design, which produces beam-disrupting wakefields, and the accelerator lattice configuration, which

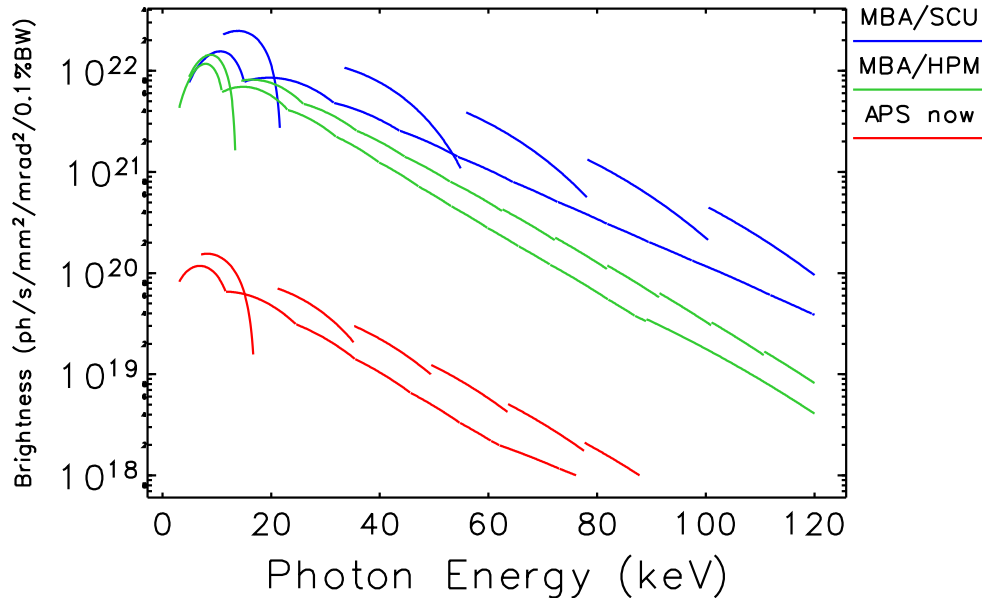


Figure 4.1. Brightness for APS today using several installed insertion devices compared to four possible undulators in APS-U. See Table ?? for list of device parameters.

includes beam energy. Smaller vacuum chamber apertures are desirable from the standpoint of magnet design to reduce pole tip fields, but doing this increases wake fields. The accelerator design presented here includes viable chamber and magnet designs commensurate with 6 GeV operation, with as few as 48 uniformly-spaced bunches, each containing 4.2 mA for a total of 200 mA. This is essentially the same bunch current presently used in the APS storage ring in 24-bunch operation at 100 mA.

4-1.5 Choice of RF Frequency

The present APS operates with an rf system at 352 MHz. Because the APS-U storage ring emittance is so small, the resulting Toushek lifetime will be correspondingly reduced, in addition to being a strong function of bunch length, with shorter bunches giving shorter beam lifetime. An extensive investigation was conducted to quantify the costs and benefits of running at a lower rf frequency, with the end goal of longer bunches and lifetime. The end result was that replacement of the existing rf plant would be quite costly, in addition to negatively impacting the types of timing x-ray experiments requiring high charge single bunch operation which would benefit most from the lower rf frequency. [1]

4-1.6 Beam Stability

A number of challenges and opportunities arise in the consideration of beam stability for the APS-U storage ring. The most significant change is associated with the factor of 13 to 15 reduction in horizontal beam size, meaning that the horizontal beam stability requirement is reduced correspond-

ingly. For the APS Upgrade, beam stability goals are based on 10% of the rms (root mean square) particle beam's phase space dimensions, implying sub-micron- and sub-microradian-scale stability levels on time scales extending from milliseconds to days. To achieve these goals, an integrated approach is being taken to first design a machine with extremely low levels of noise (e.g., power supplies, vibration suppression), and second to develop a world-leading fast orbit feedback (FOFB) architecture with closed-loop bandwidth exceeding 1 kHz. To meet the aggressive long-term drift requirements, x-ray diagnostics have been incorporated into beamline front ends, including a new high-power hard x-ray beam position monitor. In addition, mechanical monitoring systems will be used to measure and correct long-term motions of the floor (e.g. earth tides) and thermally-induced accelerator component motion.

4-1.7 Insertion Device Sources

The new storage ring will incorporate new and enhanced insertion devices to generate x-ray beams tailored to x-ray beamline requirements. Recent experience with superconducting undulators at the APS has made this technology very attractive for many applications. In addition to traditional planar hybrid permanent magnet devices, the use of revolvers will expand the flexibility of the source, allowing optimal beam properties at specific x-ray energies where needed. More exotic devices which take advantage of round beams, such as vertically-polarized undulators requiring small horizontal apertures, will now be possible. To support x-ray experiments at existing bending magnet beamlines, bending magnet radiation from high-field transverse-gradient dipole bending magnets (B:M3) will be available. Space has been allocated for optional three-pole wigglers to support bending magnet beamlines and analyses of their impact has been completed, however the B:M3 dipole radiation appears adequate for nearly all BM beamlines.

4-1.8 Swap-Out Injection

In the late 1990s, the APS pioneered top-up operation, which provides nearly constant stored beam current to x-ray experiments [2]. This has become a standard operation mode for light sources worldwide. Accumulation with existing top-up operation requires that the injected and stored bunches co-propagate around the machine with relatively large but decreasing horizontal separation (many millimeters) over many milliseconds before coalescing.

Due to very strong non-linear focussing fields, the transverse dynamic acceptance of the APS-U storage ring is expected to be quite small, making accumulation very challenging. Including in addition the presence of small horizontal apertures, bunch accumulation will not be possible in the planned machine. Instead, the injected bunch will be injected directly onto the nominal stored-beam trajectory, completely replacing the stored bunch. This “swap-out” mode involves fast kicker magnets to extract and dump the stored bunch in one sector while bringing the injected bunch from the injector machines onto the stored-beam axis in another.

References

- [1] U. Wienands et al. *Rf System Alternatives for the APS-U Storage Ring*. APS-U Document APSU-2.03-RPT-001. Argonne, IL: Argonne National Laboratory, Dec. 2016 (cit. on p. 3).

- [2] L. Emery and M. Borland. “Top-up Operation Experience at the Advanced Photon Source.” In: *Proc. of PAC 1999*. 1999, pp. 200–202. URL: <http://cern.ch/AccelConf/p99/PAPERS/TUCL4.PDF> (cit. on p. 4).

4-2 Beam Physics

This section describes the development and evaluation of the beam physics design, which is used as the basis for predicting the expected performance. The beam physics design has been iterated with the engineering designs for magnets and vacuum systems, described below, to provide assurance of feasibility.

The section begins with a description of the foundation of the beam physics analysis, namely, the lattice design. The nominal lattice design is a hybrid seven-bend achromat, patterned after the European Synchrotron Radiation Facility (ESRF) design [1], but with the addition of reverse-direction bending magnets [2, 3] (“reverse bends”) to further improve brightness. Subsequent subsections investigate the properties of this lattice in detail, beginning with an exploration of errors, correction schemes, and tolerances. These results are used to predict the likely performance of the lattice in terms of dynamic acceptance¹, local momentum acceptance, and injection efficiency. Next, the analysis turns to collective effects with a discussion of impedance, single-bunch intensity limits, and multibunch stability. Detailed simulations of the effectiveness of a passive bunch lengthening cavity are performed, including effects such as missing bunches and bunch population variation. Simulations of intrabeam scattering were also performed and are used to draw conclusions regarding the need for running with round beams. Intrabeam scattering and bunch lengthening results feed into computations of the Touschek lifetime, which again show the benefits of round beams. Because of the small aperture and relatively large emittance from the injector, it is necessary to use swap-out injection, which is described in the subsection on the injection process and systems. Finally, we discuss collimation and machine protection.

References

- [1] L. Farvacque et al. “A Low-emittance Lattice for the ESRF.” In: *Proc. of 2013 PAC*. 2013, p. 79 (cit. on p. 6).
- [2] J. Delahaye and J. P. Potier. “Reverse bending magnets in a combined-function lattice for the CLIC damping ring.” In: *Proc. PAC89*. 1990, pp. 1611–1613 (cit. on p. 6).
- [3] A. Streun. “The anti-bend cell for ultralow emittance storage ring lattices.” In: *NIM A 737* (2014), pp. 148–154 (cit. on p. 6).

¹ Dynamic acceptance includes nonlinear dynamics and physical apertures, in contrast to the dynamic aperture, which includes only nonlinear dynamics.

4-2.1 Lattice Design

The essential concept for the upgrade lattice is the well-known scaling of the natural emittance ϵ_0 with the number of dipoles N_d in the ring and the beam energy E [1]

$$\epsilon_0 \sim \frac{E^2}{N_d^3}. \quad (4.1)$$

This equation is strictly valid only for a fixed lattice structure, and implicitly assumes that the dipoles are separated by quadrupoles and that the required magnet strengths are feasible. The present APS 7 GeV storage ring has 40 sectors with two dipoles each. Although caution must be exercised in applying this equation for different lattice structures, increasing to seven dipoles per sector and reducing the energy to 6 GeV holds the promise of reducing the emittance by a factor of more than 40, from the present value of 3.1 nm to ~ 50 pm. What is important is not simply the number of separate dipoles, but the use of quadrupoles between the dipoles to create a strong-focusing lattice. This restrains the growth of the dispersion function and reduces the degree to which quantum excitation excites the beam emittance.

After extensive comparison with other options [2], the “hybrid” multi-bend achromat (HMBA) concept proposed by ESRF [3] was adopted. In addition, reverse-direction bending magnets [4, 5] were added, allowing reduction of the natural emittance to 42 pm [6] compared to 67 pm in the design without reverse bends [7]. Alternate lattice design work with larger emittance of 90 pm has also been performed to achieve better beam dynamics performance and to allow off-axis accumulation [8]. Even though the single-particle-dynamics performance is good, work on the off-axis accumulation lattice was discontinued due to lower brightness and the difficulty of accumulating high single-bunch charge, which is associated with collective effects. The lattice functions of the 42 pm reverse-bend lattice are shown in Fig. 4.2. In this concept, the dispersion is deliberately made large between the first and second, as well as between the sixth and seventh, dipoles, and all chromatic sextupoles are clustered in this dispersion bump region. As a result, the sextupoles can be longer (as there is more space) and are naturally weaker due to the larger magnitude of the dispersion. The magnitude of the dispersion is increased using a five-step longitudinal gradient in these dipoles, which also helps to minimize emittance increase. The additional “knobs” provided by the dipole field in the reverse bending magnets helps manipulate the dispersion independently of the beta functions, giving larger dispersion and better beta functions at the insertion devices. The betatron phase advance between the two dispersion bumps in each sector is set so as to cancel the leading non-chromatic effects of the sextupoles. Specifically, the phase advance in the horizontal plane is $\Delta\phi_x = 3\pi$, while in the vertical plane it is $\Delta\phi_y = \pi$. All of these factors have been found to be beneficial for the optimization of dynamic acceptance and beam lifetime in an APS-size ring, leading to a workable design with feasible sextupole strengths.

Since the early 1990s, it has been common to include both “chromatic” and “harmonic” ($\eta_x \approx 0$) sextupoles in storage ring light sources [9]. These have been found to provide significant flexibility in tuning the nonlinear dynamics of third-generation rings. Octupoles can also be used to similar effect, and are included for example in the ESRF MBA design [10]. In the APS-U design, thanks to the use of sophisticated tracking-based optimization and many independent families of chromatic sextupoles, these appear to have little benefit. In the current version of lattice, there is no space available for harmonic sextupoles. Nevertheless, the eight-pole correction magnets, of which there are four in each sector, have the potential to be powered as octupoles; this possibility will be explored

further in the future.

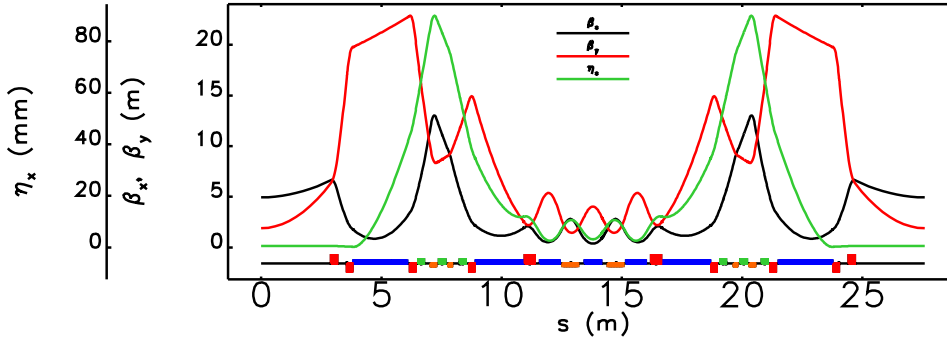


Figure 4.2. Hybrid 7BA lattice with reverse bends for the APS. The natural emittance is 42 pm. Blue blocks represent normal-direction dipoles, orange blocks represent reverse-direction dipoles, red blocks represent quadrupoles, and green blocks represent sextupoles.

4-2.1.1 Beam Energy

The natural choice of beam energy would be 7 GeV, since this would nominally preserve the high energy reach of the facility with existing insertion device (ID) designs and technology. However, two factors motivate reducing the energy to 6 GeV. The first, mentioned above, is the E^2 scaling of the natural emittance. However, a more compelling reason is the strength of the focusing quadrupoles and sextupole fields, which are challenging even for a 6 GeV ring of this circumference. This is true even though the bore radii of the magnets is greatly reduced from that of the present-day APS ring.

A more detailed examination [11] of the brightness performance of a H7BA lattice as a function of beam energy was undertaken, including the effects of intrabeam scattering. This shows that for large numbers of bunches and for photon energies below 20 keV, there is an advantage to lowering the beam energy to 5 GeV compared to 6 GeV. However, the performance above 20 keV is reduced by roughly the same factor, assuming superconducting undulators can be employed. Given this trade-off and the desire to run in a 48-bunch timing mode along with beam-lifetime challenges faced in such a lattice, it appears that 6 GeV is broadly optimal for a hard x-ray source. Even so, it should be kept in mind that slightly lowering the energy (e.g., to 5.5 GeV) may be advantageous for engineering reasons and would not have a severe impact on performance even for hard x-rays.

4-2.1.2 Constraints on the Lattice

The new lattice is constrained in a number of ways by the parameters of the existing facility. For example, the new design must have 40 straight sections, with 35 reserved for insertion device beamlines with 4.8-m-long IDs. Due to the effort involved in realigning beamlines, the ID straight sections must not move. The transverse offset of the IDs is given by the change in the radius R of the inscribed circle passing through the centers of the ID straight sections, which can be computed from the vector $(\Delta Z, \Delta X)$ between two successive straight sections using

$$\Delta R = \frac{1}{2 \sin \frac{\pi}{N}} \left[\left(\sqrt{\Delta Z^2 + \Delta X^2} \right)_{\text{mba}} - \left(\sqrt{\Delta Z^2 + \Delta X^2} \right)_{\text{now}} \right], \quad (4.2)$$

where $N = 40$ is the number of sectors. Unfortunately, constraining $\Delta R = 0$ implies transverse offsets of the bending magnet beamlines and a reduction in circumference.

The BM source points are, as now, at an angle of $9\pi/320$ from the upstream ID source point. However, compared to the present situation, the BM source points move upstream by 2.908 m with a transverse inboard offset of 39 mm. The present critical energy of the BM sources is 19.5 keV, resulting from a 7 GeV beam in a 0.6 T field. Delivering the same critical energy for a 6 GeV beam requires a field of 0.81 T, which, while not particularly high, presented significant difficulties for both the beam optics and the magnet design, given that the source dipole will have a transverse gradient. One possible solution for users requiring harder x-rays is to provide space for short wiggler magnets that may deliver photons to BM beamlines. Space was provided for 15-cm-long devices, should they be required. The impact of such devices will be described in section 4-2.3.

The circumference changes to 1103.61 m, compared to an original design circumference for the present ring of 1104 m and a present-day circumference of 1103.986 m (derived from the median rf frequency over one year). Hence, compared to present-day operations, the rf frequency increases by 342 ppm. For a given rf frequency change Δf_{rf} , the change in energy offset δ in the booster is given by

$$(\Delta\delta)_{\text{booster}} = -\frac{1}{\alpha_{c,\text{booster}}} \frac{\Delta f_{\text{rf}}}{f_{\text{rf}}}, \quad (4.3)$$

where $\alpha_{c,\text{booster}} = 9.7 \times 10^{-3}$ is the momentum compaction factor of the booster and f_{rf} is the nominal rf frequency. Because the Decker distortion [12] was applied to 35 of 40 sectors, the circumference of the storage ring already deviates from the design value, resulting in the booster being run with an energy deviation of $\sim -0.6\%$. This has the benefit of decreasing the transverse emittance from the booster. However, the additional 341 ppm change in the frequency would result in such a large change in the booster momentum offset that the beam would be unstable. Hence, either the booster circumference must be changed or it must have a separate rf source together with a timing system that can deliver the booster bunches to the desired storage ring bucket in spite of this. The latter choice is more cost-effective and provides additional potential flexibility, such as injecting on-momentum and extracting off-momentum (see Section 4-3.13.1.2).

4-2.1.3 Insertion Device Straights

The brightness of the photon beam created by an undulator depends on the emittance, beta functions, dispersion and energy spread of the electron beam, as well as the characteristics of the single-electron radiation from the undulator. For undulator radiation, an approximate description of the single-electron transverse distribution is given by [13]

$$\epsilon_r \approx \frac{\lambda}{2\pi} \quad (4.4)$$

and the beta function as

$$\beta_r \approx \frac{L_u}{\pi}, \quad (4.5)$$

where λ is the radiation wavelength and L_u is the length of the undulator.² The total phase space area of the photon beam is the convolution of the single-electron photon distribution with the

² $\epsilon_r \approx \frac{\lambda}{4\pi}$ is commonly used, but is not accurate when the undulator is detuned to maximize flux.

electron beam distribution. When the electron beam emittance is comparable to ϵ_r , brightness is sensitive to the electron beam beta function and is maximized when $\beta_x = \beta_y = \beta_r$. In the case of the APS with $L_u = 4.8$ m, this would require $\beta_{x,y} \approx 1.5$ m. In optimizing the linear optics, an approximate formula for the x-ray brightness at 20 keV was used, to prevent optimization of the emittance and mis-optimization of the beta functions at the expense of brightness. The formula is [14]

$$B \propto \frac{1}{\sqrt{\sigma_x^2 + \sigma_r^2} \sqrt{\sigma'_x{}^2 + \sigma'_r{}^2} \sqrt{\sigma_y^2 + \sigma_r^2} \sqrt{\sigma'_y{}^2 + \sigma'_r{}^2}} \frac{1}{\sqrt{4\sigma_\delta^2 + \left(\frac{0.4}{hN_u}\right)^2}}, \quad (4.6)$$

where $\sigma_{x,y} = \sqrt{\epsilon_{x,y}\beta_{x,y}}$ ($\sigma'_{x,y} = \sqrt{\epsilon_{x,y}/\beta_{x,y}}$) is the spatial (angular) size of the electron beam in the x or y plane, $\sigma_r = \sqrt{\epsilon_r\beta_r}$ is the intrinsic photon beam size, $\sigma'_r = \sqrt{\epsilon_r/\beta_r}$ is the intrinsic photon beam divergence, σ_δ is the rms fractional energy spread of the electron beam, h is the undulator harmonic, and N_u is the number of undulator periods.

A related issue is the question of the allowable vacuum chamber dimensions in the insertion device straights; this is related to details of the injection scheme. Most third-generation light sources operate in top-up mode [15], since this allows tuning for lowest emittance in spite of the deleterious effects that has on Touschek lifetime. A different operations concept known as swap-out [16, 17] gives an additional benefit, namely, the ability to tolerate very small injection aperture. This results from use of on-axis injection instead of the off-axis accumulation method used in all present-day rings. Like top-up, swap-out allows pushing the emittance of the ring to lower values, because it provides a way to deal with the concomitant reduction in dynamic acceptance.

Since the horizontal dynamic acceptance required for on-axis injection is quite small, there is no necessity to have large horizontal apertures in the ID straights. Similarly, we do not need large horizontal beta functions in order to make the real-space acceptance larger at the injection point. Hence, another significant benefit of swap-out is that it permits use of insertion devices not otherwise possible in a storage ring, such as helical devices and small-gap vertically deflecting devices.

4-2.1.4 Optimization of Nonlinear Dynamics

Nonlinear dynamics optimization was performed by using a tracking-based approach [18] that provides direct optimization of dynamic acceptance and Touschek lifetime (via local momentum acceptance) using a multi-objective genetic algorithm (MOGA) similar to those described in [19, 20]. Prior to applying MOGA, a wide-ranging tune scan was performed, similar to that described in [21]. The tune scan includes evaluation of dynamic acceptance, Touschek lifetime from local momentum acceptance, emittance, and beta functions at the IDs, among other quantities of importance. A non-dominated sort [19] identified three promising initial working points (ν_x, ν_y) , namely (95.10, 36.15), (95.15, 34.20), and (94.10, 35.15). Of these, the first is the best-developed and is presented in more detail.

In this instance, the MOGA algorithm varied two types of quantities:

- *Sextupole strengths*: The basic HMBA configuration has six sextupoles arranged in an SD-SF-SD fashion (where SD and SF stand for defocusing and focusing sextupole, respectively) within each high-dispersion area. In the simplest concept, the strengths of these sextupoles

are entirely determined by the desired chromaticity after correction. To provide additional degrees of freedom, the six sextupoles within a sector can be allowed to vary independently, which provides some measure of compensation for the fact that the scheme for cancellation of geometric aberrations is necessarily imperfect, given that the sextupoles are both thick and interleaved. Further degrees of freedom are afforded by organizing sextupole strengths with a 20-fold translational symmetry, which gives 12 sextupole “knobs.” Given that two of these knobs are constrained by the desired corrected chromaticity, up to 10 are left free for MOGA to manipulate. In some cases, simpler configurations with more symmetry are used, particularly in the early stages of an optimization.

- *Linear optics parameters:* This took one of two forms: optics targets and direct gradient variation, with the former being more commonly used. The choice of tunes is well known to have an effect on nonlinear dynamics, as it can change the distance to destructive resonances. Maximum values of beta functions, values of beta functions at the IDs, the value of dispersion in the high-dispersion area, the value of natural chromaticity, and the phase advance between the high-dispersion sections are other relevant parameters. In a typical optimization involving optics targets, most of these are placed under the influence of the MOGA algorithm, although it must be appreciated that these can only be targets, since any particular set of values may be difficult or impossible to achieve simultaneously. Direct gradient variation was found to be more productive in the later stages of refining a configuration.

A single function evaluation for MOGA typically consists of four steps, run in sequence on (typically) 32 cores using the programs `elegant` [22] and `Pelegant` [23].

1. Optional optics matching to obtain the specific linear optics targets. In addition to the targets varied by MOGA, other constraints are considered non-negotiable, such as basic geometry requirements, emittance targets, and so on, some of which are described above. The optics matching is performed with the parallel hybrid simplex optimizer [24] in `Pelegant`. Chromaticity correction is included at this stage, since linear optics has an effect on both the natural chromaticity and the effectiveness of correction sextupoles. Magnet lengths and strengths were constrained by engineering design curves, while spaces between magnets were constrained by vacuum and mechanical considerations. The five segments of the longitudinal gradient dipoles were allowed to vary in length and angle, subject to the requirement of increasing (decreasing) field and an engineering-based limit of 5.0 for the ratio of the highest to lowest field.
2. Parallel tracking is employed to determine the momentum-dependent tunes. Analysis of the momentum-dependent tunes is used to create a set of penalty function values that help delay crossing of integer resonances and ensure “rapid” crossing of half-integer resonances (or avoidance of these resonances).
3. Generation of errors for quadrupoles and sextupoles, and computation of perturbed lattice functions. As described in [18], errors are chosen to emulate the perturbations present in a reasonably well-corrected lattice.
4. Parallel tracking with said errors to determine the dynamic acceptance (DA). Analysis of the DA is used to create penalty function values that favor a large DA with a smooth boundary.
5. Parallel tracking with said errors to determine the local momentum acceptance (LMA) [25, 26] at strategic locations in the first two sectors. 20 locations were used per sector, with one location after each dipole and each sextupole, plus locations in the straight sections; these locations cover regions both of low LMA and high scattering rate. This is used for computation

of the Touschek lifetime, which gives another penalty function.

All DA and LMA tracking was performed in six dimensions, including a thin-lens rf cavity and radiation damping. The rf cavity voltage was set to give a $\pm 6\%$ bucket height. Tracking was performed for 800 turns, sufficient for overlapping of the amplitudes of adjacent probe particles in the aperture search algorithms. Physical apertures were included as well. The working apertures were a 10-mm radius round aperture in the arcs, a 4-mm radius aperture in half the IDs, and a $n = 6$, $a = 3$, $b = 3$, superelliptical aperture in the other half of the IDs. These small apertures were chosen based on previous experience with the 67-pm lattice, for which they had minimal impact.

Following optimization, solutions on the Pareto-optimal front are examined in detail to choose those that best balance the desire for large DA, smooth DA, long Touschek lifetime, and a desirable momentum-dependent tune footprint. One or more solutions are then subjected to evaluation with a large number of error ensembles, as described in section 4-2.3.

One requirement is the desire for a chromaticity of +5 in both planes, which is needed in order to ensure the ability to store over 4 mA in a single bunch. This is described in section 4-2.4. For the 67-pm lattice, it was found that chromaticities between about 4 and 7 were favorable, with lower chromaticities having issues with Touschek lifetime. It remains to be determined if a similar result will hold for the lattice with reverse bends, but it seems reasonable to assume it will.

4-2.1.5 Characterization of Nonlinear Dynamics

Figures 4.3, 4.4, and 4.5 show, respectively, the DA, LMA, and momentum tune footprint for the chosen Pareto-optimal solution. Note that the algorithm has moved both fractional tunes to 0.1, which is acceptable since operation on the coupling resonance for $\epsilon_x = \epsilon_y$ is desirable. Overall, the DA has a somewhat rectangular appearance, which is desirable. The DA is skewed slightly to the positive x side and has a total horizontal extent of about 6 mm. For comparison, the horizontal rms beam size of the incoming booster beam is about 0.65 mm (assuming $\epsilon_x = 60$ nm), so the aperture is in excess of $\pm 4\sigma_x$. The vertical DA is in excess of ± 1.4 mm, which is large compared to the assumed vertical beam size from the booster of 0.2 mm rms. Hence, the DA appears more than adequate for high-efficiency injection, which is confirmed by simulations of injection efficiency as described in section 4-2.10. The LMA is in excess of $\pm 2.5\%$, about the same as typically obtained in the APS today. Outside the dispersive regions, it is in excess of $\pm 5\%$. Hence, a reasonably long Touschek lifetime can be expected, as explored in more detail in section 4-2.3.

Figure 4.5 shows the tunes as a function of momentum offset. The momentum tune footprint crosses the half integer in the horizontal plane at about $\delta = -3.5\%$, while the vertical tune avoids this resonance over the range $\pm 4.5\%$. The horizontal tune also crosses the integer resonance for $\delta = -4.3\%$. Comparison of the tune footprint with the LMA indicates that major resonances can apparently be crossed with impunity. However, as seen below, these resonances have a greater impact during ensemble evaluation, when additional error seeds as well as higher order multipoles are added. Although it is possible to reduce the momentum tune footprint, this comes at the expense of DA, which impacts the momentum acceptance in the high-dispersion regions. This in turn reduces the Touschek lifetime.

It is often considered informative to examine the nonlinear dynamics behavior in the absence of errors

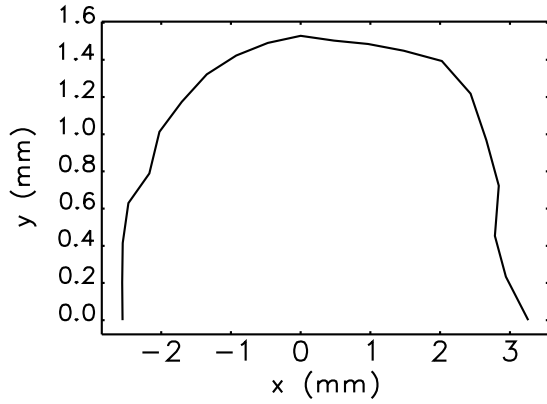


Figure 4.3. Dynamic acceptance with errors for selected Pareto-optimal solution from MOGA.

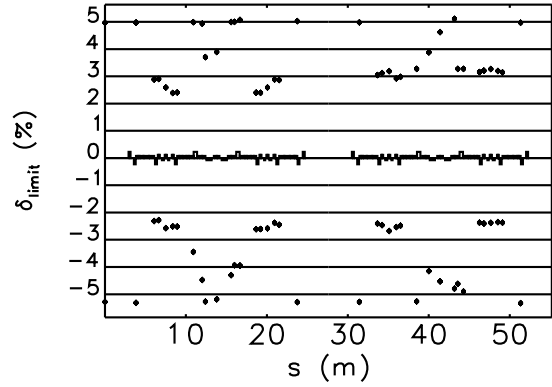


Figure 4.4. Local momentum acceptance with errors for selected Pareto-optimal solution from MOGA.

in order to gain some insight into the lattice. Toward this end, frequency maps were computed for both the (x, y) and (x, δ) planes. These have a bearing on the dynamic acceptance and the momentum acceptance.

Figures 4.6 and 4.7 show the frequency map for the transverse plane with no errors. Although the tune footprint is not small, there are no apparent strong low-order resonances. The most obvious resonance is $4\nu_y + \nu_x$, which is driven by decapole.

Figure 4.8 shows the frequency map for the horizontal and longitudinal planes, excluding synchrotron motion. The half-integer tune is visible as a gap in the color map for positive momentum deviation. In this simulation without errors, this gap indicates an inability to determine the tunes, rather than particle loss.

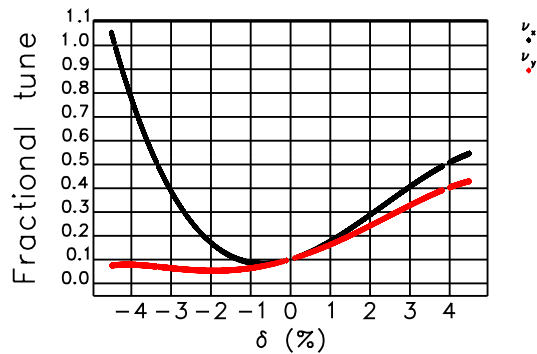


Figure 4.5. Chromatic tune dependence for the nominal lattice with no errors.

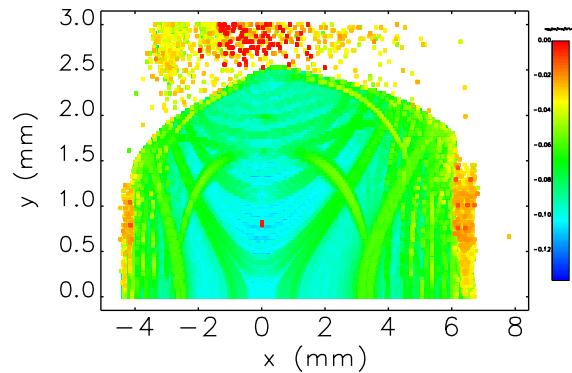


Figure 4.6. Transverse frequency map color-coded by diffusion rate for the nominal lattice with no errors.

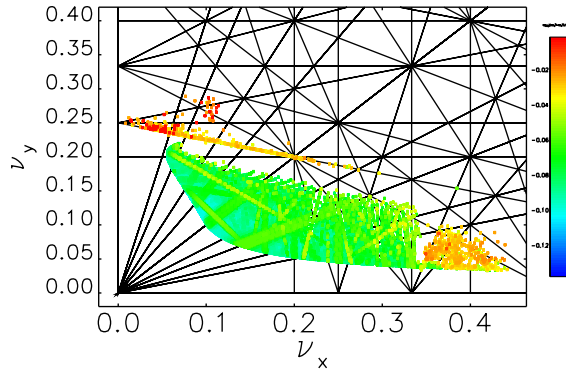


Figure 4.7. Tune-plane frequency map color-coded by diffusion rate for the nominal lattice with no errors.

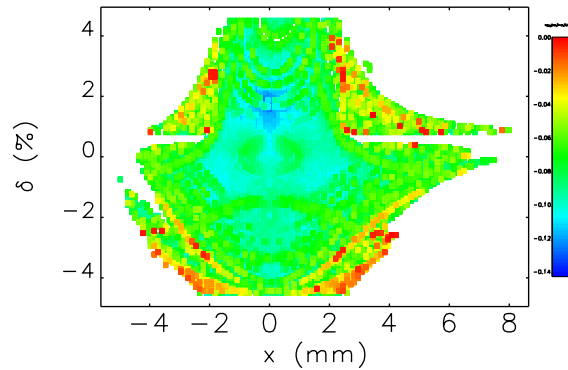


Figure 4.8. Horizontal-longitudinal frequency map color-coded by diffusion rate for the nominal lattice with no errors.

4-2.1.6 Summary of Lattice and Magnet Properties

In this section, we provide a basic summary of the properties of the optimized lattice. The lattice functions are shown in Fig. 4.2. Properties of the lattice are listed in Table 4.3. Of note are the high values of the tunes in both planes; compared to the present-day APS, the horizontal tune is 2.6 times higher, while the vertical tune is 1.9 times higher. The natural chromaticities are also significantly higher, increasing 50% for the horizontal plane and a factor of 2.5 in the vertical plane.

Magnet data is listed in Tables 4.4 through 4.6, where magnets are specified in terms of their ideal hard-edge length and strength, as used in the simulations. However, in respecting the mechanical limits on distance between magnets, the magnet length is interpreted as the insertion length, which is necessarily longer than the iron length or equivalent hard-edge length. In reality, the iron yokes and poles will be shorter than listed, and the field strength will be increased to obtain the same integrated strength for a magnet that has an *insertion* length equal to the length given in the appropriate table. This fact is taken into account in the optimization, by constraining the maximum integrated strength as a function of the simulated magnet length. For quadrupoles, the strength was limited to no more than 90% of the engineering maximum, while for sextupoles the limit was 80% of the engineering maximum. The assumed overhead is to allow for lattice flexibility and is, at this point, based on experience gained in developing many lattices.

The reverse-bending magnets Q4 and Q5 have relatively weak dipole fields, which might seem ineffective. However, these fields are very effective in adjusting the damping partition, since the dispersion is high at those locations. Further, they allow raising the maximum dispersion without harming the emittance by providing a means of bringing the dispersion back down in the M2 magnets. It is possible to move all of the reverse bending to Q4, but at the cost of making the magnet significantly more challenging; this is under study. Without reverse bending in this area, the minimum achievable emittance is 58 pm.

As mentioned above and exhibited in Table 4.4, the M1 and M2 longitudinal gradient dipoles were optimized as five nominally independent segments. The tendency is for the first segment of M1, labeled M1.1 in the table, to become very short and strong, which helps to increase the horizontal

dispersion function in the sextupoles and also reduce the emittance. This was restrained by requiring a length of at least 10 cm for the M1.1 segment and limiting the ratio of maximum-to-minimum field strength within the M1 to 5:1. Similar constraints were placed on the M2. The M3, Q8, M4 magnets require a combination of a moderately high dipole field with a significant transverse gradient, which is a challenging combination. The difficulty of obtaining a high dipole field in these magnets motivated the inclusion of an optional three-pole wiggler as a possible source for bending magnet beamlines.

As seen in Table 4.5, there are three quadrupole magnet lengths. The Q7 magnets require significantly greater length than the others in order to reduce the magnitudes of the magnetic field gradients.

Table 4.6 shows the parameters of the sextupole magnets, where the strength is the highest over a set of possible nonlinear dynamics solutions. The solutions were developed with several alternate methods [27] in addition to the one described above (which was judged to give the best overall result). The sextupoles come in two lengths, but the spread is relatively small and may be unnecessary. The S2 magnets are significantly stronger largely by virtue of being fewer in number. There is also some variation in the strengths of nominally equivalent sextupoles, which appears to be important for obtaining good Touschek lifetime. Previous iterations of the lattice have shown even larger variation, which motivates having a relatively large overhead margin (20%) for these magnets.

References

- [1] J. Murphy. *Synchrotron Light Source Data Book*. Tech. rep. BNL-42333. BNL, Jan. 1989 (cit. on p. 7).
- [2] Y.-P. Sun and M. Borland. “Alternate Lattice Design for Advanced Photon Source Multi-Bend Achromat Upgrade.” In: *Proc. IPAC15*. TUPJE071 (cit. on p. 7).
- [3] L. Farvacque et al. “A Low-emittance Lattice for the ESRF.” In: *Proc. of 2013 PAC*. 2013, p. 79 (cit. on p. 7).
- [4] J. Delahaye and J. P. Potier. “Reverse bending magnets in a combined-function lattice for the CLIC damping ring.” In: *Proc. PAC89*. 1990, pp. 1611–1613 (cit. on p. 7).
- [5] A. Streun. “The anti-bend cell for ultralow emittance storage ring lattices.” In: *NIM A 737* (2014), pp. 148–154 (cit. on p. 7).
- [6] M. Borland et al. “Lower Emittance Lattice for the Advanced Photon Source Upgrade Using Reverse Bending Magnets.” In: *these proceedings*. WEPOB01 (cit. on p. 7).
- [7] M. Borland et al. “Hybrid Seven-Bend-Achromat Lattice for the Advanced Photon Source Upgrade.” In: *Proc. IPAC15*. 2015, pp. 1776–1779 (cit. on p. 7).
- [8] Y.-P. Sun et al. “APS-U Lattice Design for Off-Axis Accumulation.” In: *Proc. NAPAC16*. WEPOB14 (cit. on p. 7).
- [9] E. A. Crosbie. “Improvement of the Dynamic Aperture in Chasman Green Lattice Design Light Source Storage Rings.” In: *PAC87*. 1987, pp. 443–445 (cit. on p. 7).
- [10] N. Carmignani et al. “Linear and Nonlinear Optimizations for the ESRF Upgrade Lattice.” In: *IPAC15*. 2015, pp. 1422–1425 (cit. on p. 7).

Table 4.3. Lattice parameters

Tunes and Chromaticities		
ν_x	95.101	
ν_y	36.101	
ν_x/N_s	2.3775	per sector
ν_y/N_s	0.9025	per sector
ξ_x	5.02	
ξ_y	5.02	
Natural ξ_x	-130.83	
Natural ξ_y	-122.01	
Lattice functions		
Maximum β_x	13.02	m
Maximum β_y	22.87	m
Maximum η_x	0.090	m
Average β_x	3.68	m
Average β_y	9.46	m
Average η_x	0.034	m
Radiation-integral-related quantities at 6 GeV		
Natural emittance	42.26	pm
Energy spread	0.127	%
Horizontal damping time	7.32	ms
Vertical damping time	16.11	ms
Longitudinal damping time	20.13	ms
Energy loss per turn	2.74	MeV
ID Straight Sections		
β_x	4.94	m
β_y	1.89	m
η_x	0.57	mm
$\epsilon_{x,eff}$	42.3	pm
Miscellaneous parameters		
Momentum compaction	3.96×10^{-5}	
Circumference	1103.61	
$\Delta f_{rf}/f_{rf}$	3.42×10^{-4}	
Damping partition J_x	2.20	
Damping partition J_y	1.00	
Damping partition J_s	0.80	

- [11] M. Borland et al. “Hybrid Seven-Bend-Achromat Lattice for the Advanced Photon Source Upgrade.” In: *Proc. IPAC15*. 2015, pp. 1776–1779 (cit. on p. 8).
- [12] G. Decker and O. Singh. “Method for Reducing X-ray Background Signals from Insertion Device X-ray Beam Position Monitors.” In: *Phys. Rev. ST Accel. Beams* 2 (11) (1999), p. 112801. URL: <http://prst-ab.aps.org/pdf/PRSTAB/v2/i11/e112801> (cit. on p. 9).
- [13] P. Elleaume. “Undulator radiation.” In: *Wigglers, Undulators, and Their Applications*. London: Taylor and Francis, 2003, p. 69 (cit. on p. 9).
- [14] S. Benson et al. “X-ray Sources by Energy Recovered Linacs and Their Needed R&D.” In: *NIMA* 637 (2010), pp. 1–11 (cit. on p. 10).
- [15] L. Emery and M. Borland. “Top-up Operation Experience at the Advanced Photon Source.” In: *Proc. of PAC 1999*. 1999, pp. 200–202. URL: <http://cern.ch/AccelConf/p99/PAPERS/TUCL4.PDF> (cit. on p. 10).

Table 4.4. Bending magnet parameters. Reverse-direction bending magnets have names beginning with “Q,” since these originated as quadrupoles in the previous lattice.

Name	Length m	Angle deg	B_0 T	B' T/m	E_c keV	$P_{d,integ}$ W/mrad	P_d W/mrad ²	Count
M1 (x80)								
M1.1	0.192	0.357	-0.650	-0.000	15.6	118.5	913.4	80
M1.2	0.233	0.267	-0.400	-0.000	9.6	72.9	561.6	80
M1.3	0.493	0.381	-0.270	-0.000	6.5	49.2	379.4	80
M1.4	0.671	0.375	-0.195	-0.000	4.7	35.6	274.2	80
M1.5	0.636	0.257	-0.141	-0.000	3.4	25.8	198.5	80
M2 (x80)								
M2.1	0.292	0.135	-0.161	-0.000	3.9	29.4	226.6	80
M2.2	0.359	0.187	-0.182	-0.000	4.4	33.2	255.6	80
M2.3	0.487	0.297	-0.213	-0.000	5.1	38.8	299.0	80
M2.4	0.308	0.222	-0.252	-0.000	6.0	45.9	353.6	80
M2.5	0.540	0.495	-0.320	-0.000	7.7	58.4	450.1	80
M3 (x80)								
M3.1	0.410	0.718	-0.612	42.071	14.7	111.6	860.0	80
M3.2	0.410	0.718	-0.612	42.071	14.7	111.6	860.0	80
Q4 (x80)								
Q4	0.244	-0.098	0.140	-68.981	3.4	25.5	196.7	80
Q5 (x80)								
Q5	0.150	-0.066	0.154	-31.590	3.7	28.2	217.0	80
Q8 (x80)								
Q8	0.646	-0.307	0.166	-73.672	4.0	30.3	233.2	80
M4 (x40)								
M4.1	0.350	0.562	-0.561	43.840	13.4	102.4	788.7	40
M4.2	0.350	0.562	-0.561	43.840	13.4	102.4	788.7	40

- [16] R. Abela et al. “Design Considerations for a Swiss Light Source (SLS).” In: *Proc. EPAC 1992*. 1992, p. 486 (cit. on p. 10).
- [17] L. Emery and M. Borland. “Possible Long-Term Improvements to the Advanced Photon Source.” In: *Proc. of PAC 2003*. 2003, pp. 256–258. URL: <http://cern.ch/AccelConf/p03/PAPERS/TOPA014.PDF> (cit. on p. 10).
- [18] M. Borland et al. *Multi-objective Direct Optimization of Dynamic Acceptance and Lifetime for Potential Upgrades of the Advanced Photon Source*. Tech. rep. ANL/APS/LS-319. APS, 2010 (cit. on pp. 10, 11).
- [19] K. Deb et al. In: *IEEE TEC* 6 (2002), p. 182 (cit. on p. 10).
- [20] I. Bazarov and C. Sinclair. “Multivariate optimization of a high brightness dc gun photoinjector.” In: *Phys. Rev. ST Accel. Beams* 8 (2005), p. 034202 (cit. on p. 10).
- [21] M. Borland, V. Sajaev, and Y.-P. Sun. “A Seven-Bend-Achromat Lattice as a Potential Upgrade for the Advanced Photon Source.” In: *Proc. of PAC 2013*. 2013 (cit. on p. 10).
- [22] M. Borland. *elegant: A Flexible SDDS-Compliant Code for Accelerator Simulation*. Tech. rep. ANL/APS LS-287. Advanced Photon Source, Sept. 2000. URL: <http://www.aps.anl.gov/Science/Publications/lsnotes/ls287.pdf> (cit. on pp. 11, 21, 37).

Table 4.5. Quadrupole data

Element Name	Length m	K_1 $1/m^2$	B' T/m	$B'L$ T	Count
Q1	0.250	3.3	-66.3	-16.6	80
Q2	0.225	-2.8	56.2	12.6	80
Q3	0.225	-2.3	45.8	10.3	80
Q6	0.225	-2.5	49.3	11.1	80
Q7	0.424	3.7	-74.5	-31.6	80

Table 4.6. Sextupole data, given as highest strength over a set of optimization methods.

Element Name	Length m	K_2 $1/m^3$	B'' T/m^2	$B''L$ T/m	Count
S01A:S1	0.230	-144.7	2896.2	664.8	20
S01A:S2	0.260	213.6	-4274.1	-1110.4	20
S01A:S3	0.230	-137.5	2752.3	631.8	20
S01B:S1	0.230	-155.6	3115.0	715.0	20
S01B:S2	0.260	240.5	-4812.5	-1250.3	20
S01B:S3	0.230	-137.5	2752.3	631.8	20
S02A:S1	0.230	-166.5	3331.9	764.8	20
S02A:S2	0.260	238.5	-4773.8	-1240.2	20
S02A:S3	0.230	-141.2	2825.1	648.5	20
S02B:S1	0.230	-159.8	3198.9	734.3	20
S02B:S2	0.260	238.5	-4773.8	-1240.2	20
S02B:S3	0.230	-141.2	2825.1	648.5	20

- [23] Y. Wang and M. Borland. “Pelegant: A Parallel Accelerator Simulation Code for Electron Generation and Tracking.” In: *AIP Conf. Proc.* 877 (2006), p. 241 (cit. on p. 11).
- [24] Y. Wang, M. Borland, and V. Sajaev. “Exploration of Parallel Optimization Techniques for Accelerator Design.” In: *Proc. of PAC 2011*. 2011, pp. 787–789. URL: <http://accelconf.web.cern.ch/AccelConf/PAC2011/papers/tuodn2.pdf> (cit. on p. 11).
- [25] C. Steier et al. “Measuring and optimizing the momentum aperture in a particle accelerator.” In: *Phys. Rev. E* 65 (5 May 2002), p. 056506. DOI: 10.1103/PhysRevE.65.056506. URL: <http://link.aps.org/doi/10.1103/PhysRevE.65.056506> (cit. on p. 11).
- [26] M. Belgroune et al. In: *Proc. of PAC 2003*. 2003, pp. 896–898 (cit. on p. 11).
- [27] C. Yao X. Sun. “Simulation Studies of a Prototype Stripline Kicker for the Aps-Mba Upgrade.” In: *NAPAC16*. WEPOB14. 2016 (cit. on p. 15).
- [28] V. Sajaev. *Private Communication*. 2014 (cit. on pp. 21, 22, 24).
- [29] V. Sajaev. *Power supply and vibration tolerance calculations for 41-pm reverse-bend lattice*. Tech. rep. AOP-TN-2017-019. APS, Apr. 2017 (cit. on pp. 22, 28, 33).
- [30] V. Sajaev. *Tolerances on longitudinal alignment of dipoles and their field integrals*. Tech. rep. AOP-TN-2017-046. APS, Sept. 2017 (cit. on p. 23).
- [31] V. Sajaev. *Private Communication*. 2013 (cit. on pp. 24, 25).

- [32] V. Shiltsev et al. “Ground Motion for Fermilab Future Collider Projects.” In: *Proc. of PAC 1999*. 1999, p. 1387 (cit. on p. 28).
- [33] S. Kim. Private communication. 2013 (cit. on p. 29).
- [34] V. Sajaev. *Orbit motion amplification factors as a function of the ground vibration correlation length*. Tech. rep. AOP-TN-2015-010. APS, Apr. 2015 (cit. on p. 30).
- [35] A. Xiao and L. Emery. *APS-U Planar and Revolver Undulator Field Quality Specifications*. Nov. 2012 (cit. on p. 30).
- [36] V. Sajaev. *Simulation of energy errors due to dipole errors*. Tech. rep. AOP-TN-2014-019. APS, Apr. 2014 (cit. on p. 35).
- [37] V. Sajaev. *Tolerances on power supply drift and ripple*. Tech. rep. AOP-TN-2016-026. APS, May 2016 (cit. on pp. 35, 36).
- [38] V. Sajaev. *BPM drift simulation*. Tech. rep. AOP-TN-2017-011. APS, Feb. 2017 (cit. on p. 35).
- [39] V. Sajaev and L. Emery. “Determination and Correction of the Linear Lattice of the APS Storage Ring.” In: *Proc. of EPAC 2002*. 2002, pp. 742–744 (cit. on p. 38).
- [40] J. Safranek. “Experimental Determination of Storage Ring Optics Using Orbit Response Measurements.” In: *NIM A 388* (1997) (cit. on p. 38).

4-2.2 Tolerances and Correction Schemes

Analysis of susceptibility to various errors is an important part of any storage ring design. There are two main types of errors that can affect a storage ring: magnet and power supply errors and magnet alignment errors. (Imperfections in magnet fields are discussed separately, in section 4-2.3.) These errors can be static, or they can change in time. Power supply and magnet errors can be random, and they can also have a systematic component. The effects of some of these errors can be corrected using beam-based measurements, both offline and in real time. This section presents tolerances for different types of errors based on analysis and modeling of the effects of errors, along with simulation of correction schemes.

4-2.2.1 Static Random Errors

Static errors are those that do not change in time or that change on very long time scales. Examples are power supply calibration errors, magnetic measurement errors, alignment errors, etc. The effect of these errors in most cases can be measured using beam-based techniques and can be subsequently corrected. Two types of static errors may be distinguished: initial errors and reproducibility errors. Initial errors are the errors expected during the commissioning of the machine, while reproducibility errors are the errors expected after turning power supplies off and then back on — for example, after shutdowns. Table 4.7 gives limits for various machine parameters and lists the types of errors responsible for deviation from ideal performance. Values for initial errors are chosen so as to provide for reasonably quick commissioning, while reproducibility goals should ensure that the storage ring can be operated without major corrections after being turned off and then back on. Tolerances for individual magnets and other systems are determined from these goals.

Table 4.7. Goals for initial errors and reproducibility in high-level machine parameters driven by static errors in subsystems

	Initial error	Reproducibility	Magnets responsible (Initial errors)	Magnets responsible (Reproducibility)
Energy	10^{-3}	10^{-4}	Dipoles	Dipoles
Orbit	2 mm	0.1 mm	Dipoles, displaced quads	Dipoles, correctors
Betatron tune	0.1	0.01	Dipoles, quads, and displaced sextupoles	Dipoles, quads
Beta functions	20%	2%	Quadrupoles, displaced sextupoles	Quadrupoles
Chromaticity	1 unit	0.1 unit	Sextupoles	Sextupoles
Nonlinear effects	TBD	TBD	Sextupoles	Sextupoles

Energy Errors

When a dipole power supply changes current, the energy of the electron beam also changes, because regardless of the dipole current, the total bending angle of the storage ring will always be 2π . In general, a dipole error also causes an orbit distortion, which results in additional bending

angle contributions from quadrupoles and sextupoles. The analysis can be simplified by assuming that the contribution from quadrupoles averages to zero (quadrupoles have positive and negative contributions), while the contribution from sextupoles can be neglected. Simulations can be used subsequently to check and refine the conclusions. The integral of the magnetic field over all dipoles divided by beam rigidity $B\rho$ is always equal to 2π :

$$\frac{1}{B\rho_0} \int B ds = 2\pi. \quad (4.7)$$

When a dipole field changes by ΔB , the energy E of the beam changes, but the total angle still stays 2π :

$$\frac{1}{B\rho_0(1 + \frac{\Delta E}{E})} \left(\int B ds + \Delta BL \right) = 2\pi, \quad (4.8)$$

where L is the length of the dipole where the field was changed. From this, the energy error due to the angle change caused by a single dipole power supply error ΔI can be simply written as

$$\frac{\Delta E}{E} = \frac{\Delta\alpha}{2\pi} = \frac{\alpha}{2\pi} \cdot \frac{\Delta\alpha}{\alpha} = \frac{\alpha}{2\pi} \cdot \frac{\Delta I}{I}, \quad (4.9)$$

where α is the nominal bending angle of the dipole(s) powered by that power supply, and $\Delta\alpha = \Delta BL/B\rho_0$. When there are several types of dipoles present in the ring, this simple expression can be extended to describe the probability distribution of the energy errors:

$$\left(\frac{\Delta E}{E} \right)_{\text{rms}}^2 = \sum_{\text{all dip PS}} \left(\frac{\alpha_i}{2\pi} \right)^2 \left(\frac{\Delta I}{I} \right)_{\text{rms}_i}^2, \quad (4.10)$$

where summation is done over all dipole power supplies, and α_i denotes the bending angle powered by a single power supply (for example, if one supply powers several dipoles, α is the combined angle of these dipoles). Equation 4.9 indicates that connecting dipoles in series instead of powering them separately increases energy sensitivity to the dipole power supply errors: if N dipoles each with bending angle $\tilde{\alpha}$ are powered separately, their combined effect is proportional to $\sqrt{\sum \tilde{\alpha}^2} = \sqrt{N} |\tilde{\alpha}|$, while if they are all connected to a single power supply, their total angle is $\alpha = N\tilde{\alpha}$, and the energy effect is proportional to $\alpha = N |\tilde{\alpha}|$.

The expression 4.10, of course, is a simplification. In reality, strong sextupoles contribute to the effect, orbit correction introduces additional bending angles, path-length constraints are introduced by the rf system, and so on. It is difficult to consider every effect, but it is easy to calculate the total effect in `elegant` [22]: when the closed orbit is calculated with fixed path length in `elegant`, energy error is one of the outputs of the calculations. To calculate the sensitivity of the energy error to dipole strength errors, 200 sets of dipole errors were generated, then the orbit was calculated and corrected [28]. Two orbit correction configurations were tested: one with all available correctors (16 per sector) and another with 6 correctors per sector. For this simulation, fractional dipole errors of 10^{-5} rms were used, M1 and M2 dipoles were connected in series, and no magnet misalignment was included. The results for the final beam equilibrium energy error are shown in Fig. 4.9. The distribution width varies by about a factor of two, so the energy error depends little on whether orbit correction is used or not, or on the orbit correction configuration itself. Figure 4.10 shows the effect of connecting all M1 and M2 dipoles in series. As expected, the amplifying effect of powering

dipoles in series on the energy error is significant, however, this is chosen as a cost-saving step for these dipoles.

The tolerances were calculated based on the simulations described above, with M1 and M2 connected as two series groups. The allowable initial dipole errors based on the energy error requirement are $2 \cdot 10^{-3}$ while the reproducibility requirement is $2 \cdot 10^{-4}$. The details of calculations are given in [28].

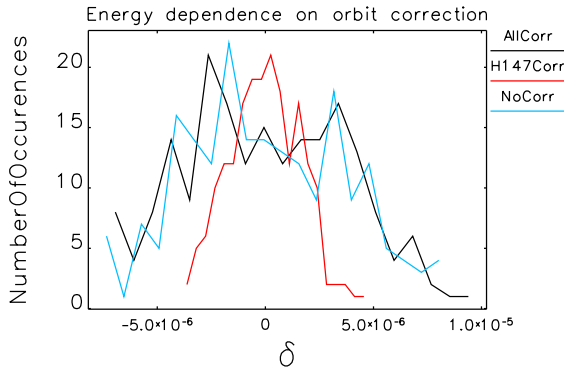


Figure 4.9. Distribution of the equilibrium beam energy errors due to dipole errors for two different orbit correction configurations (black – all correctors, red – six correctors per sector) and without orbit correction (blue).

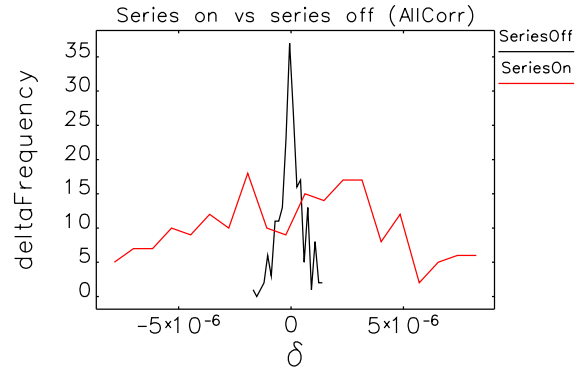


Figure 4.10. Comparison of energy errors for the cases when M1 and M2 dipoles powered in series or separately.

Orbit Errors

Initial orbit distortion is generated by dipole strength and longitudinal alignment errors and quadrupole transverse misalignments, while orbit errors after a shutdown are produced by reproducibility errors in dipole and corrector magnet power supplies. The orbit error due to a magnet error can be characterized by using the magnet amplification factor F , which gives the ratio of the orbit to the magnet strength error or displacement. The amplification factor depends on the lattice function at the location of the magnet and the betatron phase advance between the observation point and the magnet. Dipole errors, power supply errors, and quadrupole displacements are independent; therefore, the expected orbit error distribution at one location can be calculated as a sum of independent noise sources. Summation over similar types of magnets can be performed by assuming that they all have the same rms error [29]. Then, the orbit error distribution can be characterized in simplified form as

$$\begin{aligned} \Delta X_{\text{rms}}^2 = & \beta \sum_{\text{dip types}} F_{\text{dip_strength}_i}^2 \left(\frac{\Delta \alpha}{\alpha} \right)_{\text{rms}_i}^2 + \beta \sum_{\text{dip types}} F_{\text{dip_z}_i}^2 z_{\text{rms}_i}^2 \\ & + \beta \sum_{\text{quad types}} F_{\text{quad}_i}^2 u_{\text{rms}_i}^2 + \beta \sum_{\text{cor types}} F_{\text{cor}_i}^2 (\Delta \theta)_{\text{rms}_i}^2, \end{aligned} \quad (4.11)$$

where β is the beta function at the observation point, α and θ are dipole and corrector bending angles, z is dipole longitudinal misalignment, and u is quadrupole transverse misalignment. The summations are performed over different types of magnets. Quadrupole displacement should be

split into two components: girder³ displacement and misalignment of individual quadrupoles on the girders; this detail is neglected in the expression above in the interest of simplicity of presentation. For the initial orbit errors, there would be no contribution from the correctors. The orbit-related requirements in Table 4.7 were chosen to ensure that at 3σ rms the orbit still fits inside the vacuum chamber. When translated into quadrupole alignment tolerances via simulation of the amplification factors, this requirement turns out to be too demanding, as it would require girders and individual quadrupoles on girders to have rms displacements of 30 and 10 μm , respectively. This is considered unrealistic, so single-turn trajectory correction will be used to obtain the first closed orbit. This approach allows relaxing the alignment requirements. More detail is available in section 4-2.2.4.

Despite a large effect from quadrupole misalignments, it is desirable to keep dipole induced initial orbit errors small. This reduces the number of sources that must be corrected.

There are four types of dipole errors that need to be considered: dipole power supply errors, first and second field integral errors, and longitudinal misalignment. Dipole power supply errors and first field integral errors contribute in the same way, since both are “strength” errors. The longitudinal-gradient bending magnets have complicated design and can also have errors of the second field integral, which can be expressed as an equivalent longitudinal displacement of the dipole [30]. Hence, longitudinal misalignment and second field integral errors are collected under the name “longitudinal misalignment,” for convenience.

The total relative dipole strength error of 10^{-3} was already used in many simulations, and since it gives approximately 1 mm rms orbit error, this number will be used for the requirement calculations. Since the total dipole error has two independent contributions — power supply errors and first field integral errors — each contribution needs to be limited to $0.7 \cdot 10^{-3}$ rms. For convenience, the requirement for the relative first field integral error will be modified to a peak-to-peak requirement of $\pm 1 \cdot 10^{-3}$ with approximately a factor of 1.5 safety margin.

The combined effect of longitudinal misalignment and second field integral errors will also be limited to 1 mm rms orbit error. This results in the following requirements (see [30] for details):

- Longitudinal dipole misalignment: ± 1 mm;
- Second field integral error for M1 and M2: $\pm 5 \cdot 10^{-4}$ Tm².

For orbit reproducibility after shutdowns, dipole and quadrupole misalignments and field integral errors are assumed to already be compensated, and all of the error budget is assigned to dipole and corrector power supplies. Limiting the orbit non-reproducibility to 100 μm rms in both planes, the resulting requirements for dipoles and correctors are $\Delta\alpha/\alpha = 1.3 \cdot 10^{-4}$ rms and $\Delta\theta/\theta = 2.6 \cdot 10^{-3}$ rms correspondingly, assuming an equally split error budget.

Betatron Tune Errors

Betatron tune errors come from three sources: quadrupole gradients, beam energy, and orbit inside sextupoles. It is expected that in the beginning of commissioning when orbit errors are large, the

³While the final design of the mechanical support structures is not complete and may use plinths with discrete or integrated magnet assemblies in place of classical girders, the term "girders" will be used in what follows as a generic term for logical magnet groupings.

tune errors will be dominated by the orbit inside sextupoles. This effect can be described the following way:

$$\delta\nu_{\text{rms}}^2 = \left(\frac{1}{4\pi}\right)^2 \sum (\beta_i K_{2,i} L_i u_i)^2 \approx 920^2 u_{\text{rms}}^2, \quad (4.12)$$

where u is the orbit inside sextupoles in meters, β_i is the beta function at the i^{th} sextupole, and $K_{2,i}L$ is the integrated strength of the i^{th} sextupole. For simplicity, it was assumed that the orbit inside all sextupoles has the same rms displacement. This equation shows that for 1-mm rms orbit errors, the tune error will exceed 0.9. This tune error is too large to expect operation without initial correction. Therefore, during commissioning, after the first closed orbit has been established, the tune will need to be corrected. Indeed, it may be necessary to correct the tune by using first-turn data, but this has yet to be studied.

Despite the need for tune correction from the very beginning, it is still advisable to place a limit on tune error contributions from quadrupoles and dipoles. The expression for the quadrupole effect is very simple [31]:

$$\delta\nu_{\text{rms}q}^2 = \left(\frac{1}{4\pi}\right)^2 \left(\frac{\delta K_1}{K_1}\right)_{\text{rms}}^2 \sum_{\text{quad fam}} N_i (\beta_i K_{1,i} L_i)^2 = A_q^2 \left(\frac{\delta K_1}{K_1}\right)_{\text{rms}}^2 = A_q^2 \left(\frac{\Delta I}{I_{\text{max}}}\right)_{\text{rms}}^2. \quad (4.13)$$

Here, q stands for x or y, and N is the number of quadrupoles of length L in a family.⁴ K_1 stands for the gradient corresponding to the maximum current of a quadrupole power supply, because power supply quality is usually quoted in units of $\Delta I/I_{\text{max}}$. It was also assumed that all power supplies have the same $\Delta I/I_{\text{max}}$. The calculation gives $A_x = 11$ and $A_y = 26$.

The dipole errors that generate a beam energy error discussed above also affect the betatron tune. If the orbit changes due to changes in a dipole or a set of dipoles are neglected, the relation is very simple: $\Delta\nu = \xi \cdot \Delta E/E$, where ξ is the natural chromaticity. Since the natural chromaticity for the MBA lattice is large (-140 in horizontal plane), the effect on the tunes is strong. As with the beam energy errors, the actual effect of the tune error dependence on the dipole current is more complicated and was obtained from simulations [28]. The result is represented by the following empirical formula (assuming again that all dipoles have the same fractional errors):

$$\delta\nu_{\text{rms}} = 137 \cdot \left(\frac{\Delta E}{E}\right)_{\text{rms}} = 58 \cdot \left(\frac{\Delta\alpha}{\alpha}\right)_{\text{rms}}. \quad (4.14)$$

The simulation result is actually very close to the simple expression that uses the natural chromaticity.

Assuming that the tune error budget of 0.1 is distributed equally between quadrupoles and dipoles, the requirements for the initial errors are: $\Delta K_1/K_1 = 3 \cdot 10^{-3}$ and $\Delta\alpha/\alpha = 1.2 \cdot 10^{-3}$. Requirements for reproducibility are one-tenth of the initial error requirements.

Beta Function Errors

⁴Note that quadrupoles in the same family nevertheless have independent power supplies, so their effects add incoherently.

Beta function errors are generated by quadrupole errors and by orbit errors in sextupoles. Early analysis of orbit correction resulted in an expected initial beta function beating of about 20% due to orbit errors in sextupoles [31]. The same error was assumed allowable for the initial effect of quadrupole errors. Based on this assumption, a simple simulation of beta function errors due to random quadrupole errors resulted in an initial quadrupole error requirement of $1 \cdot 10^{-3}$ [31]. The requirement for reproducibility is one-tenth of the initial error requirement.

Chromaticity Errors

Chromaticity errors are generated by sextupole errors and by lattice errors. Simulations show that chromaticity errors after the beam is first stored have an rms of five units due to large lattice errors. After orbit correction is completed, the rms chromaticity error decreases to about one unit. It is assumed that the chromaticity error contribution from sextupole strengths can also be accepted at one unit. When all sextupole errors are independent, the expected effect for the chromaticity error due to sextupoles is the quadrature sum of individual effects:

$$\Delta\xi_{\text{rms}}^2 = \frac{1}{16\pi^2} \left(\frac{\Delta K_2}{K_2} \right)_{\text{rms}}^2 \sum_{\text{all sext}} (\beta \cdot \eta \cdot K_2 \cdot L)^2, \quad (4.15)$$

where β and η are beta function and dispersion at the location of a sextupole, and K_2 and L are the magnet strength and length. Simple calculation results in the initial error requirement of $2.7 \cdot 10^{-2}$. The requirement for reproducibility is one-tenth of the initial error requirement.

Static Random Errors Summary

Table 4.8 summarizes tolerances for random static errors.

Table 4.8. Summary of static rms and peak-to-peak error tolerances (peak-to-peak errors are denoted by \pm sign). Transverse alignment tolerances are discussed in section 4-2.2.4.

	Initial error	Reproducibility
Dipole PS relative error	$0.7 \cdot 10^{-3}$	$1.2 \cdot 10^{-4}$
Quadrupole PS relative error	$0.7 \cdot 10^{-3}$	$1 \cdot 10^{-4}$
Sextupole PS relative error	$2.7 \cdot 10^{-2}$	$2.7 \cdot 10^{-3}$
Corrector PS relative error	—	$2.6 \cdot 10^{-3}$
Dipole 1st integral relative error	$\pm 1 \cdot 10^{-3}$	—
Dipole 2nd integral error	$\pm 5 \cdot 10^{-4} \text{ Tm}^2$	—
Quadrupole gradient integral relative error	$\pm 1 \cdot 10^{-3}$	—
M1 and M2 dipole longitudinal alignment	$\pm 1 \text{ mm}$	—

4-2.2.2 Static Systematic Errors

There could be many different kinds of systematic errors: some of them could be related to construction of magnets while others could be connected to magnetic measurements of elements. A few such errors are examined here. Other types of systematic errors will be considered later.

Errors of Magnetic Length of Quadrupoles

If the magnetic length of a quadrupole differs slightly from the design value, the total focusing strength of the quadrupole can be easily adjusted by changing the power supply current accordingly. However, even with the same integrated strength, the quadrupole would still have a different length, which could lead to changes in the lattice. If the length difference comes from the quadrupole design, i.e., many quadrupoles have the same kind of error, then the effect will be stronger.

This effect was simulated assuming that one quadrupole family has such a systematic error. The value of the error in quadrupole length was negative 1%. The results are given in Table 4.9. Note that both tunes are changed in the same direction, and therefore, the effect cannot be corrected by simply adjusting the quadrupole strength. Assuming that all quadrupoles have the same design features that cause the length error, the total effect will be the sum of effects of all individual families from Table 4.9. Limiting the tune errors due to this effect to 0.1, the requirement for the quadrupole length accuracy will be 0.3%.

Table 4.9. Betatron tune errors due to 1% error of the quadrupole length for different quadrupole families. The total focusing strength was kept constant.

Quad family	$\delta\nu_x$	$\delta\nu_y$
Q1	0.014	0.014
Q2	0.005	0.017
Q3	0.004	0.013
Q4	0.018	0.011
Q5	0.004	0.003
Q6	0.003	0.009
Q7	0.020	0.027
Q8	0.082	0.082
M3	0.042	0.128
M4	0.014	0.036

Relative Strength Error between All Dipoles and All Quadrupoles

Presently, it isn't known exactly what magnetic measurement systems will be used for measurements of different types of magnets. To understand the scale of the effect, it can be assumed that dipoles and quadrupoles are measured by two different measurement systems that have a relative calibration error. This effect was simulated by changing all K_1 values of all quadrupoles and defocusing dipoles simultaneously by the same $\Delta K_1/K_1$ value. It was found that to keep betatron tunes within 0.1 of the design values, the calibration error between the two magnetic measurement systems should be below $7 \cdot 10^{-4}$.

4-2.2.3 Variable Errors

Variable errors are those that change in time. These errors change various beam parameters, and if these parameters can be measured in real time, the corrections, in general, can also be applied in real time. In such a case, it makes sense to calculate error tolerances considering corrections as well. The simplest example is beam orbit stability: requirements for the orbit stability are very tight. Since the orbit can be measured and corrected in real time, the actual magnet stability requirements can be made easier if the effect of orbit correction is taken into account.

The most important storage ring parameter that is susceptible to varying errors is beam orbit stability. That is why the main emphasis of this section is orbit stability. Variable errors can be split in several parts according to their frequency spectrum: slow (slower than 100 seconds), fast (between 0.01 Hz and 1 kHz), and very fast (faster than 1 kHz). The main limiting effects on the varying errors are given in Table 4.10. In the very fast band, the motion is assumed to be faster than the sample exposure time, and therefore the beam motion in this band will effectively increase the beam size. The real beam size and the contribution of the beam motion add in quadrature: $\sigma_{\text{total}}^2 = \sigma_{\text{size}}^2 + \sigma_{\text{motion}}^2$, where σ_{size} is the beam size and σ_{motion} is the rms beam motion. The allowable beam size increase is 10%, which results in $0.4\sigma_{\text{size}}$ allowable beam motion.

Table 4.10. Initial assumptions on varying errors

Range	Limit (rms)	Magnets responsible
Orbit stability		
>1 kHz	0.4σ	Dipole noise Corrector noise
0.01 Hz – 1 kHz	0.1σ	Dipole noise Corrector noise Quadrupole vibrations
<0.01 Hz	$1 \mu\text{m}$	Dipole drift Corrector drift Quadrupole position drift
Tune stability		
0.01 Hz – 1 kHz	10^{-3}	Dipole noise (through energy) Quadrupole noise Corrector noise Sextupole noise and vibration (through orbit) Orbit noise (through sextupoles)
<0.01 Hz	10^{-3}	Dipole drift Quadrupole drift Corrector drift Sextupole drift (strength and position) Orbit drift

Orbit Motion, 0.01 Hz – 1 kHz

Since most user experiments average data for more than one turn of the electron beam (and many experiments require averaging for many turns), the electron beam motion during the averaging time transforms directly into an effective increase of the source size. That is why the beam positional and angular stability are so important for the synchrotron light sources, and why the orbit stability is often given as a fraction of the beam size. For the APS Upgrade storage ring, where beam sizes will be significantly smaller than in the present APS, the importance of beam orbit stability becomes even higher. Orbit stability is mainly affected by electrical noise of the magnet power supplies and by vibration of the magnets. The effect of the power supply noise on the beam is attenuated by the eddy currents in the solid core magnets and in the vacuum chamber. Also, orbit correction is always run during user operation to counteract the beam motion. These effects need to be taken

into account if one wants to come up with realistic requirements.

To calculate the tolerances for time-varying errors, one needs a good knowledge of the spectral characteristics of all the processes involved: power supply noise and magnet vibration spectra, frequency dependence of the attenuation due to solid core magnets and the vacuum chamber, and orbit correction bandwidth. While work on measuring or calculating these effects is ongoing, some simplified assumptions were made that allow calculating preliminary tolerance requirements. The overall motion is split into three components: electrical noise in magnets, magnet vibration, and BPM vibration. While BPM vibration does not, of course, affect the beam location directly, it will affect the beam location by causing the orbit correction system to move the beam. If each component is responsible for a fraction P of the square of the beam motion, then the total motion can be written as

$$\begin{aligned}
 q_{\text{total}}^2 &= q_v^2 + q_e^2 + q_{\text{BPM}}^2 \\
 &= P_v P_{\text{girder}} q_{\text{total}}^2 + P_v P_{\text{magnet}} q_{\text{total}}^2 + P_v P_{\text{dipole_roll}} q_{\text{total}}^2 + \\
 &\quad P_e P_{\text{dip}} q_{\text{total}}^2 + P_e P_{\text{quad}} q_{\text{total}}^2 + P_e P_{\text{corr}} q_{\text{total}}^2 + \\
 &\quad P_{\text{BPM}} q_{\text{total}}^2,
 \end{aligned} \tag{4.16}$$

where v stands for vibrational, e stands for electrical, and q stands for x or y . Vibrational motion is split into motion due to girder vibration P_{girder} , vibration of separate magnets on the girder P_{magnet} , and due to dipole roll motion $P_{\text{dipole_roll}}$, while electrical noise motion is split into contributions from dipoles P_{dip} , quadrupoles P_{quad} , and correctors P_{corr} [29].

Every component of the noise goes through a series of transformations before reaching the user sample. For example, a change in bending angle due to electrical noise in a corrector is first attenuated by the vacuum chamber, then it is amplified by the lattice, and then it is attenuated by the orbit correction, which results in the final orbit motion. The orbit motion is then projected onto the sample with some transfer function. The process is illustrated in Figure 4.11. Specific

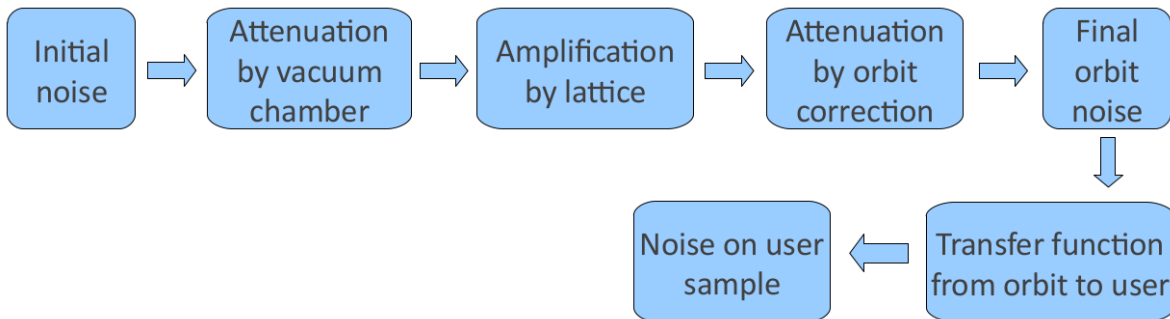


Figure 4.11. Processes affecting a noise component before its effect reaches the user sample.

assumptions about various effects are the following:

- Electrical noise has power spectral density (PSD) that is inversely proportional to frequency ($1/f$ dependence) and extends in both directions without limit. This is so called “pink” noise that is common in electronic devices.
- Vibrational noise of the girders follows the motion of the floor and has $1/f^3$ PSD dependence (this dependence is based on several publications and our preliminary measurements) [32].

Only two modes are presently included – displacement and pitch/yaw, both modes have the same spectrum.

- Vibrational motion of the magnets on the girders follows the same spectrum behavior as the girder motion, but the motion of different magnets on the girder is uncorrelated. This assumption is somewhat arbitrary. The main sources of the uncorrelated motion of magnets on girders are thought to be water supply system vibration and girder deformations. Measurements of the vibration due to water supply are planned on the present APS girders; the girder deformation modes' effect will also be analyzed later.
- The BPM motion has the same spectrum and magnitude as the girder motion because BPMs move with girders (or $q_{\text{girder}} = q_{\text{BPM}}$). Electrical noise of BPMs is expected to be around 100 nm and will be considered as a (small) part of the BPM motion budget.
- The attenuating effects of the solid core magnets and vacuum chamber were calculated using the program OPERA. The resulting field ratio as a function of frequency is shown on Fig. 4.12 [33]. The PSD attenuation ratio (which is the square of the field attenuation ratio shown in the figure) can be approximated as $1/\sqrt{f}$ in the range from 1 Hz to 100 Hz and as $1/f$ above 100 Hz. It is assumed, conservatively, that this attenuation does not affect motion due to vibrational noise. It also, obviously, does not affect the BPM motion.
- Lattice amplification of the electrical noise is frequency independent, while for vibrational noise the amplification decreases for low frequencies due to coherent floor motion. There is no amplification of the BPM noise.
- Orbit correction is an integral controller that has PSD dependence of f^2 and is effective up to a bandwidth of f_{bw} . Orbit correction only attenuates motion caused by electrical and vibrational noise, but not the motion due to BPM vibration.
- The motion caused by the electrical noise is transferred to the sample without attenuation because the sample motion and electrical noise are independent, while vibrational and BPM caused motion is attenuated at low frequencies due to coherence of the floor motion.
- Any possible resonant lines in the motion and power supply noise spectra are neglected because their location and power are not presently known. Preliminary measurements show that the total contribution of spectral lines to the total noise does not exceed 50%; therefore, neglecting them should underestimate the beam motion by no more than a factor of two.

Some of the assumptions are illustrated in schematic form in Fig. 4.13, where the shape of the noise spectrum is given as well as the shape of vacuum chamber attenuation, lattice amplification, and orbit correction attenuation. The resulting PSD of the beam orbit motion is the product of the four functions shown in the schematic. The multiplication and integration of the resulting PSD were done numerically. The lattice parameters were used to calculate the orbit motion amplification factors F , and the results are summarized in Table 4.12.

As was mentioned before, the lattice amplification factors for vibrational motion should decrease when the ground motion correlation length becomes large. We simulated the effect by generating random girder displacements with different correlation lengths. Figure 4.14 shows the amplification factors as a function of correlation length of the ground motion. One can see that for correlation lengths around 50 m, the lattice amplification factors go down to 1. Without direct measurements of the correlation length frequency dependence, it is assumed that 50 m corresponds approximately to 0.1 Hz. The assumption is loosely based on the literature, but the measurements of the APS floor are planned. The following spectral dependence of the amplification factors was assumed: constant factor corresponding to independent motion of girders at high frequency down to 0.2 Hz, 1 from

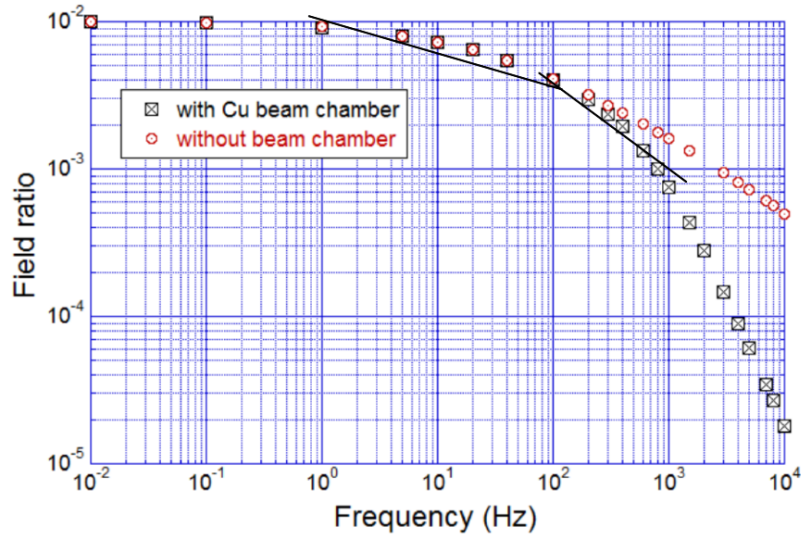


Figure 4.12. AC magnetic field attenuation due to losses in both the solid iron yoke of the quadrupole magnet and the copper wall of the vacuum chamber. The field attenuation is approximated as $1/f^{1/4}$ between 1 Hz and 100 Hz and as $1/f^{1/2}$ above 100 Hz (black lines).

0.1 Hz down, and smooth transition between 0.1 and 0.2 Hz. The details of the simulations can be found in [34].

During machine studies, some measurements must be performed without orbit correction running—response matrix measurement, for example. Therefore, orbit motion due to vibrational and electrical noise needs to be below some limit even without orbit correction. From present experience, a limit of $1\ \mu\text{m}$ seems to be reasonable. The same orbit amplification factors as in Table 4.12 can be used for calculations, only there will be no attenuation due to orbit correction. Response matrix measurement involves subtracting two measured orbits, and therefore the noise that is much slower than the duration of two orbit measurements gets eliminated. We assume that the measurement will be done on a one-second time scale, so the noise below 1 Hz will not contribute to the accuracy of the response measurement. The frequency range of interest when considering motion without orbit correction is therefore from 1 Hz up. The response measurement will also be done with averaging, which allows for attenuation of high-frequency noise. For calculations here, a low-pass filter with 1 Hz cut-off frequency was used for averaging. The apportioning of the budget motion for both cases (with and without orbit correction) is given in Table 4.11.

Effect of insertion devices

One effect that has yet to be discussed is the orbit perturbation from variation in the strength of insertion devices (e.g., by changing the gaps). This process is in general rather slow, as a full gap closure takes longer than a minute, and the perturbation itself is a smooth ramping process. Similarly, superconducting undulators have limits on the rate of change of current in order to prevent quenching and generation of excessive heat. For ramping sources of orbit distortion the resulting global orbit error is proportional to the rate of the distortion change multiplied by a time constant characteristic of the orbit correction [35]. The relevant time constant is the iteration frequency of

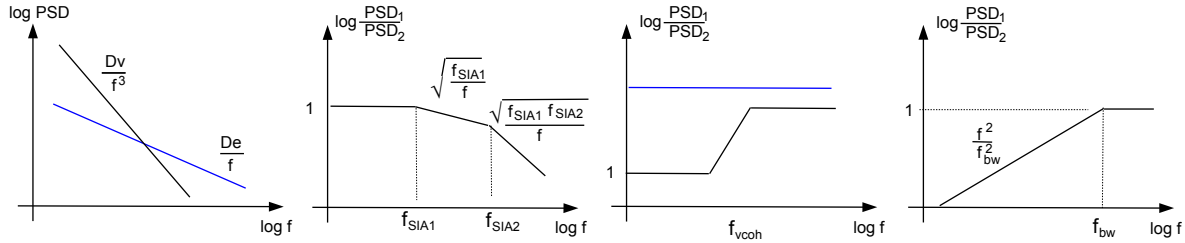


Figure 4.13. From left to right: Power spectral density of electrical (blue) and vibrational noise (black) with power amplitudes D_e and D_v ; electrical noise attenuation due to solid iron core and vacuum chamber with bandwidths f_{SIA1} and f_{SIA2} ; lattice amplification factors: blue – for electric noise, black – for vibrational noise; beam motion attenuation due to orbit correction with bandwidth f_{bw} .

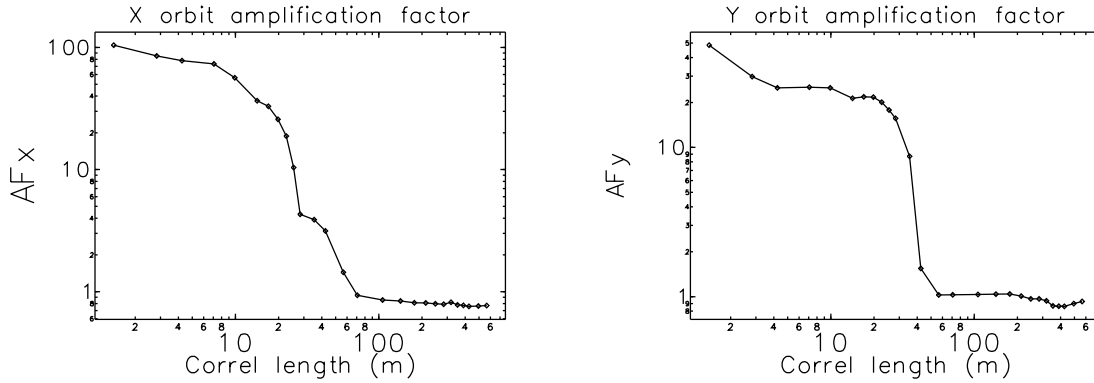


Figure 4.14. Lattice amplification factor dependence on the ground motion correlation length. An amplification of 1 means that everything moves together, so no relative motion is detected.

the orbit correction divided by the fraction of the correction that is applied at each step. For the present APS, the orbit correction time constant is 0.25 sec, which is defined by the parameters of the slow orbit correction since the fast orbit correction has very low gain at low frequencies. For the APS Upgrade it is expected that the time constant will be 0.001 sec. So while the overall orbit stability requirement for the APS Upgrade will be about 20 times more stringent than for the present APS (ratio of the horizontal beam sizes because ID effects mostly contribute to horizontal orbit motion), the orbit correction time constant for the APS Upgrade will be 200 times smaller. Therefore, the insertion device effect on the global orbit is expected to be much smaller than it is now. In other words, the insertion devices perturb the orbit only in the low-frequency part of the spectrum where orbit correction has very high efficiency. That is why the contribution of insertion devices on the orbit stability was neglected in the considerations above. Detailed, quantitative consideration of this effect will be pursued later when a model of the orbit correction system is available.

Tune Variation, 0.01 Hz – 1 kHz

Table 4.11. Budget apportioning for beam motion

		User operation, orbit correction on	Beam studies, orbit correction off
Total motion budget		0.1 σ (1.7 μm , 0.4 μm) 0.01 – 1000 Hz	1 μm 1 – 1000 Hz
Portion of mean square motion due to:			
power supply noise	P_e	0.29	0.59
vibrational noise	P_v	0.01	0.4
BPM motion	P_{BPM}	0.7	0.01

Table 4.12. Orbit motion amplification factors normalized by $\sqrt{\beta_{ID}}$

	Symbol	Units	X	Y
Girder motion amplification	F_{girder}	$\text{m}^{-1/2}$	29	38
Quadrupole motion amplification	F_{magnet}	$\text{m}^{-1/2}$	63	81
Corrector noise amplification	F_{corr}	$\text{m}^{1/2}$	0.012	0.02
Dipole noise amplification	F_{dipole}	$\text{m}^{1/2}$	0.24	
Dipole roll amplification	$F_{\text{dipole_roll}}$	$\text{m}^{1/2}$		1.6

As with static errors, the main sources of tune variation are quadrupole and dipole power supply noise and orbit noise in sextupoles. The effect of the quadrupole and dipole errors on the tune is given by equations 4.13 and 4.14. It is assumed that no tune correction is running in this bandwidth. However, the attenuation effect due to the solid core magnets and vacuum chamber discussed above is still present and needs to be taken into account. Integrating the attenuation function shown on the middle plot of Fig. 4.13 gives the total attenuation coefficient of 0.77 in the considered bandwidth. This means that the values of $\Delta I/I$ (or $\Delta\alpha/\alpha$) obtained from equations 4.13 and 4.14 can be multiplied by 1/0.77.

Another possible source of tune variation is sextupole power supply noise. To estimate this effect, it was assumed that the orbit error in sextupoles is 100 μm rms (girder alignment tolerance). By using the expression for the tune change due to focusing errors, and assuming that orbit errors in sextupoles are independent (which is probably an overestimation, given the small phase advance between the SD-SF-SD strings on each girder), the following equation for the tune distribution width can be written:

$$\begin{aligned} \Delta\nu_{\text{rms}}^2 &= \sum_{\text{sext}} \left(\frac{1}{4\pi} \beta \Delta K_2 x L \right)^2 = x_{\text{rms}}^2 \left(\frac{\Delta K_2}{K_2} \right)^2 \sum_{\text{sext fam}} \left(\frac{\beta K_2 L}{4\pi} \right)^2 N \\ &\approx x_{\text{rms}}^2 \left(\frac{\Delta K_2}{K_2} \right)^2 \times \left(570 \frac{1}{\text{m}} \right)^2. \end{aligned} \quad (4.17)$$

Here the first summation is done over all sextupoles, the second summation is done over sextupole families, assuming that all sextupoles within a family have the same K_2 and β , and N is the number of sextupoles in a family. The final number given is the largest of the two planes and corresponds to the vertical plane.

It turns out that the most important effect on tune stability comes from orbit noise in sextupoles.

The consideration is similar to 4.17, but this time the orbit in nearby sextupoles cannot be considered independent. The sextupoles are located in triplets with very small phase advance inside the sextupole triplets. Therefore, the orbit inside a sextupole triplet is just proportional to the square root of beta function. The orbit in different triplets can be considered independent because they are separated in phase advance and could have orbit correctors between them. The total tune variation can be written as

$$\Delta\nu_{\text{rms}}^2 = \left(\frac{L}{4\pi}\right)^2 \sum_{\text{triplets}} \left(\sum \beta_i K_{2i} x_{\text{rms}i}\right)^2. \quad (4.18)$$

Here the first summation is over different sextupole triplets, while the second summation is over sextupoles within one triplet. All 80 sextupole triplets are nearly identical (with small differences in K_2), therefore the summation over triplets is simple. Normalizing x_{rms} to the rms displacement at ID locations gives

$$\Delta\nu_{\text{rms}q}^2 = 80 \left(\frac{x_{\text{IDrms}} L}{4\pi}\right)^2 \left(\sum \beta_{iq} K_{2i} \sqrt{\frac{\beta_{ix}}{\beta_{\text{ID}x}}}\right)^2 = (A_q \cdot x_{\text{IDrms}})^2, \quad (4.19)$$

where again q stands for X or Y. Calculations give $A_x = 370$ 1/m and $A_y = 190$ 1/m. For normal user operation, the requirement for the orbit stability at ID locations x_{ID} is one tenth of the beam size. This gives the following tune variation due to orbit motion: $\nu_x = 2 \cdot 10^{-4}$ and $\nu_y = 5 \cdot 10^{-5}$. For the case when orbit correction is not running, the expected tune variation due to orbit motion in sextupoles is $\nu_x = 3.7 \cdot 10^{-4}$ and $\nu_y = 1.9 \cdot 10^{-4}$.

Summary of Tolerances, 0.01 Hz – 1 kHz

Requirements for electrical noise and magnet vibration were considered through their effects on orbit stability with and without orbit correction and on betatron tune variation. A summary of the requirements, derived from the above considerations, is given in Tables 4.13 and 4.14. More details about tolerance calculations in this bandwidth can be found in [29].

It is important to note that most of the vibration requirements are dictated by the stability requirements of the non-user operation (beam studies), mainly to have quiet orbit during the response matrix measurement. This happens because the orbit correction is assumed to not be running during the measurements. If only user operation is considered in the requirement calculations, some numbers in Table 4.14 could be considerably relaxed. Understanding this, the work is ongoing concerning how to relax the requirements. Options under consideration are an AC lock-in response matrix measurement and a response matrix measurement with the orbit correction running in some way.

Drift tolerances (variations below 0.01 Hz)

There are several effects that contribute to slow variations of orbit and other parameters in a storage ring: power supply drifts lead to slow lattice parameter variation; mechanical motion of BPMs leads to orbit motion and could thus lead to lattice changes as well; changes in ID gaps also result in focusing changes. These effects will be considered in this section.

Table 4.13. Summary of rms electrical noise tolerances for 0.01-1000 Hz bandwidth.

Magnet type	Requirement	Based on
Correctors	$2 \cdot 10^{-4}$	Orbit stability
Dipoles M3-M4	$2 \cdot 10^{-5}$	Orbit stability
Dipoles M1-M2	$2.3 \cdot 10^{-5}$	Tune stability
Quadrupoles	$2.5 \cdot 10^{-5}$	Tune stability
Sextupoles	$2 \cdot 10^{-3}$	Tune stability

Table 4.14. Summary of vibrational tolerances. Two bandwidths are given. The numbers in this table are the most demanding requirements based on either stability requirement with or without orbit correction.

	X	Y	X	Y
	(rms)	(rms)	(rms)	(rms)
	1-100 Hz		0.1-1000 Hz	
Girder vibration	20 nm	20 nm	200 nm	200 nm
Quadrupole vibration	10 nm	10 nm	100 nm	100 nm
Dipole roll vibration	—	0.2 μ rad	—	2 μ rad

It is assumed that power supply drifts will be dominated by environmental temperature variation. In this case, all power supplies change simultaneously in one direction, and the overall behavior is oscillatory (for example, repeating 24-hour variation of temperature in the tunnel). To simulate such drift, one just needs to apply single-step magnet changes to obtain the response for any parameters of interest. Any effect of power supply drift on the orbit will be corrected by the orbit correction, and therefore, the orbit stability will be defined by the BPM stability, not power supply stability. Only parameters like tunes, beta functions, and beam energy will be affected by the drifts. The drift effects of the longitudinal-gradient dipole power supplies need to be simulated separately because these power supplies will be located in a separate room with supposedly better temperature regulation. Table 4.15 shows accelerator parameter changes due to fractional-strength-error (FSE) changes of 10^{-4} . To see the effect of temperature change in different parts of the tunnel, the changes were applied to the entire ring, to six sectors (one storage ring zone), and to a single sector. One can see that the parameters that change the most are betatron tunes.

Table 4.15. Lattice parameter changes due to 10^{-4} fractional strength change of quadrupoles and dipoles

Parameter	Quadrupoles and transverse-gradient dipoles			Long.-gradient dipoles
	Entire ring	6 sectors	1 sector	
$\Delta\nu_x$	$2.3 \cdot 10^{-2}$	$3.4 \cdot 10^{-3}$	$5.6 \cdot 10^{-4}$	$-1.6 \cdot 10^{-2}$
$\Delta\nu_y$	$2.9 \cdot 10^{-2}$	$4.4 \cdot 10^{-3}$	$7.3 \cdot 10^{-4}$	$-1.3 \cdot 10^{-2}$
$\Delta E/E$	$5.2 \cdot 10^{-5}$	$7.8 \cdot 10^{-6}$	$1.6 \cdot 10^{-6}$	$7.3 \cdot 10^{-5}$
$\Delta\beta_x/\beta_x$	$3.2 \cdot 10^{-3}$	$3.5 \cdot 10^{-3}$	$2.6 \cdot 10^{-3}$	$1.9 \cdot 10^{-3}$
$\Delta\beta_y/\beta_y$	$1.9 \cdot 10^{-3}$	$1.7 \cdot 10^{-3}$	$1.7 \cdot 10^{-3}$	$1.1 \cdot 10^{-3}$

As shown earlier, the effect on tunes (and energy) can depend on whether orbit correction is running

[36]. To see the effect of orbit correction, the simulations were run with and without orbit correction for the case when both focusing magnets and longitudinal gradient dipoles change together by the same amount. Table 4.16 shows the results for the tunes. One should keep in mind that depending on the orbit correction configuration, the numbers could change slightly. For the final drift tolerances, the case of all magnets changing together with orbit correction running will be taken (bottom right number in Table 4.16). The details of the PS drift simulations can be found in [37].

Table 4.16. Tune change due to 10^{-4} FSE error on all magnets with and without orbit correction

Parameter	No OC	With OC
$\Delta\nu_x$	$6.5 \cdot 10^{-3}$	$3.5 \cdot 10^{-3}$
$\Delta\nu_y$	$1.7 \cdot 10^{-2}$	$1.5 \cdot 10^{-2}$

Another source of drift is the mechanical motion of BPMs. The BPM drifts will be dominated by the thermal longitudinal expansion of the vacuum chamber that will lead to some transverse deformation due to buckling. The process is unpredictable and random: different parts of the chamber will move in random directions, and the same type of chambers in different sectors will behave differently. The transverse motion of the chamber will result in BPM motion; the orbit correction will make the beam follow the BPMs and thus change the real orbit. The possible consequences of this effect are changes in betatron tunes, beta functions, and beam energy. When simulating these effects, it was assumed that only BPMs outside of ID straight sections are allowed to drift. A summary of the simulation results is given in Table 4.17, while details of the simulations can be found in [38].

Table 4.17. Various rms errors resulting from BPM drift simulations

BPM change	Tunes	Beta functions	Emittances
3 μm rms	$1 \cdot 10^{-3}$	0.3%	0.05 μm

One more source of drift is the change of ID gaps. A single 4.8-m long U27 ID closed to the minimum gap changes vertical tune by 0.001 and causes rms beta function beating of 0.6%. The effect of many undulators on the tune is additive, which, if left uncorrected, could lead to tunes shifts exceeding 0.01. The details of ID gap correction are not worked out yet, but it is envisioned that a gap feedforward will be applied to the nearest Q1 and Q2 quadrupoles. The feedforward could be local if beta function correction is deemed necessary, or global if only tunes are important.

Table 4.18 summarizes the requirements based on the drift simulations. In this table, 3 μm rms BPM drift limit from Table 4.17 was loosely transformed to $\pm 5 \mu\text{m}$ requirement with some safety margin.

Table 4.18. Summary of drift simulations and corresponding rms requirements

	Tune effect	Beta function effect	Requirement
BPM drift	$1 \cdot 10^{-3}$	0.3%	$\pm 5 \mu\text{m}$
PS drift	$1.5 \cdot 10^{-3}$	—	$\pm 1 \cdot 10^{-5}$
ID gaps	$2 \cdot 10^{-3}$	0.5%	Tune feedforward

AC line ripple tolerances

An AC line ripple is a narrow-band power supply noise that comes from the AC line imperfections. The lowest harmonic of the AC line ripple is assumed to be 360 or 720 Hz. At this frequency, there must be some attenuation of the variation of the magnetic field due to the magnet solid cores and vacuum chamber. The simulated attenuation factor was shown earlier in Fig. 4.12. At the assumed frequency of the AC ripple, the attenuation is about a factor of 5. Attenuation measurements will be conducted in the future to confirm this number.

If the outputs of all power supplies change in phase, then the effect of the AC ripple can be represented by exactly the same simulation as the drift simulation above. One can directly use results given in Table 4.15, column “Quadrupoles and transverse-gradient dipoles, entire ring,” (longitudinal-gradient dipoles have completely different power supplies, so they are excluded). The resulting ripple amplitude can be relaxed by the attenuation factor. In reality, the ripple phase will be the same within a double sector, but phases between double sectors will be different, and it is expected that the phase differences between double sectors will be random and small (this corresponds to different double sectors being powered by different transformers). Simulations showed that under this assumption, the variations of the tunes, energy, and beta functions differ very little from the numbers given in Table 4.15. Based on these numbers, the amplitude of the AC ripple is required to be below $2 \cdot 10^{-5}$ to limit the contribution into the tune variation below 0.001.

The effect of ripple on the orbit was also simulated. It was found to be negligible after taking into account the attenuation of the varying fields by the solid core magnets and vacuum chamber and attenuation of the orbit motion by the orbit correction.

Ripple from switching power supplies

The switching frequencies start at 20 or 40 kHz. At these frequencies, the field attenuation due to solid core magnets and vacuum chamber reaches about a factor of 1000. Once again using numbers from Tables 4.15, and limiting the tune variation to 0.001, gives a current ripple requirement of $3 \cdot 10^{-3}$. Orbit motion is negligible.

Individual glitches

Using simple formulas for the orbit or tune change due to a single source shows that a glitch of 10^{-3} gives an orbit change of about $2 \mu\text{m}$ or a tune change of $5 \cdot 10^{-4}$. These numbers, or even factor of 10 larger numbers, are acceptable.

The final requirements for power supply drifts, ripple, and glitches are summarized in Table 4.19 and more details can be found in [37].

Table 4.19. Summary of drift and ripple requirements coming from tune stability requirement of 0.001 peak to peak. Attenuation is taken from Fig. 4.12 but could be changed later if measurements would show a different effect.

24-hour drift peak-to-peak	10^{-5}
AC line ripple peak-to-peak	$2 \cdot 10^{-5}$
High-frequency switching ripple peak-to-peak	$3 \cdot 10^{-3}$
Single glitch	10^{-3}

4-2.2.4 Simulation of Orbit and Lattice Correction

The very small emittance in the MBA lattice is achieved by much stronger focusing than in the present APS ring. For example, maximum quadrupole strengths increase nearly five-fold in the new lattice compared to the present APS lattice. Stronger focusing inevitably leads to larger natural chromaticity and thus a nearly seven-fold increase in sextupole strength is needed, resulting in relatively small dynamic aperture and a short lifetime even for the ideal lattice. Misalignments of the strong quadrupoles generate large orbit errors, which, in the presence of very strong sextupoles, leads to large lattice and coupling errors. Add to this smaller vacuum chamber gaps that are required to achieve high gradients in the magnets, and the required rapid commissioning becomes a significant challenge.

Another issue with highly nonlinear lattices is the proper evaluation of lattice performance in the presence of lattice and alignment errors. It is well known that errors degrade the performance of a machine by breaking symmetry and introducing new resonances. In order to evaluate the lattice in the presence of errors, it is necessary to introduce some errors in the simulation. Introducing realistic errors would lead to very large orbit and lattice distortion, because real machines never operate without some sort of correction to reduce initial orbit and lattice errors. One strategy to account for the correction is to introduce only very small magnet errors (for example, quadrupole strength and tilt errors) that statistically reproduce the final lattice errors expected to be achieved in real life after orbit and lattice correction. This approach assumes that the nonlinear lattice behavior is defined only by the final lattice distortion that is the combination of large magnet errors and their corrections. Even though this assumption seems reasonable, it is best to use the real values of the errors, correct their effect, and then evaluate the nonlinear behavior of the lattice in order to remove any doubts.

To address both the issues of the possibility of fast commissioning and the use of real errors in simulations, a start-to-end simulation of machine commissioning was performed, taking into account as many errors as possible. All simulations were done using `elegant` [22]. The simulated commissioning procedure closely follows the steps that will be performed during commissioning. Before proceeding with the commissioning, the nominal quadrupole strengths are adjusted to move betatron tunes away from integer and coupling resonances to reduce their negative effect during initial steps of the commissioning (the design fractional tunes are 0.10 in both planes, they are adjusted to 0.18 and 0.24). The procedure includes the following steps:

- Generate errors for all elements according to Table 4.20 using Gaussian distributions with 2σ cut off.
- Correct trajectory until a closed orbit is found:
 - Perform “one-to-best” trajectory correction until the beam has reached the end of the machine.
 - Perform “global” trajectory correction starting with a small number of singular values (SV) and iterating the correction while increasing the number of SVs and recording a closed orbit if it exists. Before each iteration, the correctors that are close to the limit are reduced by some predetermined fraction.
 - After the SV scan is completed, choose the configuration with the best orbit.
- Perform closed orbit correction using a small number of correctors and the same process of increasing number of SVs while keeping the corrector strength from reaching the limits as

described in the global trajectory correction:

- Adjust tunes after each iteration to keep them away from integer resonances.
- If orbit correction is diverging, perform very “gentle” optics correction with a very small number of SVs and a very small correction fraction.
- Stop when orbit errors are reduced below a limit or when the number of SVs has reached a limit.
- Reduce BPM errors by a factor of 10 – assuming that at this point the beam-based BPM offset measurements are performed.
- Repeat orbit correction with a gradually increasing number of SVs, as described above, but using more correctors.
- Keep increasing number of correctors while repeating the orbit correction procedure until orbit errors are reduced below the requested level.
- Perform lattice correction, iterating between beta function correction and coupling minimization, while correcting the orbit between iterations (using one-step simple orbit correction).
- Adjust emittance ratio to a predetermined operational value by exciting the nearest difference resonance using skew quadrupoles.

Table 4.20. Various rms errors used for start-to-end commissioning simulation

Girder misalignment	100 μm
Elements within girder	30 μm
Initial BPM offset errors	500 μm
Dipole fractional strength error	$1 \cdot 10^{-3}$
Quadrupole fractional strength error	$1 \cdot 10^{-3}$
Dipole tilt	$4 \cdot 10^{-4}$ rad
Quadrupole tilt	$4 \cdot 10^{-4}$ rad
Sextupole tilt	$4 \cdot 10^{-4}$ rad

A standard correction procedure that was developed for the present APS [39] is used for lattice correction, and is based on the response matrix fit [40]. First, a response matrix measurement is simulated. BPM noise, BPM gain, corrector calibration errors, and BPM and corrector tilts are added to the simulated response matrix. For measurement and calculation speed, only ten correctors per plane are used. Based on the present experience, the measurement time should not exceed five minutes. After the response matrix is generated, the response matrix fit is run to derive focusing and coupling errors.

The entire simulation procedure is automated, and the commissioning is simulated for 200 different error sets. The procedure is able to successfully correct orbit and optics in 98% of all cases. The remaining 2% of the cases can be commissioned with some human intervention. The correction results are statistically analyzed for many parameters, such as orbit and lattice perturbations, correctors strengths, emittances, etc. The analysis is done the following way: a single number is calculated for every error set (for example, rms of the relative difference between the final and ideal horizontal beta functions), then the histogram of these numbers is calculated. Figure 4.15 shows results of the orbit correction — the rms of the residual orbit is expected to be around 100 μm . Figure 4.17 shows the results of the lattice correction — beta functions are expected to be corrected to within 2%, while the horizontal dispersion error is expected to be 1 mm. The expected value for the vertical dispersion is below 2 mm.

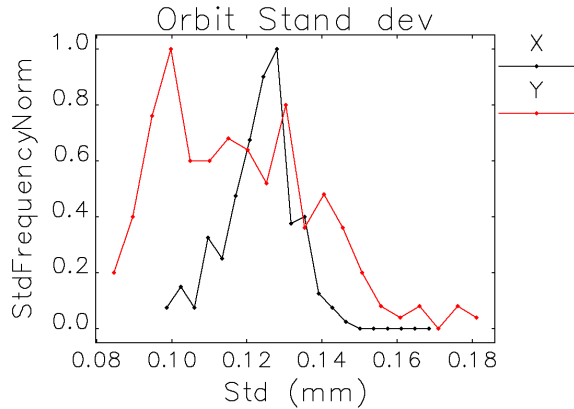


Figure 4.15. Final orbit errors.

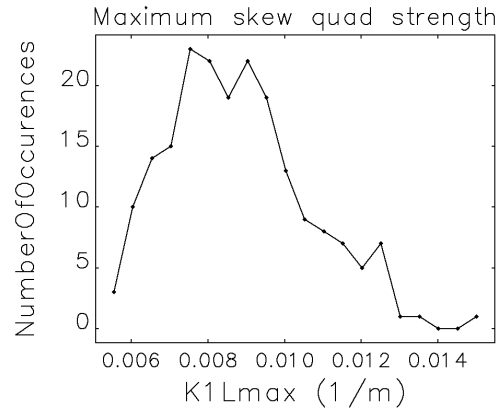


Figure 4.16. Probability distribution of the required maximum skew quadrupole integrated strength.

As was mentioned before, x-y coupling is first minimized, then adjusted to provide the required value of the emittance ratio (it was 10% for the data shown here) by exciting the nearest difference resonance using skew quadrupoles. Figure 4.18 presents emittances before and after coupling adjustment, showing that the low horizontal emittance of ~ 42 pm is not significantly affected by the errors or by the emittance ratio adjustment. If a “round beam” is required, the tunes are moved to the coupling resonance after the lattice correction is complete. Emittance plots presented here are given with tunes away from the coupling resonance.

The simulation data was also used to define the required maximum skew quadrupole strength. Figure 4.16 shows the expected probability distribution for the required maximum skew quadrupole strength. The 95-percentile value is 0.12 1/m.

4-2.2.5 Simulation of Beam Size Stability

Operation with $\kappa = \epsilon_y/\epsilon_x \approx 1$ is desirable in order to maximize the beam lifetime and reduce the impact of intrabeam scattering. The procedure for setting up the lattice described in the last section involves decoupling using skew quadrupoles to achieve $\kappa = 0.1$ with the fractional tunes moved apart by ~ 0.1 . However, the stability of the beam size and divergence when the tunes are moved together is a concern. In particular, the concern is that achieving stable beam sizes and divergences will require a very high level of tune stability.

This was simulated using the ensembles from the commissioning simulation. For each ensemble, 100 gaussian-distributed random values of the fractional tune separation were generated, with an rms parameter of $\sigma_{\Delta\nu} = 5 \times 10^{-3}$ and a cutoff of 3 sigma. All the Q1 and Q2 quadrupoles in a differentially series fashion (i.e., all Q1’s changed by the same amount and all Q2’s changed by the same amount) to achieve each value of the tune separation. With this completed, the equilibrium beam moments were computed. Statistics were then performed across the 100 tune separation instances for each ID source point, giving the fractional standard deviation of the beam sizes and divergences, rms tilt angle, etc. These were then histogrammed across all ensembles and all source

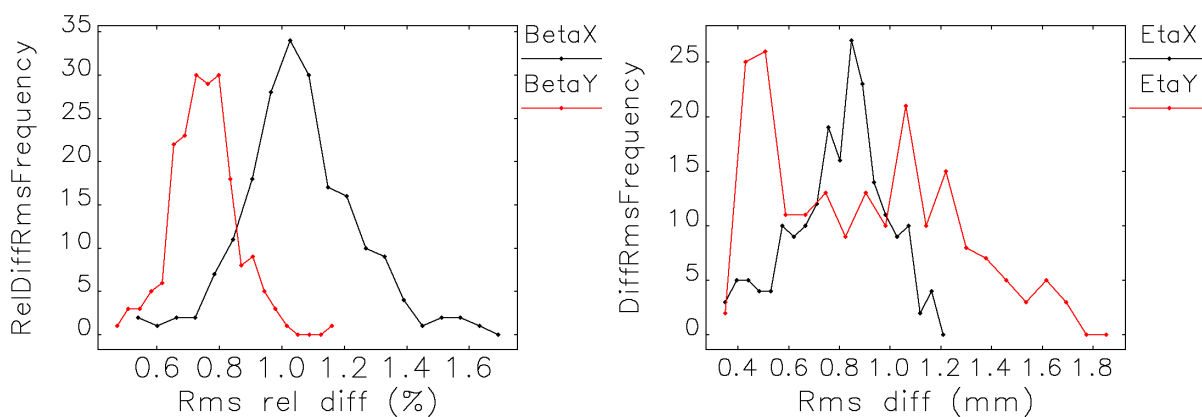


Figure 4.17. (Left): Final beta function errors. (Right): Final dispersion errors. Vertical dispersion distribution is the result of adjusting coupling from the minimum number to the requested 10%.

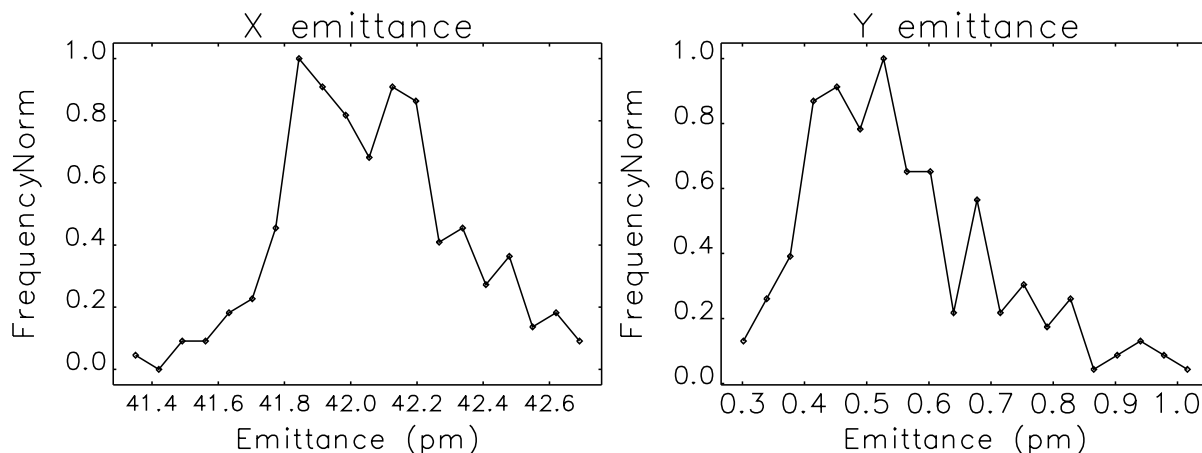


Figure 4.18. Distribution of horizontal (left) and vertical (right) emittance after lattice correction but before adjusting coupling.

points.

Figure 4.19 shows the histogram of the standard deviations of the fractional beam size variation. The variation is well under 10%, even for the rather extreme assumption of $\sigma_{\Delta\nu} = 5 \times 10^{-3}$. Figure 4.20 shows the histogram of the tilt angles in $x'-y'$ and $x-y$ space. The maximum values, excluding some clear outliers, are about 0.2 rad or less than 12 degrees, which seems tolerable. Given that this simulations imply a much larger tune variation than the specified 10^{-3} , it appears that beam size and tilt variation due to tune variation should not be an issue.

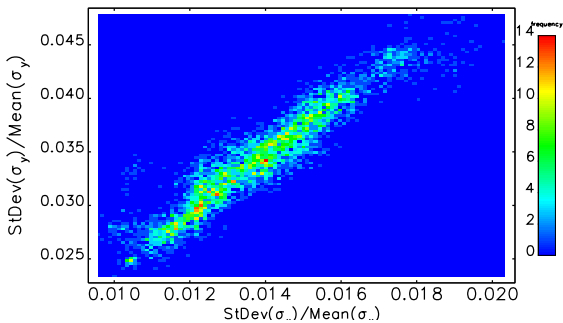


Figure 4.19. Distribution of standard deviation of beam sizes at IDs, normalized to the average beam size at IDs, assuming 5×10^{-3} rms variation in tune separation.

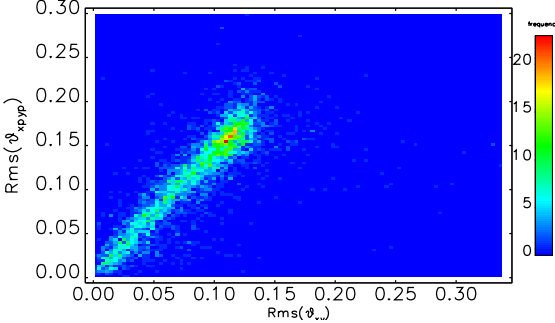


Figure 4.20. Distribution of rms tilt angles at IDs, assuming 5×10^{-3} rms variation in tune separation.

4-2.3 Lattice Evaluation

As described in [1], MOGA optimization of the nonlinear dynamics includes errors that are chosen so as to mock up the level of lattice errors and coupling that are expected in a reasonably well-corrected machine. This is intended to ensure that the lattice is robust against similar errors, rather than only against the specific set of errors used in MOGA optimization. However, it is necessary to verify that this is indeed the case. Toward this end, lattice evaluation was performed, which involves simulating a large number of error ensembles and determining statistics of the dynamic acceptance, lifetime, and other quantities. This starts from the results of simulations of orbit and lattice correction, as described in section 4-2.2.4. Physical apertures are included in the evaluation process, as detailed below.

4-2.3.1 Magnet Multipole Errors

Multipole errors are deviations of the field of a magnet from the ideal field. Most commonly, multipole errors are expressed as a fraction of the main magnet field. A $2(m+1)$ -pole main field, of multipole order m , may be described in terms of its normal and skew components, given respectively by

$$B_m = \left. \frac{d^m}{dx^m} B_y(x, y) \right|_{x=0, y=0} \quad (4.20)$$

and

$$A_m = \left. \frac{d^m}{dx^m} B_x(x, y) \right|_{x=0, y=0}. \quad (4.21)$$

Similarly, the normal and skew components B_n and A_n may be defined for any error multipole of order n . In terms of these quantities, the fractional normal $2(n+1)$ -pole error at the reference radius R is then

$$b_n = \frac{B_n R^n / n!}{|B_m + iA_m| R^m / m!}, \quad (4.22)$$

while the fractional skew error is

$$a_n = \frac{A_n R^n / n!}{|B_m + iA_m| R^m / m!}. \quad (4.23)$$

Typically, only one of A_m or B_m is non-zero.

The effects of multipole errors in the magnets are included at this stage, and doing so allows determining tolerances on such errors. In addition, insertion devices are not included in the MOGA optimization, but must be considered when the lattice is evaluated; this is done as a separate step, after determination of multipole error tolerances.

Multipole errors in dipoles, quadrupoles, and sextupoles can result from limitations of the design or from various construction errors. Multipole errors of the former type are systematic errors and are generally restricted to certain orders. Multipole errors of the latter type are random errors and may have any order. `elegant` allows specifying both types of error by giving an average value and an rms value for each multipole error. Because of the number of possible multipole errors, the search space for determining tolerances is practically unbounded, and a scheme must be developed to limit the range of possibilities.

Systematic multipoles have been computed for several of the dipole, quadrupole, and sextupole designs based on OPERA simulations. For normal-direction dipoles, systematic multipoles have been computed for the designs of the M1, M3, and M4 magnet types. These have been used for the simulations, with the M2 terms taken as identical to the M1 terms. The systematic fractional multipole errors, normalized to the dipole field, are listed in Table 4.21. Table 4.22 lists the values for the reverse-bend dipoles; these seem large only because the values are normalized to the relatively weak dipole field.

The multipole error levels for the Q1, Q2, Q3, Q6, and Q7 quadrupoles are listed in Tables 4.23 through 4.27. The tables show edge/body terms, which provide a more accurate method of simulation [2]. In addition to the edge and body multipoles, pseudo-multipoles are included [3, 4] in some situations (see below). Systematic multipoles for the sextupole magnets design are listed in Table 4.28.

Random multipole errors were included for dipoles, quadrupoles, and sextupoles, using gaussian distributions with a $2\text{-}\sigma$ cutoff. For dipoles, the flat-field and gradient magnets are treated differently

- For M1 and M2, the rms value for the sextupole was 2×10^{-4} , while for higher multipoles up to 18-pole it was 1×10^{-4} .
- For dipoles with gradients (M3, M4, Q4, Q5, and Q8), the random multipoles use the same distribution as for ordinary quadrupoles (see below).

For quadrupoles, a wealth of data is available from the National Synchrotron Light Source II (NSLS-II) [5]. These data give the rms values for multipole components from sextupole up to 40-pole and are thought to be applicable, in part, because the ratio of magnet bore to reference radius is nearly identical. In that case, the fractional random multipole errors scale linearly with the bore radius for all orders, and a factor of 2.5 increase (the ratio of NSLS-II to APS-U bore radius) may be expected from this fact alone. In addition, the construction of the APS-MBA magnets is more complex, with more degrees of freedom, which was accounted for with an additional factor of 2. Since the NSLS-II magnets were individually shimmed to correct multipoles below the decapole, and as this is not possible for the APS-MBA magnets, an additional factor of 2 was applied for sextupole and octupole errors. Finally, all fractional multipoles were rounded up with a resolution of 0.5×10^{-4} . The resulting random multipole errors are shown in Table 4.29.

For sextupoles (and quadrupoles), a theory exists [6] that connects construction errors such as random radius errors, pole placement errors, splitting errors, and rotation errors to multipole errors. This theory can be used in cases where other applicable data are lacking, e.g., for the sextupoles. Based on comparison of the scaled NSLS-II quadrupole data to the output of this theory, an rms error level of $30 \mu\text{m}$ was assumed for each construction error component and used in computing the random multipole error level for the sextupoles, which are listed in Table 4.30.

4-2.3.2 Beam Dynamics Effects from Undulators

Insertion devices can also contribute to decreased acceptance. There are three distinct effects.

- Vertical focusing is naturally present in a planar, horizontally-deflecting device. This introduces a tune error and beta-function beating in the vertical plane.

Table 4.21. Systematic normal multipoles for normal-direction dipoles

Order	M1,M2 10^{-4}	M3 10^{-4}	M4 10^{-4}
1	11.2	0.0	0.0
2	-12.3	1.5	0.8
3	0.7	-0.3	3.9
4	-10.1	-1.5	4.6
5	-5.7	5.7	1.3
6	-6.4	-3.0	-3.8
7	-0.8	0.4	-1.7
8	-0.1	-1.2	2.1

Table 4.22. Systematic normal multipoles for reverse-direction dipoles

Order	Q4 10^{-4}	Q5 10^{-4}	Q8 10^{-4}
2	-14.4	1.5	14.5
3	9.0	13.1	-24.7
4	-18.9	-21.8	56.2
5	16.8	20.8	-49.4
6	-6.2	-18.5	-13.1
7	12.7	21.8	17.5
8	-15.2	-19.7	-16.0

- A typical insertion device does not have a simple sinusoidal field that is uniform in x and y . Rather, it may kick particles at different amplitudes. This is usually characterized by a kickmap [7]. Use of a kickmap also provides accurate modeling of the focusing effect.
- Real-world insertion devices have multipole errors due to imperfections. Based on much experience at the APS, it is well known that these can be reliably reduced to small values. Hence, the existing APS specifications are used, as listed in Table 4.31

Although the insertion devices for the MBA lattice are not fully specified and designed, it is possible to get an idea of the possible impact of the IDs on the beam dynamics by using kickmaps for some existing devices. The kickmaps for six devices are as follows:

- NSLS-II in-vacuum undulators with periods of 20, 21, and 22 mm. These kickmaps were provided by Weiming Guo (NSLS-II) for a 3 GeV beam and were scaled to our energy of 6

Table 4.23. Q1 normal systematic multipoles at 10 mm

Order	Body 10^{-4}	Edge 10^{-4}	Integrated 10^{-4}
5	15.4	-9.0	-2.5
9	-2.1	-0.3	-2.7
13	-2.6	-0.3	-3.2

Table 4.24. $Q2$ normal systematic multipoles at 10 mm

Order	Body 10^{-4}	Edge 10^{-4}	Integrated 10^{-4}
5	14.0	-10.1	-6.0
9	-2.0	-0.4	-2.7
13	-2.5	-0.3	-3.1

Table 4.25. $Q3$ normal systematic multipoles at 10 mm

Order	Body 10^{-4}	Edge 10^{-4}	Integrated 10^{-4}
5	14.4	-10.2	-5.7
9	-2.0	-0.5	-2.9
13	-2.5	-0.3	-3.1

GeV.

- APS out-of-vacuum undulators with periods of 28, 30, and 36 mm. These kickmaps are based on fitting and tracking for 3D field maps [9, 10] and were scaled from 7 GeV to 6 GeV.

To simplify assembly of the lattice, two ~ 2.4 -m devices of the same period were installed in each straight, with a different device type used in each successive straight.

Because these devices will have an effect on the vertical tune and this was found to impact the vertical dynamic aperture, it is necessary to perform tune correction. This was done with a global knob for the Q1 and Q2 magnets. No attempt is made to reduce lattice function beats, since it appears to be unnecessary.

Additional ID effects include changes in the emittance due to additional energy losses, which tend to reduce the emittance, and additional quantum excitation, which tends to increase it. These are discussed in the context of intrabeam scattering effects and Touscheck lifetime in Section 4-2.8.1.

4-2.3.3 Effect of Errors on Dynamic and Momentum Acceptance

The multipole errors described above and the corrected lattice ensembles described in section 4-2.2.4 were used to assess the robustness of the lattice. The assessment involved computing the dynamic

Table 4.26. $Q6$ normal systematic multipoles at 10 mm

Order	Body 10^{-4}	Edge 10^{-4}	Integrated 10^{-4}
5	14.4	-10.2	-5.7
9	-2.0	-0.5	-2.9
13	-2.5	-0.3	-3.1

Table 4.27. $Q7$ normal systematic multipoles at 10 mm

Order	Body 10^{-4}	Edge 10^{-4}	Integrated 10^{-4}
5	15.2	-8.4	-1.6
9	-2.9	0.4	-2.1
13	-2.3	-0.3	-2.9

Table 4.28. Nominal systematic fractional normal multipole errors for sextupoles at 10 mm

Order	Normal 10^{-4}
8	-303
14	-14

acceptance and the local momentum acceptance, then using these results to determine the beam lifetime. The DA and LMA determination involved tracking for 1000 turns, including the main rf and harmonic rf systems set to provide a bucket height of $\pm 4.5\%$ with ideal bunch lengthening. The value of $\pm 4.5\%$ was used because it was found that larger bucket height did not increase the LMA, which is smaller than the results from MOGA (compare Fig. 4.4). This is thought to be a result of MOGA optimizing very well for a specific set of errors, the results of which do not entirely carry over for another set of (similar) errors.

Several cases were modeled and are compared in terms of the dynamic and local momentum acceptances. All cases included the same physical apertures:

- Standard ID chambers in sectors 1-35, unless otherwise noted below. These chambers have a horizontal semi-axis of 8 mm and a vertical semi-axis of 3 mm.
- Helical SCU chamber with an inside radius of 3 mm in Sector 4.
- $n = 6$ -superelliptical chamber with $a = 3$ mm and $b = 3$ mm in Sector 33. This is for a horizontal-gap SCU.
- Photon absorbers at locations and with horizontal apertures as specified in the vacuum design. These do not limit the linear acceptance but are included for completeness and to accurately locate the losses.
- Septum aperture, which is nominally a $n = 6$ superellipse with $a = 4$ mm and $b = 3$ mm in the Sector 39 straight section. The semi-axes are reduced to 3.7 mm and 2.7 mm, respectively, to account for orbit distortion inside the stored beam chamber from the leakage field.
- Kicker apertures, in the sector 38 and 39 straight sections. These are elliptical with $a = 6.7$ mm and $b = 4.2$ mm.
- Swap-out dump and vertical collimator: these ± 4.7 -mm vertical apertures are inside the A:M1 magnets in sectors 39 and 1, respectively. The collimator runs from the end of the A:M1.1 segment to the end of the A:M1.4 segment.
- Whole-beam dumps and horizontal collimators: these nominally-identical ± 4.8 -mm horizontal apertures are upstream of the A:Q4 magnets in sectors 37, 38, 39, 40, and 1. They are near the point of maximum horizontal beta and dispersion function, and so are well-positioned to

Table 4.29. Nominal rms values for random fractional multipole errors for quadrupoles and transverse-gradient dipoles at 10 mm

Order	Normal 10^{-4}	Skew 10^{-4}
2	10.5	16.5
3	12.5	3.5
4	3.0	3.0
5	5.5	2.0
6	1.5	2.0
7	2.0	1.0
8	0.5	0.5
9	1.0	0.5
10	0.5	0.5
11	0.5	0.5
12	0.5	0.5
13	0.5	0.5
14	0.5	0.5
15	0.5	0.5
16	0.5	0.5
17	0.5	0.5
18	0.5	0.5
19	0.5	0.5

intercept losses due to Touschek scattering and beam dumps.

Using these apertures, a number of cases were simulated, including:

- *Case 0*: No multipole errors.
- *Case 1*: Add systematic multipole errors using edge/body terms for quadrupoles. Also, include edge pseudo-multipoles on quadrupoles [11, 4].
- *Case 2*: Also add random multipole errors.
- *Case 3*: Also add steering and skew-linked multipoles.
- *Case 4*: Also add ID kickmaps and ID multipole errors, with tune compensation as described above.

Table 4.30. Nominal rms values for random fractional multipole errors for sextupoles at 10 mm

Order	Normal 10^{-4}	Skew 10^{-4}
1	0.0	0.0
2	0.0	0.0
3	8.9	8.9
4	9.1	5.5
5	4.5	0.9
6	2.6	1.8
7	0.7	0.7
8	0.8	0.3

Table 4.31. Effects of ID errors, original tolerance values [8], and achieved rms of distribution

Component	Units	Limit	Achieved rms of distribution
$\int B_x ds$	G-cm	100	50
$\int B_y ds$	G-cm	100	25
$\int (dB_x/dx) ds$	G	50	65
$\int (dB_y/dx) ds$	G	50	45
$\int (d^2 B_x/dx^2) ds$	G/cm	200	120
$\int (d^2 B_y/dx^2) ds$	G/cm	100	130
$\int (d^3 B_x/dx^3) ds$	G/cm ²	300	150
$\int (d^3 B_y/dx^3) ds$	G/cm ²	50	80

Figure 4.21 compares the DA for these 5 cases. The largest effect comes from the random multipole errors, followed by ID effects. Systematic and correction multipoles have very small effects, which are nearly invisible when viewed in this fashion. Use of edge/body multipoles gives results very similar to those obtained for integrated multipoles. Finally, ID kickmaps and multipole errors have a negligible effect. Based on previous comparisons, increasing the apertures for the HSCU and HGSCU would improve the DA, but not dramatically.

The expected emittances of the booster beam are 60 nm (16 nm) for the x (y) plane, giving rms beam size of 0.55 mm (0.17 mm). The 10th-percentile DA is thus approximately $\pm 4\sigma_x$ and $\pm 7\sigma_y$. Including possible emittance growth from high charge related effects, the most pessimistic emittances of the booster beam are 100 nm (20 nm) for the x (y) plane, giving rms beam size of 0.71 mm (0.19 mm). The 10th-percentile DA is then still approximately $\pm 3.1\sigma_x$ and $\pm 6.3\sigma_y$. Even with effective trajectory errors of several hundred microns, the DA appears adequate for high-efficiency capture. This is verified by simulations of injection that include additional sources of errors, as presented in 4-2.10.3.

The LMA is most meaningfully compared in terms of the Touschek lifetime. To this end, an approximate calculation was performed for each of the 100 LMA results for each of the cases described above. (A more detailed and accurate lifetime analysis is given in 4-2.8.1, with substantially improved results.) This calculation assumes that the rf systems are set to give the necessary bucket half-height to match each LMA, with the 4th-harmonic cavity set to ideally lengthen the bunch. Using these parameters, intrabeam scattering (IBS) is computed for the corresponding rms bunch duration assuming $\epsilon_y = \epsilon_x$. The results of the IBS computations are then used together with the LMA results to compute the Touschek lifetime. The results in Fig. 4.22 for 324-bunch, 200-mA mode show that there is little difference among the several of the above cases.

Further studies were performed to probe the effects of larger multipole errors in the lattice magnets. In particular, DA and LMA runs were performed in which each type of error was doubled. (The six “types” are random and systematic multipoles in dipoles, random and systematic multipoles in quadrupoles, and random and systematic multipoles in dipoles.) In comparison with the nominal case, only doubling of the random errors in quadrupoles had a significant effect. In this instance, the DA was slightly smaller. While further study is needed (e.g., combining cases with higher multipoles of all types) it seems probable that some multipole error requirements can be relaxed. This is different from what was found for the 67-pm lattice, for which increasing the random multipole errors in quadrupoles had a strong effect on the LMA. Part of the future efforts will be use of

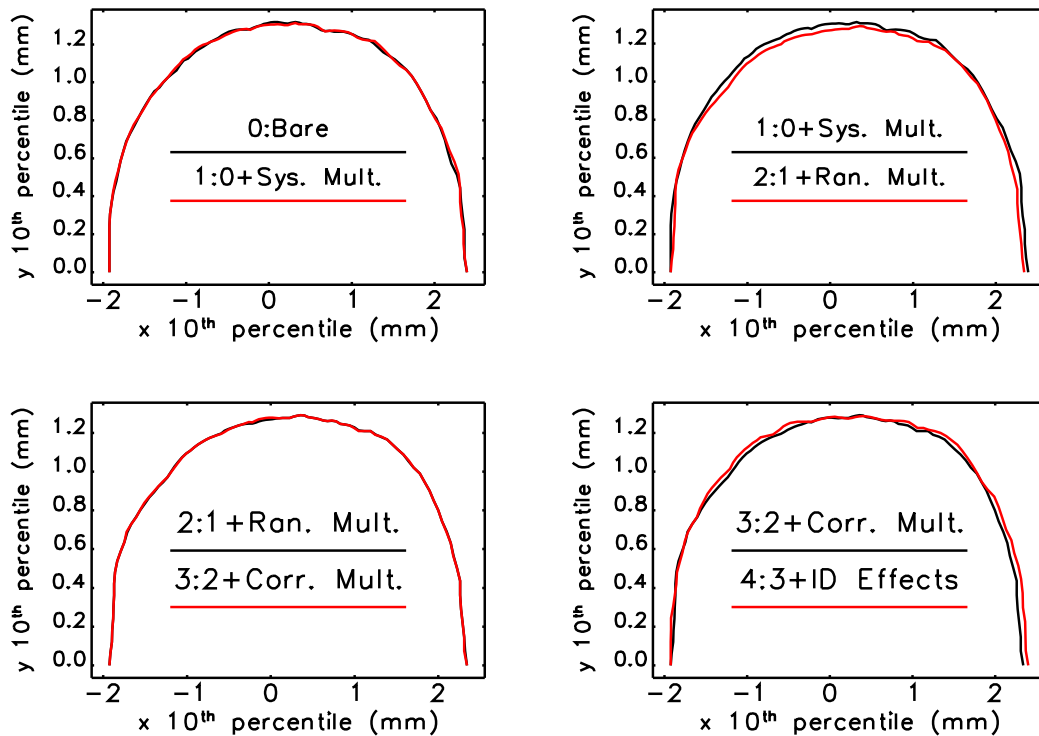


Figure 4.21. 10^{th} -percentile dynamic acceptance contours for five cases. See text for details.

mechanical stack-up simulations to determine probable random errors in various types of magnets [12].

References

- [1] M. Borland et al. *Multi-objective Direct Optimization of Dynamic Acceptance and Lifetime for Potential Upgrades of the Advanced Photon Source*. Tech. rep. ANL/APS/LS-319. APS, 2010 (cit. on p. 42).
- [2] M. Borland and R. Lindberg. “Modeling of Dipole and Quadrupole Fringe-Field Effects for the Advanced Photon Source Upgrade Lattice.” In: *Proc. NAPAC 16*. THPOA13 (cit. on p. 43).
- [3] G. E. Lee-Whiting. “End effects in first-order theory of quadrupole lenses.” In: *NIM A 76* (1969) (cit. on p. 43).
- [4] E. Forest. *Beam Dynamics: A New Attitude and Framework*. CRC Press, 1998 (cit. on pp. 43, 47).
- [5] A. Jain. *Private Communication*. 2014 (cit. on p. 43).
- [6] K. Halbach. “First Order Perturbation Effects in Iron-Dominated Two-Dimensional Symmetrical Multipoles.” In: *NIM A 74* (1969), p. 147 (cit. on p. 43).
- [7] P. Elleaume. “A New Approach to Electron Beam Dynamics in Undulators and Wigglers.” In: *Proc. of EPAC 1992*. 1992, pp. 661–663 (cit. on p. 44).

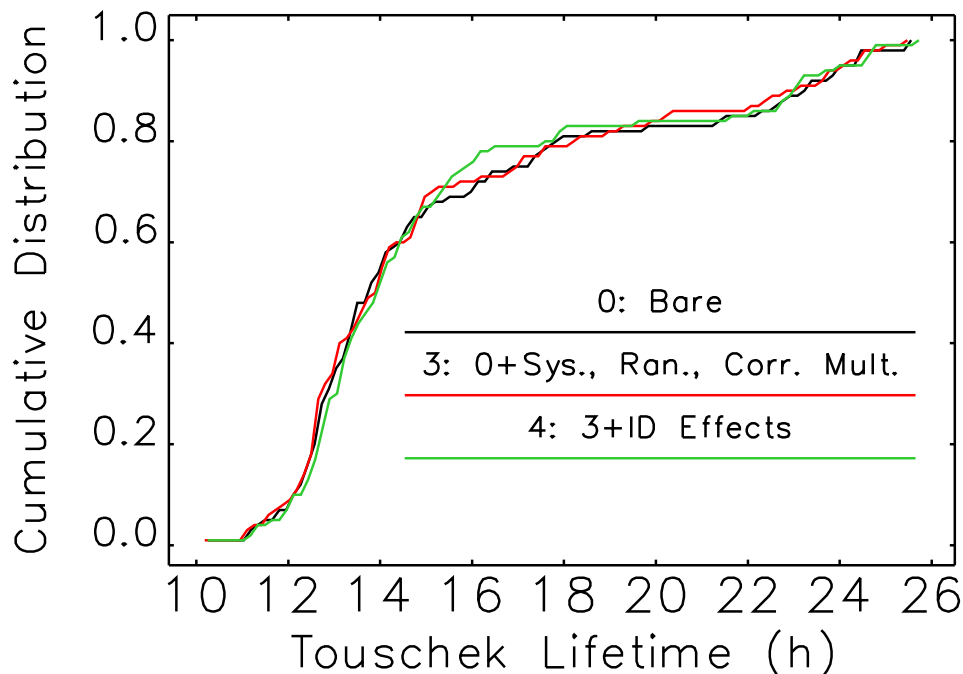


Figure 4.22. Cumulative distributions of approximate Touschek lifetime for several cases for 200 mA, 324-bunch, round-beam mode, as described in the text. A more detailed and accurate lifetime analysis is given in 4-2.8.1.

- [8] Y.-C. Chae and G. Decker. “Advanced Photon Source Insertion Device Field Quality and Multipole Error Specification.” In: *Proc. of PAC 1995*. 1995, pp. 3409–3411. URL: <http://cern.ch/AccelConf/p95/ARTICLES/RAR/RAR24.PDF> (cit. on p. 48).
- [9] A. Xiao. Private communication. 2014 (cit. on p. 45).
- [10] M. Jaski. Private communication. 2014 (cit. on p. 45).
- [11] G. E. Lee-Whiting. In: *NIM A* (1969) (cit. on p. 47).
- [12] J. Liu et al. “Field Quality from Tolerance Stack Up in R&D quadrupoles for the Advanced Photon Source Upgrade.” In: *NAPAC16*. 2017, pp. 904–906 (cit. on p. 49).
- [13] Y. Chae. “Impedance Database and Its Application to the APS Storage Ring.” In: *Proc. of PAC 2003*. 2003, pp. 3017–3019 (cit. on p. 53).
- [14] Y. Chae and Y. Wang. “Impedance Database II for the Advanced Photon Source Storage Ring.” In: *Proc. of PAC 2007*. 2007, pp. 4336–4338 (cit. on p. 53).
- [15] Y. Chae. “The Impedance Database Computation and Prediction of Single Bunch Instabilities.” In: *Proc. of PAC 2007*. Invited Talk. 2007 (cit. on p. 53).
- [16] R.R. Lindberg and A. Blednykh. “Instability thresholds for the Advanced Photon Source multi-bend achromat upgrade.” In: *Proc. of IPAC 2015*. 1822, p. 1882 (cit. on p. 53).

-
- [17] I. A. Zagorodnov and T. Weiland. “Field Solver for Particle Beam Simulations without Numerical Cherenkov Radiation.” In: *Phys. Rev. ST Accel. Beams* 8 (2005), p. 042001 (cit. on p. 54).
- [18] W. Bruns. *The GdfidL Electromagnetic Field simulator*. URL: <http://www.gdfidl.de> (cit. on p. 54).
- [19] M. Borland. *elegant: A Flexible SDDS-Compliant Code for Accelerator Simulation*. Tech. rep. ANL/APS LS-287. Advanced Photon Source, Sept. 2000. URL: <http://www.aps.anl.gov/Science/Publications/lnotes/ls287.pdf> (cit. on p. 55).
- [20] S. Krinsky and J. M. Wang. “Longitudinal instabilities of bunched beams subject to a non-harmonic rf potential.” In: *Particle Accel.* 17 (1985), p. 108 (cit. on p. 56).
- [21] D. Boussard. *Observation of microwave longitudinal instabilities in the CPS*. Report LabII/RF/INT/75-2. CERN, 1975 (cit. on p. 57).
- [22] M. Borland. *Comparison of ID aperture options for the 41-pm lattice*. Tech. rep. AOP-TN-2017-006. APS, Jan. 2017 (cit. on p. 58).
- [23] M. Borland et al. “Simultaneous Simulation of Multi-Particle and Multi-Bunch Collective Effects for the APS Ultra-Low Emittance Upgrade.” In: *Proceedings of the 2015 International Computational Accelerator Physics Conference*. 2015, pp. 61–65 (cit. on pp. 58, 72).
- [24] R. R. Lindberg, M. Borland, and A. Blednykh. “Collective Effects at Injection for the APS-U MBA Lattice.” In: *Proc. of NA-PAC 2016*. 2016 (cit. on pp. 58, 59).
- [25] A. Piwinski. *Wakefields and Ohmic Losses in Round Vacuum Chambers*. CERN-HERA-92-11. CERN, 1992 (cit. on pp. 60, 64).
- [26] K. Bane and M. Sands. *The Short-Range Resistive Wall Wakefields*. SLAC-PUB-95 7074. SLAC, 1995 (cit. on p. 60).
- [27] G. R. Lambertson. “Dynamic Devices – Pickups and Kickers.” In: *Physics of Accelerators*. Ed. by M. Month and M. Dienes. 153. AIP, 1987, p. 1414 (cit. on p. 65).
- [28] D. A. Goldberg and G. R. Lambertson. *Dynamic Devices – a Primer on Pickups and Kickers*. Tech. rep. LBL-31664. LBL, Nov. 1991 (cit. on p. 65).
- [29] A. Blednykh, W. Cheng, and S. Krinsky. “Stripline beam impedance.” In: *Proc. of PAC 2013*. 2013 (cit. on p. 65).
- [30] R. E. Collin. *Field Theory of Guided Waves*. John Wiley & Sons, 1991 (cit. on p. 65).
- [31] J. H. Billens and L. M. Young. *Poisson Superfish*. LANL (cit. on p. 65).
- [32] X. Sun and C. Yao. “Simulation Studies of a Prototype Stripline Kicker for the APS-MBA Upgrade.” In: *Proc. of NA-PAC 2016*. 2016, pp. 874–876 (cit. on p. 65).
- [33] E. Koukovini-Platia, G. Rumolo, and C. Zannini. “High frequency electromagnetic Characterization of NEG Properties for the CLIC damping rings.” In: *Proc. of IPAC 2014*. 2014, p. 2384 (cit. on p. 68).
- [34] G. Goubau. “Surface Waves and their Application to Transmission Lines.” In: *J. Appl. Phys.* 21 (1950), p. 1119 (cit. on p. 69).
- [35] J. Musson and S. Rubin K. Cole and. “Application of Goubau Surface Wave Transmission Line for Improved Bench Testing of Diagnostic Beamline Elements.” In: *Proc. of PAC 2009*. 2009, p. 4060 (cit. on p. 69).
-

- [36] www.cst.com. *CST Microwave Studio Suite*. 2013 (cit. on p. 69).
- [37] H. Wiedemann. *Particle Accelerator Physics*. 2nd. Vol. I. Springer, 1998 (cit. on p. 72).
- [38] D. Sagan. “On the Physics of Landau Damping.” In: *Am. J. Phys.* 62 (1994), p. 450 (cit. on p. 73).
- [39] C. Pellegrini. “On a New Instability in Electron-Positron Storage rings (The Head-Tail Effect).” In: *Nuovo Cimento* 64.2 (Nov. 1969). <http://link.springer.com/content/pdf/10.1007/BF02754905.pdf>, p. 447 (cit. on p. 73).
- [40] J. Paterson et al. “Fast Damping of Transverse Coherent Dipole Oscillations in SPEAR.” In: *IXth Int. Conf. of HEAC*. Also a SLAC-PUB-1433, <http://www.slac.stanford.edu/pubs/slacpubs/1000/slac-pub-1433.html>. 1974, p. 339 (cit. on p. 73).
- [41] R. Lindberg. Private communication. 2017 (cit. on p. 73).
- [42] M.G. Minty, A.W. Chao, and W.L. Spence. “Emittance Growth Due to Decoherence and Wakefields.” In: *Proc. of PAC 1995*. 1995, pp. 3037–3039 (cit. on p. 74).
- [43] G.V. Stupakov and A.W. Chao. “Study of Beam Decoherence in the Presence of Head-Tail Instability Using a Two-Particle Model.” In: *Proc. of PAC 1995*. 1995, pp. 3288–3290 (cit. on p. 74).
- [44] C. Yao et al. “AN FPGA-BASED BUNCH-TO-BUNCH FEEDBACK SYSTEM AT THE ADVANCED PHOTON SOURCE.” In: *Proc. of PAC 2007*. <http://accelconf.web.cern.ch/AccelConf/p07/PAPERS/MOPAN116.PDF>. 2007, p. 440 (cit. on p. 75).
- [45] R. A. Bosch, K. J. Kleman, and J. J. Bisognano. “Robinson instabilities with a higher-harmonic cavity.” In: *Phys. Rev. ST Accel. Beams* 4 (2001), p. 074401 (cit. on pp. 75, 77).
- [46] L. Emery. *User’s Guide to Program clinchor*. http://www.aps.anl.gov/Accelerator_Systems_Division/Operations_Analysis/manuals/clinchor_V1.0/clinchor.html (cit. on p. 78).
- [47] L. Emery. “Required Cavity HOM DeQing Calculated from Probability Estimates of Coupled Bunch Instabilities in the APS Ring.” In: *Proc. of PAC’93*. Washington DC, May 1993, p. 3360. URL: http://accelconf.web.cern.ch/AccelConf/p93/PDF/PAC1993_3360.PDF (cit. on p. 78).
- [48] R. Siemann. “Instability Growth Rate Calculations for High Energy Storage Rings.” In: *IEEE Transactions on Nuclear Science*. Vol. NS-28. 3. Proceedings of the 1981 PAC. June 1981, pp. 2437–2439. URL: http://cern.ch/AccelConf/p81/PDF/PAC1981_2437.PDF (cit. on p. 78).
- [49] J. Hagel and B. Zotter. “PC-BBI, a Program to compute Bunched Beam Instabilities on a PC.” In: *Proc. of EPAC 1990*. 1990, p. 1717. URL: http://accelconf.web.cern.ch/AccelConf/e90/PDF/EPAC1990_1717.PDF (cit. on p. 78).
- [50] K. Thompson and R. D. Ruth. “Transverse coupled bunch instabilities in damping rings of high-energy linear colliders.” In: *Phys. Rev. D* 43 (1991), pp. 3049–3062. DOI: [10.1103/PhysRevD.43.3049](https://doi.org/10.1103/PhysRevD.43.3049) (cit. on p. 78).
- [51] D. Teytelman and J. Byrd. *Private Communication*. Jan. 2017 (cit. on pp. 78, 81).
- [52] Computer Simulation Technology. *CST Studio Suite 2010*. <http://www.cst.com> (cit. on p. 78).

4-2.4 Impedance and Single-Bunch Stability

The maximum single-bunch current in a storage ring is determined by the physics during and directly after the injection of additional charge. In the usual method of injection with accumulation (which is presently used at the APS), the current reaches a limit when the added charge equals the amount lost by the stored and injected beam during the injection process. In the swap-out method of injection planned for the APS Upgrade, the full bunch charge must be stably injected into an empty bucket. The number of electrons lost in either method depends on a number of factors, including the size of the dynamic aperture relative to the emittance of the injected bunch, treated in Section 4-2.3, and the errors in the injection system as discussed in Section 4-2.10; nevertheless, any injection scheme is ultimately limited by collective effects whose influence increases with the stored bunch current. Hence, insuring that the full 4.2 mA/bunch can be stably injected requires a thorough understanding of the various collective effects that may limit single-bunch current. The sources of collective effects may include electron cloud, ions, and impedance elements in the ring. Observations indicate that electron cloud effects typically do not cause serious problems in electron storage rings, and they are not expected to play a role at the APS-U; ions may cause some issues depending on the pressure and bunch pattern, and will be discussed further in Section 4-2.6. On the other hand, the perturbations due to impedances/wakefields will always be present, and have in the past been observed to cause various instabilities that often limit the single-bunch current. To be more specific, transverse wakefields drive transverse beam instabilities that typically limit the single-bunch current in storage rings like the APS, while longitudinal wakefields predominantly lead to bunch lengthening (which usually eases operational requirements) and an increase in energy spread (which is typically not too detrimental). Longitudinal and transverse impedances will continue to be the dominant drivers of collective effects for the APS Upgrade, so that understanding and calculating the impedance is critical for accurate simulations—and thus accurate predictions—of the ring performance. Based on such simulations, the impedance cost of various vacuum component designs can be assessed, and limits will be imposed on sources of impedance to ensure that the desired parameters, including the single-bunch current, are achieved.

A method for calculating impedances and using these results in predictive simulations of the storage ring has already been developed and implemented at the APS. This impedance model has successfully reproduced various impedance-driven collective effects observed in the APS ring [13, 14, 15, 16], and can be extended to the APS upgrade in a straightforward manner once the primary impedance sources have been identified and analyzed. The next subsection briefly describes the APS-U impedance model that has been developed, after which simulation predictions of the longitudinal collective effects, including bunch lengthening and the onset of the microwave instability, are presented. Following this it is shown how a transient instability at injection can lead to particle loss at high (4.2 mA) single-bunch current; fortunately, simulations indicate that a modest transverse feedback system can cure this instability. Next, a more detailed discussion of the longitudinal impedance and rf-heating associated with important wakefield sources, including the BPM-bellows assembly, the injection and extraction kicker, and the in-line photon absorbers, is presented. To complement and cross-check the simulation efforts described above, the planned rf measurement technique is briefly introduced in Section 4-2.4.4. Finally, this section concludes with an overview of the findings, and what additional efforts are being made to proceed toward the final design.

Table 4.32. Elements that contribute to the resistive wall and geometric impedances. Here, the full gap refers to the diameter for circular chambers and the major \times minor axes for elliptical chambers, and BPM = beam position monitor.

Resistive wall			Geometric contributions			
Metal	Full gap	Length	Sector ($\times 40$)		Ring	
			Element	Number	Element	Number
Cu	22 mm	224 m				
Al	22 mm	590 m	BPM-bellows	14	Injection kicker	4
SS	22 mm	80 m	In-line absorber	19	Extraction kicker	4
Al	16 \times 6 mm	170 m	Gate valve	4	Small-gap ID BPM	30
Al	6 mm	20 m	Flange	47	352 MHz rf-cavity	10
Al	140 mm	20 m	ID transition	1	Rf transitions	3
			Crotch absorber	2	4 th harmonic cavity	1
			Pumping cross	5		

4-2.4.1 Impedance Model

It is important to recognize that any attempt to model collective effects will only be as good as its ability to properly identify and model the various sources of impedance in the ring. For the APS-U this is done largely by relying on the experience obtained while developing the impedance model for the present APS, and by carefully studying the methods and models developed at other storage rings. Table 4.32 summarizes the various components that contribute to the impedance model for the upgrade vacuum system. First, the resistive wall contribution is calculated by applying the analytic formulas appropriate for the round and elliptical chambers listed in Table 4.32. The resistive wall contributes the largest source of transverse impedance, due, in particular, to the narrow gaps of the insertion device (ID) straight sections. In contrast, the geometric impedance depends on the detailed cross-sectional variation of various components along the vacuum vessel, so that computing it requires additional numerical simulation tools and methods.

The geometric contribution is built from the individual impedances/wakefields generated by various elements around the ring. A list of these wakefield-producing components is also tabulated in Table 4.32. The geometric impedance for each of these elements is computed from the Fourier transform of the wakefield, and the wakefields themselves are obtained from finite-difference time domain codes. The wakefields produced by components possessing axial symmetry (such as the flange gaps) are computed with the 2D ECHO code [17], while the commercial finite-difference time domain code GdfidL [18] is used to calculate most of the wakefields from structures that vary in 3D. To balance numerical efficiency and accuracy, each of these codes models the (point particle) wakefields with the wake potential generated by a gaussian bunch with a 1-mm rms length, as this approximation has had good success in predicting the onset of various instabilities in the current APS. In addition, numerical tests with similar MBA lattices have been performed by using wake potentials derived from shorter electron bunches, and these have proven to give the same results in terms of the single-bunch current limit. Since using this “pseudo-Green function” derived from a 1-mm bunch is equivalent to filtering the point-charge impedance by a Gaussian filter whose frequency width is ~ 50 GHz, this implies that collective effects in the APS-U are insensitive to frequency components of the impedance that are higher than this. As a point of reference, the zero-current frequency spectrum of the electron bunch including the higher-harmonic cavity (HHC)

Table 4.33. Characterization of the longitudinal impedance contribution of various impedance elements in terms of the total (ring summed) $\Im(Z_{\parallel})/n$ and the loss factor of a 50-ps bunch.

Impedance source	Number	$\Im(Z_{\parallel})/n$ (Ω)	$k_{\text{loss}}(\sigma_t = 50 \text{ ps})$ (V/pC)
BPM-bellows	560	0.048	0.090
In-line absorber	760	0.060	0.045
Gate valve	160	0.020	0.002
Flange	1880	0.011	$< 10^{-3}$
ID transition	40	0.0018	$< 10^{-3}$
Crotch absorber	80	0.0070	0.002
Pumping cross	200	0.0015	$< 10^{-3}$
Inj/ext kickers	8	0.0075	0.94
Small-gap ID BPM	30	0.0013	0.008
352 MHz rf-cavity	10	0.001	3.8
Rf transitions	3	0.018	0.84
Resistive wall	NA	NA	2.18
Total	NA	0.18	7.9

is ~ 3.2 GHz.

The longitudinal impedance contributions are summarized by their $\Im(Z_{\parallel})/n$ and loss factor in Table 4.33. The former gives a rough estimate of the relative contribution to the microwave instability, while the latter quantifies the energy loss to wakefields; the zero-current bunch length of 50 ps was chosen to compute the loss factor because κ_{loss} is typically negligibly small for the > 70 ps bunch length expected at equilibrium in 48 bunch mode. Table 4.32 indicates that the BPMs and in-line photon absorbers are a dominant source of longitudinal impedance, largely because there are so many in the ring. Specific design choices for these components along with expected levels of rf heating will be discussed further in Section 4-2.4.3.

The transverse impedance is also of critical importance, as it can drive instabilities in the transverse plane at high current. The driving terms of these transverse instabilities scale as the product of the local dipole impedance with the beta function, so that we plot the beta function-weighted transverse impedances in Figure 4.23. The biggest source of transverse impedance is due to the resistive wall in the narrow gap insertion device straights. This can be recognized as the large contribution at $f \rightarrow 0$ that falls off $\sim |f|^{-1/2}$ at higher frequency. The next two largest contributions come from the BPM-bellows and the in-line photon absorbers, which also contribute nearly all the narrow resonance-like peaks seen in Figure 4.23. It should be noted that slight variations in individual components will tend to broaden these resonance lines and decrease their amplitudes. To test what effect this might have, simulations were run that compared the instability threshold from a sum of identical resonator impedances with ones that varied in frequency. It was found that the differences between these cases were minimal; if anything, varying the resonator parameters slightly increased the stability threshold, which implies that assuming all components are the same is at worst slightly conservative.

4-2.4.2 Predictions of collective beam dynamics from tracking

Once sources of impedance have been identified and modeled, they are then used with the tracking code `elegant` [19] to predict various collective effects in the APS-U. To this end, several methods

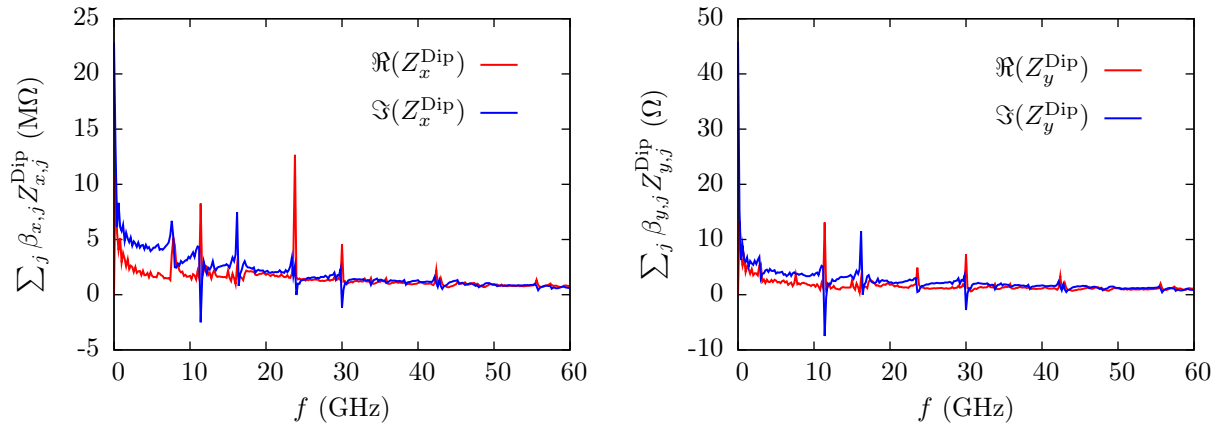


Figure 4.23. Beta function-weighted transverse dipole impedance for the APS-U ring.

of modeling wakefields within `elegant` have been developed. The simplest such model lumps all sources of impedance into a single “impedance element” that is then applied once per turn. This method is used in the present APS model, and has proven to be quite accurate when the collective response is built up over many turns, as is the case for the longitudinal dynamics and most transverse instabilities. The longitudinal impedance is determined by summing the impedance contribution from all components in the ring, $Z_z^{\text{tot}}(\omega) = \sum_j Z_{z,j}(\omega)$ for each component j , while the total transverse impedance of the ring is found by weighting the individual geometric contributions by their respective local lattice functions and summing. More precisely, the total geometric impedances along x and y are given by

$$Z_x^{\text{tot}}(\omega) = \frac{1}{\beta_x} \sum_{\text{elements } j} \beta_{x,j} Z_{x,j}(\omega) \quad Z_y^{\text{tot}}(\omega) = \frac{1}{\beta_y} \sum_{\text{elements } j} \beta_{y,j} Z_{y,j}(\omega), \quad (4.24)$$

where the lattice functions at element j are denoted by $\beta_{x,j}$ and $\beta_{y,j}$, while β_x and β_y are the lattice functions at the location where the impedance element is applied. The lumped (total) impedance is then applied at a single location in `elegant`, and the results of particle tracking are used to determine the influence of collective effects. Particle tracking also uses a lumped model, wherein the entire ring lattice is represented by a single element that includes nonlinearities in the transverse and longitudinal motion, as well as a lumped synchrotron radiation model. The main and harmonic rf systems are modeled as ideal cavities tuned for a nominally flat potential, which lengthens the bunch without beginning to split it. The lumped impedance model has been applied to assess how the longitudinal impedance lengthens the bunch as a function of current, to predict the current at which the microwave instability occurs, and to determine the current at which the transverse impedance drives instabilities from equilibrium. The longitudinal predictions are made by tracking 100,000 particles in `elegant` over 30,000 turns for a range of initial currents, and averaging the last 15,000 turns once equilibrium has been reached. Results from this study are summarized in Fig. 4.24. Figure 4.24(a) shows the predicted bunch length as a function of current, while Fig. 4.24(b) shows how the energy spread increases above the microwave instability threshold of about 1.7 mA. This current is almost three times the 0.63 mA/bunch in 324-bunch mode, but well below the 4.2 mA/bunch planned for 48 bunch mode. As a point of reference, Wang and Krinsky’s version [20]

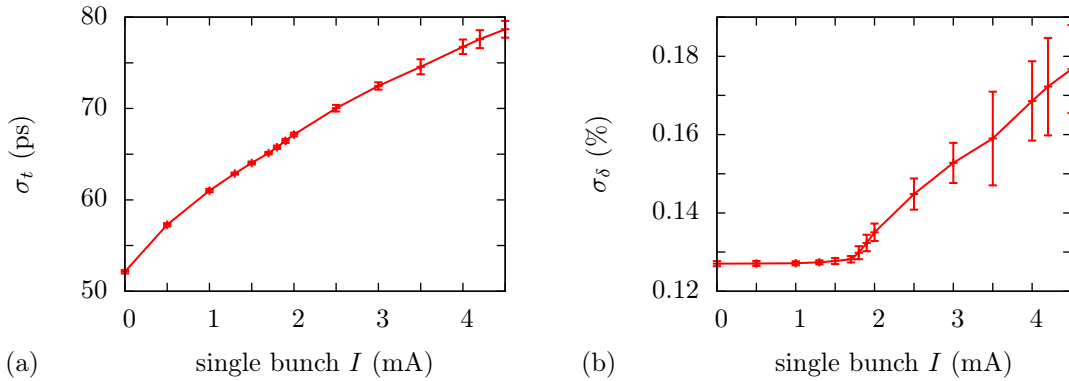


Figure 4.24. Bunch lengthening (a) and energy spread increase (b) as a function of current. Error bars denote $\pm 2\sigma$ fluctuations.

of the Boussard criterion [21] gives

$$I_{\text{MWI}}^{\text{Boussard}} = \sqrt{\frac{\pi}{2}} \frac{\gamma \alpha_c I_A \sigma_z Z_0}{C_R |Z_{\parallel}/n|} \approx 0.5 \text{ mA}, \quad (4.25)$$

where the Alfvén current $I_A \approx 17 \text{ kA}$, the impedance of free space $Z_0 \approx 377 \Omega$, and C_R is the ring circumference. It is well-known that the Boussard criterion typically underestimates the microwave instability threshold by a factor of 2 or more, which is consistent with the difference between the estimate in (4.25) and what is shown in the tracking studies.

Error bars in Figure 4.24 show expected $\pm 2\sigma$ levels of fluctuation in the bunch length and energy spread, which become rather significant above the microwave instability threshold. Nevertheless, the present APS operates in hybrid mode with a single bunch current that is more than two times larger than the microwave instability threshold with no apparent difficulties, and it is anticipated that the APS-U can do the same.

Before proceeding further, it may be useful to compare the results plotted in Figure 4.24 with those in the section on beam dynamics with the HHC presented in Figure 4.63. The latter simulates collective dynamics in the presence of a passive HHC as a function of the total ring current, showing how the rms bunch length and energy spread evolve as the increasing current drives both a larger voltage in the HHC and larger collective wakefields. Here, on the other hand, Figure 4.24 uses a prescribed harmonic voltage that exactly flattens the rf potential, so that in effect it describes the longitudinal collective dynamics under the assumption that the full 200 mA is always driving the HHC. This is why, for example, Figure 4.24 here shows the onset of the microwave instability at a single bunch current of 1.75 mA when the bunch is $\sim 65 \text{ ps}$ long, whereas the self-consistent HHC simulations of Figure 4.63 shows evidence of the microwave instability between 1 and 1.5 mA when $\sigma_t \approx 30 \text{ ps}$. In addition, Figure 4.63 shows that overstretching the bunch to $\sim 100 \text{ ps}$ reduces the severity of the microwave instability at full 4.2 mA/bunch current, such that both the energy spread increase and its fluctuation is half of what is plotted here in Figure 4.24(b).

Additional simulations using the same method of tracking with the lumped impedance were also done to determine the single-bunch instability threshold. These simulations tracked 200,000 macroparticles over 30,000 passes for various initial bunch currents. Once equilibrium was established after

15,000 turns, the beam was perturbed by 100 microns in x and y to initiate any potential instability, and the simulation output was investigated for evidence of undamped transverse oscillations and/or particle loss⁵. Results predict the APS-U to be safe from transverse instabilities starting from equilibrium by a rather large margin at the operational chromaticity of $+5/+5$; in particular, it was found that the beam does not go unstable until the single-bunch current reaches about 10 mA, which is well above the required 4.2 mA/bunch in 48 bunch mode. While at these currents the beam displays significant longitudinal fluctuations due to the microwave instability, the high instability threshold current is quite encouraging. In fact, one might wonder if the vacuum design is too conservative, and that perhaps something like smaller ID gaps might be possible. Leaving aside the fact that other simulations show that smaller ID gaps have detrimental effects on the dynamic aperture [22], it turns out that there are transient collective instabilities during and after injection that lead to a much more stringent limit on the single bunch current that can be injected into the ring. This is because the longitudinal mismatch between the injected booster beam and the APS-U storage ring causes the bunch to tumble in the rf bucket, which leads to longitudinal substructure and local current peaks in the injected bunch. The longitudinal dynamics in turn drives anomalously strong transverse wakefields and a transient transverse instability that can result in beam loss [23, 24].

Proper simulation of collective effects during injection provides a unique challenge. Because the injection process occurs over a relatively small ($\lesssim 500$) number of turns and involves distributions of particles that are far from equilibrium, it appears that a full accounting of physics within a single turn will be important. For this reason, injection simulations employ element-by-element tracking—both with and without errors—including synchrotron radiation, the full array of physical apertures, and an impedance that is distributed over the ring. The distributed impedance model is composed of 15 impedance elements per sector, with one located at the midpoint of every ID straight section, and the other 14 placed next to each BPM. Each impedance element is repeated 40 times around the ring for the tracking, and includes both resistive wall and geometric contributions that are weighted by the relative β -function in a manner analogous to Eq. (4.24). As one example, the impedance element at the middle of any straight section includes 1/40th of the total resistive wall component of all narrow gap IDs, and 1/40th of the geometric contribution of all 8 injection/extraction kickers, all 30 narrow gap BPMS, and the rf cavities and transitions; as another example, each impedance element at the AP5 BPM situated between the Q7 quadrupole and the M3 dipole contains the resistive wall component from about 1.6 m of the arc in addition to the geometric contributions from 3 flanges, 1 BPM-bellows assembly, 1 in-line photon absorber, and 1 pumping cross.

The distributed impedance model was then applied to simulations of the injection process into the APS-U ring. These simulations track 200,000 particles element-by-element through the ring, and assume that the initial booster beam has a nominal rms bunch length and energy spread of 100 ps and 0.12%, respectively, while the transverse emittances are $\varepsilon_x \times \varepsilon_y = 60 \times 16$ pm. In this case, the bunch is $\sim 30\%$ longer while the energy spread 50% smaller than the ring equilibrium, in addition to being mismatched to the flattened rf potential provided by the fourth harmonic cavity. In 324-bunch mode the single bunch charge is sufficiently low such that little to no transverse oscillations are excited, and 100% of the injected beam can be stored. On the other hand, in 48-bunch mode simulations predict that the initial longitudinal tumbling in the rf-bucket drives strong transverse wakefields that in turn drive a vertical instability. The resulting vertical motion reaches the wall

⁵The simulations are insensitive to the initial perturbation, with displacements of 50 and 200 microns giving nearly identical predictions.

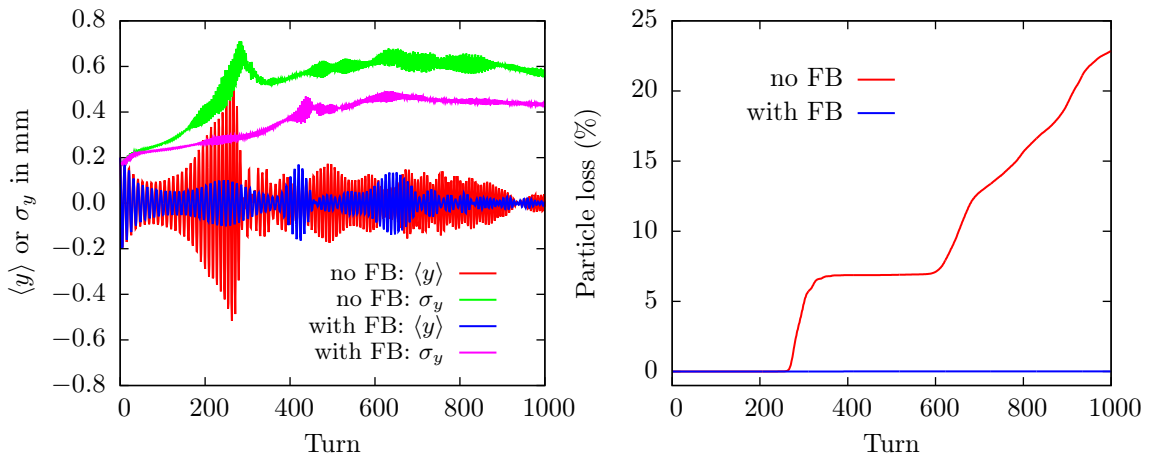


Figure 4.25. Collective transverse dynamics at injection. (a) compares vertical beam size and centroid dynamics assuming no feedback (no FB) to that including transverse feedback (with FB). (b) plots the corresponding particle loss.

Table 4.34. Level of transverse feedback required for stable injection assuming different longitudinal distributions from the booster. The bunch duration $\sigma_t = 100$ ps unless listed otherwise.

	$\sigma_\delta = 0.12\%$	$\sigma_\delta = 0.15\%$, $\sigma_t = 80$ ps	$\sigma_\delta = 0.18\%$	$\sigma_\delta = 0.2\%$
Required maximum feedback kick	1 μrad	0.5 μrad	0.5 μrad	0.4 μrad

and the beam loses a significant amount of charge as shown by the “no FB” (no feedback) case in Figure 4.25(a) and (b). This instability can be controlled and the beam loss eliminated by applying bunch-by-bunch transverse feedback. A simulation including feedback is shown as the “with FB” case in Figure 4.25(a) and (b), where the feedback system is simulated using the TFBPICKUP and TFBDRIVER element in *elegant* including a 6-turn FIR filter and a maximum kick strength of 1 μrad . For the present simulation, the feedback pickup and driver were both placed in the center of the ID straight, which is not ideal; nevertheless, the feedback strength required can be readily achieved with the present APS feedback amplifiers.

In addition, the required feedback strength can be further reduced if the longitudinal phase space from the booster is better matched to that of the storage ring, and simulations indicate that increasing the energy spread beyond 0.12% is particularly beneficial. The increased energy spread could be achieved by operating the booster with a mean beam energy $\sim 1\%$ below the design orbit (rather than the presently used -0.6%), which would also have the added benefit of reducing the transverse emittance. The required feedback strength is summarized in Table 4.34 for several different assumptions regarding the longitudinal distribution out of the booster.

Finally, some simulations of previous APS-U lattices showed that lattice errors could potentially exacerbate instabilities at injection and significantly affect injection efficiency [24]. However, it has since been understood that this sensitivity to errors is caused by energy offsets of the closed orbit in the presence of large second-order chromatic terms. The present lattice has reduced the vertical second-order chromaticity by more than a factor of two, and the commissioning scheme now does a much better job in correcting any energy offset. Hence, it is expected that lattice errors should not

play a large role, and in fact injection simulations that include errors have so far shown that lattice errors play only a minor role. Additional injection simulations with collective effects are planned for the future to test a wider range of error sets and to refine the requirements on the transverse feedback system.

4-2.4.3 Longitudinal Impedance and Rf Heating

As mentioned previously, the transverse wakefields limit the maximum stable current, while longitudinal wakefields predominantly lead to bunch lengthening, increased energy spread, and rf heating of vacuum chamber components. The last of these can become a serious issue if vacuum components are not properly designed. For a Gaussian bunch with N_e electrons, the energy ΔE lost by the bunch is $\Delta E = \kappa_{\text{loss}}(eN_e)^2$, where the loss factor κ_{loss} depends on the bunch length σ_z and the longitudinal impedance Z_{\parallel} (or wakefield W_{\parallel}) in the following manner,

$$\kappa_{\text{loss}} = \frac{1}{\pi} \int_0^{\infty} d\omega e^{-\omega^2 \sigma_z^2 / c^2} \Re Z_{\parallel}(\omega) = \frac{c}{\pi} \int_0^{\infty} d\tau \frac{e^{-\tau^2 / 2\sigma_z^2}}{\sqrt{2\pi}\sigma_z} W_{\parallel}(\tau). \quad (4.26)$$

Here, the co-moving coordinate $\tau \equiv s - ct$, while W_{\parallel} and Z_{\parallel} are the longitudinal wakefield and its associated impedance. When the material conductivity is moderate to high, the total loss factor can be decomposed into a sum of the geometric loss factor and the resistive-wall loss factor:

$$\kappa_{\text{loss}} = \kappa_{\text{loss}}^{\text{rw}} + \kappa_{\text{loss}}^{\text{geo}}. \quad (4.27)$$

For simple structures, the geometric loss factor can be derived analytically, but in most cases the geometry is sufficiently complex so that $\kappa_{\text{loss}}^{\text{geo}}$ can only be calculated numerically. The following analysis focuses on a bunch length of 15 mm at full current, which is the length expected due to the bunch-lengthening harmonic cavity alone (i.e., without including the effects of longitudinal wakefields). At equilibrium, Fig. 4.24(a) shows that the bunch length in 48-bunch mode is expected to be > 70 ps, but the bunch length may be significantly shorter than this during the first injection cycle prior to establishing sufficient voltage in the HHC (see Fig 4.63). Nevertheless, preliminary analysis shows that the quadratic scaling of P_{loss} with current typically more than makes up for the increase in κ_{loss} at smaller bunch lengths.

The resistive wall wakepotentials have been derived analytically for a round vacuum chamber by Piwinski in Ref. [25]; along the axis the longitudinal wakepotential is expressed as

$$W_{\parallel}(\tau) = \frac{r_e m c^2 N_e}{2b\sqrt{2\mu_r Z_0 \sigma_{\text{cond}}}} \left| \frac{\tau}{\sigma_z} \right|^{3/2} e^{-\tau^2 / 4\sigma_z^2} \times \left[I_{1/4} \left(\frac{\tau^2}{4\sigma_z^2} \right) - I_{-3/4} \left(\frac{\tau^2}{4\sigma_z^2} \right) - \text{sgn}(\tau) I_{-1/4} \left(\frac{\tau^2}{4\sigma_z^2} \right) + \text{sgn}(\tau) I_{3/4} \left(\frac{\tau^2}{4\sigma_z^2} \right) \right], \quad (4.28)$$

where $I_n(x)$ is the modified Bessel function of the first kind, b is the chamber radius, r_e the classical electron radius, $Z_0 \approx 120\pi \Omega$ is the impedance of free space, σ_{cond} is the material's electrical conductivity, and μ_r its relative permeability. Bane and Sands demonstrated in Ref. [26] that Piwinski's result is valid when the rms length of the Gaussian electron bunch satisfies $\sigma_z \gg (2b^2 / Z_0 \sigma_{\text{cond}})^{1/3}$; for the APS Upgrade this condition requires σ_z to be much longer than 10 microns, which is well-satisfied.

Many vacuum elements have a complex geometry in which electromagnetic fields can be accumulated over many passes, which results in a steady state power deposition in the structure commensurate with the power loss of the electrons. The power loss P_{loss} depends on the loss factor κ_{loss} and bunch parameters via the equation

$$P_{\text{loss}} = \kappa_{\text{loss}} \frac{I_{\text{ave}}^2}{M} T_0, \quad (4.29)$$

where I_{ave} is the total average current, T_0 is the revolution period, and M is the number of bunches. Of particular concern is rf heating for the BPM-bellows assemblies, because for these components the conductive and radiative cooling is typically inefficient, while active cooling is essentially non-existent. Here, a preliminary analysis of the rf heating of these two components is presented, followed by a brief discussion of impedance considerations associated with the injection/extraction kickers and the in-line photon absorbers. The focus is on these elements because they are either dominant sources of impedance (in-line absorbers), are particularly sensitive to heating (kickers), or both (BPM-bellows).

Before proceeding, it should be noted that the level of rf heating depends critically on the bunch length, which in turn depends upon the voltage and tuning of the bunch-lengthening HHC. In addition, rf heating will change with the precise bunch shape, but comparisons of the loss factor obtained from simulated bunch shapes with those of Gaussian bunches with the same rms width show agreement to $\sim 10\%$. The following calculations focus on a 15-mm Gaussian bunch length to be conservative, because this is the smallest bunch length possible if the HHC is operating as desired. However, if the HHC is entirely detuned one may expect $\sigma_z \approx 10$ mm at 4.2 mA/bunch, which would lead to additional the rf heating. The goal is for components to continue to function even at these bunch lengths, even though it is expected that normal operations will have to be modified if the HHC is not working. On the other hand, there are no plans to over-design components to account for improper tuning of the HHC that could potentially result in bunch shortening. Rather, the HHC system must be designed to detect and prevent such a situation.

4-2.4.3.1 BPM-bellows assembly A CAD-generated model of the full BPM-bellows assembly used for the tracking-based impedance model is shown in Fig. 4.26(a). In this section, the impedance analysis of the BPM buttons is done separately from that of the bellows so that the behavior of each may be separately determined; in addition, it was found that summing the separate contributions for the BPMs and bellows resulted in an impedance that is a rather accurate approximation to the impedance of the entire assembly. A magnified GdfidL representation of a single BPM button is shown in Fig. 4.26(b). The BPM button is 8 mm in diameter and 2 mm thick, while the BPM pin dimensions have been tailored to best match the characteristic impedance to 50 Ohm (the minimum pin diameter is 0.65 mm). Wakefield analysis of the large-aperture BPM began with a GdfidL model comprised of four such buttons arranged symmetrically and at a 12 mm distance from the beam axis. The lowest resonance mode due to the button geometry is expected to have a frequency $f_{H11} \sim 11$ GHz, which is well outside the spectrum of the 50 ps electron bunch that has $f_{\text{rms}} \approx 3.2$ GHz. For this reason, the BPM impedance plotted in Figs. 4.27(a) and (b) show no resonances within the bunch frequency spectrum. The longitudinal long-range wakepotential driven by a $\sigma_z = 15$ mm ($\sigma_t = 50$ ps) electron bunch is shown in Fig. 4.27(c). The wakepotential is largely inductive and decays to zero as the distance becomes large. Finally, the geometric loss factor as a function of the bunch length is shown in Fig. 4.27(d). As indicated by the graph, the loss factor for a 15-mm bunch

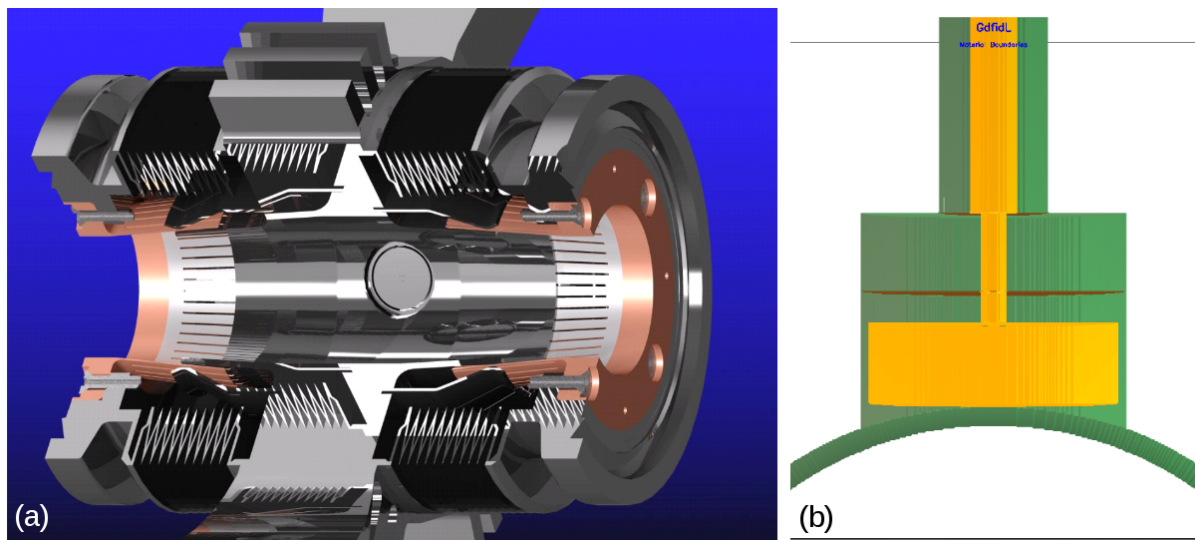


Figure 4.26. a) CAD model of the BPM-bellows assembly. b) GdfidL model of a single BPM button.

length is $\kappa_{\text{loss}} = 0.1 \text{ mV/pC}$, which results in an estimated power loss of $P_{\text{loss}} = 0.33 \text{ W}$ over four BPM buttons in 48 bunch mode at 200 mA.

This level of rf-heating appears to be manageable, but additional simulations that include heat transfer are planned. In addition, the longitudinal wakepotential in normal operation of 48 bunches and 200 mA ring current are expected to further lengthen the bunch to be as long as 21–25 mm rms. In this case, Fig. 4.27(d) shows that the loss factor will decrease by almost a factor of two, and the rf-heating will reduce to a little less than 0.19 W. On the other hand, if for some reason the bunch-lengthening cavity is not functioning as desired, the bunch length may decrease to about 10 mm, which would lead to an approximately 80% increase in heating. Additional work will be done, including heat transfer and ANSYS simulations, to determine if these heat loads can be tolerated. If not, one may have to place different limits on the maximum-allowed operating current, depending on whether the bunch-lengthening cavity is on or off. Finally, the discussion here assumes a gaussian bunch for concreteness, but at full current the microwave instability results in a turbulent bunch shape, and furthermore the lifetime is maximized for an overstretched, “double-humped” bunch like that shown in Figs. 4.61 and 4.69. Recent work has shown that these effects may change the predicted levels of rf losses by typically $\lesssim 50\%$, so that at least this level of safety margin must be accounted for in the design.

The bellows are shown in Fig 4.26(a), where the rf-meshed fingers are colored silver and located near each end. The rf fingers are made of GlidCop plated with $13 \mu\text{m}$ of silver, and when perfectly aligned exhibit very good contact with the vacuum chamber. The nominal vacuum chamber is essentially an 11 mm stainless steel cylinder coated with 2.5 microns of rhodium. The rf finger thickness is tapered from 0.5 mm at the root down to 0.2 mm at the tip. The small thickness provides good flexure contact with the circular chamber surface, while still being thick enough to shield electromagnetic fields down to the revolution frequency f_0 in the storage ring: at f_0 the skin depth in the rf-finger is approximately 0.13 mm, which is about one-third of the average thickness of each finger.

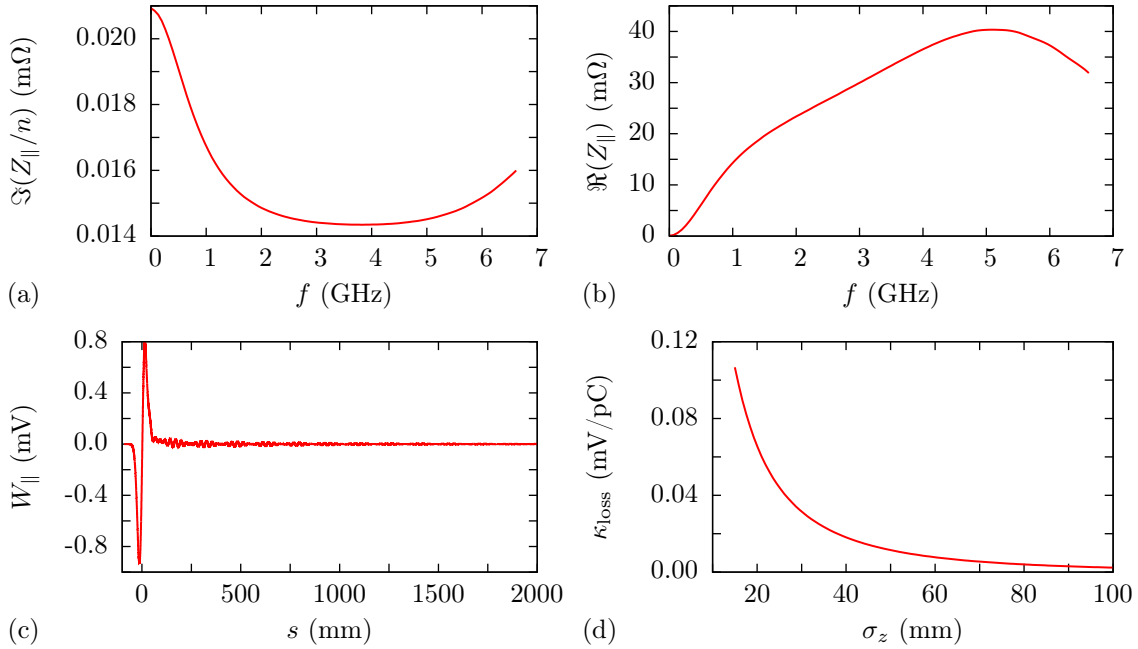


Figure 4.27. BPM button longitudinal impedance and wakepotential analysis. a) The imaginary part of the longitudinal impedance divided by $n = f/f_0$, with the revolution frequency $f_0 \approx 271.6$ kHz. b) The real part of the longitudinal impedance. c) The geometric wakefield. d) The loss factor as a function of bunch length.

The bellows geometry can be represented by the axially symmetric 2D model sketched in Fig. 4.28(a) if the electron bunch is sufficiently long. Further analysis shows that this representation gives a reasonable approximation to the generated wakefields for electron bunches as short as 1 mm in length. Hence, the spaces between the rf-fingers contribute very little to the impedance over the frequencies of interest. The geometric impedance of the bellows as computed by GdfidL is shown in Fig. 4.28(b)-(c), and the corresponding wakefield is plotted in 4.28(d). The geometric loss factor associated with this wakefield/impedance is much smaller than that due to the resistive wall for the long bunches that are planned at the APS Upgrade; at a bunch length of 15-mm the geometric loss factor $\kappa_{\text{loss}}^{\text{geo}} = 0.001$ mV/pC, which is about fifty times smaller than the contribution of the resistive wall, $\kappa_{\text{loss}}^{\text{rw}} = 0.05$. The resistive wall loss factor as a function of bunch length is shown in Figure 4.28(e), including a 32-mm-long rhodium-coated stainless steel pipe with electrical conductivity $\sigma_{\text{Rh}} = 23 \times 10^6$ S/m at a radius of 11mm, and the 27.2-mm-long silver-coated rf fingers at an average radius of 11.75 mm, whose electrical conductivity $\sigma_{\text{Ag}} = 62 \times 10^6$ S/m. Using the total loss factor $\kappa_{\text{loss}} = 0.051$ mV/pC, the total power loss per bellows is $P_{\text{loss}} = 0.14$ W for $M = 48$ bunches at $I_{\text{ave}} = 200$ mA. The next step is to estimate the impedance of the bellows when the rf-fingers are vertically offset by an amount within the required specifications of 0.5 mm, determine the resulting power loss, and assess its effect on rf finger contact with the inner surface of the vacuum chamber.

The preliminary assessment is that the rf-heat loads of both the BPM and bellows assemblies are small, and appear to be manageable in the absence of active cooling. Nevertheless, further study, including detailed simulations of the predicted heat transfer, will be done in the future; this is par-

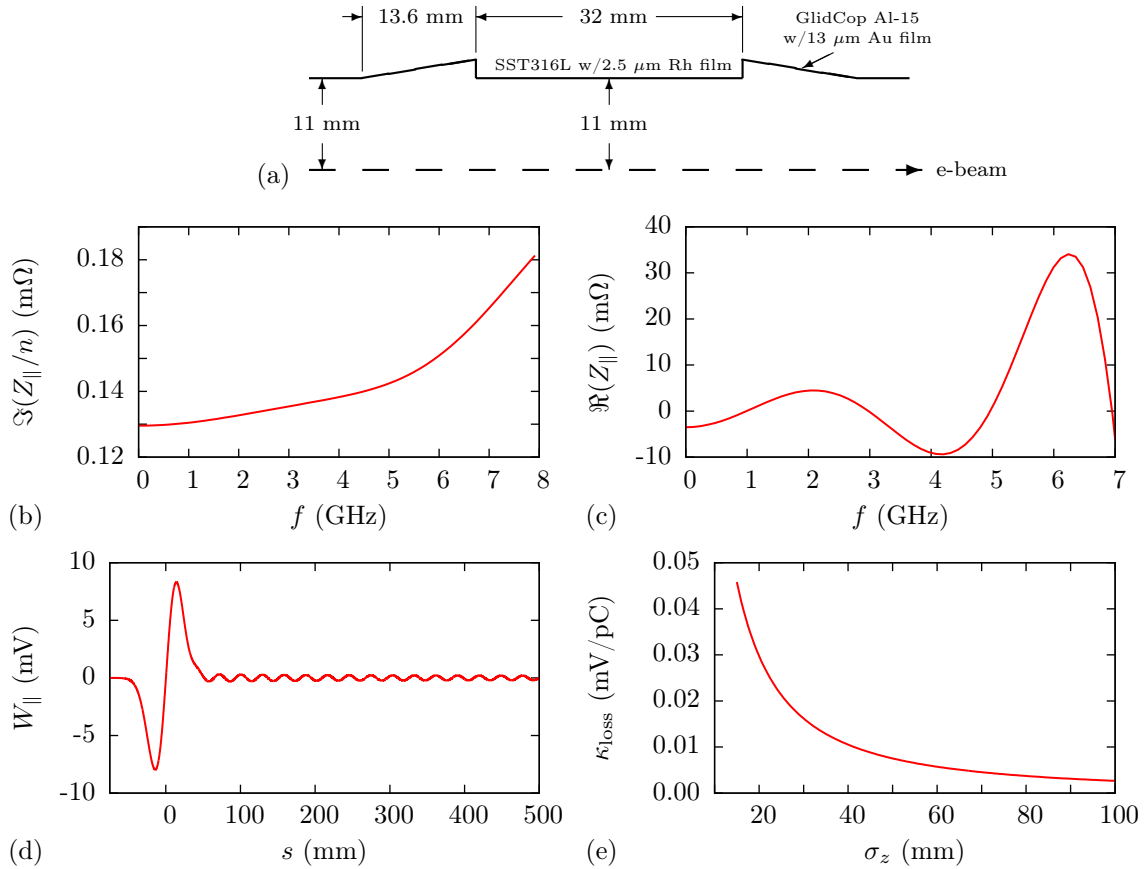


Figure 4.28. Bellows longitudinal impedance and wakepotential analysis. a) Simplified 2D model with geometric dimensions from the full model. b) The imaginary part of the longitudinal impedance divided by $n = f/f_0$. c) The real part of the longitudinal impedance. d) The geometric wakefield. For clarity the plot only shows the wakefield for $s \leq 0.5$ m, but is calculated out to $s = 3$ m. e) The resistive wall loss factor vs. bunch length calculated analytically [25] for the bellows geometry shown in (a).

ticularly important since these two elements have been the source of rf-heating-related difficulties at other storage rings. A similar style of analysis of other impedance elements from Table 4.32, including the flanges, gate valves, and in-line absorbers, have shown comparable results to those mentioned for the BPMs and bellows. The rf-heat loads produced by the geometric wakefields are generally negligible for the anticipated bunch length > 50 ps when the bunch-lengthening cavity is on, and are still quite manageable provided $\sigma_t \gtrsim 30$ ps. Nevertheless, the stripline injection/extraction kickers will require additional analysis, since preliminary calculations have found that the predicted heating varies according to the exact geometry of the transitions into and out of the kicker body, and with the precise shape of the kicker blades. In addition, the kicker feedthroughs can be particularly sensitive to increases in temperature, and are typically difficult to cool. The following summarizes some of the work completed to characterize the kicker impedance and verify that it will work as designed.

4-2.4.3.2 Injection/extraction kickers Lambertson [27, 28] has presented a very interesting and comprehensive discussion of pick-ups and kickers. Following his formalism, the longitudinal and transverse beam impedances are given by [29]

$$Z_{\parallel}(k) = g_{\parallel}^2 Z_{\text{ch},\parallel} [\sin^2(kL) - i \sin(kL) \cos(kL)] \quad (4.30)$$

$$Z_{\perp}(k) = \frac{g_{\perp}^2 Z_{\text{ch},\perp}}{kb_{\text{min}}^2} [\sin^2(kL) - i \sin(kL) \cos(kL)], \quad (4.31)$$

where k is the wave number, L is the longitudinal length of the electrodes, b_{min} is the minimum distance between the beam axis and the electrodes, g_{\parallel} and $Z_{\text{ch},\parallel}$ are the longitudinal geometric factor and characteristic impedance of the stripline, respectively, while g_{\perp} and $Z_{\text{ch},\perp}$ are their transverse counterparts. The characteristic impedances $Z_{\text{ch},\parallel}$ and $Z_{\text{ch},\perp}$ for the geometry presented in Fig. 4.29 were estimated using the structure capacitance C using $Z_{\text{ch}} = 1/cC$ [30]. The capacitance, in turn, was determined from the 2-D POISSON electrostatic code [31] by computing the stored energy W_e for a given voltage electrode V_p via $C = 2W_e/V_p^2$. When both electrodes are set to the same voltage V_p the capacitance corresponds to that of the longitudinal (common) mode, while setting the electrodes with opposite polarity $\pm V_p$ determines the transverse (differential) mode.

The APS-U stripline prototype kicker geometry [32] consists of two 720-mm-long electrodes located inside of a “double-omega shaped” chamber with maximum radius $d = 20$ mm and at a distance of $b = 4.5$ mm from the chamber center. For the electrode geometry in Fig. 4.29, we calculated the following parameters for the two electrodes: $g_{\parallel} = 0.99$, $g_{\perp} = 0.996$, $Z_{\text{ch},\parallel} = 33.01 \Omega$, and $Z_{\text{ch},\perp} = 25.07 \Omega$. The idealized real longitudinal and transverse impedances are calculated using Eqs. (4.30) and (4.31), and then compared with numerically calculated results from the 3D GdfidL code in Fig. 4.30. As can be seen from the figure, the predictions of Eqns. (4.30) and (4.31) closely follow the real part of the impedance determined from the numerical simulation up to frequency $f \approx 2.5$ GHz, meaning that the electrodes are well-matched to the characteristic impedance up to 2.5 GHz; at higher frequencies some mismatch becomes apparent. Work continues to improve the impedance matching at frequencies above 2.5 GHz, and to assess whether the high-voltage pulsed sources may permit the distance between the electrode blades and the beam to be increased.

Finally, Fig. 4.30(c) includes the longitudinal wakefield of a 12 mm bunch, while Fig. 4.30(d) plots the loss factor as a function of bunch length. At a bunch length of 15 mm the plot indicates that the lost beam power is approximately 350 W. Of this 305 W of total power, CST simulations indicate

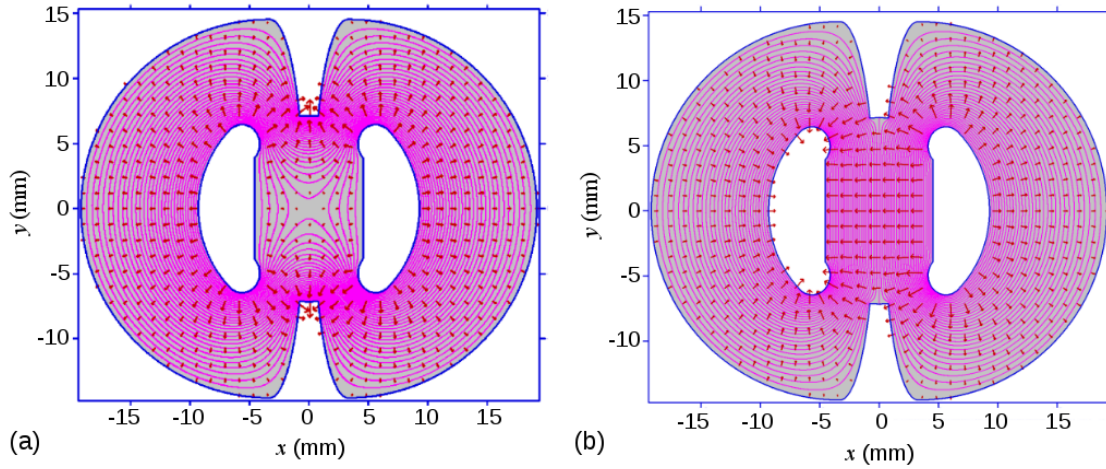


Figure 4.29. Cross-sectional view of the stripline kicker geometry in the middle of the structure. a) Longitudinal excitation: two electrodes inside omega shape chamber at equal positive voltages. b) Transverse excitation: two electrodes at opposite sign voltages.

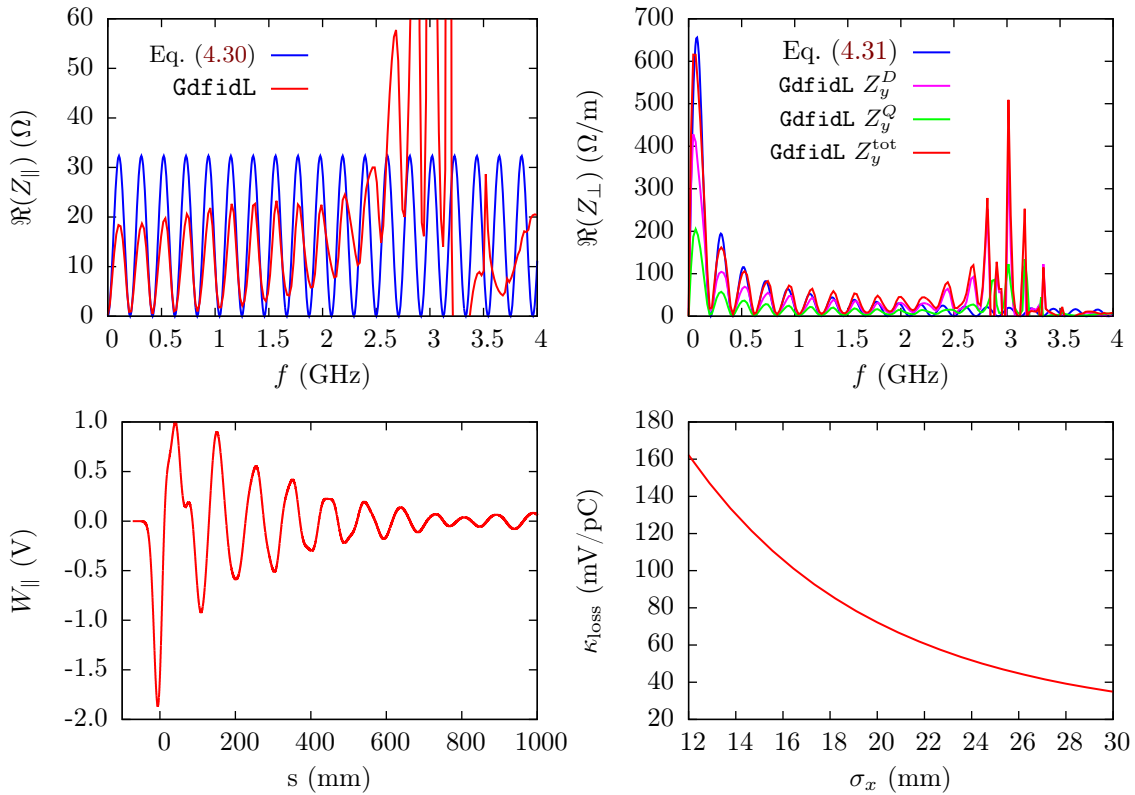


Figure 4.30. Impedance and wakefield calculations for injection/extraction kickers. a) Compares the theory with GdfidL calculations for the longitudinal impedance. b) Compares the theory with GdfidL calculations for the transverse impedance. c) Plots the longitudinal wakefield out to 1 m, although the calculation extends to 15 m. d) plots the loss factor as a function of bunch length.

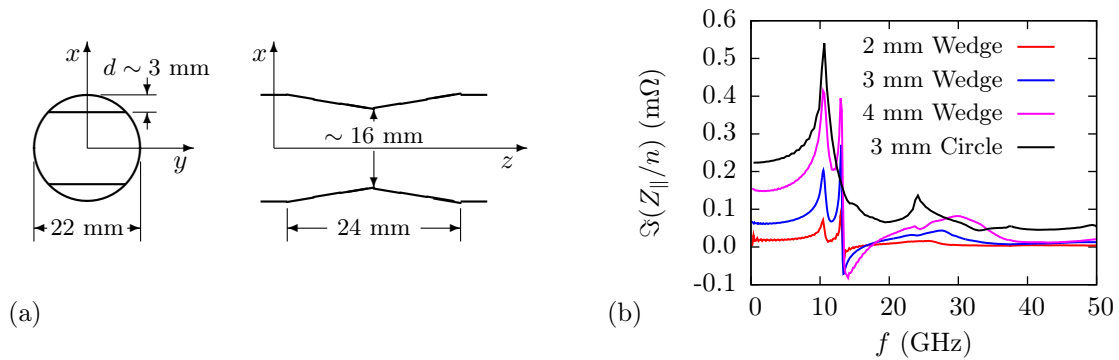


Figure 4.31. a) Geometry of the in-line photon absorber design. b) Comparison of the $\Im(Z_{\parallel}/n)$ for different protrusion depths d of the absorber. Black line shows the result for a cylindrically symmetric absorber for reference.

that about 265 W will be transported out the feedthrough ports, with 165 W going to the upstream ports and the remainder out the downstream ports. This predicted level of power, when scaled by the difference in beam current and geometry, is broadly consistent with the ~ 45 W power observed in the feedthroughs of the present APS feedback system in 24-singlet mode. Furthermore, these measurements were used to verify the CST simulation methodology, with the simulated power in both the upstream and downstream ports agreeing with the measurement to better than 10%. Design of the feedthrough and power supply circuits will account for the beam-induced power. In addition, handling the remaining ~ 80 W of power will present a challenge, particularly for the 15 W that is predicted to be dissipated in the kicker blades. One possible solution that can reduce the impedance and increase conductivity involves copper plating the blades. Alternatively, recent experience with the high-voltage supplies indicate that the blade separation may be increased, which would also reduce the surface currents and rf heating.

4-2.4.3.3 In-line photon absorbers This section is concluded with a brief discussion of how impedance considerations informed the design of the in-line photon absorbers. The main purpose of these absorbers is to mask sensitive components, such as the BPM-bellows assembly, from synchrotron radiation. Ray tracing simulations indicate that the absorbers must protrude into the chamber by typically 2–4 mm to provide the required protection, and that 19 such absorbers are required in each sector. Because there are so many absorbers, they result in a large source of impedance within the ring that must be managed to the extent possible.

The basic design for the in-line absorbers was chosen to be a double wedge that is 24 mm long, and is shown in Fig. 4.31(a). This length allows for a small-angle taper to reduce the impedance, while still being short enough so that the absorber can be machined out of a flange. To minimize the impedance, the constriction only occurs in the horizontal plane, and is mirror symmetric in both planes to eliminate any on-axis transverse wakefields that would otherwise inflate the emittance. The resulting impedance is summarized by the $\Im(Z_{\parallel}/n)$ plotted in Fig. 4.31(b), where the impedance for three different absorber protrusion depths d are compared. The impedance is comparable to that of the bellows, and is less than half what it would be if the absorber were cylindrically symmetric.

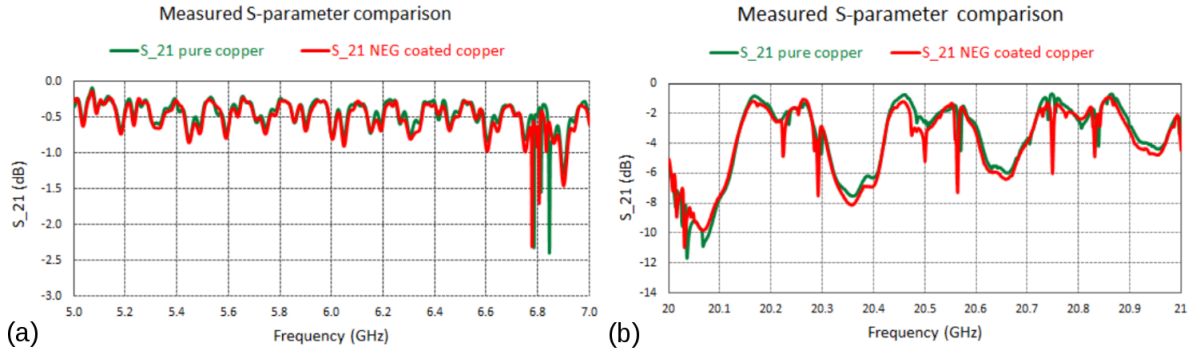


Figure 4.32. Measured S_{21} transmission coefficient before (green) and after (red) coating the copper chamber with a 1.5 micron-thick NEG coating. (a) Plots S_{21} from 5-7 GHz, while (b) plots the same near 20 GHz. The measurements indicate that the impedance cost of the NEG coating is negligibly small.

4-2.4.4 Rf measurements and the impedance test stand

An experimental effort is also underway to perform impedance-related measurements on various vacuum components as a way to complement, validate, and cross-check electromagnetic simulations. The first experiments used the traditional coaxial wire technique to assess the impedance associated with the non-evaporative getter (NEG) coating planned for the copper FODO section. The goal of this experiment was to attempt to verify that the planned 1.5 micron thick coating is largely invisible to the beam over a wide spectral range. To do this, the reference $S_{21}(\omega)$ transmission coefficient of a one meter long, 22-mm diameter copper chamber was first measured. Next, the chamber was sent out for NEG coating, after which the S_{21} was measured again. Measurements showed that the NEG coating contributed a negligibly small impedance for frequencies below 20 GHz, as predicted by simulations; examples of the measured S_{21} transmission coefficient are shown in Fig. 4.32(a) and (b). Above 20 GHz, simulations that use the NEG resistivity found in Ref. [33] predict there to be small but measurable linear dependence of the impedance on frequency due to the NEG, but the data did not indicate any clear difference between the coated and uncoated chambers. To be more precise, the measured difference between the pure copper and the NEG-coated copper at low frequencies (~ 5 GHz) was 0.15 dB or less, which was comparable to the $\lesssim 0.1$ dB difference in S_{21} found when the same chamber was measured on two separate days. Around 20-30 GHz, the measured difference between coated and uncoated chambers were $\lesssim 1$ dB, while measurements of the same chambers that were separated by several weeks were repeatable to within ± 0.5 dB. Hence, we can conclude that the measurement is consistent with the NEG coating having little to no impedance cost up to 30 GHz, and that it at most increases the high-frequency impedance by $\sim 50\%$. Since the resistive wall contribution of the FODO section represents about 9% (1%) of the total $Z_{\parallel}^{\text{rw}}$ (Z_{\perp}^{rw}), the contribution of the NEG to the total ring impedance is a truly negligible contribution. Hence, the measurements are consistent with the expectation that the impedance cost of the NEG coating is very small for frequencies $\lesssim 30$ GHz, and should not adversely affect operations at the APS-U.

The next set of experiments is designed to measure the geometric impedance of a variety of APS-U vacuum components, including the BPM-bellows assembly, the gate valve, rf-liner options for flanges, and potentially other components, such as the injection/extraction kicker. The primary goal here is to validate the electromagnetic simulations and verify that the manufactured part has

similarly low impedance to that predicted by simulations of ideal CAD models. A Goubau-line-based impedance stand has been designed and manufactured to perform these experiments, and measurements should begin by the summer of 2017. The Goubau-line (G-line) is a transmission line that uses a single, dielectric-coated conducting wire to propagate Sommerfeld-like surface waves [34]. The radial electric and axial magnetic fields of these waves fall off $\sim 1/r$ nearby the wire, so that they can be used to model the Coulomb field of a relativistic electron beam [35]. The waves are launched using impedance-matching cones as shown in the CST Microwave Studio [36] image in Fig. 4.33(a); these simulations show the G-line can make useful measurements over a wide range of frequencies, from ~ 100 MHz up to tens of GHz. In addition, they have the advantage of using a single thin wire that can be precisely controlled with minimal perturbations to the fields within the device under test.

As a first verification of the G-line impedance measurement concept, CST was used to simulate the S_{21} transmission coefficient for three different conditions:

1. For the G-line setup with a 22-mm diameter reference pipe.
2. For the G-line setup with the 22-mm diameter pipe leading to a small cavity.
3. For the pipe and cavity only.

Figure 4.33(b) shows the results of this test, which predict that the two cavity resonances can be easily extracted from the G-line measurement. The simulated measurement also shows some extra, smaller features around the primary resonances that do not yet have a clear explanation. Additional simulations are being done to try and determine if these effects are simulation artifacts or intrinsic to the measurement. Nevertheless, this initial test is quite encouraging, and work is now being done to simulate the measurement setup including MBA vacuum components.

4-2.4.5 Future Directions of Collective Effects R&D

The outlook for single-bunch stability in the APS Upgrade is good — present calculations show that the target current of 4.2 mA per bunch can be stably stored in the APS-U lattice, and that injection transients can be controlled with a suitable transverse feedback system. Nevertheless, work continues to pursue the reduction and/or optimization of the impedance of certain components, particularly the BPM-bellows assembly and the injection and extraction kickers.

Other means to validate the impedance modeling described above are also being pursued. For example, recent measurements to determine the dependence of the APS dynamic aperture on bunch charge have shown good agreement with simulation predictions. An informal collaboration with Brookhaven has also been developed to compare modeling methods and code predictions on both the APS and NSLS-II rings. In conjunction with these studies, a better understanding of the role of each APS-U impedance element in the single-bunch current limit is required, so that sources of impedance may be identified and reduced.

The last area of ongoing work involves the longitudinal impedance and rf heating. While preliminary analysis appears to show that rf-heating issues are manageable, there are plans to perform more simulations of the heat transfer and predicted rise in temperature. In addition, because the bunch lengthening due to both impedance and the harmonic cavity depend on current, some additional analysis of the impedance-induced energy loss at less than 200 mA is planned. The expectation

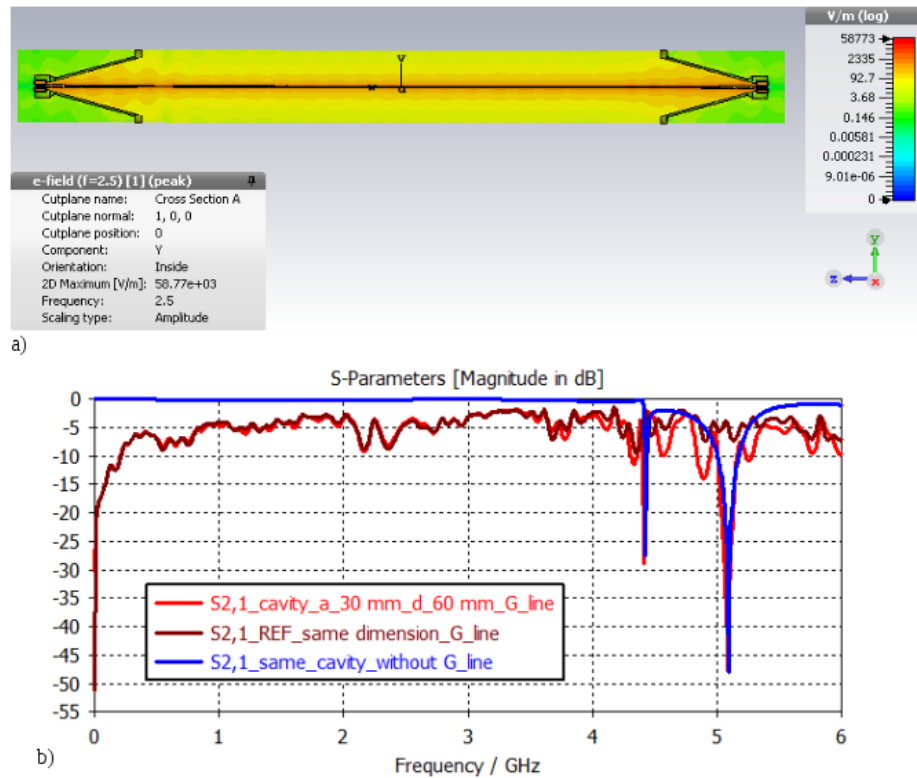


Figure 4.33. (a) Simulation of field matching for the G-line steup. (b) Test S_{21} transmission coefficient simulated for the reference G-line measurement (light red), the test cavity G-line measurement (dark red), and directly from CST.

is that this heating will be less since the energy loss scales as the current squared, but this must be explicitly verified because the loss factor κ_{loss} may depend strongly on σ_t when the longitudinal impedance contains resonances associated with trapped higher order modes. There is also the need to incorporate overstretched bunch shapes and the effect of high-frequency components that exist in microwave-unstable beams.

4-2.5 Multi-bunch Stability

Each circulating bunch leaves behind a wakefield or ions (from the residual gas) that will affect the motion of bunches behind it. If there is a resonance between the long-range wakefields and the beam frequencies, positive feedback may occur and, at large enough beam charge, produce an instability. The main concern is not so much suffering a strong instability that causes beam loss, but creating a small, sustained bunch oscillation in any plane, which would effectively increase the emittance of the electron beam.

The long-range wakefields from the present 352 MHz accelerating rf cavities are the strongest in the ring. The destabilizing effect of resonating cavities are well known in the literature, and will be presented here in the context of the APS Upgrade lattice. The ion effects will be covered in section 4-2.6. The other long-range effect is that of the resistive wall impedance, which will be significant in the smaller apertures of the APS-U. However, since the spectrum is broad, the driving term for multi-bunch instabilities will be weak. Its effect has been explored in comprehensive multi-particle tracking and found to be controllable with weak feedback [23]. Note that the short-range resistive wall impedance is significant for single bunch stability, and is included in the single bunch effect of section 4-2.4.

Stability depends on whether the various natural and applied damping effects can suppress these aforementioned driving effects. In the transverse planes, potentially strong damping effects come from the chromaticity of the optics, while a moderately strong damping effect in the longitudinal plane comes from the Landau damping due to the bunch-lengthening higher-harmonic cavity (HHC). Of course, bunch-by-bunch feedback systems covering all planes can be designed to damp multi-bunch instabilities that have reasonable growth rates. In an approximation, one can treat the damping and driving terms separately and determine from the total effect whether the beam will be stable or not. In the more complicated conditions of the APS-U ring (i.e., in the presence of the HHC and high bunch charge) one cannot treat the damping and driving terms separately, and tracking would have to be done to verify stability.

Each of these effects is explored in the following sections.

4-2.5.1 Damping Effects

There are four damping effects to be considered: synchrotron radiation damping, head-tail damping, Landau damping from the bunch-lengthening cavity, and active feedback. An accurate estimate of these is necessary because the total damping available may influence the design of the harmonic cavity, as well as the decisions as to whether to build bunch-by-bunch feedback systems and better dampers for the accelerating cavities.

Synchrotron radiation damping, present in electron rings, is well understood [37], and occurs in all three planes of motion. Its strength depends on the optics of the MBA lattice, and there is little uncertainty as to its value. This damping works independently on the individual particle motion (namely, it provides incoherent damping), so it is intensity-independent. There could be some increased damping from the extra energy emitted from insertion devices for x-ray production, and that contribution can also be calculated. Here, a conservative assessment of the instability will be made by ignoring the extra radiation damping from the insertion devices, since this depends on

the ID gap and is potentially highly variable.

Though it is readily calculated and appears in all storage ring parameter tables, the synchrotron radiation damping is relatively weak in comparison with the other intensity-dependent and Landau damping effects. As will be shown, the synchrotron radiation damping alone in the MBA lattice is insufficient to counter all multi-bunch instabilities, even though it is typically sufficient for similar high-energy electron rings like the APS.

A much stronger damping effect is the combination of coherent damping and head-tail damping, either of which can dominate over the other. Coherent damping (also known as Landau damping – see [38] for an overview) is the apparent damping effect of the bunch from having particles of different betatron tunes, say from momentum spread and non-zero chromaticity. There is no special force applied to particles or to the centroid besides normal optics. Any initial centroid motion is reduced after some number of turns. Synchrotron radiation emitted from electrons, a diffusion effect, will ensure that the beam does not re-cohere afterwards, as opposed to what could happen to a proton beam.

Head-tail damping involves a wakefield that applies a force to the centroid of each of the z -slices of the bunch, either damping or increasing the amplitude of an initial oscillation. With positive chromaticity, the effect is to damp the oscillation. This stabilization of the high-current single bunch is, of course, the reason that the APS-U was chosen to operate at a relatively high positive chromaticity [39, 40].

The damping provided by both effects scales linearly with chromaticity. The damping mechanism through chromaticity is regarded as a general-purpose cure for many instabilities in the transverse planes. The cost of this cure is usually a lower lifetime. There is no chromaticity-related damping counterpart for the longitudinal plane, although some weak Landau damping from rf bucket nonlinearity will occur, and be mentioned later.

Recent tracking investigations revealed that the strong damping of centroid motion of a kicked bunch was due to the decoherence from the momentum spread and the chromaticity, rather than the head-tail damping. A visual indication of this is that the decay in amplitude is not exponential, and is independent of charge [41]. The equivalent damping rate was 6800 s^{-1} . In comparison, the APS ring has a strong head-tail damping, as tracking in the APS ring shows a damping that depends on charge.

To demonstrate that this coherent damping works to inhibit multi-bunch instabilities, simulations of the MBA beam were performed with a fictitious “strong” dipole HOM intended to produce a multi-bunch instability. The beam and lattice were setup with 48 bunches totaling 200 mA, with a chromaticity of 5 in both planes and with longitudinal and transverse short-term wake-field impedances of the previous subsection. The bunch-lengthening cavity was detuned to 12 kHz to make the bunch profile flatter in order to allow the beam energy oscillations to settle sooner. (It was found that energy oscillations delayed the transverse instability.) The shunt impedance of a single dipole HOM ($\sim 760 \text{ MHz}$) optimally tuned to drive an instability in the x plane was varied in strength and the expected growth rate in x (Equ. 4.34) was calculated without regard to any damping. For the high end of the range of shunt impedances, a transverse multi-bunch instability in the x -plane occurred in a few 100’s of turns and an exponential growth rate was fitted to the

turn-by-turn dipole HOM response. For the low end of shunt impedances, no instability was seen. Figure 4.34 shows the correspondence with the fitted growth rate and the expected growth rate. An apparent threshold occurs at 6000 ± 200 1/s, which demonstrates the subtraction of some fixed

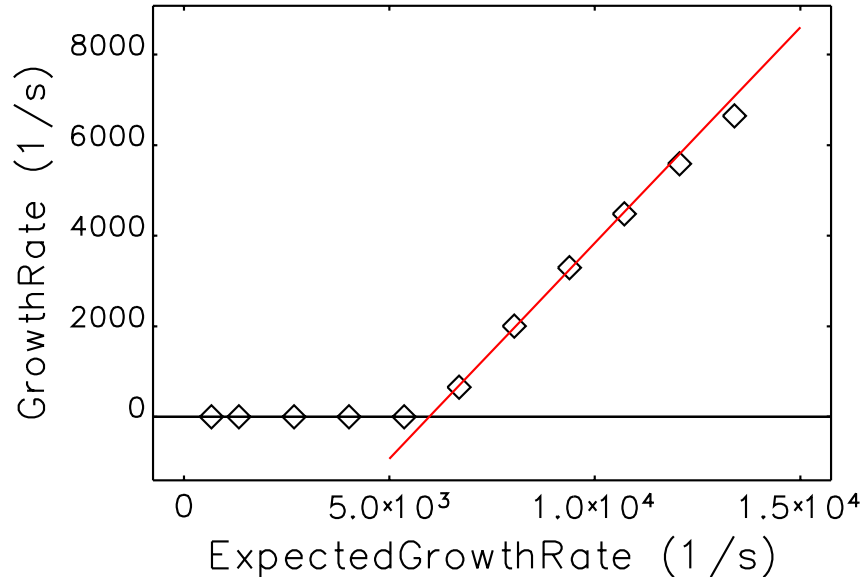


Figure 4.34. Coherent damping demonstrated in multi-bunch instability simulations. Growth rates are fitted from turn-by-turn simulation data of a single dipole HOM. Expected growth rate are calculated.

damping rate from the expected growth rate. This threshold value doesn't exactly equal the value obtained from kick-damp simulation (6800 1/s), difference of which could be due to slightly different configurations of, say, bunch lengthening cavity tuning, in the various types of simulations. The dependence of coherent damping on such configuration variations should be investigated further.

The coherent damping as previously determined from kick-damp simulations is the value listed in Table 4.35.

To explain the difference between the APS and MBA lattice transverse centroid damping, we observe that, although the impedance and wake-fields in both rings are similar, the frequency at which the head-tail effect samples the impedance are much different. Assuming a chromaticity of 5, the chromatic frequency $\xi f_0/\alpha_c$ for APS is 4.8 GHz while that of MBA is 34 GHz. Since the impedance is much smaller at 34 GHz than at 4.8 GHz (see Fig. 4.23), the head-tail effect is lessened in the MBA.

We recently found references [42, 43] discussing the competition between decoherence and head-tail damping.

The next damping effect to consider is that of a bunch-by-bunch feedback system. A separate system is required for each plane, as they require separate and optimized strip lines for detecting beam position and applying an impulse to the beam at each passage. (A cavity is required for the longitudinal plane.)

The present APS bunch-by-bunch transverse feedback system [44] adds a significant amount of transverse-plane damping to single-bunch motion, of the order of 7000 1/s. Using a realistic model of the future feedback system for the MBA lattice, it is expected that a similar amount of damping can be provided. Table 4.35 provides the actual values obtained at the APS, and assumes the same will be obtained for the MBA ring.

A feedback system working in the longitudinal plane could greatly supplement the small damping from synchrotron radiation damping. If synchrotron radiation damping in the longitudinal plane is not enough, there are several possible routes to ensure stability, including building new rf dampers for the cavities, building a longitudinal feedback system, relying on individual cavity temperature tuning, or relying on the Higher-Harmonic Cavity (HHC) for bunch-lengthening to produce Landau damping.

Although the APS-U plans to rely on both new rf dampers for the cavities and on individual cavity temperature tuning, Landau damping will also play a role in the longitudinal plane, and its filamentation effect is often seen in tracking.

Landau damping occurs in a group of oscillators that has a frequency spread, so that the coherent motion of all oscillators is not sustained for long. In the case of the longitudinal plane motion, the HHC at optimum setting for bunch length also creates the largest spread of synchrotron frequencies for the individual particles. The growth of an instability is stopped if the following condition on its growth rate G and the rms angular frequency spread σ_ω is met,

$$G < F\sigma_\omega, \quad (4.32)$$

where F is a coefficient dependent on the frequency distribution and theory used. Reference [45] (near equation 18 therein) gives $F = 0.31$. We will refer to $F\sigma_\omega$ as the Landau “damping rate.”

Table 4.35 summarizes the damping in the three planes of motion relevant to the suppression of multi-bunch instability.

Table 4.35. Summary of damping rates from various mechanisms

Mechanisms	Horizontal (s ⁻¹)	Vertical (s ⁻¹)	Longitudinal (s ⁻¹)
Synchrotron radiation ^a	137	62	50
Coherent ^b	6800	6800	N/A
Active feedback	3600	10000	690 ^c
HHC damping rate	N/A	N/A	188
Expected minimum passive damping rate	6800	6800	238
Expected minimum active damping rate	10000	17000	740

^a Lattice 42pm-Version0

^b Chromaticity setting of 5.0

^c This is a specification from tracking simulations in 4-2.9.5

4-2.5.2 Cavity Impedance

The strongest wakefield source for multi-bunch instability is expected to be the higher-order modes (HOMs) of the rf cavities. Twelve of the sixteen 352-MHz copper rf cavities will be retained in the new ring, thus making the higher-order-mode impedance effect similar to (or perhaps less than) that of the existing ring. As will become apparent, changes in ring parameters compared to the present-day APS make the beam dynamics relatively less favorable for stability in the vertical plane.

The formula for growth rates for symmetric bunch patterns and a single HOM gives the general dependence on ring parameters; when a HOM is exactly resonant with the beam frequency, the growth rate of the worst multi-bunch mode is

$$G_s = \frac{\alpha_c I_{\text{total}}}{2(E/e)\nu_s} (R_s f_{\text{HOM}}) \exp(-\omega_{\text{HOM}}^2 \sigma_t^2) \quad (4.33)$$

for the longitudinal plane and

$$G_{x,y} = \frac{f_0 I_{\text{total}}}{2(E/e)} (\beta_{x,y} R_t) \exp(-\omega_{\text{HOM}}^2 \sigma_t^2) \quad (4.34)$$

for the transverse planes, where α_c is the momentum compaction, I_{total} is the total stored current, E/e is the beam energy in eV units, ν_s is the synchrotron frequency, R_s is the shunt impedance (circuit model) of the monopole HOM, f_{HOM} is the frequency of the HOM resonator, $\omega_{\text{HOM}} = 2\pi f_{\text{HOM}}$, σ_t is the bunch length, f_0 is the revolution frequency, $\beta_{x,y}$ is the betatron function at the location of the rf cavities, and R_t is the transverse shunt impedance (circuit model) of the dipole modes. The exponential factor is a bunch form factor, which is close to unity for the HOM frequencies of interest in the 352-MHz cavities.

Figure 4.35 shows a set of monopole HOMs for the 352-MHz cavity with a curve evaluated from Eqn. (4.33) using a growth rate limit equal to the synchrotron radiation damping rate. There are five modes above threshold in each cavity. This gives an idea of the problem at hand.

Table 4.36. Comparison of ring parameters relevant to multi-bunch instabilities

Quantity	APS ring	MBA ring ^a	Ratio in growth rate
Number of cavities	16	12	0.63
Total current (mA)	150 ^b	200	1.33
Energy (GeV)	7	6	1.17
Momentum compaction	2.83×10^{-4}	3.96×10^{-5}	0.14
Synchrotron frequency (kHz)	2.1	0.56 ^c	3.8
Cavity β_x/β_y (average at exact locations)	19.6/3.4	5.2/2.7	0.27/0.79

^a 42pm-Version0

^b Though APS operates at 100 mA, we are stable at 150 mA

^c With HHC off. With HHC on, there will be a large spread of f_s centered at 0.1 kHz.

Table 4.36 compares the ratios of factors contributing to the growth rates for the APS and APS-U, while Table 4.37 summarizes the overall change, plus the ratios in synchrotron radiation damping rates for reference. The longitudinal plane estimation doesn't include the effect of the harmonic cavity to lengthen the bunch; this effect will significantly change the dynamics, but does not allow for a simple treatment. First, the synchrotron frequency will decrease in value by a large factor,

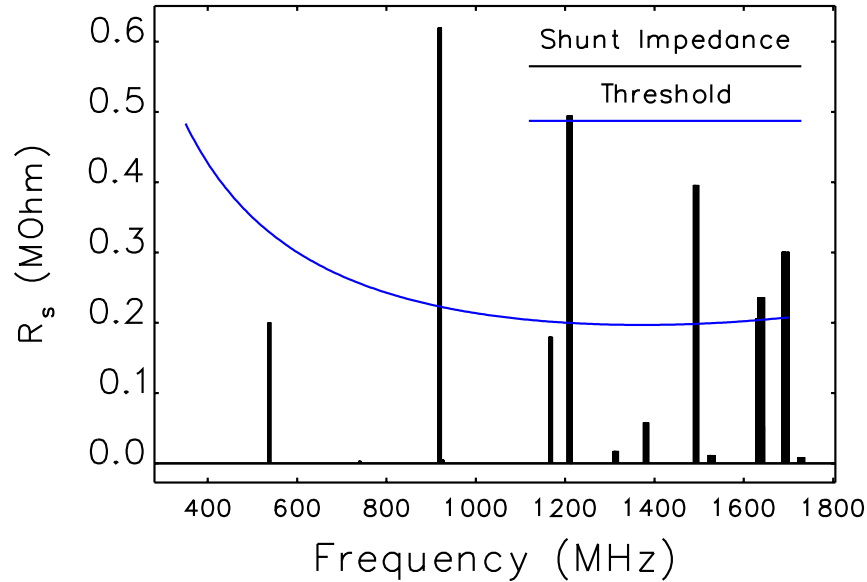


Figure 4.35. Shunt Impedances of damped 352-MHz cavity. Ensembles of HOM families with stepped frequencies appear as thick lines. Threshold is calculated using bunch form factor for $\sigma_z = 2.5$ cm.

Table 4.37. Summary of ring parameters relevant to multi-bunch instabilities relative to APS ring

Plane	Total ratio in growth rate	Ratio in SR damping
Longitudinal	0.51	0.24
Horizontal	0.26	1.31
Vertical	0.77	0.60

which makes multi-bunch modes more unstable. However, a large frequency spread is introduced at the same time (almost equal to the average synchrotron frequency), which will mitigate this worsening effect. Tracking studies presented in section 4-2.9.5 show that the general conclusions derived here also hold when the rf potential includes the HHC; similar work was done previously in Ref. [45]. Since the harmonic cavity may be off during operations, the simulations should be done for both off and on cases, but have thus far only been done when the HHC is in operation.

The bunch lengthening cavity will have its own HOMs, which will have to be included in the multi-bunch stability analysis. Since the cavity is superconducting, it will be heavily damped, with quality factors (Qs) ranging in the 1000's—much less than the twelve regular 352-MHz cavities. It is therefore expected that the bunch lengthening cavity will not provide much of an additional HOM-driven instability effect as compared to the 352-MHz cavities.

4-2.5.3 Monte Carlo Calculation of Growth Rates

The calculation described is limited to the case where HHC is off, although it is expected that qualitatively similar behavior will be seen when the HHC is included.

Presently, only four of the sixteen APS cavities are fitted with an antenna damper that damps the lowest (and strongest) longitudinal HOM by a factor of 8. For the Monte Carlo calculations of possible beam modes, the analysis assumes that all 12 APS-U cavities will have dampers equivalent to the existing ones. Even with dampers, it appears that the ring will not be stable against longitudinal-plane coupled motion unless the frequencies of each cavity can be tuned by varying the cavity temperature and unless a feedback system is implemented. The HOMs of the HHC were not included, but, as noted above, the effect is expected to be small.

The Monte Carlo calculation of growth rates [46, 47] involves randomizing the resonant frequency of the HOM resonator parameters (f , R/Q , and Q) [48, 49] used in a normal mode calculation. The modal analysis method [50] assumes that bunches move rigidly as single macro-particles at a single natural frequency in each plane; thus it does not handle the possibility of decoherence from frequency spread or from chromaticity. As mentioned earlier, the decoherence is assumed to be a separate damping effect, whose strength will be compared to the growth rates of the instability.

The normal mode calculation determines the frequency shift and growth rates of all multi-bunch modes in a beam of N bunches. If one or more of these N -bunch modes comes in resonance with any HOM resonator, the growth rates of these modes will be relatively high. To account for some uncertainty regarding the precise values of the HOM frequencies, a simple model of frequency randomness that assumes a uniform distribution of width $\pm f_0$ has been adopted for the calculation. The randomization of the HOM frequency is intended to represent the various drifts and operating conditions that affect all of the HOM frequencies. One source of drift is any variation in the cavity temperature; recent experiments [51] found that the thermal expansion of Cu can vary the HOM frequencies by 10 - 20 kHz per degree C. In addition, the randomization will take into account the uncertainty in the HOM frequency changes when the cavities will be tuned to 125 kHz nominally above the present main rf frequency (the circumference of the APS-U will be reduced by 0.4 m).

In addition to the randomness just described, the model also includes the fact that the original APS 352-MHz cavities were built with systematic length steps of 0.3 mm, which creates a spread among the HOM frequencies while keeping the fundamental-mode frequency virtually constant. This is crucial in reducing shunt impedance peaks and the potentially very high growth rates of multi-bunch modes. The frequency stepping was recently re-confirmed with spectrum analyzer measurements of revolution harmonics in the cavities induced by a 10 mA single bunch. Figure 4.36 shows the measured frequency stepping for the HOM near 537 MHz, which will also be included in the simulations.

The original calculation of the HOM parameters was done in 1991 with the 2D code URMEL using a simplified 2D model of the cavity. Recently, a calculation that included 3D structure, such as coupler and tuners, was performed with CST Microwave Studio [52]. The resonator parameters turned out essentially the same. The simulations provide the cavity R/Q and Q , which are hard to measure in installed cavities, while the stepped frequencies are determined from the measurements as explained above. URMEL simulations can provide up to 75 HOMs per cavity over a range of 537 MHz to 2 GHz, while the spectrum analyzer measurements and longitudinal feedback experiments only found 4 easily-identifiable HOMs in the longitudinal plane, which are in the range 537 - 1210 MHz. The Monte Carlo simulations of longitudinal growth rates were performed with the lowest 15 HOMs below beam pipe cut-off of 1.64 GHz (see Fig. 4.35). Since four of these monopole HOM families were measured by the spectrum analyzer at the APS, the measured frequency was used

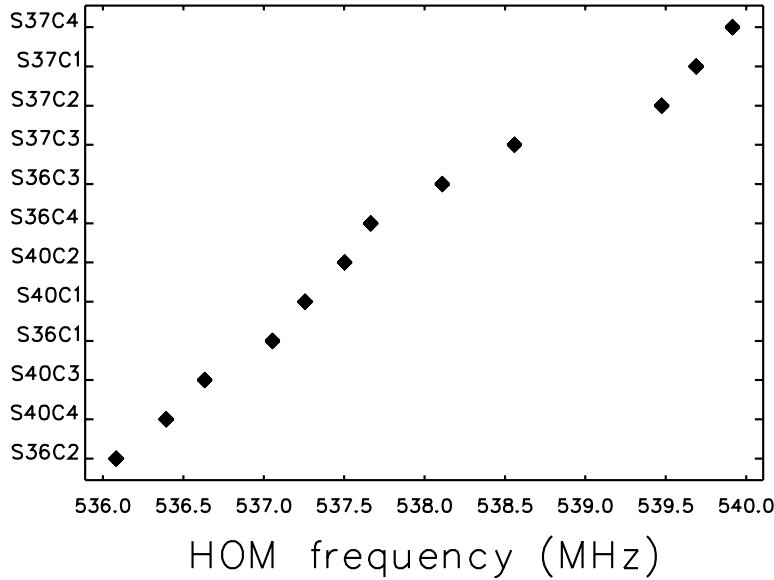


Figure 4.36. Measured HOM frequency across the 12 cavities of the APS that will be included in the APS-U. The resolution is $\sim(1/2)f_0$ because the HOM are excited by the stored beam.

as the starting frequency point for these modes. The above-cutoff, higher-frequency HOMs are assumed to be further damped by the environment of the cavities in the straight section, which is a reasonable explanation for why the present APS does not suffer greatly from HOMs.

For the transverse plane, the lowest 14 dipole HOMs found by URMEL were used, assuming that they are undamped. These HOMs were not measured or studied in the APS storage ring since presently no multi-bunch transverse instabilities are observed, and similar results are expected from the APS-U because of the strong coherent damping.

For each realization of possible HOM frequencies of the 12 cavities, all beam mode complex frequencies (frequency shift and growth rates) are calculated, and the value of the highest growth rate in each case is retained for histogramming. The cumulative distribution function (CDF) (i.e., the integral of the histogram) of the highest growth rate is plotted rather than the histogram itself. This presentation allows for a better comparisons of different cases. Two hundred seeds were used to obtain sufficiently smooth distributions.

Figure 4.37 shows the CDFs of the maximum growth rates in the three planes, assuming that all 12 cavities are outfitted with the present HOM damper that damps the lowest 537 MHz mode. Shown here are the results for 48 bunches, while plots for 324 bunches are virtually the same if not better, because there is a lower probability of overlap of HOMs of different families. Absent a feedback system and the HHC, the synchrotron radiation damping would be the only source of damping in the longitudinal plane. Thus, the CDF for the longitudinal plane shows instability for the majority of the seeds. For the transverse planes, the computed growth rates are typically well below the anticipated total damping rates, which include coherent damping.

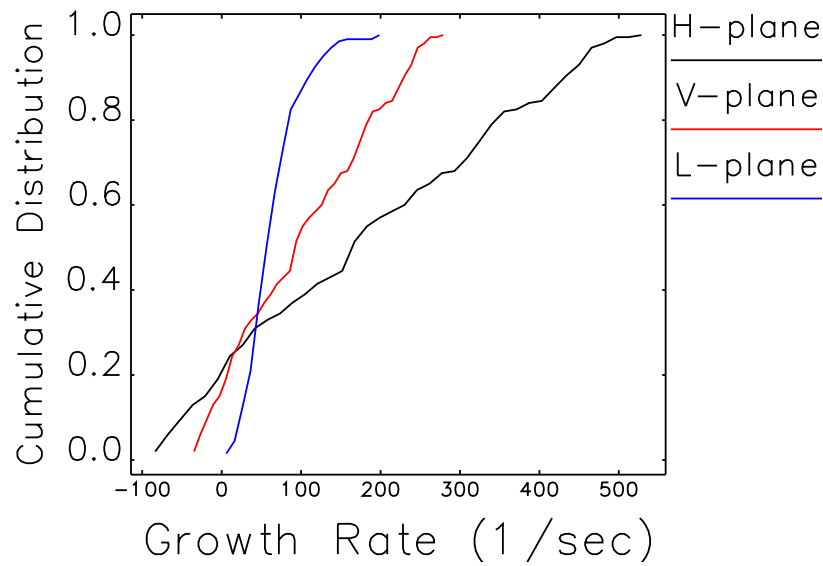


Figure 4.37. Distribution of net growth rates of worst beam modes in the three planes with 12 cavities with monopole HOM dampers. The net growth rate values have the synchrotron radiation damping rates subtracted.

At some point it was thought that the longitudinal instability could be eliminated by controlling the HOM frequencies using the cavity temperature, because this was the case for the APS operations. Such a temperature-tuning process was investigated in simulation for the MBA lattice case by first identifying which cavity or cavities have a HOM that interacts with the beam. In practice, the longitudinal bunch-by-bunch feedback system planned for the APS-U would be used to do this measurement. Then, the frequency of the offending HOM(s) would be adjusted by changing the temperature of the associated cavity. This was simulated by assuming that for each cavity targeted for tuning, the fundamental is returned to resonance while the frequency shift for all HOMs follow the uniform scaling model

$$\frac{\Delta f_{\text{HOM}}}{f_{\text{HOM}}} = -\alpha_{\text{Cu}}\Delta T, \quad (4.35)$$

where α_{Cu} is the expansion coefficient of Cu, $17 \times 10^{-6} \text{ }^\circ\text{C}^{-1}$. The tuning amount Δf_{HOM} was set to be $+0.05f_0$ for the offending HOM, which corresponds to about $-2 \text{ }^\circ\text{C}$. Since the temperature tuning of any cavity may move a different HOM into resonance with the beam, the modal analysis is recomputed after each tuning, and the process of identifying the driving HOM(s), shifting f_{HOM} by an additional $+0.05f_0$ via temperature tuning, and computing the multi-bunch growth rates is repeated until a converged distribution is achieved.

The results of this iterative process are summarized in Fig. 4.38, which shows the cumulative distributions at each stage. In many of the cases the maximum growth rate can be reduced, but not below the synchrotron radiation damping rate. Upon detailed examination of some representative cases, one sees that as the strongest HOM of one cavity is moved away from a beam mode frequency, another HOM from the same cavity moves into a different beam mode frequency. There are simply too many significant HOMs per cavity (4) for temperature-tuning to work in all cases. The process was repeated with only the two most significant HOMs per cavity, and there, the temperature tuning worked to greatly reduce the growth rate distribution below the damping rate. In the APS only one HOM (undamped 538 MHz in 12 cavities) is significant and this HOM can be temperature-tuned without consequences even though the cavity temperatures are not independent, but controlled in groups of four.

Even with the limited success of temperature tuning of the HOM frequencies, it is regarded as an important part of the program to reduce instabilities along with bunch-by-bunch feedback and relying on Landau damping of a HHC system. Furthermore, the general procedure of temperature tuning has been tested at the present APS, which has shown that the present water cooling system can both move f_{HOM} by the amount required and hold it stable to the level necessary for the APS-U [51].

In addition to the main rf cavities, the HHC resonating at 1408 MHz has its own set of HOMs (design is complete). However, this superconducting cavity is not expected to play a major role in driving multi-bunch instabilities, both because it has been designed with damping to reduce the effects of its HOMs, and because it is one cavity in addition to the 12.

When the HHC is turned on, a large spread in particle frequencies occurs and the point-bunch modal analysis described above is not applicable. As bunch oscillations start to grow in amplitude, the natural frequency also changes, thus leaving the resonance and invalidating the method. However, the improvement in growth rates obtained from frequency tuning mentioned above is likely to hold in this different longitudinal focusing case. In any case, a tracking-based approach has been used

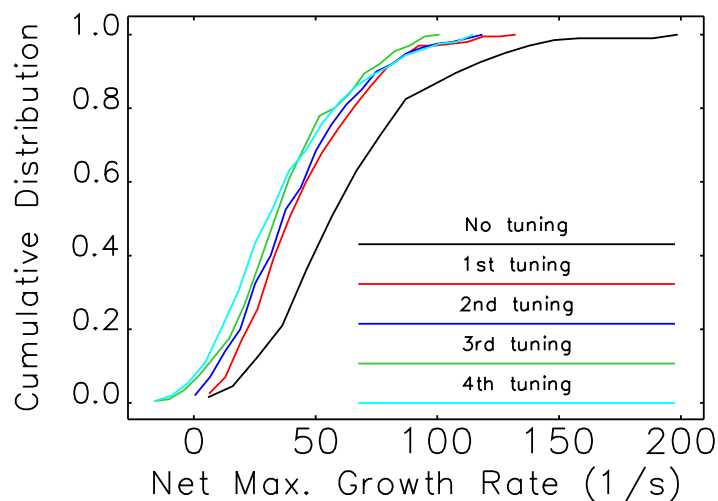


Figure 4.38. Limited effect of temperature tuning on the distribution of net growth rates of the worst beam modes in the longitudinal plane.

to assess the net growth rates for the HHC case, as presented in section 4-2.9.5. These studies find high growth rates for some cases (sans temperature tuning), which further reinforces the need for a longitudinal feedback system.

Table 4.35 summarizes the present analysis of the stability condition for multi-bunch modes in the three planes excluding feedback. The transverse planes are clearly stable because of the anticipated coherent damping from chromaticity.

Table 4.38. Summary of stability conditions with HHC off

	Growth Rate ^a (s ⁻¹)	Damping Rate ^b (s ⁻¹)	Stability
Horizontal	485	6800	Yes
Vertical	255	6800	Yes
Longitudinal	150	50	No, need T tuning and feedback

^a Worst 98th percentile.

^b Expected damping rates from Table 4.35 excluding feedback.

4-2.5.4 Conclusion for Instability from Cavity Impedance

Transverse coherent damping is expected to be strong in the nominal MBA lattice, and thus, the lower synchrotron radiation damping rate won't be an issue for the transverse plane.

In the longitudinal plane, a temperature tuning procedure for the individual cavities and a feedback system are necessary for HHC off or on. The performance and requirements for a longitudinal feedback system are described in Section 4-2.9.5. HOM dampers that cover the bandwidth below

cut-off of 1.6 GHz for the monopole HOMs should be evaluated as an alternative to a feedback system.

4-2.6 Ion Trapping and Instabilities

Ions are produced in an accelerator when the beam ionizes residual gas inside the vacuum chamber. If the beam is negatively charged, ions can become trapped in the beam's potential, and their density may increase over time. If this happens, the motion of the ions will couple to the beam, possibly leading to a transverse (usually vertical) instability. The strength of the instability is generally proportional to the average beam current, and inversely proportional to the beam size [1].

Because the APS-U storage ring is planned to run with high charge, low emittance electron bunches, trapped ions could be very dangerous for beam stability. However, if the beam density is sufficiently high, the ions can receive a very strong kick from a single bunch, and escape before the next bunch arrives. In this regime we should be safe from instability, since the ions will not persist long enough to couple to the bunch motion. This section will discuss the possibility of ion trapping and instability for various modes of operation at the APS-U storage ring. This question is covered both from the perspective of analytical calculations and computer simulations. A scheme is proposed for mitigating the instability if it does occur, by using gaps in the bunch train. Finally, the question of ion-induced emittance growth is briefly discussed.

4-2.6.1 Trapping Criteria

For a machine without an ion-clearing train gap [2], Bacconier and Brianti [3] derived a simple expression for determining whether a given ion will be trapped by the beam. Ions with mass number larger than the "critical mass" given by Eq. (4.36) will be trapped; lighter ions will not.

$$A_{x,y} = \frac{N_e r_p S_b Q}{2\sigma_{x,y}(\sigma_x + \sigma_y)} \quad (4.36)$$

Here N_e is the bunch population, $r_p = 1.5 \times 10^{-18}$ m, S_b is the bunch spacing, σ_x and σ_y are the horizontal and vertical beam sizes, and Q is the charge number of the ion ($= 1$ for a singly ionized molecule). Note that this equation actually gives two criteria, for trapping in the horizontal and vertical plane (A_x and A_y). In order for an ion to be trapped, it must meet both criteria (so $A_{crit} \equiv \max(A_x, A_y)$).

Because the beam size will vary along the ring, the critical mass numbers will also vary. This means that a given ion may be trapped in some parts of a lattice, but not others. To quantify this, a script was written which calculates A_x and A_y around the ring for a given lattice and emittance ratio, and compares them to the mass number for common gasses to determine which will be trapped.

Table 4.39 gives the fraction of the APS-U lattice that will trap singly-ionized H_2 ($A_{crit} = 2$), CH_4 ($A_{crit} = 16$), CO ($A_{crit} = 28$), and CO_2 ($A_{crit} = 44$) ions. Results are given for four different emittance ratios. With flatter beams ($\varepsilon_y / \varepsilon_x = 0.1$), no ion trapping is expected. With rounder beams ($\varepsilon_y / \varepsilon_x > 0.1$), heavier ions will be trapped in a portion of the lattice. Note that all these results are for 324-bunch mode ($N_e = 1.4 \times 10^{10}$, $S_b = 3.4$ m). In 48-bunch mode ($N_e = 9.6 \times 10^{10}$, $S_b = 23$ m), $A_{crit} > 700$ for the entire ring, so ions will definitely not be trapped.

It is important to understand which part of the lattice will trap ions. Figure 4.39 compares the

Table 4.39. Percent of lattice that will trap ions in 324-bunch mode, for different emittance ratios

Emit. Ratio	ε_x (pm)	ε_y (pm)	% H ₂	% CH ₄	% CO	% CO ₂
0.1	40	4	0	0	0	0
0.2	39	8	0	0	0	17
0.4	36	14	0	0	12	26
1.0	29	29	0	4	27	32

trapping parameters for the APS-U lattice to the mass numbers for different gasses. An ion will be trapped at a given point in the lattice if its mass number is greater than A_{crit} . By comparing this picture to the lattice functions, it becomes clear that trapping occurs primarily in the multiplet sections.

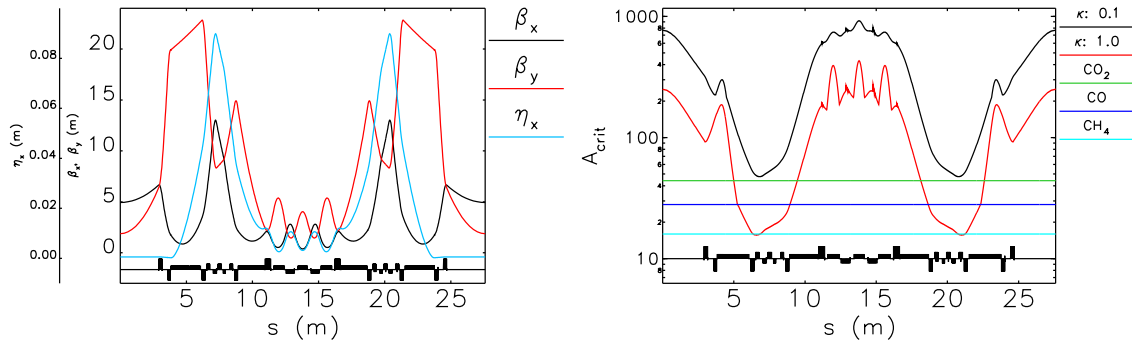


Figure 4.39. Left: lattice functions for one sector of the APS-U lattice. Right: critical mass for different emittance ratios, compared with the mass numbers of common gasses.

4-2.6.2 Instability Simulations

To evaluate the possibility of ion instability in the APS-U, we used an ion simulation code developed at SLAC [4], which models the interaction between the beam and ions at multiple points (~ 800) around the ring. This code was previously used to study an ion-induced tune shift in the PAR [5]. In this code the ions are modeled using macroparticles, but the beam is rigid (with only centroid motion allowed). Thus it can model ion trapping and beam instability, but not emittance growth. All simulations shown in this section were done for 324-bunch mode, with 200 mA total current.

The simulations incorporate realistic vacuum profiles, generated using the CERN codes SynRad+ and MolFlow+ [6, 7]. As described in Section 4-3.3.3, these codes give a predicted partial pressure for different gas molecules around the ring, as a function of beam scrubbing time, for specific beam current. To be consistent with the gas scattering lifetime calculations (Section 4-2.8.2), the second-worst of four possible PSD models was used for the ion simulations.

Figure 4.40 compares pressure profiles for one sector of the storage ring at 200 mA, after 100 and 1000 A-hrs of beam scrubbing. The 100 A-hr case corresponds to early operation at full current, while the 1000 A-hr case corresponds to roughly one year of operation at full current. The pressure variation through the sector is quite significant. In particular, the pressure is high in the multiplets,

due to a lack of distributed pumping. Unfortunately, as shown in Fig. 4.39, this is exactly where ion trapping is most likely to occur.

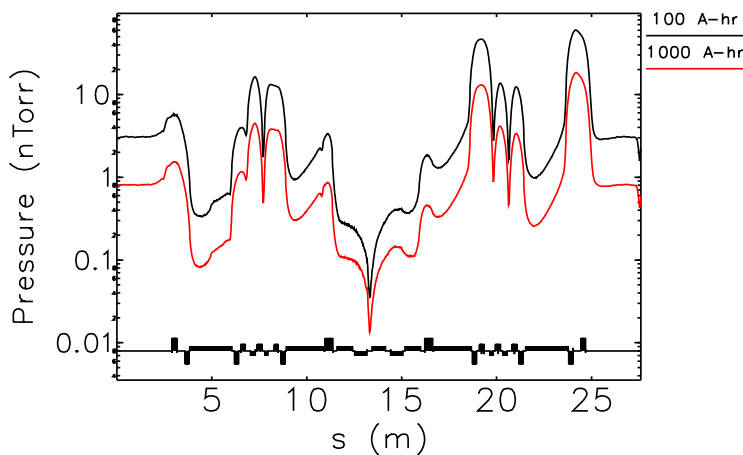


Figure 4.40. Pressure profiles for one sector of the APS-U storage ring, calculated by MolFlow+.

Figure 4.41 plots the simulated ion density vs. time for round beams (emittance ratio = 1.0) and flat beams (emittance ratio = 0.1), and for 1000 A-hr and 100 A-hr beam conditioning. As predicted by the calculation, no trapping is observed for the flat beam cases (i.e., the ion density does not increase with time), while ions are trapped in the round beam case. Of course, the density is higher for 100 A-hr than for 1000 A-hr.

As shown in Fig. 4.42, the trapped ions in the round beam case do lead to an instability, even after 1000 A-hrs of beam conditioning. The instability initially grows very quickly, then saturates when the beam motion reaches about 10% of the vertical beam size, after which it grows much more slowly. Even this small amount of beam motion is enough to shake out some of the ions, leading to a reduction in the ion density (which can be seen clearly in Fig. 4.41). Thus the instability is to some extent self-limiting, though unfortunately not to the extent that it stops growing altogether.

The flat beam simulations also show an instability, though with a much lower growth rate than the round beam case. The growth rate is roughly 320/sec for 1000 A-hrs, and 1000/sec for 100 A-hrs. These values are much smaller than the effective coherent damping rate (6800/sec) and the damping expected from the transverse feedback system (10000/sec), given in Table 4.35 (these effects are not included in the simulation). Therefore we expect flat beams to be relatively safe from coherent ion instability (though emittance growth is still possible—see Section 4-2.6.5). However, since flat beams are undesirable for beam lifetime, other options should be considered.

4-2.6.3 Train Gaps

One common technique for mitigating ion instability is to use gaps between bunch trains, to allow the ions to clear out [2]. However, as discussed in 4-2.9.6, the missing bunches can cause transients in the RF system, leading to variations in the bunch length, phase, and lifetime along the train. One way to minimize these impacts is to distribute the missing charge to the bunches adjacent to the

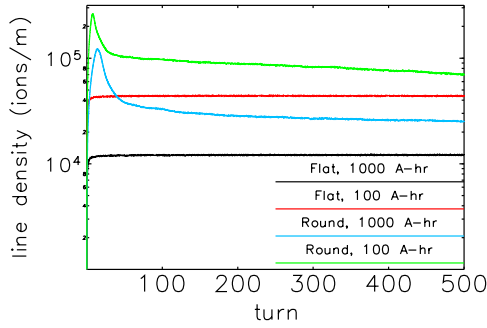


Figure 4.41. Simulated ion density for 324 bunches, 200 mA.

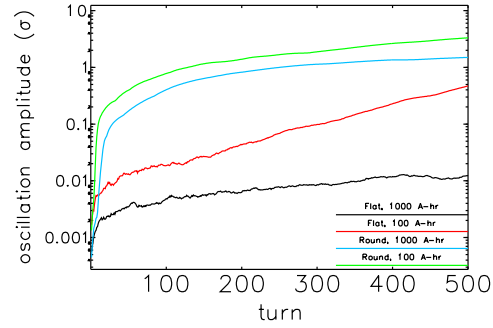


Figure 4.42. Ion instability amplitude (in units of vertical beam size) for 324 bunches, 200 mA.

gaps. An example of this scheme is shown in Fig. 4.43, which depicts four trains with a two bucket gap between them. The bunches before and after the gaps then have double charge. Simulations have shown that the impact of this arrangement on the RF system should be relatively modest (Section 4-2.9). In addition, the high charge bunches before the gap will provide a stronger kick to the ions, helping with the clearing process.

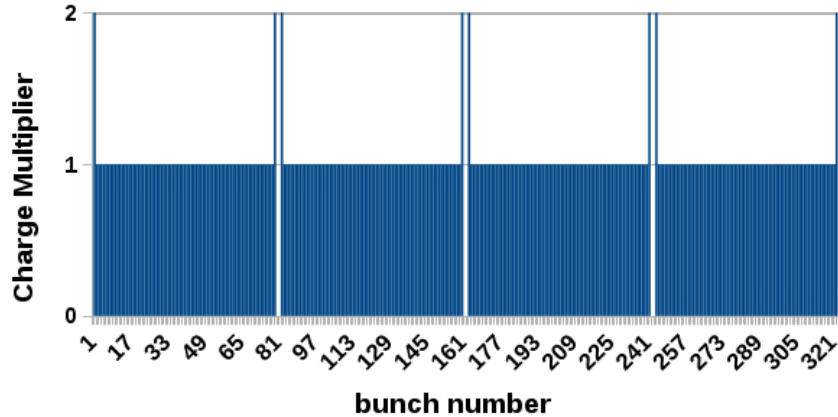


Figure 4.43. Bunch population with ion clearing gaps.

The ion simulation code described above has been modified to allow for multiple trains, with extra charge in the bunches before and after the train gaps. Two parameters that can be varied in this model are the number of bunch trains and the size of the gap between trains. Increasing the number of buckets in the gap did not have an appreciable effect on the simulated instability growth rate, because even a two bunch gap is effective at clearing out the ions (the minimum A_{crit} for the gap is 76).

Increasing the number of bunch trains has a much more significant effect. Figure 4.44 shows the growth of the ion density vs. turn number for different numbers of trains (with 1000 A-hr pressure profiles). All of these simulations used a two bunch gap, with one double-charge bunch before and after the gap. Even with two trains, the peak ion density is reduced by more than an order of

magnitude; using more trains further reduces the density. The instability growth rate (Fig. 4.45) is also significantly reduced with two trains—from $\sim 43000/\text{sec}$ to $\sim 1400/\text{sec}$. The growth rate is further reduced with more trains; with 18 trains it is essentially zero. For 100 A-hrs the ion density is considerably higher (Fig. 4.46) as is the growth rate (Fig. 4.47), amounting to $\sim 6200/\text{sec}$ for 2 trains and $\sim 500/\text{sec}$ for 18 trains. Again, we expect these slow growing instabilities to be effectively damped by feedback and coherent damping (with effective damping rates of $10000/\text{sec}$ and $6800/\text{sec}$, respectively).

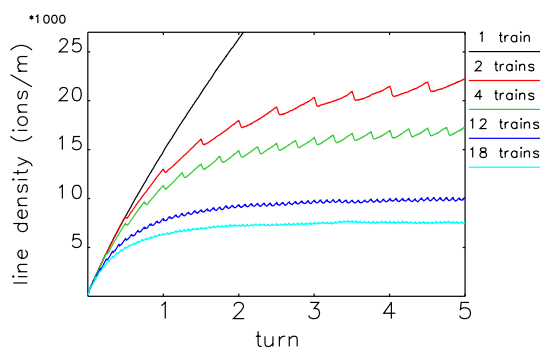


Figure 4.44. Simulated ion density for 324 bunches, round beams, 1000 A-hrs, and 2-bunch gaps.

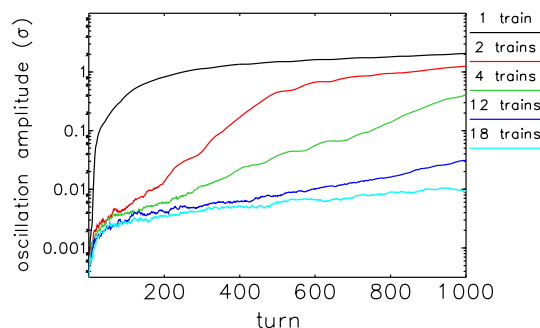


Figure 4.45. Vertical ion instability amplitude for 324 bunches, round beams, 1000 A-hrs, and 2-bunch gaps.

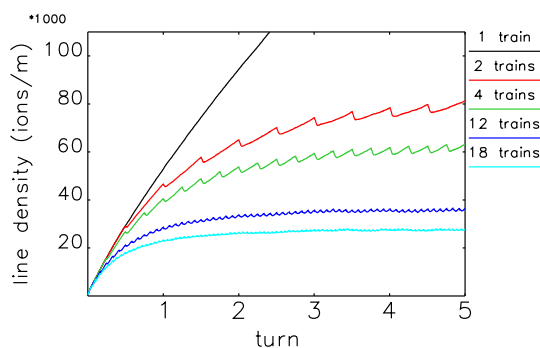


Figure 4.46. Simulated ion density for 324 bunches, round beams, 100 A-hrs, and 2-bunch gaps.

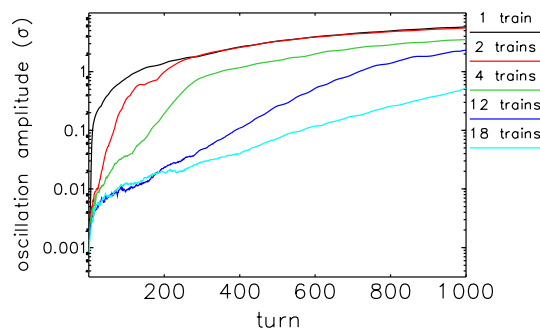


Figure 4.47. Vertical ion instability amplitude for 324 bunches, round beams, 100 A-hrs, and 2-bunch gaps.

4-2.6.4 Commissioning and Early Operation

Commissioning and early operation may present several challenges that push in opposite directions. Some conditions may exist that will push the use of many bunches and round beams; among these are imperfectly corrected nonlinear dynamics and lack of a functioning higher harmonic cavity, both of which would result in low Touschek lifetime. Other conditions may exist that will motivate the use of few bunches and flat beams. Chief among these is ion trapping, which may be worsened by high vacuum pressure due to insufficient conditioning time. A compromise may be the use of relatively few bunches with round beams.

Hence, it is likely that during the ramp up to full current, the APS-U will be operated with a relatively small number of equally spaced bunches, so ions should not be trapped. For example, Fig. 4.48 plots the instability growth rate vs number of bunches after 5 A-hrs of beam conditioning, with 25 mA total current. Below the ion trapping threshold (108 bunches for round beams, or 144 bunches for flat beams), the instability growth rate is very low, and should be easily contained with feedback and coherent damping.

As the vacuum chamber conditions, we can increase the number of bunches and bunch charge while staying below the threshold of ion instability. As shown in Fig. 4.49, at 100 A-hr and 200 mA the instability growth rate for round beams is low for 144 (or fewer) bunches. Around this time, operations can transition to 324 bunch mode, with either train gaps or flat beams.

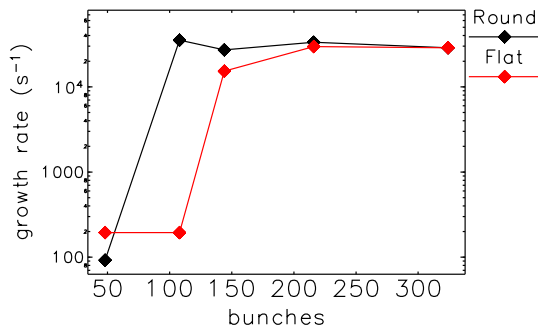


Figure 4.48. Vertical ion instability with 25 mA and 5 A-hr beam conditioning, as a function of number of bunches.

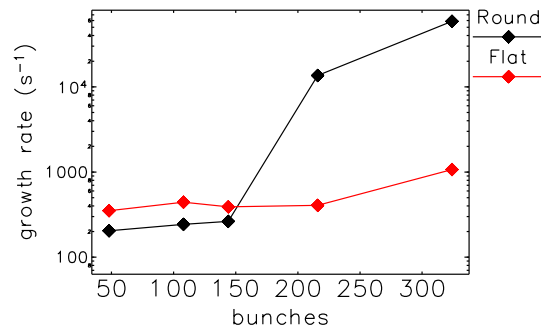


Figure 4.49. Vertical ion instability with 200 mA and 100 A-hr beam conditioning, as a function of number of bunches.

4-2.6.5 Emittance Growth from Ion Effects

Because the simulation code used to obtain the above results assumes a rigid beam, it is not able to model emittance growth due to ions. This is of particular concern because significant emittance growth will change the trapping criteria, potentially trapping more ions and leading to further emittance growth and/or instability. Ion effects are presently being incorporated into *elegant*, which will allow us to model intra-bunch effects such as emittance growth and decoherence. In addition, this will enable self-consistent modeling of ion effects in combination with other elements, including feedback and impedance. We plan to benchmark this simulation against measurements of ion-induced emittance growth in the PAR (Section 4-3.13.2).

References

- [1] H.G. Hereward. *Coherent Instability due to Electrons in a Coasting Proton Beam*. Tech. rep. CERN-71-15. July 1971 (cit. on p. 84).
- [2] D. Villevald and S. Heifets. *Ion Trapping in the SLAC B-factory High Energy Ring*. Tech. rep. SLAC-TN-06-032. June 1993 (cit. on pp. 84, 86).
- [3] Y. Baconnier and G. Brianti. *The Stability of Ions in Bunched Beam Machines*. Tech. rep. CERN/SPS/80-2. Mar. 1980 (cit. on p. 84).

- [4] L. Wang et al. “Suppression of beam-ion instability in electron rings with multibunch train beam fillings.” In: *Phys. Rev. ST Accel. Beams* 14 (8 Aug. 2011), p. 084401. DOI: 10.1103/PhysRevSTAB.14.084401. URL: <http://link.aps.org/doi/10.1103/PhysRevSTAB.14.084401> (cit. on p. 85).
- [5] J. Calvey, K. Harkay, and CY. Yao. “Ion Effects in the APS Particle Accumulator Ring.” In: *NAPAC16*. THPOA14. 2016 (cit. on p. 85).
- [6] M. Ady and R. Kersevan. “Introduction to the latest version of test particle Monte Carlo Code MolFlow.” In: *Proc. IPAC 2014*. IEEE, 2014, p. 2348. URL: <http://accelconf.web.cern.ch/AccelConf/IPAC2014/papers/wepme038.pdf> (cit. on p. 85).
- [7] R. Kersevan. “SYNRAD, a Monte Carlo Synchrotron Radiation Ray Tracing Program.” In: *Proc. PAC 1993*. IEEE, 1993, p. 3848. URL: http://accelconf.web.cern.ch/AccelConf/p93/PDF/PAC1993_3848.PDF (cit. on p. 85).

4-2.7 Intrabeam Scattering

Due to the ultra-low emittance, intrabeam scattering (IBS) will potentially have a significant effect on the beam emittance and energy spread. The program `ibsEmittance` [1] was used to evaluate IBS effects. This program uses the Bjorken-Mtwingwa formalism [2]. It finds the emittances and energy spread such that the total growth rates equal the synchrotron-radiation damping rates in all planes, assuming a fixed ratio κ of vertical to horizontal emittance. To provide a preliminary analysis of the effects of IBS, the rms bunch length was taken to be 15.6 mm, which is the value with an ideally tuned 4th-harmonic cavity in the absence of wakefields. Without 4th-harmonic cavity, the IBS is much stronger with short bunch length which largely increase emittance and energy spread, especially for 48 bunch mode. The ratio of bunch length to energy spread is assumed to be fixed, so the bunch lengthens if the energy spread increases due to IBS. Figure 4.50 shows the equilibrium effects of IBS for 48-bunch and 324-bunch fills. At equilibrium, the IBS growth rate in 48-bunch mode is about 10% of the radiation damping time.

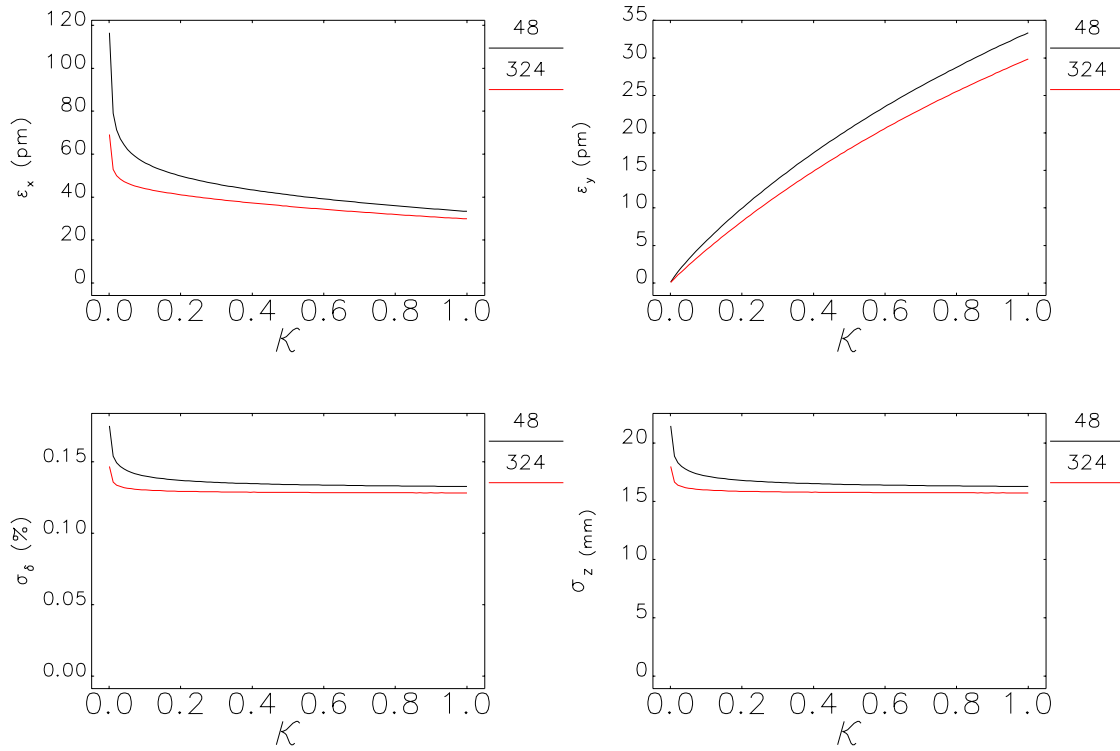


Figure 4.50. Effect of IBS on emittances, energy spread, and bunch length for 48-bunch and 324-bunch fills at 200 mA as a function of the assumed emittance ratio $\kappa = \epsilon_y/\epsilon_x$.

Close examination of Fig. 4.50 shows that even for 324 bunches, the sum $\epsilon_x + \epsilon_y$ is larger than ϵ_0 . In the absence of IBS, the sum of the transverse emittances is given by [3]

$$\epsilon_x + \epsilon_y = \epsilon_0 \frac{2\tau_x\tau_y + \tau_y(\tau_y - \tau_x)\sin^2\theta}{2\tau_x\tau_y + \frac{1}{2}(\tau_y - \tau_x)^2\sin^2\theta}, \quad (4.37)$$

while the ratio is

$$\frac{\epsilon_y}{\epsilon_x} = \frac{(\tau_y + \tau_x) \sin^2 \theta}{4\tau_x + (\tau_y - 3\tau_x) \sin^2 \theta}, \quad (4.38)$$

where τ_x and τ_y are the radiation damping times, and $\theta : [0, \pi/2]$ is the coupling angle. As θ is varied from 0 to $\pi/2$, ϵ_y/ϵ_x varies from 0 to 1. Since $J_x > 1$, $\tau_x \neq \tau_y$, and hence $\epsilon_x + \epsilon_y \geq \epsilon_0$. In particular, for $\theta = \pi/2$

$$\epsilon_x + \epsilon_y = \epsilon_0 \frac{2\tau_y}{\tau_x + \tau_y} \approx 1.38\epsilon_0, \quad (4.39)$$

where the final expression makes use of values from Table 4.3. This explains the “excessive” value of $\epsilon_x + \epsilon_y$ for 324 bunches.

In addition to impacting the emittance, IBS can increase the energy spread. However, as Fig. 4.50 shows, the effect is significant only for $\kappa \ll 0.1$, and then only for 48-bunch mode. Since those conditions would give a very short Touschek lifetime, they are not considered for operations and this effect is not a concern. Note however, that in 48-bunch mode with $\kappa \approx 1$, the microwave instability will result in a considerable increase in the energy spread, as shown in 4-2.4 and 4-2.9.

The impact of IBS on the brightness can be roughly gauged by taking the ratio of $\epsilon_x\epsilon_y$ computed with IBS to the same product computed without IBS. As seen in Fig. 4.51, the impact of IBS is significant for very low κ , but is otherwise fairly moderate. For 324-bunch mode, a $\sim 40\%$ improvement is seen for $\kappa = 1$ compared to the maximum, while for 48-bunch mode, a much smaller improvement is possible. (The impact on the x-ray photon brightness depends on the undulator length, beta functions, and the photon energy, so this just gives a rough idea.) The increase in lifetime for 324-bunch mode with $\kappa = 1$ is nearly 60% compared to that for $\kappa = 0.1$, as seen in Table 4.40. Hence, if necessary, the lifetime can be significantly improved using $\kappa = 1$, with modest impact on the brightness.

References

- [1] A. Xiao. “Study of IBS Effects for High-Brightness Linac Beams.” In: *Proc. of Linac 2008*. 2008, pp. 296–298 (cit. on p. 91).
- [2] J. D. Bjorken and S. K. Mtingwa. “Intrabeam Scattering.” In: *Part. Accel.* 13 (1983), p. 115 (cit. on p. 91).
- [3] R. Lindberg. Private communication. 2014 (cit. on p. 91).

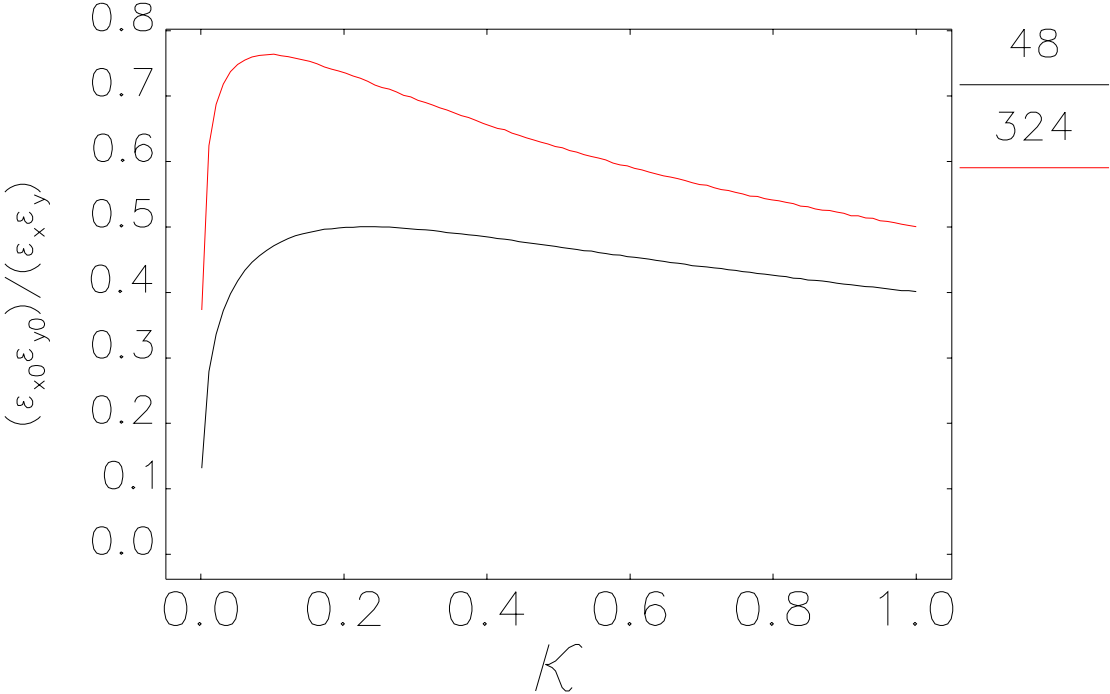


Figure 4.51. Ratio of electron beam brightness with IBS to that without IBS as a function of the emittance ratio, for various numbers of bunches in a 200 mA fill. The nominal rms bunch length is 15.6 mm.

4-2.8 Beam Lifetime

There are two primary contributions to the beam lifetime: Touschek scattering and gas scattering. Touschek lifetime has been presented above, but the computations used the simplified assumption of a Gaussian longitudinal distribution with an rms bunch length (duration) of 15 mm (50 ps). This section provides a more detailed treatment of Touschek lifetime, along with a detailed analysis of gas scattering lifetime.

The quantum lifetime is extremely long since the rms beam sizes are more than an order of magnitude smaller than the dynamic acceptance. Similarly, the rms energy spread is more than an order of magnitude smaller than the minimum local momentum aperture. Hence, the quantum lifetime contribution can be safely ignored.

4-2.8.1 Touschek Lifetime including Harmonic Cavity

As mentioned above, one of the primary reasons for including a harmonic cavity is the desire to increase the Touschek lifetime. Ideally, one would model this by self-consistently simulating the Touschek scattering rate in the presence of the impedance, rf cavities, and IBS. However, this is computationally intensive, so an approximate procedure was used that nonetheless goes beyond the simple approach made in section 4-2.3.

Unlike those results, the rf bucket half-height is fixed at 4.5%, which exceeds the LMA seen in all ensembles. This allows using a fixed set of rf parameters for all ensembles, reducing the amount of tracking by a factor of 100. Since reducing the rf voltage to match the LMA for each ensemble would allow longer bunches, this simplification may underestimate the Touschek lifetime at the lower end of the range by $\sim 10\%$. (The estimate is based on a comparison of the ideal bunch duration with 4.5% bucket half-height and 3.0% bucket half-height, ignoring impedance effects.) As will be seen, the increase in the estimated Touschek lifetime that results from using the detailed longitudinal distribution is much larger than this.

In this procedure, the tracking described in section 4-2.9 provides slice-by-slice information on the energy spread and charge for a representative bunch, sampled every turn over 1000 turns. For each tracking simulation with the HHC, 10 samples of these results are used with the program `ibsEmittance` [1] to compute the emittance, energy spread, and bunch length in the presence of IBS. (This program is described in more detail in section 4-2.7.) In doing this, the transverse beam parameters are taken from computations of the equilibrium 6D beam moments for each of 100 ensembles as discussed in section 4-2.3. The results of these calculations are IBS-inflated emittances and energy spread for each bunch sample and for each ensemble. This data is used with the program `touschekLifetime` [2] to perform slice-by-slice computation of the Touschek lifetime. Results are averaged over bunch samples, then statistics are performed over ensembles.

The `touschekLifetime` program also takes as input the local momentum aperture data from `elegant` tracking simulations, as described in section 4-2.3. The results for Case 4 were used for these tracking simulations. Simulations were performed for both 48- and 324-bunch fills at 200 mA for various values of the harmonic cavity detuning frequency Δf_h . To maximize the lifetime, the emittance ratio was close to 1, with exact values varying from ensemble to ensemble according to the lattice simulations.

Figures 4.52 and 4.53 show the Touschek lifetime results for round-beam mode for 48 and 324 bunches, respectively. To be conservative, the 10th-percentile values are taken as input to subsequent calculations. Referring to these values, the Touschek lifetime for 48-bunch mode is increased by 75% when the HHC Δf_h is tuned to 9 kHz.

For 324-bunch mode, the Touschek lifetime increases more than three-fold, using the case with $\Delta f_h = 11$ kHz as the optimum. The relatively larger improvement compared to 48-bunch mode is a result of having significant bunch lengthening already for 48-bunch mode due to the microwave instability. As Δf_h is lowered past 11 kHz, the Touschek lifetime decreases, owing to the fact that the bunch is being split into two somewhat distinct, higher-density sub-bunches. At $\Delta f_h = 8$ kHz, the beam is mildly unstable.

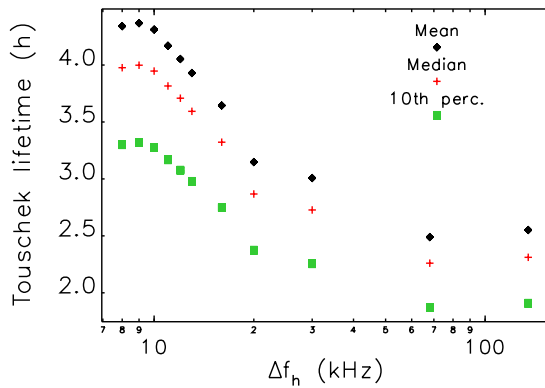


Figure 4.52. Touschek lifetime results over 100 ensembles for 48-bunch mode at 200 mA, as a function of HHC detuning.

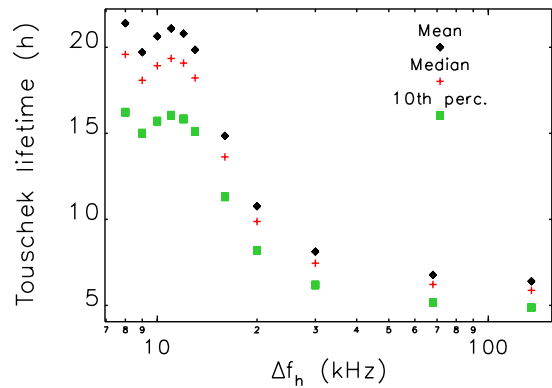


Figure 4.53. Touschek lifetime results over 100 ensembles for 324-bunch mode at 200 mA, as a function of HHC detuning.

The results above assumed that all insertion devices (IDs) are open. In user operations, the energy loss due to IDs may be as high as 1.3 MeV per turn, which is significant compared to the nominal energy loss per turn of 2.7 MeV. Hence, the damped emittance will be smaller, which may increase IBS effects and decrease the Touschek lifetime. This was evaluated by adding energy loss ΔU_{ID} of up to 1.3 MeV per turn using two 2.4-m-long, 27-mm-period insertion devices in each of the 35 user straight sections. The field in the devices was adjusted to get the desired energy loss. An iterative method was used to determine the value of Δf_h that maximizes the Touschek lifetime for each value of ΔU_{ID} , for both 48- and 324-bunch modes.

Once this was determined, IBS and Touschek lifetime were computed using a simplification of the above procedure. In particular, the rms bunch length was used in the IBS calculations and, instead of performing calculations for all 100 ensembles, the 10th-percentile LMA was used as a conservative input. Figure 4.54 shows the variation in Touschek lifetime for 48- and 324-bunch modes with $\kappa = 1$. For 48-bunch mode, the decrease is just over 10%, while for 324-bunch mode, a nearly 25% decrease is observed. This results from stronger IBS in 48-bunch mode, but more importantly from the fact that the energy spread in 48-bunch mode is kept relatively constant by the microwave instability. Figure 4.55 shows that the variation in the emittance is $\sim 20\%$, corresponding to a $\sim 10\%$ variation in beam size and divergence. It is at first surprising that the variation in Touschek lifetime and

emittance are similar in magnitude, but different in functional dependence on ΔU_{ID} . The reason is that the energy spread varies more weakly than the emittance, even in 324-bunch mode. This, coupled with the fact that the energy spread contribution dominates the beam size in the regions with the smallest momentum acceptance, makes the lifetime variation differ from the emittance variation.

Figure 4.55 assumes that there is no canting of IDs. Since canting changes the residual dispersion in the straight sections, it might change the results. To check this, a comparison was made of the natural emittance for when all 70 devices (again 2.4-m-long, 27-mm-period devices were used) are canted to the case when all 70 devices are inline. The difference was greatest when all devices were closed to give $\Delta U_{ID} = 1.3$ MeV, but amounted to an increase of less than 1 pm. Since only a fraction of the IDs will in fact be canted, the effect is expected to be negligible.

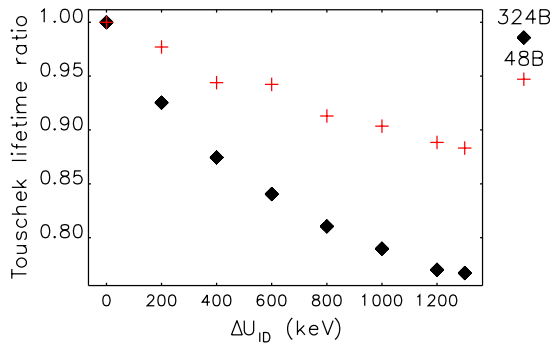


Figure 4.54. Variation in Touschek lifetime as a function of energy loss from IDs, assuming optimized HHC settings.

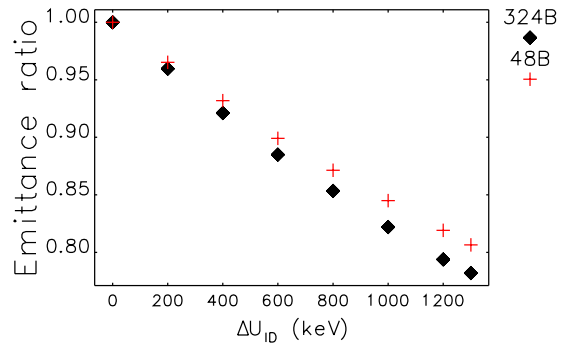


Figure 4.55. Variation in emittance as a function of energy loss from IDs, assuming optimized HHC settings.

4-2.8.2 Gas Scattering Lifetime Based on Species-Specific Pressure Profiles

The gas scattering lifetime includes contributions from elastic gas scattering and gas bremsstrahlung [3]. The elastic gas scattering lifetime is computed from the DA, while the gas bremsstrahlung lifetime is computed from the LMA. As with the Touschek lifetime, the DA and LMA make use of the Case 4 results from section 4-2.3 which includes not only errors, but realistic physical apertures in the arcs and IDs. In addition, the gas scattering calculations made of the species- and position-dependent gas pressure profiles, described in section 4-3.3.3. Several sets of profiles were provided, all based on simulations with MOLFLOW+/SYNRAD+ [4, 5]. These profiles differ in the data used for modeling photon-stimulated desorption (PSD), in the assumed number of ampere hours accumulated, and in the stored beam current. Four PSD models were used, as described in section 4-3.3.3, for three different conditions

1. 25 mA with 5 $A \cdot h$ dose. This is a plausible condition for the beginning of user operations.
2. 200 mA with 100 $A \cdot h$ dose. This is a plausible condition following the ramp-up to 200 mA, which would take place during the first year of operation.
3. 200 mA with 1000 $A \cdot h$ dose. This is a plausible condition following an additional year (5000 hours) of operation at 200 mA.

An example of the local scattering rates and corresponding pressure data is shown in Fig. 4.56.

Table 4.40 lists the elastic and bremsstrahlung-scattering lifetimes, τ_e and τ_b respectively, along with the total gas-scattering lifetime τ_g , for each condition and each PSD model. The lifetimes are worst for the Grobner model, and best for the Foerster model. There is significant disagreement among the models and no clear method of choosing among them. To introduce a measure of conservatism without excessive pessimism, the Foerster model was first discarded, then the median of the remaining values taken. Note that these results are for the lattice operated on the difference resonance, giving $\epsilon_y/\epsilon_x \approx 1$. For operation with $\epsilon_y/\epsilon_x \approx 0.1$, the DA and LMA are slightly reduced, giving slightly lower gas scattering lifetime.

Table 4.40. Gas-scattering lifetime results from calculations using species-specific pressure data

Model	τ_e h	τ_b h	τ_g h
25 mA after 5 A·h			
Foerster	49.2	49.5	24.7
Grobner	16.4	17.6	8.5
Halama	18.2	19.4	9.4
Mathewson	14.4	15.6	7.5
Notional	16.4	17.6	8.5
200 mA after 100 A·h			
Foerster	60.0	60.5	30.1
Grobner	8.8	9.4	4.5
Halama	12.7	13.7	6.6
Mathewson	16.5	17.7	8.5
Notional	12.7	13.7	6.6
200 mA after 1000 A·h			
Foerster	244.4	251.0	123.8
Grobner	26.2	28.3	13.6
Halama	45.4	49.0	23.6
Mathewson	74.6	79.9	38.6
Notional	45.4	49.0	23.6

4-2.8.3 Total Lifetime and Beam Parameters

Combining the Touschek and gas scattering lifetimes gives the total lifetime, which is listed in Table 4.41. The 10th-percentile lifetime for the 324-bunch mode is nearly 10 hours, while that for 48-bunch mode is just over 3 hours. This table also lists the required time between injections to maintain the droop in bunch current at 10% or less. For the 10th-percentile lifetime, the injection intervals are between 10 and 23 s, which is relaxed given that the injector runs at 2 Hz. Delivering 15.3 nC in a single shot has its challenges, as described in section 4-3.13. For 324 bunch round beam mode, the lifetime gain is roughly 60% compared to the brightness mode with 10% coupling, as shown in Table 4.41. For 48 bunch mode, it may not be possible to operate with flat beam, as lifetime is already very short.

To reduce radiation levels outside the shielding wall, it is desirable to keep the lifetime relatively long. The “APS Safety Assessment Document” states that the shielding calculations were performed for a 10-h beam lifetime with a 7 GeV, 360 mA beam. Assuming the implied radiation power is

the maximum acceptable, the corresponding lifetime requirement for the upgrade lattice at 200 mA and 6 GeV is $\tau \geq 4.8$ h. This is readily achieved for 324-bunch mode, but not for 48-bunch mode, where even the median value is below 4 hours. However, the 4.8-h number is based on the original APS shielding calculations. Updated calculations in Section 4-3.12.3.6 indicate that, under the assumption of good average injection efficiency, the required lifetime is considerably lower. Since computed injection efficiency is very high, it appears that lifetime even for 48-bunch mode is adequate.

Still, the 4.8-h value can be meaningfully be used as an ALARA goal. Given a gas scattering lifetime of 23.6 hours, as listed in Table 4.40, the required Touschek lifetime for a total lifetime of 4.8 hours is 6.0 hours. This is approximately the 85th-percentile of the Touschek lifetime distribution for 48-bunch mode. It is thought that the variation in the Touschek lifetime is related to variations in the quality of the orbit and optics correction, both of which can be improved over time in an operating machine. In addition, methods such as on-line optimization can be employed. Hence, long-term improvements of the lifetime to the desired value are expected to be possible. Of course, collimation and supplemental shielding will be used as needed to localize losses and reduce the radiation levels outside the shield wall. These matters are discussed in section 4-2.11 and section 4-3.12.

Table 4.41. Final beam parameters and total lifetime including IBS, impedance, harmonic cavity effects, Touschek scattering, and gas scattering, based on evaluation with 100 ensembles with errors and realistic apertures.

N_b	f_b MHz	Charge nC	κ	ϵ_x pm	ϵ_y pm	σ_δ 10^{-4}	σ_t ps	$\tau_{10^{th}}$ h	ΔT_{inj} s	$\tau_{50^{th}}$ h	ΔT_{inj} s
48	13.034	15.3	0.99	31.9	31.7	1.56×10^1	104	2.91	21.8	3.42	25.6
324	87.983	2.3	0.99	30.0	29.9	1.30×10^1	88	9.51	10.6	10.63	11.8
324	87.983	2.3	0.10	44.0	4.2	1.32×10^1	88	5.96	6.6	6.64	7.4

References

- [1] A. Xiao. “Study of IBS Effects for High-Brightness Linac Beams.” In: *Proc. of Linac 2008*. 2008, pp. 296–298 (cit. on p. 94).
- [2] A. Xiao and M. Borland. “Touschek Effect Calculation and Its Application to a Transport Line.” In: *Proc. of PAC 2007*. 2007, pp. 3453–3455. URL: <http://cern.ch/AccelConf/p07/PAPERS/THPAN098.PDF> (cit. on p. 94).
- [3] F. C. Porter. “Luminosity lifetime at an asymmetric e^+e^- collider.” In: *NIM A* 302 (1992), pp. 209–216 (cit. on p. 96).
- [4] M. Ady and R. Kersevan. “Introduction to the latest version of test particle Monte Carlo Code MolFlow.” In: *Proc. IPAC 2014*. IEEE, 2014, p. 2348. URL: <http://accelconf.web.cern.ch/AccelConf/IPAC2014/papers/wepme038.pdf> (cit. on p. 96).
- [5] R. Kersevan. “SYNRAD, a Monte Carlo Synchrotron Radiation Ray Tracing Program.” In: *Proc. PAC 1993*. IEEE, 1993, p. 3848. URL: http://accelconf.web.cern.ch/Accelconf/p93/PDF/PAC1993_3848.PDF (cit. on p. 96).

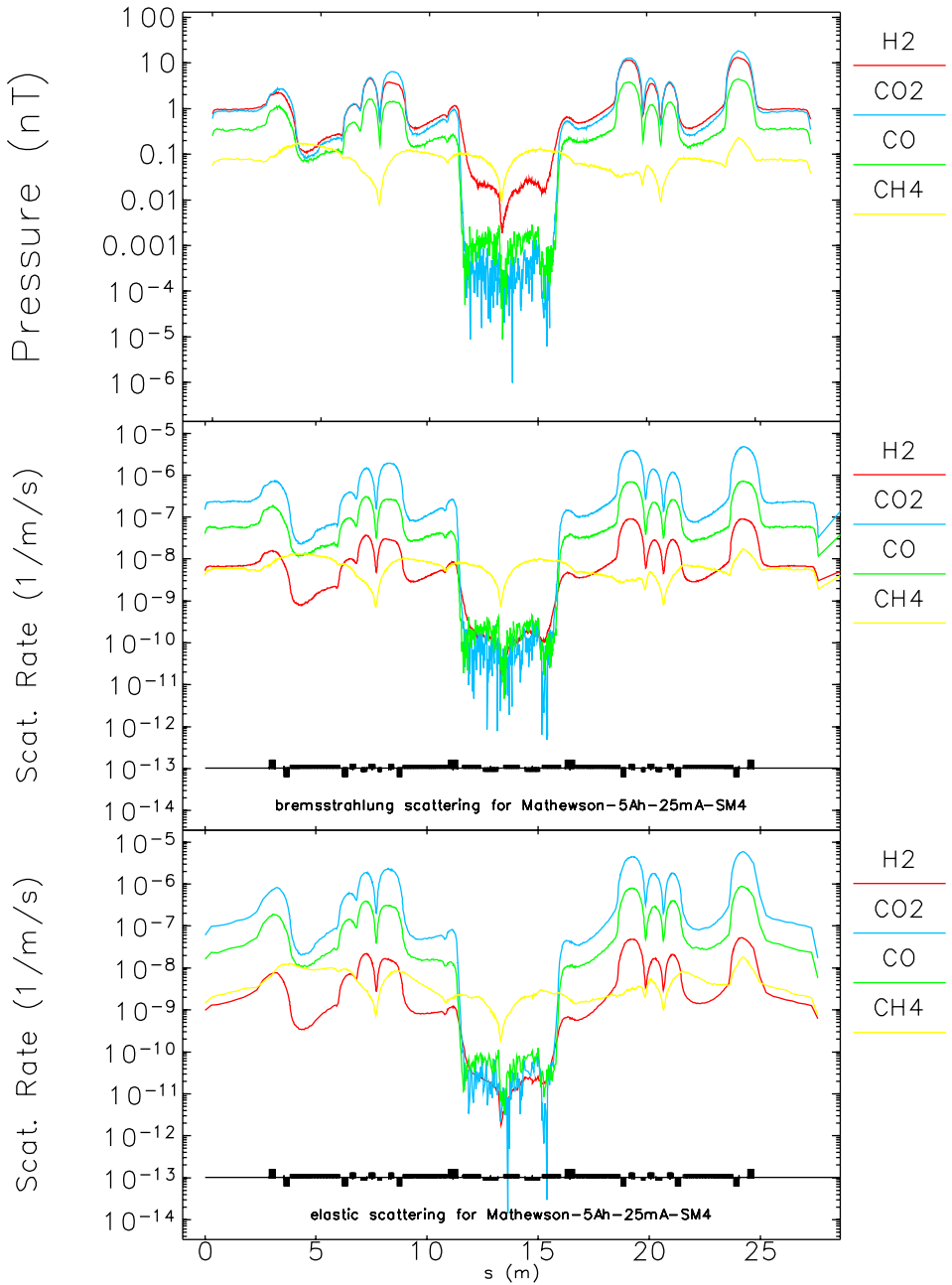


Figure 4.56. Local gas scattering rates computed using data from MOLFLOW/SYNRAD and elegant. This example shows results using PSD data from Mathewson, assuming 5 A · h dose and 25 mA operating current.

4-2.9 Beam Dynamics with Bunch-Lengthening Cavity

As seen above, lengthening the bunch is necessary to increase the Touschek lifetime. It also serves to limit the emittance-diluting effects of IBS and reduce rf heating of the beam position monitors, bellows, and other vacuum perturbations. An effective way to lengthen the bunch is using an HHC, which flattens out the rf potential created by the main rf cavities. This section describes beam dynamics simulations with such a cavity.

Approximate calculations performed with TAPAs [1] indicate that lengthening the bunch to 52 ps rms is possible while maintaining 4.5% bucket half-height using a fourth-harmonic cavity having a voltage of about 850 kV. For comparison, the zero-current bunch length is about 14 ps rms for a nominal main rf voltage of 4.4 MV. A third-harmonic cavity would be more effective, giving a 62 ps rms bunch duration, but would require 1.2 MV. The fourth-harmonic was selected since the power handling requirements of the external couplers (used for adjusting the Q) are more manageable.

Tracking studies allow simulating this in much more detail. Even in the simplest case, they can include the exact time-dependence of the rf fields and self-consistent interaction of the beam with the cavity mode. This is particularly important given that a passive cavity is being pursued to reduce cost and complexity. In addition, tracking studies can include longitudinal and transverse impedances, as well as higher-order beam transport effects. Beyond this, tracking studies permit exploration of issues such as bunch population variation, missing bunches from a train of equi-spaced bunches, the transient effect of a lost bunch, and other details.

4-2.9.1 Theoretical Expectations

The HHC provides bunch lengthening by reducing the local slope, and hence longitudinal focusing, of the total accelerating voltage, as depicted in Fig. 4.57. The expression for the total voltage $V(t)$ from the rf systems is given as

$$V(t) = V_o [\sin(\omega_o t + \phi_o) + k \sin(n\omega_o t + \phi_n)], \quad (4.40)$$

where V_o , ω_o , and ϕ_o are, respectively, the voltage, frequency, and phase offset of the main rf, and kV_o , $n\omega_o$, and ϕ_n are, respectively, the voltage, frequency, and phase offset of the harmonic rf. A maximally flat voltage can be obtained by setting the first and second derivatives of Equation (4.40) to zero while additionally requiring that $V(t=0) = U_r$, where U_r is the energy loss per turn.

Neglecting potential well distortion and the longitudinal impedance, Equation 4.40 along with the equation for synchrotron motion gives a first-order approximation to what can be expected from inclusion of an HHC. The longitudinal phase space motion can be described by a Hamiltonian [2, 3] with a potential, $W(t)$, of the form

$$W(t) = \int_0^t [eV(\tau) - U_r] d\tau. \quad (4.41)$$

The resulting instantaneous electron current is [2, 3]

$$I(t) = C \exp\left(\frac{-W(t)}{T_o \alpha_c E \sigma_s^2}\right), \quad (4.42)$$

where T_o is the revolution period, α_c is the momentum compaction factor, E is the nominal beam energy, σ_δ is the rms fractional momentum spread, and C is such that $\int I(t)dt$ over suitable limits to cover the entire bunch is equal to the bunch charge.

The instantaneous current for a few scenarios with a 48-bunch fill is shown in Fig. 4.58. The ideal scenario represents the maximally flat potential with $V_o = 4.1$ MV and $n = 4$. The over- and under-stretched cases represent an HHC over-voltage and under-voltage, respectively. Clearly the peak current with no HHC is substantially reduced with the HHC. The rms bunch durations are 12, 50, 69, and 40 ps for no HHC, the ideal, over-stretched, and under-stretched scenarios, respectively.

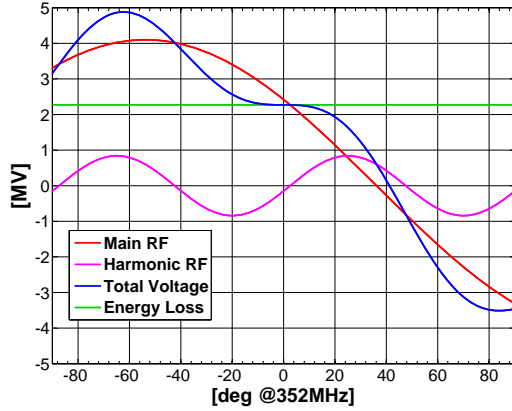


Figure 4.57. Rf voltages for a maximally flat total voltage using a 4th harmonic cavity for bunch lengthening.

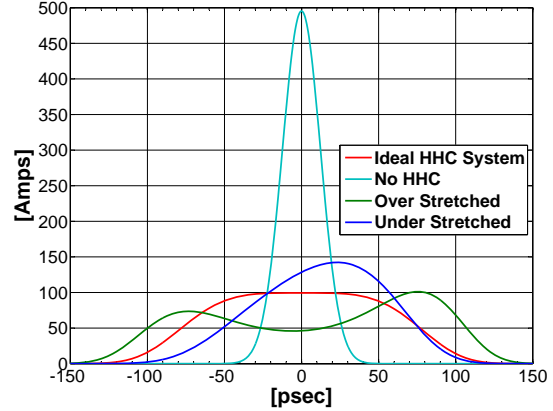


Figure 4.58. Instantaneous current for 48-bunch fill with 200 mA beam current, 4.1 MV main rf voltage, and $n=4$, for various bunch-lengthening conditions.

The parameters of Equation (4.40) with $V_o = 4.1$ MV and $n = 4$ for the ideal case shown in Fig. 4.58 are $\phi_o = 143.8$ deg, $kV_o = 0.84$ MV, and $\phi_n = -10.36$ deg. Since ϕ_n is negative, the beam loses energy to the harmonic cavity. This can also be understood by realizing that the harmonic voltage is negative at the beam center, $\omega_o t = 0$, in Fig. 4.57. This implies that the beam can be used to completely drive the cavity without the use of an rf power source. This is what is considered to be a passive system.

In a passive system, the resultant harmonic voltage is determined by the beam current, the cavity loaded Q (Q_l), and the cavity detuning ($\Delta f = f_h - n f_o$, where f_h is the cavity resonant frequency, and $n f_o$ is the harmonic drive frequency). In turn, since the harmonic voltage determines the beam current profile $I(t)$ according to equations (4.41) and (4.42), the solution of both the harmonic voltage and the beam current profile in a passive system has to be self-consistent.

In fact, the instantaneous currents for the scenarios shown in Fig. 4.58 are self-consistent solutions, which were determined by a technique which is similar to that used in Ref. [4]. The cavity parameters were: for the ideal case, $Q_l = 2.3 \times 10^5$, $\Delta f = 16.3$ kHz; for the over-stretched case, $Q_l = 6 \times 10^5$, $\Delta f = 14$ kHz; and for the under-stretched case, $Q_l = 6 \times 10^5$, $\Delta f = 18$ kHz. In all cases, the main rf voltage is equal to the ideal $V_o = 4.1$ MV with $\phi_o = 143.8$ deg, which can be forced since the main rf cavities must be driven by an RF power source to make up for the total beam energy losses.

As noted, this treatment excludes certain effects such as potential well distortion and the longitudinal

impedance of the storage ring vacuum chambers. These can be included self-consistently by using a tracking simulation.

4-2.9.2 Simulation Methods

The simulations make use of parallel `elegant` [5, 6]. Ten elements are needed:

- **ILMATRIX**: Provides fast, symplectic single-turn beam transport simulation that incorporates longitudinal, chromatic, and transverse nonlinearities. This element is configured by a script that processes output from `elegant`'s `twiss_output` command.
- **SREFFECTS**: Provides fast lumped-element simulation of synchrotron radiation. This element is also configured by a script that processes output from the `twiss_output` command.
- **WATCH**: Provides bunch-by-bunch beam phase space and bunch-by-bunch statistical data during tracking.
- **HISTOGRAM**: Provides bunch-by-bunch histograms during tracking. Used to record the longitudinal density.
- **RFCA**: Simulates an idealized, externally-driven rf cavity, imposing a $V \sin \omega_m t$ energy change on particles, where $\omega_m = 2\pi f_m$ is the angular frequency of the main cavities. This element provides the generator-driven part of the main cavity fields.
- **CHARGE**: Imparts charge to macroparticles and allows changing the charge during a tracking run. In combination with `elegant`'s `modulate_elements` command, allows slowly ramping up the beam current to achieve a quiet start.
- **RFMODE**: Simulates a beam-driven cavity mode. This is needed for the beam-driven part of the main cavity fields as well as for the beam-driven fields in the passive harmonic cavity. In addition to the bunch-to-bunch effects of the resonating fields, this element implicitly includes the short-range wake resulting from the fundamental cavity modes.
- **ZLONGIT**: Simulates the short-range wake, excluding the rf cavities. The geometric impedance is computed using GdfidL [7], while the resistive wall impedance is computed analytically. This is described in more detail in section 4-2.4.
- **TFBPICKUP**: Simulates a pickup to be used for bunch-by-bunch feedback. In this case, the pickup is assumed to be an ideal detector of energy offset with a filter that averages over 10 turns.
- **TFBDRIVER**: Simulates a driver to be used for bunch-by-bunch feedback, based on data from a **TFBPICKUP** element.

The tracking studies presented here used 48 or 324 bunches, with each bunch represented by a number of macro-particles. Earlier studies showed that 100,000 macroparticles per bunch were needed to ensure convergence of the results for 48 bunch mode, where the microwave instability is in play.

Table 4.42 shows parameters of the cavities, as used in the simulations.

4-2.9.3 Choice of Loaded Q and Detuning

To provide bunch lengthening, the HHC must be detuned to the positive side. This also means that it is Robinson anti-damping [8]. If the HHC is not detuned sufficiently, the beam will be

Table 4.42. Assumed cavity parameters

System	Revolution Harmonic	R/Q (ohm)	Loaded Q	Number of cavities
Main	1296	208	9100	12
Harmonic	4 * 1296	109	variable	1

unstable because the Robinson damping from the main cavities will be insufficient to overcome this anti-damping. In addition, the induced voltage and the anti-damping effect are influenced by the loaded Q of the HHC, which can be controlled using variable couplers. Earlier studies concluded that a loaded Q of $Q_l = 6 \times 10^5$ for the HHC was effective, allowing significant bunch lengthening while maintaining stability. Although more explorations of the optimum value are planned, this value is assumed in all subsequent simulations.

In addition to the loaded Q for the HHC, the detuning of both the HHC and main cavities is free to vary within some limits. At 200 mA and in the absence of the HHC, the ideal detuning of the main cavities is approximately -17 kHz. Depending on the amount of power transferred to the HHC load, this value may decrease by up to approximately 1 kHz. Further decreasing the detuning of the main cavities will somewhat increase the Robinson damping, but this was not found to have a strong effect. For this reason, the main cavities are assumed to be detuned so as to minimize reflected power.

The sole remaining knob is the detuning of the HHC, which was varied in the tracking simulations. Figure 4.59 shows the rms bunch duration as a function of the detuning of the harmonic cavity. As expected, as the cavity is tuned toward resonance, the bunch becomes longer. The cavity voltage (not shown) rises to slightly over 1 MV. There are differences for 324 and 48 bunch mode, due to the microwave instability's impact on the latter. This is verified by Fig. 4.60, which shows the rms fractional energy spread. As the cavity is tuned closer to resonance and the bunch lengthens, the microwave instability is partly suppressed and the energy spread in the 48-bunch fill approaches the nominal value. The rms bunch length in the two fill patterns eventually converges, becoming dominated by the fact that the bunch is nearly split in two; hence the still-higher energy spread for 48-bunch mode has diminished impact. In the case of 324 bunches, tuning too close to the resonance results in oscillation of the bunch length and energy spread.

As the bunch duration changes, the bunch shape also changes, deviating strongly from a simple gaussian shape. This is shown in Figs. 4.61 and 4.62. As shown in section 4-2.8.1, the maximum Touschek lifetime is obtained for overstretched bunches, i.e., bunches that are partly separated into two bunches. For 48-bunch mode, the optimum is near $\Delta f_h = 9$ kHz, while for 324-bunch mode, the optimum is near $\Delta f_h = 11$ kHz.

The simulation results just shown are for a 200-mA beam that has equilibrated. It is also of interest to understand the properties for beams of intermediate current. This was simulated assuming uniform 48-bunch fills with total current from 1 mA to 200 mA. These results are shown in Fig. 4.63, where it is seen that at low current, the nominal energy spread and bunch duration are obtained. As the current increases, the bunch length also increases, as would be expected. At a total current of approximately 70 mA (about 1.5 mA per bunch), the energy spread starts to increase, marking the onset of the microwave instability. This is somewhat lower than discussed in section 4-2.4, which is

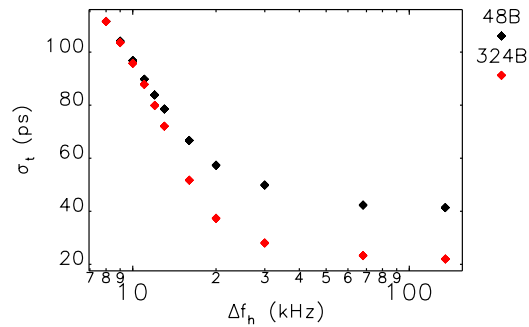


Figure 4.59. Rms bunch duration for 48- and 324-bunch modes as a function of the harmonic cavity detuning Δf_h .

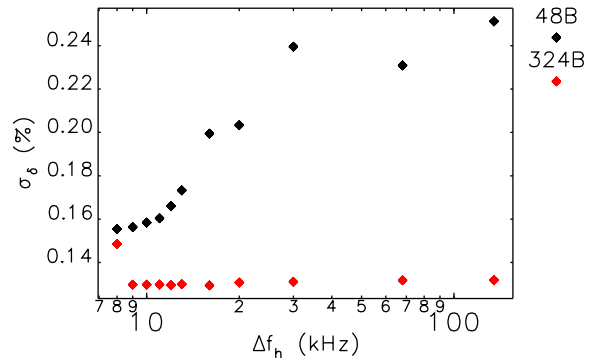


Figure 4.60. Rms energy spread for 48- and 324-bunch modes as a function of the harmonic cavity detuning Δf_h .

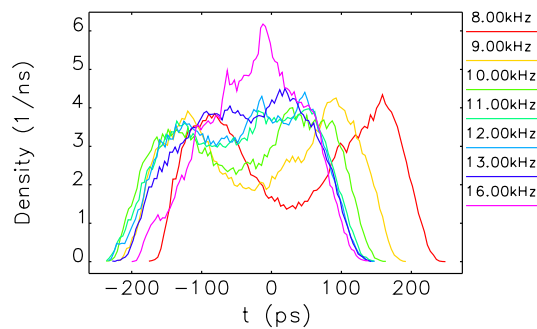


Figure 4.61. Samples of the longitudinal bunch density normalized to unit area for 48-bunch mode for various values of Δf_h .

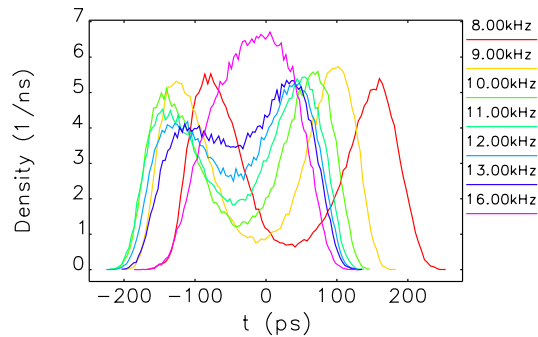


Figure 4.62. Samples of the longitudinal bunch density normalized to unit area for 324-bunch mode for various values of Δf_h .

understandable since in that section the bunch was assumed to be ideally lengthened, whereas in the present case the lengthening is limited by the relatively low HHC voltage at low current.

The bunch length continues to grow as the beam current increases, since the HHC voltage is also increasing. The energy spread largely stabilizes as a result. Again, the results are different from those in section 4-2.4, since in that section the bunch is not overstretched as it is here.

4-2.9.4 Effects of Bunch Population Variation

The population of individual bunches in the train is expected to vary as a natural result of the periodic filling and swapping out of single bunches, in addition to variations in the injected charge per pulse and in the injection efficiency. Nominally, a bunch will be replaced when it has lost 10% of its original charge. It is thus expected that bunch charge will vary quasi-linearly from 105% to 95% of nominal, with a random pattern around the ring.

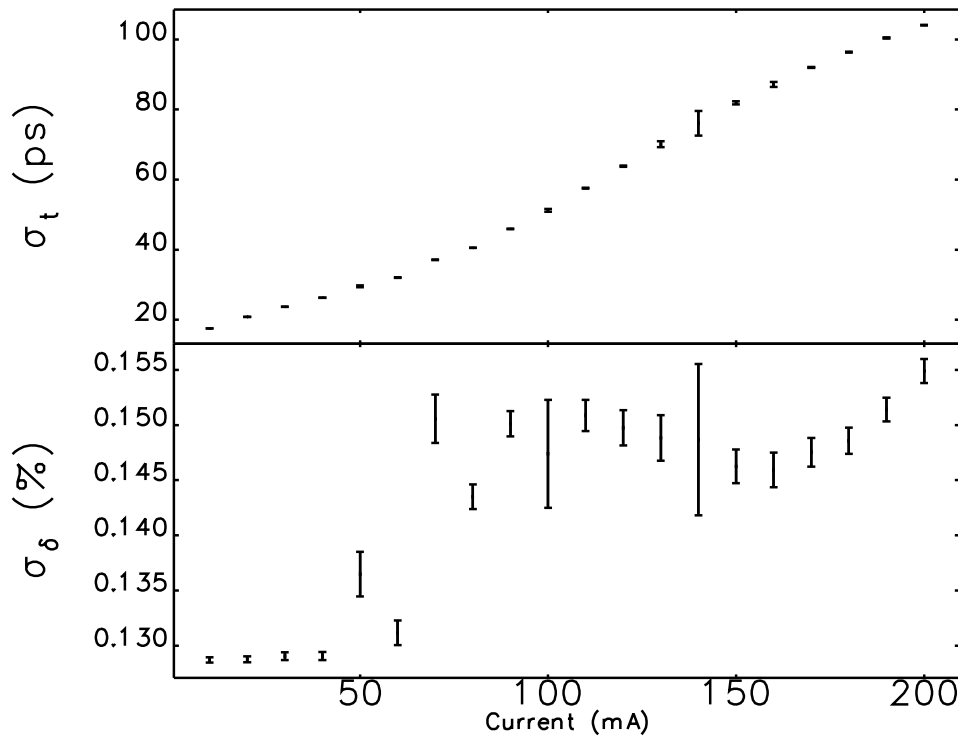


Figure 4.63. Rms bunch duration and rms energy spread as a function of total current for a 48-bunch fill, with fixed $\Delta f_h = 9.0$ kHz and $Q_L = 6 \times 10^5$.

To simulate this, ten random 48-bunch beams were generated, each with a bunch population that varies linearly through the expected range, but with the bunches in random order. Each beam was tracked to equilibrium using the approach described above. The results were then analyzed to determine the distribution in bunch duration across all bunches and all cases. As seen in Fig. 4.64, the variation is negligible. The standard deviation of the bunch duration distribution is less than 1 ps, compared to a bunch duration of over 100 ps. Hence, the effect on the Touschek lifetime is expected to be at the 1% level. The variation in bunch arrival time was also computed, and found to be much less than the rms bunch duration.

4-2.9.5 Multibunch Instabilities

Multibunch instabilities are discussed in Section 4-2.5 using a point-particle model that cannot fully include the effects of the harmonic cavity. Tracking studies of these instabilities have also been performed, including not only the accelerating mode of the main cavities and the main mode of the passive harmonic cavity, but also the higher-order monopole and dipole modes of the main cavities. (The HOMs of the harmonic cavity are ignored as the shunt impedances are very low, resulting in very low growth rates.)

The tracking used 15 monopole modes in each of the 12 main cavities. The mode frequencies are to some extent unknown, so 10 sets of possible frequencies were used. The 10 sets correspond to various percentiles of the growth rates predicted by `clinchor` [9] simulations. (The tracking also

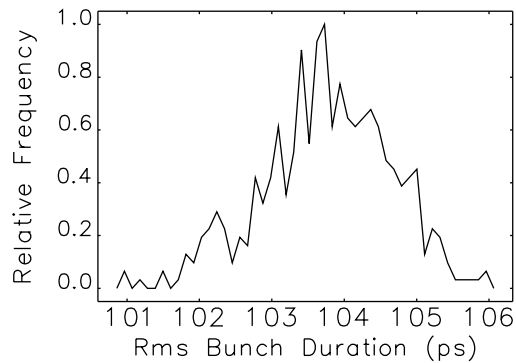


Figure 4.64. Distribution of rms bunch duration when the charge per bunch varies by 10% due to nonuniformity of the fill.

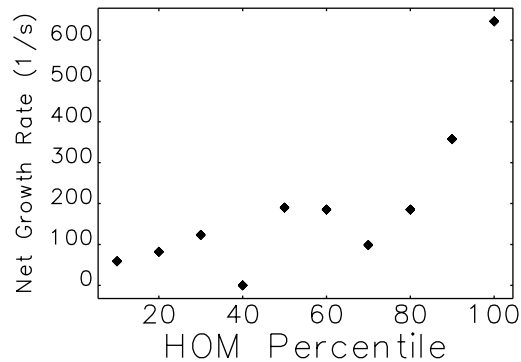


Figure 4.65. Net growth rates of multi-bunch instabilities for 48-bunch, 200-mA beam for various randomized HOM frequencies, labeled by the expected percentile of the growth rate.

included dipole modes, but these were never observed to cause instability and won't be discussed further.)

The first round of simulations was designed to determine the growth rates in the absence of longitudinal feedback (LFB). To start, a 48-bunch, 200-mA beam is brought to equilibrium by ramping the current from 0, with LFB turned on with no strength limit. After 200 mA is achieved, feedback is gated off and the HOMs are activated. Tracking continues for 15,000 turns or until amplitudes are excessive (as indicated by loss of beam or particles outside the rf bucket). Taking the envelope of $\langle \delta \rangle$ over all bunches as a function of turn provides a signal that reflects the amplitude of the dominant beam modes. An exponential is fit to this signal, giving a net growth rate (instability growth rate less synchrotron radiation damping rate). Figure 4.65 shows the net growth rates for the various HOM sets. The simulated rates are generally higher for the higher percentile frequency sets, as expected.

Based on these results, it seems advisable to have a strong, fast LFB system, which is indeed planned. Of course, it should also be possible to mitigate the issue to some extent with temperature tuning of the cavities. The highest growth rate corresponds to a growth time of ~ 1.5 ms, or ~ 420 turns, which is less than a synchrotron period. Hence, the LFB system probably cannot wait for a momentum offset to turn into a phase offset before acting, but should measure the momentum offset and act quickly. The LFB used in the simulations averages the momentum offset over 10 turns, then computes and applies the required momentum kick to reduce the momentum offset by 2.5%, subject to a strength limit. The 2.5% value was obtained through several trials and is subject to further optimization.

Because of the low synchrotron tune, there is a concern that the momentum offset signal needed by the LFB will be confused with orbit motion. Although details remain to be worked out and validated, multiple beam position monitors (BPMs) in dispersive and nondispersive regions can be used to separate out these various signals. One promising concept is to take advantage of the $\approx 3\pi$ horizontal betatron phase advance between the two high-dispersion regions within each sector.

Additional simulations were performed with LFB limited to a practical strength of 4 kV. Figure 4.66 shows that the required strength is 3-4 kV in steady-state conditions. The 100th-percentile case could not be stabilized with the feedback limited to 4 kV.

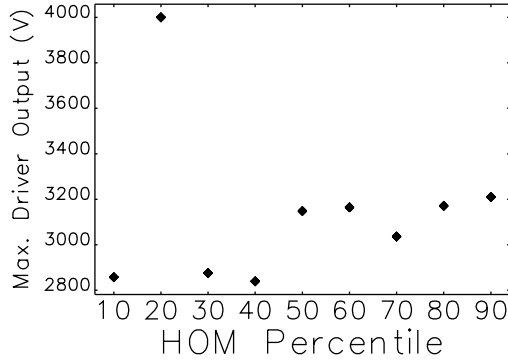


Figure 4.66. Maximum LFB driver output in steady-state conditions for 48-bunch, 200-mA beam for various randomized HOM frequencies, labeled by the expected percentile of the growth rate.

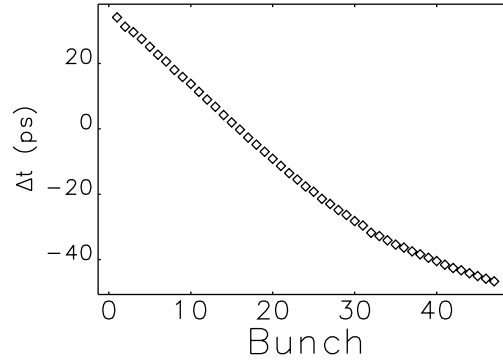


Figure 4.67. Equilibrium bunch centroids for 48-bunch fill after kicking out of bunch 0.

Further simulations were performed to understand possible transient requirements. Ideally, when a bunch is depleted, it is replaced by a full-current bunch. This is done by extracting and dumping the depleted bunch and immediately injecting the replacement. However, it may happen that a depleted bunch is extracted, but the replacement bunch is not injected. This might result from a last minute malfunction in the injector, for example. In this case, the voltage in the rf cavities will exhibit transients, which will modulate the bunch duration and phase bunch-by-bunch.

This scenario was modeled directly by first bringing a 200-mA, 48-bunch beam to equilibrium by using the procedure described above. After equilibration, a single bunch was kicked out, after which tracking continued for an additional 12,000 turns. Of interest is the transient behavior following the extraction of the bunch, the longitudinal distribution when equilibrium is reached, and the strength of the longitudinal feedback system.

It was found that a limit of 4 kV on the strength of the longitudinal feedback system was sufficient (smaller values were not tried for all the cases), except for the 100th-percentile case, which was unstable even before the bunch was lost. In all other cases, the LFB pegs at 4 kV immediately after the loss, but is able to stabilize the beam. Some limited excitation of several HOMs is seen after the bunch is lost, but this does not cause an instability.

After kicking out a bunch, the return to equilibrium takes about 5000 turns, after which there is a clear spread in the bunch lengths. Figures 4.67 and 4.68 show, respectively, the equilibrium arrival time centroids and rms bunch durations after equilibrium, obtained from averages over the last 5000 turns. (These results are from an earlier round of simulations with 10 main rf cavities; however, the results for 12 rf main rf cavities should be very similar.) The centroids vary by about 80 ps, which is a significant fraction of the rms bunch duration. The rms bunch duration also varies, though

only by about 10%, so a dramatic change in Touschek lifetime is not expected. The shapes of the bunches, shown in Fig. 4.69, are skewed in different directions at the two ends of the bunch train.

Hence, simulations show that accidentally kicking out a single bunch is a manageable situation with modest longitudinal feedback. Many users might not notice the incident, and normal operation could resume after the missing bunch is injected. More of a concern is that one HOM set could not be stabilized even with a uniform fill; more work on temperature tuning and optimized LFB is needed to address this case.

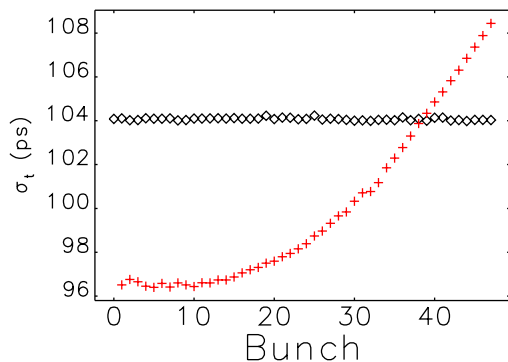


Figure 4.68. Equilibrium rms bunch durations for 48-bunch fill after (black) kicking out bunch 0, compared to values with all bunches present (red).

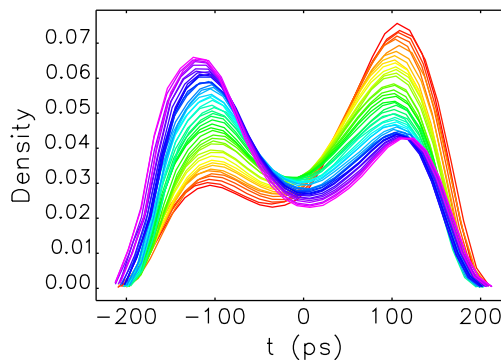


Figure 4.69. Equilibrium bunch shapes for bunch 1 (red) through 47 (magenta) after bunch 0 is lost.

4-2.9.6 Effects of Bunch Train Gaps

In order to suppress ion effects (see 4-2.6), it may be necessary to include gaps in the bunch train for 324-bunch mode. This of course implies running with fewer than 324 bunches.

A well-known issue with bunch train gaps is that they introduce transients in the rf systems, which result in modulation of the bunch arrival times, durations, and shapes. Particularly for long gaps, this can significantly reduce the beneficial effect of the harmonic cavity on the Touschek lifetime. This was simulated by introducing various numbers of two-bunch gaps — which are adequate to clear ions, see section 4-2.6 — into the 324-bunch train, keeping the total current constant at 200 mA. The Touschek lifetime was computed for each bunch using 100 samples of the longitudinal distribution, assuming for simplicity that the momentum acceptance was $\pm 2.5\%$. (This permits valid comparisons of ratios of loss rates and lifetimes.) As shown in Fig. 4.70, there is a $\sim 13\%$ variation in the lifetime depending on the position within the bunch train.

A potentially better approach is to introduce self-compensating gaps [10]. This idea starts with the observation that the filling time of the main cavities is about $6 \mu\text{s}$, while the filling time of the superconducting harmonic cavity is much longer. Anything that smooths the apparent current distribution on time scales $\lesssim 6 \mu\text{s}$ will reduce transient beam-loading effects. If the charge from the gaps is added to the nearest remaining bunches, rather than being spread among all the remaining bunches, this can be accomplished. For example, in creating a two-slot gap, there would be one

double-charge or “guard” bunch on either side of the gap. The guard bunches offer the additional benefit of providing a two-fold larger kick to ions, thus improving the effectiveness of the ion clearing gap.

Since the guard bunches have double the charge, they will also have roughly half the Touschek lifetime of the other bunches. Figure 4.71 shows that the Touschek lifetime of the bunches with nominal charge is very nearly constant, whereas that for the guard bunches is, to within 10%, half of the nominal value. There is little variation in the results for different numbers of gaps, although the average lifetime will of course decrease as the number of gaps increases. Inspection of the longitudinal distributions shows that the nominal-charge bunches are very uniform.

While it may appear from this comparison that the compensated scheme should have a large advantage in terms of the overall loss rate, this is not the case. The guard bunches not only have half the lifetime, they have twice the charge, and so contribute four times the loss rate as the normal bunches. Figure 4.72 compares the loss rate for the two schemes using two-bunch gaps, showing a small advantage for small numbers of gaps that declines and becomes a disadvantage as the number of gaps (and thus the number of guard bunches) increases. Variations on this scheme, e.g., having more, weaker guard bunches for each removed bunch, should provide reduced loss rates but less effective ion clearing. One such variation is shown in Fig. 4.72 as “Guard*2”: in this case, the charge from the removed bunches is distributed to two surrounding bunches on each side of the gap. This has lower total loss rate than the original scheme, with similar uniformity of bunch shapes. Of course, the ability to clear ions is somewhat diminished.

In summary, the introduction of ion-clearing gaps into the 324-bunch train has some effect on Touschek lifetime. This can be mitigated using a guard-bunch scheme, though the effectiveness of the scheme diminishes when the gaps are short or when there are many gaps. Perhaps the greatest benefit of the guard-bunch scheme is to provide superior ion clearing.

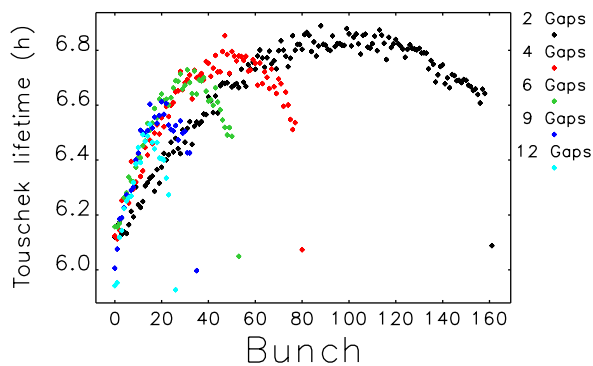


Figure 4.70. Touschek lifetime for unique bunches when various numbers of simple two-bunch gaps are used in the nominally 324-bunch fill.

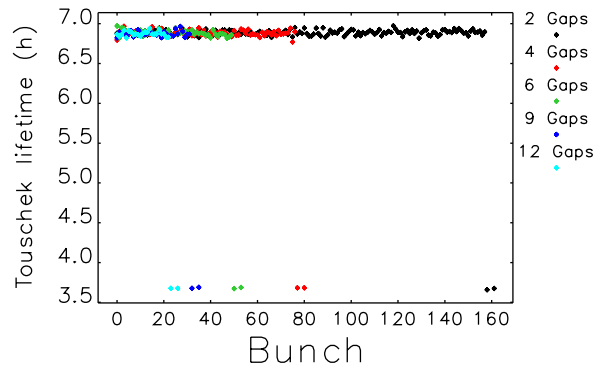


Figure 4.71. Touschek lifetime for unique bunches when various numbers of compensated two-bunch gaps are used in the nominally 324-bunch fill.

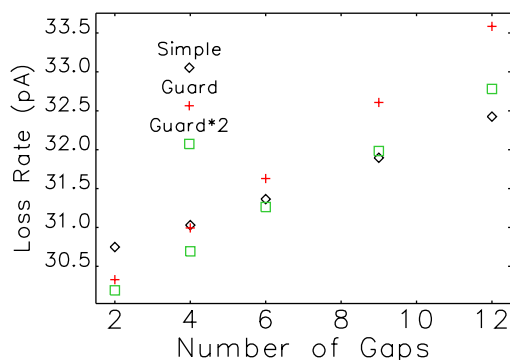


Figure 4.72. Loss rate due to Touschek scattering for two gap schemes as a function of the number of two-bunch gaps, along with a modified guard-bunch scheme.

References

- [1] M. Borland. “Recent Improvements to TAPAs, the Android Application for Accelerator Physics and Engineering.” In: *NAPAC16*. 2017, pp. 625–627 (cit. on p. 100).
- [2] A. Hofmann and S. Myers. “Beam Dynamics in a Double RF System.” In: *Proc. of 11th International Conference on High-Energy Accelerators*. 1980, pp. 610–614 (cit. on p. 100).
- [3] J. Haissinski. “Exact Longitudinal Equilibrium Distribution of Stored Electrons in the Presence of Self-Fields.” In: *IL Nuovo Cimento B* 18 (1 1973), pp. 72–82. URL: link.springer.com/article/10.1007/BF02832640 (cit. on p. 100).
- [4] P. F. Tavares, A. Andersson, and A. Hansson. “Equilibrium Bunch Density Distribution with Passive Harmonic Cavities in the MAX IV 3 GeV Storage Ring.” In: *Proc. of IPAC 2013*. 2013, pp. 1790–1792 (cit. on p. 101).
- [5] Y. Wang and M. Borland. “Pelegant: A Parallel Accelerator Simulation Code for Electron Generation and Tracking.” In: *AIP Conf. Proc.* 877 (2006), p. 241 (cit. on p. 102).
- [6] Y. Wang and M. Borland. “Implementation and Performance of Parallelized elegant.” In: *Proceedings of the 2007 Particle Accelerator Conference*. 2007, pp. 3444–3446. URL: <http://cern.ch/AccelConf/p07/PAPERS/THPAN095.PDF> (cit. on p. 102).
- [7] W. Bruns. “GdfidL on Massive Parallel Systems.” In: *Proc. of LINAC 2002*. 2002, pp. 418–420 (cit. on p. 102).
- [8] R. A. Bosch, K. J. Kleman, and J. J. Bisognano. “Robinson instabilities with a higher-harmonic cavity.” In: *Phys. Rev. ST Accel. Beams* 4 (2001), p. 074401 (cit. on p. 102).
- [9] L. Emery. *User’s Guide to Program clinchor*. http://www.aps.anl.gov/Accelerator_Systems_Division/Operations_Analysis/manuals/clinchor_V1.0/clinchor.html (cit. on p. 105).
- [10] M. Borland. *Touschek lifetime for the 41-pm lattice in 324-bunch mode with compensated gaps*. Tech. rep. AOP-TN-2017-001. APS, Jan. 2017 (cit. on p. 108).

4-2.10 Swap-out Injection Design and Performance

An on-axis vertical injection scheme was adopted for the MBA lattice design. It utilizes fast stripline kicker technology, which works together with a direct current (DC) Lambertson septum, and performs single-bunch “swap-out” injection [1, 2]. In this implementation of swap-out injection, the stored bunch with the least bunch current is extracted and dumped in the swap-out dump located inside the A:M1 magnets in sector 39 and a fresh bunch is injected immediately into the same bucket in the ID straight of sector 39. A conceptual layout of the extraction/injection region is shown in Fig. 4.73.

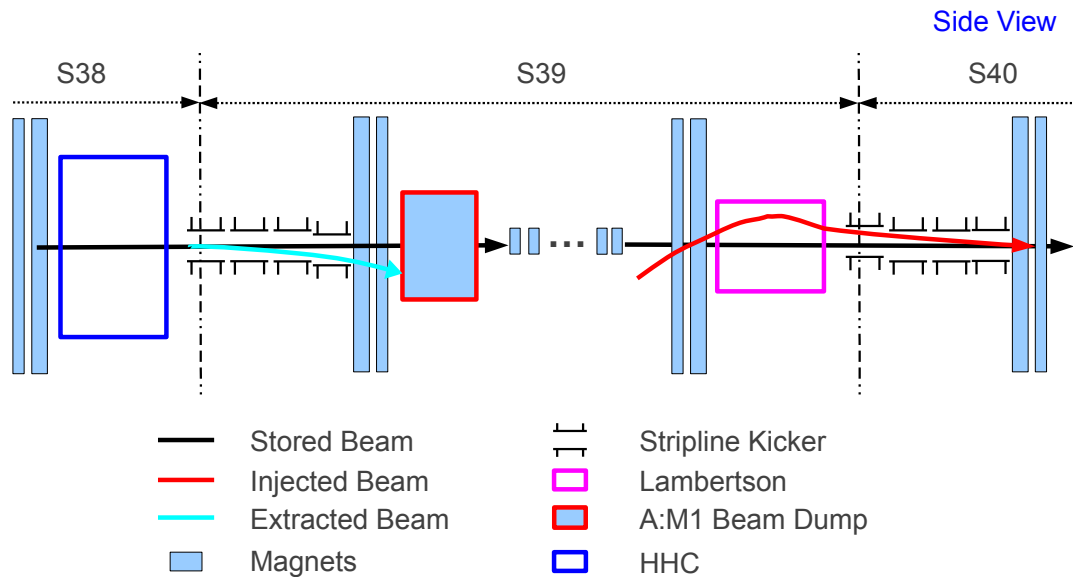


Figure 4.73. Schematic layout of extraction-injection region. Red line shows the current BTS line configuration. Blue box shows the section requiring modification for APSU.

This injection scheme has many advantages. First, the swap-out approach reduces the requirements for the dynamic aperture of the lattice because the injected beam is put directly on axis and does not experience any residual oscillations, thus allowing for lower emittance. For the same reason, it also benefits round-beam operation mode, which is important for obtaining longer beam lifetime, and greatly reduces the impact of collective effects at injection [3]. Second, performing injection within a single straight section avoids interference with the lattice optimization and possible lattice evolution. Third, injection in the vertical plane reduces the required stripline strength due to the smaller vertical beam size, which makes smaller-gap striplines possible and reduces the required injected/stored beam orbit separation at the exit of the septum. Among the disadvantages are the cost of the fast stripline kicker technology and the requirement for high injector charge since the entire bunch needs to be replaced in full.

4-2.10.1 Injection Line Design

The injection line design process consisted of three steps:

1. Design the on-axis injection section of the storage ring (SR).
2. Match the Booster to SR (BTS) transport line to the existing APS tunnel structure.
3. Perform optical function matching of BTS line to the APS-U ring.

Injection section of SR

A schematic of the injection section together with the projected injected beam orbit is shown in Fig. 4.74. Two basic requirements need to be satisfied: first, the horizontal separation between stored and injected beams (D1) at the exit of the last magnet (Q1 in the plot) has to be large enough to allow the injected beam chamber to get through the open space between the magnet poles; second, the vertical separation (D2) at the exit of the Lambertson septum magnet has to be larger than $(3\text{mm} + 2\text{mm} + 3\sigma_{inj})$, where 3-mm is the vertical half-gap of the vacuum chamber, 2-mm is the Lambertson wall thickness, and σ_{inj} is the vertical beam size of the injected beam. The Lambertson magnet is slightly tilted about the z axis to provide a gentle vertical bend that brings the injected beam trajectory close to $y = 0$ when it passes through magnets Q1 and Q2; this avoids passing through a pole or coil of either magnet.

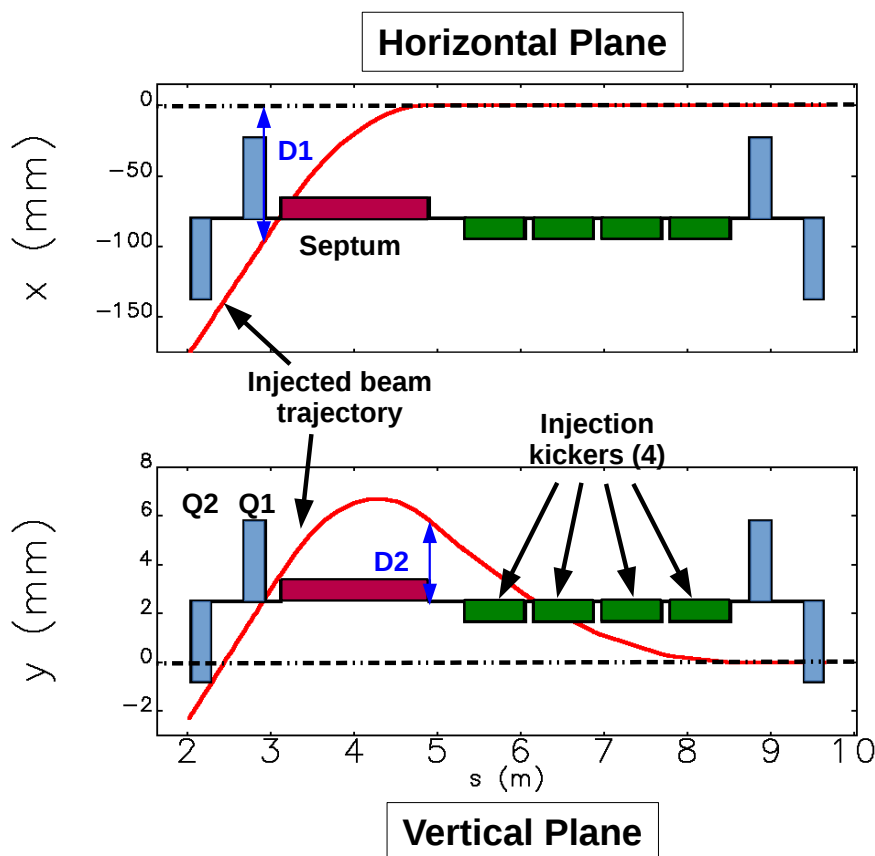


Figure 4.74. Layout of the on-axis injection section and the projected injected beam orbit.

Based on these requirements, the main design parameters are then determined and optimized by considering difficulty, risk, and availability of suitable technology. These parameters are listed in

Table 4.43. The main requirement on the fast stripline kickers is the kick strength of 1 mrad per meter of insertion length with a minimum gap of 9 mm (assuming the pulser voltage can reach ± 15 kV). To allow for a uniform stripline design, the kicker next to the septum is required to be shifted up vertically by 1 mm to accommodate the large injected beam trajectory at the entrance, as shown in the vertical projected trajectory in Fig. 4.74.

Table 4.43. Main parameters of injection elements

Title	Description	Value	Unit
Stripline	Length	0.72	m
	Gap	9	mm
	Pulser Voltage	± 15	kV
	Kick Angle	0.72	mrad
Lambertson	Length	1.78	m
	Wall Thickness	2	mm
	Field Strength	1	T
	Bending Angle	89	mrad
	Tilt Angle	93	mrad
	Stored Beam Half Aperture (x×y)	4×3	mm

Based on the selected parameters, the $\pm 3\sigma_{inj}$ injected beam envelope at various locations is listed in Table 4.44, where σ_{inj} is computed with $\varepsilon_{x,inj} = 100$ nm, $\varepsilon_{y,inj} = 20$ nm, and $\sigma_{\delta,inj} = 0.0012$, where $\varepsilon_{x(y),inj}$ and $\sigma_{\delta,inj}$ are the injected beam emittance and energy spread, respectively. It is assumed for now that the injected beam is shielded from the magnetic field of the storage ring elements (B:M1, Q1 and Q2) through which it passes. Effects from stray fields of these magnets will be evaluated in detail as the engineering design develops.

Table 4.44. Injected beam envelope ($\pm 3\sigma$) at specified locations for different injection configurations

Name	Location	x^- (mm)	x^+ (mm)	y^- (mm)	y^+ (mm)
B:M1	Exit	-180.5	-175.0	-3.73	-1.09
Q2	Entrance	-176.0	-170.6	-3.44	-0.83
	Exit	-156.0	-150.7	-2.17	0.32
Q1	Entrance	-120.0	-114.9	0.12	2.39
	Exit	-97.8	-92.8	1.53	3.67
Lambertson	Entrance	-81.3	-76.4	2.58	4.63
	Exit	-2.15	2.15	5.18	6.48
Kick-1	Entrance	-2.12	2.12	4.11	5.33
	Exit	-2.11	2.11	2.07	3.25

Matching of BTS line layout

As shown in Fig. 4.74, the injected beam trajectory needs to be matched in both the horizontal and the vertical direction. This is realized by two slightly tilted dipoles in the BTS, which act together

with the tilted septum magnet and stripline kickers to bring the injected beam on axis. Since the new BTS line must also fit into the existing tunnel, only the SR side of BTS line is modified for matching the geometry; the Booster side of APS BTS line layout is unchanged, see Fig. 4.75. The

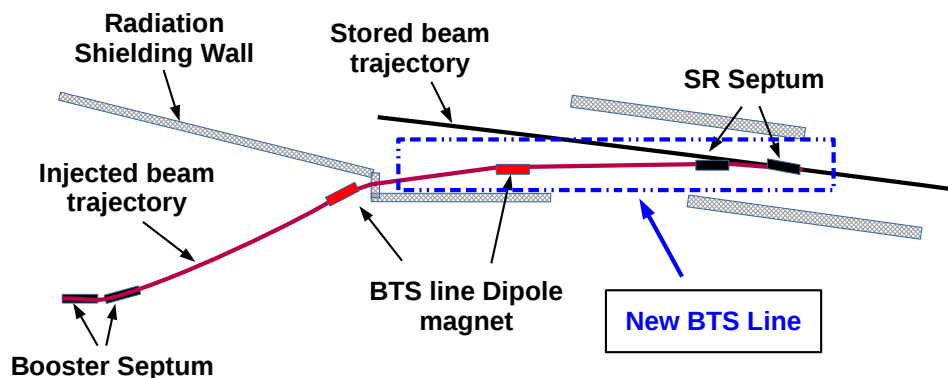


Figure 4.75. Schematic layout of APS injection region.

matched BTS line geometry is shown in Fig. 4.76. Note that, besides the septum magnet, which merges the injected and stored beam vacuum chambers into one, the centerline of the last magnet of BTS line is separated from the SR centerline by 30 cm to allow easier installation of hardware.

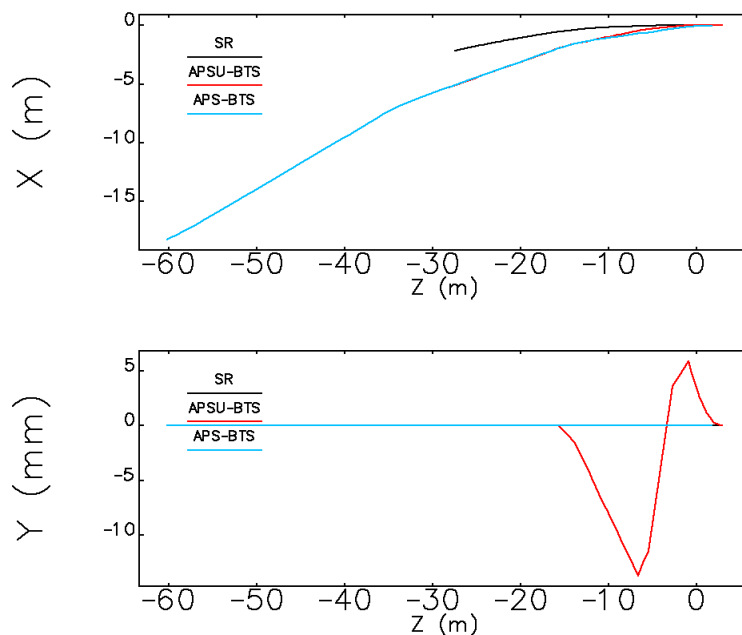


Figure 4.76. BTS line layout, upper plot – horizontal plane, lower plot – vertical plane. Black line – SR; red – APS-U BTS line; blue – APS BTS line.

Matching of BTS line optics

The BTS line optical functions are matched to the SR at the injection point using the 132-nm Booster lattice as input, see Fig. 4.77. As in the present BTS design, it consists of two dispersion

suppression sections at the beginning (Section A) and end (Section C), with one dispersion free section in the middle (Section B):

- Section A: dispersion suppression section. This section can also allow moderate optical function adjustments to change the input to downstream sections. The same magnet layout is kept in this section as in the current BTS line.
- Section B: dispersion-free section. This section is used for optical function matching and adjustment. It will also provide space for installation of various instruments to measure injected beam properties, e.g., beam emittance measurement.
- Section C: Final optical and geometry matching section. The transfer line in this section has weak vertical bends (see Fig. 4.76), and therefore it generates vertical dispersion. Two weak skew quadrupoles are installed in this section to correct the vertical dispersion at the injection point.

The main parameters of the BTS magnets are listed in Table 4.45

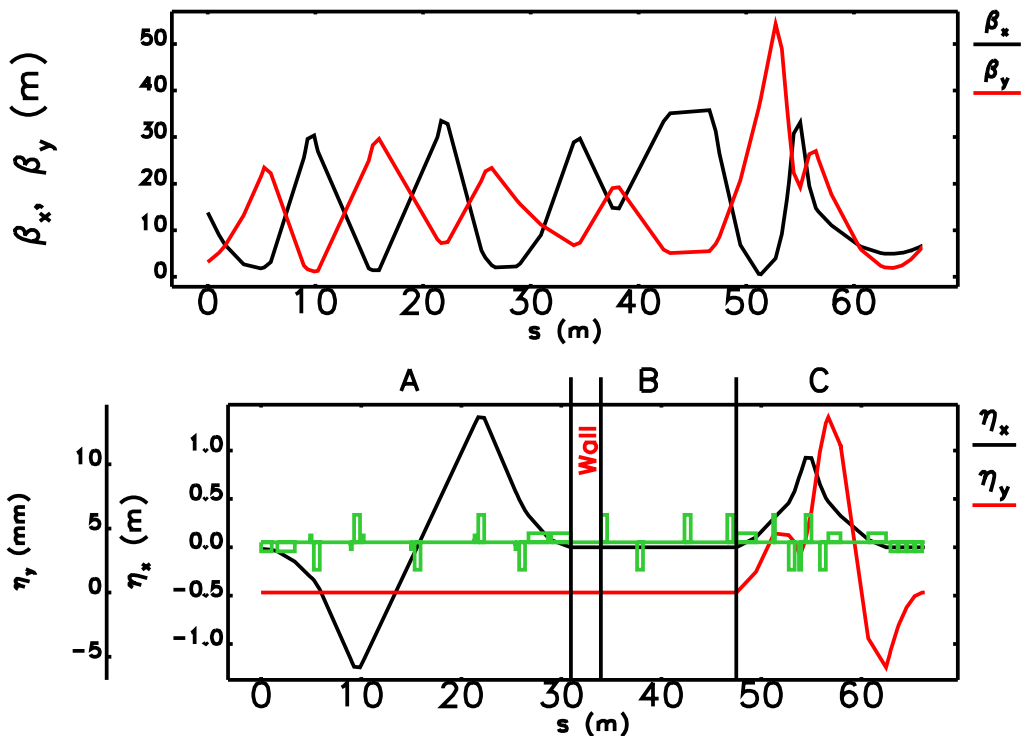


Figure 4.77. Optical functions of the BTS transfer line. The last optical and geometry matching section has two weak skew quads to correct the vertical dispersion to zero at the injection point.

4-2.10.2 Swap-out Extraction Section

The swap-out extraction kickers are located at the beginning of sector 39, sharing the same ID straight section with the bunch lengthening high harmonic cavity (HHC), as shown in Fig. 4.73. As a result, the entire swap-out injection process is largely transparent to the rf systems, so there

Table 4.45. *BTS line main magnet parameters*

Name	Length m	Angle deg	$K1$ m^{-2}	New Magnet	New Location
BTS:AQ1	0.6	—	-0.590	No	No
BTS:AQ2	0.6	—	0.596	No	No
BTS:AQ3	0.6	—	-0.441	No	No
BTS:AQ4	0.6	—	0.563	No	No
BTS:AQ5	0.6	—	-0.330	No	No
BTS:AB1	1.938	4.437	—	No	No
BTS:AB2	1.938	4.437	—	No	No
BTS:BQ1	0.6	—	0.411	No	No
BTS:BQ2	0.6	—	-0.417	No	Yes
BTS:BQ3	0.6	—	0.137	No	Yes
BTS:BQ4	0.6	—	0.379	No	Yes
BTS:BB1	1.938	6.218	—	No	Yes
BTS:CB1	1.2	3.691	—	Yes	Yes
BTS:CQ1	0.6	—	-0.669	No	Yes
BTS:CQ2	0.6	—	1.111	No	Yes
BTS:CQ3	0.6	—	-0.501	No	Yes
BTS:CSQ1	0.2	—	0.029	Yes	Yes
BTS:CSQ2	0.2	—	-0.026	Yes	Yes

are no significant beam loading changes when the swap-out is successfully performed. (See 4-2.9.5 for a discussion of transients that occur when swap-out fails.) To support this, sector 39 includes four stripline kickers in the straight section and one vertical collimator in the A:M1 magnet. Of these four stripline kickers, the last one is used as a pre-kicker, as discussed below, to reduce the energy density of the dumped bunch when it hits the swap-out dump (see 4-2.11.3 for discussion of the necessity of this). The other three are used to kick the bunch into the dump ~ 250 turns after the pre-kicker fires. If any one extraction kicker out of the three does not pulse, the bunch is still dumped at the intended location. The worst case is when the first extraction kicker misses the pulse; this moves the dump location to the downstream end of the swap-out dump. The layout of the extraction section, including vacuum chamber size variation, the first turn of pre-kicked beam trajectory, beam orbit and dump location for normal operation, and the worst case of misfiring of the first stripline kicker, is shown in Fig. 4.78. As with the injection section, when using a 9-mm-gap stripline kicker, the last stripline kicker is shifted down vertically by 1 mm to accommodate the dumped beam trajectory.

As described in 4-2.11.3, because of the high energy density in the bunch, it is inadvisable to extract a bunch into the swap-out dump without taking steps to inflate the bunch volume. One way to do this is using a spoiler, but there is no material that can be used for this purpose that will not be destroyed. However, decoherence following a small vertical kick has been found adequate for this purpose. In this scheme, the bunch to be extracted is pre-kicked some time prior to when it needs to be extracted. The combination of lattice nonlinearity and the impedance results in decoherence of the centroid motion, inflating the emittance of the bunch.

The simulation methods are similar to those employed in simulation of whole-beam dumps, as described in 4-2.11.4. The effect of the pre-kick is modeled using element-by-element tracking,

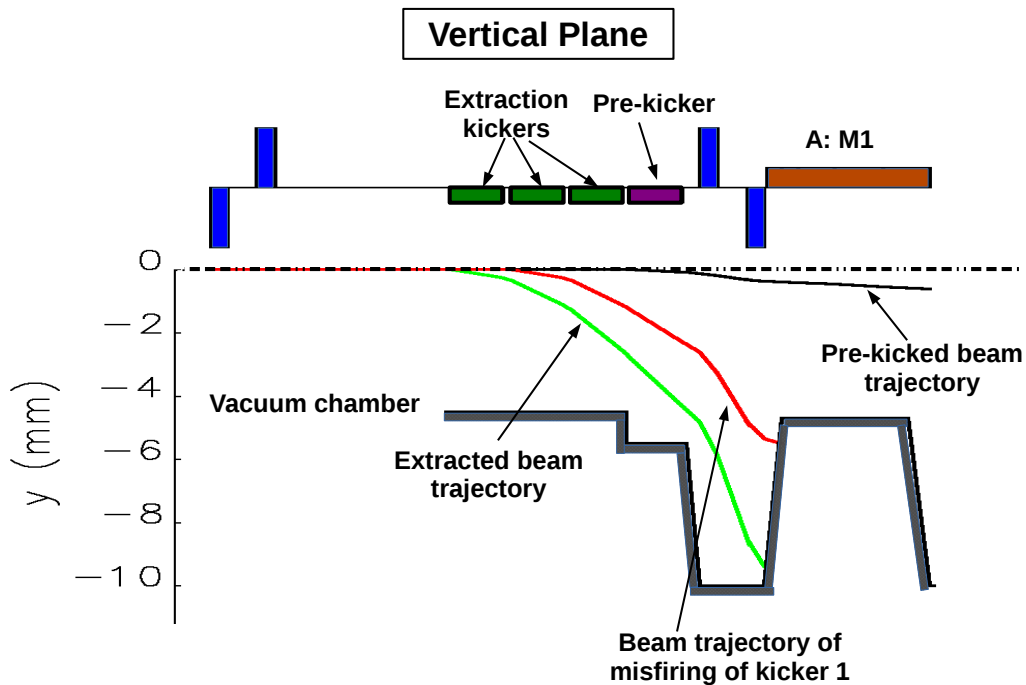


Figure 4.78. Layout of swap-out extraction section and dumping beam trajectory at different scenario.

including the element-by-element impedance model. Lattice errors are included using one of the error sets from the commissioning simulation, which gives realistic coupling of horizontal and vertical motion. The magnitude of the pre-kick was varied and it was found that a kick of 0.20 mrad was sufficient to cause significant inflation of the emittance without any beam loss. Beam loss needs to be avoided as it may not be sufficiently localized. In addition, excessive inflation of the emittance is to be avoided as it would make it more difficult to localize the loss point.

The decoherence process requires several hundred turns to effectively expand the bunch prior to swap-out. As an illustration, Fig. 4.79 compares the particle density on the face of the dump if nothing is done with the density when a 2.16 mrad extraction kick is given to the bunch 250 turns before extraction. The configuration is similar, but not identical to what is shown in Fig. 4.78. The particle density is reduced by a factor of ~ 100 as a result of the pre-kick. At this point, the bunch can be safely extracted into a copper dump. Because of the potential to damage the dump if the decoherence kicker fails to fire, the extraction kickers will be gated on a signal derived from the decoherence kicker's actual high-voltage waveform. In this way, if the pre-kicker does not fire, or does not fire with sufficient amplitude or correct timing, swap-out will not occur. See Section 4-3.12.4 for further discussion on machine protection.

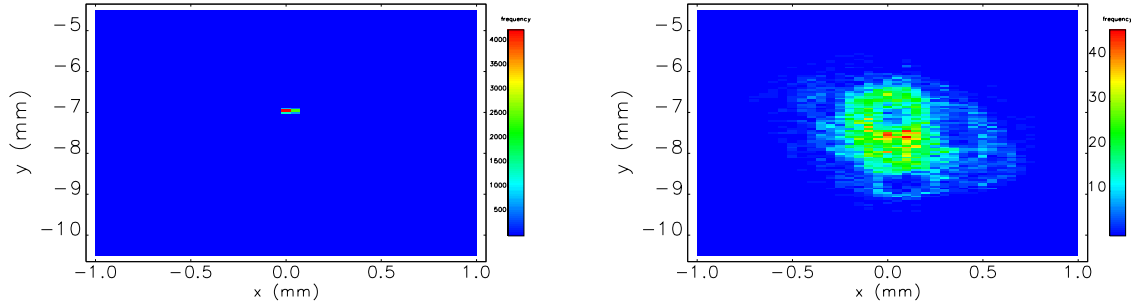


Figure 4.79. Bunch 0 transverse distribution at swap-out dump if extracted without (left) and with (right) a pre-kick. The two plots are on a fixed x - y scale and illustrate the large reduction in particle density with the pre-kick.

4-2.10.3 Injection Performance

Many imperfections can occur during the injection process, which may be organized in several categories: optical function mismatch, longitudinal mismatch, and injected beam trajectory error. The perturbation amplitude (A_u) is used to quantify the total perturbation strength, with u for x or y and $A_u = \gamma_u u^2 + 2\alpha_u uu' + \beta_u u'^2$.

4-2.10.3.1 Optical mismatch. Optical function ($\beta_{x,y}, \alpha_{x,y}, \eta_{x,y}, \eta'_{x,y}$) mismatch at the injection point is largely a static error that has contributions from the booster and storage ring systems. To evaluate the possible optical function mismatch originating from the booster, some knowledge of the booster to storage ring (BTS) transport line is required. Since a detailed BTS lattice design was only recently available, the current BTS line design, with an arbitrary matrix added at the end to match optical functions at the injection point, was used as the simulation model.

Modeling of optics mismatch was performed by adding strength and tilt errors to the BTS line magnets. Based on present experience, the rms relative strength errors were set to 1% and rms tilt errors were set to 1 mrad. Assuming that the beta functions at the exit of the BTS line will be corrected with accuracy of 10% or better, only the error sets that have beta function error at the exit of 10% or below are chosen for further simulations. This results in α mismatch being larger than β mismatch, which follows the assumptions that beta function is easier to measure than its slope. 5000 random cases were used to calculate the rms variation in the optical functions, which are then used in simulations of injection.

Optical errors of the storage ring itself are also important. To include this, the corrected ensembles obtained during lattice commissioning simulations (section 4-2.3) are used, which automatically includes optical and orbit errors.

4-2.10.3.2 Longitudinal mismatch. Longitudinal mismatch errors have static and randomly varying components. Static rf phase and energy errors can be reduced to a low level by beam-based

tuning using turn-by-turn BPMs in regions with high dispersion. Assuming a very conservative turn-by-turn resolution of $10\ \mu\text{m}$ with peak dispersion of $89\ \text{mm}$ gives an energy resolution of $\sim 0.01\%$. This corresponds to very small residual energy and phase errors, so these static effects are ignored. Energy jitter from the booster originates in power supply ramping errors, which was measured to be approximately $\sim 0.01\%$; a very conservative value of 0.5% was used in the simulations. A level of $100\ \text{ps}$ rms for the timing jitter between the arriving beam and the rf systems of the storage ring appears consistent with maintaining high injection efficiency and was chosen as a preliminary value for this specification. Further exploration of this requirement is needed, including self-consistent simulation of the jitter of the incoming beam relative to the kickers and of the kickers relative to the external clock.

The nominal booster energy spread for -0.6% -off-momentum operation is $\sigma_\delta = 0.103\%$, with a natural emittance of $64\ \text{nm}$. For a booster rf voltage of $9\ \text{MV}$, an rms bunch duration of $\sigma_t = 65\ \text{ps}$ is expected. These will both be inflated to a presently unknown degree by collective effects in the booster. At present, it is assumed that the combination of this factor and the above errors will increase the effective booster longitudinal phase space to $\sigma_\delta = 0.12\%$ and $\sigma_t = 100\ \text{ps}$, while the transverse emittances are $60\ \text{nm}$ and $16\ \text{nm}$, for the horizontal and vertical, respectively. (Note that these emittances are smaller than those used above for determining the required apertures in the injection components.)

The beam is assumed to be Gaussian, which will of course be mismatched to the storage ring bucket due to the presence of the harmonic cavity. Bucket mismatch is included by simulation of a fully-optimized harmonic cavity in the ring.

4-2.10.3.3 Trajectory error. Injected beam trajectory error also has static and random components. For simplicity in simulations, these have been assumed to be purely random, i.e., varying from shot to shot.

For injected beam pulse-to-pulse jitter (x, x', y, y') , the jitter amplitude has been obtained from APS operations [4]. In the vertical plane, the measured jitter corresponds to a beam center spreading over a $\Delta A_y = 0.3\ \text{nm}$ area in phase space. In the horizontal plane, the jitter mostly comes from booster septum strength error, which is measured as 1.1×10^{-4} . This corresponds to a beam center spreading over a $\Delta A_x = 5\ \text{nm}$ area in phase space. To simplify the simulation, errors are set in terms of the equivalent trajectory error at the injection point, using $\Delta u = \sqrt{\Delta A_u \beta_u}$. The values are $\sigma_{\langle x \rangle} = 180\ \mu\text{m}$ and $\sigma_{\langle y \rangle} = 27\ \mu\text{m}$ (see [5] for related discussion). The main error source is the booster septum strength error, which causes the horizontal injected beam trajectory error.

Strength errors from storage ring injection elements will also contribute to trajectory errors. Jitter from the stripline kickers will produce vertical trajectory errors. Based on earlier studies of loss rates [5], a limit of $\Delta A_y = 20\ \text{nm}$ was established, which corresponds to $\sigma_{\langle y \rangle} \approx 230\ \mu\text{m}$. Similarly, jitter on the septum will contribute an equivalent $\sigma_{\langle x \rangle} \approx 24\ \mu\text{m}$ to the horizontal trajectory. The various equivalent errors are added in quadrature to obtain the Gaussian width of the trajectory errors in x and y .

4-2.10.3.4 Summary and results. Table 4.46 summarizes the errors used in the simulations. Using these values, tracking studies of injection efficiency were performed in a fairly literal fashion. The tracking included element-by-element synchrotron radiation, main and harmonic rf cavities, edge and body multipoles on quadrupoles, body multipoles on sextupoles and dipoles, ID apertures, arc apertures, photon absorbers, and collimators. The values used are the same as used in Case 4 of the ensemble evaluation for dynamic and momentum acceptances. 1000-turn tracking was performed, after verifying that tracking for 1500 turns made little difference.

Table 4.46. Errors used in simulations of injection efficiency

Quantity	Value	Units	Sources
Δx	182	μm	Septum jitter, trajectory error
Δy	232	μm	Kicker jitter, trajectory error
$\Delta\delta$	0.5	%	Booster energy (very conservative)
Δt	100	ps	Relative rf phase
$\Delta\beta_x$	0.44	m	BTS optics errors
$\Delta\beta_y$	0.10	m	BTS optics errors
$\Delta\alpha_x$	0.044		BTS optics errors
$\Delta\alpha_y$	0.039		BTS optics errors
$\Delta\eta_x$	0.017	m	BTS optics errors
$\Delta\eta_y$	0.003	m	BTS optics errors
$\Delta\eta'_x$	0.005		BTS optics errors
$\Delta\eta'_y$	0.001		BTS optics errors

Tracking was performed for the first 50 corrected ensembles. For each ensemble, 25 jitter instances were used, with different jitter instances for each ensemble. For the incoming beam properties, we used $\epsilon_x = 60$ nm, $\epsilon_y = 16$ nm, $\sigma_\delta = 0.12\%$, and $\sigma_t = 100$ ps, as noted above. Tracking studies show that the vertical emittance increases dramatically, to a typical value of 60 nm, as a result of injection errors and cross-plane coupling. For the same reason, the increase in the horizontal emittance is moderated and it typically remains near the initial 60 nm value.

In order to improve accuracy, the tracking studies used uniformly-distributed particles with Gaussian weights. The coordinate values cover $\pm 4\sigma$ in all dimensions. This provides superior sampling of outlying particles compared to a simpler simulation with Gaussian-distributed coordinates. Simulations were performed for the configuration described in 4-2.3.3 as Case 4, which includes all apertures, systematic and random multipole errors, correction multipoles, and ID effects. To assess the effect of the booster emittance, several runs were performed:

- Nominal emittances as described above.
- Increased booster emittances 25% to $\epsilon_x = 75$ nm and $\epsilon_y = 20$ nm.
- Increased booster emittances 50% to $\epsilon_x = 90$ nm and $\epsilon_y = 24$ nm.

Even with the inflated emittance, the predicted injection losses are low, with a high probability of losses below the few percent level. This is seen in Fig. 4.80, which shows the cumulative distribution of the injection efficiency. For the nominal emittances, the losses are below 2% in 90% of cases. Even for the most extreme situation (50% increase in both emittances), the losses are below 5.1% in 90% of cases. Further, since the various cases represent the end result of the automated commissioning algorithm, it is expected that improvements will be possible with targeted effort.

Figure 4.81 shows the locations of the lost particles for the nominal beam parameters. In spite of the fact that the collimators limit the linear acceptance, most of the losses are at the two smallest gap IDs in sectors 4 (HSCU) and 33 (HGSCU). This suggests that reduction of the collimator apertures should be explored, although in the horizontal this would entail reducing the maximum achievable Touschek lifetime.

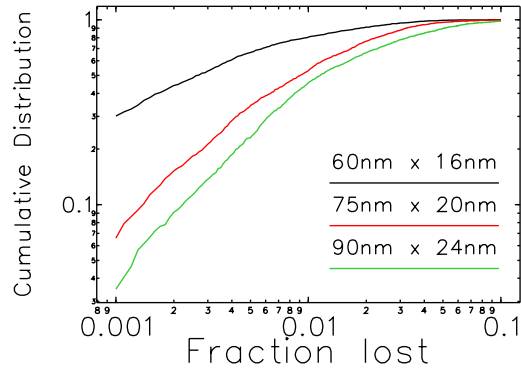


Figure 4.80. Cumulative distribution of fraction of injected particles that are lost, for various assumptions of horizontal and vertical emittance of the injected beam.

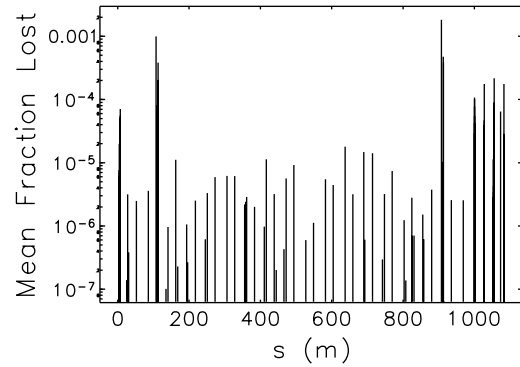


Figure 4.81. Locations of injection losses for the nominal 60nm by 16nm injected beam emittances.

Future developments in injection modeling will increase the realism and further refine requirements. Improvements will include simulation of the kickers using the measured waveforms, which will include effects of pulser jitter and arrival time jitter. In addition, field non-uniformity in the kickers together with details of transport through the septum and upstream ring magnets will be included.

4-2.10.4 Perturbations to Stored Beam

So far, the analysis has only looked at the variation in injection efficiency. However, the stored beam may also be perturbed by a residual kick that originates from a prolonged kicker waveform tail, an after-pulse from the kicker power supply, or a reflection from the stripline kicker structure. The effect can have systematic and random components. The systematic error is the same for all kickers, for example, a kick due to long waveform tail. The overall effect on the beam of all extraction and injection kickers is therefore weaker than the simple sum due to phase advance between extraction and injection sections. To study the effect, the perturbation amplitude (A_y) is used to quantify the total perturbation strength, with $A_y = \gamma_y y^2 + 2\alpha_y y y' + \beta_y y'^2$, where y and y' are perturbed stored bunch center coordinates at a watch point, and γ_y , α_y , and β_y are the corresponding optical functions.

The A_y values are calculated at different residual kick levels, with the static error (from a non-zero waveform tail) at 0%, 1%, 2%, 3%, 4% and 5% and the random error (from amplitude variation and timing jitter) at 1%, 2%, and 3% of the designed kick strength. At each error level, 20,000 random cases are simulated. Figure 4.82 shows the maximum A_y value over 20,000 random cases at different error levels (with linear interpolation between simulated points). This result will provide guidance in establishing the system tolerances.

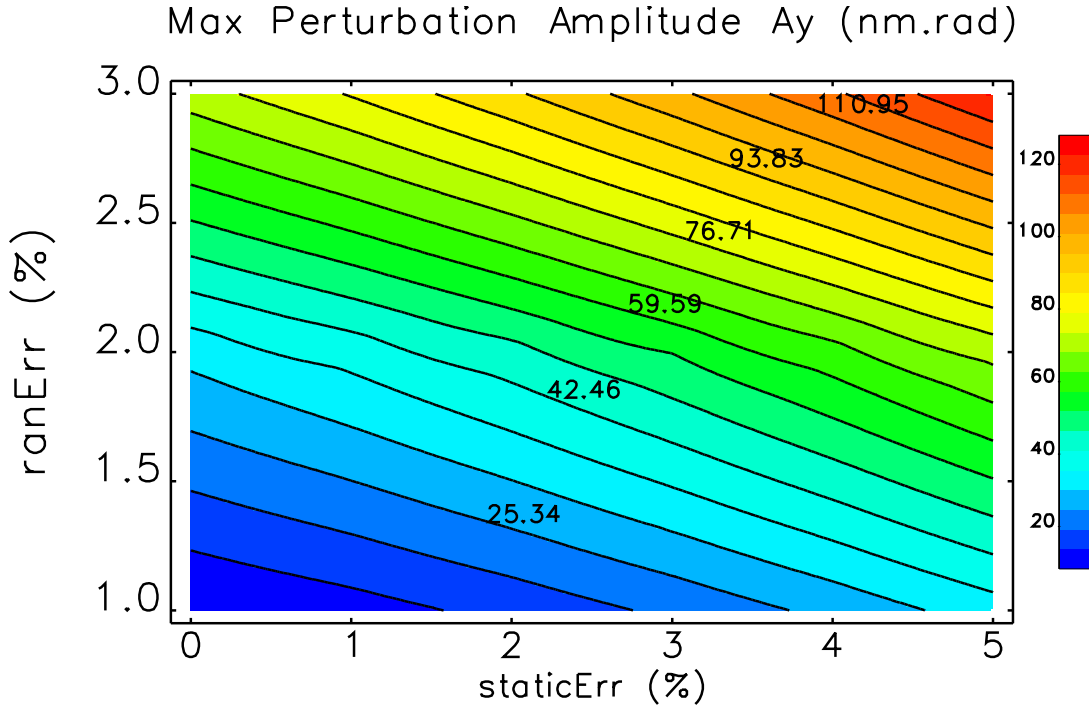


Figure 4.82. Maximum stored-beam perturbation amplitude A_y vs. stripline kicker error levels (in percentage of full kick strength).

Perturbations to nearby bunches

The most difficult-to-avoid perturbation to the stored beam is from a prolonged waveform tail, which mostly affect the 324-bunch mode. In this case, the bunch current is small and thus the simulation ignored collective effects.

Three cases with the largest A_y values among the 20,000 cases, at a systematic error of 5% and random error of 3% (Gaussian-distributed), were chosen for further simulation. A uniformly-distributed bunch[6], which covers a Gaussian volume of $\varepsilon_x = 45$ -pm, $\varepsilon_y = 30$ -pm, $\delta p/p = 0.0016$ and $\sigma_l = 30$ -mm with a cut-off of 5 sigma, is used for tracking through our 100 optical error ensembles for 1,000 turns. Each particle has an associated weight which is derived from its probability in a Gaussian distribution. The total loss rate is then the sum of lost particles' associated weights, rather than the sum of the number of lost particles. Figure 4.83 shows the cumulative distribution of fraction of stored particles that are lost for these three cases. We can see that for most perturbation amplitudes and the most unfavorable optical errors, the maximum stored beam loss rate is about 0.012%, which is very small, therefore, the tolerable stripline error seen by the stored bunches of 5% for the systematic error plus 3% random error is consistent with very good operation.

This simulation doesn't include collective effects, which could cause particle loss at a smaller perturbation amplitude when bunch charge is high. Hence, the specifications above for 324-bunch mode, being somewhat conservative, allow margin for collective effects. These may exist even for 324-bunch mode, particularly for the double-charge guard bunches that will be used when introducing gaps in the 324-bunch train (see 4-2.6.3). More detailed evaluation will be needed in the future.

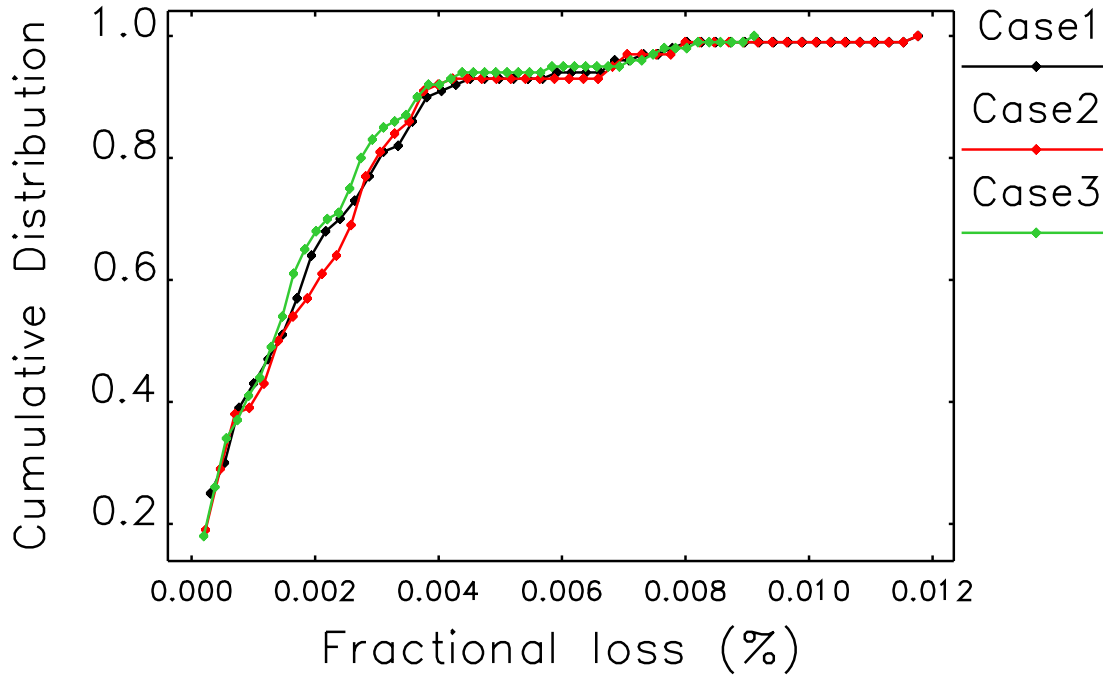


Figure 4.83. Cumulative distribution of fraction of stored particles for the three maximum perturbation cases.

For 48-bunch mode, a preliminary simulation showed that a 0.15 mrad kick error can be tolerated, which is equivalent to $A_y \approx 42$ nm.rad. Thus the tolerance for any reflection or after pulse of stripline kicker at the next-nearest bunch in this mode is set to 3% for the systematic error plus 1.5% random error, or equivalent combinations, which can be seen from Fig. 4.82.

In addition to losses, the affected stored bunches have their emittance significantly inflated, as Fig. 4.82 makes clear. Assuming that the two nearest bunches are affected, and including the fact that the newly-injected bunch has similarly large emittance, the dip in brightness following an injection event will amount to $3/324$, or about 1%.

References

- [1] R. Abela et al. “Design Considerations for a Swiss Light Source (SLS).” In: *Proc. EPAC 1992*. 1992, p. 486 (cit. on p. 111).
- [2] L. Emery and M. Borland. “Upgrade Opportunities at the Advanced Photon Source Made Possible by Top-up Operations.” In: *Proc. of EPAC 2002*. 2002, pp. 218–220 (cit. on p. 111).
- [3] R. Lindberg, M. Borland, and A. Blednykh. “Collective Effects at Injection for the APS-U MBA Lattice.” In: *NAPAC16*. WEPOB08. 2016 (cit. on p. 111).
- [4] L. Emery. *BTS Trajectory Jitter Measurements over the Years*. Tech. rep. OAG-TN-2006-024. APS, June 2006 (cit. on p. 119).
- [5] A. Xiao et al. “Simulation study of injection performance for the Advanced Photon Source upgrade.” In: *Proc. IPAC15*. 2015, pp. 1816–1818 (cit. on p. 119).

- [6] A. Xiao. Private communication. 2016 (cit. on p. 122).

4-2.11 Beam Dumps and Collimation

The beam dump and collimation system serves several purposes, including:

1. Radiation safety — particle loss should be localized as much as possible so that radiation levels in occupied areas can be minimized with the use of local shielding.
2. Machine protection — sudden loss of beam, e.g., from a swap-out extraction or from a whole beam dump, must be managed in such a way that machine components are not damaged. This is a particular concern given the energy density in the electron beam.
3. Insertion device (ID) protection — particle loss at the location of permanent-magnet IDs in particular should be kept as low as possible to reduce demagnetization.

The dump and collimation system is designed with consideration of the existing APS tunnel shielding structure, which has a thicker continuous shielding wall in Zone F (see section 4-3.12.3), extending from sector 37 to sector 1. These are preferred sectors for collimators and beam dumps. In sector 1, any such objects should ideally be in the upstream, “A,” part of the sector, since the shield wall becomes thinner around the location of the S02A:M2 dipole.

Both horizontal and vertical collimators are used in this system. Their physical apertures were introduced in 4-2.3.3, where they are included in simulations of single-particle dynamics. What follows is a more detailed description

1. Whole-beam dump/Horizontal collimators: This is for machine protection. When an error is detected, e.g., mis-steering of an x-ray beam from an undulator that could result in damage to a vacuum chamber, it is necessary to dump the entire beam. This will be performed by tripping both rf systems. Simulation shows that the dumped beam power density is so high that it will carve a groove in any kind of material. To prevent damage to other components, such losses are localized to a set of horizontal dumps located on upstream side of the A:Q4 magnets in sectors 37, 38, 39, 40, and 1. These dumps, which have a nominally ± 4.8 -mm horizontal aperture, are near the point of maximum horizontal beta and dispersion function. Multiple dumps are used, thus covering a spread in betatron phase angles, to make sure that beams can be always dumped to at least one of these specially-designed components even when including other machine errors. Another feature of these horizontal collimators is that the collimating surface should be vertically movable to provide a fresh surface after a dump. The nominal aperture of the dumps/collimators was chosen to avoid reducing the maximum-achievable Touschek lifetime while still intercepting most Touschek-scattered particles. The beam stay clear (BSC) aperture, defined by a free betatron oscillation, is limited by the smallest ID aperture in sectors 4 (HSCU) and 33 (HGSCU). Installation of beam collimators in the BTS line is under consideration.
2. Swap-out beam dump/Vertical collimators: Bunches that are extracted as part of swap out are directed to this dump. As described in 4-2.10.2, the swap-out bunch is kicked first by a weak stripline kicker (pre-kicker), after which there is a delay of about 250 turns to allow decoherence, which reduces the energy density by two orders of magnitude. Following this, another three stripline kickers are fired to dump the bunch vertically and without damage to the dump itself. Physically, the swap-out beam dump is a ± 4.7 -mm vertical collimator located inside the A:M1 magnet in sector 39. This location not only has large vertical beta function, but also benefits from extra shielding provided by the magnet. A vertical collimator of the

same design is installed in sector 1. This one is intended to localize the incoming injected beam loss which could come from either a larger-than-normal injected beam trajectory jitter or a misfiring of injection kicker. The BSC aperture in vertical plane is limited by this swap-out beam dump and vertical collimator aperture size.

The BSC aperture over one sector is shown in Fig. 4.84.

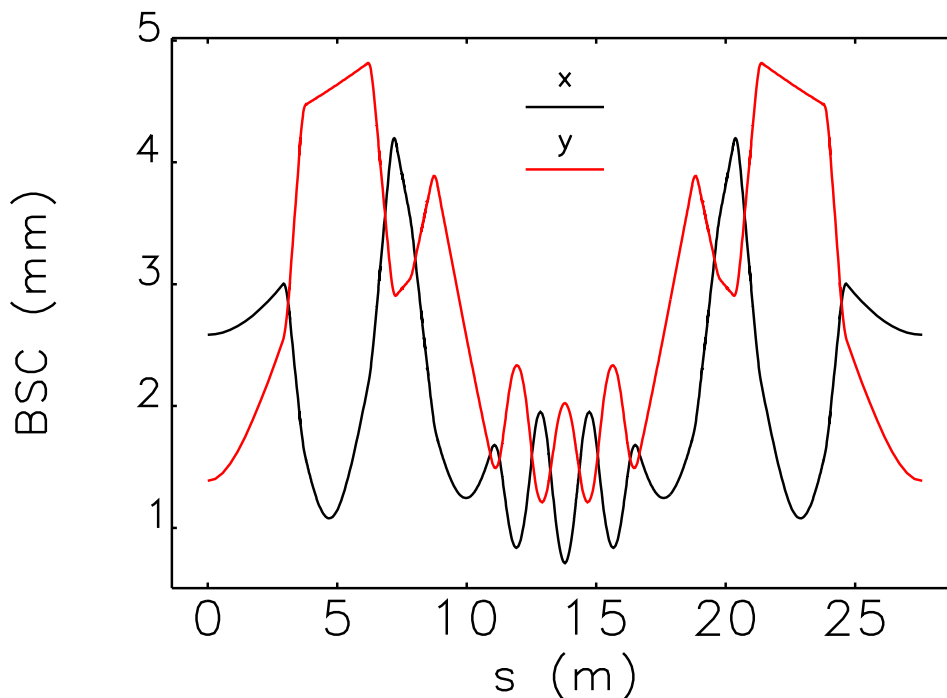


Figure 4.84. The BSC aperture over a sector. The horizontal aperture is limited by the smallest ID aperture; The vertical aperture is limited by the vertical collimator aperture.

4-2.11.1 Collimation of Touschek Losses

As described above, collimators are also used to catch the lost particles from injection, Touschek scattering, and gas scattering. Simulations of injection were described in 4-2.10.3; the corresponding loss distribution is shown in Fig. 4.81.

The Touschek beam loss distribution was also simulated, using a Monte Carlo approach that directly models the scattering [1, 2]. Using the apertures described just above (and in 4-2.3.3), the loss distribution was obtained for several cases of errors (also described in 4-2.3.3).

In particular, the Touschek beam loss simulation was performed using three optical errors from one hundred optical error ensembles. These reflect the minimum, average, and maximum calculated Touschek beam lifetime. The beam parameters used for simulation are: $\varepsilon_{x,y} = 34\text{-pm}$, $\sigma_t = 100\text{-ps}$, $\sigma_\delta = 0.16\%$, approximately representing a 48-bunch fill with HHC, IBS, and an emittance

ratio of ~ 1 (see Table 4.71). Table 4.47 summarizes the simulation results. The table lists the “calculated” and “simulated” Touschek lifetimes. The “calculated” lifetime is based on Piwinski’s method and assumes a hard-edged local momentum aperture (LMA), as used in other calculations in this document, e.g., 4-2.3.3. The “simulated” lifetime refers to the results of Monte Carlo simulation of Touschek scattering. This differs from the “calculated” lifetime because the LMA is not in fact hard-edged, but has a fuzzy boundary owing to randomness in the scattering process, which introduces variation in the betatron oscillation amplitude of the scattered electrons.

The ID losses are mostly confined to the two smallest gap IDs in sectors 4 (HSCU) and 33 (HGSCU)—both are superconducting IDs and are less sensitive to the radiation damage than permanent magnet IDs. The total beam loss energy is very small, $\sim 0.03\text{W}$ per ID. The results for the minimum-lifetime case are shown in Fig. 4.85.

Table 4.47. Summary of Touschek beam loss distribution

	Minimum Lifetime	Average Lifetime	Maximum Lifetime	Unit
Calculated Lifetime	2.66	4.39	7.15	h
Simulated Lifetime	1.91	5.77	6.98	h
Total Loss	6.67	2.21	1.83	$\times 10^8$ -p/s
Loss @ ID straight	9.39	14.83	7.32	%
Loss @ Collimator location	86.55	75.55	80.40	%
Loss @ Other locations	4.06	9.62	12.28	%

These results and those from injection modeling show that the collimation scheme works as expected for localizing the Touschek beam loss but is less effective for the injected beam loss. This is owing to the fact that the injected beam losses mostly result from larger betatron oscillation, rather than energy oscillation. Combined with the presence of very small apertures in two of the IDs, this makes collimation of the injected losses difficult. Further studies are planned of the collimation scheme, including the optimum collimator aperture.

While the gas scattering beam loss has yet to be simulated, inferences can be made based on simulations of other loss mechanisms. Elastic gas scattering mostly changes particles’ betatron oscillation amplitudes, so the loss distribution pattern is expected to be similar to the injected beam loss pattern. Inelastic gas scattering mostly changes particle energy, so the loss distribution pattern is expected to be similar to the Touschek scattering loss pattern.

4-2.11.2 Swap-out Beam Dump

The vacuum chamber of the Advanced Photon Source Upgrade (APS-U) storage ring (SR) must maintain vacuum integrity during a variety of loss scenarios from the 6-GeV, 200-mA circulating electron beam. Of particular concern are planned “swap-out” dumps associated with replenishing SR bunches, and unplanned beam dumps where the entire stored charge of the ring is lost. The SR design calls for fill patterns ranging from 48 to 324 bunches, representing a total charge of 737 nC (4.6×10^{12} electrons). The total stored energy in the beam is 4420 J; thus in a 48-bunch fill, each bunch has a nominal energy of 92 J.

Elegant simulations yield rms beam sizes of $\sigma_x = 12 \mu\text{m}$ and $\sigma_y = 8 \mu\text{m}$ for the 42-pm Multi-Bend

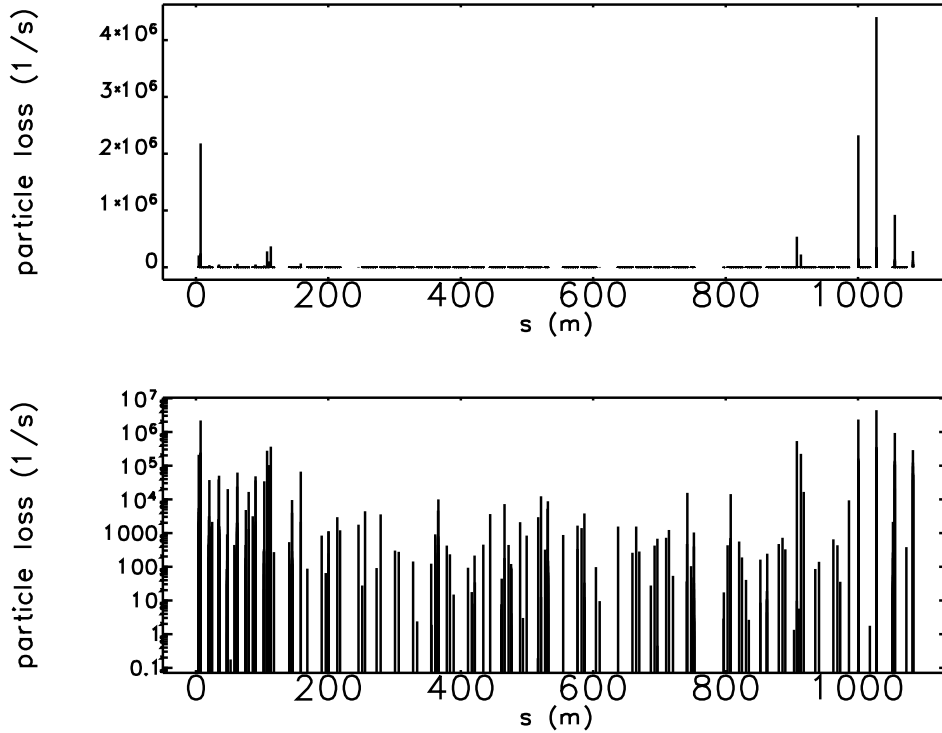


Figure 4.85. Locations of Touschek losses (minimum lifetime case): linear scale (upper); log scale (bottom).

Achromat (MBA) SR lattice [3]. The moderate energy and small beam cross section entail a large deposited energy density in vacuum chamber wall material, regardless of composition.

At 7 GeV and 100 mA, the present APS SR beam is capable of damaging materials it intercepts, in spite of having a much larger cross section ($\sigma_x = 280 \mu\text{m}$ and $\sigma_y = 10 \mu\text{m}$). This was seen experimentally for both copper and tungsten [4]. Hence, it is important to carefully consider both the material and strategy for the beam dumps for the APS-U.

The potential for damage to the vacuum chamber, collimator, or other beam-facing component can be assessed by examining the thermal diffusion of beam-deposited energy. Assuming cylindrical symmetry, the diffusion equation for the temperature distribution may be expressed as [5],

$$\frac{\partial}{\partial t}T(r, t) = \alpha \nabla^2 T(r, t) + S(r, t), \quad (4.43)$$

where $S(r, t)$ is the thermal source term, L_{diff} is a characteristic diffusion length and α is the thermal diffusivity. By inspection, a simple scaling relation can be obtained for the thermal diffusion time,

$$t_{\text{diff}} = \frac{L_{\text{diff}}^2}{\alpha} \quad (4.44)$$

In the present case, we assume L_{diff} to be the rms size of the beam. In aluminum, $\alpha = 9.7 \times 10^{-5} \text{m}^2 \text{s}^{-1}$. Taking the geometric mean of the σ values mentioned above as the characteristic

dimension gives $t_{\text{diff}} = 1 \mu\text{s}$. This time is long compared with the interaction time of a single bunch with the swap-out dump, which is determined by the pulse length of about 235 ps FWHM. Hence, thermal diffusion should not play a role in single bunch energy deposition. However, this time is relatively short with respect to the time for a full beam dump ($\approx 10 \mu\text{s}$), so diffusion should help reduce temperature rise in that case.

Energy deposition was examined in various materials and different geometries using the matter-particle interaction program MARS [6, 7, 8]. For normal incidence beam, simple rectangular block geometry is employed.

4-2.11.3 Energy Deposition Simulations

Energy deposition was examined in various materials and different geometries using the matter-particle interaction program MARS. For the normal-incidence beam that is generally appropriate for the swap-out dump, simple rectangular block geometry is employed. Small-volume geometry arrays are required to accurately assess the dose.

4-2.11.3.1 Geometry Both a rudimentary collimator design as well as simple block geometries have been modeled with MARS to understand energy deposition and heating from APS-U beam loss. Normal-incidence beam dose distributions are evaluated with the block geometry shown in Fig. 4.86. Here the central 1.02-mm x 1.02-mm x-y region of the collimator is divided into 51 equal 0.02-mm x 0.02-mm x 10 mm geometry voxels to record dose. The dark bar across the center of Fig. 4.87 is the fine mesh region shown in cross section in Fig. 4.86. The black region to the right of the geometry is where scattered particle trajectories are collected for later simulations.

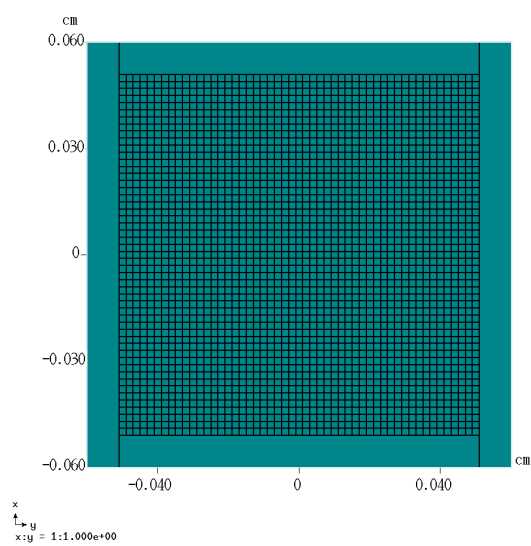


Figure 4.86. Normal-incidence x - y block geometry for the central section.

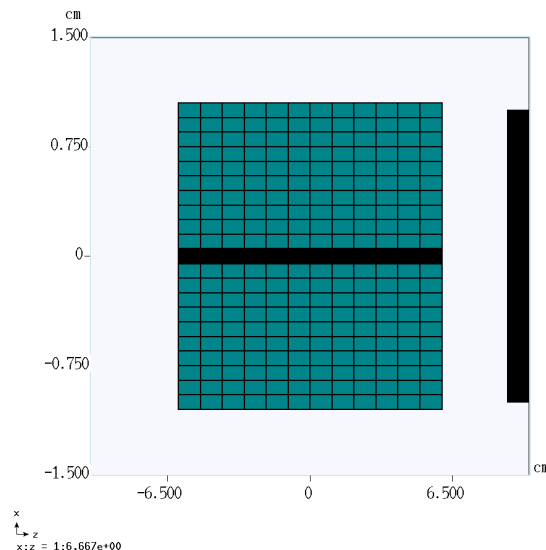


Figure 4.87. Normal-incidence x - z block geometry, showing the densely-gridded central section as a dark band.

As mentioned above, *elegant* simulations predict rms beam sizes in the 42-pm MBA lattice to be

$\sigma_x = 12 \mu\text{m}$ and $\sigma_y = 8 \mu\text{m}$. This implies very high power densities within the electron beam. A simulated dose distribution for a single swapped-out bunch in 48-bunch mode in the upstream collimator segment is presented in Figure 4.88. The transverse distribution is read externally from

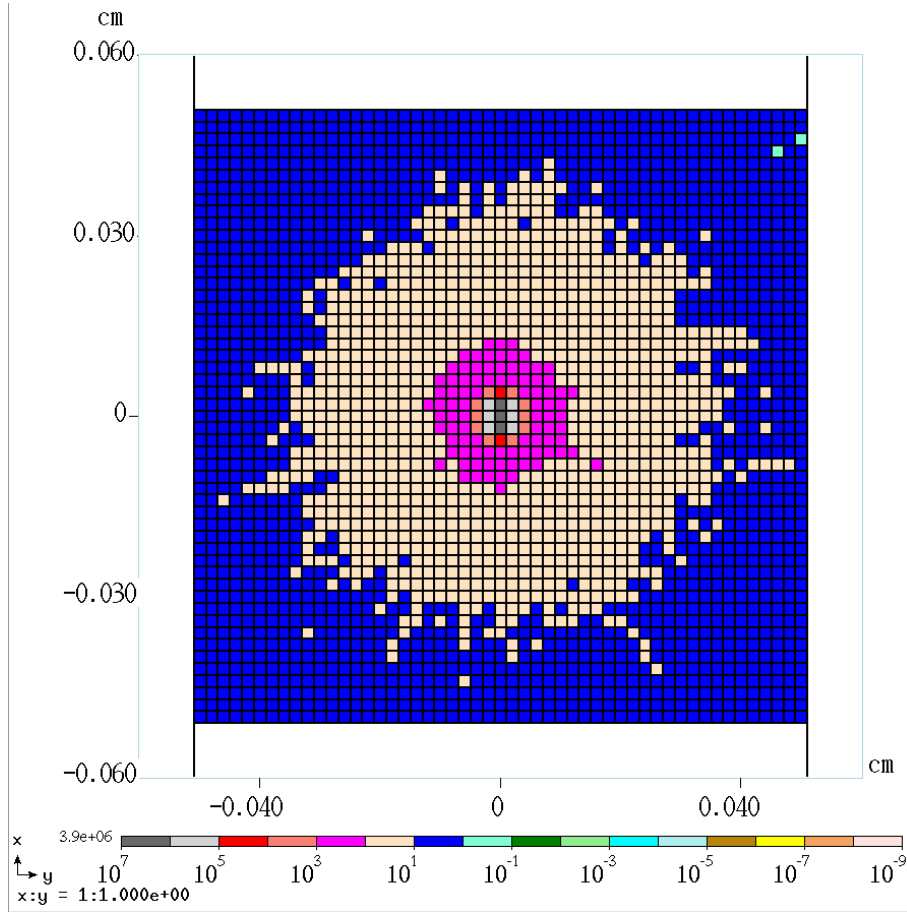


Figure 4.88. Transverse total dose distribution in the upstream collimator segment.

elegant output or internally modeled in MARS with an equivalent Gaussian where $x'=y'=0$. Simulations typically employed 10^6 trajectories to model the initial electron distribution. The maximum dose is obtained for several candidate materials including graphite, aluminum, and titanium alloy TiAl6V4 (TiA) containing by weight 6 percent Al and 4 percent V. A naive estimate of peak temperature excursion can be determined as,

$$\Delta T = \frac{DA_w}{C_m}, \quad (4.45)$$

where D is the dose, A_w the atomic weight, and C_m the molar specific heat. Peak dose and temperature rise for operational swap-out beam dumps without transverse beam size modification is listed in Table 4.48. In reality, C_m varies with temperature [9]; also for large dose, enthalpy associated with phase changes must be included. MARS includes the effect of temperature-dependent specific heat [10]; however, the temperature excursion must be below the melting point. For ΔT above phase transition temperatures, energy deposition output from particle-matter interaction codes like MARS are used as input to separate analyses such as ANSYS [11].

Table 4.48. Peak dose in candidate collimator material for a single, unmodified swapped-out bunch out of 48

Material	Dose (MGy)	C_m (Jmole ⁻¹ K ⁻¹)	A_w (g mole ⁻¹)	ΔT (K)	Melting Temp. (K)
Graphite	4.1	8.52	12.0	5777	3915*
Aluminum	3.9	24.2	26.98	3498	933
Titanium alloy	3.6	24.89	47.87 [†]	6923	1900-1950
Copper	3.6	24.44	63.55	9361	1358
Tungsten	3.6	24.27	183.84	2.7×10^4	3695

*sublimation
[†]Ti only

Empirically, we have found that when Eq. 4.45 predicts ΔT to exceed the melting temperature for a given material, that material will suffer damage. Examples in the present APS SR of materials damaged by beam dumps include copper and tungsten; however, aluminum components exposed to the beam have never shown beam-induced failure. In the former case, the melting temperatures were exceeded according to Eq. 4.45; whereas, in the latter it was not. Generally lower-Z, lower density material such as carbon or aluminum can survive a beam dump without mechanical failure; however, because of the very high energy densities of the APS-U beam, the collisional (local heating) component [12] is sufficient to damage essentially any solid material.

As described in 4-2.10.2, if the swap-out bunch is kicked first by a weak stripline kicker (pre-kicker), then only dumped after a delay of about 250 turns to allow decoherence, there is a significant reduction in the energy density, which allows the bunch to be dumped without damaging the dump. With the transverse bunch size broadened by decoherence, the dose deposited in potential collimator material is now greatly reduced. Employing the decohered beam sizes indicated in Figs. 4.89 and 4.90, MARS predicts peak ΔT values of 16.8K, 11.9K, 19.4K, 44.8K, and 269K in graphite, aluminum, TiA, copper, and tungsten, respectively. Peak axial ΔT profiles from MARS geometry regions for these five materials are plotted in Fig. 4.91. The peak temperature excursions after decoherence show a large reduction compared with those prior to decoherence listed in Table 4.48. Note that the turn-250 integrated profile shown in Fig. 4.90 has been shifted by its centroid value, $y_0 = -7.48$ mm, for comparison with the turn-0 profile.

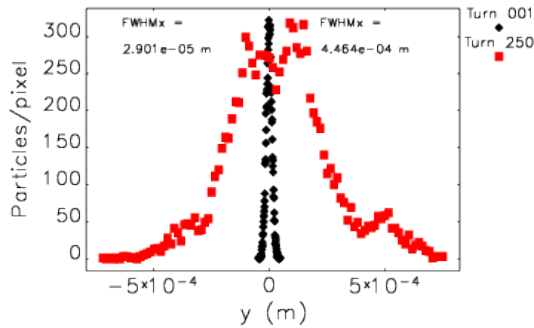


Figure 4.89. Integrated swap-out bunch x-profiles at turn 0 and turn 250.

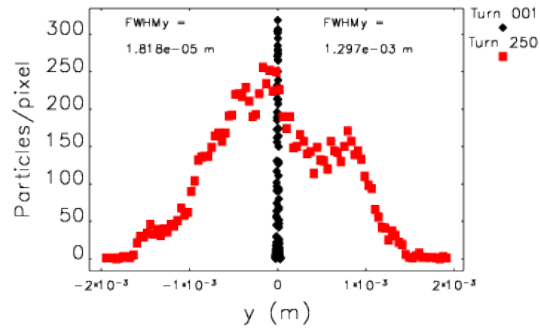


Figure 4.90. Integrated swap-out bunch y-profiles at turn 0 and turn 250.

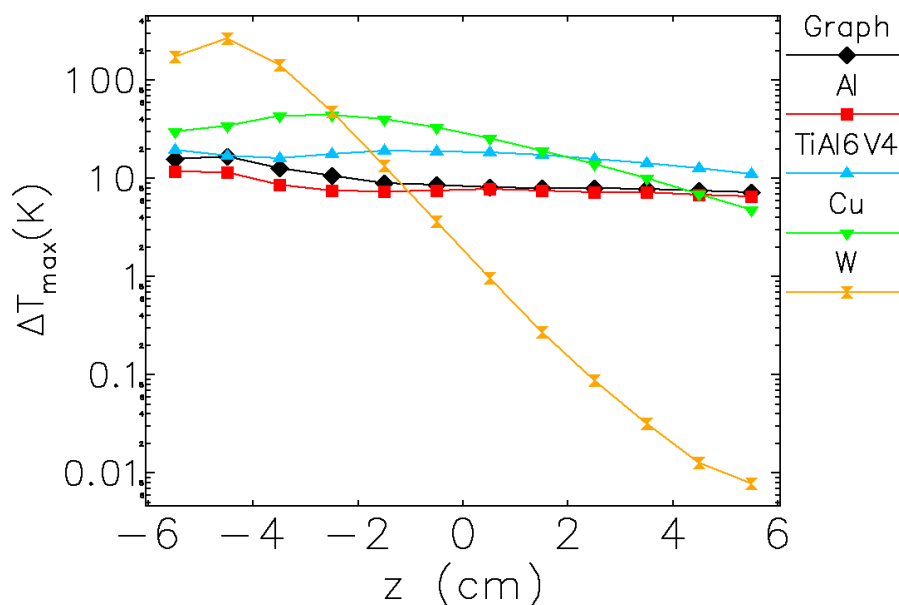


Figure 4.91. Longitudinal peak ΔT distributions for a single decohered bunch.

4-2.11.4 Whole-beam dump

As the name suggests, the whole-beam dump is intended as the location where the entire beam can be dumped at once. This will happen, for example, when the rf systems are tripped under the command of the machine protection system or personnel protection system.

Based on the above analysis, there is good reason to expect that the whole-beam dump might be damaged by the beam. To assess this possibility, beam dump simulations were performed for 48-bunch mode with $\Delta f_h = 9\text{kHz}$, using 10k particles per bunch in order to reduce running time. The collimation configuration was slightly different from the more recent concept described above, in terms of the exact position and aperture of the dump. Tracking was performed for 10,000 turns to find the equilibrium using a lumped-element model, including lumped-element impedances, main and harmonic rf, and feedback systems. After turn 10,000, the simulation switched to an element-by-element model [13] including element-by-element synchrotron radiation, transverse and longitudinal impedance, main and harmonic rf systems, and physical apertures. Shortly after this, the generator for the main rf cavities was muted and the cavities began to ring down. The transverse and longitudinal feedback systems were simultaneously switched off so they do not fight the decay of the beam energy.

Figures 4.92 through 4.95 show properties of bunch 0 starting just after the switch to element-by-element tracking. The decay of the momentum centroid begins at pass 2 when the rf drive is muted. The beam sizes do not change much until the beam actually begins to be lost. This implies high particle density on any surface struck by the beam.

The collimation in the beam tracking simulations is idealized and does not include out-scatter or

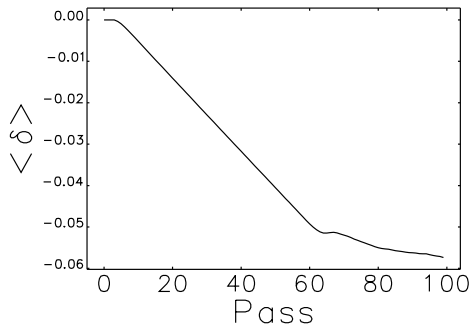


Figure 4.92. Fractional momentum offset of bunch 0 vs. pass, where the rf is muted at pass 2.

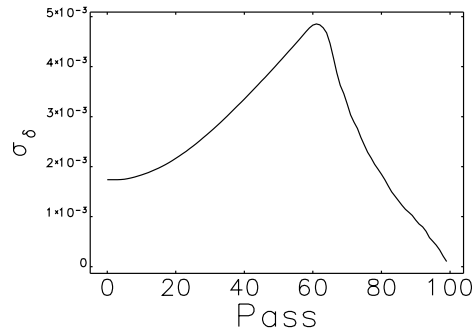


Figure 4.93. Fractional momentum spread of bunch 0 at the end of sector 40 vs. pass, where the rf is muted at pass 2.

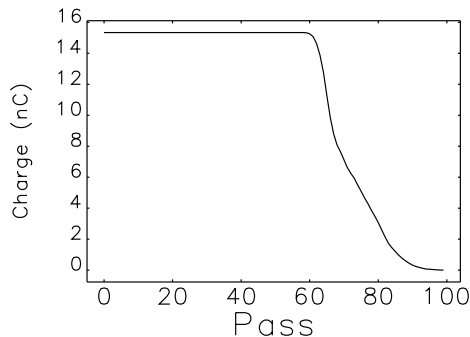


Figure 4.94. Charge in bunch 0 vs. pass, where the rf is muted at pass 2.

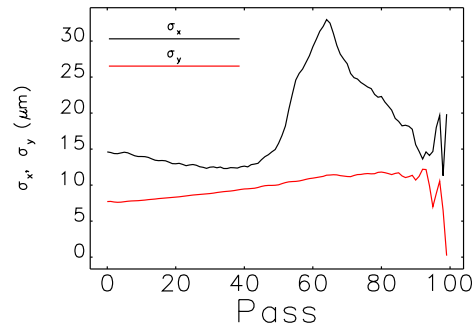


Figure 4.95. Horizontal and vertical beam size of bunch 0 at the end of sector 40 vs. pass, where the rf is muted at pass 2.

shower generation. However, it accurately reflects the distribution of the beam when it first impacts dump. All of the lost electrons first strike this dump, making this a worst-case scenario. Inspection of Fig. 4.94 shows that 50% of the beam is dumped within 10 turns.

As was the case for the swap-out dump, the loss distribution from these tracking simulations is used as input for MARS simulations. An anamorphic view of the MARS beam dump geometry is presented in Fig. 4.96. The vacuum beam pipe is composed of aluminum with an ID of 22 mm and an OD of 24.54 mm, yielding a wall thickness of 1.27 mm. Within the beam pipe is the collimator, tapered slightly on the downstream side. The loss distribution strikes the dump on the inboard side with an average x' of -3.2 mrad. The beam impinges on the wall at this relatively shallow angle causing the dose to be spread in the z-direction along the dump. After the first 7.5 cm, the dump wall flares conically at an angle that matches the average x' of the beam. The conical section extends for an additional 7.5 cm making the total dump length 15 cm. At the downstream end of the geometry is a 1-cm thick disk of iron representing the location of a magnet.

Based on experience in the present APS ring, we expect a whole beam loss event (for which there

is no decoherence) will lead to localized mechanical damage of the dump, in the form of a groove carved by the beam. For the APS-U, the energy density is even higher, which strongly indicates that the dump will experience localized mechanical failure, particularly if materials of higher density and atomic number are used. A trade-off exists between the desire to stop the dumped beam quickly and the amount of damage that the dump will sustain. Figure 4.97 shows the longitudinal distribution of peak dose calculated using MARS for aluminum, titanium-alloy, copper, and tungsten in the dump geometry of Fig. 4.96. The dose is calculated in 5-mm steps in the z-direction. (Because of space limitations in the machine and the fact that the beam streams through graphite with relatively weak interactions ($X_{o,graph}/\rho_{graph} = 19.3$ cm), at this time it is no longer being considered as a beam dump material.) In addition, the simulations strongly suggest that aluminum is the best material for the beam dump for several reasons that are discussed below. 2-D x-z distributions of

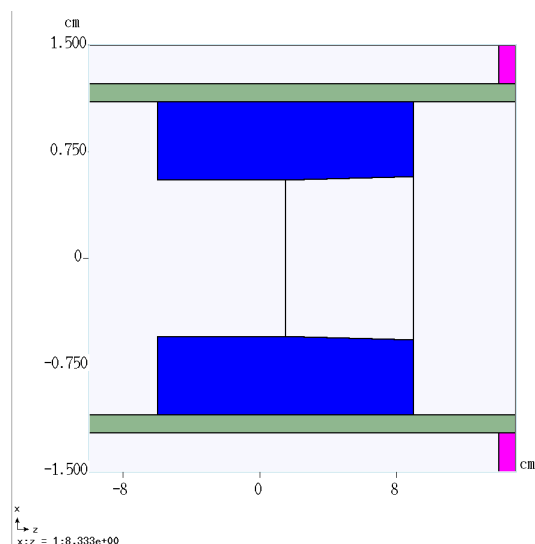


Figure 4.96. X-Z view of beam dump geometry.

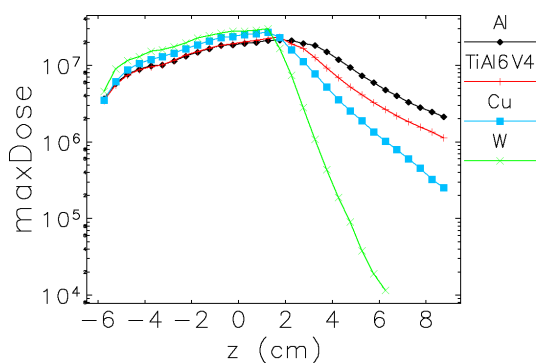


Figure 4.97. Peak dose (Gray) versus z for various materials during a beam dump.

electron/positron fluence (FLE, no. per cm^2) and total dose (PDT, Gy) for aluminum are given in Figs. 4.98 and 4.99.

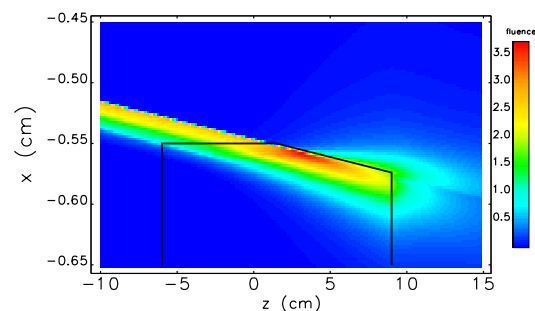


Figure 4.98. Electron-positron fluence from a whole beam dump in Al (10^{15}cm^{-2}).

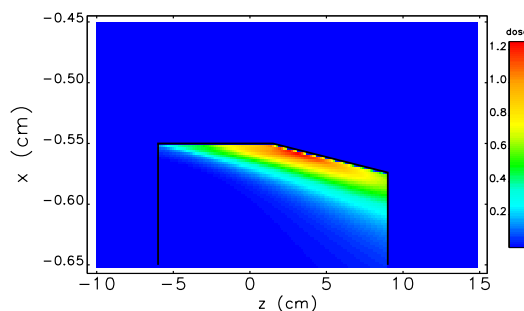


Figure 4.99. Total dose in Al (MGy). Note, the dose is integrated across the region shown in Fig. 4.86.

Again, based on APS experience, dose causing temperature excursions in excess of the melting temperature can lead to localized mechanical damage. In aluminum, a dose of 1 MGy leads to a temperature excursion of approximately 1000K according to Eq. 4.45, well in excess of the melting point of 933K. Thus, regions where dose exceeds 1 MGy are expected to exhibit mechanical damage in aluminum. The same dose in tungsten, with its higher atomic weight, yields a temperature excursion naively calculated to be 7600K; however, the ratio of excursion to melting temperatures in W is not that different from Al. Therefore, setting 1 MGy of absorbed dose as an approximate threshold for damage is a reasonable rule-of-thumb. In the present APS ring, modeling beam dumps on aluminum vacuum chamber components yield temperature excursions just below the melting point [14]. Beam-strike damage has not been observed on any aluminum vacuum surface in the present ring. A 1-MGy rule-of-thumb is roughly an order of magnitude less than the hydrodynamic regime threshold of 15 MGy [15, 16]. As seen in Fig. 4.100, this threshold is exceeded for peak dose in aluminum. All materials modeled (including graphite) exhibit a peak dose of approximately 20 MGy.

The total dose x-y distributions in the 5-mm axial slice near maximum dose are presented in Figs. 4.100 for aluminum. The electron-positron fluence (FLE) distributions 5 cm downstream of

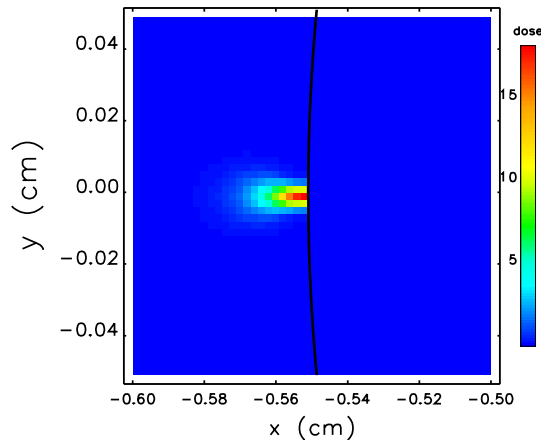


Figure 4.100. Total dose (MGy) in the transverse plane near peak in Al.

the beam dump , as well as the resultant total dose in the adjacent beam pipe wall and magnet iron, are shown in Figs. 4.101 and 4.102, respectively. The simulations show that most of the energy in the beam exits the dump. In particular, of the 4600 J in the beam, only 23 J are predicted to be deposited in an Al dump; for Cu and W dumps, the numbers are 260 J and 410 J, respectively. However, the fluence results, Figs. 4.98 and 4.101, show that the beam is significantly broadened in the transverse plane. Hence, the dump acts more like a spoiler, particularly in the case of Al. Additional simulations will be undertaken to determine the locations at which these electrons and positrons are eventually lost and how those losses might be localized. One option is a second collimating structure downstream of the A:Q4, but the details have yet to be explored.

While copper, titanium, and tungsten all absorb more energy locally, based on the downstream shower and dose patterns, aluminum appears to be the best choice for the beam dump. The

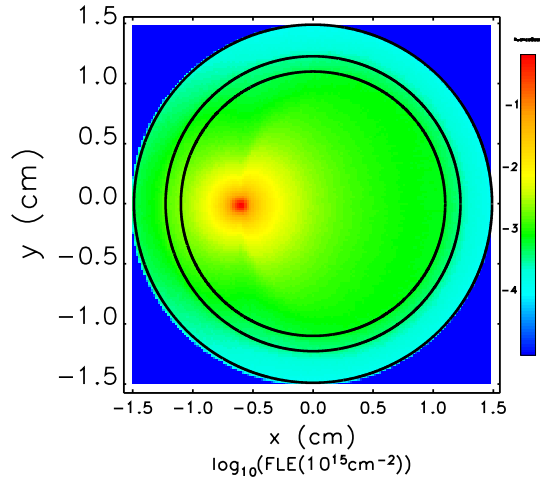


Figure 4.101. FLE 5 cm downstream from an aluminum beam dump.

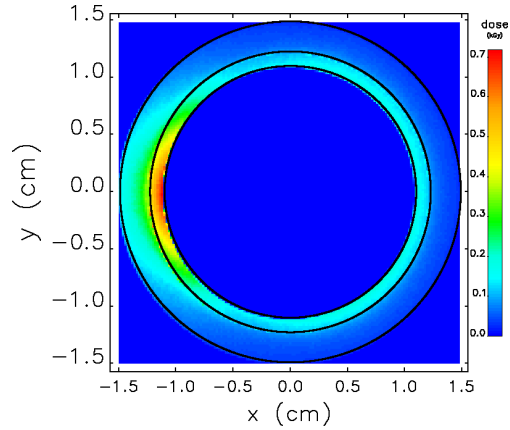


Figure 4.102. Total dose (kGy) in the beam chamber wall and adjoining magnet iron, for an aluminum beam dump.

radiation length in aluminum (X_o/ρ) is 8.9 cm, making the axial extent of an Al dump roughly $1.5X_o$. The dump length is sufficient to scatter the beam while minimizing the absorbed energy and thus damage to the wall. Maximum dose in the magnet iron and the adjacent beam pipe are presented in Table 4.49; ΔT calculated from Eq 4.45 are also given. As can be seen in the table and figures, the temperature excursions are relatively small. Because vaporized material from the dump is likely to settle on nearby vacuum chamber walls, it makes the most sense for these materials to be the same.

Table 4.49. Whole-beam peak dose in magnet iron and adjacent beam pipe.

Dump Material	Wall Dose (kGy)	Fe Dose (kGy)	ΔT Wall (K)	ΔT Fe (K)
Al	0.7	0.65	0.78	1.4
TiA	2.0	2.0	2.2	4.4
Cu	1.7	2.2	1.9	4.9
W	1.4	1.5	1.6	3.3

With an aluminum dump, the downstream profiles indicate the FWHM extent of the shower is 1.11 mm in x and 0.93 mm in y. The cross sectional area of the shower is now roughly equivalent to that of the decohered swap-out bunch. As mentioned, further simulations will be needed to assess possible damage to materials elsewhere in the ring. Another reason for choosing an Al dump is that doing so reduces the neutron dose. Spectra for the downstream shower are presented in Figs. 4.103 and 4.104. At the dump, local maximum neutron fluence levels drop from $6.6 \times 10^{12} \text{cm}^{-2}$ with W to $2.3 \times 10^{11} \text{cm}^{-2}$ for Al.

Simulations indicate the beam dump will be damaged after every whole-beam loss event; therefore, the dump will be moved after each event to expose an undamaged surface at the probable strike

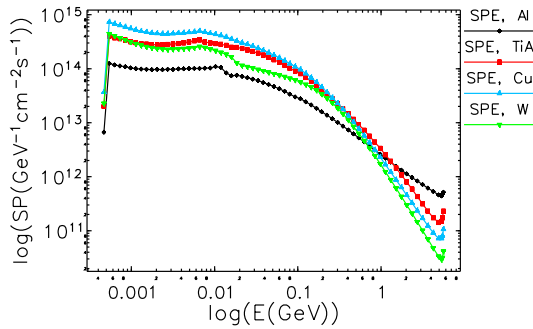


Figure 4.103. Downstream electron-positron spectra for different dump metals.

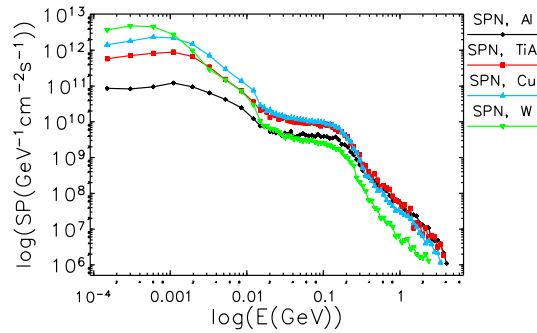


Figure 4.104. Downstream neutron spectra for different dump metals.

location. The motion can be either translational or rotational; however, rotation in the cylindrically-symmetric geometry would be the most natural.

An important point to keep in mind is that the MARS model is static; however, if material in the beam dump is heated sufficiently, the material may enter a hydrodynamic regime and move over the course of the dump. Such motion may lead to a change in the dump mechanical configuration and downstream dose distributions. For example, losses may then be spread over several of the dumps (a total of five are presently included).

One alternative to the present concept would involve an abort kicker system with a dedicated dump beam line; however, because of the energy density in the beam, any failure of that system could result in significant damage to the vacuum chamber.

References

- [1] A. Xiao and M. Borland. “Monte Carlo simulation of Touschek effect.” In: *Phys. Rev. ST Accel. Beams* 13 (2010), p. 074201 (cit. on p. 126).
- [2] A. Xiao and M. Borland. “Beam loss simulation and collimator system configurations for the Advanced Photon Source upgrade.” In: *NAPAC16*. WEPOB22. 2016 (cit. on p. 126).
- [3] R. Lindberg M. Borland. *Beam dump simulations for the 41-pm lattice*. Tech. rep. AOP-TN-2016-057. APS/ASD/AOP, 2016 (cit. on p. 128).
- [4] J.C. Dooling and M. Borland. *Beam Energy Deposition in the Sector 37 Scraper*. Tech. rep. AOP-TN-2011-039. APS/ASD/AOP, 2011 (cit. on p. 128).
- [5] J. Dooling R. Lindberg. *Diffusion of heat during beam loss*. Tech. rep. AOP-TN-2012-030. APS/ASD/AOP, 2012 (cit. on p. 128).
- [6] N.V. Mokhov. *The Mars Code System User’s Guide*. Tech. rep. Fermilab-FN-628. Fermilab, 1995. URL: <https://mars.fnal.gov> (cit. on p. 129).
- [7] S.I. Striganov N.V. Mokhov. *MARS15 Overview*. Tech. rep. Fermilab-Conf-07/008-AD. Fermilab, 2007 (cit. on p. 129).

- [8] N.V. Mokhov et al. “MARS15 code developments driven by the intensity frontier needs.” In: *Prog. Nucl. Sci. Technol.* 4 (2014), pp. 496–501 (cit. on p. 129).
- [9] A.-M. Zahra et al. “Heat capacities of aluminium alloys.” In: *Journal of Materials Science* 30 (1995), pp. 426–436 (cit. on p. 130).
- [10] N. Mokhov. *Private Communication*. October 2014 (cit. on p. 130).
- [11] Nikolai V. Mokhov. *BEAM-MATERIALS INTERACTIONS*. Tech. rep. Fermilab-PUB-13-603-APC. Dec. 2013 (cit. on p. 130).
- [12] *ESTAR: Stopping Powers and Ranges for Electrons*. <http://physics.nist.gov/PhysRefData/Star/Text/ESTAR.html> (cit. on p. 131).
- [13] R. Lindberg, M. Borland, and A. Blednykh. “Collective Effects at Injection for the APS-U MBA Lattice.” In: *NAPAC16*. WEPOB08. 2016 (cit. on p. 132).
- [14] Jie Liu et al. “Mechanical Design and Analysis of an Electron Beam Advanced Photon Source.” In: *Proceedings of the MEDSI 2014 Conference, Melbourne, Australia-October 2014*. 2014, pp. 1–6 (cit. on p. 135).
- [15] Nikolai V. Mokhov. “Beam-Materials Interactions.” In: *Reviews of Accelerator Science and Technology* 6 (2013), pp. 275–290 (cit. on p. 135).
- [16] N.V. Mokhov and F. Cerutti. “Beam-Material Interactions.” In: *Proc. of the Joint International Accelerator School: Beam Loss and Accelerator Protection Newport Beach, US, 5-14 November 2014*. 2016, pp. 83–110 (cit. on p. 135).

4-2.12 Ray Tracing Guidelines

Ray tracing is used to identify direct line-of-sight from dipole radiation source points to accelerator components such as photon absorbers, vacuum chamber walls, flanges, bellow liners, and gate valves. Accelerator components must be designed to tolerate the heating from intercepted radiation. To be conservative, a hard-edge model is assumed for the dipole field; this overestimates the intercepted power for the inboard edge of the ray. Standard ray tracing typically only concerns the horizontal plane and horizontal orbit errors; that is, only the in-plane synchrotron radiation produced in the dipole fields is traced. Given the strong dipole fields and small vacuum chamber apertures in the upgrade machine, the out-of-plane radiation is also potentially an important source of heating, especially for non-ideal orbits. For the APS Upgrade, 2D (x,s) ray tracing and 3D (x,y,s) photon tracking have been carried out for a beam orbit centered in the magnets (see section 4-3.3.2, Figure 4.119). The next step is to include realistic orbit errors.

The most probable source of a large orbit perturbation is a single-source orbit distortion caused by a single dipole kick at one location in the ring. This could be caused by a magnet power supply trip, mistakenly changed magnet setting, or a poorly-compensated local steering bump elsewhere in the machine. Misdirected insertion device beams are limited by using interlocked beam position monitors located at opposite ends of each insertion device straight section, the so-called beam position limit detectors (BPLDs). Selected BPMs in the arcs between insertion devices will also be interlocked to control dipole sources. These devices, distributed around the ring, also serve as an interlock on the global orbit distortion. When the global orbit becomes large enough, the beam will be lost on an aperture limitation (it could be a real aperture limit or a BPLD interlock limit). The physical aperture limitations are obviously larger than BPLD interlock limits, therefore the physical aperture limitations are considered first. Unlike the present APS, where the smallest physical apertures are nearly identical ID vacuum chambers that are located everywhere around the ring, in the APS Upgrade the smallest horizontal apertures will be localized dumps/collimators and the septum magnet chamber.

To generate all possible closed orbits, two fictitious horizontal corrector magnets are used at locations with identical horizontal beta functions, separated by $\Delta\phi_x = \pi/2$. They are placed on either side of a straight section. If the kicks from two correctors are $A \cos\theta$ and $A \sin\theta$, where θ changes from 0 to 2π , then all possible orbits of a given amplitude A are sampled. The value of A is then also varied in order to vary the amplitude of the orbit distortion. Figure 4.105 gives all possible closed orbits shown at the beginning of the storage ring lattice (beginning of sector 1). Different colors correspond to different orbit amplitudes A . One can see that for large amplitudes, closed orbits are possible only for some phases. It is interesting to note that even though Fig. 4.105 looks similar to betatron phase space, it is actually not the same thing. This plot will be referred to as “orbit phase space.”

After the set of all possible orbits is generated, one can look at the cross-section of these orbits at any location. First, Fig. 4.106 shows the orbit phase space in the middle of the first 16 ID straight sections. One can see that the orbit phase space rotates and repeats itself approximately every 8 sectors, which corresponds to the tune of 0.125 (original tune is 0.10 but it shifts up for large orbits). This feature emphasizes the difference from the betatron phase space — the betatron phase space follows the lattice symmetry and repeats every two sectors. Just as orbits in the middle of ID straight sections do not repeat after every sector, the orbits inside dipoles do not repeat from

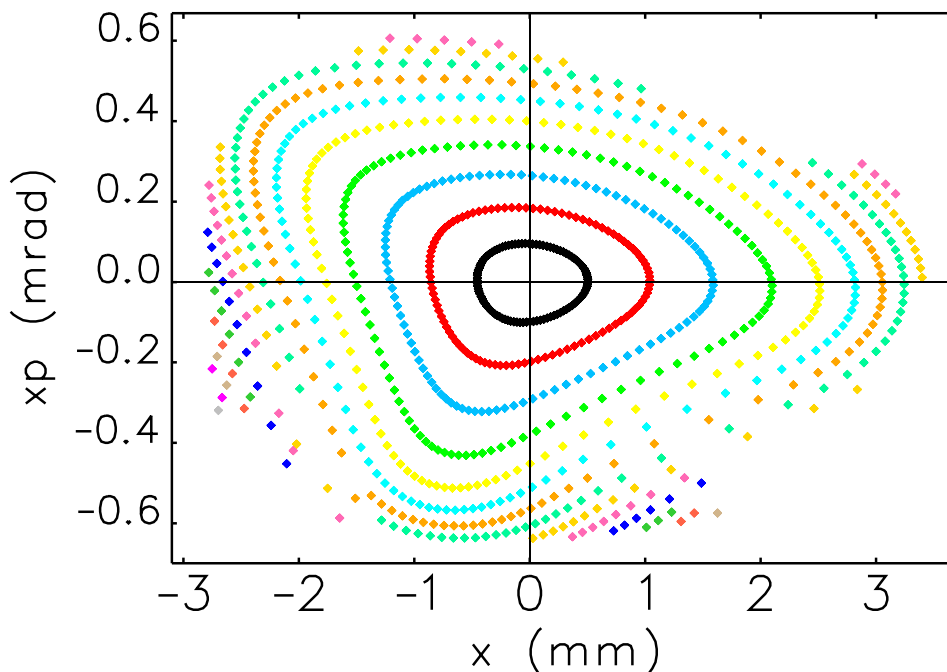


Figure 4.105. Possible closed orbits generated by two orthogonal correctors. Different colors correspond to different orbit amplitudes A .

sector to sector either. However, since the vacuum chamber design will be the same in every sector, the orbits inside that dipole from all sectors are combined together to get all possible orbits inside that dipole type.

The program that is presently used to trace all possible synchrotron radiation rays uses ideal betatron ellipses $\gamma x^2 + 2\alpha x x' + \beta x'^2 = \mathcal{A}$ to represent all possible orbits at any location. To allow the use of this program, the betatron ellipses that encompass the real orbit phase spaces are also calculated. Figures 4.107 and 4.108 show the orbit phase spaces at the entrance to all dipoles as well as encompassing betatron ellipses. Table 4.50 gives the values \mathcal{A} for all dipoles.

Table 4.50. Betatron ellipse constants \mathcal{A} for ellipses that encompass all possible orbits in dipoles

Dipole name	Ellipse amplitude (μm)	Dipole name	Ellipse amplitude (μm)
A:M1	3.5	A:Q4	3.9
A:M2	7.9	A:Q5	9.2
A:M3	8.0	A:Q8	7.9
A:M4	8.0	B:Q8	7.9
B:M3	7.9	B:Q5	11
B:M2	8.0	B:Q4	4.8
B:M1	3.7		

One can see in Figures 4.107 and 4.108 that orbit phase space of magnets M1 and Q4 is not far from elliptical, while for the rest of the magnets the ellipses have to be rather large to fit all orbits inside,

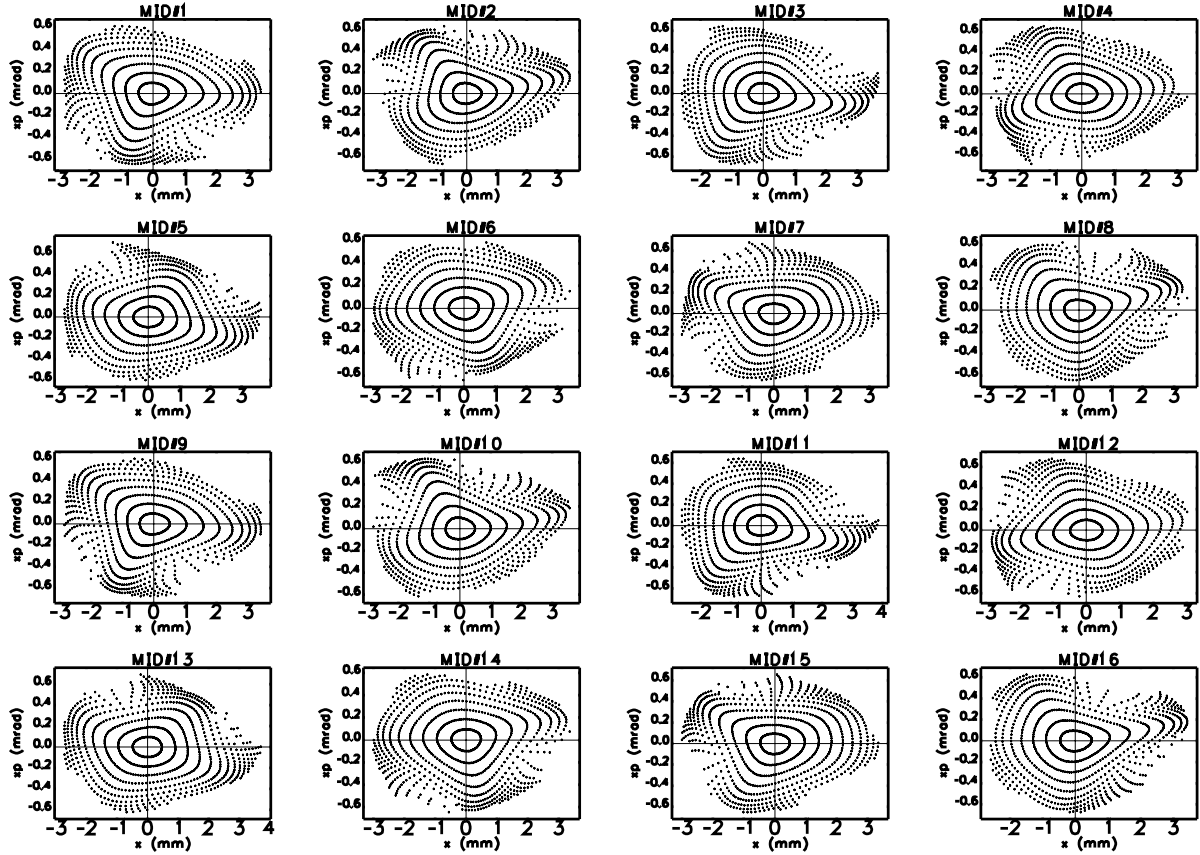


Figure 4.106. Possible closed orbits at the middle of consecutive ID straight sections.

and using these ellipses for ray tracing could lead to significant over estimation of the possible orbits. To be more precise, one can generate the set of points on the outer boundary of the dipole entrance orbit phase space, then transform those points along the dipole using the following expression:

$$\begin{bmatrix} x_1 \\ x'_1 \end{bmatrix} = \begin{bmatrix} \sqrt{\frac{\beta_1}{\beta_0}} (\cos \psi + \alpha_0 \sin \psi) & \sqrt{\beta_0 \beta_1} \sin \psi \\ \frac{\alpha_0 - \alpha_1}{\sqrt{\beta_0 \beta_1}} \cos \psi - \frac{1 + \alpha_0 \alpha_1}{\sqrt{\beta_0 \beta_1}} \sin \psi & \sqrt{\frac{\beta_0}{\beta_1}} (\cos \psi - \alpha_0 \sin \psi) \end{bmatrix} \times \begin{bmatrix} x_0 \\ x'_0 \end{bmatrix}, \quad (4.46)$$

where subscript 0 corresponds to the dipole entrance, subscript 1 corresponds to the point of interest along the dipole, and ψ is the betatron phase advance between the points. Figure 4.109 shows the orbit phase space for entrance and exit of the dipole A:M2. The red symbols on the left plot (dipole entrance) show the boundary of the phase space obtained by analyzing all points on that plot for maximum amplitude at every phase ψ . The red symbols on the right (dipole exit) are obtained by applying expression (4.46) to the red symbols on the left plot. One can see that the transformation works well.

So far, the orbits that were considered were limited by the physical aperture. The maximum orbit can also be limited by the Beam Position Limiting Detectors (Beam Position Monitors with interlocks). Usually, BPLDs are used to protect the vacuum chamber from the radiation generated by Insertion Devices (IDs) and therefore are placed around ID straight sections. The BPLD limits are usually much smaller than the physical aperture, and the orbit phase space at these kick magnitudes

is close to true betatron ellipses. Since ID BPLDs are located all around the ring and at the same beta function, one can write for the limiting ellipse:

$$\mathcal{A} = \frac{x_{\text{BPLD}}^2}{\beta_{\text{BPLD}}}, \quad (4.47)$$

where x_{BPLD} and β_{BPLD} are the BPLD trip limit and the beta function at the BPLD location, respectively. For example, if the BPLD trip limit is 1 mm and the beta function is 6 m, the ellipse constant is $\mathcal{A} = 0.17\mu\text{m}$.

It is important to emphasize that the consideration above only refers to a single-source orbit distortion. Deliberate steering inside a dipole magnet can generate larger orbits, but it is considered an unlikely event and is not presently covered.

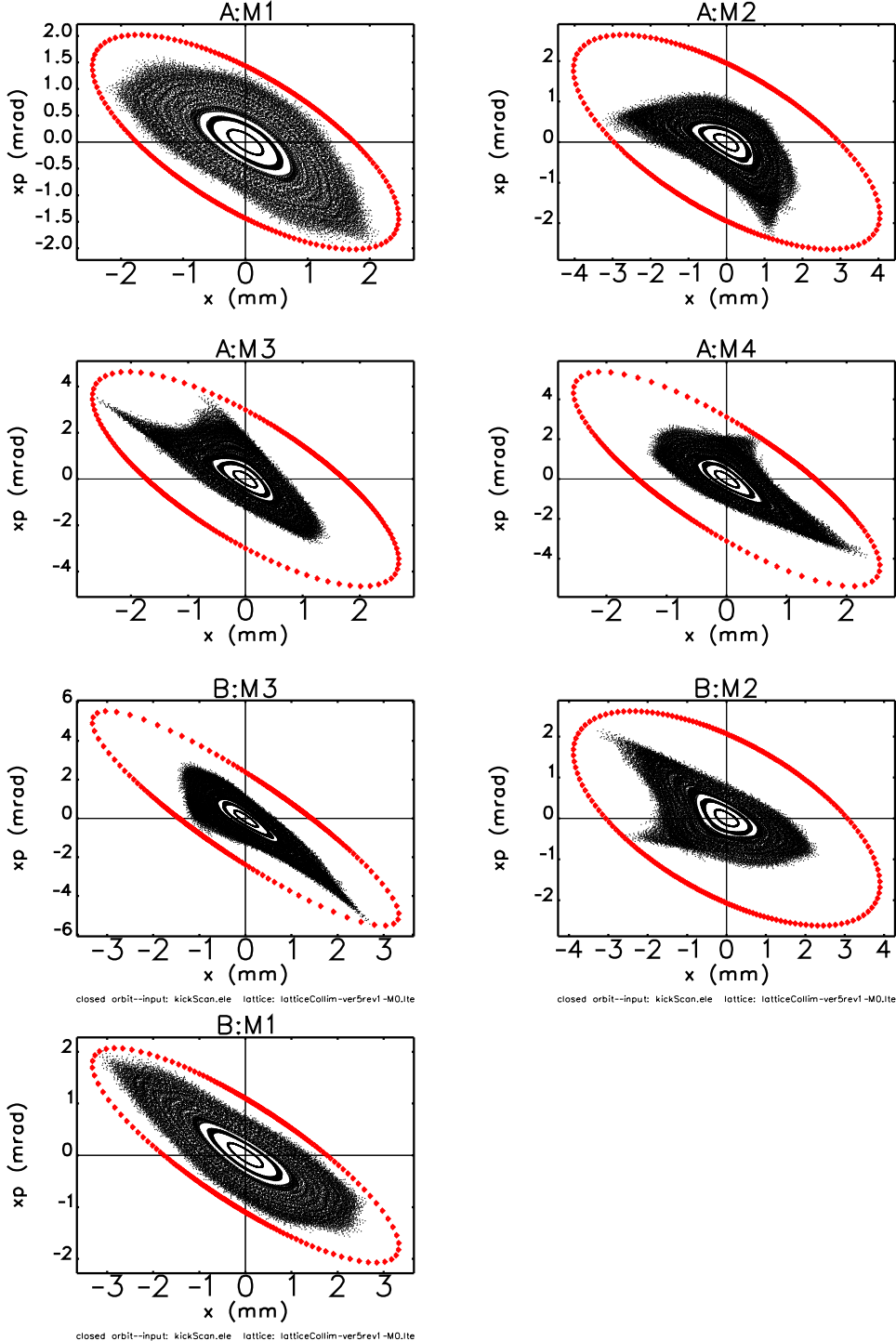


Figure 4.107. Orbit phase space at the entrance to seven non-reverse bending dipoles. Betatron ellipses encompassing the orbit phase space are also shown.

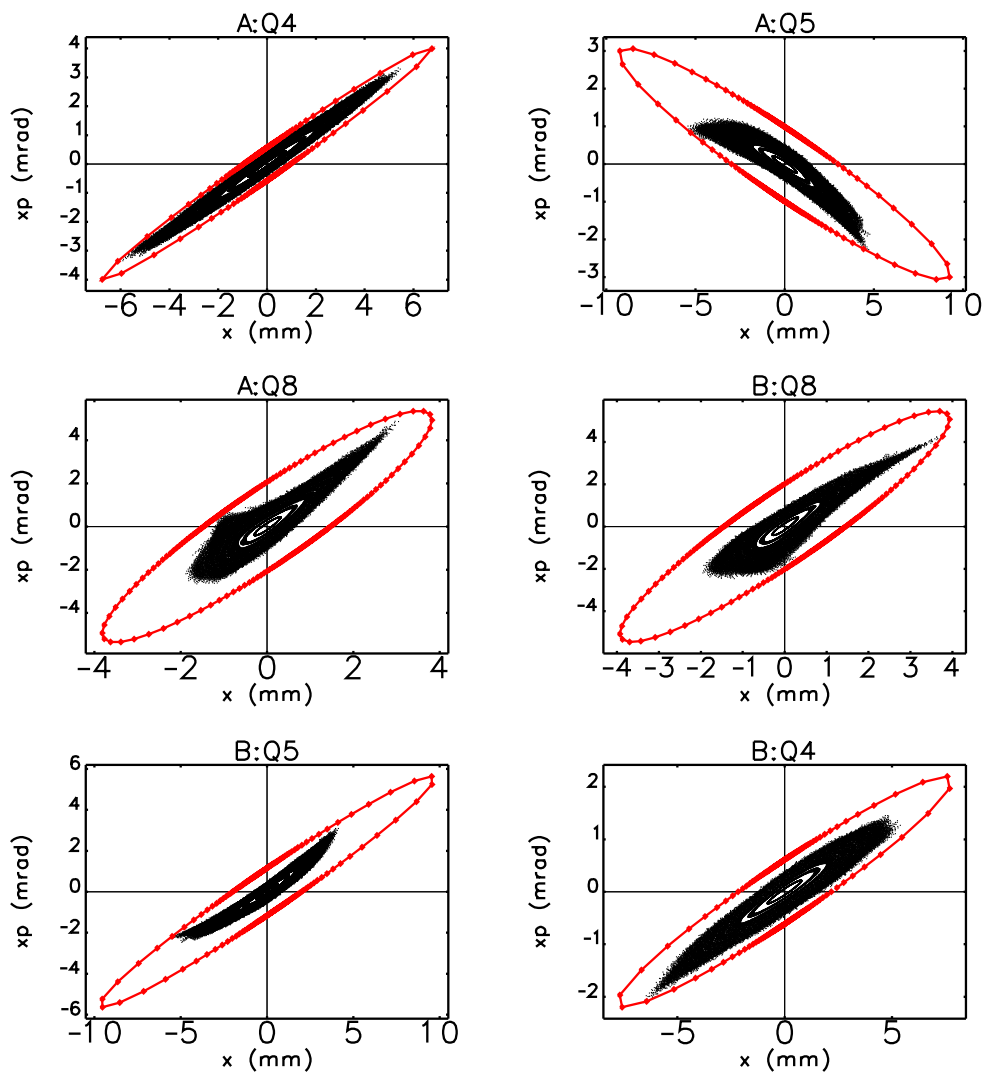


Figure 4.108. Orbit phase space at the entrance to reverse bending dipoles. Betatron ellipses encompassing the orbit phase space are also shown.

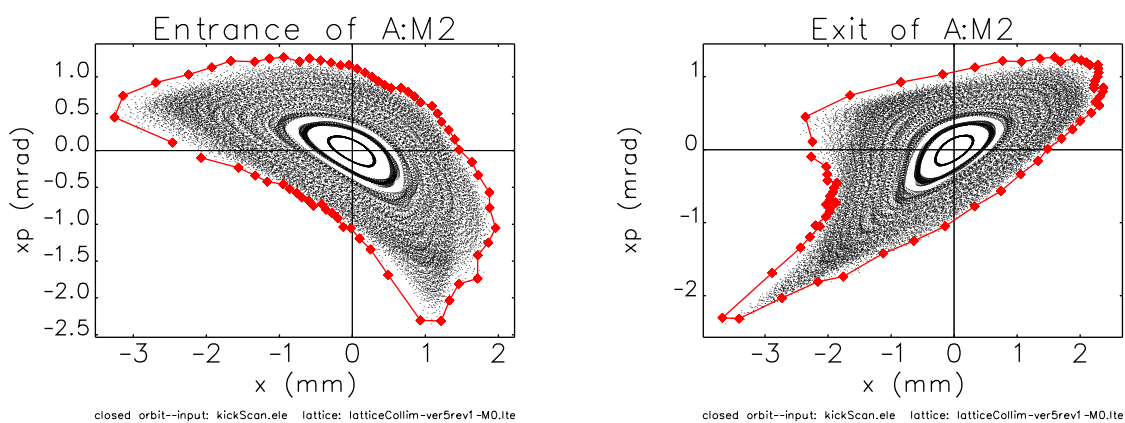
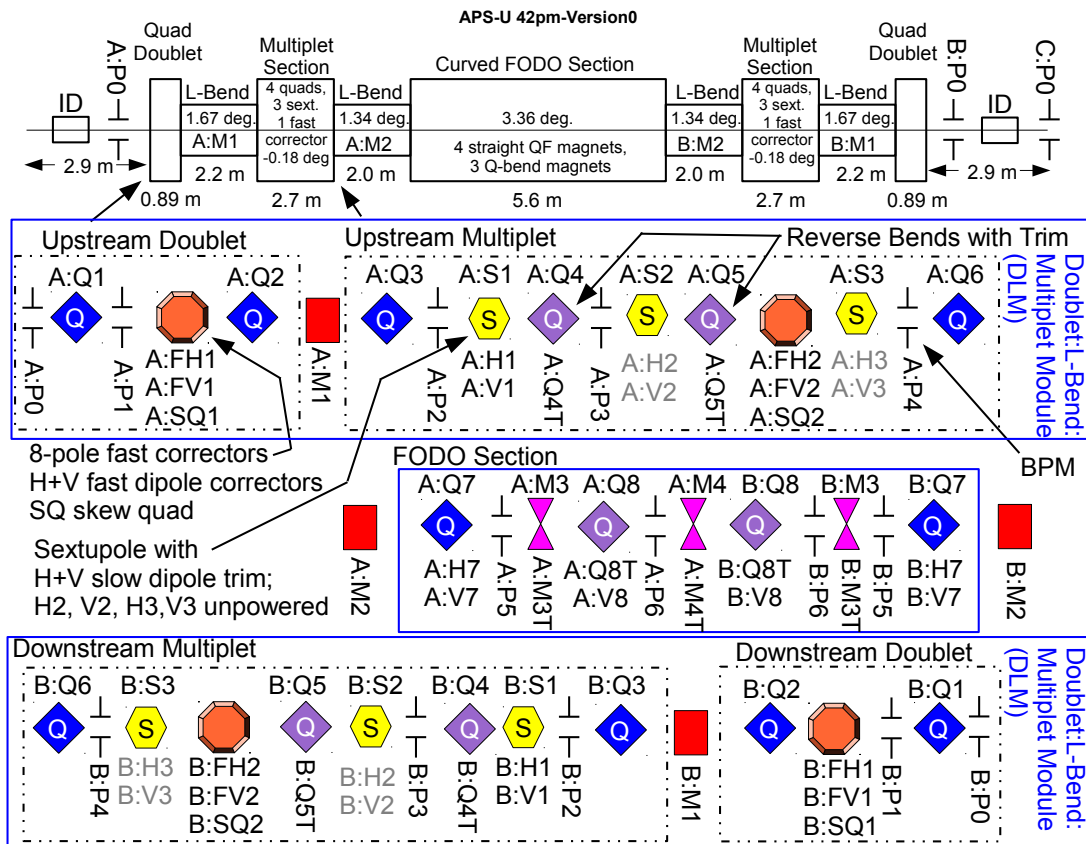


Figure 4.109. Orbit phase at entrance (left) and exit (right) of the dipole A:M2. Red symbols on the left plot outline the boundary of the phase space and are obtained by simple analysis of all the points on the plot. Red symbols on the right are obtained by applying expression (4.46) to the red symbols on the left plot.

4-3 Implementation

4-3.1 Introduction

The APS-U storage ring has 40 sectors, each consisting of 10 functional modules: two quadrupole doublets, four longitudinal-gradient dipoles, two multiplets, a curved FODO section, and an insertion device straight section (see Figure 4.110). Each quadrupole doublet section contains two quadrupole magnets and one combined-function corrector magnet providing horizontal steering, vertical steering, and skew quad capability. The straight multiplets each contain two quadrupole magnets, two reverse bends, three sextupole magnets, and one fast corrector. The center reverse bends Q4 and Q5 are simply quadrupole magnets offset horizontally, making them function as transverse-gradient dipoles which deflect the beam (weakly) outboard. The curved FODO section contains two strongly focusing quadrupoles, two strongly focusing reverse bends, three strongly defocusing transverse-gradient dipole magnets, and an optional three-pole wiggler (3PW) magnet to support bending-magnet x-ray beamlines. Synchrotron radiation from dipole A:M4 and/or B:M3 can also be used as sources of x-rays for the bending magnet beamlines. All together, each sector contains seven dipoles, 10 standard quadrupoles, 6 reverse bends, six sextupoles, and four fast steering correctors totalling 33 lattice magnets / sector, or 1,320 magnets for the entire 40 sectors. This is in addition to insertion device sources tailored to beamline requirements.



The 10 functional modules are grouped into three large magnet assemblies with the M2 dipoles bridging between them. The upstream doublet / L-bend / multiplet (DLM) module contains a dozen magnets, as does the downstream DLM assembly. The central curved FODO section contains 7 relatively large lattice magnets in addition to space to accommodate an optional three-pole wiggler. The DLM and FODO assemblies have been made as large as practicable to facilitate rapid installation.

In addition to 35 standard MBA insertion-device straight sections, three straight sections are reserved for 12 rf cavities. One straight section contains fast swap-out extraction kickers and a superconducting bunch-lengthening harmonic cavity, and one contains an injection septum and four fast injection kickers.

The vacuum systems will be closely integrated with the magnet assemblies and generally use cylindrical chambers with 11-mm inner radius and 1-mm wall thickness designed to satisfy impedance requirements. The minimum magnet pole tip radius is 13 mm. Non-evaporable getter (NEG) - coated round chambers in the FODO section are combined with uncoated antechamber-style and round chambers in the other sections of the arcs. Beam position monitor pickup electrodes with integral bellow assemblies and flanges facilitate chamber assembly. Water cooling and strategically placed discrete photon absorbers are used to handle heating from synchrotron radiation.

For fast orbit feedback (FOFB), four fast combined-function dipole correctors in each sector are used to stabilize the insertion device and three-pole wiggler / bending magnet source points. Each fast corrector has windings for horizontal dipole, vertical dipole, and skew quadrupole field components. Slow dipole trim windings are included on all sextupole magnets and the FODO section quadrupoles. In addition, 14 electron beam position monitors per sector and, in sectors with beamlines, four x-ray beam position monitors are used for orbit alignment and feedback.

Power supplies are located on top of the storage ring enclosure, using existing s-shaped conduit penetrations for cabling, and existing cabinets for the power supplies themselves. The majority of main magnet as well as trim and corrector windings, are powered by individual power supplies. Two families of dipoles will be powered in series. Sextupoles and quadrupoles will be powered by ultrastable unipolar power supplies while correctors and trim windings will have bipolar supplies. Power supplies will be monitored with a unified fast data acquisition system, integrated with the fast orbit feedback data network and accelerator timing systems.

A high-resolution absolute beam size monitor will be used to quantify the emittance. In addition, two relative beam size monitors will be used in conjunction with skew-quad windings located on the fast corrector magnets to control horizontal/vertical coupling. These new diagnostics will be complemented by the existing 35-BM diagnostic beamline.

Additional diagnostics to monitor total beam current, bunch current, x-ray beam position and intensity, vacuum chamber motion, and beam loss are provided.

An enhanced control system based on the Experimental Physics and Industrial Controls System (EPICS) will be provided, and it will include high-speed data acquisition, channel- and service-oriented application programming interfaces, and instrument-embedded input-output controllers (IOCs).

To preserve beam lifetime, a superconducting harmonic cavity bunch-lengthening system will be used, which will be closely integrated with the existing rf, controls, and timing systems.

4-3.1.1 Key Design Drivers

Each of the technical subsystem designs is influenced by specific objectives, which have driven the design process. In the area of magnet design, adjacent quadrupole and sextupole magnets must be aligned at the level of $30\ \mu\text{m}$ rms due to the very high gradients to assure successful commissioning and adequate dynamic acceptance. The short installation window dictates that a method will be needed for transporting groups of magnets (modules) into the accelerator enclosure while preserving magnet-to-magnet alignment.

Accurate placement of extremely strong quadrupoles and transverse-gradient dipoles along a curved trajectory in the FODO section using carefully-designed magnetic measurement and fiducialization techniques will be required.

The magnet support structures must preserve the magnet-to-magnet alignment while allowing placement of modules relative to each other at the level of $100\ \mu\text{m}$ rms, all the while suppressing magnet vibration at the level of $10\ \text{nm}$ rms.

The chosen parameters are a balance between using small magnet apertures to achieve the highest magnetic field gradients, in contrast to beam impedance and vacuum chamber conductance issues, which tend to favor the use of larger chamber and magnet apertures. A pole-tip radius of 13 mm and vacuum chamber inner diameter of 11 mm, with a 1-mm wall thickness in the multipole magnets, have been chosen for the design, consistent with a workable machine.

The high density of magnets, 33 per sector, and the small magnet aperture severely constrain the space available for vacuum and diagnostic components, chamber cooling, and chamber supports. A hybrid vacuum system combining lumped pumping, distributed NEG pumping, and NEG-coated chamber sections is envisioned, satisfying physics requirements.

Thousands of power supplies will be used to drive all of the main, trim, and corrector magnets, in many cases with very tight absolute calibration requirements and with resolution and stability below the level of 10 ppm. Fast bipolar power supplies for orbit stabilization will operate at frequencies up to 10 kHz. Demonstrating that all installed power supplies are performing at this level will require efficient and comprehensive testing and quality assurance (QA) procedures during the pre-installation phase.

Diagnostic and controls systems will be used to contend with electrical and vibrational noise, wake-field effects, and long-term effects, like earth tides and thermal drift, providing stability on time scales extending up to a week or longer. To achieve a level of beam stability commensurate with the significantly reduced transverse beam dimensions, several different beam and mechanical position diagnostics will be required. These will be coupled with an array of fast steering corrector magnets into a high-speed orbit feedback data network, with fast computer processors used to correct the orbit at 22.6 kHz.

A targeted and integrated set of R&D plans has been used to demonstrate that the physics and

stability requirements for the APS-U machine will be met.

4-3.2 Magnets

Each sector has four longitudinal gradient dipoles, three transverse gradient dipoles, six reverse bend gradient dipoles, ten quadrupoles, and six sextupoles - a total of 29 main magnets. In addition, each sector has four fast multi-function corrector magnets, one in each doublet section between Q1 and Q2, and one in the each multiplet section. The layout of these magnets within a sector is shown in Figure 4.110, and a summary of the different main magnet types is given in Table 4.51.

Table 4.51. Summary of MBA magnet types

Magnet type	Q1	Q2,Q3,Q6	Q4	Q5	Q7	Q8	S1,S3	S2	M1, M2	M3	M4
Qty/Sector	2	2	2	2	2	2	2	2	2	2	1
Qty total	80	240	80	80	80	80	160	80	160	80	40
Insertion length (m)	0.250	0.225	0.244	0.150	0.424	0.646	0.230	0.260	2.225, 1.986	0.820	0.700
Pole tip material	VP	ST	VP	ST	VP	VP	ST	VP	ST	VP	VP
Trim winding?	No	No	H	H	H+V	H+V	H ^a +V ^a	H ^a +V ^a	No	H	H

^a S2, S3 trim windings unpowered.

ST = low carbon steel

VP = vanadium permendur

There are three types of dipole bending magnets: longitudinal-gradient dipoles (L-bends), transverse-gradient dipoles (Q-bends), and reverse-bend dipoles (R-bends). The M1 and M2 L-bends have different field strength profiles along their length. The field strength profiles of A: M1 and B: M1 mirror each other longitudinally, as do A: M2 and B: M2. The Q-bend transverse gradient dipoles (M3 and M4) and R-bends resemble quadrupole magnets where the beam axis is offset from the geometrical center of the magnet to create both dipole and quadrupole field components. The three Q-bends, located in the FODO section of Figure 4.110, come in two varieties: the two M3 magnets are identical, while the single M4 at the center of the sector is unique, with its own length and field strength. There are three varieties of R-bends: two Q4 magnets, two Q5 magnets, and two Q8 magnets per sector.

The 10-quadrupole magnets in each sector come in four sizes: Q1, Q2, Q3/Q6, and Q7. Magnets Q3 and Q6 are identical and have a slot opening for a photon beam chamber. The Q2 magnet does not have an opening for a photon beam chamber, but is the same length as Q3/Q6. Q2, Q3, and Q6 use the same coils and are located in the doublet and multiplet sections shown in Figure 4.110, and have solid steel cores. Quadrupoles Q1 and Q7 use vanadium permendur pole tips to achieve a high field strength. The Q7 magnet is a multi-function magnet capable of producing a quadrupole field, vertical dipole field, and a horizontal dipole field.

All sextupole magnets have the same cross section. The S1 and S3 are 230 mm long while the S2 is 260 mm long. All sextupoles are solid steel core multi-function magnets capable of producing a sextupole field, vertical dipole field, and a horizontal dipole field. The S2 sextupole will have trim coils but will not be supplied with trim power supplies. S1 and S3 use steel pole tips, while S2 has vanadium permendur pole tips to meet the high magnet strength requirements. All six sextupole magnets are located in the two-multiplet sections, as shown in Figure 4.110.

In multi-function magnets, such as the sextupole magnets, a high magnetic efficiency is needed to minimize the cross talk between the field components. To illustrate the problem, Figure 4.111 shows the effect that a sextupole field has on the horizontal and vertical dipole trim fields in the S1/S3

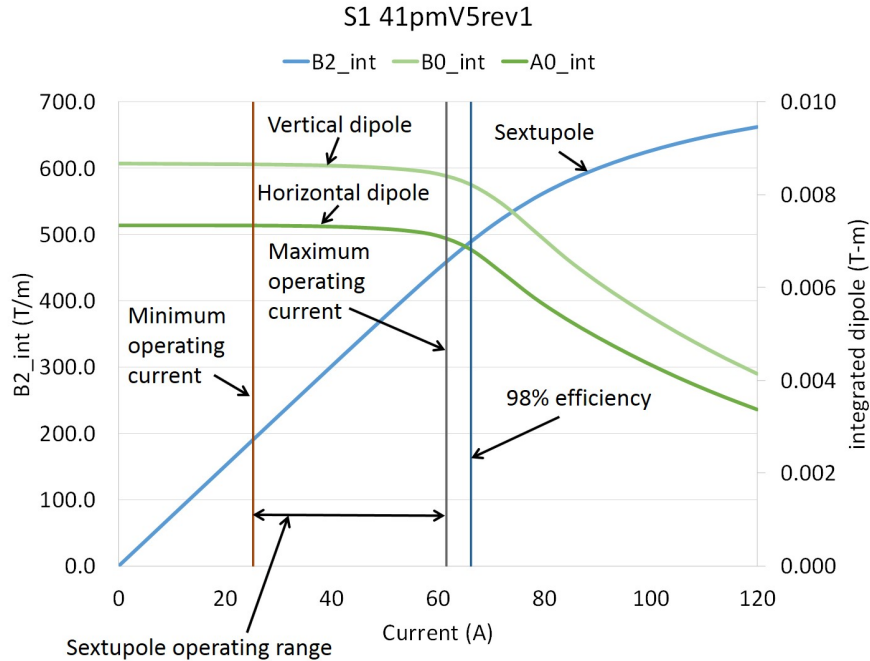


Figure 4.111. Effect of S1/S3 sextupole current on sextupole and dipole fields. Both horizontal and vertical dipole correction currents are set and held at the maximum (10 A) while the sextupole current is turned up. Saturation in the poles result in a decrease in the dipole field for high values of the sextupole field.

magnet. As the sextupole field gets larger, saturation in the poles causes the dipole fields to drop rapidly when the sextupole current is above the current indicated by the 98% sextupole efficiency line. Changing the dipole field while the sextupole current remains constant has a similar, but much smaller (and negligible) effect on the sextupole field. The operating range of this sextupole magnet must stay below the current that corresponds to a 98% magnet efficiency in order for the dipole fields to stay within 7.1% of their value in the absence of a sextupole current. A 98% magnet efficiency rating also creates a well-designed yoke [1].

The magnet efficiency is defined as the ratio between the actual field and the field that would be produced if the core had infinite permeability. Figure 4.112 shows the integrated field for a sextupole magnet with steel poles along with the integrated field for the same sextupole magnet made out of a core with infinite permeability. For currents below the 98% efficiency limit, the fields are nearly identical. Above that current limit, the fields diverge quickly. The guideline used to design the sextupole magnets is to keep the operating current below the 98% efficiency limit. This will minimize the cross talk between the main field and the corrector fields. Quadrupole, reverse bend, and transverse gradient dipole magnets are designed to 90% minimum magnet efficiency. Defining the magnet efficiency limit this way determines the magnet lengths with allowable magnetic saturation.

All magnets except correctors are water cooled. Consistent with the present APS designs, the pressure drop between supply and return for the de-ionized water is 0.62 MPa (90 psi). The supply pressure is 1.03 MPa (150 psi) with pressure spikes reaching 1.72 MPa (250 psi). The supply

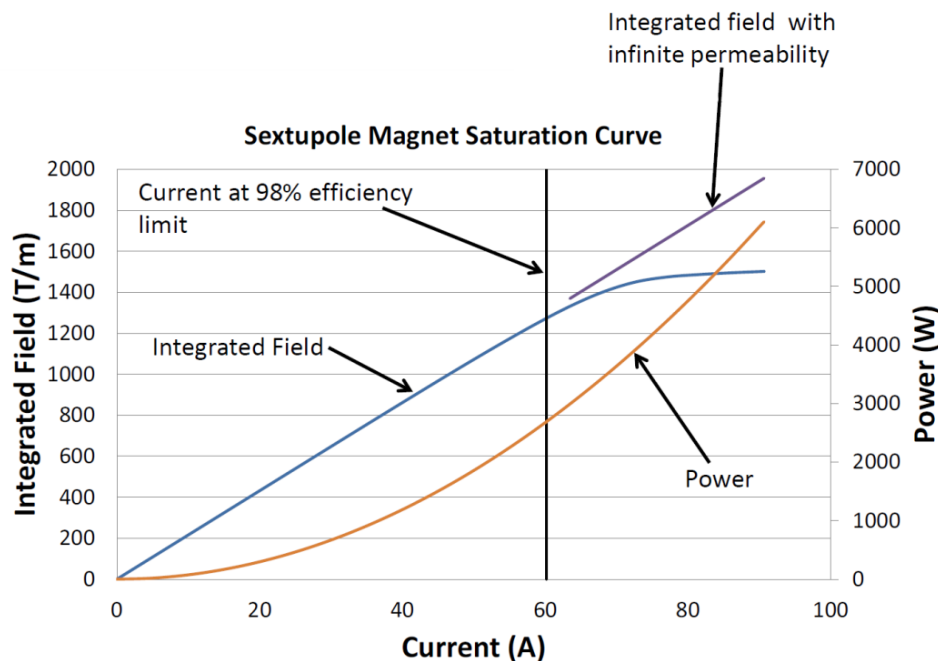


Figure 4.112. Effect of current on integrated field and power, showing sextupole magnet saturation. Design guideline – operate magnets at or better than 98% efficiency.

temperature is 25.6°C. All magnets are designed to have a temperature rise of no more than 10°C (exceptions are made on a case-by-case basis).

At the start of the magnet design effort, the most demanding version of each type of magnet was identified, and subsequent design effort was focused on that magnet. Thus, design work on the L-bend magnets has been focused on M1 rather than the lower-field M2, with a similar approach taken for the other magnet types. The magnets have been modelled and simulated as single stand-alone magnets. Extensive 2D and 3D magnetic modeling studies have led to the preliminary magnet designs described in the following sections.

Cross talk analyses between adjacent magnets has been studied. Cross talk studies have been done between the Q2 and M1 magnets and the corrector and Q1 and Q2 magnets. These results have shown negligible field quality issues between magnets. Further analysis is needed to examine the magnet-to-magnet coupling that may occur between the corrector and the Q5 and S3 magnets.

4-3.2.1 Quadrupole Magnets

Table 4.52 lists the parameters for the quadrupole magnets. The “insertion length” given is the physical length of the complete magnet and includes the space needed for the coils. The types of magnet as determined by their pole tip materials are also listed: Q2, Q3, and Q6 with their steel poles, and Q1 and Q7 with vanadium permendur poles. All quadrupole magnets have a 13-mm aperture radius and a 10-mm vertical gap between pole tips.

The Q1, Q2, Q3, and Q6 are single-function magnets. All quadrupole magnets are designed to

Table 4.52. Summary of quadrupole magnet parameters

Magnet identification		Q1	Q2	Q3	Q6	Q7
Insertion length	m	0.250	0.225	0.225	0.225	0.424
Pole tip material		VP	ST	ST	ST	VP
Aperture (diameter)	mm	26.00	26.00	26.00	26.00	26.00
Integrated gradient, max. magnitude	T	18.26	13.86	11.33	12.21	34.76
Integrated gradient, nom. magnitude	T	16.60	12.60	10.30	11.10	31.60
Integrated gradient, min. magnitude	T	12.45	9.45	7.73	8.33	23.70
Current at max. integrated gradient	A	205.00	173.37	135.52	147.03	203.96
Current at nom. integrated gradient	A	177.96	152.40	122.75	132.64	174.76
Current at min. integrated gradient	A	130.30	112.34	91.66	98.85	127.66
Power at max. integrated gradient	W	2503	1656	1314	1548	2364
Power at nom. integrated gradient	W	1886	1279	1080	1260	1736
Power at min. integrated gradient	W	1013	697	602	703	928
Inductance	mH	18.9	16.8	18.0	18.0	44.3
Central gradient max.	T/m	89.3	78.2	62.9	67.9	97.8
Vertical/Horizontal integrated dipole max. (at magnet center)	T-m					0.0189
Current at max. vertical/horizontal dipole	A					10
Power at max. vertical/horizontal dipole	W					407

ST = low carbon steel

VP = vanadium permendur

operate over a range from 75% to 110% of the nominal integrated strength. The Q7 magnet is a multi-function magnet producing both vertical and horizontal dipole fields as well as a quadrupole field.

In the case of the Q7 magnet, there are three coils in each of the four coil packs to produce vertical and horizontal dipole fields in addition to the main quadrupole field. Table 4.52 shows the parameters for the Q7 quadrupole magnet.

Figure 4.113 shows the flux density, B , in a cross-section view for one quadrant of the Q1 quadrupole magnet. It represents the values of $|B|$ in the center of the magnet. The maximum field is 2.1 T at the corners of the pole tip.

Figure 4.114 shows a 3D calculation for the same magnet. The values of $|B|$ shown by the colors are the values at the surface of the magnet. As expected, the 3D calculation shows that the highest saturation is still at the pole tips, but the saturation level is higher at the upstream and downstream ends of the pole tips.

Even a perfectly symmetric magnet will produce some higher-harmonic field components, and these quadrupoles are no exception. Tolerances are set on how big these components can be compared to the main field. All harmonics are determined at a reference radius of $R = 10$ mm. Harmonics of orders other than the quadrupole must have a value that is generally significantly less than 0.1% (10 units, where a “unit” is one part in 10^4) of the quadrupole term. Detailed requirements on field quality are described in section 4-2.3.1. The harmonics present in the field of a perfectly symmetric quadrupole magnet (the “allowed” harmonics) are b_5 , b_9 , b_{13} , and b_{17} , i.e., the 12-, 20-, 28-, and 36-pole harmonic components, respectively. For the Q1 quadrupole magnet, these harmonics were

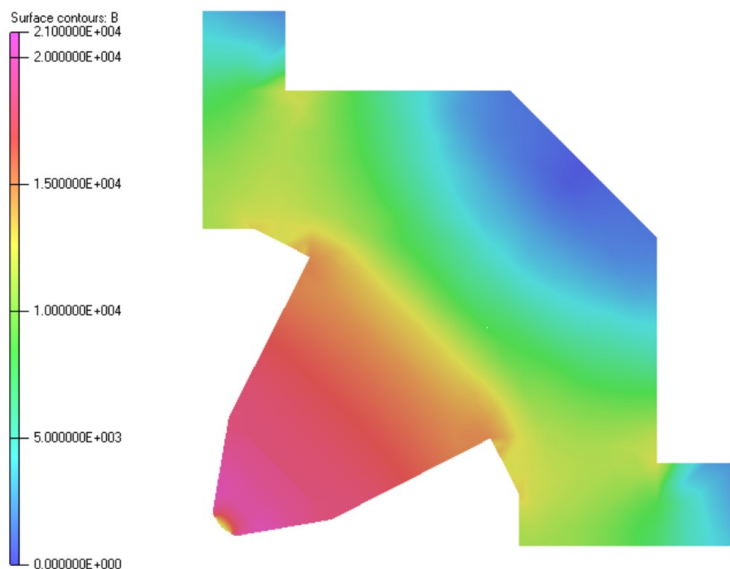


Figure 4.113. Flux density, B , in a cross-sectional view of the first quadrant of a Q1 quadrupole magnet at maximum current. This cross-section is taken at the axial center of the magnet (in the beam direction). The highest value of $|B|$ is 2.1 T, at the corners of the pole tip.

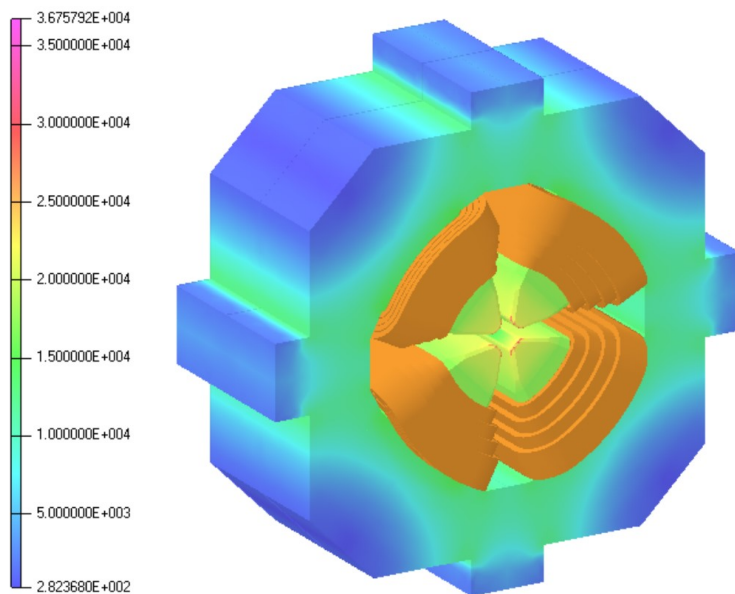


Figure 4.114. Q1 quadrupole 3-D calculation for the flux density. The values of $|B|$ shown here are for the surface of the magnet. The highest value, 3.7 T, occurs at the upstream and downstream ends of the pole tips.

calculated to be $b_5 = -2.4$, $b_9 = -4.3$, $b_{13} = -2.5$, and $b_{17} = -0.1$ units, which are within specifications. The remaining quadrupole magnets are expected to have similar values. The b_5 harmonic can be adjusted by modifying the end and tip chamfers, but this will result in some loss of field strength.

4-3.2.2 Sextupole Magnets

The S1 and S3 sextupole magnets have an insertion length of 230 mm and are identical. The S2 magnet is 260 mm long. Table 4.53 lists the parameters for these sextupole magnets. All sextupole magnet designs are multi-function magnets, designed to produce a sextupole field, a horizontal dipole field, and a vertical dipole field. There are three coils in each of the six coil packs, one coil pack per pole, to produce vertical and horizontal dipole fields in addition to the main sextupole field. The S1 and S3 sextupole magnets have steel pole tips, while the S2 sextupole magnet uses vanadium permendur pole tips to meet the higher field requirements. All sextupole magnets have a 14-mm aperture radius and a 10-mm vertical pole tip gap. The sextupole magnets are designed to operate over a range from 50% to 120% of the nominal integrated strength.

Table 4.53. Summary of sextupole magnet parameters.

Parameter	Unit	Value	
Magnet identification		S1, S3	S2
Insertion length	m	0.256	0.256
Pole tip type		ST	VP
Aperture (diameter)	mm	28.00	28.00
Integrated B'' , max. magnitude	T/m	917.76	1500.36
Integrated B'' , nom. magnitude	T/m	764.80	1250.30
Integrated B'' , min. magnitude	T/m	382.40	625.15
Current at max. integrated sextupole	A	61.44	87.60
Current at nom. integrated sextupole	A	50.87	71.91
Current at min. integrated sextupole	A	25.35	35.73
Power at max. integrated sextupole	W	436	992
Power at nom. integrated sextupole	W	300	668
Power at min. integrated sextupole	W	75	165
Inductance	mH	19.5	21.8
Central B'' , max.	T/m ²	5081.5	7131.3
Vertical integrated dipole field max.	T-m	0.0087	0.0099
Current at max. vertical dipole	A	10.0	10.0
Power at max. vertical dipole	W	217	247
Horizontal integrated dipole field max.	T-m	0.0073	0.0084
Current at max. horizontal dipole	A	10.0	10.0
Power at max. Horizontal dipole	W	165	186

ST = low carbon steel

VP = vanadium permendur

Figure 4.115 shows the flux density $|B|$ in a cross-sectional view calculated for the first quadrant of the S1 sextupole magnet at maximum current. A design goal is that all harmonics of the sextupole magnets be significantly less than 0.1% (10 units) of the main harmonic (here the sextupole), when determined at a reference radius of $R = 10$ mm (see section 4-2.3.1). The calculated values for S1 are $b_8 = -304$ and $b_{14} = -14$ units. These harmonics exceed the design goal, mainly due to the large vertical pole tip gap compared to the small pole tip radius. If the vertical pole tip gap is reduced from 10 mm to 7 mm, the b_8 harmonic can be reduced to less than 10 units, but a 7-mm vertical pole tip gap interferes with the vacuum chamber cooling channel. Investigations indicate that these elevated levels will not have a significant impact on accelerator performance.

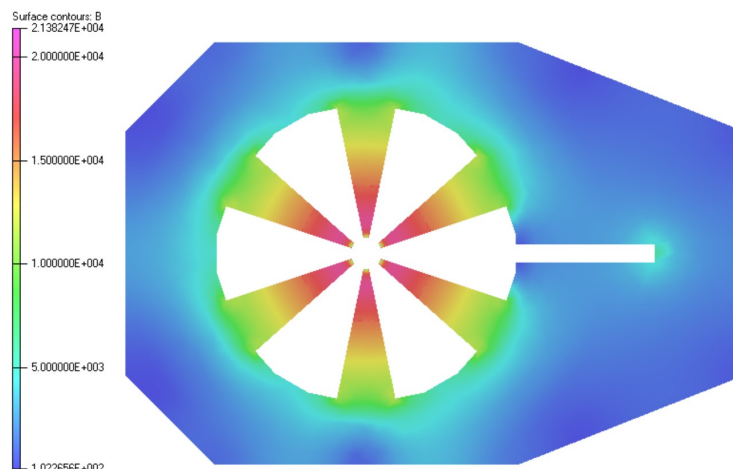


Figure 4.115. Flux density $|B|$ in a cross-sectional view of the sextupole magnet at maximum current. The cross-section is taken at the axial center of the magnet.

4-3.2.3 Longitudinal-Gradient Dipoles

Longitudinal-gradient dipole magnets (L-bends) have a vertical magnetic field that varies along the particle beam trajectory. Table 4.54 shows the functional specifications for the two types of L-bends: M1 and M2. For the convenience of beam optics analysis, each magnet is divided into five sections with different field strengths and lengths. The specified minimal gap between poles is 27 mm. A total of 80 of each type will be fabricated. All M1 magnets will be connected in series and powered by a single power supply. The other circuit combines all M2 magnets. Each M1 magnet must be magnetically identical to all the others (to within the tolerances listed in the tolerances document), by use of trim windings and adjustable end shields.

Table 4.54. Functional specifications of the M1 and M2 magnets

M1 Dipole			M2 Dipole		
B (T)	L_{eff} (m)	$B \times L_{\text{eff}}$ (T-m)	B (T)	L_{eff} (m)	$B \times L_{\text{eff}}$ (T-m)
0.650	0.192	0.12472	0.161	0.292	0.04706
0.400	0.233	0.09312	0.182	0.359	0.06524
0.270	0.493	0.13316	0.213	0.487	0.10360
0.195	0.671	0.13096	0.252	0.308	0.07742
0.141	0.636	0.08986	0.320	0.540	0.01729
Total	2.225	0.57182		1.985	0.46621

Based on the study of the R&D longitudinal-gradient dipole magnet built with a continuously varying gap, a more complex design with uniform gap is proposed which can more accurately match the specified stepped field; this was assumed for the accelerator lattice optimization. Figure 4.116 shows this L-bend magnet model (a) and yoke (b), which approximates the specified fields in Table 4.54 but matches the specified stepped field. A final magnet design will be determined after the completion of the R&D program that approximates the specified fields in Table 4.54 for the final 42 pm lattice.

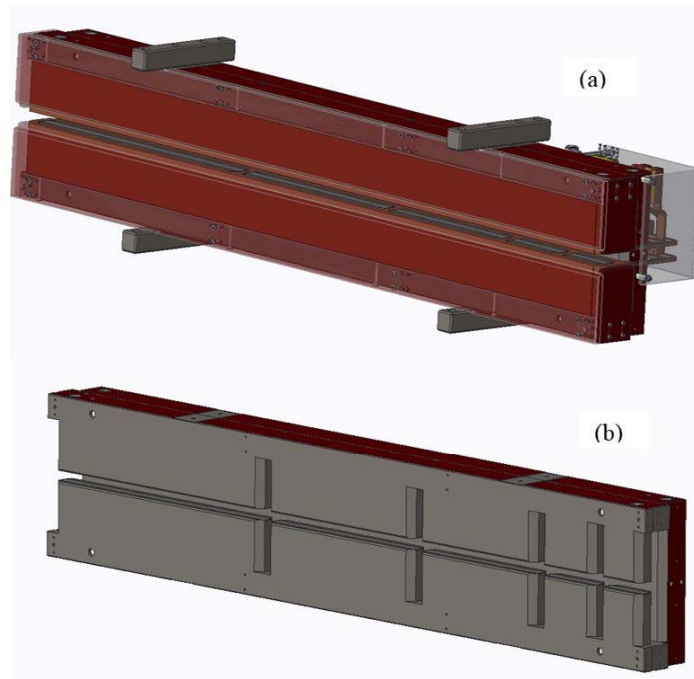


Figure 4.116. (a) Prototype M1 L-bend magnet with uniform gap and (b) M1 yoke.

4-3.2.4 Transverse-Gradient Dipoles

Transverse-gradient dipoles (Q-bends) resemble a quadrupole magnet but are distinguished from a simple quadrupole in that the beam axis is offset from the geometrical center of the magnet. This is done so that both dipole and quadrupole field components are present on the beam axis. The Q-bend magnets come in two types, as shown in Table 4.55. The M3 and M4 magnets are of different lengths: the insertion length of M3 is 820 mm; that of M4 is 700 mm. Both types of Q-bend magnets are of solid steel construction with vanadium permendur pole tips to achieve the high field strength. The quadrupole field strength operating range is from 95% to 105% of the nominal integrated strength.

The integrated dipole strength must remain constant throughout the quadrupole operation range. To accomplish this, vertical dipole coils are used to provide a correction field that compensates for the change in dipole field as the quadrupole excitation is changed.

These vertical dipole coils are separate from the quadrupole coils, so separate power supplies are needed. When the current through the quadrupole coils is set to produce the nominal quadrupole field, the dipole field created by the geometrical offset equals the required integrated dipole field, so the dipole coils are not powered (or have a very small current setting). The dipole correction coils are only used when the quadrupole field is operated at other than the nominal value, when they are used in order to maintain the required integrated dipole field. The drawback of powering the dipole coils is that they also introduce a sextupole component. Compensation of this sextupole component using other ring sextupoles was successful with earlier versions of the accelerator lattice, and it is expected that the same can be accomplished for the present 42 pm lattice. Figure 4.117 shows a 2D cross-section of the M4 Q-bend magnet. The geometrical offset is indicated by the 10-mm-radius

Table 4.55. Q-bend magnet parameters

Parameter		M3	M4
Insertion length	m	0.820	0.700
Pole tip type		VP, curved	VP, curved
Aperture (diameter)	mm	43.40	41.60
Integrated gradient, max. magnitude	T	36.22	32.21
Integrated gradient, nom. magnitude	T	34.50	30.68
Integrated gradient, min. magnitude	T	32.77	29.15
Current at max. integrated gradient	A	253.69	230.01
Current at nom. integrated gradient	A	206.36	199.04
Current at min. integrated gradient	A	183.32	176.01
Power at max. integrated gradient	W	9401	8726
Power at nom. integrated gradient	W	6220	6534
Power at min. integrated gradient	W	4909	5110
Inductance	mH	104.1	86.1
Integrated dipole field	T-m	-0.5018	-0.3927
Vertical dipole current at max. integrated gradient	A	26.590	17.270
Vertical dipole power at max. integrated gradient	W	1340	486
Central gradient, max.	T/m	47.8	50.4
Vertical integrated dipole max. (at magnet center)	T-m	0.113	0.0642
Current at max. vertical dipole	A	30	20
Power at max. vertical dipole	W	1704	651

VP = vanadium permendur

circle in the pole gap.

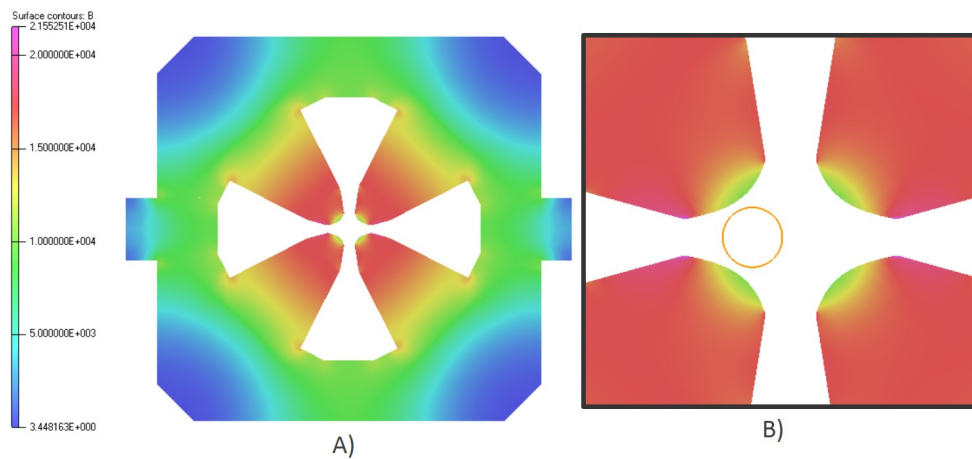


Figure 4.117. Cross-section of the M4 Q-bend magnet. A) Whole magnet. B) Close up of pole tips with 10 mm radius.

The M3 and M4 magnets have a 21.7-mm and 20.8-mm pole tip radii, respectively, along with a minimum pole tip vertical gap of 10 mm. All Q-bend harmonics are required to be significantly less than 0.1% (10 units) at a reference radius of $R = 10$ mm with the dipole as the main field (see section 4-2.3.1). The pole tips of the magnets are machined with a curve to match the corresponding radius. Unlike the pole tips, the pole bases, core, and coils are machined straight.

4-3.2.5 Reverse-Bends

Reverse-bend dipoles (R-bends) are essentially quadrupole magnets, but are distinguished from a simple quadrupole in that the beam axis is offset from the geometrical center of the magnet. This is done so that both dipole and quadrupole field components are present on the beam axis. These are similar to the Q-bends except that the dipole field polarity is reversed. The R-bend magnets Q4, Q5, and Q8 are of different lengths: the insertion length of Q4 is 244 mm; Q5's is 150 mm; and Q8's is 646 mm. The Q5 R-bend magnet is solid steel construction while the Q4 and Q8 use vanadium permendur pole tips to achieve the high field strength. The quadrupole field strength operating range is from 95% to 105% of the nominal integrated strength. The Q8 R-bend magnet has curved pole tips while the Q4 and Q5 magnets have straight pole tips.

The integrated dipole strength must remain constant throughout the quadrupole operation range. To accomplish this, vertical dipole coils are used to provide a correction field that compensates for the change in dipole field as the quadrupole excitation is changed.

These vertical dipole coils are separate from the quadrupole coils, so separate power supplies are needed. When the current through the quadrupole coils is set to produce the nominal quadrupole field, the dipole field created by the geometrical offset equals the required integrated dipole field, so the dipole coils are not powered (or have a very small current setting). The dipole correction coils are only used when the quadrupole field is operated at other than the nominal value, when they are used to maintain the required integrated dipole field. The drawback of powering the dipole coils is that they also introduce a sextupole component. Compensation of the dipole-coil-induced sextupole component on quadrupole magnets using other ring sextupoles was successful with earlier versions of the accelerator lattice, and it is expected that the same can be said of the design presented here. The Q8 magnet has a horizontal dipole field corrector that is also for vertical beam correction.

The Q4, Q5, and Q8 magnets have a 28.7-mm, 31.0-mm, and 29.0-mm aperture radii, respectively, along with a minimum pole tip vertical gap of 10 mm. All R-bend harmonics are required to be significantly less than 0.1% (10 units) at a reference radius of $R = 10$ mm with the quadrupole as the main field (see section 4-2.3.1).

4-3.2.6 Magnet Trims and Fast Correctors

Some of the magnets include provisions for adjustment or correction of the field. For others, corrections are still under investigation.

The L-bend magnets must be magnetically identical to each other (to within the tolerances listed in the tolerance section). This is achieved by the use of trim windings and adjustable end shields. Trim windings for the L-bend magnets remain under investigation.

An eight-pole laminated fast corrector magnet will produce vertical and horizontal dipole fields as well as a skew quadrupole field. The corrector magnet is 158 mm long and capable of bending the stored beam by 300 micro radians. The maximum required integrated skew quadrupole field is 0.25T. There will be four fast corrector magnets in each sector.

The Q7 and Q8 quadrupole magnets include separate vertical and horizontal corrector windings.

The maximum required field for the correctors is 11 mT. Table 4.52 lists the maximum integrated fields for these magnets.

When the vertical dipole winding is energized on a quadrupole magnet, a large normal sextupole component is also introduced. Similarly, the horizontal dipole comes with a large skew sextupole component. These sextupole components have been evaluated and accepted in the lattice design.

4-3.2.7 Magnet Modules

There are four longitudinal gradient dipoles (L-bend), three transverse gradient dipoles, sixteen quadrupoles, six sextupoles, and four fast corrector magnets in each sector. Individual multipole magnets are grouped together and integrated with the girder and plinth to form magnet modules. There are two Doublet-L-bend-Multiplets (DLM) modules, one FODO module in the middle, and two L-bend dipoles in between the DLM and the FODO module in each sector. The DLM module consists of six quadrupoles, three sextupoles, two fast correctors, and one L-bend dipole magnet. The FODO module consists of four quadrupole magnets and three transverse gradient dipole magnets.

The tight magnet-to-magnet alignment tolerance requirements are achieved within a module through machined datum reference frames and mating surfaces. The common magnetic centerline of the module is then identified and fiducialized through magnetic measurements of the magnet module assembly. The alignment tolerance between magnet modules is more relaxed, and this allows for efficient survey and alignment procedures during the installation period. All required utilities and instrumentation are incorporated into the modules.

4-3.2.8 Magnetic Measurements

All magnets will be measured to ensure that they meet the field quality requirements. These measurements will also provide data on field strengths in various magnets needed for operation of the accelerator. The magnetic centers of multipoles in the quadrupole doublet and the multiplet sections will be measured to verify alignment and to define the overall magnetic axis of these assemblies. The magnet assemblies will be installed in the machine using this information. Magnets in the FODO section will be fiducialized individually using a wire-based system, and then installed in the FODO assembly using either survey or precision-machined surfaces on the support structure.

4-3.2.8.1 Rotating Coil Measurements of Multipole Magnets The field quality in the multipole magnets, such as the quadrupoles and the sextupoles, is described in terms of the normal and skew field harmonics, as defined in Equation (4.20) - Equation (4.23). These field harmonics can be measured most conveniently and accurately by a system of rotating coils. With a good rotating coil system, the field harmonics can be measured with a resolution of ~ 10 ppm of the main field component (0.1 “units”) or better. The strength of the main field component can be measured with a repeatability of 50-100 ppm over a long production run. The absolute accuracy of the main field component depends on the calibration method used. There is a plan to calibrate the field strengths measured by rotating coils against Hall probe scans in a few quadrupoles and sextupoles. It is estimated that the main field components can be calibrated with an absolute accuracy of $\sim 0.1\%$ or better.

Even small rotational imperfections of the rotating coil cause significant errors in the measurement of harmonics [2]. Rotating coil designs have been developed to implement bucking of the main harmonic term and the next lower order term (feed-down term) to ensure accurate measurements even in the presence of small rotational imperfections. These designs use printed circuit technology developed at Fermilab[3] to build these coils at minimal cost. A complete measurement system has been built and fully tested with the Demonstration Modular Multiplet (DMM) magnets during the R&D phase.

In production, rotating coils will be used to measure the main field strength and field harmonics as a function of current in individual magnets. Measurements of quadrupole and sextupole magnets will require rotating coils of different designs. Several such rotating coil systems will be needed in production to meet the requirements of measuring different types of magnets, and to achieve the required measurement throughput. Some magnets will have integrated horizontal and vertical steering correctors. The corrector strengths and harmonics will be measured in such magnets as a function of current, with the main magnet coil set to a nominal current.

The Q-bends M3 and M4, and the quadrupole Q8 in the FODO section, are combined function magnets and are curved. A procedure has been developed to measure the field quality in such magnets using a short rotating coil at several axial and transverse positions [4]. The procedure is validated using computed field maps in a M4 magnet and will be refined further using a R&D M4 magnet.

4-3.2.8.2 Wire-Based Measurements Wire-based techniques, such as the vibrating wire or the stretched wire, can measure the magnetic axis of a multipole magnet with a precision of a few micrometers [5]. For example, a vibrating wire system was used at NSLS-II to align several multipoles on a girder within ~ 0.006 mm rms [6]. A new “rotating wire” technique has been developed at APS-U that achieves comparable accuracy with significantly reduced measurement time. To simplify integration of magnets into assemblies, the magnets to be mounted on a common support structure will be aligned using precision-machined reference surfaces. This assumes that the mechanical and magnetic centers of the multipoles coincide. An assembly of multipoles on a common support structure will be measured using the rotating wire technique to determine the alignment between various elements and to define an overall best fit “assembly axis” which can be used for installation in the storage ring. In the 42 pm lattice design, the Q4 and Q5, quadrupoles in the multiplet section are combined function magnets producing slight reverse bends. The multiplet assembly, therefore, is no longer straight. The bending angles, however, are quite small (< 2 mr) in Q4 and Q5 and it will still be possible to carry out alignment measurements using a straight rotating wire, although the maximum rotation radius that can be used will be somewhat limited. It is expected that an alignment of better than 0.030 mm rms will be achieved without the need to shim individual magnets, but any magnet found to be unacceptably misaligned (offset of more than ~ 0.06 mm, say) will be shimmed to improve the overall alignment. Another reason to use shims would be to correct magnetic roll angles in magnets that do not meet the ± 0.4 mrad magnetic roll specification

The Q-bends M3 and M4, as well as the Q8 magnet in the FODO section, will have strong quadrupole and dipole components, and will be curved. No established technique exists to measure the magnetic axis of such magnets. As part of ongoing R&D, it has been shown[4] that a wire-based technique

could be used to measure the magnetic axis in these curved magnets with appropriate data analysis to account for the curvature. This concept will be tested and refined with the help of measurements in a R&D M4 magnet. This method will be used to measure the magnetic axis of a stand-alone curved magnet, and relate it to magnet fiducials. Measurement of the relative alignment between all the magnets in the FODO section, although possible in principle, has many practical difficulties that may limit the usefulness of such measurements. The magnets in the curved FODO section will therefore be aligned based on mechanical features and the alignment will be verified by survey and utilizing fiducialization data in individual magnets.

4-3.2.8.3 Hall Probe Measurements The longitudinal gradient dipoles M1 and M2 (L-bends) are ~ 2.22 m and ~ 1.98 m long, respectively, with bend angles of 1.637 and 1.336 degrees. The dipole field in these magnets varies in the axial direction by as much as a factor of 4.6. The axially varying field, coupled with the fact that the field integral is required along a curved trajectory with varying curvature, makes rotating coils somewhat unsuitable for providing useful magnetic measurements. The field in these magnets is best described by a full field map that can be measured by a Hall probe. These magnets are designed as C-shaped magnets with an open gap on one side. This design will facilitate the insertion of a Hall probe arm from the side. High resolution Hall probes that can be read in an analog mode will be used to carry out on-the-fly measurements on a rectangular grid on the magnet midplane to minimize the time required to complete a field map measurement. The Hall probe system will be similar to what is currently used at the APS for undulator measurements. The Hall probes will be calibrated in-house against nuclear magnetic resonance (NMR) measurements in a reference magnet to ensure good absolute accuracy. If necessary, the end shields in the L-bend dipoles will be adjusted to keep the strengths of all magnets within a tight tolerance band. In addition to the L-bend dipoles, Hall probe maps will be measured in a few multipole magnets of each type to obtain generic field profiles to characterize the field in the ends of the multipole magnets, and to calibrate absolute field strengths measured by rotating coils.

References

- [1] J.T. Tanabe. *Iron-Dominated Electromagnets*. World Scientific Publishing Co. Pte. Ltd, 2005, pp. 97–129 (cit. on p. 151).
- [2] Animesh Jain. “Harmonic Coils.” In: *Proc. of CERN Accelerator School on Measurement and Alignment of Accelerator and Detector Magnets*. Also found in CERN-98-05. 1998, pp. 175–217. URL: <http://cds.cern.ch/record/1246517/files/p175.pdf> (cit. on p. 161).
- [3] J. DiMarco. “Rotating Circuit Board Probes for Magnetic Measurements.” In: *Proc. of the 15th International Magnetic Measurement Workshop*. 2007. URL: <https://indico.fnal.gov/getFile.py/access?contribId=27&sessionId=15&resId=2&materialId=slides&confId=1093> (cit. on p. 161).
- [4] Animesh Jain. “Rotating Coil and Wire Measurements for the Advanced Photon Source Upgrade.” In: *3rd PACMAN Workshop*. 2017. URL: https://indico.cern.ch/event/600191/contributions/2520340/attachments/1430059/2196296/PACMAN3_Jain.pdf (cit. on p. 161).
- [5] Animesh Jain. “Precision Alignment of Multipoles on a Girder for NSLS-II.” In: *Proc. of the 17th International Magnetic Measurement Workshop*. 2011. URL: <http://immw17.cells.es/presentations/Thu05-IMMW17-AJain.pdf> (cit. on p. 161).

- [6] Animesh Jain. “Production Measurements for NSLS-II: Lessons Learned.” In: *Proc. of the 18th International Magnetic Measurement Workshop*. 2013. URL: <https://indico.bnl.gov/getFile.py/access?contribId=21&sessionId=8&resId=1&materialId=slides&confId=609> (cit. on p. 161).

4-3.3 Vacuum System

4-3.3.1 Requirements and Constraints

The principal purpose of an accelerator vacuum system is to minimize interaction between the particle beam and gas molecules. Such interactions contribute to instability and gradual loss of beam. For the APS-U storage ring, the vacuum system must limit residual gas pressures so that the lifetime associated with gas scattering is no less than 30 hours while operating at 200 mA after 1000 Ah of machine operation. In addition, the vacuum system must provide an in-vacuum flight path for extracted x-ray beams, intercept unwanted bending magnet radiation, and provide suitable access and mechanical stability for beam diagnostics. Moreover, to reliably serve APS users, the system must be robust enough for a lifespan of at least 25 years over which 5000 hours of beam per year are provided to users with 95% availability.

In addition to functional requirements, numerous design constraints are associated with interfaces to other technical systems. These include adequately limiting the electromagnetic interaction between the vacuum system and the beam, ensuring mechanical fit between vacuum components and magnets, ensuring that vacuum components do not compromise required magnet field strength and quality, keeping gas bremsstrahlung and other stray radiation within acceptable levels, providing signals as-needed for control and equipment protection systems, and making sure that the time needed for installation is accommodated by the project schedule.

4-3.3.2 System Design

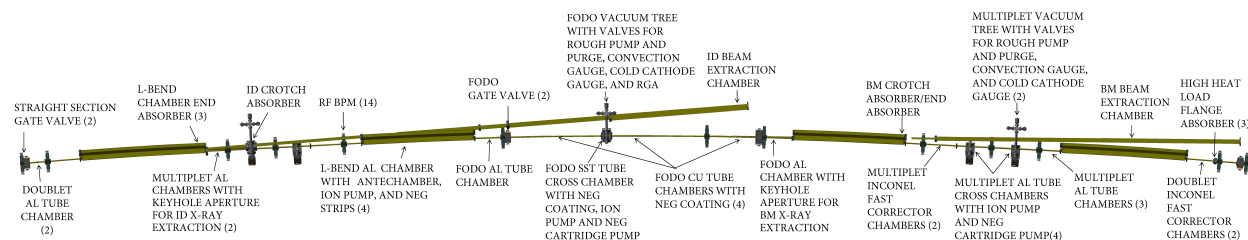


Figure 4.118. Layout for the vacuum system in a typical storage ring arc.

Space available for vacuum components inside of and between magnets in an MBA machine is apt to be limited and the APS-U storage ring is no exception. Aside from the longitudinal gradient dipoles (L-bends), the storage ring magnets provide little more than a 26 mm diameter opening inside of the magnet poles. In addition, space outside the poles and between the magnet coils is generally not enough to fit an “antechamber,” a secondary portion of the vacuum chamber conventionally used to house photon absorbers and distributed pumping. Whereas in the past antechambers have allowed bending magnet radiation to be intercepted at a few locations per sector, in an MBA storage ring there is typically little option but to intercept that radiation on the chamber walls. This is problematic for a number of reasons. First, the heat load, which will exceed 1 kW/m in portions of the APS-U storage ring, must be managed. In addition to the possibility of damage to the chambers from this heat, the thermal growth of the chambers must be managed so that critically aligned components, like beam position monitors (BPMs), are not excessively disturbed. In addition, the gas load due to photon-stimulated desorption (PSD), which typically exceeds thermal outgassing during machine operation by a factor of 10, must be effectively pumped to ensure adequately

low vacuum pressures. This, however, is hampered by the limited gas conductance of the small aperture chambers. Because of the limited available space, pumping options consist of placement of pumps between magnets, where they may fit, and non-evaporable getter (NEG) coatings inside the chambers.

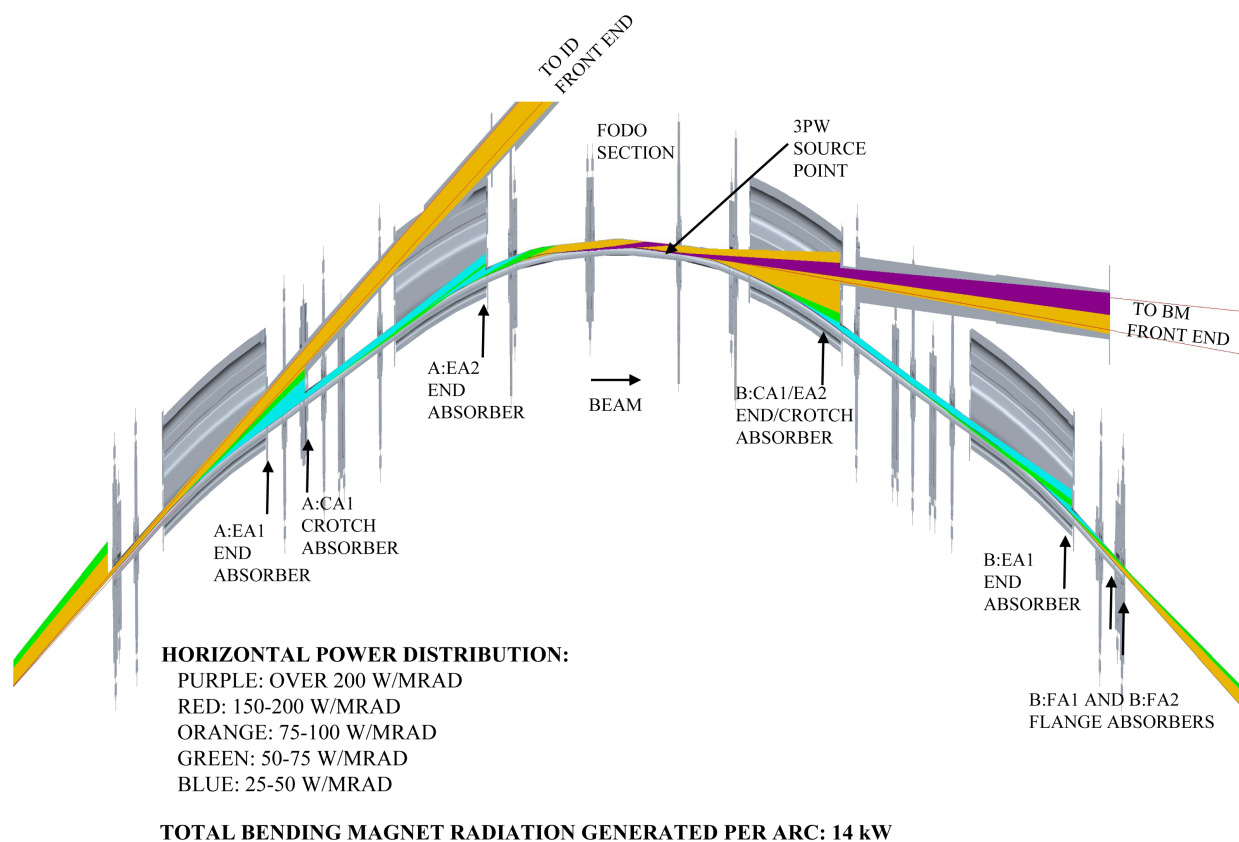


Figure 4.119. Synchrotron radiation power distribution in a typical storage ring sector.

The design of the storage ring vacuum system addresses these challenges with an approach that is tailored to some basic properties of the lattice and magnet designs. First, the synchrotron radiation that must be managed inside of magnets in the multiplet sections of the arc is relatively low in power and flux. Because of this, the design requirements of the chambers in these areas are significantly relaxed from both a thermal and vacuum standpoint. Second, the longitudinal gradient dipole, or “L-bend,” magnets, which combined extend over one third of the length of the arc, are open on the outboard side, permitting chambers with antechambers that allow for distributed pumping and use of dedicated photon absorbers which are thermally decoupled from the vacuum chamber. In addition, the wide horizontal aperture of these chambers helps to accommodate extraction of x-ray beams to both the insertion device and bending magnet beamlines. Finally, where the synchrotron radiation that must be intercepted inside of magnets is unavoidably high in power and flux, in the central FODO section, more sophisticated chambers with an aggressive thermal design and coatings to suppress PSD may be used [1]. The layout of the vacuum system in a typical storage ring arc is shown in Figure 4.118 and the distribution of radiation generated in bending magnets in Figure 4.119.

Instrumentation for pumping and pressure monitoring in the system is strategically located. Pumping

is provided by: 45 L/s ion pumps mounted to each of the five cross chambers and four L-bend section vacuum chambers, 200 L/s NEG cartridge pumps at each of the five cross chambers, a pair of 2 m long NEG strips installed inside each of the L-bend chambers, and activated NEG-coating inside of the FODO chambers. Monitoring of residual gasses is provided by a convection gauge and cold cathode gauge located at one of the vacuum crosses in each of the two multiplet sections and at the vacuum cross located in the FODO section. In addition, a residual gas analyzer (RGA) monitors the composition of residual gases at the cross chamber in the FODO section where maintaining the pumping functionality of NEG coatings requires strict prohibition of certain gas species.

4-3.3.3 System Design Analysis

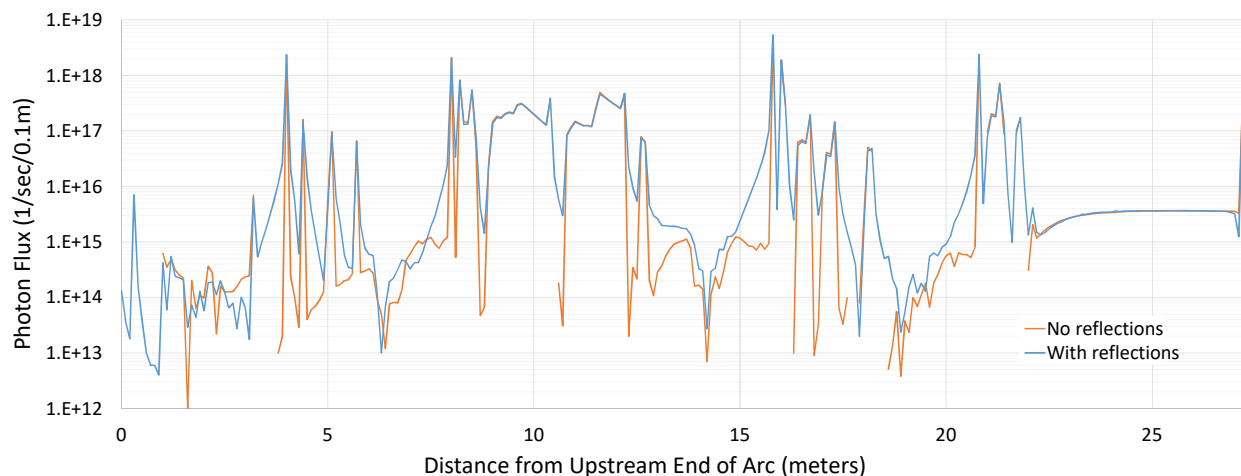


Figure 4.120. The difference in photon flux distribution in the storage ring at 200 mA operation when reflections are accounted for.

4-3.3.3.1 Computer Simulations for a Precise Understanding of Synchrotron Radiation Loads and Residual Gas Pressures The dominant gas load in a vacuum system for an accelerator like the APS storage ring is PSD so a precise prediction of residual gas pressures in such a system begins with a precise understanding of absorbed photon flux during machine operation. Accomplishing this requires understanding not only where photons are first incident on surfaces inside the vacuum system, but also where the photons that are reflected from those surfaces end up. SynRad+, a program developed at CERN which uses the Monte Carlo method for statistical modeling, is used to predict the distribution of both primary and secondary photons using numerical models of the beam parameters and magnets, along with a CAD model of the vacuum system as inputs [2]. The results of SynRad+ simulations showing the large effect that reflection has on the distribution of absorbed photons are shown in Figure 4.120.

Another program developed at CERN, MolFlow+ [3] uses the vacuum system CAD model and absorbed photon flux generated by SynRad+ along with pumping and outgassing assumptions to generate detailed predictions of residual gas in the system. MolFlow+ also uses the Monte Carlo method but, in this case, to model the statistical behavior of gas molecules so as to accurately capture the effective gas conductance that results in complex chamber geometries. To best account for the largest source of uncertainty in the vacuum pressure predictions, PSD yield, simulations have been conducted using aluminum PSD data from four independent studies [4]. Pressure profiles assuming

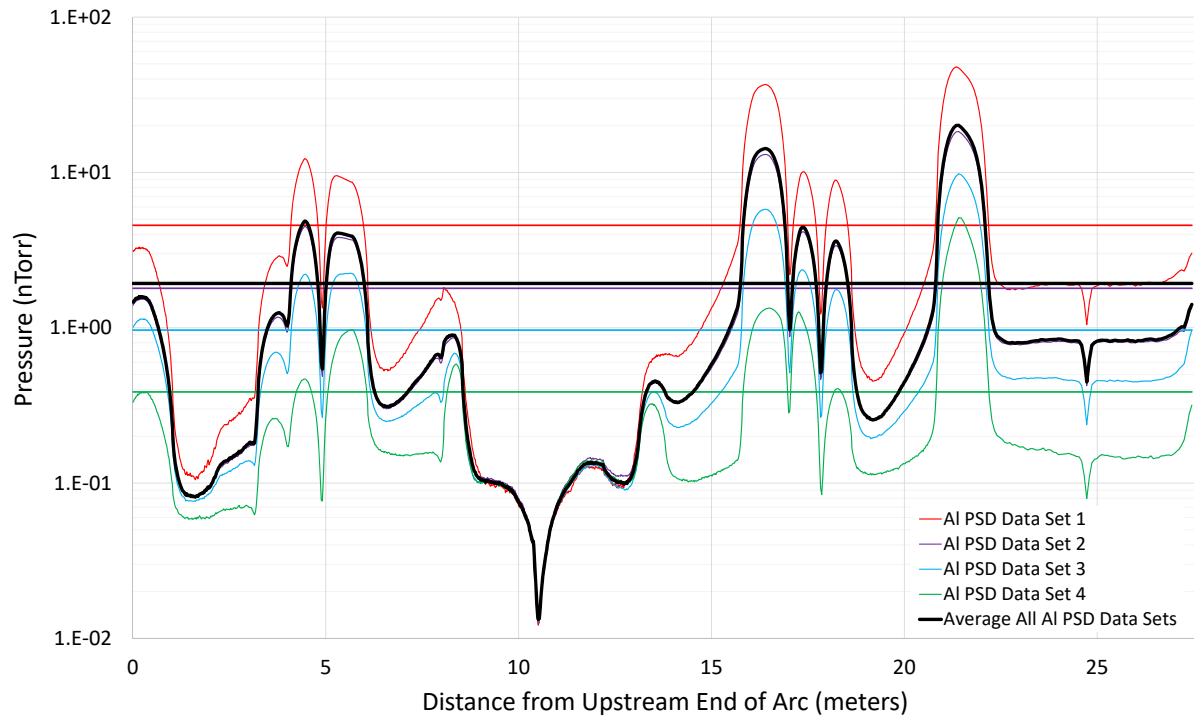


Figure 4.121. Vacuum pressure distribution in a typical storage ring sector at 200 mA operation after 1000 Ah conditioning.

the preliminary design based on a 42 pm lattice are shown in Figure 4.121. The results suggest that after baking and 1000 Ah of beam scrubbing, the expected average pressure will be 1.9 nTorr with error ranging over a factor of approximately 2.5. Figure 4.122 shows how the simulation results are also being used to predict how residual pressure will decrease over the course of machine operation. Even though simulations with differing PSD assumptions result in somewhat different pressures after a given amount of conditioning, the rates by which the pressure is reduced with conditioning are found to be in good agreement. Finally, simulations have been conducted to understand the composition of the residual gases, which is important for accurate predictions of beam lifetime and ion trapping. The distribution of pressures found given gas-specific pumping speeds reported by pump manufacturers and a typical set of aluminum PSD data is given in Figure 4.123.

4-3.3.3.2 Numerical Ray Tracing to Understand Bending Magnet Radiation under Off-Normal Steering Conditions

Photon absorbers must not only protect sensitive components from synchrotron radiation generated under design particle beam trajectories, they must also protect these components when the beam is mis-steered, intentional (for beam study purposes, for example) or not. To ensure that all possible mis-steering scenarios are adequately addressed, a method has been developed which assumes only how the particle beam transverse positional and directional phase space is constrained by a physical limiting aperture and lattice parameters [5]. Possible synchrotron radiation rays are computed by finely discretizing the phase space domain along a dense locus of points the particle beam trajectory inside each of the bending magnets. These rays are propagated until an absorbing surface is encountered. Two analyses are performed. First, the

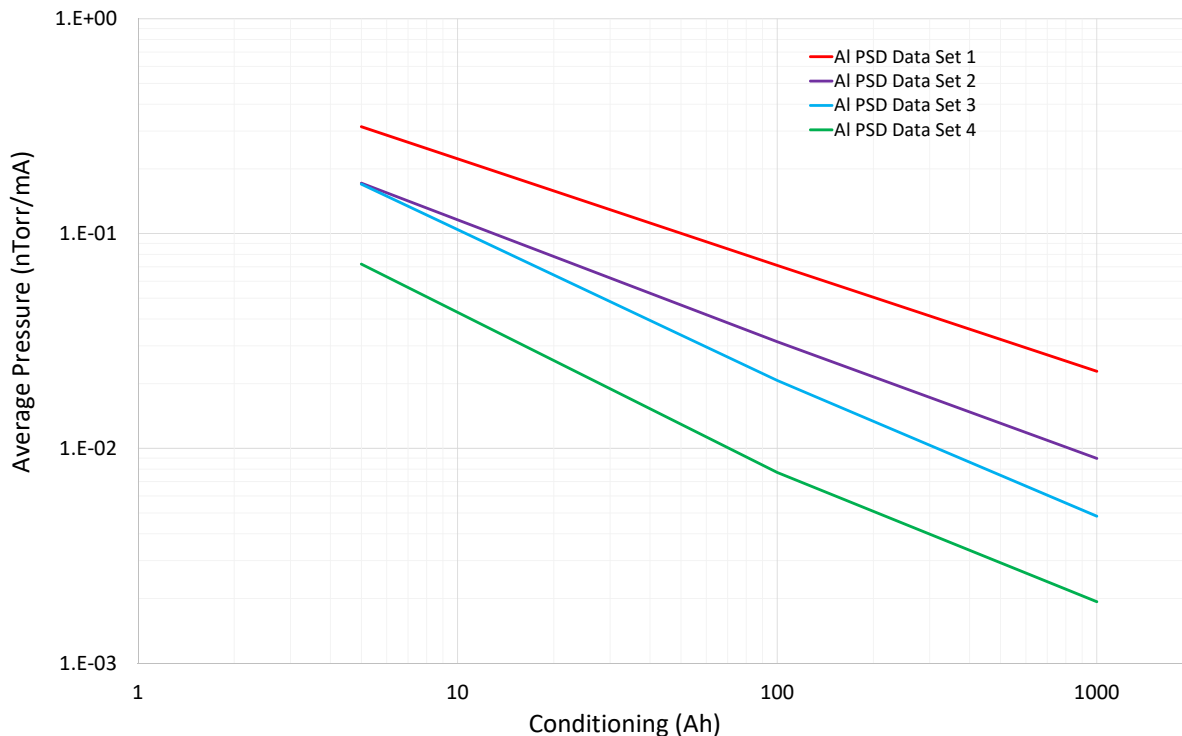


Figure 4.122. Reduction in pressure with beam conditioning.

maximum horizontal apertures that are allowed at each of the absorbers to cast sufficiently long shadows are determined (Figure 4.124). Simultaneously, it is verified that absorbers which shadow specifically in the vertical direction are not needed. Next, worst-case absorbed power scenarios are identified by finding the greatest linear and areal power densities that are possible on each absorber surface, which informs design analysis of the photon absorbers. Confidence in the results from these numerical methods is established by comparing results computed for ideal steering conditions with those found using traditional methods of ray tracing by geometric construction.

4-3.3.4 Component Design

4-3.3.4.1 Doublet and Multiplet Section Vacuum Chambers In the two quadrupole doublet and two straight multiplet sections, extruded aluminum chambers with a simple circular cross section are used (Figure 4.125). Explosion-bonded joints are employed to transition to chain-clamped stainless steel CF-type flanges at each end. Inline photon absorbers, which typically reduce the horizontal aperture outboard of the particle beam by 3 mm, are machined from the aluminum portion of the explosion-bonded transition at the downstream end of the chamber. A water-cooling channel on the outboard side of the chamber is used to remove the heat deposited by bending magnet radiation. The channel on the inboard side is reserved for the option of baking the chambers with electrical heater rods. At the upstream end of the first straight multiplet section in each sector, special versions of these chambers feature a keyhole-shaped aperture, with the additional pocket needed to clear extracted insertion device x-ray beams.

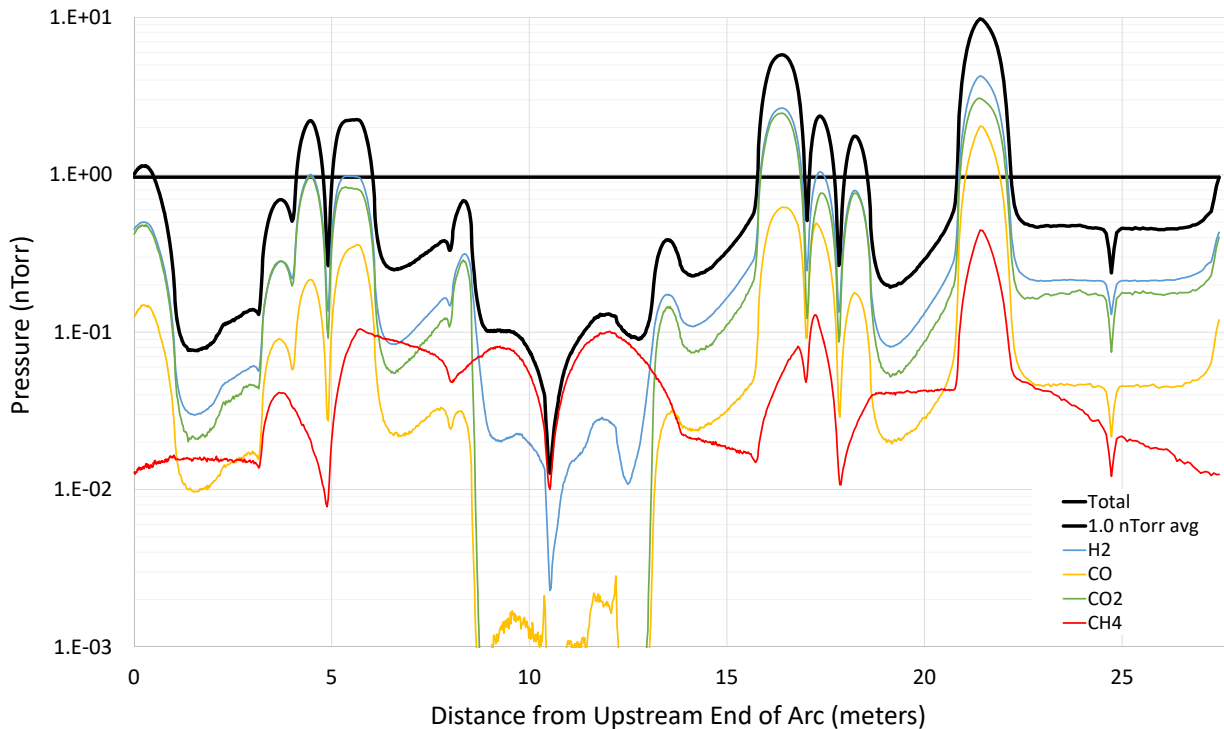


Figure 4.123. Residual gas composition at 200 mA operation after 1000 Ah conditioning.

A variety of other special chambers are also needed in these sections. Inside each of the multiplet sections is a chamber cross that provides four flanged ports to which pumps and gauges (described above) and right angle valves for venting and rough pumping are mounted. The bodies of the crosses are built entirely from aluminum and are water-cooled so that they, like most of the other chambers, may intercept bending magnet radiation. Like the standard aluminum tube chambers, flanges are stainless steel joined to the chamber by an explosion-bonded joint. Special chambers are also needed for the fast corrector magnets. These chambers are similar to the standard tubular chambers, although instead of aluminum they are made of Inconel, a non-magnetic nickel alloy with particularly low electrical conductivity which is needed to avoid excessive eddy current shielding of the time-varying fast corrector fields. To minimize the resistive wall impedance that would otherwise result, the chambers are plated internally with copper 1-2 microns thick. Water cooling channels on both the inboard and outboard side of the fast corrector chambers will ensure that the temperatures and material stresses resulting from absorption of bending magnet radiation on the chamber walls are adequately controlled. The symmetry of the water channels about the vertical plane helps to minimize the distortion of the fast corrector fields as modified by the presence of the chamber. Stainless steel chain-clampable flanges are jointed to the chamber bodies by TIG welding.

4-3.3.4.2 L-bend Section Vacuum Chambers In the L-bend magnet sections, chambers are built using an aluminum extrusion that provides a large antechamber (Figure 4.126). The vacuum volume in the particle beam portion of the chamber is connected to that in the antechamber by an 8 mm tall slot through which radiation from bending magnets and insertion devices is allowed

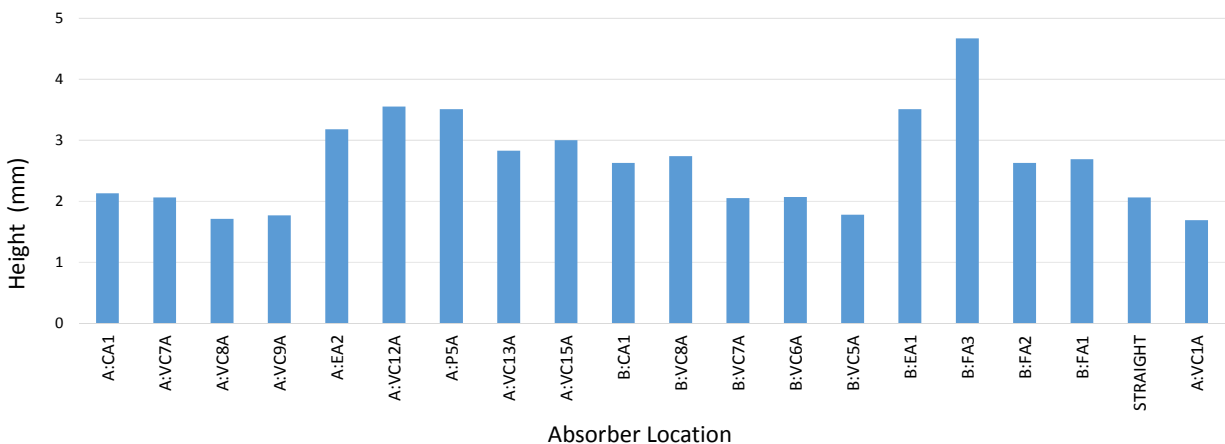


Figure 4.124. Minimum heights of photon absorbers required to protect sensitive components under all conceivable mis-steered beam scenarios.

to pass. The chamber geometry has been evaluated to ensure that electromagnetic modes excited by the particle beam will not be trapped. NEG strips mounted inside the chamber are supported by a linkage of carrier assemblies made of formed pieces of stainless steel sheet riveted together with ceramic spacers for electrical isolation between the strip and the chamber. An electrical feedthrough flange at one end of the chamber allows the NEG strips to be activated using a low voltage DC electrical current. Flanges are joined to the ends of the chamber via an explosion bonded aluminum-to-stainless steel transition plate which is welded to the chamber body using automated welding machines that have been used successfully for many years for vacuum chamber fabrication at Argonne.

4-3.3.4.3 FODO Section Vacuum Chambers The FODO section will make use of chambers with a cross-section similar to that described for the quadrupole doublet and multiplet sections (Figure 4.127). Like the standard doublet and multiplet section chambers, the outer two chambers are made of aluminum. The three central chambers, however, are made of copper for good thermal conductivity between the inner surface of the chamber receiving the synchrotron radiation and the adjacent water channel. Portions of the chambers where especially intense synchrotron radiation will be intercepted are made of GlidCop, an aluminum dispersion-strengthened alloy with exceptional material strength which is generally preserved under welding and brazing operations. To join the water-cooling channels to the chamber body with minimal material distortion and loss of material strength, electron beam welding is used. Flanges at each end of the copper chambers are joined by brazing to a GlidCop tube which is subsequently welded to the chamber body. The downstream flange brazement incorporates a GlidCop photon absorber with a dedicated water-cooling channel. The copper chambers are also NEG-coated to suppress PSD and provide distributed pumping when activated. To minimize both the disruption to magnets and the time required for activation of the NEG coating, low profile heater jackets roughly 0.4 mm thick will be permanently installed on the chambers. In addition to the tubular chambers, a NEG-coated stainless steel cross chamber is centrally located in the FODO section to which pumps and gauges and right angle valves for venting and rough pumping are mounted, similar to those in multiplet sections.

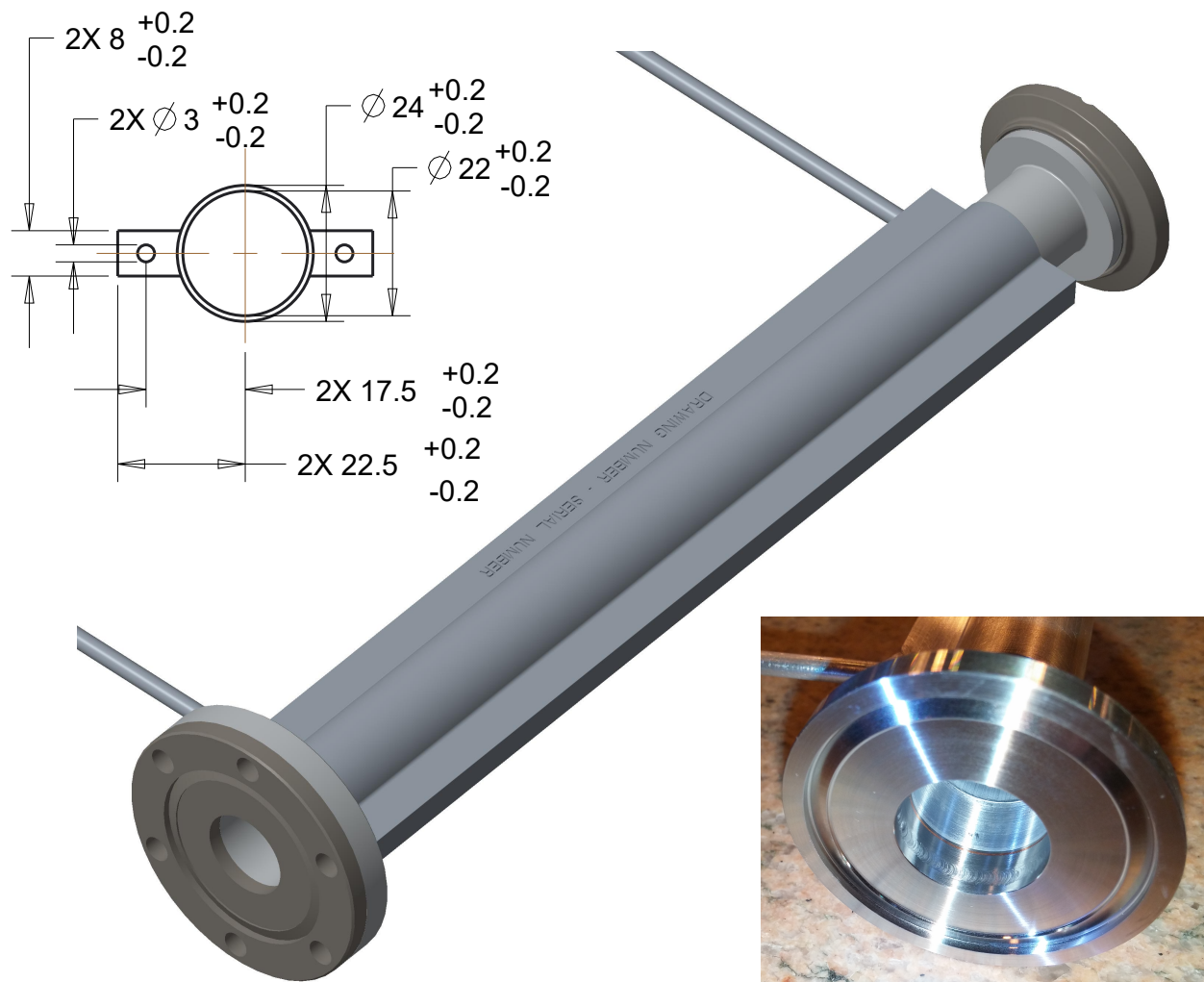


Figure 4.125. Standard aluminum doublet and multiplet section vacuum chamber.

4-3.3.4.4 Photon Absorbers In addition to the inline absorbers built into the various vacuum chambers, a number of dedicated photon absorbers separately mounted to chambers will also be provided. Of these are four “end absorbers” which protect the downstream end of the L-bend chambers, two “crotch absorbers” which protect the junctions formed between the x-ray beam extraction lines and the particle beam chamber, and two “flange absorbers” which protect the BPM and gate valve immediately preceding the straight section. The power loads for these absorbers are given in Table 4.56. The designs of these absorbers generally seek to make the best use of available space by using coaxial water cooling supply and return paths. At locations with relatively low thermal loads, absorbers feature hollow copper bodies with baffles to direct water flow inside. Renderings of the CAD model of one of the latter type of absorbers and example results from computational fluid dynamics (CFD) and thermal finite element method (FEM) simulations, which have been performed to demonstrate general feasibility of the designs, are shown in Figure 4.128. CAD models of the crotch absorbers planned for extraction of x-ray beams to the ID and BM beamlines are shown in Figure 4.129.

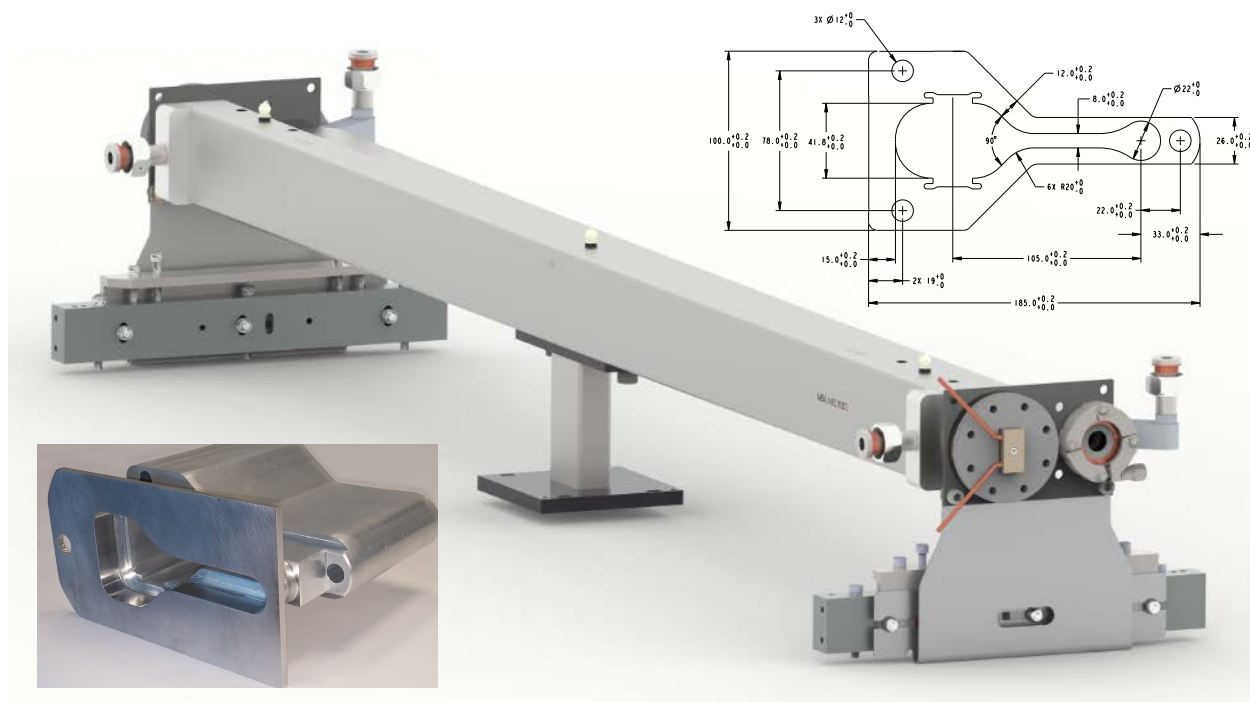


Figure 4.126. Aluminum L-bend section vacuum chamber.

4-3.3.4.5 Integrated Beam Position Monitor with Bellows Assemblies The sector arc vacuum system includes fourteen stainless steel rf BPM blocks, each providing four electrically-isolated feedthroughs to capacitive “buttons” which are used by diagnostic systems for precisely sensing beam location. To provide requisite thermal and vibrational stability of the BPMs and to allow thermal growth of chambers during operation and maintenance activities, all but one of the BPM blocks is nested between a pair of bellows. The interior surface of the BPM block is coated with silver and inside each bellows, a flexible GlidCop shield is used. Together, these help to reduce electrical impedance and rf-heating by providing a smooth, electrically-conductive path for surface currents induced by the beam. An early version of the BPM design was previously reported [6]. However, an updated design shown in Figure 4.130 features a different scheme for the sliding finger

Table 4.56. Power incident on photon absorbers

Location	Absorbed Power (W)	Peak Power Density at Normal Incidence (W/mm ²)
A:EA1	12	120
A:CA1	1015	241
A:EA2	469	355
B:CA1	2404	180
B:EA2	867	180
B:EA1	572	332
B:FA3	400	141
B:FA2	164	83
B:FA1	155	74

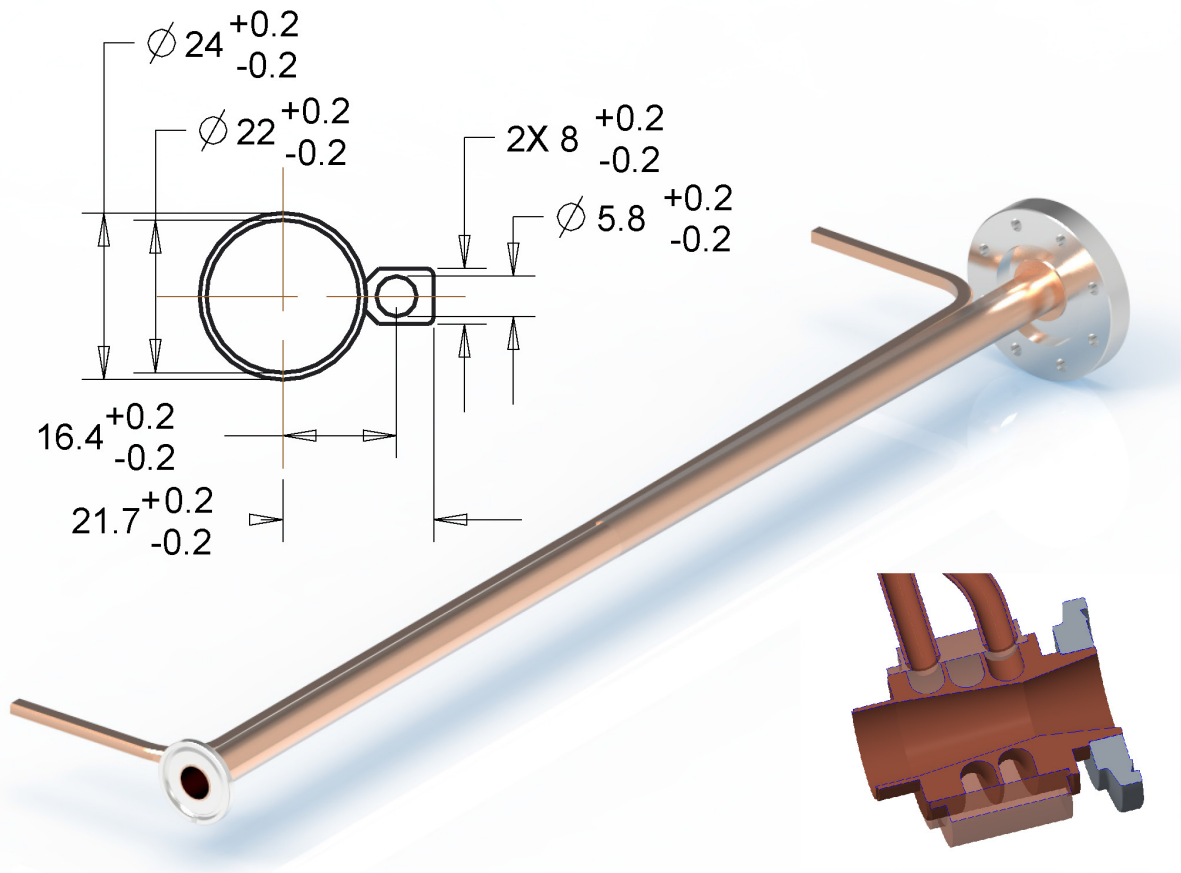


Figure 4.127. Copper FODO section vacuum chamber with independently-cooled inline photon absorber.

contacts that are used in the rf shield, based on an approach that has now been used successfully at many accelerator facilities [7]. The new design makes use of an additional set of springs outside the shield, rather than spring loading the fingers themselves, to provide the contact pressure needed for good electrical continuity. In this way, adequate contact pressure and electrical continuity is assured as the copper fingers relax mechanically over time. Also, because the copper fingers in the new design make contact on the outside of the rigid portion of the liner, they are less apt to collapse and obstruct the particle beam.

4-3.3.4.6 Mechanical Supports The mechanical support arrangement for vacuum components in the sector arcs is designed, foremost, to provide needed mechanical drift and vibrational stability for rf BPMs. In addition, the supports are expected to prevent contact between vacuum chambers and magnet poles. Delivering on these requirements is a particular challenge in MBA machines because of spatial constraints, which must allow for the thermal growth of vacuum chambers that serve a double function as photon absorbers. Installation and maintenance activities also benefit if the support scheme can accommodate thermal growth in the system during bake out and activation of NEG-coated chambers without disassembly or loss of alignment. To best achieve these two objectives, mechanical supports are used to mechanically fix the vacuum system at all BPMs,

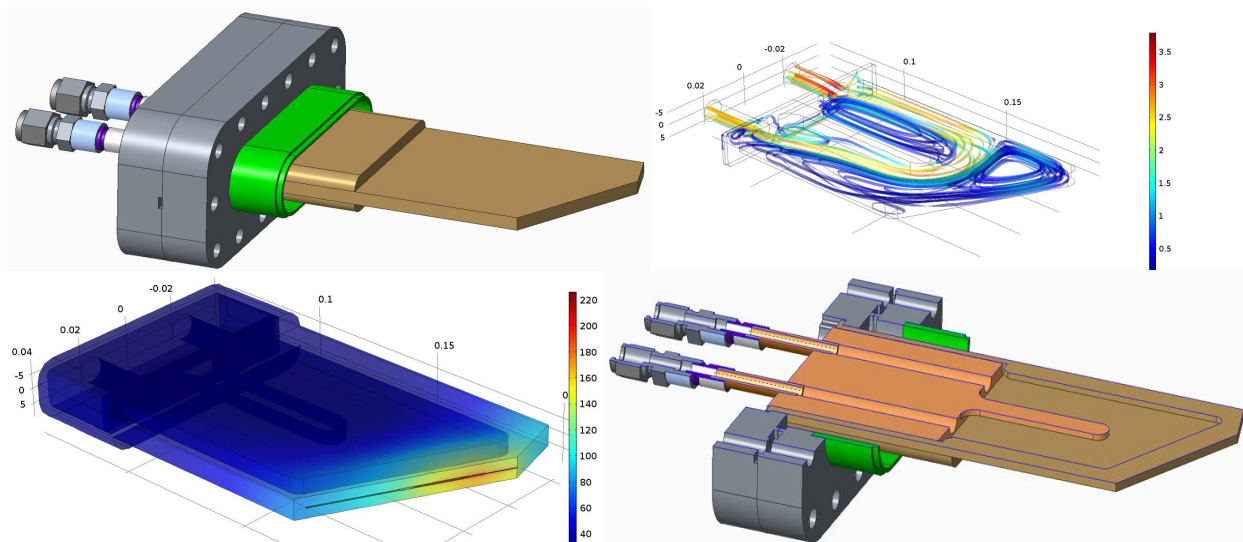


Figure 4.128. Typical end absorber with examples of CFD and thermal FEM simulation data.

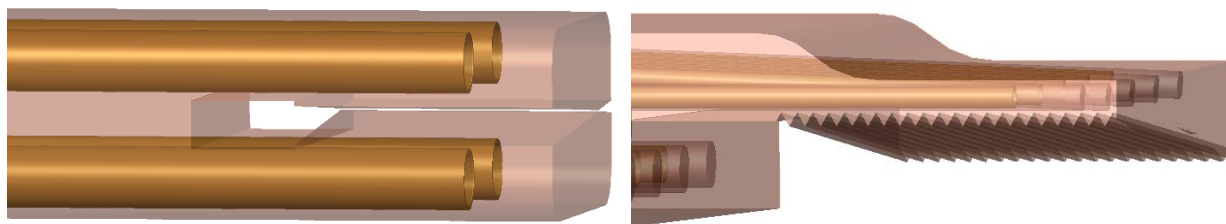


Figure 4.129. CAD models of crotch absorbers for x-ray beam extraction to ID beamlines (left) and BM beamlines (right).

locations where heavy components such as ion pumps are present, and locations which act to evenly distribute the compression of bellows when chambers are heated. Elsewhere, the supports utilize flexures which allow motion along the beam direction but which are rigid in other directions. A rendering of a typical flexure-based support used for tubular chambers is shown in Figure 4.131.

4-3.3.5 Zone F Straight Sections

Five storage ring sectors, 36 through 40, comprise Zone F. While the arc portions of these sectors are nearly identical to those elsewhere around the ring, the straight sections are occupied with special purpose hardware needed for machine operation - the injection septum magnet, rf cavities which maintain the energy of the stored beam, beam feedback and conditioning systems, and diagnostics. Integrating this hardware within the straight sections and to the neighboring arc sections requires a number of vacuum chambers, photon absorbers, rf-shielded bellows, and vacuum pumps. Specifying the vacuum components needed in these areas requires, first and foremost, a clear plan of how all of the various pieces will fit together in the limited space that is available. To accomplish this, CAD models and layouts have been generated for each of the straight sections. In addition, ray tracing has been conducted to understand what photon absorbers will be needed, at what locations,

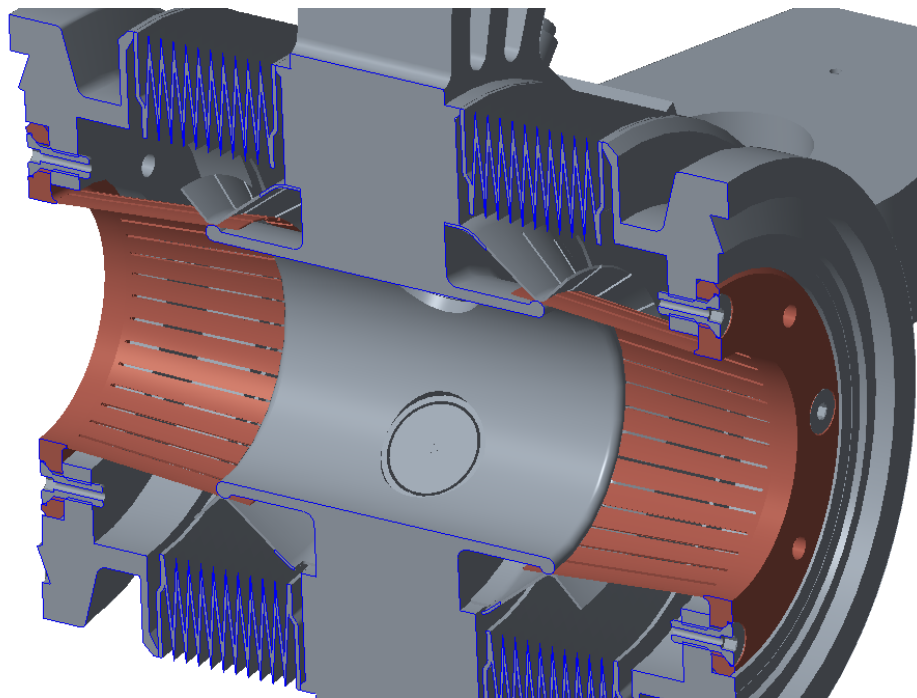


Figure 4.130. Concept for a beam position monitor assembly with GlidCop bellows liner.

and how much power they must intercept. The CAD model of the sector 37 straight section is an example of this work (Figure 4.132). Items shown in solid line are needed to upgrade the machine whereas items in phantom line are existing.

References

- [1] B. Stillwell et al. “Conceptual Design of a Storage Ring Vacuum System Compatible with Implementation of a Seven Bend Achromat Lattice at the APS.” In: *Proc. IPAC 2014*. IEEE, 2014, p. 2409. URL: <http://accelconf.web.cern.ch/AccelConf/IPAC2014/papers/wepme059.pdf> (cit. on p. 165).
- [2] R. Kersevan. “SYNRAD, a Monte Carlo Synchrotron Radiation Ray Tracing Program.” In: *Proc. PAC 1993*. IEEE, 1993, p. 3848. URL: http://accelconf.web.cern.ch/Accelconf/p93/PDF/PAC1993_3848.PDF (cit. on p. 166).
- [3] M. Ady and R. Kersevan. “Introduction to the latest version of test particle Monte Carlo Code MolFlow.” In: *Proc. IPAC 2014*. IEEE, 2014, p. 2348. URL: <http://accelconf.web.cern.ch/AccelConf/IPAC2014/papers/wepme038.pdf> (cit. on p. 166).
- [4] J.A. Carter. “Benchmarking and Calibration of Monte Carlo Vacuum Simulations with SynRad and MolFlow+.” In: *Proc. of IPAC2016*. 2016, pp. 3695–3697 (cit. on p. 166).
- [5] K. Harkay. *Private Communication*. 2016 (cit. on p. 167).
- [6] B.K. Stillwell et al. “Conceptual Design and Analysis of a Storage Ring Beam Position Monitor for the APS Upgrade.” In: *Proc. IPAC 2015*. IEEE, 2015, pp. 1170–1172. URL: <http://accelconf.web.cern.ch/AccelConf/ipac2015/papers/mopwi012.pdf> (cit. on p. 172).

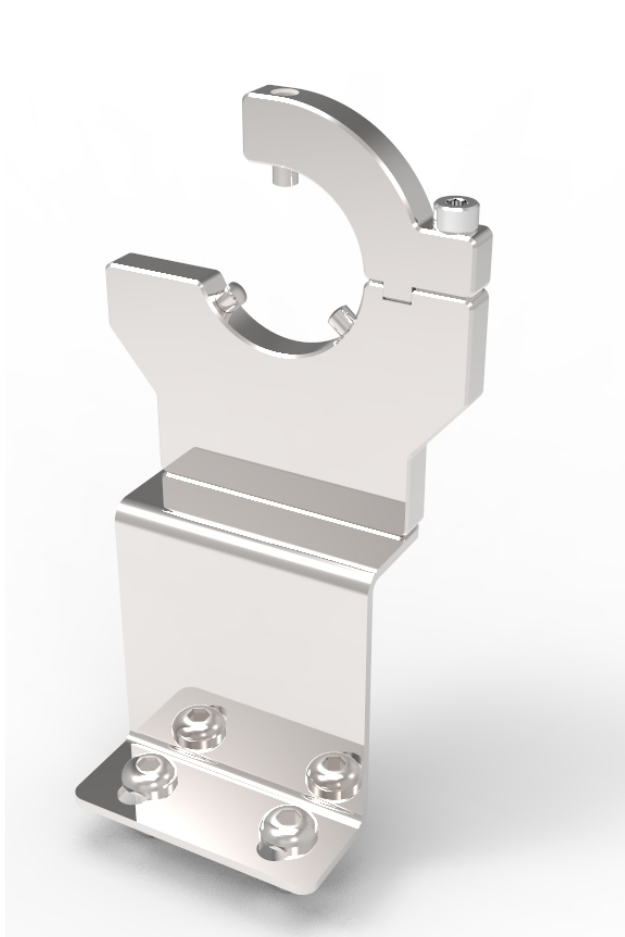


Figure 4.131. Render of an adjustable flexure-based chamber support.

- [7] M.E. Nordby, N. Kurita, and C-K. Ng. “Bellows Design for the PEP-II High Energy Ring Arc Chambers.” In: *Proceedings of PAC 1995*. 1995, pp. 2048–2050. URL: <http://www-spires.slac.stanford.edu/pubs/slacpubs/6750/slac-pub-6992.pdf> (cit. on p. 173).

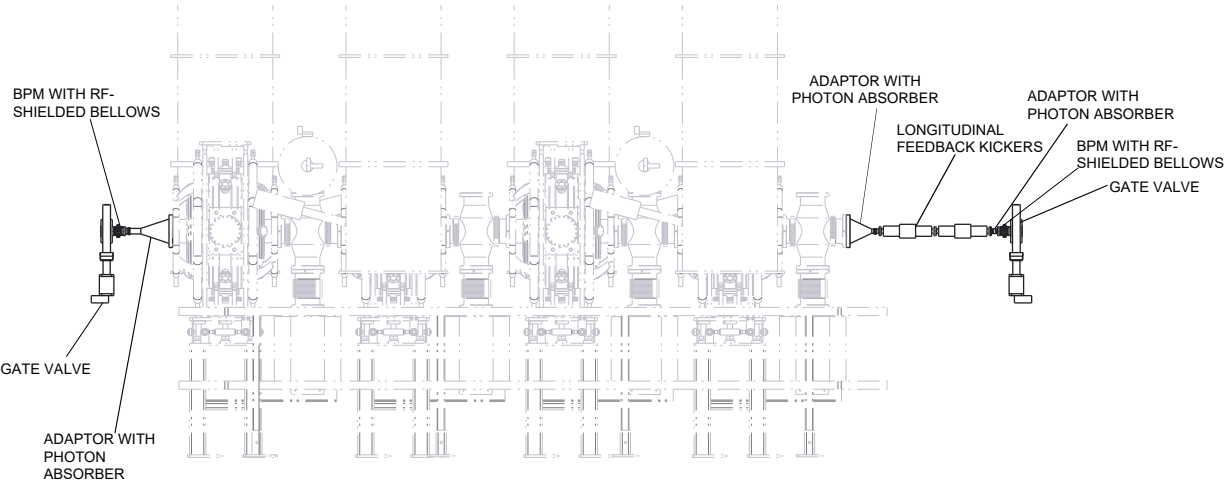


Figure 4.132. CAD model of the sector 37 straight section used to develop integrated design.

4-3.4 Magnet Support and Alignment System

The new magnet lattice requires the magnet support structures to be mechanically and thermally stable in order to satisfy the stringent physics requirements. The magnet alignment requirements are shown in Table 4.20. The vibration and stability requirements are shown in Table 4.14. In addition, the key design drivers outline a short installation window, dictating that ease of installation and alignment is a significant consideration in the magnet support structure design. These constraints inform all aspects of the design process. From simulation, to testing, each step is used to evaluate the preliminary design against the requirements.

Each storage ring sector consists of three large modules with two L-bend magnets bridging between them. Figure 4.133 shows one of these 40 sectors of the proposed storage ring lattice. The upstream Doublet L-bend Multiplet (DLM) module A supports the quad doublet, an L-bend, and the multiplet magnets. In the center of the sector is the curved Focusing Defocusing (FODO) module which supports seven large bending / focusing magnets. The downstream DLM module B is a mirror image of the upstream DLM module A. Each module contains a concrete plinth grouted to the floor, upon which is an alignable support girder, which in turn supports the individual magnet strings, vacuum system, and auxiliary hardware. Each of these modules will be delivered to one of the five “super doors” that are located on the inner circumference of the storage ring. From the super door, each module will be transported via the storage ring aisle all the way to the final installation location.

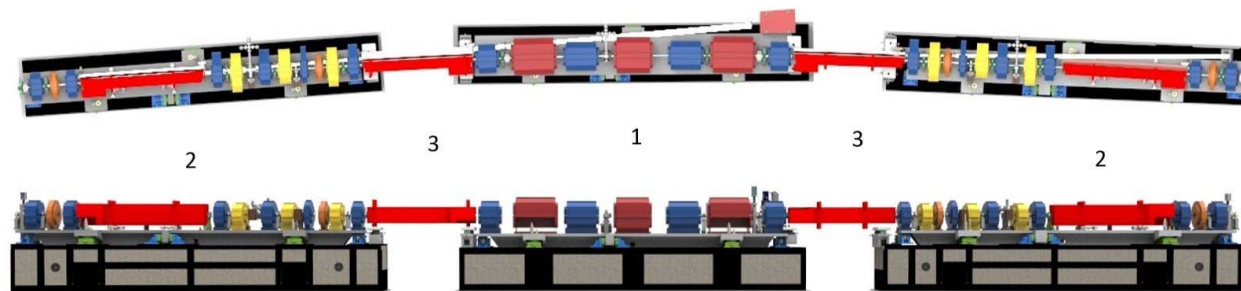


Figure 4.133. Plan and elevation views of the APS Upgrade lattice. The different magnet groups include (1) curved FODO, (2) DLM modules, and (3) M2 L-bend dipoles. The quad-doublet, M1 L-bend dipoles, multiplet, and curved FODO magnets are all supported on unique plinths, while the M2 L-bend dipoles are supported from the ends of these plinths.

4-3.4.1 Support Concept

Each of the magnet modules consists of a plinth grouted to the floor and a three-point, semi-kinematic mount for the magnet support structures. The groups of individual magnets are mounted on top of the rigid magnet support structure. Figure 4.134 shows the details of the FODO module. Each plinth will be rigidly bonded to the storage ring floor using epoxy grout. Plinths are fabricated using a welded steel frame filled with reinforced concrete. Each plinth is bathtub-shaped to allow the large cross-section girder to extend down into the plinth body. Similar to other facilities, concrete was chosen because it is economical, readily available, and has excellent mechanical and thermal properties. Each support girder is made of ductile cast iron with cross-sections resembling a hollow rectangular box with a T-top. In addition to supporting the magnets, all vacuum system

components are mounted to the girder. The support girder geometries are optimized to minimize weight while providing a very stiff structure that maximizes the first vibrational mode frequency and minimizes static deflection. The casting process allows economic fabrication of the optimized support girder geometries.

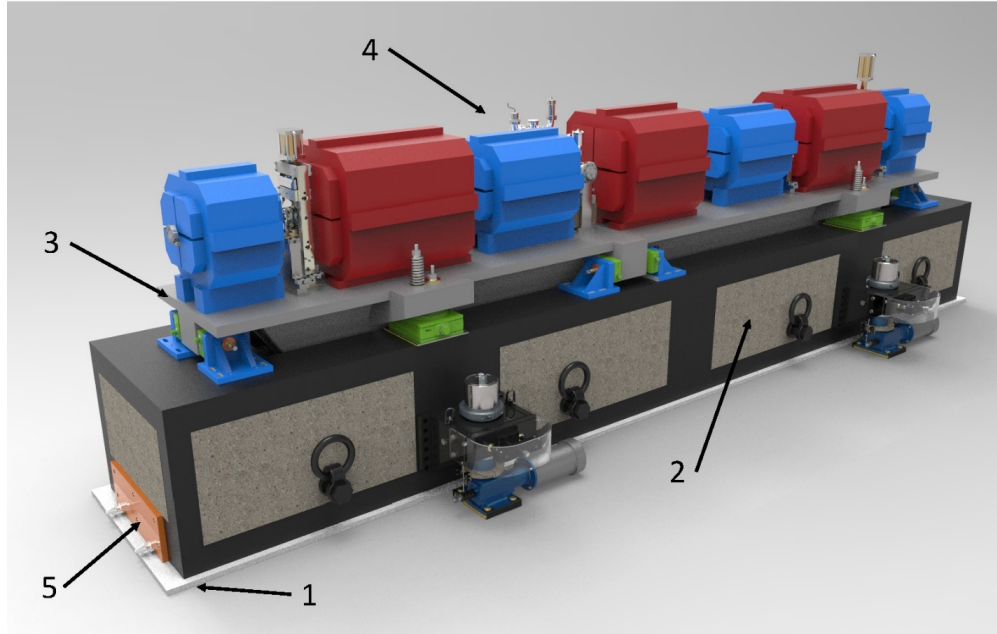


Figure 4.134. Preliminary FODO module assembly consists of (1) epoxy grout, (2) concrete/steel plinth, (3) cast iron support girder, (4) individual magnets and vacuum system, and (5) quick attach plate for the air caster system tug.

In order to meet the previously mentioned schedule, maintenance, and physics requirements, the magnet support system is designed with:

1. A high-stiffness girder,
2. An alignment system that is easily adjusted both inside and outside of the tunnel, and
3. Provisions for locking the system during transport.

Special consideration has been given to the girder and support system such that the magnet modules meet the alignment requirements, shown in Table 4.20, while also providing the necessary vibrational and stability requirements shown in Table 4.14. Alignment requirements are met with features on the girder providing the necessary magnet-to-magnet alignment. The details of the plinth and alignment mechanisms are shown in Figure 4.135. The vertical supports and the lateral and longitudinal pushers all use commercially available wedge jacks. In this semi-kinematic system, the three vertical adjusters constrain the vertical displacement, pitch, and roll. Lateral pushers constrain the lateral displacement and yaw. Finally, the longitudinal pusher constrains the longitudinal displacement. The ability to preload these wedge jacks is provided to increase the support stiffness. The system is described as “semi-kinematic” because there will be a certain amount of over-constraint due to the friction between the components. Plinths will be aligned to better than ± 1 mm vertically and ± 2 mm laterally prior to grouting. Three removable support outriggers provide the necessary six degrees of freedom for this alignment. After alignment, each plinth will be grouted to the storage

ring floor. The top of each plinth will be roughly at the same elevation after grouting. Because the storage ring floor varies as much as 22 mm in elevation around the storage ring, the grout thickness for each plinth will vary. After the epoxy grout has cured and the plinth has been bonded to the floor, the support outriggers will be removed and sent back to the assembly facility where they will be used for the next plinth installation.

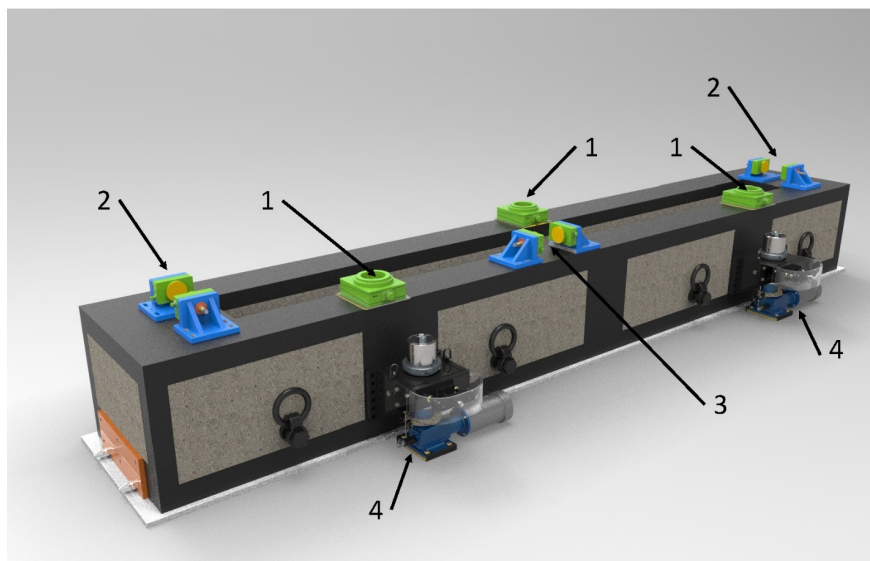


Figure 4.135. Plinth and alignment mechanisms without the magnet assembly. The alignment mechanism components are (1) three-point vertical supports with spherical bearings and slip plates to decouple translation and rotation from the vertical motion, (2) lateral pushers to provide lateral and yaw constraint and alignment while decoupling vertical motion, (3) longitudinal pusher to provide longitudinal constraint and alignment while decoupling vertical motion, and (4) support outriggers (three total) to provide six degrees of freedom for plinth alignment.

The FODO module, the upstream DLM module A and the downstream DLM module B are all of similar design with standardized support and alignment system components. Having similar designs for all of the magnet modules simplifies the design process and alignment procedures. Similar to the curved FODO section, Figure 4.136 shows the details of the preliminary design for the DLM module A assembly. The M1 L-bend dipole magnet is mounted directly to the DLM module girder and may be adjusted by ± 2 mm in the Z-direction to account for variations of the magnet vertex location.

The M2 L-bend dipole magnets are not part of either the FODO or DLM modules, but span between them. The L-bend dipole magnets have less stringent requirements for vibrational stability than other magnets within the lattice. Each M2 L-bend is supported on a separate (from the FODO or DLM) support and alignment system that mounts to the shelves on the ends of the concrete plinths. Similar to the other magnet module designs, the M2 L-bend dipole magnets have a six degree of freedom semi-kinematic support and alignment system that use commercially available wedge jack mounts for the three vertical supports. Lateral and longitudinal pushers are integrated with the baskets in which the wedge mounts sit. The vacuum chamber for the M2 L-bend dipole magnet is mounted directly to the magnet with its own support and alignment system. The vacuum chamber will be aligned to the magnet during pre-installation, and the assembly will be installed as a unit

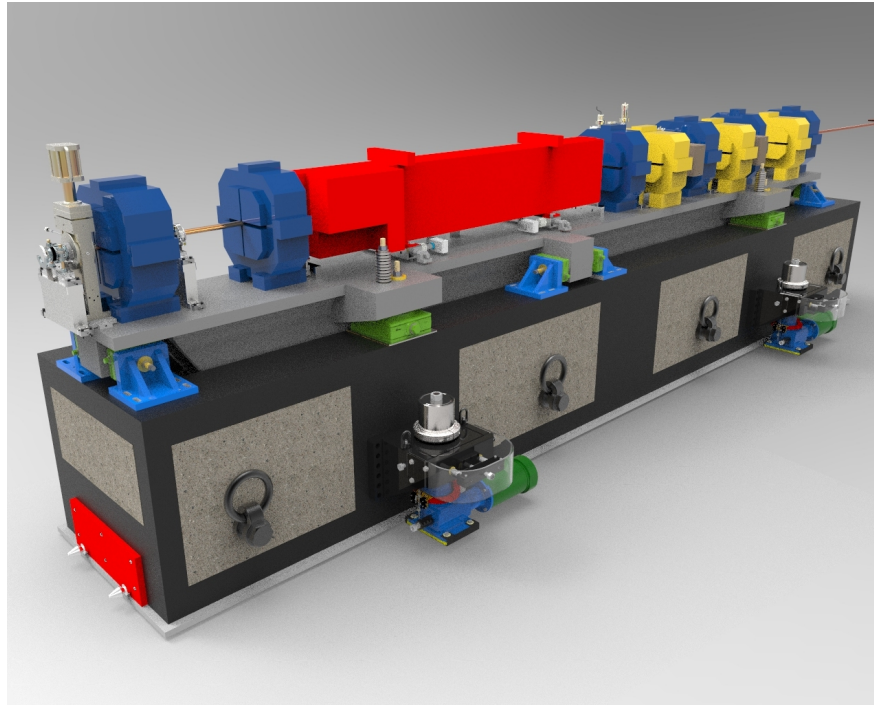


Figure 4.136. Preliminary DLM module A assembly. All of the magnet modules have similar designs with standardized support and alignment system components.

in the storage ring. A rendering of the M2 L-bend dipole magnet resting on the semi-kinematic support and alignment system is shown in Figure 4.137.

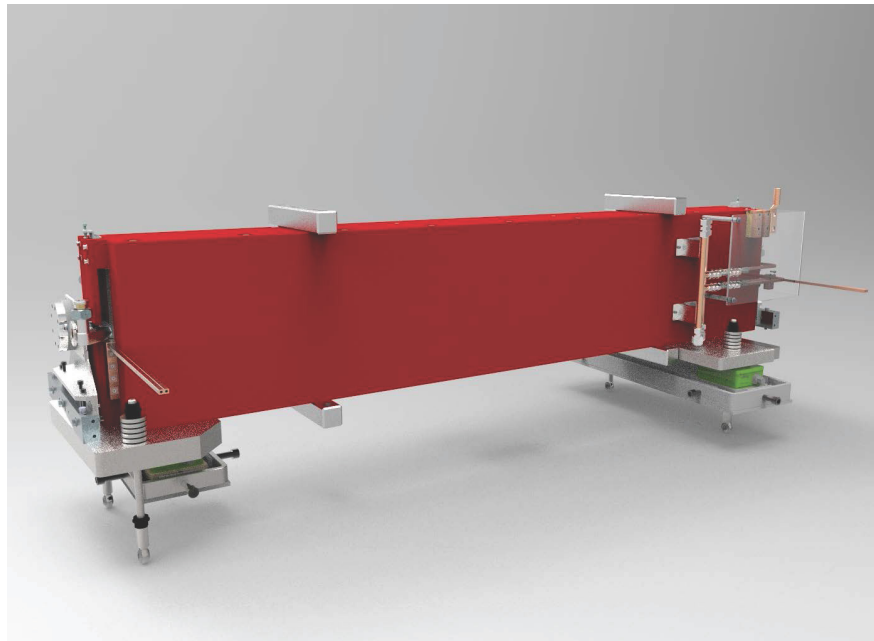


Figure 4.137. Preliminary M2 L-bend dipole magnet assembly resting on the semi-kinematic support and alignment system.

4-3.4.2 Support System Vibration and Stability

Vibrational and stability requirements are being addressed with a focused R&D effort to develop a methodology that enables accurate prediction of final design vibrational performance using FEA modeling tools. This predicted performance can then be compared against the vibration requirements of Table 4.14, providing a high level of confidence before any physical articles are manufactured. This methodology has been demonstrated with free boundary condition tests of the DMM module. Key to this methodology are experimentally determined support properties. Figure 4.138 shows a comparison of the first experimentally measured mode and the first finite element calculated mode. The results agree within 5%. Higher order modes were accurately predicted as well.

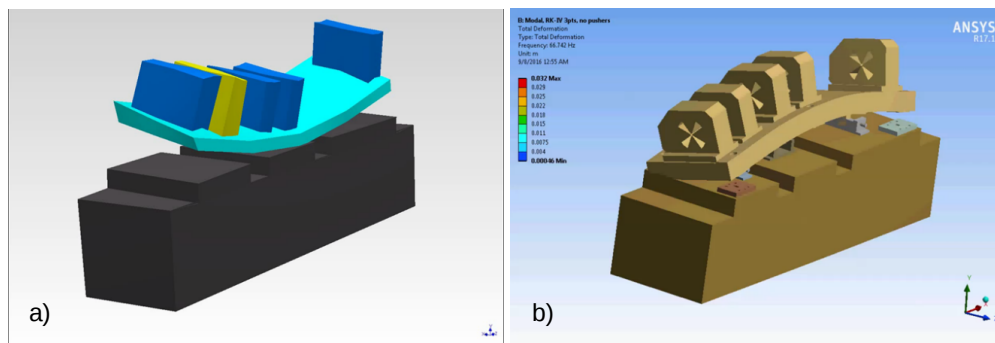


Figure 4.138. Images comparing the a) DMM experimentally measured first mode of 64 Hz, and the b) DMM FE calculated first mode of 67 Hz. The simulation differed from the experiment by 5%.

Knowledge of the existing APS storage ring vibration is very useful for evaluating the magnet module designs. Recent storage ring floor vibration measurements, as shown in Figure 4.139, indicate that 90% of the integrated RMS motion between 1 and 100 Hz is contained within the frequency band of 1 to 23 Hz for the transverse motion, and 1 to 44 Hz for the vertical motion. Therefore, a system with a first mode involving X-direction motion above 23 Hz, and the first mode involving Y-direction motion above 44 Hz should not significantly amplify floor motion. Combining the vetted modeling process and the measured storage ring vibration enable direct evaluation of the preliminary design against the vibration requirements of Table 4.14. Applying this methodology to the DLM design shows that the first mode is 42 Hz, as shown in Figure 4.140.

The set of calculated mode shapes, along with an experimentally-determined damping ratio of 0.02, were then used to estimate the power spectral density function at the magnet pole tips with the measured storage ring floor displacement data as an input. The expected tip motion was found to be 13 nm rms on a 1-100 Hz bandwidth as shown in Figure 4.141. The corresponding integrated RMS motion of the floor in the X direction in the frequency range of 1-100 Hz is 11 nm. The pole tip motion can be compared to the girder-to-girder motion specification of Table 4.14.

Magnet-to-magnet motion has not yet been predicted for the FODO or DLM. However, recent tests of the DMM show the magnet-to-magnet motion is approximately 4.3 nm rms in the transverse and 5.8 nm rms in the vertical on a 2-100 Hz bandwidth, as shown in Figure 4.142. Since the relative motion between magnets is negligible below 2 Hz, the DMM vibration results show the DMM as tested would meet vibration specifications in Table 4.14. The DMM as tested is much less rigid

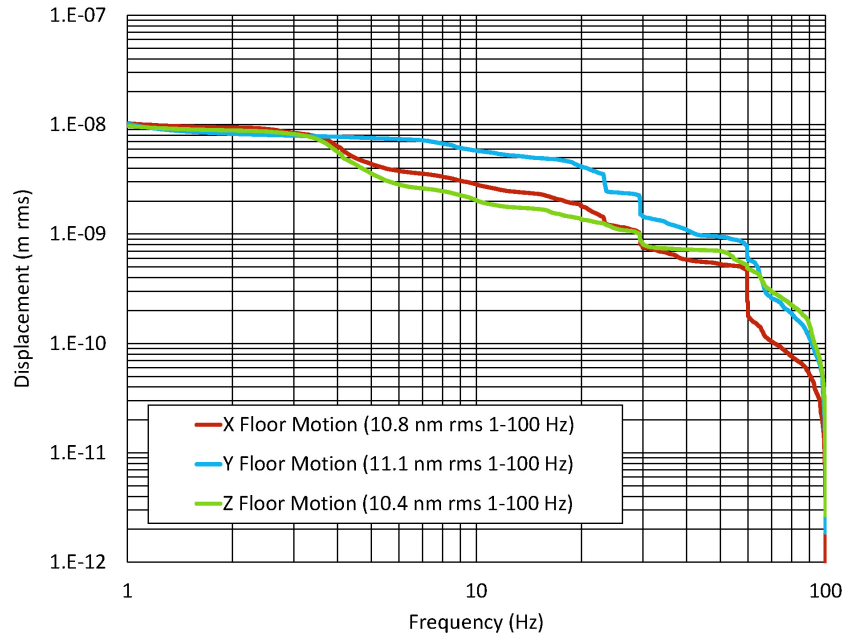


Figure 4.139. APS storage ring tunnel sector 28 integrated floor motion on a 1-100 Hz bandwidth showing the transverse (X), vertical (Y), and longitudinal (Z) components.

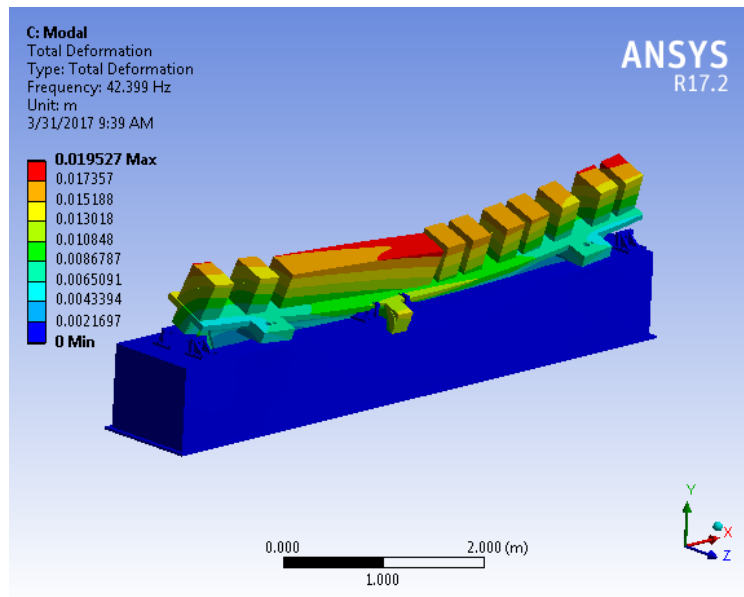


Figure 4.140. Simulated first mode of the DLM module, 42 Hz.

than the FODO or DLM designs. The stiffer FODO and DLM designs are expected to perform at least as well.

Large relative motions between magnet modules is problematic. The influence of the storage ring floor motion on the magnet modules directly affects the electron beam motion. Conversely, if the

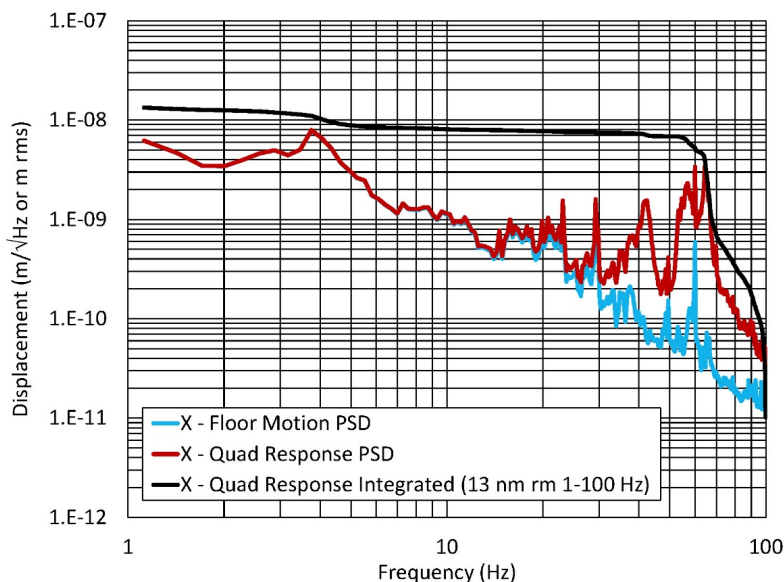


Figure 4.141. The FE-calculated DLM response. The floor motion (blue), quadrupole motion (red), and the integrated quadrupole motion (black) are shown. The quadrupole motion can be taken to be the same as the girder motion.

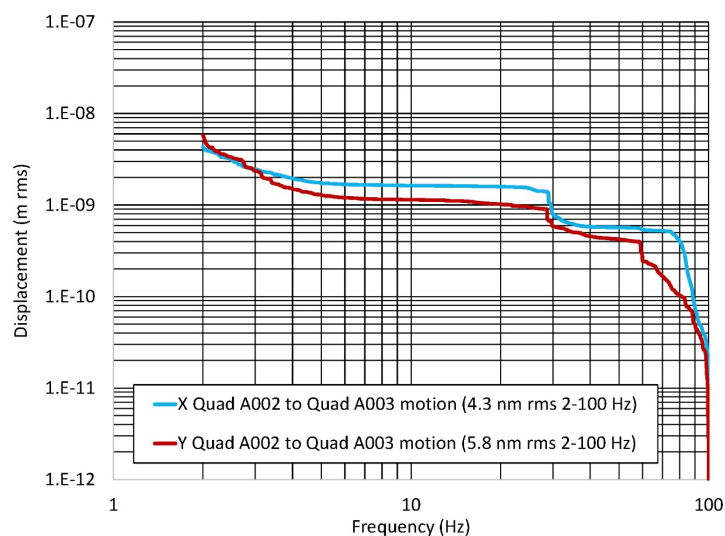


Figure 4.142. The measured quadrupole-to-quadrupole motion on the DMM.

absolute motion of the floor is relatively high, the relative motion can still be at an acceptable level. Figure 4.143 compares the transverse and vertical relative motions at points 9 m apart, to the absolute floor. The separation distance of 9 m represents the distance between the center of one magnet module to the center of another magnet module. The plots of the square root of the PSD clearly show that in low frequencies, the relative motion is below the level of the absolute motion. For instance, at a 9 m separation distance, the 0.1 to 10 Hz band-limited RMS levels of the

relative motion are 33 nm and 9 nm in the transverse and vertical directions, respectively, whereas the absolute motions are 94 nm and 119 nm.

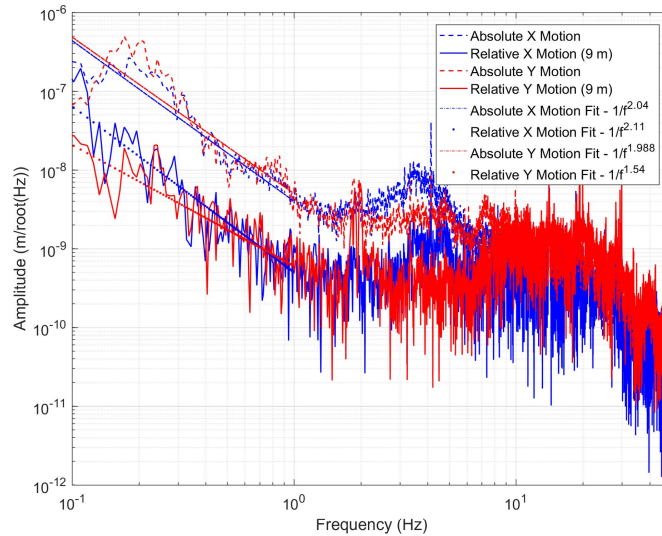


Figure 4.143. Chart showing the square root of the absolute and relative motion PSDs of the APS storage ring floor at a 9 m separation for both the transverse (X) and vertical (Y) directions. Curves fit to the region between 0.1 and 1 Hz are also shown. Both absolute motions and the X direction relative motion follow $1/f^2$, whereas the Y direction relative motion grows at a slightly lower rate, following $1/f^{1.5}$.

4-3.4.3 Magnet and Plinth Transport and Assembly

The large combined weight of each module requires that extra consideration be given to rigging and transport. The 6.3 m long FODO module has a mass of approximately 27,000 kg. The DLM modules will have slightly less mass than the FODO module but their length will be close to 6.5 m. To meet the installation schedule, the magnet modules will be fully assembled during pre-installation and will later be transported to the storage ring as complete assemblies.

The FODO prototype has shown that strict machining tolerances used to position magnets can still be maintained on a longer, more massive girder. Flatness of the FODO prototype girder, supported on three points with dummy magnets installed, measured 10 microns, well within positioning tolerances.

Rigging features have been incorporated into the design of the plinths to allow hoisting and transport of fully assembled magnet modules. Features have been incorporated into the support and alignment system design that allow the magnet support girder assembly to be rigidly locked down to the plinth during transport. Each fully assembled magnet module will be transported on a flatbed truck to one of the five super doors where it will be unloaded and placed on the three support outriggers. The height of the support outriggers will be pre-set such that the air casters can easily slip under the plinth. Air tugs will then be connected to the ends of the plinth. To ensure proper operation of the air casters the floor must be properly prepared, which will include covering small cracks

with aluminum tape and covering large cracks with plastic sheeting. When the air caster system is energized, the plinth will lift off the ground and will then be driven by the air tugs into the storage ring to the installation location.

The rigging and in-facility transport of the modules have been demonstrated. A prototype FODO module was recently delivered via flatbed truck to the APS. The FODO module was lifted off the flatbed truck, using two heavy-duty fork lifts (Versa-Lifts), and placed on cribbing. Air casters were then placed under the module, air tugs attached, and the unit was driven by the air tugs into the test area. Figure 4.144 shows the prototype FODO module after the air caster system was installed and prior to moving the unit into the test area. The two heavy-duty fork lifts can be seen on the right-hand side of the picture.



Figure 4.144. Prototype FODO module being moved into the test area using an air caster system after it was unloaded from a flatbed truck using two Versa-Lifts in tandem.

The air caster system offers precise positioning and control of the fully assembled magnet module. Pre-surveyed marks on the storage ring floor will indicate where a particular magnet module plinth needs to be located. Once in location, the air caster system will be de-energized and the plinth will lower until it once again sits on the three support outriggers. The air caster system tugs, air pads, and quick attach plates will then be removed from the plinth. The support outriggers will be used to locate the plinth. After the plinth location has been set, a grout frame will be placed around the plinth base and epoxy grout will be poured underneath the plinth. The support outriggers will be removed and sent back to the assembly facility for the next module installation after the grout has cured a minimum of twenty-four hours.

4-3.4.3.1 Transport Test In production, the magnet modules will be assembled off-site and completely pre-aligned units will be transported into the storage ring. There will be no time to re-align magnets on the girder in the SR tunnel, so importance of stability of alignment during transport is very significant. As part of the rigorous testing program, the DMM was subjected to a transportation test. After the baseline magnet mapping, the DMM plate with magnets was loaded on a truck and went for a test ride. Then the second set of magnetic measurements were taken and later the whole assembly, including plinth, was driven around the site and then re-measured. The

positioning of magnets repeated within $5 \mu\text{m}$, the three sets of data are plotted in Figure 4.145 and Figure 4.146 .

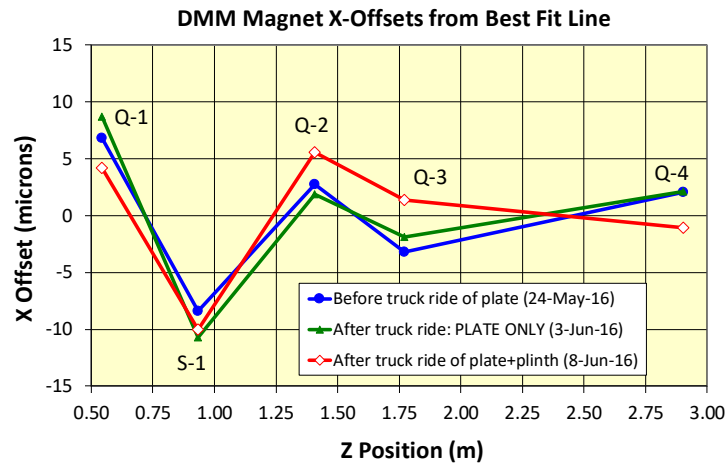


Figure 4.145. DMM magnet alignment before and after the transport tests.

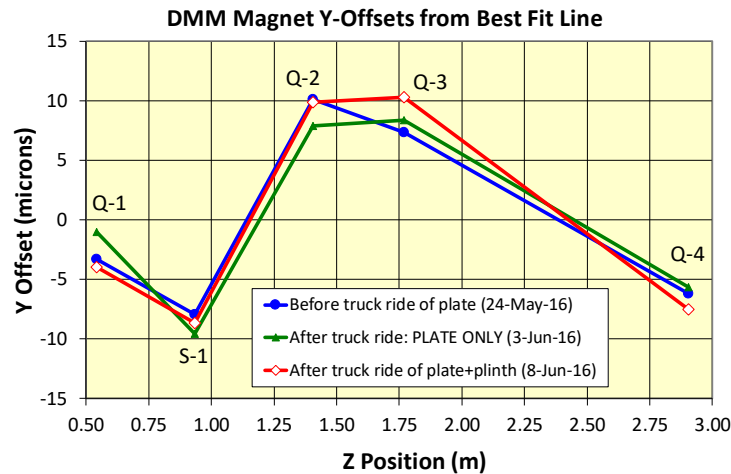


Figure 4.146. DMM magnet alignment before and after the transport tests.

4-3.4.4 Alignment Strategy

The very strict alignment and vibrational tolerances as well as a short installation period are the main driving forces behind the design of the support structures and alignment system. The early involvement of survey and alignment personnel is important for a successful design of a system that will be functional, easy to use, and satisfies physics requirements. The magnet support and alignment system is designed in a modular fashion for a fast installation of pre-assembled units in the storage ring. To speed up the alignment process of magnet modules in the storage ring, a three-point, semi-kinematic, six degree of freedom (DOF) support and alignment system is adopted throughout

the design of all module supports. Typically, top to bottom, magnet groups are mounted on a girder (magnet support structure) supported by a concrete plinth via a three-point, semi-kinematic alignment system. Each concrete plinth is equipped with three temporary outriggers that provide a six DOF alignment system for the whole assembly prior to grouting the plinth to the storage ring floor.

The S&A group is involved in providing QA measurements, prototype testing, and validating design performance. Survey data are also important for establishing several key design parameters, like range of the adjustment system and overall height of the support structure. Table 4.57 lists tolerances relevant to alignment that were derived from the APS-U accelerator physics requirements. The tolerances can be divided into three groups, each requiring a different approach and methodology to meet the requirements. The absolute global tolerances (1 mm level) will be met by survey techniques and APS geodetic control network. The relative 100 μm tolerances of girder to girder alignment will be achieved by survey measurements, free network bundle adjustment, and relative girder to girder smoothing without engaging the APS reference control. The within girder tolerance of 30 μm component-to-component alignment will be accomplished by a combination of mechanical design, machining tolerances, magnetic measurements, and employment of the cutting-edge metrology instrumentation for the fiducialization.

Table 4.57. Survey and Alignment assembly and installation tolerances at the start of commissioning

Parameter	Value	Units
Storage-ring Circumference	30	mm
Plinth assembly placement during installation (vertical)	± 1	mm
Plinth assembly placement during installation (lateral)	± 2	mm
Girder to Girder alignment	100	μm rms
Elements within a girder, magnet-magnet	30	μm rms

Retrofitting an existing facility with a new machine has some downsides but also many significant advantages. Some of the positives from the alignment perspective are intimate knowledge of building behaviour, and existing survey networks. Having over twenty years of floor settlement data is one of the benefits of upgrading the existing APS storage ring tunnel. The charts of storage ring settlement between 1993 and 2015, shown in Figure 4.147, indicates a few standout areas (around sectors 6, 16, and 33) with noticeably larger settlement. These areas correlate with location of wetlands that were relocated and backfilled prior to building construction. Closer analysis of the data reveals that the settlement in these areas has decreased over time. The settlement rate was about 0.45 mm/year over the first ten years but slowed down about fivefold during the second decade to approximately 0.09 mm/year. The worst monitored location settled 6.51 mm in total over 22 years, while uplift of the worst point was only 0.86 mm total. Based on this historical survey data, the range of the girder adjustment system was set at ± 13 mm (X,Y,Z) for all APS-U support structures.

Existing APS geodetic reference frame and tunnel control networks will be used for alignment of new components. In a similar fashion, the APS right-handed Cartesian coordinate system with the same orientation and origin as the geodetic coordinate system has been used for lattice calculations. The APS primary vertical control network, secondary vertical control network in the storage ring, and storage ring 3D network will be surveyed before MBA lattice installation and alignment. The storage ring 3D network constellation will be densified as needed before the resurvey. Laser trackers

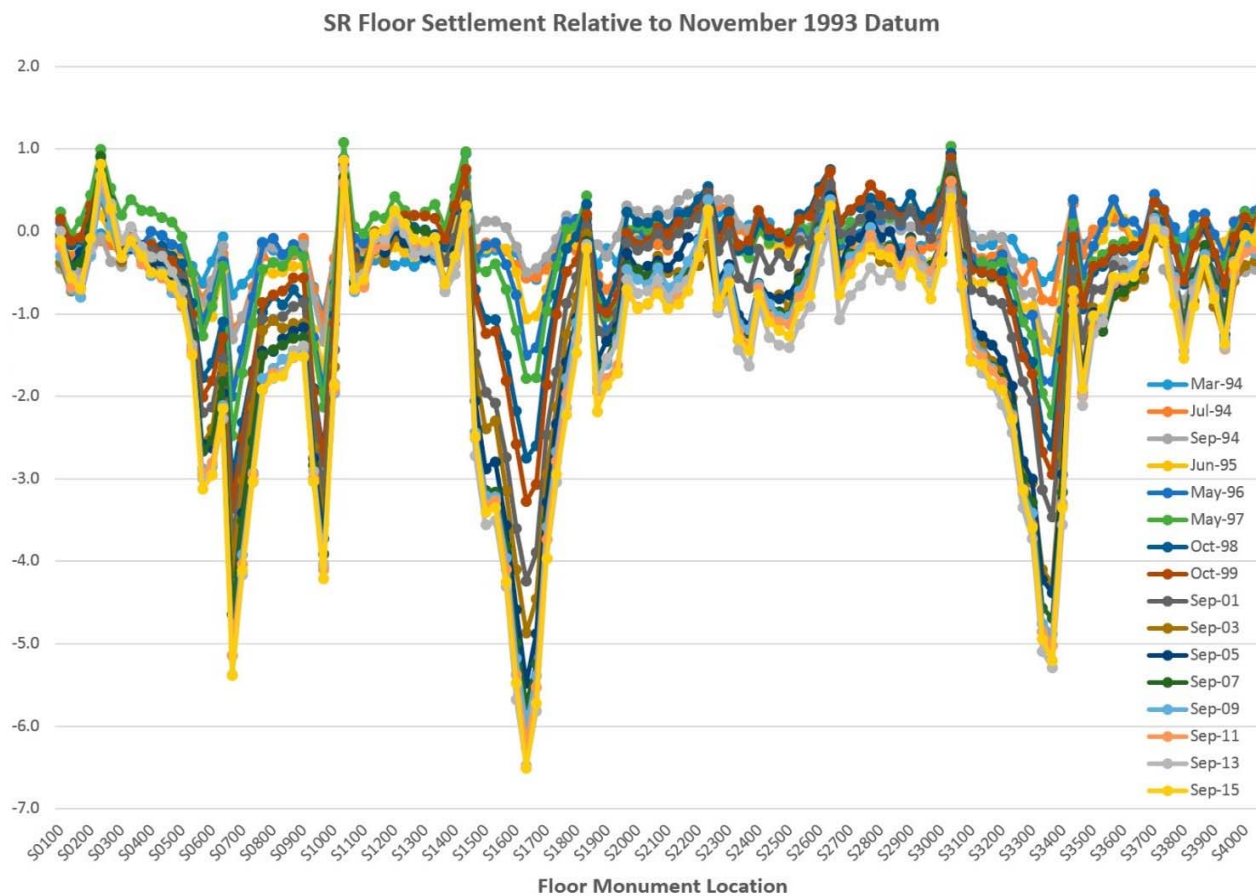


Figure 4.147. APS Storage Ring floor settlement 1993-2015.

and digital levels will be the key instruments used for control network measurements.

The tunnel control networks are established a quarter of the storage ring at a time. Once the network is established, the installation of the magnet and plinth module assemblies can begin. Plinth modules are brought into position by tug and air casters. A combination of coarse positioning fixtures and stops will be used to locate the assembly within 1-2 mm of the final lateral and longitudinal positions. Mechanical jacking screws are then used to set the elevation of the plinth top within 1 mm, and the plinth is grouted in place. The magnet modules can then be aligned to 100 μm rms by the magnet support structure alignment mechanism. The remaining installation steps, such as joining the vacuum chambers into a fully integrated sector arc, are performed after the magnet modules are aligned.

The alignment, smoothing, and mapping operations are performed once all of the components are fully installed and assembled in the tunnel. Component fiducialization and alignment of components in the storage ring will be accomplished by a combination of laser trackers, articulating arm coordinate measuring machines, and optical tooling equipment. High redundancy of collected data analyzed by least-squares adjustment software will provide statistical confidence of positional ac-

curacy. Absolute positional tolerances will be met by aligning girders first with reference to the storage ring control network. In the second step, smoothing, each girder will be mapped relative to its neighbors without any constraints of the control monuments, and adjustment will be applied to the girders to meet the relative tolerances. Smoothing will eliminate propagation of systematic errors of the control network into the relative alignment of the sections. As a final step, after the smoothing adjustments have been applied, the entire storage ring will be mapped and evaluated for QA purposes.

4-3.5 Power Supply System

4-3.5.1 Overview

The general approach to powering the MBA magnets is much the same as for the existing APS. All the multipole magnets, Q-bend dipoles, trim, and corrector windings are powered by individual DC-to-DC power converters. Two stand-alone power supplies provide power to the M1 and M2 families of longitudinal-gradient dipoles, which are each powered in series. According to the design in the Magnets section, 1002 unipolar, 921 slow-bipolar and 322 fast-bipolar power supplies are required. Magnet power supply requirements are listed in the following tables:

- Quadrupoles (incl. auxiliary windings): Table 4.60
- Bending magnets (incl. auxiliary windings): Table 4.61
- Reverse-bending quadrupoles (incl. auxiliary windings): Table 4.62
- Sextupoles (incl. auxiliary windings): Table 4.63
- Fast correctors: Table 4.64

A generic block diagram of a magnet power converter is shown in Figure 4.148. Unipolar or bipolar DC-DC converters will be supplied with unregulated DC power from common transformer/rectifier units (four per sector). Magnet currents are monitored by precision DC current transducers (DC-CTs) that are external to the power supplies and stay with the magnet “slots” when converters are replaced. Since the external DCCTs are outside of the current regulation loop, they provide independent readback verification of magnet currents. Keeping the DCCT and its electronics with the magnet slot allows a new converter to be calibrated to provide exactly the same output current as the converter being replaced. These DCCTs will also be the essential components of the overall calibration scheme. The diagram assumes that the current regulation is internal to the DC-DC converter.

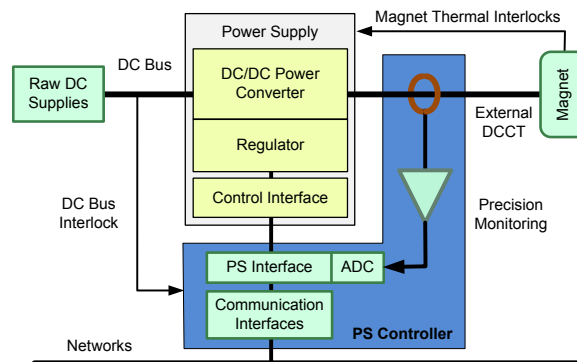


Figure 4.148. Magnet power supply generic block diagram

The power supply controller provides the communication interfaces between the power supplies and multiple networks, including the EPICS-based controls network, a bulk data network, and a synchronized data acquisition (DAQ) system. Common power supply controllers are used to control multiple power supplies in one power supply cabinet. Besides providing monitoring and controls for the power converters themselves, the power supply controllers monitor thermal conditions of the

cabinets and conditions of the DC busses.

Requirements for power supply stability and accuracy are more demanding than for those of the present APS. The main multipole and dipole magnets require 10-ppm-class unipolar power supplies, and calibration will be traceable to magnet measurement data.

The large number of power supplies means that reliability and availability are critical issues for MBA operation. For example, in order for the power supply system as a whole to cause no more than one beam-trip per 10 days (i.e. 240-hr MTBF), the individual power supplies must achieve effectively MTBFs of several hundred-thousand hours. Twenty years of APS operations has shown that such high availability can indeed be achieved, albeit non-trivially, and can be achieved without resorting to costly redundancy schemes or so-called High-Availability designs. In FY 2014, the ensemble of 1600 magnet power supplies in the present APS caused only nine beam trips in 5000 hours of user operation (544hrs MTBF).

Based on the power ratings, output polarities, and output bandwidths, four power supply types are needed:

1. Unipolar DC power supplies with output powers of several hundred kilowatts and output currents of several hundred amperes for the series-connected M1 and M2 dipole families;
2. Unipolar DC power supplies with output currents up to 280 A and a power rating in kilowatt ranges to power quadrupole, sextupole, and M3 and M4 dipole magnets;
3. Slow bipolar DC power supplies with output currents up to +/-15A and power ratings of several hundreds of watts for slow correctors, skew quadrupoles, and dipole trim coils;
4. Fast corrector power supplies that can make fast changes in its output voltage and current to meet the requirement from the fast beam correction magnets. The power rating of the fast corrector power supplies is similar to that of the slow DC power supplies. These will be four-quadrant power supplies.

The four power supply types are summarized in Table 4.58.

Table 4.58. DC Power Supply Types and Parameters

	Unipolar stand-alone		Unipolar DC-DC	Bipolar (slow)	Bipolar (fast)
Magnet families	M1	M2	M3-M4, Q1-Q8, S1-S3	M3,M4,Q4,Q5,Q8,S1	Fast correctors
Quantity	1	1	1000	921	160
Input voltage (v)	480, 3-ph	480, 3-ph	40 DC	40 DC	40 DC
Output current (A)	441	245	280	+/-15	+/-15
Power (kW)	584	416	9.8	0.525	0.525
Resolution (bits)	18	18	18	16	16
Initial accuracy (ppm) ^(a)	100	100	100	100	100
Repeatability (ppm) ^(a)	100	100	100	100	100
Current stability (ppm) ^(a)	10	10	10	100	100
Reproducibility (ppm) ^(a)	10	10	10	100	100
Small-signal bandwidth					10 kHz

Notes

^a Parts-per-million of rated current

4-3.5.2 Stand-alone Unipolar Power Supplies for M1 and M2 Dipole Strings

Stand-alone commercial power supplies will power the 80-magnet strings of the M1 and M2 dipole families. Preliminary parameters and the power ratings for the M1 and M2 dipole magnets are listed in Table Table 4.59.

Table 4.59. Parameters of M1 and M2 Dipole Magnets (Excludes busbar losses, which are expected to be <2%)

Dipole	Quantity	Magnet specs		Calculated from magnet specs			
		I_{max} (A)	P_{max} (W)	R (mΩ)	V_{max} (V)	V_{total} (V)	P_{total} (kW)
M1	80	441	7304	37.6	16.6	1325	584
M2	80	245	5200	86.6	21.2	1698	416

Although the two strings have different ratings, the same power supply model is assumed for each string in order to simplify power supply support and maintenance. Taking into account power losses in the approximately one-kilometer-long bus and the margins for reliability, the required ratings for the power supplies will be greater than the numbers listed in the table. Since these supplies will be provided stand-alone, the preliminary design is to use commercial power supplies that will meet the stability requirement.

4-3.5.3 Unipolar DC-DC Power Converter System

The preliminary design for the unipolar DC power supply system is based on a commercial DC-DC power converter unit specified at 10 parts-per-million stability, and customized to meet APS-U needs. The modifications are mostly in the input and output stages of the commercial power supply in order to utilize the existing APS DC distribution system. It is anticipated that two or more models will be needed to cover the wide range of operating currents.

Two different current regulation configurations, the current regulation loop inside power supply or the current regulation loop outside power supply, have been verified to be able to produce the required stable current. The choice of the configuration will be determined during the production procurement process. Figure 4.149 shows both regulation configurations.

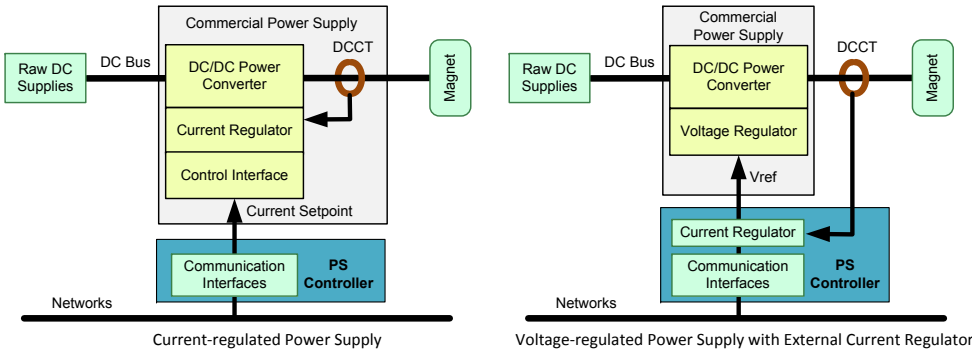


Figure 4.149. Block diagram of the unipolar power supply system.



Figure 4.150. Prototype fast corrector power supply.

4-3.5.4 Bipolar DC-DC Converter System for Trims, Slow Correctors, and Skew Quads

The total number of slow bipolar DC power supplies is 921, which includes 760 power supplies for trims coils in the main magnets and 161 power supplies for skew quadrupole magnet coils.

The preliminary design of the slow bipolar DC power supplies is very similar to the design for the bipolar DC power supply system for the fast correctors, which will be described in detail in section 4-3.5.5. The major difference is in the size of the output filter. Being a power supply without need of changing the output quickly, a much larger filter can be used in the output stage of the circuit to significantly reduce the ripple in the output voltage and hence the ripple current in the magnet. A lower PWM frequency, 125 kHz, will be used to control the MOSFET devices for smaller switching losses.

4-3.5.5 Bipolar Power Supply System for Fast Correctors

There are four fast-correction magnets in each sector, driven by eight power supplies: four in the vertical plane and four in the horizontal plane for use in fast orbit corrections.

The power supply requirements for the fast correctors are similar to those for the slow bipolar power supplies with the addition that the output current needs to have a small-signal and -3dB bandwidth of 10 kHz in order to minimize the power supply impact on the closed-loop performance of the fast-orbit-feedback (FOFB) system.

The preliminary design of the fast corrector power supplies is based on the prototype power supply developed through the R&D activities (Figure 4.150). The power supply is a switching-mode DC-DC converter utilizing a standard H-bridge topology with four MOSFET as the switching devices, as shown in Figure 4.151.

The power supply receives an analog signal from the power supply controller as the reference for the output current. The output current is sensed with a DCCT for its superior performance in the stability and the gain accuracy. The current feedback loop uses a phase-lead compensator in addition to a standard proportional-and-integral compensator to minimize the phase delay at high frequencies. A block diagram of the current regulation loop is shown in Figure 4.152.

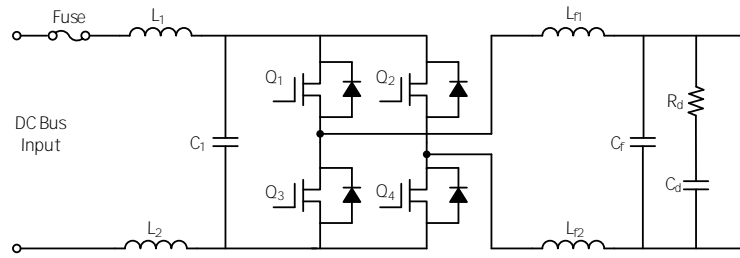


Figure 4.151. Block diagram of an H-bridge switching circuit for fast corrector power supplies.

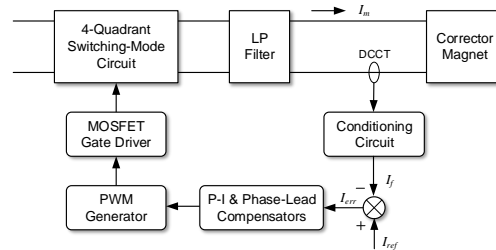


Figure 4.152. Fast Corrector Power Supply Current Regulation Loop.

A 250-kHz unipolar-voltage PWM method is used to control the on-off duty cycle of each MOSFET device. The PWM method interleaves four switches to produce an effective 500-kHz switching frequency from the H-bridge circuit. The advantage of high switching frequency is that the size of the output filter can be small.

The input of the power supply uses the APS' existing 40-volt DC distribution system, which is fed from four three-phase diode-rectified DC raw power supplies with little filtering at the outputs. To reduce the ripple components in the DC bus voltage, an L-C low-pass filter is used at the input circuit of the power supply. A soft-start circuit will be used to reduce the inrush current so that the power supply may be swapped without turning off the DC distribution system.

The output stage of the power supply contains a critically damped L-C filter. The filter is necessary to reduce the high frequency components in the output voltage to reduce the electromagnetic interferences. The cut-off frequency of the filter is designed at 159 kHz (determined by available commercial L and C components) and it does not significantly affect the dynamical performance of the power supply.

The MOSFET devices are mounted on a common heatsink that is forced-air cooled. Two 40-mm fans are used to provide the require cooling with redundancy to improve the reliability. The fan speed is PWM-controlled proportional to the output current with a minimum speed of 50%.

4-3.5.6 Power Supply Controllers

There are two types of power supply controllers, one for the unipolar power supplies and one for the bipolar power supplies, including the fast corrector power supplies. There are a total of 200 unipolar power supply controllers and 200 bipolar power supply controllers. Each controller is installed in a

cabinet that houses the type of the power supplies to be controlled by the controller.

Figure 4.153 shows a preliminary design of the power supply controller that utilizes a System on Chip (SoC) Field Programmable Gate Array (FPGA) as the core processor with multiple interfaces and protocols to communicate with power supplies and other accelerator systems. The design shares many functions that are common to both the unipolar power supplies and the bipolar power supplies. The main differences are in the digital and analog input and output where the two types of power supplies have different requirements.

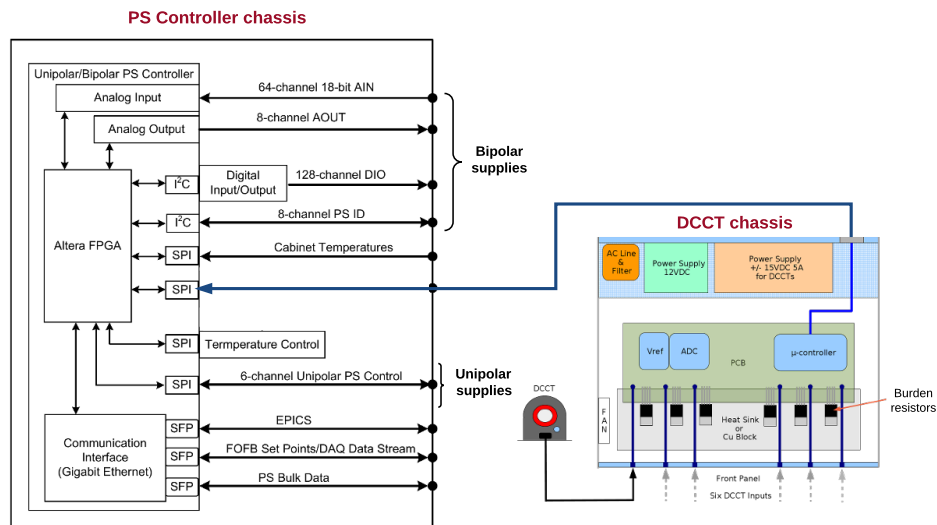


Figure 4.153. Power Supply Controller function diagram and external DCCT interface.

For the bipolar power supplies, each controller sends analog references for the output current to up to eight bipolar power supplies. The analog input module (18-bit AIN) reads analog signals from each power supply. The digital input/output monitors the power supply status and performs the reset and on or off functions. Every bipolar power supply has an embedded unique serial number and the serial number is read by the controller through digital I/O.

For the unipolar power supplies, a serial peripheral interface (SPI) will be used to communicate with the vendor designed power supplies for all necessary control and monitoring purposes. The SPI can accommodate a change rate of the setpoints up to 10 Hz with a latency much less than 10 msec.

Precision 32-bit ADCs (20 bit ENOB) for digitizing the independent DCCT readbacks are housed in a separate temperature-controlled chassis together with the DCCT electronics and burden resistors.

A high-speed communication interface common to both types of the power supplies is based on a Gigabit Ethernet designed by LBNL. The communications with this interface include EPICS, FOFB/DAQ, and bulk data communication. The EPICS communication provides general power supply supervisory functions. FOFB/DAQ link to the FOFB system receives the set points for the fast corrector power supplies at 22.6 kHz with a latency less than 10 microseconds.

External measurements of output current and other important parameters from both unipolar and bipolar power supplies can be streamed back and synchronized with the global RTFB clock at 22.6 kHz through this interface to the DAQ system for global time-correlation with other accelerator events. A memory buffer stores the current waveforms for at least one second. Waveforms can be read back with time-stamps through a dedicated bulk data network for postmortem analysis when triggered by an internal event such as a glitch in the output current or an external event such as a beam motion or a beam loss.

Each power supply controller will have a temperature input to monitor the ambient temperatures in the power supply cabinet or relay racks to correlate the power supply performances with the environment conditions. The temperature sensor may be installed on the cooling water manifold to monitor the water temperature in the case of unipolar power supplies.

4-3.5.7 External Current Measurement and Calibration System

The output currents of both the bipolar and unipolar power supplies require independent measurement for verification. The precision of the measurement needs to be 18 bits or better for the unipolar power supplies but may be an order of magnitude more relaxed for the bipolar power supplies. The common precision ADC circuit in Figure 6 will be used for both types of power supplies, although the bipolar power supplies may not need such a high precision.

In order to maintain the accuracy of the current measurement system, particularly for the unipolar power supplies, a calibration system will be installed to allow automated, in situ calibration of all 1000 channels. This system will provide precise, NIST-traceable calibration current to a multi-turn calibration winding inside each DCCT. The calibration winding multiplies the calibration current by a factor of 1000, allowing the full range up to 300 A to be calibrated using a 300 mA precision current source. The known calibration current will allow an end-to-end calibration of each channel, including the DCCT, the burden resistor, and the precision ADC circuit.

Three calibration schemes have been tested in the R&D program. Scheme 1 calibrates multiple DCCTs with one common calibration current. The issue with this scheme is the number of DCCTs that can be connected in series and driven by one calibration current source is small due to the winding resistance and the available voltage from the current source. Scheme 2 uses an additional DCCT with a calibration winding of 100 turns and a null circuit with a power supply to produce a large calibration current, 10 A for example, from a small precision current reference. Scheme 3 uses an incremental calibration method that relies on a stable power supply to produce the main current through the DCCT at large incremental steps, 10A steps for example, and uses a small calibration current to calibrate DCCTs between steps. All three schemes proved to be able to achieve the goal of the calibration, but each if used alone has limitations in the engineering implementation. The preliminary design proposes to use a scheme, derived from scheme 1 and scheme 2, that uses a small current standard to produce the required calibration current through a null circuit for the DCCTs in one power supply cabinet. Since the required current standard is small, a few miliamperes, one current standard is capable of delivering the current to many cabinets connected in series. Figure 4.154 illustrates how the proposed scheme works.

In this scheme, DCCT-1 through DCCT-6 are the external DCCTs in one power supply cabinet. Each DCCT has a built-in calibration winding with 1000 turns. DCCT-cal is a calibration DCCT

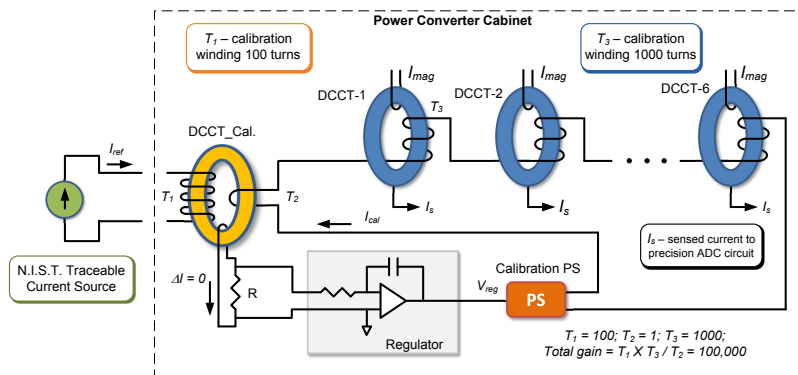


Figure 4.154. Precision current measurement system in-situ calibration diagram.

with a 100-turn calibration winding. A null circuit and small power supply can produce a calibration current 100 times the current from an NIST traceable standard. The total current gain in the circuit is 100,000, which means a reference current of three milliamperes can perform a 300 A full range calibration.

The resistance of the 100-turn calibration winding is typically less than 1Ω . With a few milliamperes in the winding, the voltage drop will be only a few millivolts. Therefore, one precision current source can drive many 100-turn calibration windings in series, making the total number of the precision current sources small and maintainable.

Typically, the external current measurement calibration will be done during a shutdown period. However, with the proposed design, an *in situ* calibration of a single channel or a set of channels, can be done by delivering an opposite calibration current through the calibration windings. This may be particularly desirable during the machine commissioning to check the performance of individual power supplies.

4-3.5.8 Power Supply Communication Structure

Figure 4.155 shows the preliminary design of the power supply communication structure in a double sector. It has three communication links for different controls and communication purposes. Links 1 and 2 are used for the power supply operations and slow monitoring, while Links 3 and 4 are used for fast monitoring and diagnostics.

Link 1 interfaces with the EPICS-based controls network. It delivers the DC set points to the unipolar power supplies. It handles the power supply logistics such as ON and OFF commands and interlock or fault resets. It reads back the monitored stationary signals such as the interlock conditions, the magnet temperatures, and other power supply status. The set points for the slow bipolar power supplies and the fast corrector power supplies may also be sent through this link under certain operation or power supply maintenance modes.

Link 2 is for delivering the bipolar power supply set points, including the set points for both slow and fast bipolar power supplies. It connects the bipolar power supply controller to the power supply interface hardware in the double-sector-controller chassis of the orbit feedback system. Link 2 also

provides an interface for the synchronized data read back from both bipolar and unipolar power supplies. Through this link, the power supply output current and other important data can be streamed back synchronously with the global orbit feedback clock at a frequency of 22.6 kHz.

Link 3 interfaces with the bulk data network. The captured power supply waveforms will be sent through this link.

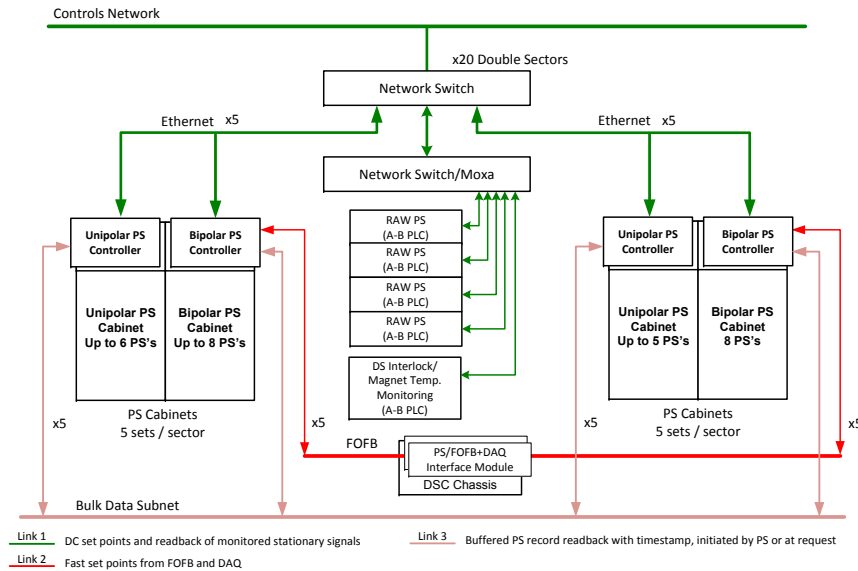


Figure 4.155. Double sector power supply communication structure.

4-3.5.9 Double Sector Configuration and Layout

In the existing APS Storage Ring, the power supply layout is partitioned into 20 identical double sectors. In each double sector, there are four AC-to-DC raw power supplies, named T1 through T4, with associated DC distribution system to deliver DC power to 10 power supply cabinets. The voltage level of the raw DC power supplies is configurable from 40 V to 72 V. The total power capacity of the DC distribution system is 496 kW per double sector, more than the power requirement by the APS-U power supplies. Each double sector has an interlock relay rack that houses the cooling water interlocks, the dipole magnet thermal interlocks, and a control unit to control the raw DC power supplies in the double sector. The preliminary design proposes to move the temperature readbacks of the thermocouples on the magnet windings from each power supply, which is the monitoring scheme in the present machine, to the central location in the double-sector interlock relay rack. Commercial PLC-based thermocouple modules will be used to read the magnet temperatures.

The existing converter cabinets for the unipolar power supplies are designed with safety interlocks on the rear doors. If the door is open, the interlock circuit will trip off the raw DC power supplies and remove the DC power to the cabinets. The front doors of the cabinets are not interlocked since there is no access to live electric circuits from the front. For the new 19-inch relay racks for the bipolar power supplies, there will not be exposed electrical circuit and, therefore, there will not be a requirement for door interlocks.

Because of the existing design of the connections between the DC bus and the unipolar power supplies, the DC bus has to be de-energized and LOTO'd before replacing a power supply. However, in the case of the bipolar power supplies, the DC bus may be left 'on' during a power supply replacement since the connectors with recessed contacts are used at the DC power input, which means a hot swap is possible.

The APS-U power supplies will have a very similar double sector layout: retaining the raw DC power supplies, the DC distribution system, the power supply cabinets, and the double sector interlocks. The output voltages of the raw DC power supplies will be reconfigured to have a uniform 40 V. Since the APS-U will have more power supplies, the existing power supply cabinets do not have sufficient space to house all the power supplies, particularly the bipolar power supplies, without limiting it to a modular design. To avoid this constraint, ten 19-inch relay racks will be added in each double sector to house the bipolar power supplies and the bipolar power supply controllers. Each 19-inch relay rack may contain up to eight bipolar power supplies.

The new double sector layout is illustrated in Figure 4.156, where DCU-PS represents the unipolar DC power supplies, FCB-PS represents the fast corrector bipolar power supplies, and DCB-PS represents the slow DC bipolar power supplies.

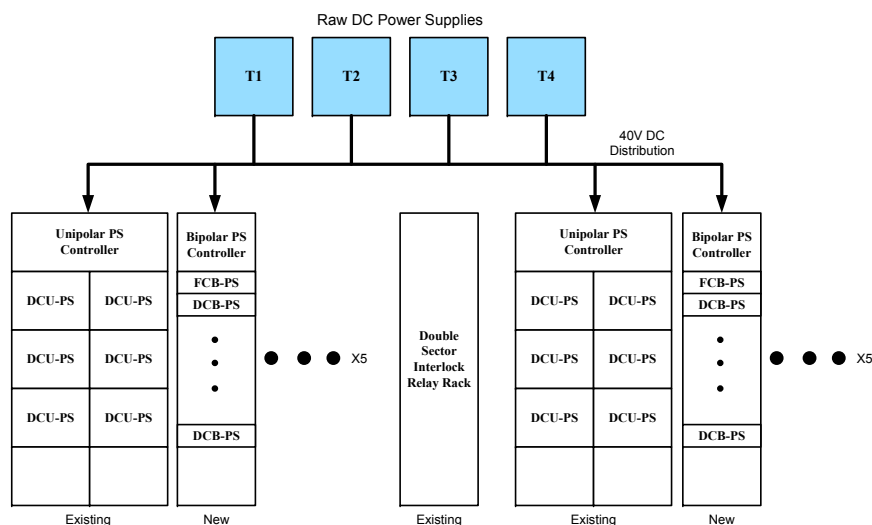


Figure 4.156. Double sector power supply layout.

Table 4.60. Power supply parameters for straight quadrupole magnets

Magnet type		Q1	Q2	Q3	Q6	Q7
Magnets/sector		2	2	2	2	2
Magnets total (40 sectors)		80	80	80	80	80
Num. main power-supplies (40 sectors)		80	80	80	80	80
Unipolar / bipolar		Unipolar	Unipolar	Unipolar	Unipolar	Unipolar
Max. operating current	A	205.0	173.4	135.5	147.0	204.0
Min. operating current	A	140	118	92	100	139
Min. standardization current	A	93	79	61	67	97
Max. power (each magnet)	W	2503	1656	1314	1548	2364
Initial accuracy after installation ^(a)	ppm	100	100	100	100	100
Magnet-to-magnet repeatability ^(a)	ppm	100	100	100	100	100
Output current settability ^(d)	ENOB	18	18	18	18	18
Reproducibility after shutdown ^(b)	ppm	10	10	10	10	10
Current stability (AC rms)	ppm	10	10	10	10	10
Aux windings (each magnet)		None	None	None	None	H+V
Num. aux power supplies (40 sectors)						160
Max current per winding (nom.)	A					± 15 ^(c)
Output current settability ^(d)	ENOB					16

Notes

^a Preliminary apportionment of physics total error budget for achieving first-turn orbit

^b Preliminary apportionment of physics total error budget for routine operation, post optics correction

^c Output current for bipolar supplies should be smooth and linear through zero

^d ENOB: Effective number of bits relative to full scale

Table 4.61. Power supply parameters for bending magnets

Magnet type		L-bend		Q-bend	
		M1	M2	M3	M4
Magnets/sector		2	2	2	1
Magnets total		80	80	80	40
Num. main power-supplies (40 sectors)		1	1	80	40
Unipolar / bipolar		Unipolar	Unipolar	Unipolar	Unipolar
Max. operating current	A	441	245	254	230
Min. standardization current	A	286	122	127	115
Max. power (each magnet)	W	7304	5200	9401	8726
Initial accuracy after installation ^(a)	ppm	100	100	100	100
Magnet-to-magnet repeatability ^(a)	ppm	100	100	100	100
Output current settability ^(d)	ENOB	18	18	18	18
Reproducibility after shutdown ^(b)	ppm	10	10	10	10
Current stability (AC rms)	ppm	10	10	10	10
Aux windings (each magnet)		None	None	H-trim	H-trim
Num. aux power supplies (40 sectors)				80	40
Max current per winding	A			$\pm 15^{(c)}$	$\pm 15^{(c)}$
Max power per winding	W			TBD	TBD
Output current settability ^(d)	ENOB			16	16

Notes

^a Preliminary apportionment of physics total error budget for achieving first-turn orbit

^b Preliminary apportionment of physics total error budget for routine operation, post optics correction

^c Output current for bipolar supplies should be smooth and linear through zero

^d ENOB: Effective number of bits relative to full-scale

Table 4.62. Power supply parameters for reverse-bending quadrupole magnets

Magnet type		Q4	Q5	Q8
Magnets/sector		2	2	2
Magnets total		80	80	80
Num. main power-supplies (40 sectors)		80	80	80
Max. operating current	A	280	142	219
Min. operating current	A	223.2	126	189
Min. standardization current	A	126	67	102
Max. power (each magnet)	W	6162	1162	6010
Initial accuracy after installation ^(a)	ppm	100	100	100
Magnet-to-magnet repeatability ^(a)	ppm	100	100	100
Output current settability ^(d)	ENOB	18	18	18
Reproducibility after shutdown ^(b)	ppm	10	10	10
Current stability (AC rms)	ppm	10	10	10
Aux windings (each magnet)		H-Trim	H-Trim	H+V-trim
Num. aux power supplies (40 sectors)		80	80	160
Max current per winding	A	$\pm 15^{(c)}$	$\pm 15^{(c)}$	$\pm 15^{(c)}$
Output current settability ^(d)	ENOB	16	16	16
Max power per winding	W	TBD	TBD	TBD

Notes

^a Preliminary apportionment of physics total error budget for achieving first-turn orbit

^b Preliminary apportionment of physics total error budget for routine operation, post optics correction

^c Output current for bipolar supplies should be smooth and linear through zero

^d ENOB: Effective number of bits relative to full-scale

Table 4.63. Power supply parameters for sextupole magnets

Magnet type		S1	S2	S3
Magnets/sector		2	2	2
Magnets total		80	80	80
Num. main power-supplies (40 sectors)		80	80	80
Max. operating current	A	62	88	62
Min. operating current	A	25	35	25
Min. standardization current	A	30	44	30
Max. power (each magnet)	W	436	992	436
Initial accuracy after installation ^(a)	ppm	100	100	100
Magnet-to-magnet repeatability ^(a)	ppm	100	100	100
Output current settability ^(d)	ENOB	18	18	18
Reproducibility after shutdown ^(b)	ppm	10	10	10
Current stability (AC rms)	ppm	10	10	10
Aux windings (each magnet)		H+V-Trim		
Num. aux power supplies (40 sectors)		160		
Max current per winding	A	$\pm 15^{(c)}$		
Max power per winding	W	TBD		
Output current settability ^(d)	ENOB	16		

Notes

Only S1 aux. windings are powered.

^a Preliminary apportionment of physics total error budget for achieving first-turn orbit

^b Preliminary apportionment of physics total error budget for routine operation, post optics correction

^c Horizontal and vertical trim windings are not powered on the S2 and S3 magnets

^d ENOB: Effective number of bits relative to full-scale

Table 4.64. Power supply parameters for 8-pole fast corrector magnets

Magnet Coil		Horizontal	Vertical	Skew Quad
Magnet circuits/sector		4	4	4
Magnet circuits total		161	161	161
Num. power-supplies (40 sectors)		161	161	161
Max. operating current (dc)	A	$\pm 15^{(c)}$	$\pm 15^{(c)}$	$\pm 15^{(c)}$
Max. real power per circuit	W	90	90	90
Max. voltage per circuit	V	30	30	30
small-signal bandwidth	kHz	10	10	
Initial accuracy after installation ^(b)	ppm	100	100	100
Magnet-to-magnet repeatability ^(a)	ppm	100	100	100
Output current settability ^(d)	ENOB	16	16	16
Reproducibility after shutdown ^(b)	ppm	100	100	100
Current stability (AC rms)	ppm	100	100	100

Notes

^a Preliminary apportionment of physics total error budget for achieving first-turn orbit

^b Preliminary apportionment of physics total error budget for routine operation, post optics correction

^c Output current for bipolar supplies should be smooth and linear through zero

^d ENOB: Effective number of bits relative to full-scale

4-3.6 Beam Injection and Extraction Systems

4-3.6.1 Overview

Injection into the MBA storage ring will employ vertical on-axis injection with bunch swap-out, as described in Section 4-2.10. This is a two-step process, where the bunch circulating in the target rf bucket is first kicked out of the machine and the incoming full-charge bunch is then kicked on-axis into the same rf bucket.

As shown in Figure 4.157, the design concept uses two groups of four fast pulsed kickers located in two separate sectors of the storage ring: the extraction group kicks out the bunch that occupies the target bucket of interest; and the injection group kicks the incoming bunch on-axis and into the now-empty rf bucket. Both sets of kicker pulses must be short enough that bunches upstream and downstream of the target bunch are not unduly disturbed.

Kicking out the target bunch requires two kicks: first a low-amplitude “pre-kick” is applied using one of the four extraction kickers in order to decohere the bunch and reduce power densities. Some 200-300 turns later, a larger kick from the remaining three extraction kickers sends the bunch to the swap-out dump.

The injection similarly has four kickers, but all are used to bring the injected beam on-axis. Each kicker comprises a dual-blade stripline rf structure and dual-channel fast high-voltage pulser. In addition, the injection section contains a Lambertson DC septum that deflects the incoming beam both horizontally and vertically upstream of the four kickers. Key requirements are given in Table 4.65.

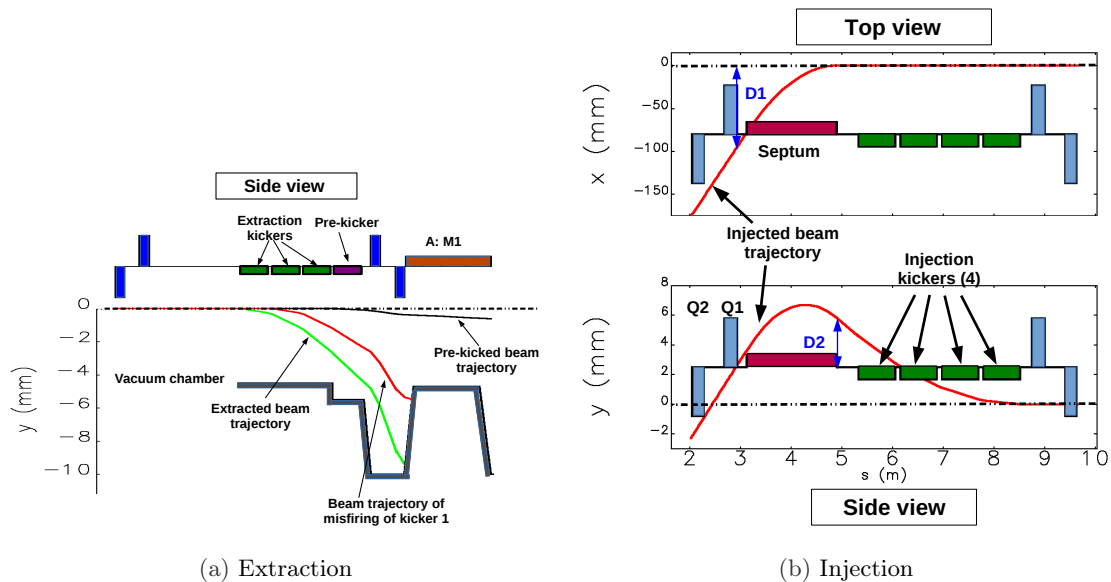


Figure 4.157. Layouts for Extraction and Injection sections.

Table 4.65. Fast kicker parameters

Parameter	Units	Value
Kick direction		y-plane
Total kick Angle	mrad	2.88
Number of kickers		4
Kicker strength	mrad/m	1
Length of each kicker	m	0.72
Peak-to-peak blade voltage (nominal)	kV	30 (± 15)
Aperture at kicker	mm	>9
Good-field region	mm \times mm	$\pm 2.3 \times \pm 1$
Field uniformity	% of center field	2
Minimum bunch spacing (324-bunch mode)	ns	11.4
Maximum residual kick to stored beam	% amplitude	3
Blade length	mm	720
Gap between blades	mm	9
Blade shape		“D”
Vertical offset relative to beam - Injection	mm	1
Vertical offset relative to beam - Extraction	mm	1

4-3.6.2 Lambertson DC Septum

Lambertson septum magnets have been used in many accelerators, such as the extraction system for the Spallation Neutron Source [1] and the injection/extraction system for the Large Hadron Collider [2].

Because the APS booster and storage ring are both at the same elevation, the vertical on-axis injection scheme requires a Lambertson septum to be used in the injection section. To ensure that the injected beam trajectory is close to the midplane when it passes through the storage ring magnets upstream of the septum, the septum is also slightly tilted about the z-axis.

Key parameters for the Lambertson septum are given in Table 4.66. To address the design challenges implicit in the specification, a novel concept that cancels out the leakage field was developed and applied to the APS-U septum design. The concept involves placing the US (upstream) end of the stored beam chamber under the side leg to create a positive B_y field leakage that cancels out the negative B_y leakage field created at the DS (downstream) by the small septum thickness. Almost all the integrated leakage field in the stored beam chamber is cancelled. Furthermore, the concept helps to reduce the integrated skew quadrupole field and normal sextupole in the stored beam chamber.

The septum magnet was designed with Opera 3D, as shown in Figure 4.158. The coil is 14 layers with 4 turns per layer, wound around the top pole. The gap between the top and bottom poles, which provides space for the injected beam, was set at 10 mm. An illustrative 2D picture of the magnetic flux lines, obtained with Opera-2D, is shown in Figure 4.159. From this, it is apparent how the leakage field at the up- and downstream ends cancels, leading to low deflection of the stored beam.

The stored beam chamber is located in the bottom pole. The width of the top pole is 6.5 cm, while the width of the bottom pole is 6 cm and the yoke thickness is 4 cm. The septum thickness varies along the magnet, from 4.56 mm at the US end to 2 mm at the DS end. The upstream and

Table 4.66. Lambertson septum parameters. The field uniformity specifications are preliminary, subject to further beam dynamics studies.

Parameter	Value	Unit
Length	1.78	m
Thickness DS end	2	mm
Thickness US end	4.56	mm
Beam separation at DS septum	5.5	mm
Septum thickness tolerance	50	μm
Field Strength	1	T
Bend Angle	89	mrad
Tilt Angle	93	mrad
Stored beam deflection angle	<100	μrad
Aperture of stored beam chamber	8 x 6	mm
Field uniformity ($\Delta B/B$), $\pm 2\text{mm}$ beam vicinity	≤ 0.001	

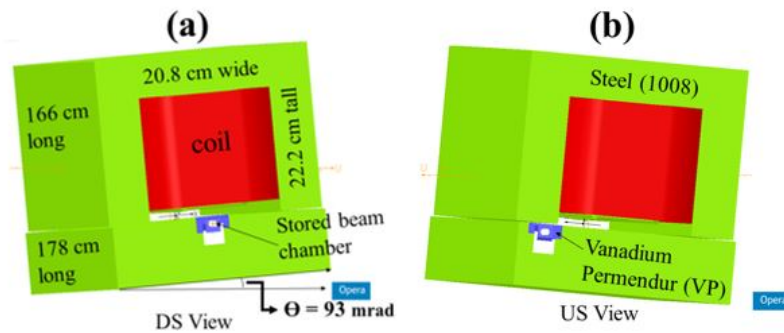


Figure 4.158. The septum magnet viewed from the stored beam chamber at DS (a) and US (b) ends.

downstream X centers of the stored beam chamber are separated by 7.887 cm, resulting in a 47.5 mrad rotation of the stored beam chamber in the XZ-plane against the magnet axis. To reduce leakage field seen by the stored beam, the iron around the stored beam chamber was cut off and made into an open space, as shown in Figure 4.158. The material of the stored beam chamber was selected to vanadium permendur to utilize a higher magnetic permeability to shield the field better than iron.

Figure 4.160 (a) and (b) show the trajectories of the injected and stored beams with a peak field of 1.06 T at the gap center. The trajectories in Figure 4.160 (a) are referenced to the storage ring coordinate system which was set at the US end, while (b) is referenced to the magnet coordinate system for which the origin is the center of the gap. The outgoing angle, α_2 , in Figure 4.160(b), was to the mechanical tilt angle of the stored beam chamber in XZ-plane, which is 47.5 mrad from the magnet axis.

The X position of the injected beam at the DS exit of the septum magnet was set to match the center of the stored beam chamber, resulting in the trajectory of the injected beam matching the stored beam trajectory at the DS end as in Figure 4.160 (a) and (b). The total deflecting angle of

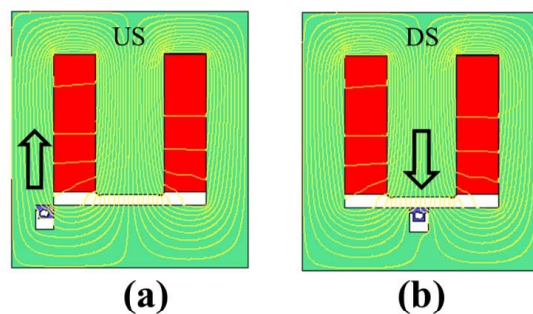


Figure 4.159. Calculated magnetic flux density distribution over the septum magnet calculated with an Opera-2D model, with the different colors representing different flux densities. The injection beam-pipe aperture is located immediately below the center pole of the magnet.

the injected beam, $\alpha = \alpha_2 - \alpha_1$, was confirmed as -89 mrad from the trajectory in Figure 4.160 (b), matching the required angle in the specifications. Further details of the beam trajectories and constraints can be found in the Beam Physics section [4-2.10].

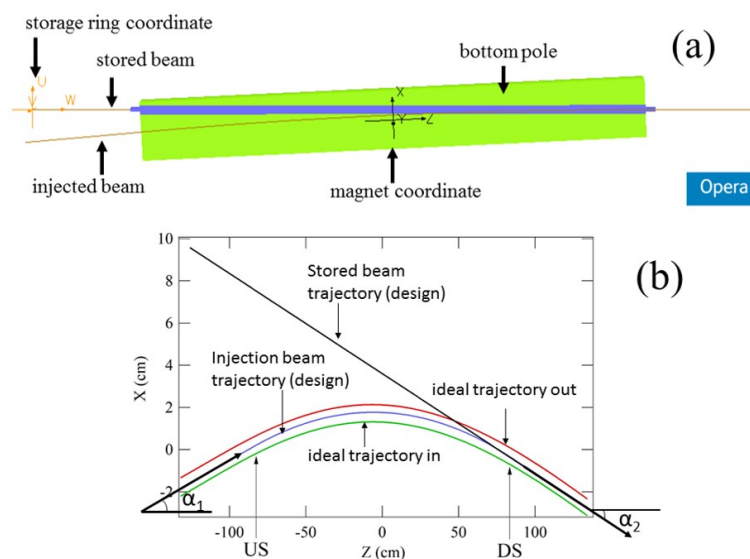


Figure 4.160. Septum magnet top view (a) of the injected and stored electron beam trajectories in the storage ring coordinate system (all other parts except the bottom pole are hidden); (b) Plots of injected and stored electron beam trajectories in the magnet coordinate system. The ideal trajectory (in)board and (out)board show the allowed range of the injected beam in the XZ-plane using an ideal field.

4-3.6.3 Stripline rf Design

Table 4.67 lists the key specifications for the injection/extraction kickers. A two blade stripline design was chosen with a line impedance of 50 Ω to avoid high-voltage reflections that may disturb

adjacent bunches, to improve high-voltage compatibility, and to take advantage of commercial-availability high-voltage components connectors, attenuators, and cables. Similar devices have been developed at DAΦNE and KEK [3] and [4].

Table 4.67. Specifications of the injection/extraction kickers. The good-field region and field uniformity specifications are preliminary, subject to further beam simulations.

Injection scheme	Swap-out
Kick direction	y-plane
Minimum bunch spacing (ns)	11.4
Residual kick to stored beam (% amplitude)	3
Kicker strength (mrad/m)	1
Total kickers	4
Length of a kicker (m)	0.72
Aperture at kicker (mm)	>9
Good field region (mm × mm)	$\pm 2.3 \times \pm 1$
Field uniformity (% of center field)	2

Figure 4.161 (a) illustrates the operating principles and timing constraints. Bunches traveling from left to right are separated by 11.4 ns and travel through a stripline of length L_s . High-voltage pulses fill the stripline structure from right to left. In order to avoid disturbing the bunch arriving ahead of the target bunch, the high-voltage pulse cannot start filling the structure until the bunch ahead of the target bunch has left the structure, which must then be filled in time for the target bunch to arrive at the upstream end of the structure. The structure must remain filled until the target bunch has left, and then be emptied again before the next bunch arrives.

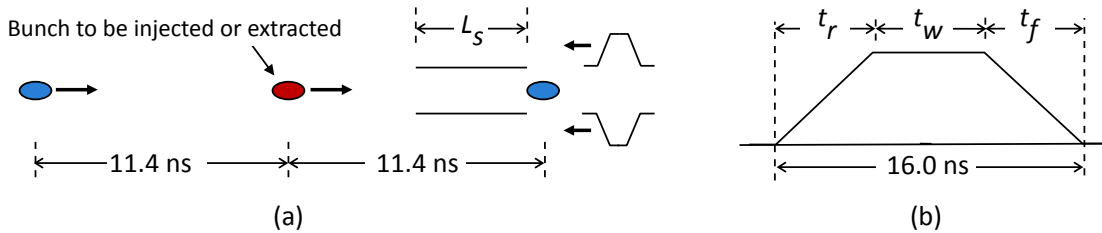


Figure 4.161. Kicker pulse shape requirements: (a) intra-bunch spacing, (b) pulse shape.

Figure 4.161 (b) illustrates the ideal high-voltage pulse shape. The total kick experienced by the target bunch is a function of the field-integral while the bunch is inside the structure. Since the high-voltage pulse and the bunch travel in opposite directions, the flat-top must be twice the electrical length of the stripline, with additional allowances for jitter and the 3-sigma bunch length. Any variation in voltage along the flat-top will be seen as shot-to-shot kick-amplitude jitter and a non-uniform kick over the length of the bunch.

The vertical kicker stripline geometry was optimized to match the differential impedance to 50 Ω while allowing some mismatch in the common mode impedance, the mode which will be excited by the beam. A ‘vaned’ outer body geometry is adopted, which provides better common-mode impedance matching, while ‘D’ shaped blades are used to improve field uniformity within the good field region. Tapered end-sections match the impedance of the kicker deflecting cavity to the APS-U beam pipe and impedances of the high-voltage feedthroughs to the striplines. Optimization was performed by running a multi-objective sddsoptimize [5] process with a 2-D electrostatic simulation

program [6]. The 3-D simulation using CST Studio [7] was performed starting from the optimized 2-D geometry in order to further validate the design-parameter optimization from the 2-D simulation and to evaluate the entrance/exit tapered sections. Figure 4.162 shows the optimized geometry. Table 4.68 lists the 2-D optimized parameters.

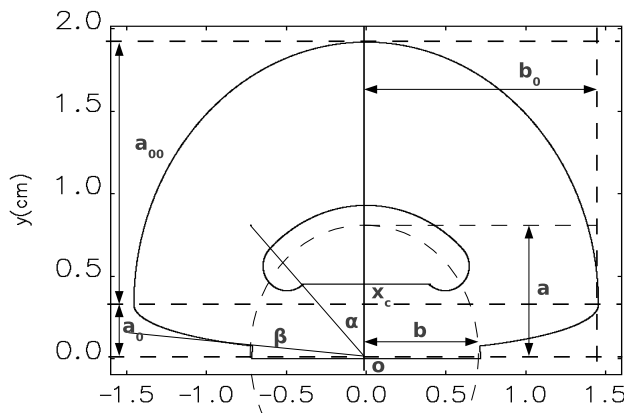


Figure 4.162. Upper half of the stripline kicker model; geometric-parameters for optimization.

Table 4.68. Optimized fast stripline geometric parameters. See Figure 4.162 for meanings of the listed quantities.

Parameter	Value	Unit
a	7.80	mm
b	7.15	mm
α	43.83	degree
β	84.27	degree
a_0	2.87	mm
a_{00}	15.91	mm
b_0	14.54	mm
x_c	19.19	mm

The outer conductor consists of two connected half-ellipses defined by the half-axes (a_0, b_0) and (a_{00}, b_0) ; the center x_c ; and the two vanes on the horizontal plane. The inner blade is defined by an ellipse with axes (a, b) and by the thickness of the blade. Figures 4.163 and 4.164 show the field distribution and S-parameters of the model, respectively. Table 4.69 lists the 3-D simulation results.

Table 4.69. Kicker simulation results with applied /pm15 kV pulse

Parameter	Value	Units
Z_{diff}	49.6	Ω
Z_{comm}	63.1	Ω
Ave. E_x	3.015	MV/m
E_{max}	6.77	MV/m
Variation in field	1.4	%

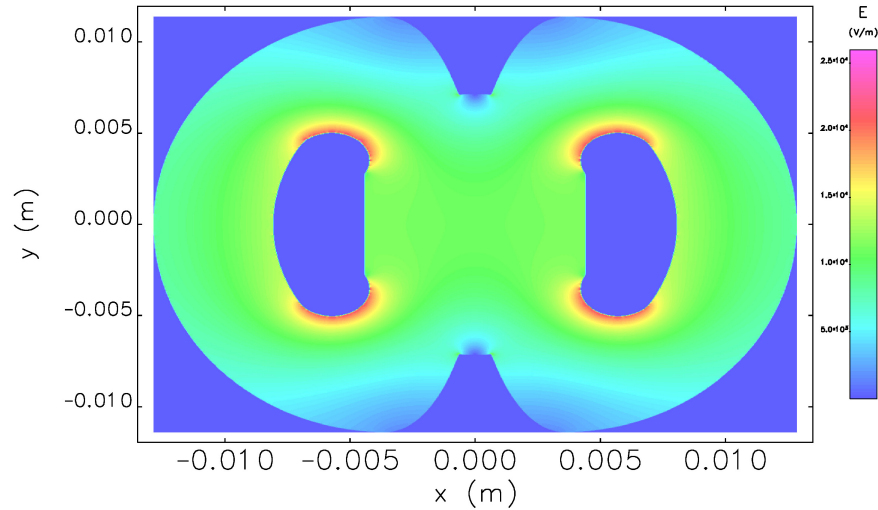


Figure 4.163. *E*-field distribution of the 2-D stripline kicker model. The deep-blue color represents the blades and the outer shell of the kicker. The geometry is rotated 90-degrees relative to Figure 4.162 and the actual working orientation.

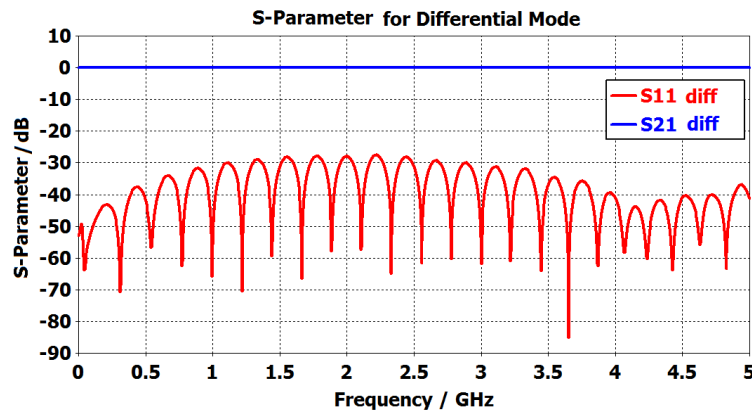


Figure 4.164. Differential-mode *S*-parameters of the stripline kicker.

4-3.6.4 High-Voltage Feedthrough

The high-voltage vacuum feedthroughs serve as insulator, vacuum seal, and blades support. Key specifications were: an impedance of $50 \pm 5 \Omega$ and bandwidth $> 1 \text{ GHz}$, sustain bake-out at 150 C, and compatibility with ultra-high vacuum and high levels of radiation. Given that suitable off-the-shelf feedthroughs were not readily available, a custom feedthrough was developed in conjunction with Cosmotec Corporation. A cross-sectional view and photograph of the feedthrough prototype are shown in Figure 4.165 and Figure 4.166, respectively.

4-3.6.5 Stripline Mechanical Design

The mechanical design of the stripline kicker is driven not only by the physics requirements shown earlier in Table 4.65, but also by achievable manufacturing tolerances, which must be factored into

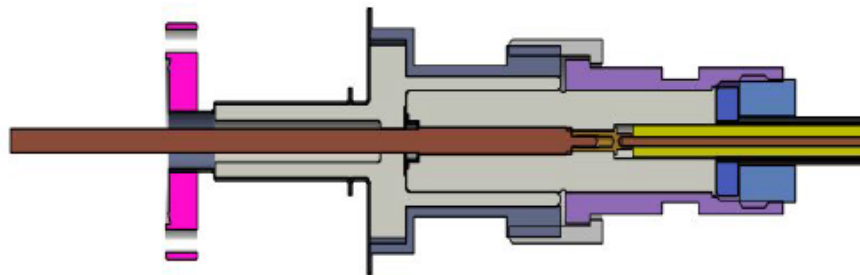


Figure 4.165. Cross-sectional view of prototype feedthrough design.



Figure 4.166. Finished prototype feedthrough.

the design geometries. Considering the electromagnetic design and current machining practices, the following fabrication constraints were developed for the vertical kickers:

- The blades must be fully-supported by the feedthroughs.
- The stripline kickers are of a 2-blade type design with a main body, taper transitions, feedthroughs, and end-cap flanges.
- The gaps between blades and body must be greater than or equal to 2 mm in order to keep local high-voltage concentration below 13 MV/m (the breakdown field-strength at ± 15 kV in 1 nano-torr vacuum).
- The gaps between blade ends of adjacent kickers must be at least 100 mm to provide space for a flanged bellows section and to avoid mechanical interference between feedthroughs.

The kicker body is 61.8 cm long and is machined from a solid 316-L stainless steel bar using wire EDM (Electrical Discharge Machining). Further machining to improve the inside surface finish will be done through electropolishing. Geometries of the main body and tapered transitions are shown in Figure 4.167

The tapered end-sections are high-vacuum furnace brazed to the kicker body using CuSil braze alloy (72% Ag, 28% Cu).

The blades are made from CDA101 high purity copper and are 720 mm long, as seen in Figure 4.168, and are attached to the feedthrough inner conductor with internal brass studs. During operation of the kicker, the expected differential expansion between the blades and outer stainless steel body is calculated to be a few micro-inches. This is negligible over the 720 mm blade length and does not

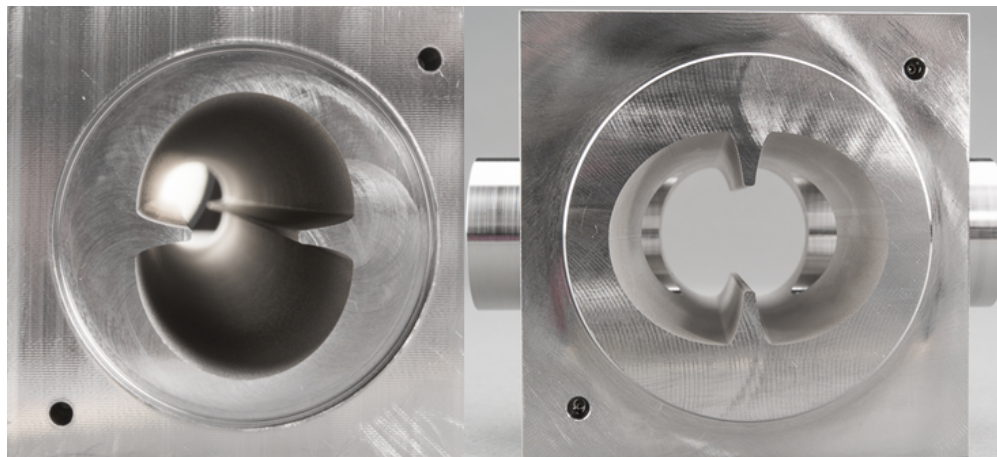


Figure 4.167. Body (Left) and tapered transition (Right) parts for the vertical kicker.

perturb the electromagnetic performance of the device in any meaningful way.

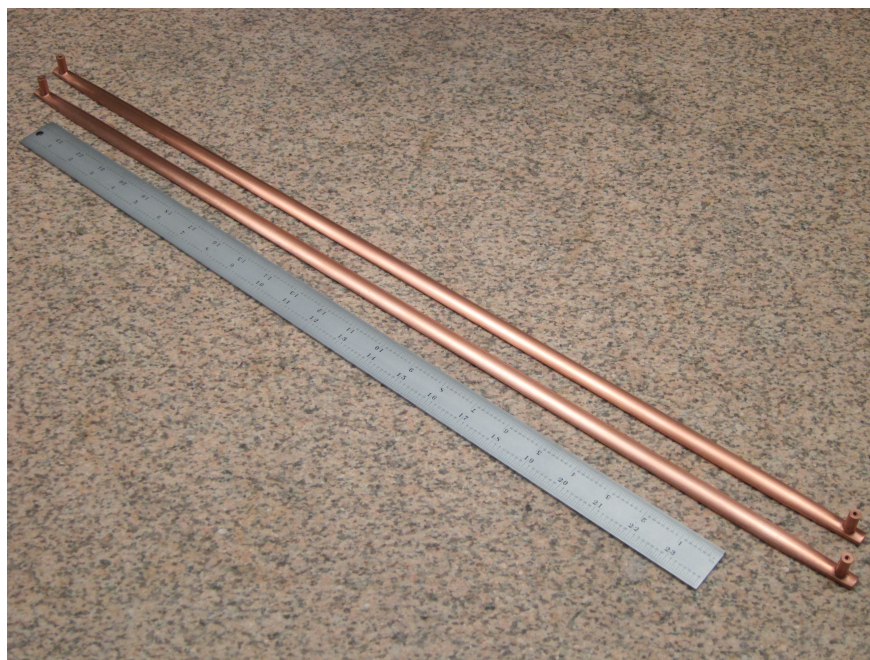


Figure 4.168. Photograph of the stripline blades manufactured for the prototype kicker.

Electrical and mechanical tuning techniques have been developed and tested on a prototype unit. In the final assembly, the measured stripline blade separation was 8.75 mm and the center of the blade gap aligned with the center of the kicker body better to a level than the resolution of our coordinate measuring machine (CMM). The measured angular offset of the blades were all less than 0.3 degrees. With these measurements the prototype unit was successfully tested with a 7 GeV electron beam and achieved all required operating parameters: 1 mrad/m deflection, 30 kV peak voltage, and 1 nano-torr vacuum.

Figure 4.169 shows the finished kicker assembly prior to being installed in the APS injector test

beamline. During this assembly, coordinates on the parts were measured and compared to the desired geometric shape. For the blade the maximum deviation from the ideal blade thickness was measured to be +75 microns, while for the body the maximum deviation in the middle of the large elliptic arc was measured to +200 microns. These measured deviations are all within the acceptable tolerance.

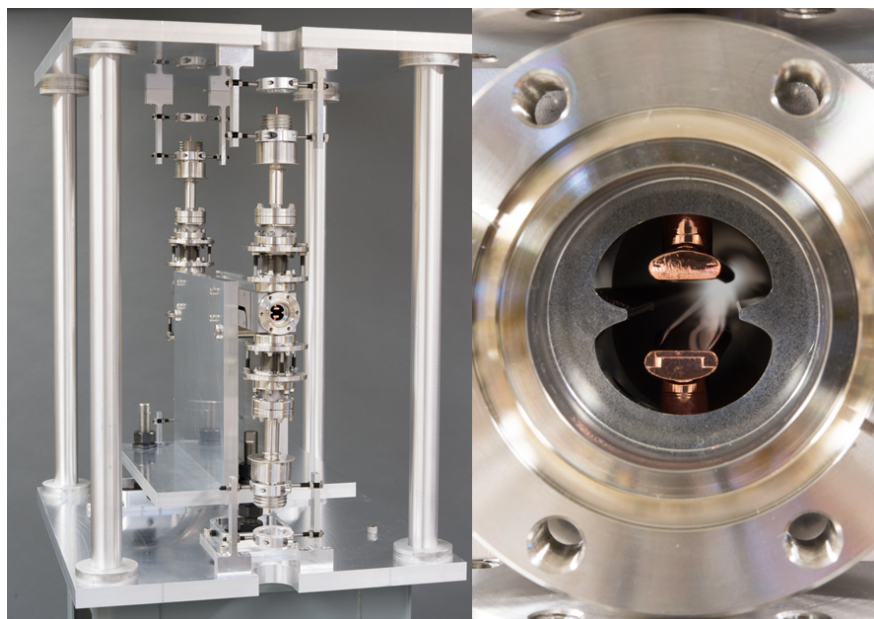


Figure 4.169. Prototype kicker assembly prior to beam testing (Left). The kicker copper stripline blades and a view down the bore of the kicker beam aperture (Right).

4-3.6.6 End-to-end Simulations

Both 2D and 3D simulations have been performed on the optimized geometry with CST studio[7] in order to further validate the design-parameter optimization from the 2-D simulation and to evaluate the end-point geometries [8]. A 3D kicker model is developed based on 2D simulation results, as shown in Figure 1, and CST Microwave Studio (MWS) is applied.

Figure 4.170 shows the kicker-assembly model used for 3D end-to-end TDR simulations. Differential-mode and common-mode TDR simulations were compared with actual TDR measurements from the prototype kicker prior to installation.

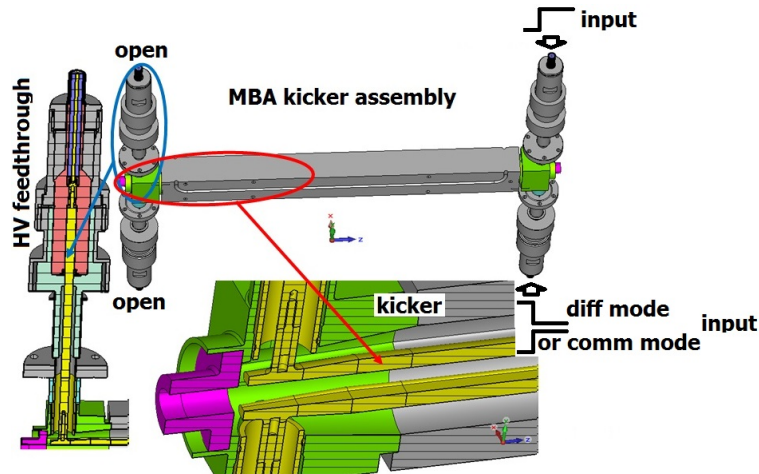


Figure 4.170. Model of kicker assembly for end-to-end TDR simulations.

Figure 4.171 shows good agreement of the differential-mode and common-mode TDR simulations with actual measurements. The simulation correctly shows all the features, and except for the finest structure, the magnitudes of impedance changes are consistent with the measurements. Impedance-changes for the finer structures are likely a result of under-estimating a rise-time for the injected pulse in the simulation.

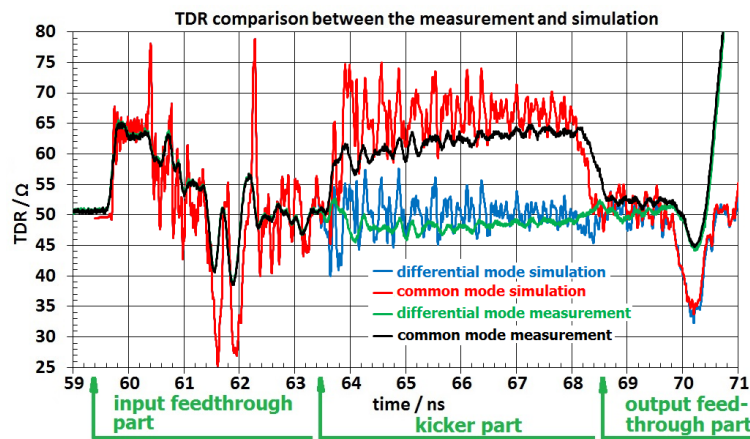


Figure 4.171. Comparison of differential-mode and common-mode TDR measurements with simulations.

4-3.6.7 Fast High-Voltage Pulser

Specifications for the high-voltage pulsers that drive the stripline kickers are listed in Table 4.70. The specifications are based on a 324-bunch fill pattern.

The reference pulse shape is trapezoidal, as shown in Figure 4.161. There are two key timing criteria: start-to-end, the total pulse length should be short enough to not unduly disturb the upstream and downstream bunches; the flat-top length should exceed the round-trip electrical length of the

stripline. In both cases, pulse jitter and a 6-sigma bunch length need to be taken into account. In practical terms, the allowable residual kick to the nearest upstream and downstream bunches is a function of the acceptable induced beam losses in those bunches, as discussed in Section 4-2.10.4.

Achieving the combination of high peak voltage and nanosecond-scale rise- and fall-times is challenging and technology options are limited.

Table 4.70. Fast pulser specifications. The timing jitter specifications are preliminary, subject to further beam dynamics studies.

Parameter	Value	Unit
Maximum output voltage per channel	20	kV
Dual outputs	\pm polarity	
Maximum rise time (10 – 90 %)	4.5	ns
Maximum fall time (90 – 10%)	4.5	ns
Flat top width (at 90%)	5.9	ns
Maximum pulse tail amplitude	3	%
Amplitude stability	1	%
Maximum time jitter between two channels (rms)	0.1	ns
Maximum output time jitter to external trigger (rms)	0.1	ns
Maximum skew between 2 channels	0.1	ns
Maximum pulse rate (continuous)	10	Hz
Maximum burst rate (pulsed) (2-sec. bursts at 3 min. intervals)	300	Hz

The preliminary design for the MBA kickers uses commercially-available pulsers. Three pulsers procured for the R&D phase all met the performance specifications, and one of the pulsers successfully supported tests of the prototype kicker in the BTX line, described in Section 4-3.6.9. However, reliability of the commercially-available pulsers remains a concern, and alternatives are being investigated.

As part of the investigation into alternative pulsers, the physics impact of a pseudo-gaussian pulse shape was investigated. The disadvantages compared with the trapezoidal pulse with a flat top are the non-uniformity of the kick and greater sensitivity to timing jitter. Nevertheless, simulation results with realistic errors indicate that the degradation of injection performance is still tolerable [9].

4-3.6.8 Pulser Timing

Figure 4.172 shows a block diagram of timing for extraction/injection. The kicker triggers will be generated by precision delay generators, such as the Stanford Research DG645. This particular device provides four pulsed outputs suitable for driving four dual-channel pulsers. The four dual-channel extraction- and injection-kicker pulsers will each be driven by a single four-channel delay generator. A timing reference from the APS injection timing system provides the trigger for the two delay generators.

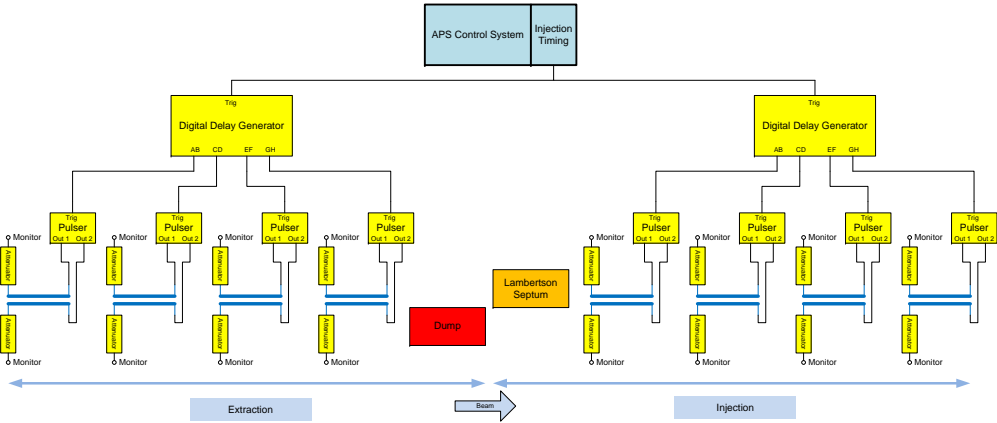


Figure 4.172. Extraction/Injection block diagram, showing timing.

4-3.6.9 Prototype Kicker Tests

Beam tests have been performed with the prototype kicker installed in the booster extraction test line (BTX) line using two different FID pulsers. Preliminary results up to the nominal working voltage of ± 15 kV were previously reported [10].

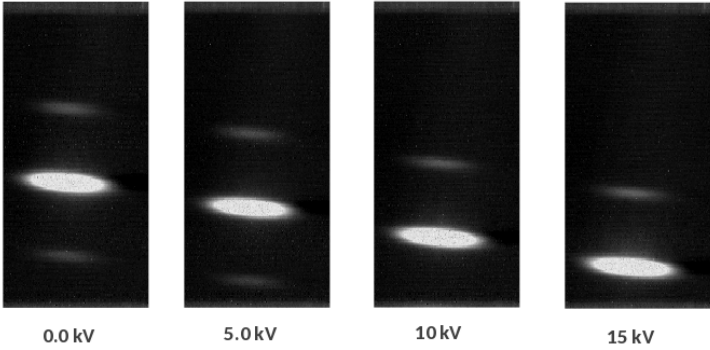


Figure 4.173. Beam spot deflection for kicker amplitudes from 0 kV to 15 kV.

Figure 4.173 shows the beam spot imaged on the downstream screen for kicker voltages between 0 kV and 15 kV. Results of post-processing of the image centroids to obtain deflection in microns as a function of kicker amplitude are shown in Figure 4.174. The measured kick angle at ± 15 kV was 0.66 mrad for 7 GeV beam (0.77 mrad scaled to 6 GeV).

More recently, beam tests using a second FID pulser have allowed measurements of deflection up to an applied voltage up to ± 30 kV.

Measurements of effective kick strength for these second tests were made by scanning the pulser trigger delay relative to the bunch arrival time and the displacement of the y-centroid of the beam image on the downstream screen was recorded. Figure 4.175 shows the results of the timing scans at several kicker voltages [11].

In summary, the prototype kicker and pulser have been operated for more than 6 months at 20 kV

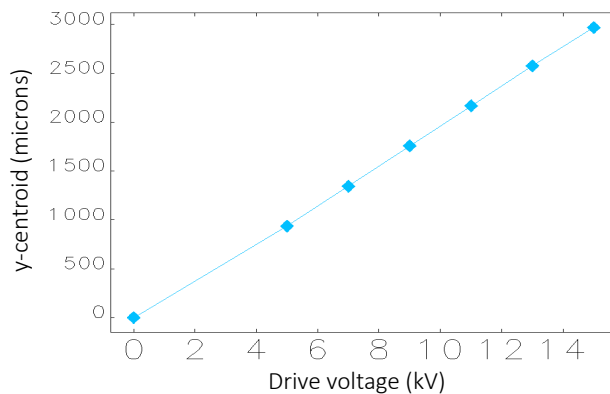


Figure 4.174. Measured y -centroid position as a function of kicker amplitude for 7 GeV beam. The maximum deflection corresponds to a kick angle of 0.66 mrad at ± 15 kV

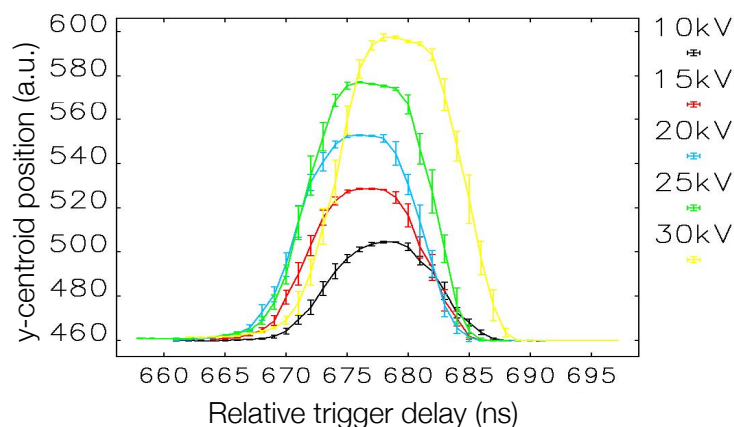


Figure 4.175. Measurement of kick strength at several voltages vs pulser trigger delay. Note that the right-side edge of the pulse is the leading (upstream) edge

and at 30 kV for about an hour without issue and with no evidence of any voltage withstand limitations. The feed-through and stripline kicker design are therefore considered ‘qualified’ for higher than the required nominal operating levels. The commercial pulser performed as expected at the required voltage and flat-top width. The residual kick from the waveform tail is about 3 %, which satisfies the physics requirement for the nearest bunches, although further reduction is desirable. At higher voltages, the pulser waveforms have obvious slopes in the ‘flat-top’ region, and there are voltage-dependent time-shifts. The cause and the impact of these effects require further investigation.

References

- [1] J. Rank et al. “The extraction Lambertson septum magnet of the SNS.” In: *Proc. of PAC 2005*. 2005, p. 3847 (cit. on p. 206).

-
- [2] S. Bidon et al. “Steel septum magnets for the LHC beam injection and extraction.” In: *Proc. of EPAC 2002*. 2002, p. 2514 (cit. on p. 206).
 - [3] D. Alesini and others. “Design, test, and operation of new tapered stripline injection kickers for the e^+e^- collider DAΦNE.” In: *Phys. Rev. ST Accel. Beams* 13 (2010), p. 1111002 (cit. on p. 209).
 - [4] T. Naito and others. “Multibunch beam extraction using the strip-line kicker at the KEK Accelerator Test Facility.” In: *Phys. Rev. ST Accel. Beams* 14 (2011), p. 051002 (cit. on p. 209).
 - [5] M. Borland et al. “SDDS-Based Software Tools for Accelerator Design.” In: *Proc. of PAC 2003*. 2003, pp. 3461–3463 (cit. on p. 209).
 - [6] M. BORLAND. *estat, Private Communication*. 1989 (cit. on p. 210).
 - [7] www.cst.com. *CST Microwave Studio Suite*. 2013 (cit. on pp. 210, 214).
 - [8] C. Yao X. Sun. “Simulation Studies of a Prototype Stripline Kicker for the Aps-Mba Upgrade.” In: *NAPAC16*. WEPOB14. 2016 (cit. on p. 214).
 - [9] A. Xiao and J. Carwardine. *Possibility and specifications of a Gaussian waveform pulser for the APS-MBA upgrade*. Tech. rep. AOP-TN-2017-028. May 2014 (cit. on p. 216).
 - [10] C. Yao et al. “Preliminary Test Results of a Prototype Fast Kicker for Aps Mba Upgrade.” In: *NAPAC16*. WEPOB24. 2016 (cit. on p. 217).
 - [11] A. Xiao et al. *Beam Test Report of MBA Prototype Kicker with the 30-kV FID Pulser*. Tech. rep. AOP-TN-2017-027. May 2017 (cit. on p. 217).

4-3.7 Orbit Positioning and Stabilization

4-3.7.1 Introduction

An ultra-stable orbit will be essential for taking advantage of the MBA beam properties, and with extremely small transverse beam dimensions (Table 4.71), tolerances for orbit stability and drift are very challenging. Relative to what is achieved at the APS today, improvements are necessary in the measurement of the beam trajectories (especially long-term drift) and the effectiveness of the orbit feedback system. These are discussed in sections 4-3.8.2 and 4-3.7.4, respectively.

General considerations for orbit positioning and stabilization are:

- During initial commissioning, obtain trajectory for the first several turns in order to close the orbit, store beam, and allow correction of the optics.
- Stabilize the particle beam at x-ray source points within a fraction of the beam size, both AC and long-term (days / weeks).
- Recover the orbit through the ID straight sections after machine maintenance / studies periods in order to restore x-ray source positions within a fraction of the beam size.
- Center the particle beam in the lattice multipole magnets at the level of a few tens of microns.

Table 4.71. Insertion device source parameters for 42pm v0 lattice.

κ	ϵ_x pm	ϵ_y pm	σ_δ %	σ_t ps	β_x m	β_y m	η_x mm	σ_x μm	σ'_x μrad	σ_y μm	σ'_y μrad
$N_b = 48$	$f_b = 13.0 \text{ MHz}$		$Q_b = 15.3 \text{ nC}$								
0.99	31.9	31.7	0.156	104	4.9	1.9	0.57	12.6	2.5	7.7	4.1
$N_b = 324$	$f_b = 88.0 \text{ MHz}$		$Q_b = 2.3 \text{ nC}$								
0.99	30.0	29.9	0.130	88	4.9	1.9	0.57	12.2	2.5	7.5	4.0
0.10	44.0	4.2	0.132	88	4.9	1.9	0.57	14.7	3.0	2.8	1.5

4-3.7.2 Beam Stability Tolerances

Beam size and angular divergence for the 42-pm preliminary-design lattice are substantially smaller than for the 67-pm conceptual design lattice, and achieving beam stability requirements based on 10% of the beam size will be considerably more difficult to achieve in the vertical plane for flat-beam mode ($\kappa = 0.10$).

For the preliminary design, the horizontal beam stability requirement is based on 10% of the smallest expected horizontal beam size ($\kappa = 0.99$, round-beam mode), while the vertical requirement in microns will remain at the conceptual design values, with 10% of beam size being an operational goal.

Shown in Table 4.72 are the beam stability requirements for the APS-U storage ring. These are stated in terms of AC rms orbit motion from 0.01-1000 Hz and long-term drift (anything slower than 100-second period). It is anticipated that most user applications would be insensitive to orbit motion at higher frequencies [1, 2, 3]. There are, however, certain application areas that are pushing for higher data sampling rates and that orbit stabilization criteria at higher frequencies may need

to be revisited at a later stage.

It remains an open question how orbit stabilization requirements might be impacted should specific use-cases emerge where this is no longer the case.

Table 4.72. Beam stability tolerances at insertion device source points

Plane	AC rms Motion (0.01-1000 Hz)		Long Term Drift (7 Days)	
	Horizontal	1.3 μm	0.25 μrad	1.0 μm
Vertical	0.4 μm	0.17 μrad	1.0 μm	0.5 μrad

A more detailed discussion on beam stability tolerances can be found in the Physics section of this report in section 4-2.2.

4-3.7.3 Sources of Orbit Motion

As has been discussed in section 4-2.2.3, magnet vibration and magnet power supply noise place fundamental limits on the achievable level of beam stability. In addition, mechanical motion of the BPM pickup electrodes/sensors themselves contribute to beam instability in a way dependent on the orbit feedback implementation. Stable air temperature in the accelerator tunnel and diagnostic system electronics racks is critical to minimize long-term drift.

The performance of the orbit feedback system has two dimensions: spatial effectiveness (extent to which the orbit feedback system has access to the spatial modes present in the orbit errors), and closed-loop frequency response. For very low frequencies, the gain of the feedback regulator is essentially infinite, meaning that all disturbances observed on the BPMs are completely removed by the feedback system, in which case *long-term drift in the orbit is defined by the long-term stability of the orbit position measurements.*

4-3.7.3.1 Vibration There are a number of important vibration-related concerns for the APS Upgrade. Mechanical vibration of the multipole magnets will cause orbit kicks. Turbulent flow in the cooling water circuits must be avoided. The design of the support structures is critical in minimizing amplification of ground motion. The APS Upgrade accelerator vibration tolerances have been determined through analysis of the impact of accelerator component motion on the beam orbit, beam position through the ID source points, and the betatron tune (see section 4-2.2.3). Vibration tolerances are distinct from (static) alignment tolerances and are listed in Table 4.14.

The APS Upgrade differs from most storage-ring synchrotron constructions [4, 5], in that it will be built in an existing storage ring tunnel. This decision has some important advantages over a greenfield site when it comes to meeting the vibration tolerances. First, the vibration levels and the effects of on-site and off-site sources can be well characterized. Second, both through the operating history and independent measurement, the APS can be considered a quiet facility, with non-APS researchers measuring daytime vibration levels on the order of 11 nm rms on a 0.08 to 100 Hz bandwidth [6].

Four important areas have been considered:

1. Quantification of the existing storage ring vibration levels and identification/inventory of sources.
2. Mitigation of any vibration sources or problems that are determined to impede meeting the vibration specifications.
3. Design of the magnet, vacuum chamber, and BPM systems and supports such that they meet the vibration tolerances for the existing environment.
4. Testing of subsequent accelerator component designs in the existing APS environment.

Details of vibration studies and planning can be found in section [4-3.4.2](#).

4-3.7.3.2 Temperature Stability The principal thermal effects that impact the APS storage ring and associated technical systems are air temperature stability in the storage ring tunnel and on the mezzanine, and temperature stability of the cooling water for the vacuum chambers. The original specification for tunnel temperature stability was $\pm 1^\circ\text{C}$. This specification has generally been met; however, enhanced accelerator performance (e.g., ultra-low emittance) and a higher level of beamline sophistication make this level of stability insufficient. The goal for MBA is to maintain tunnel air temperature stable within $\pm 0.1^\circ\text{C}$. Major issues and limitations in the original system include the following: air-handling units were designed for a large heating capacity and are unable to provide the fine control now needed; air from the experimental hall is designed to infiltrate the storage ring tunnel, so temperature variations in the experimental hall impact the storage ring; and tunnel air temperature stability is affected by chilled water temperature and outdoor air temperature.

Air temperature stability in the storage ring tunnel at the level of $\pm 0.1^\circ\text{C}$ has been demonstrated at select locations on a 1-week time scale. This followed many incremental improvements over the past several years. This level of stability should be good enough for the APS Upgrade; but it must be achieved throughout the storage-ring tunnel and over time periods of weeks/months, not just in select locations over a period of a week. Conversely, air-temperature stability on the storage-ring mezzanine is not adequate for sensitive electronics, such as BPM electronics, power supply control electronics, etc. Rather than attempting to improve the overall air temperatures in the large volume of the storage-ring mezzanine and experiment hall, internal temperatures of the affected electronics racks will be stabilized where needed.

4-3.7.4 Orbit Feedback System

APS currently uses two orbit correction systems, running simultaneously but independently, and at different sample rates:

- Real-time orbit feedback (RTFB) corrects the global orbit at ~ 1.6 kHz using 160 bpms and 38 fast correctors per plane and has a closed-loop bandwidth of ~ 80 Hz [7][8]. As illustrated in Figure [4.176](#), the RTFB is implemented in a network of 20 ‘local controllers’ housed in VME crates (one crate per two sectors). Each local controller receives data directly from the two nearby sectors of bpms and streams new setpoints to nearby corrector power supplies (two correctors total per plane). RTFB is capable of correcting down to DC, but with only one fast corrector per sector it has limited spatial resolution. Consequently, its frequency response is

intentionally rolled off below a fraction of a hertz, with the second system (Datapool) taking over the lower frequencies and stabilizing the DC orbit.

- Datapool uses several hundred correctors and boms to correct the DC global orbit and compensate low-frequency disturbances. Datapool is built using SDDS tools, and originally ran on a workstation in the main control room with an update interval of several seconds. It has since been ported to an EPICS IOC and runs at 10Hz. The large numbers of correctors and boms give excellent orbit-correction spatial resolution, but the closed-loop bandwidth is limited to ~ 1 Hz, primarily due to transport delays and eddy currents in the thick aluminum vacuum chambers of the slow correctors.

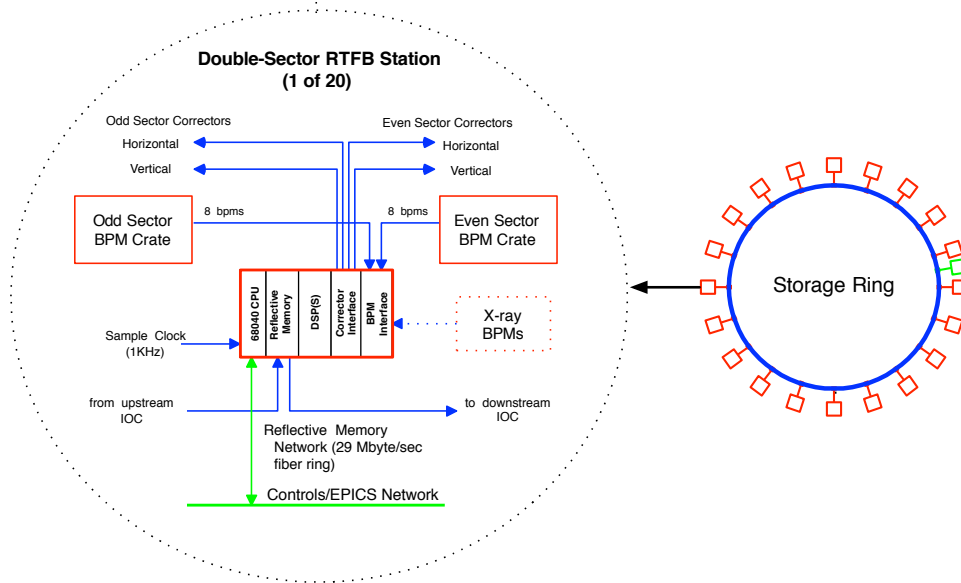


Figure 4.176. Architecture for the present APS RTFB that is the basis of the preliminary design for the APS Upgrade.

Both RTFB and Datapool perform global rms orbit correction, with corrector deltas being computed from the vector of measured bpm deltas using the standard inverse Response-Matrix (RM) transformation:

$$\mathbf{R}^{inv} \cdot \delta \mathbf{p} = \delta \mathbf{c} \quad (4.48)$$

where \mathbf{R}^{inv} is the inverse response matrix, $\delta \mathbf{c}$ is a vector of bpm position errors, and $\delta \mathbf{p}$ is a vector of corresponding corrector deltas that become the error terms in the feedback controller.

Computation of the product of the 38 by 160 inverse response matrix and the 160 by 1 vector of bpm values is partitioned amongst the 20 local controllers, where each local controller computes the product for the rows in the inverse RM that correspond to its local correctors. This partitioning is illustrated in Figure 4.177. The inverse RM is computed off-line and uploaded to the local controllers as vectors of parameters.

The vector of 160 bpm errors is assembled via a reflective memory network. At the start of each RTFB sample tick, each local controller is responsible for reading the current values for its local boms and pushing them to the reflective memory network. Each local controller contributes a total

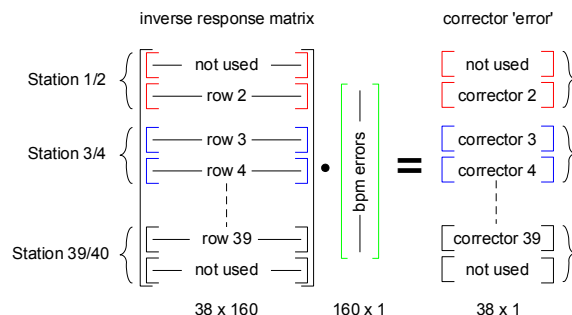


Figure 4.177. Partitioning the inverse-response matrix computations to the local controllers.

of eight bpm values (four per sector), and the complete vector is available once all twenty local controllers have pushed their respective individual bpm values to reflective memory. The frequency responses of all the fast correctors are assumed to be identical, allowing the 38 correctors to be treated as 38 decoupled scalar control loops.

4-3.7.5 APS-Upgrade Fast Orbit Feedback System

The preliminary design for the APS-U fast orbit feedback system (FOFB) uses the same architecture as the present APS RTFB. A feedback controller (FPBC) is located in every odd-numbered sector (20 FBCs total). The feedback controllers receive bpm values from local bpm processors turn by turn, and pushes them to the fast data network for distribution to the 19 other feedback controllers. There are 560 bpm's in total. Every 44.1 μ sec, the feedback controllers read the latest orbit vector from the fast data network and computes and distributes new setpoints to both fast and slow correctors in its double-sector. In total, there are 160 fast (wide-bandwidth) correctors and 320 slow correctors per plane. A block diagram of the feedback controllers is shown in Figure 4.178.

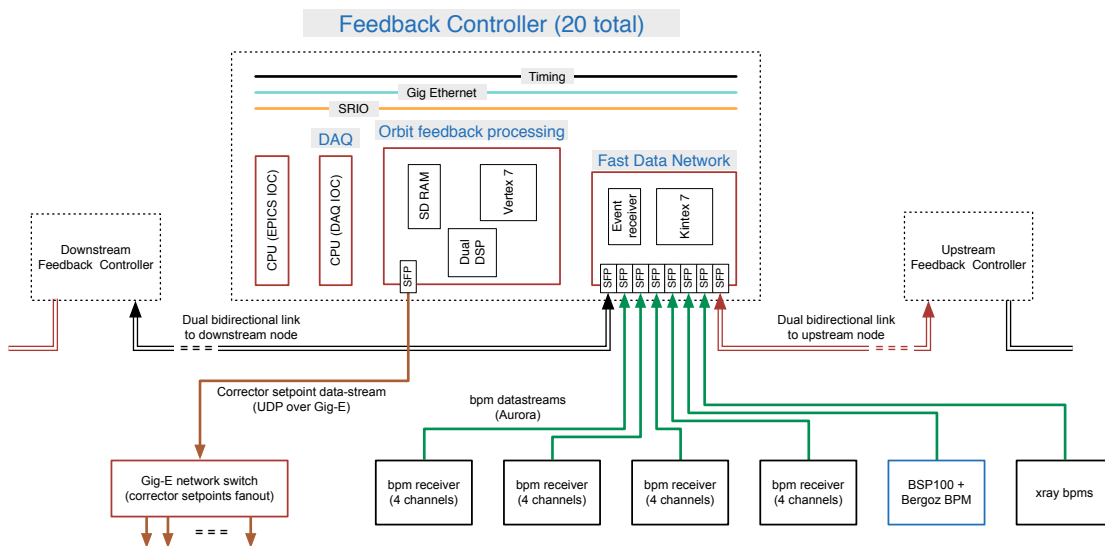


Figure 4.178. Fast orbit feedback controller.

Orbit feedback processing is partitioned between a Virtex-7 FPGA and TMS320-C6678 multi-core DSPs. Serial data interfaces and pre-processing such as bpm turn-by-turn filtering are handled by the FPGA, while the DSPs performs orbit correction computations, feedback control, and ‘tick-by-tick’ data analysis functions. Basing the implementation on a TMS320-series, DSP allows us to benefit from the code and 20 years of code-development for the TMS320-series devices used on the present real-time feedback system (TMS320-C40). There is a factor of 4000 difference in processing performance between the 1980’s C40 DSPs and the modern C6678 device (160 GFLOPS vs 40 MFLOPS).

The most-recent BPM values are streamed turn-by-turn over serial fiber links. There is one link per bpm processor (corresponding to four bpms in both planes).

Setpoints for all 32 (fast and slow) corrector power supplies in the double sector are assembled into a single UDP packet that is distributed over a dedicated gigabit ethernet link to a high-performance ‘cut-through’ network switch for distribution to the 10 corrector power supply controllers in the double sector.

The fast data network links the feedback controller with its upstream and downstream neighbors over dual bidirectional synchronous high-speed serial data links. Together, the interconnection of twenty feedback controllers forms a redundant birectional ring with a maximum of nine ‘hops’ between any one FBC and all others. BPM data is distributed and pushed to DSP local memory every $7.36\mu\text{sec}$.

The DAQ gives access to timestamped synchronous data from all feedback controllers. BPM data is collected turn-by-turn, while other channels are collected once per $44.1\mu\text{sec}$ tick.

The goal for APS-U is to achieve a closed-loop bandwidth of ~ 1 kHz with sufficient spatial resolution to independently control each x-ray source-point. Key differences between the APS-U FOFB and the present RTFB include:

1. Four fast correctors per sector instead of one, which allows independent control of position and angle at every source-point (see Figure 4.179).
2. A single unified orbit feedback system using all fast and slow correctors.
3. An orbit correction sampling rate of 22.6 kHz instead of the present 1.6 kHz.
4. New corrector magnets and power supplies with fast response and wide bandwidth.

Table 4.73 compares the APS-U parameters with the present RTFB/Datapool system.

4-3.7.6 Long-Term Orbit Drift

Limitations on minimizing the long-term orbit drift are entirely reliant on the quality of the measurements of the orbit trajectory through the source points. The orbit feedback system will faithfully track the readings from the beam position monitors, but without further information can do nothing to compensate for any movement of the bpm vacuum chamber. The APS Upgrade preliminary design derives a composite slow readback of beam position from multiple sensors, comprising RF bpms around the ID source-points, photon bpms on the beamline frontend, and mechanical-motion sensors on the rf and photon bpm vacuum chambers. Mechanical motion sensors (MMS) and photon

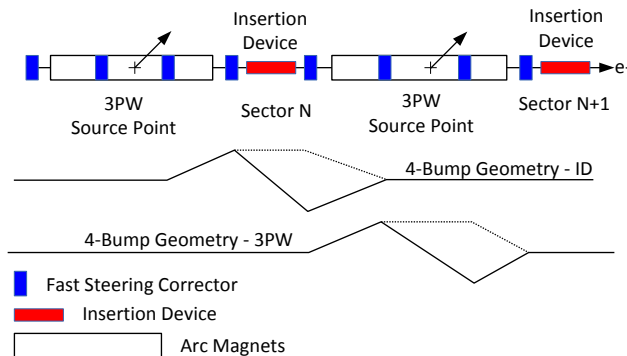


Figure 4.179. Orbit feedback spatial requirements - two correctors between adjacent x-ray source-point are needed to control position and angle independently.

Table 4.73. Comparison of orbit feedback system parameters

Parameter	APS-U	Present APS	
	Unified-RTFB	RTFB	Datapool
Revolution frequency	271 kHz	271 kHz	271 kHz
BPM sample rate	Turn-by-turn	1.6 kHz	10 Hz
BPM orbit vector distribution rate	Turn-by-turn (goal)	1.6 kHz	10 Hz
Fast corrector setpoint update rate	22.6 kHz	1.6 kHz	10 Hz
Rf bpms (per plane)	570	160	360
ID X-ray bpms (per plane)	90	-	50
Fast correctors (per plane)	160	38	-
Slow correctors (per plane)	320	-	300
Closed-loop bandwidth	DC – 1 kHz (goal)	1 Hz – 80 Hz	DC – 1 Hz

bpms are covered in more detail in Section 4-3.8.5.

4-3.7.7 Unified Feedback Algorithm

The unified feedback algorithm, recently developed at the APS [9] allows both ‘slow’ and ‘fast’ correctors to be used in orbit feedback down to DC while still taking advantage of the full available bandwidth of the fast correctors. For DC orbit correction and steering, it is desirable to have all correctors available to participate in correction in order to have as many spatial modes available as possible. For AC orbit motion correction, just the fast correctors are used and there must be a hand-over from using many correctors at DC to using fewer correctors for AC.

In the present APS, this is achieved using a highpass crossover filter to roll off the response of RTFB towards DC, and then Datapool takes over for the lower frequencies. This approach has been used successfully at the APS for more than 15 yrs, there is necessarily a limit to the orbit motion attenuation that can be achieved around the crossover frequency in order to avoid the two systems fighting.

The unified feedback algorithm uses a different approach to isolating the responses. The fast corrector channels are configured for operation down to DC instead of rolling off their low-frequency response, and the inverse response-matrix coefficients are formulated conventionally. The slow-

corrector channels are also (still) configured for operation down to DC, but their inverse response-matrix coefficients are generated using a modified formulation, where the fast corrector channels are treated as if they respond instantaneously. This forces the spatial modes of the slow corrector channels to be orthogonal to all spatial modes of the fast corrector channels. As a result, the two systems can both operate down to DC without fighting.

The unified feedback algorithm has been tested with the present APS User operations selection of bpms and correctors for both RTFB (@ 1.6 kHz) and Datapool (@ 10 Hz). Figure 4.180 compares the closed-loop step responses of standard Operations mode with frequency overlap compensation with unified mode where both RTFB and Datapool correct down to DC. The settling times for both RTFB and datapool correctors are several times shorter than for standard mode.

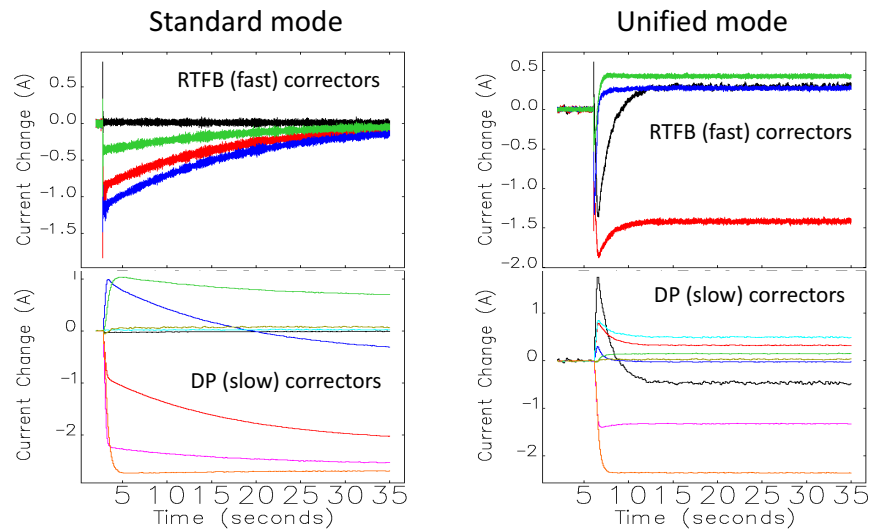


Figure 4.180. Transient responses of RTFB+Datapool in standard mode (left) and in unified mode (right). Datapool updates at 10 Hz, RTFB updates at 1.6 kHz.

Tests of unified mode at 22.6 kHz sampling rate were performed during the APS-U orbit feedback prototype tests at Sector 27 (see Section 4-3.7.10).

4-3.7.8 Fast Corrector Magnets

A prototype fast corrector magnet has been developed at Brookhaven. As yet there are no beam-based tests with the prototype magnet in place, but the frequency response has been measured in the magnet-measurement facility at the APS and are included here for reference purposes. Figure 4.181 shows the measured small-signal transfer function of the magnetic field inside the vacuum chamber with respect to magnet current. Amplitude is shown on a linear scale normalized to the amplitude at 1 Hz.

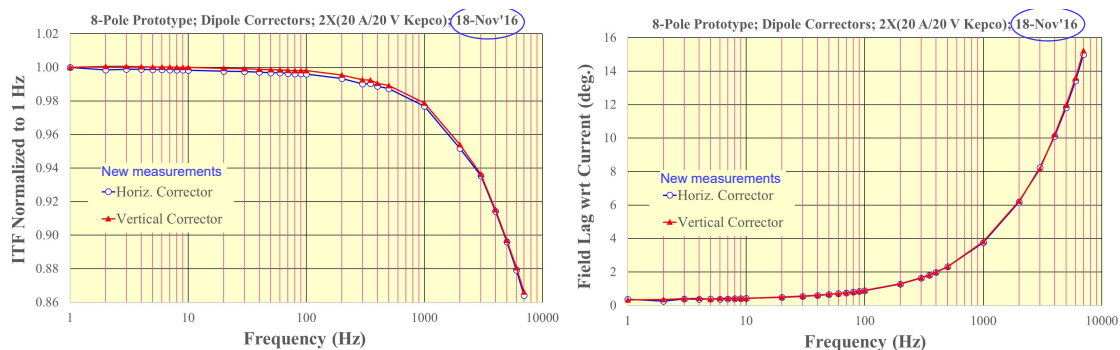


Figure 4.181. Fast corrector prototype: measured amplitude (left) and phase responses (right) of the magnetic field inside the vacuum chamber.

4-3.7.9 Prototype Development and Testing - ‘4x4’ tests

A prototype feedback controller was developed for the APS-U beam stability R&D at Sector 27, in order to demonstrate the functionality of one of the twenty nodes shown in Figure 4.178. The controller prototype is built around a commercial high-performance DSP/FPGA processor (Commagility AMC-V7-2C6678).

The Sector-27 ‘4x4’ tests used a single 4-channel Libera Brilliance+ bpm processor together with four existing fast corrector power supplies and setpoint data links. Orbit correction operated at the full 22.6 kHz rate. A signal-flow diagram for the 4x4 test is shown in Figure 4.182. Figure 4.183 shows the signal-flow implementation on the processor board.

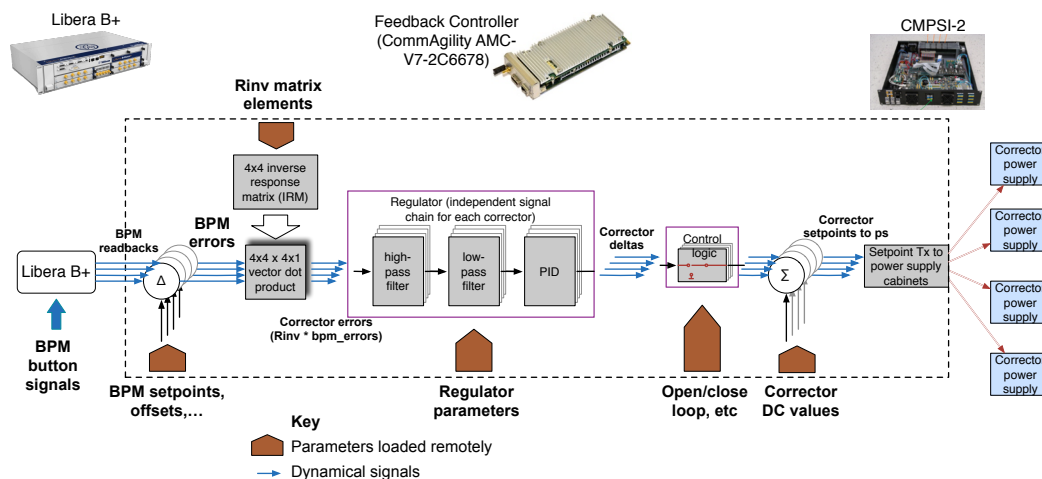


Figure 4.182. Feedback-controller signal flow diagram for the S27 ‘4x4’ tests.

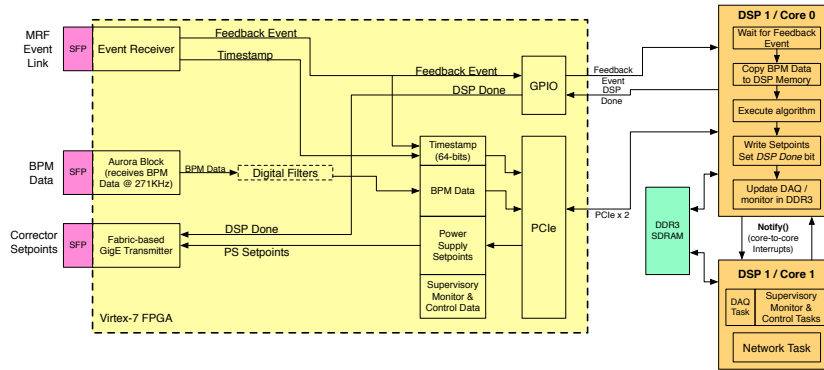


Figure 4.183. FBC signal flow hardware implementation for the S27 ‘4x4’ tests.

The main objective of the 4x4 tests was to demonstrate orbit feedback operation at 22.6 kHz and show the corresponding performance improvement over the present system running at 1.6 kHz. The performance improvement was demonstrated by comparing the transient responses. Both the RTFB (existing system) and S27 4x4 prototype were configured for ‘local bump’ orbit feedback, each in different sectors of the storage ring. With both systems running closed-loop, a global orbit disturbance was generated by applying a step change in current to one of the unused fast correctors. This allowed simultaneous measurement of the responses of the two systems to the same identical disturbance. Figure 4.184 shows the transient responses of the two systems. The symbols in the plots correspond to individual datapoints. The response time for the S27 prototype running at 22.6 kHz is a factor four faster and the peak amplitude of the disturbance is 30% lower than for RTFB running at 1.6 kHz.

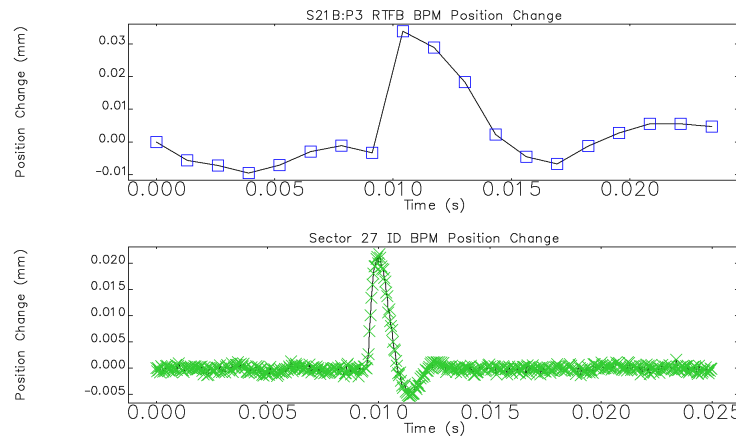


Figure 4.184. Closed-loop transient responses to the same disturbance. Top: RTFB at 1.6 kHz; Bottom: S27 4x4 prototype at 22.6 kHz. The symbols correspond to individual datapoints.

4-3.7.10 Prototype Development and Testing - ‘16x8’ Integrated Tests

A principle objective of the 16x8 tests was to demonstrate operation of a single feedback controller at 22.6 kHz with a representative configuration and numbers of correctors and bps. Main components

of the tests were: four Libera Brilliance+ bpm processors (16 bpms total); four (fast) correctors driven by newly-developed prototype fast corrector power supplies and setpoint links; and four (slow) correctors driven by existing corrector power supplies and links. The full layout of the 16x8 test is shown in Figure 4.189.

4-3.7.10.1 Unified feedback algorithm at 22.6 kHz correction rate In Section 4-3.7.7 the unified feedback algorithm was described, and the performance compared with standard mode using RTFB and Datapool. Shown in Figure 4.185 is the response of the S27 prototype FOFB in unified mode with four fast and four slow correctors, all receiving setpoints from the S37 FOFB prototype at 22.6 kHz. The speed of recovery should be compared with that of RTFB + Datapool, which was shown in Figure 4.180. The setting time is improved by about a factor four over that of the RTFB+Datapool combination.

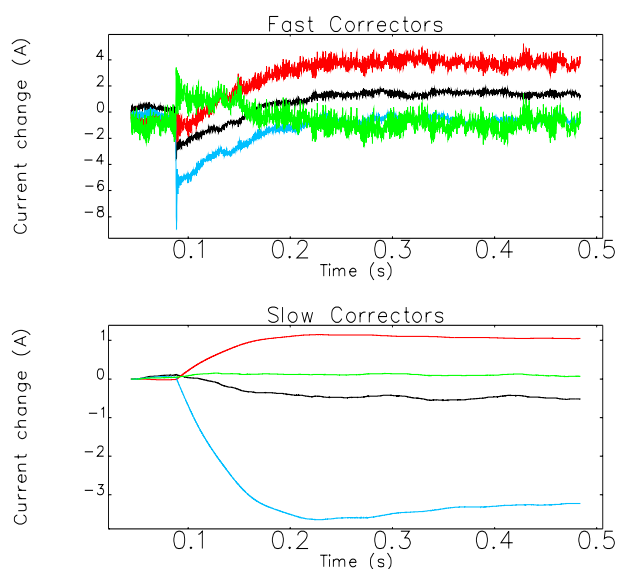


Figure 4.185. Response of correctors to a $50\mu\text{m}$ angle bump for unified mode. Both ‘fast’ and ‘slow’ correctors receive their setpoints at 22.6 kHz.

4-3.7.10.2 Fast corrector latency and response time Orbit-feedback specific specifications for the fast corrector power supplies were a small-signal bandwidth of 10 kHz and a maximum latency of $10\mu\text{sec}$ for the setpoint datastream. Compliance with the specifications has been demonstrated through a combination of bench tests (section 4-3.5.5) and beam-based measurements during the 16x8 tests.

Figure 4.186 shows the measured responses of the orbit to step changes in setpoints to four different correctors with the original and the new prototype power supplies. The horizontal axis shows the individual $44\text{-}1\mu$ ‘ticks’ in the feedback controller. Time ‘zero’ is the discrete time step when the setpoint was sent to the power supply. The limitation on risetime with the new prototype power supplies is the corrector magnet itself, which was the same for both tests.

A more precise, albeit indirect, measurement of the setpoint latency was obtained from timing

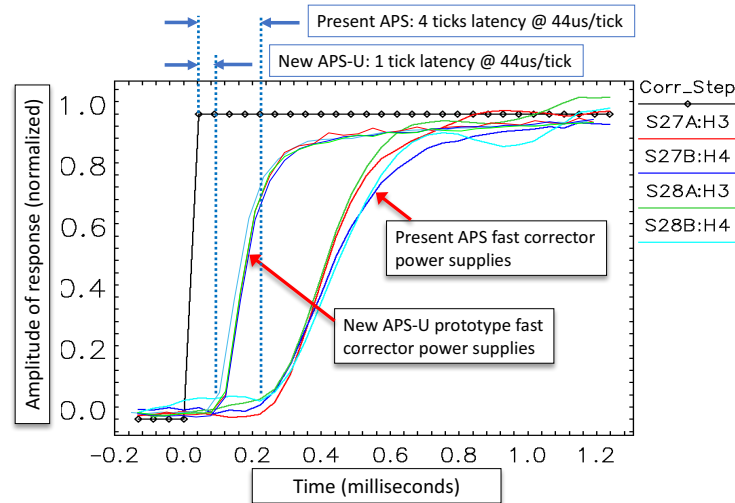


Figure 4.186. Open-loop step responses of a new fast corrector prototype with that of the present RTFB. Both latency and rise-time have been improved.

measurements of the code execution times in the feedback controller and a measurement of the end-to-end latency. Figure 4.187 shows the execution times for the 16x8 tests with the new prototypes. The end-to-end latency is obtained by measuring the arrival-time of the setpoint at the power supply relative to the start of the $44.1\mu\text{sec}$ tick. The setpoint transport latency inferred from this measurement is $6.1\mu\text{sec}$.

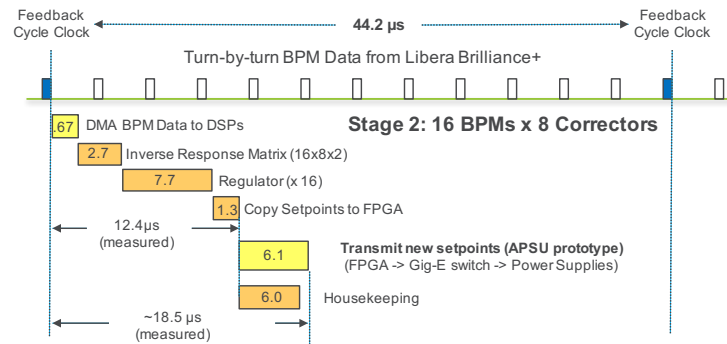


Figure 4.187. Execution time measurements for the '16x8' test using new prototype power supplies.

4-3.7.10.3 Closed-loop orbit correction bandwidth With prototype fast corrector power supplies installed in all four fast-corrector locations in Sector 27/28, we have achieved closed-loop unity-gain bandwidths of 700 Hz. Resulting improvements in cumulative rms orbit motion for the horizontal plane are shown in Figure 4.188.

4-3.7.10.4 Feedback controller processor comparisons The hybrid DSP/FPGA implementation was selected for the Conceptual Design phase over an all-FPGA implementation. Experience

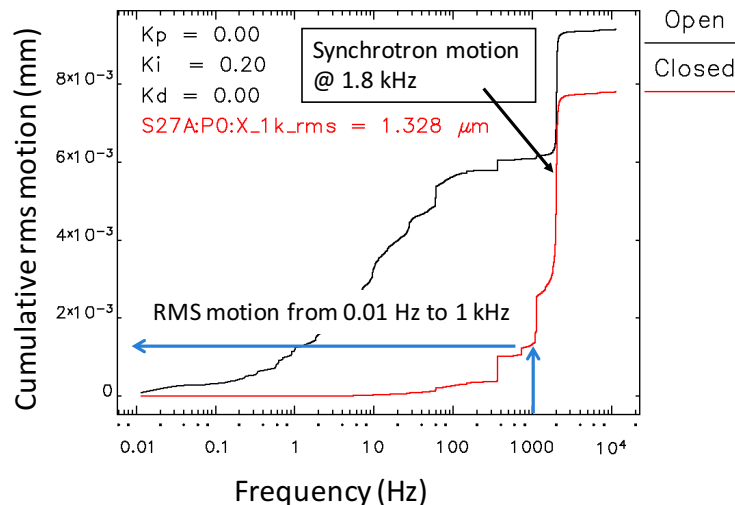


Figure 4.188. Cumulative horizontal-plane RMS beam motion measured at Sector 27 with unified feedback running at 22.6 kHz.

Table 4.74. Implementation and processor comparisons

Parameter	Present RTFB	S27 '4x4'	S27 '16x8'	APS-U FOFB ⁽¹⁾
BPM processing rate	1.6 kHz	22.6 kHz	Turn-by-turn ⁽²⁾	Turn-by-turn ⁽²⁾
Corrector ps setpoint rate	1.6 kHz	22.6 kHz	22.6 kHz	22.6 kHz
Orbit feedback processing:	C40 ⁽³⁾ (40 MFLOPS) -	C6678 ⁽³⁾ (320 GFLOPS) Xilinx Virtex-7	C6678 ⁽³⁾ (320 GFLOPS) Xilinx Virtex-7	C6678 ⁽³⁾ (320 GFLOPS) Xilinx Virtex-7
Platform	VME	microTCA	microTCA	microTCA
Node-to-node links	Reflected Memory (29 Mbyte/sec)	-	LBNL design (5 Gbit/sec)	LBNL design (>5 Gbit/sec)

⁽¹⁾FOFB = Fast orbit feedback system

⁽²⁾Turn-by-turn rate is 271 kHz

⁽³⁾Texas Instruments TMS320 series

with the prototype feedback controller has been strong validation that the hybrid DSP/FPGA is the right approach for this project at this time. Table 4.74 compares implementation of the FOFB preliminary design for APSU with those of the 4x4 and 16x8 tests and of the original RTFB.

4-3.7.10.5 Summary

1. We have demonstrated closed-loop orbit feedback at 22kHz (highest of any light-source so far)
2. We have demonstrated a new unified algorithm that combines slow and fast correctors
3. We are right at spec for AC stability for vertical and below spec for horizontal (400 nm and 1700 nm respectively)

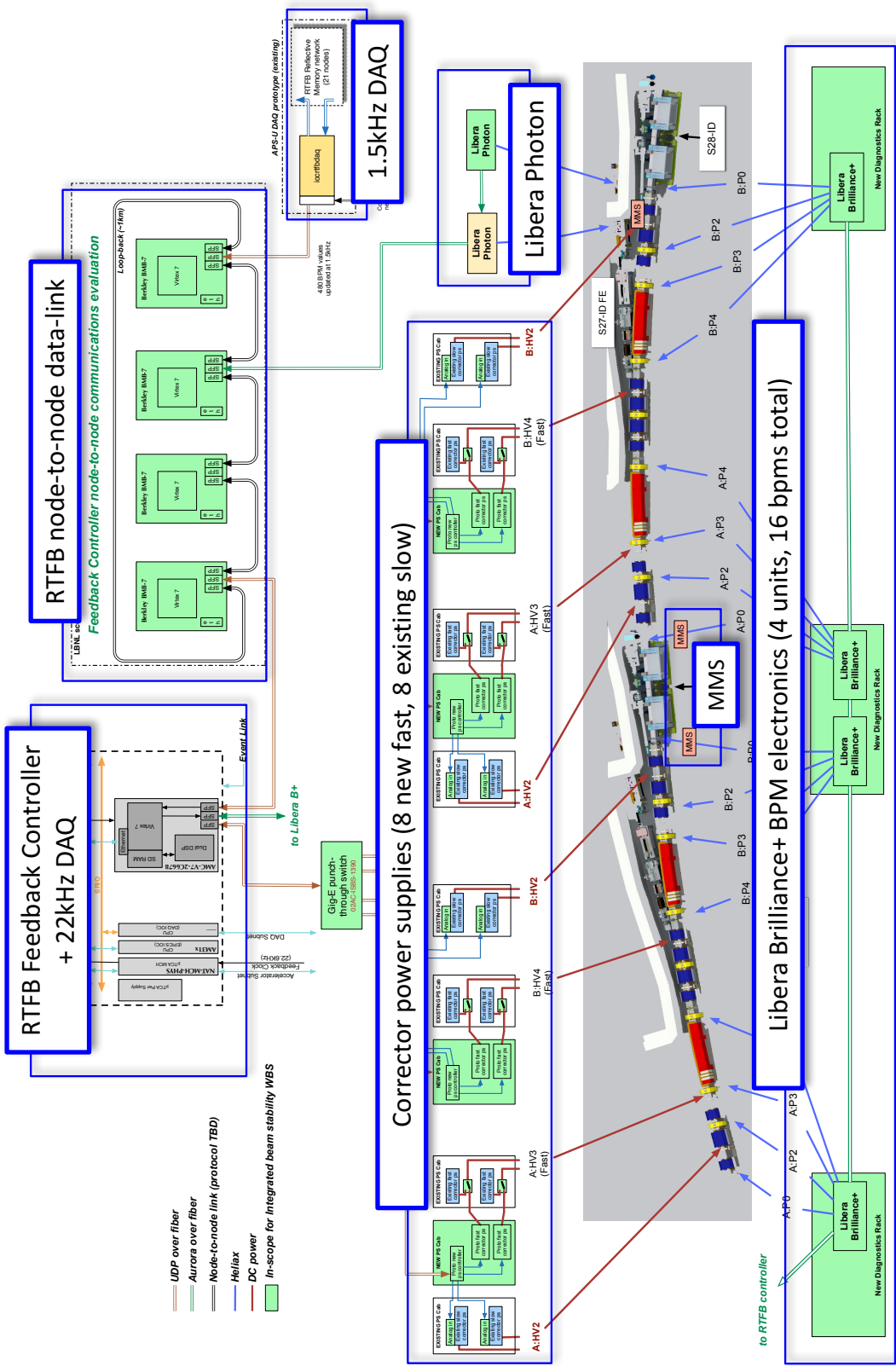


Figure 4.189. Hardware configuration for the S27 '16x8' integrated beam stability tests.

References

- [1] J. Carwardine et al. *Five-year plan for APS beam stabilization*. 2005. URL: https://icmsdocs.aps.anl.gov/docs/groups/aps/documents/report/aps%5C_1192147.pdf (cit. on p. 220).
- [2] L. Young and M. Borland. *Email exchange related to beam motion and emittance increase*. APSU_1426487. 2011 (cit. on p. 220).
- [3] O. Singh and G. Decker. “Beam Stability at the Advanced Photon Source.” In: *Proc. of PAC 2001*. 2001, pp. 3268–3270 (cit. on p. 220).
- [4] *NSLS-II Preliminary Design Report*. Tech. rep. Brookhaven National Laboratory, 2007. URL: <http://www.bnl.gov/nsls2/project/PDR/> (cit. on p. 221).
- [5] *MAX-IV Conceptual Design Report*. Tech. rep. MAX IV Laboratory (cit. on p. 221).
- [6] Various authors. *Compilation of ground motion measurements*. Tech. rep. Webpage compilation of world-wide accelerator vibration measurements, as made by DESY researchers. DESY, 2003. URL: <http://vibration.desy.de> (cit. on p. 221).
- [7] J. Carwardine and F. Lenkszus. “Real-Time Orbit Feedback and the APS.” In: *BIW98 AIP Conference Proceedings 451*. 1998, pp. 125–144 (cit. on p. 222).
- [8] Y. Kang, G. Decker, and J. Song. “Damping Spurious Harmonic Resonances in the APS Storage Ring Beam Chamber.” In: *Proc. of PAC 1999*. 1999, pp. 3092–3094 (cit. on p. 222).
- [9] N. Sereno and J. Carwardine. *Unified Formulation of Orbit Feedback Using Slow and Fast Correctors*. Tech. rep. DIAG-TN-2014-012. Nov. 2014 (cit. on p. 226).

4-3.8 Diagnostics

4-3.8.1 Diagnostic Systems Overview

Diagnostics for the MBA lattice will feature major upgrades to rf and x-ray bpm systems, a new beam size monitoring system, and updates to many existing legacy systems already installed in the storage-ring, as summarized in Table 4.75. The largest systems are the rf and x-ray bpps, with the significant addition of a mechanical motion sensing system to correct for long-term drift and low frequency chamber vibration. The bpm and mechanical motion systems will be used together with a new realtime orbit-feedback system with a factor of 10 higher closed loop bandwidth and integration of both slow and fast correctors into the feedback algorithm. Legacy systems, such as current monitors and the multi-bunch feedback system, will be updated to meet requirements.

Steering through the centers of the quads will be critical, and requires 12 rf BPMs in the arcs sector. There will be an additional two high-quality rf bpps at the ends of the insertion device (ID) straight sections, and three for canted undulator straights, and two additional hard-x-ray bpps and associated x-ray intensity monitors in each high-heat-load front-end. The first optic enclosure exit mask outside the shield wall will be similarly instrumented for flux and white beam position monitoring. Canted undulator beamlines will have four x-ray bpps in their front-ends.

Table 4.75. MBA diagnostic systems

Diagnostic System	Quantity/Sector	Total
Arc rf bpps	12	480
ID rf bpps ([A,B]:P0)	2	80
Canted ID rf bpps (C:P0)	1	10
ID x-ray bpm electronics (non-canted)	2	50
ID x-ray bpm electronics (canted)	4	40
ID x-ray-intensity monitor	2	70
BM x-ray bpm electronics	2	52
Mechanical-motion systems	1	35
Beam-size monitors		3
Fast orbit-feedback system		1
Transverse multi-bunch feedback system		1
Current monitors		2
Bunch-current monitor		1

The in-tunnel x-ray diagnostics components and their electronics are considered part of the front-end. One RF cavity section (A:M1 source) will be used for a high-resolution absolute beam-size diagnostics to measure the achieved emittance in both x- and y-planes. One additional RF cavity section and one BM front end will be used for relative beam-size monitors to provide fast beam-size data for automated feedback control of beam sizes in x- and y-planes. A mechanical motion sensing system comprising hydrostatic-level sensors, capacitive proximity-sensors and perhaps other monitors will be needed to assure long-term beam alignment of the accelerator in relation to the beamline axis. The mechanical motion system will monitor the position of rf bpm straddling the ID vacuum chambers and x-ray bpps in the associated front-ends.

The following existing storage ring systems will be upgraded to satisfy MBA requirements:

- A fast multi-bunch transverse feedback system will be required in order to increase beam lifetime and monitor betatron tunes.
- Two current-monitors will be required: an average-current monitor and a bunch-current monitor for monitoring the current in individual bunches during swap-out injection.
- A beam-loss monitoring system, adapted from an existing system, will be installed in the storage-ring enclosure for monitoring losses in the high-charge (up to 20 nC/pulse) bunches coming from the injector.

4-3.8.2 RF Beam Position Monitors

RF bpms provide the primary measurement of the electron beam trajectory through the insertion device (ID) straight sections and in the storage ring arcs. Each sector will contain 12 bpms in the arcs and 2 additional rf BPMs at the ends of the ID straight section. Canted sectors will require an additional BPM between insertion devices. In cases of canted ID straights, an additional bpm may be installed between insertion devices depending on cost, needs and technical feasibility. The baseline design utilizes 410 high-resolution BPMs with commercial electronics. The less critical locations will re-use 160 existing BPM processors from the present APS storage-ring. The plan also includes the installation of 40 new shielded EMI cabinets for BPMs, and feedback electronics, and new heliax cables.

The new BPM assembly has been designed in coordination with the vacuum design group[1]. The BPM assembly features integrated shielded bellows on both flanges and pick-up electrodes that are welded to the stainless steel body. The button electrodes are 8 mm in diameter and the vacuum chamber is 22 mm in diameter.

The bellows-isolated BPM assembly shown in Figure 4.190 has been designed and simulated. The electromagnetic performance for full BPM assembly was simulated with CST Microwave Studio. The simulations indicate an overall power dissipation for the BPM assembly of 0.42 watts when the design 48 bunch and 200 mA beam parameters are used for excitation. The ASD/AOP group also simulated this assembly using Gdfidl and found good agreement in power dissipation estimates. Power dissipation is a critical parameter that will be studied and measured when beam testing is conducted.

The first prototype BPM electrodes are shown in Figure 4.191. A rigorous plan to test prototype BPM electrodes is planned for the fall of 2017. The new machine will require 570 BPMs and each BPM requires four button electrodes totaling 2,280 button electrodes. BPM prototypes from two vendor sources are being evaluated. The BPMs have been electrically and mechanically tested and inspected. The unit shown below was tested using a Time Domain Reflectometer (TDR) where a fast pulse is injected into a test port and the reflected power and time of arrival is measured. The results of the TDR test were in good agreement with the simulated data shown in Figure 4.192.

We will install four prototype buttons in a test vacuum chamber in the APS storage-ring in September 2017. This test will be a significant milestone for qualifying the rf BPM button design in the APS storage ring.

In order to achieve the beam stability goals, low noise BPM electronics are essential. APS-U has opted to use commercial BPM electronics for preliminary design that meet the demanding beam

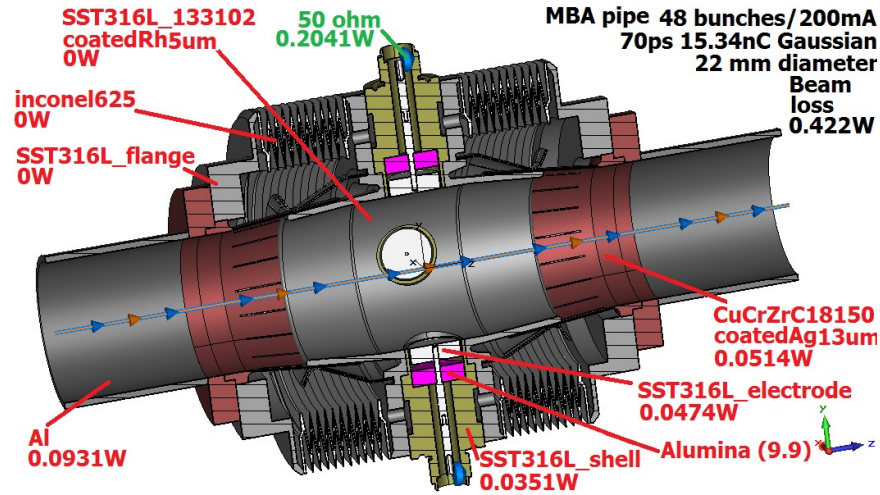


Figure 4.190. MBA BPM assembly cross-section.

stability requirements shown in Table 4.72. Each BPM processor, as shown in Figure 4.193, consists of four channels of BPM button electrode inputs, a timing module, Software/EPICS IOC, Fast data stream (FDS) packet structure, and a Gigabit Data Exchange (GDX) module for interfaces to the feedback controller (FBC) and machine protection interlock [2].

The commercial electronics are based on FPGA technology similar to those used at several other light sources around the world [3]. The new BPM architecture features digital signal processing which enables improved long-term stability in addition to low noise fast data acquisition for orbit feedback. Turn by-turn (TBT) and analog-to-digital (ADC) buffered data is available on demand for machine studies. The electronics consist of four processing modules: a fast ADC module with 16-bit resolution running at 108 MHz; an interconnection board that performs all the control actions for all modules in the chassis; a timing module (TIM) that performs synchronization and distribution of clocks and trigger signals to all modules in the chassis; and a Gigabit Data Exchange (GDX) module that provides fast data links for orbit feedback, controls TBT DAQ, and the beam mis-steering interlock. There will be 35 interlocks, or one per ID. The interlock is a separate FPGA processor that takes as input bpm data and insertion device gap switch position and has an output to the machine protection system (MPS).

The (GDX) module provides fast links for filtering and transmitting TBT fast acquisition data to the orbit feedback system. The GDX board also has a dedicated user area for implementation of customized processing such as filtering. The GDX provides TBT streaming data to an external data acquisition system (DAQ) and the beam mis-steering interlock. When the beam angle exceeds a user specified limit, the interlock trips the MPS system and the beam is dumped.

The commercial BPM processors show excellent noise performance, approaching $2 \text{ nm}/\sqrt{\text{Hz}}$, and long-term stability at the level of 200 nm peak-to-peak over a 24-hour period [3]. The commercial BPM processors satisfy the APS-U's long-term and AC beam-stability requirements [4] as measured in the APS storage ring and extrapolated to APS-U BPM design.



Figure 4.191. MBA BPM electrodes.

4-3.8.3 X-ray Beam Position Monitors

To improve the measurements of the ID photon beam trajectories, each ID beamline front-end includes a high-power grazing-incidence insertion device x-ray beam position monitor (GRID-XBPM) and associated intensity monitor to provide more direct measurement of the photon beam trajectories for slow orbit control at the ID source points [5]. Measurements of mechanical motion of the RF bpm and GRID x-ray bpm vacuum chambers will allow correction of the locations of the bpm sensors from temperature variations or ground settlement using an offset subtraction scheme.

The GRID-XBPM system, which is based on hard x-ray fluorescence, will provide users with much better beam stability than the present legacy photoemission-based system. The photoemission system suffers from systematic offsets due to the soft radiation emitted by bending magnet fringe fields and multipoles. Compensation of these offsets requires an involved feedforward scheme, resulting in correction only at the level of tens of microns.

The next generation XBPM systems are based on hard x-ray fluorescence from copper for high heat load front ends (HHLFE) and hard x-ray Compton scattering for canted undulator front-ends (CUFE) that have lower power density. These upgrade XBPMs are only sensitive to positions of hard x-rays at the core of the undulator beam and have much smaller systematic offsets. Two GRID-XBPM systems were installed in 27-ID and 35-ID front ends in May 2014. After commissioning, the unit in 27-ID has been utilized in the orbit feedback controls for two years and meets APS-U long-term performance requirements. The unit in 35-ID has been used as a test platform for readout detectors development. The development of Compton XBPM has made significant progress: A prototype has been fully tested in a 24-ID first optics enclosure with satisfactory results. It was moved into a 26-ID front end in May 2017 and is being tested with two inline undulators. Commercial FPGA-based x-ray bpm processing electronics are under evaluation to determine their

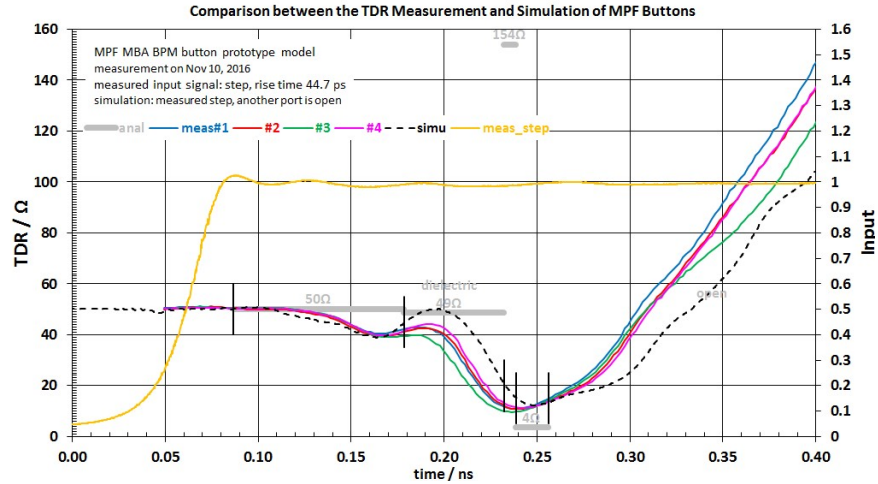


Figure 4.192. MBA BPM button assembly TDR data.

suitability for high resolution GRID and Compton XBPMs. The in-house designed BSP-100 [6] modules and current amplifiers will be used for intensity monitoring in ID beamlines. BSP-100 modules and current amplifiers will be also used for XBPMs in all BM beamlines, including user beamlines and in-tunnel beam size monitors.

4-3.8.4 Beam Size Monitor (BSM)

We plan to build one absolute beam size monitor for reliable emittance measurements and two relative beam size monitors for automatic feedback control of beam emittance and for measurements of beam energy spread. Table 4.76 summarizes the available sources for the APS-U beam size monitors. The tabulated data shows: (1) The most suitable source for the emittance measurements is the A:M1 source, accessible from all ID ports. Its horizontal size is determined by the beam emittance with negligible contribution from the energy spread. Its vertical beam size is three times as large as that of the 3PW source, advantageous for vertical coupling measurements. Finally, the A:M1 source sizes are proportional to the ID source sizes used by most APS users. (2) The most suitable source for the beam energy spread measurements is the three-pole wiggler (3PW). Its horizontal size is dominated by the product of the dispersion and the beam energy spread. The contribution from the horizontal emittance is only a small perturbation. (3) The bend magnet source B:M3 is between the previous two. It is not optimized for either emittance nor beam energy spread measurements, but sufficient for relative beam size measurements. Its advantage is the ease of access from many unused BM front ends.

To avoid competing for precious insertion device real estate, we will use two ID ports in the RF sectors (No. 36 - 40), or more precisely AM ports, one for absolute beam size monitor (ABSM) and the other for relative beam size monitor (RBSM). The large vertical beam size is highly beneficial for relative BSM to provide stable coupling information. We will also use one BM port to take light from the B:M3 source and measure the beam energy spread (absolute horizontal beam size), and relative changes of horizontal and vertical beam sizes. While the relative BSM beamlines will be entirely contained in the tunnel, the absolute BSM beamline will be extended into the experimental floor by drilling through the tunnel wall, and building a shielded station on the experimental floor. The



Figure 4.193. Commercial BPM processing electronics.

extension is necessary for suitable optical magnification and adequate space for monochromators and high-resolution imaging detectors.

Table 4.77 lists the lattice functions and expected e-beam sizes at the A:M1 source points. During normal operations, the beam sizes are between $7\ \mu\text{m}$ and $25\ \mu\text{m}$. We need to develop absolute beam size monitors with $3.2\ \mu\text{m}$ rms resolution with a possible future upgrade to support low-coupling studies and operations. The required resolution for the absolute beam size monitor is defined by the criterion that the increase of measured beam sizes due to finite imaging resolution should not exceed 10% of the actual beam sizes: $\sqrt{\sigma_e^2 + \sigma_r^2} < 1.1\sigma_e$, where σ_e and σ_r are the rms e-beam size and monitor resolution, respectively. To support an automatic feedback system for stabilizing beam sizes, we also plan to develop relative beam size monitors with $7\ \mu\text{m}$ rms resolution, which provide stable, adequate signals for feedback system with the bandwidth of 1 Hz or better. Table 4.78 summarizes the beam size monitor resolution requirements. In the following subsections, we will describe the designs of the beamline on the ID ports. The design of the BM relative BSM beamline will differ only slightly.

The angular exit aperture of the APS-U ID port is 1.5 mrad on each side of the insertion device axis, with respect to the nominal ID source point. Since the B:M1 and A:M1 sources are further upstream and downstream from the ID source point, respectively, the actual accessible radiation fan from A:M1 is over 3-mrad wide on the inboard side, and the fan from B:M1 is about 1-mrad wide on the outboard side. The first optical elements of the relative BSM will be a $50\ \mu\text{m}$ tungsten foil mounted on a water-cooled copper frame located 10 m from the ID source point on the M2 magnet chamber. This foil has three imaging apertures spanning from -0.9 mrad to -0.5 mrad on the inboard side and one imaging aperture on the outboard side of the beamline axis. The first optical elements of the absolute BSM will be a $25\ \mu\text{m}$ tungsten foil mounted on a water-cooled copper frame located 10.25 m from the ID source point. This foil has three imaging apertures spanning from -1.5 mrad to -1.1 mrad on the inboard side of the beamline axis. Table 4.79 summarizes the dimensions and

Table 4.76. Electron Beam Sizes in APS-U Storage Ring Sources

Source	3PW	B:M3	A:M1.1	ID (ref)
Access port	BM	BM	ID	ID
Observation angle in beamline (mrad)	0.0	-2.2	-1.5	0.0
Horizontal beta functions (m)	1.30	0.70	1.63	4.94
Vertical beta functions (m)	2.44	4.85	19.85	1.89
Horizontal dispersion (mm)	7.1	3.1	0.26	0.57
Energy spread in Timing Mode (%)	0.156	0.156	0.156	0.156
Horizontal emittance in Timing Mode (pm)	31.9	31.9	31.9	31.9
Horizontal beam size from emittance (μm)	6.4	4.7	7.2	12.5
Horizontal beam size from energy spread (μm)	11.0	4.9	0.4	0.9
Total horizontal beam size (μm)	12.8	6.8	7.2	12.6
Vertical emittance in Timing Mode (pm)	31.7	31.7	31.7	31.7
Vertical beam size for Timing Mode (μm)	8.8	12.4	25.1	7.7
Vertical emittance in Brightness Mode (pm)	4.2	4.2	4.2	4.2
Vertical beam size for Brightness Mode (μm)	3.2	4.5	9.1	2.8

the functions of these apertures. Monochromators and detectors at the end of the beamline will be used to extract beam size information from the pinhole images cast by these apertures.

Table 4.77. Electron Beam Sizes and Monitor Resolution Requirements for A:M1 Source

	Horizontal		Vertical	
	Beta functions at A:M1 source (m)	1.63		19.85
APS-U operating mode	Timing	Brightness	Timing	Brightness
Emittance (pm)	31.9	44	31.7	4.2
Beam size (μm)	7.2	8.5	25.1	9.1
Resolution for 10% error (μm)	3.2	3.7	10.9	4.0

Table 4.78. Beam-size-monitor resolution requirements

Monitors	Absolute beam-size monitor	Relative beam-size monitor
Quantity	One	Two
Port (tentative)	37-ID	40-ID and 32-BM
Resolution	3.2 μm	7 μm
Bandwidth	> 0.01 Hz	> 1 Hz
Notes	Beam-size uncertainty < 10%	Feedback-control of beam sizes

4-3.8.4.1 Relative Beam Size Monitor and X-ray Beam Position Monitor The relative beam size monitor system includes two apertures for emittance monitoring and two beam position monitors for maintaining the alignment of the collimator optics. The monochromators and detectors described in this section are installed in all beam size monitor beamlines.

4-3.8.4.1.1 Relative Beam Size Monitors: Aperture No. 3 & 4 The relative beam size monitors [7] position two detector slits upstream of the 20-keV, fixed-energy monochromator.

Table 4.79. Beam Size Monitor Imaging Apertures

Index	Function	Angle (mrad)	Width	Height	Energy	Beam Size Range
1	XBPM-B	+1.0	0.5 mm	0.25 mm	20.4 keV	($\pm 250\mu\text{m}$)
2	XBPM-A	-0.5	0.25 mm	2.5 mm	20.4 keV	($\pm 250\mu\text{m}$)
3	Vertical relative BSM	-0.7	250 μm	25 μm	20.4 keV	5 - 100 (μm)
4	Horizontal relative BSM	-0.9	25 μm	250 μm	20.4 keV	5 - 100 (μm)
5	X-ray Pinhole	-1.1	25 μm	25 μm	20.4 keV	8 - 100 (μm)
6	Fresnel diffractometer	-1.3	70 μm	70 μm	8.4 keV	4 - 16 (μm)
7	Young's double slits	-1.5	200 μm	2 \times 8 μm	8.4 keV	1 - 5 (μm)

These detector slits and the two imaging apertures form two collimators in the horizontal and vertical planes, respectively. Two detectors, I_{0x} and I_{0y} , will be located upstream of the detector slit assemblies to measure the photon flux passing the imaging slits. Two more detectors, I_x and I_y , will be located downstream of the monochromator to measure the 20-keV photon flux passing through the 10- μm detector slits. Figure 4.194 shows the ratio of the two detector signal intensities (I_{0x}/I_x) as a function of the source size. As we can see from the figure, the smaller the source size, the higher the x-ray flux through the detector pinhole, and the lower the ratio I_{0x}/I_x . It is clear that the ratio is sensitive to the source size changes down below 5- μm source size.

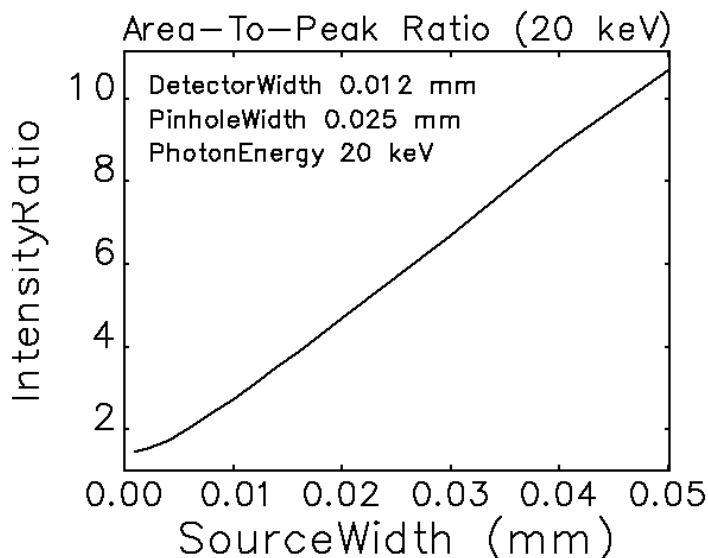


Figure 4.194. Ratio of x-ray flux through a collimator made from two pinhole slits, one 25 μm at 10 m and another 12 μm at 20 m from the source.

4-3.8.4.1.2 Source Position and Beam Angle Monitors: Apertures No. 1 and 2 Since our relative BSM is based on measuring the photon flux through a narrow collimator aimed at the center of the source, the stability of the source positions and beam angles is very important for accurate measurements. We need to monitor in real-time the source positions and beam angles in both planes so the orbit feedback system can keep them stable. Since no mechanical motion sensors are installed in the beam size monitors to compensate for the motion of the storage ring chamber

and the RF beam position monitors, we used x-ray monitors to measure the source position and the beam angles. These monitors are again pinhole cameras: they use two pinholes as the imaging apertures for A:M1 and B:M1 sources, and two quad silicon PIN diodes downstream of the fixed-energy monochromator. When the two source positions are held constant, the alignment of the relative BSMs can be properly maintained.

4-3.8.4.2 Absolute Beam Size Monitors The absolute beam size monitor uses three imaging apertures for an x-ray pinhole camera, a Fresnel diffractometer, and a Young's double slits interferometer. As shown in Table 4.76, the three diagnostics are designed to cover different beam size ranges with sufficient overlap with each other. The monochromator and detectors described in this section for relative beam size monitor are installed in the absolute BSM beamline, and, when the energy spread measurement is needed, also in the BM beamline.

4-3.8.4.2.1 X-ray Pinhole Camera: Aperture No. 5 The x-ray pinhole camera uses 20-keV x-ray photons through the fixed-energy monochromator. The 25- μm square pinhole aperture is optimized for the photon wavelength and the source and imaging distances. Figure 4.195 shows the calculated intensity profiles at 20 keV for RMS source sizes from 4 μm to 20 μm . The profiles can clearly be resolved down to 8 μm . A high-resolution x-ray camera made of thin scintillators and microscope cameras will be used to read out the images and profiles. During normal operations, this camera will be used for measuring vertical profiles. However, both X and Y beam profiles can be useful for characterizing beam instabilities.

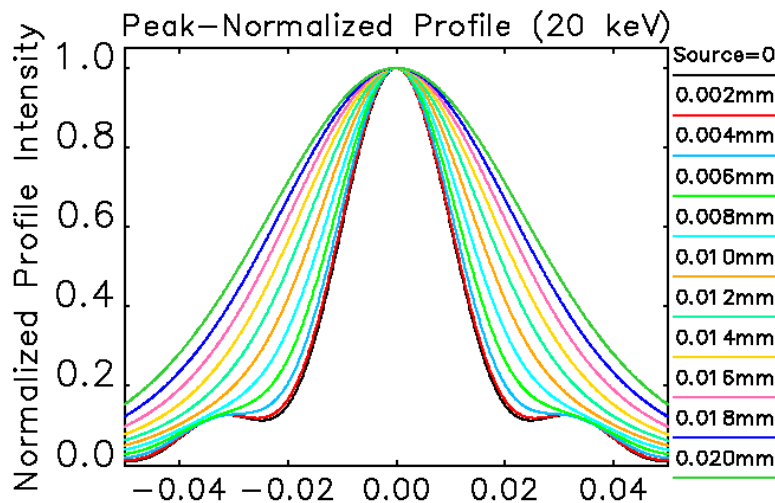


Figure 4.195. Calculated intensity profiles at 20 m from the source from a 20-keV x-ray pinhole camera using a 25 $\mu\text{m} \times 25 \mu\text{m}$ imaging pinhole located 10 m from the source.

4-3.8.4.2.2 Fresnel Diffractometer: Aperture No. 6 The Fresnel diffractometer uses a 70 μm square aperture. At 8.4 keV x-ray energy, it produces a diffraction profile with a minimum at the center. Finite source sizes fill the central valley, the larger the beam size, the shallower the

valley, the higher the central minimum. Figure 4.196 shows the diffraction profiles for beam sizes from $2\ \mu\text{m}$ to $18\ \mu\text{m}$. The change of source size can clearly be resolved between $4\ \mu\text{m}$ and $16\ \mu\text{m}$.

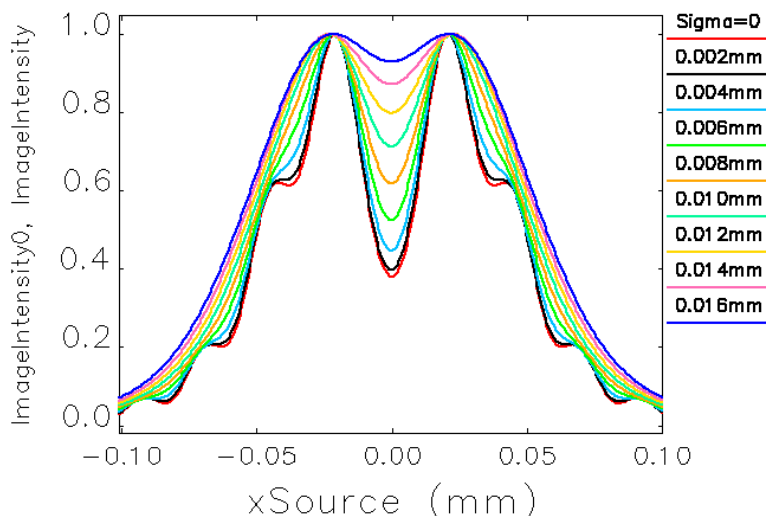


Figure 4.196. Calculated Fresnel diffraction pattern at 20 m from the source from a $70\text{-}\mu\text{m}$ aperture at 10-m, using 8.4-keV x-rays.

4-3.8.4.2.3 Young’s Double-Slit Interferometer: Aperture No. 7 As shown in Table 4.76, the vertical beam sizes may be below $3\ \mu\text{m}$ at the A:M1 for emittance ratio below 1%, and at the B:M3 for emittance ratio below 10%. The Young’s double-slit interferometer [7], using a pair of $8\text{-}\mu\text{m}$ -high slits with $100\text{-}\mu\text{m}$ spacing, can be used to measure the vertical beam sizes. Figure 4.197 shows the diffraction profiles for vertical beam sizes from $1\ \mu\text{m}$ to $7\ \mu\text{m}$. The change of source sizes can clearly be resolved down to $1\ \mu\text{m}$.

4-3.8.5 Mechanical Motion Monitoring

In order to achieve long-term beam stability goals, all sources of mechanical motion of critical in-tunnel beam position monitoring devices must be carefully evaluated and appropriately addressed. Studies conducted at APS sector 27 confirm that the bpm’s move mechanically more than the $1\ \mu\text{m}$ as chamber water [8] and air temperature and beam current change. To quantify this type of motion for the APS accelerator tunnel and experiment hall floor, a prototype system based on capacitive detectors and hydrostatic levels has been developed, as shown in Figure 4.198 [8, 9]. This system will be used to correct for bpm mechanical motion in the orbit feedback system.

The Mechanical Motion System (MMS) has provided design insight for the vacuum chamber and beam position monitor supports. The MMS shown in Figure 4.198 consists of very sensitive non-contact capacitive detectors mounted on extremely low expansion super Invar rods. Capacitive detection is a very sensitive technique for detecting small displacements. It works by detecting the change in impedance of a parallel plate capacitor as the spacing or area changes. Two conducting electrodes are formed by the vacuum chamber [10] and detector separated by about 500 microns. Any change in the capacitance, due to a change in its area or spacing, is demodulated and converted

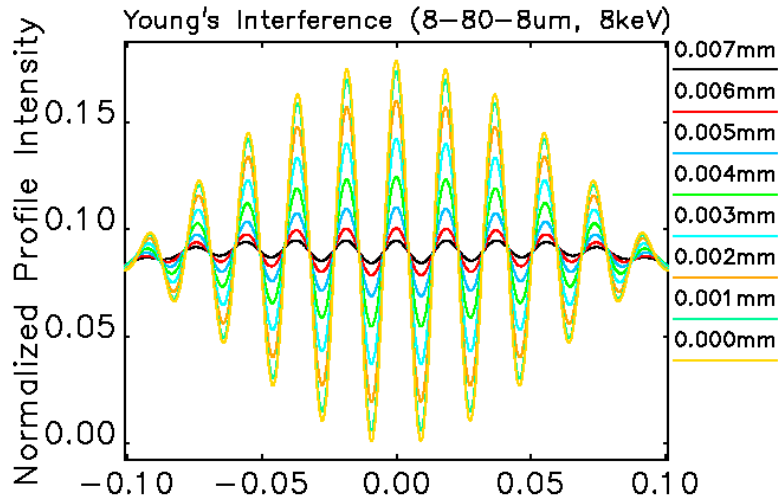


Figure 4.197. Calculated 8.4-keV x-ray interference pattern at 20 m from the source from a Young's double slits with two 8 μm slits at spacing of 100 μm located at 10 m from the source.

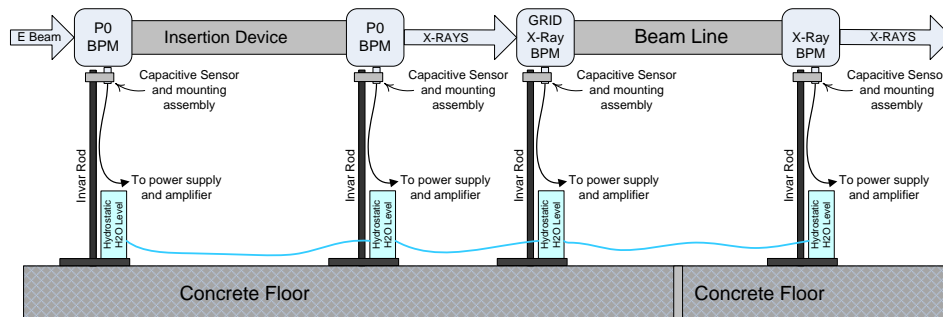


Figure 4.198. Capacitive and hydrostatic level mechanical motion monitoring for both ID vacuum chamber and GRID X-ray BPM support.

to DC. Capacitance detection has the advantage of very high position resolution (10 nanometer), zero hysteresis, zero power dissipation at the point of measurement, high linearity (0.01% is possible), insensitivity to crosstalk, simplicity, and the ability to be made from very stable materials, such as Invar. We are using commercial electronics, which is a multi-channel measuring system that is modular [11]. The controller can support up to four synchronized channels with an integrated Ethernet interface. The capacitive detection system will monitor movement of the BPM relative to the floor directly below.

A Hydrostatic Leveling System (HLS) complements the capacitive BPM motion detection system shown in Figure 4.198. In the baseline design, the HLS measures the relative ground motion between the two insertion device (ID) rf BPMs and the GRID X-ray BPM location in the APS accelerator tunnel. The fundamental principle of the HLS [12] is that any fluid seeks its own level. Given four reservoirs connected by a half full pipe or tube, the fluid level in each reservoir will be at the same absolute elevation, determined by the balance between gravity and air pressure. For small systems, the absolute elevation can be relative to some reference such as mean sea level. For larger

systems, the curvature of the earth and other gravitational effects need to be considered. Given a reference point, such as the bottom or top of the housing, the relative level of the fluid will vary as the sensor is moved up or down with respect to all the other sensors. The new electronics used for the capacitance sensing system will be similar for the HSL system with some minor modifications.

The upgrade will require instrumenting 35 IDs BPMs and 35 X-ray BPMs for 280 channels of capacitive detectors. These detectors will provide mechanical position data of the detectors, which will be used in a feed forward compensation loop to remove any residual mechanical motion for the bpm measurements. Included in preliminary design are 140 hydrostatic detectors located at the ID P0 rf BPMs and GRID BPM locations. These detectors will measure ground motion and be used to compensate for localized ground motion in each of the 35 locations. The MMS has also provided critical information on the accelerator vacuum chamber, cooling water, and tunnel air handling system impact on beam stability. These systems have significant impact on mechanical bpm detector stability and improvements are ongoing at this time. The MMS data has also motivated the design implementation for the ID BPMs, which has been changed from a vacuum chamber mounted button type BPM similar to the APS today to a bellows isolated BPM shown in Figure 4.190. The BPM will be isolated from the negative effect of the chamber cooling water and additional vibrations when mounted directly to the vacuum chamber. We are also designing and testing as part of R&D an ultra-stable Invar support similar to the NSLS II support with the goal of eliminating specific mechanical motion instrumentation at each sector.

4-3.8.6 Bunch Length and Bunch Purity Monitoring

The longitudinal characteristics of the electron beam are pertinent to accelerator operations and user experiments: Harmonic cavities are used to lengthen the electron bunches to improve the e-beam life time and measurements of the bunch lengthening and the longitudinal profile, providing direct information on the effect of the harmonic cavities. For Mossbauer scattering experiments, impurity bunches in the stored bunch train have an adverse impact on the quality of the data. Table 4.80 lists the required measurement accuracy for bunch length and bunch purity monitors.

Table 4.80. Specifications of bunch length and purity monitors

Monitor	Bunch length monitor	Bunch purity monitor
Quantity	One	One
Dynamic range	50 - 150 ps rms	Main bunch 1 - 10 mA
Tolerance/Limit	$\pm 10\%$ error	Limiting sensitivity 10^{-8}
Notes	6 ps rms resolution	

Figure 4.199 shows the conceptual design of the bunch length and bunch purity monitor. They will share one B:M3 source located at the 35-BM source point. A retractable water-cooled mirror (M0) will pick up the visible light from the wiggler source and transport it out of the tunnel onto the experimental floor area through the existing transport line. When the mirror is retracted below the beamline axis, x-rays passing through the front end will be used for measuring the bunch purity.

The retractable mirror will be supported by remotely-controlled kinematic mounts which will allow alignment of the transport with synchrotron radiation. This is important since the APS-U will not

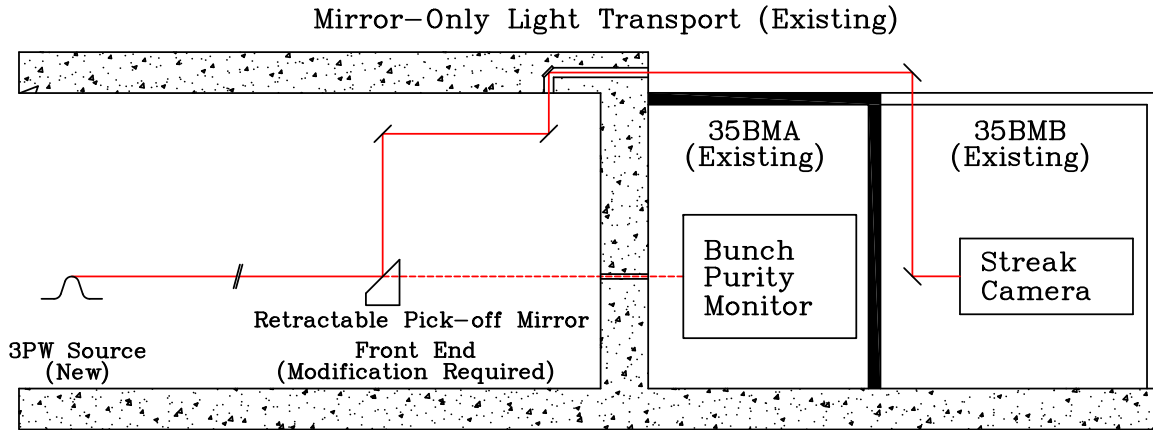


Figure 4.199. Bunch length monitor and bunch purity monitor beamline layout.

have the alignment target in the old storage ring, and its vertical aperture will be reduced from 5.7 mrad to under 2 mrad. An existing spherical mirror-based optical transport will project the beam image inside the hutch 35-BM-B. A commercial streak camera will be used to measure the longitudinal profile of the visible light pulse with a resolution of 6-ps or better [13].

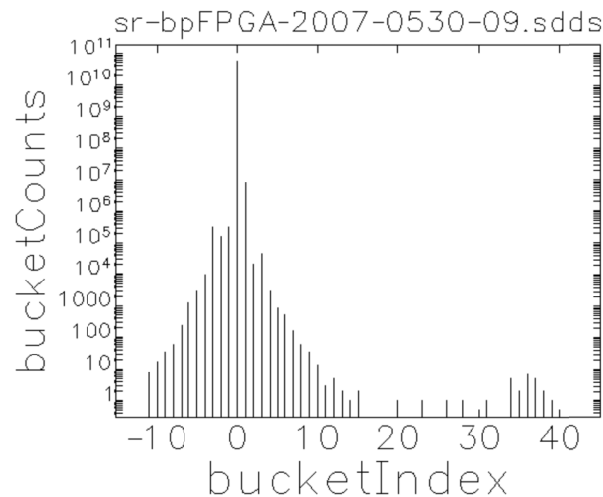


Figure 4.200. A week-long recording of bunch purity histogram demonstrated a dynamic range of eleven decades.

The x-rays passing on through the front end of the inboard side of the M0 mirror will be used for measuring the bunch purity in experimental station 35-BM-C. Fast silicon avalanche photodiodes (APD) will be used as detectors, and APS-developed FPGA fast electronics will be used to implement a time-correlated single photon counting (TCSPC) technique. This technique has been used in the APS for the last ten years with a possible dynamic range of eleven decades as illustrated in Figure 4.200 [14].

In summary, the existing 35-BM bunch length and bunch purity monitors will be reused with one major modification: The bunch length monitor will require a new M0 mirror to pick up visible light beam and align it to the streak camera.

4-3.8.7 Current and Loss Monitoring

Two diagnostic systems that are currently deployed at the APS will be reused or upgraded for the MBA ring. These systems include current monitors and beamloss monitors. Both systems must be able to operate with 200 mA, which is double the present SR average current. Due to the new vacuum chamber dimensions, new current monitor DCCTs will need to be purchased from a commercial vendor.

We plan on reusing the existing beamloss monitors which will save significant engineering time and costs. We will need new hardware to mount the detectors to the storage ring chambers and new high-voltage and signal cables.

4-3.8.8 Longitudinal Feedback System

The APS-U storage ring operates at twice the beam current of the present APS ring. At the same time, the synchrotron tune is reduced to about 620 Hz due to the lower momentum compaction and will be much lower again when the BLS is fully engaged. With these parameters, multi-bunch instability growth rates will be higher than in the present APS storage ring while at the same time the radiation damping rate will be lower due to the lower beam energy. For these reasons the need for a longitudinal bunch-by-bunch feedback system is foreseen. Detailed modelling studies of multibunch stability are described in sections 4-2.5 and 4-2.9.5 of this report.

In a recent study carried out in collaboration with Dimtel, Inc.[15], several HOMs were investigated in the present APS storage ring and found to be in reasonable agreement with expectations, thus confirming the cavity parameters and the coupling to the beam. While at the APS, only the dominant HOM near 537 MHz drives an instability sufficiently strong to overcome the radiation damping, a number of the other modes are expected to have growth rates in the APS-U storage ring that will exceed the radiation damping, see Figure 4.201. (Note that this figure is in essence the same as Fig. 4.35 except that the $1/\omega$ frequency dependence has been removed.)

As explained in section 4-2.5, one method of reducing these growth rates is “HOM tuning” by means of changing the cavity temperature. This method is employed in the present APS storage, controlling the cavity temperature by sector to prevent instability due to the $m = 36$ mode driven by the cavity HOM near 537 MHz. For APS-U, the fundamental rf frequency will be different by about 125 kHz. This changes the aliasing of the cavity HOMs to spatial beam modes as well as the frequency of the HOMs themselves but is not expected to significantly change the widths of the HOMs. One result of the Dimtel study has been the temperature coefficients and the widths of several cavity HOMs (which were found to be within 10% of the estimate using the temperature coefficient of copper); putting that together with the shifted spectrum will allow determination of the degree of temperature control needed for APS-U to keep the growth rates within limits that can be controlled by a reasonable feedback system. Figure 4.38 shows an example of the effectiveness of this approach as determined using a Monte-Carlo technique.

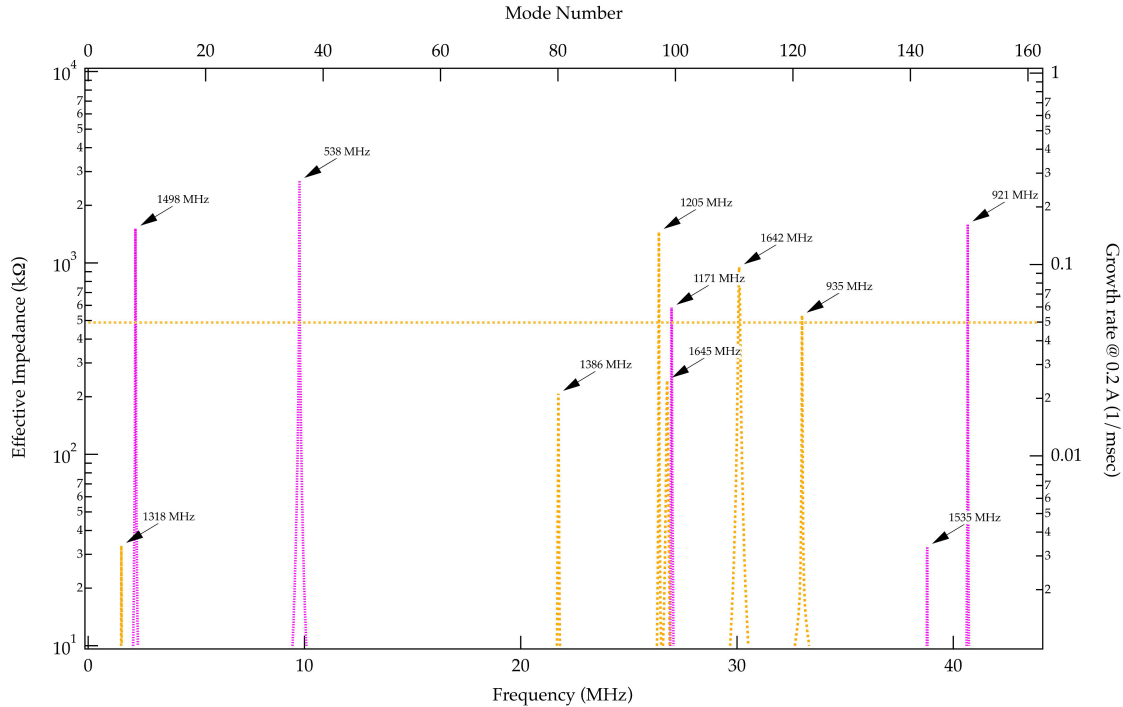


Figure 4.201. Aliased impedance spectrum of the beam modes arising from the HOM spectrum of the 352-MHz rf cavities, for one cavity, from Ref [15]. The growth rates on the right-hand scale are for the APS-U beam of 200 mA at 6 GeV, 324 bunches. The dashed horizontal line indicates radiation damping in the longitudinal plane.

The primary parameters for the LFB system are the system bandwidth needed to damp all modes anticipated to grow, the gain necessary to reduce growth rates below the radiation damping with comfortable margin, and the maximum energy kick, which needs to be sufficient to avoid saturation due to transients and system noise at the highest gain desired. For APS-U, the system bandwidth shall be wide enough to facilitate operation at the highest number of bunches; it is chosen to cover a range from near 0 to 60 MHz which includes operation with 432 bunches—compared to the APS-U design specs of 324 bunches—to avoid limiting upgrade potential of APS-U. The maximum kick is 5.9 kV, to be achieved with two kickers, with an upgrade path to about 8.3 kV without changing the kicker structures should the need arise.

A rough estimate for the gain required can be derived as follows: With the fundamental rf system only, a 1° phase excursion of a bunch translates to about 4.8 MeV energy offset given the parameters of the APS-U storage ring. In Ref.[15], the fastest growth rate is estimated at 0.24/ms for mode 36. An operational rule-of-thumb is that the feedback damping rate should equal or exceed twice the growth rate, therefore 0.5/ms damping from the feedback system is desired, which translates to 9 kV/turn at this amplitude. Therefore the system should have a gain of 9 kV/ $^\circ$ to be able to control this particular mode up to 1° of amplitude. At this gain, a phase noise of 0.4° translates to a kicker voltage of 3.6 kV, within the capability of the system and kicker design. This sets a limit on the phase noise in the rf system as the feedback system will detect this noise (which is mostly mode-0 motion) and will drive the kicker accordingly. Filtering will reduce this noise amplification, but with the low and diffuse synchrotron frequency when the BLS is active, the degree of the filtering

that can be applied is not yet clear. It is noted that the injection phase transient may saturate the output, however, this only applies to the injected bunch and not the stored ones. While the feedback will saturate for this particular bunch it is only a small fraction ($1/48$ or $1/324$ depending on the fill pattern) of the driving force for any particular mode and therefore this saturation will not significantly affect the modal damping.

The maximum practical damping—for a defined synchrotron frequency of 620 Hz—is evaluated in the same study to be somewhat less than $1/\text{ms}$ if reasonable operational margins are to be maintained. It appears then that net growth rates of up to $0.5/\text{ms}$ are within reach of the feedback system. It is therefore prudent to install dampers for the dominant modes in all rf cavities for APS-U. Radiation damping will help but is too small to make a significant difference.

The estimates apply in this form to the single rf-frequency without the BLS. The BLS changes the phase-energy relationship, but more importantly, also the dynamics of the relation. Landau damping *may* provide an additional $0.2/\text{ms}$ in damping—see section 4-2.5 in this report—however, it is noted that high growth rates are still seen in multi-particle tracking simulations that include the BLS, as reported in section 4-2.9.5.

4-3.8.8.1 System Layout If it follows the now-conventional architecture, the feedback system will have a layout as shown in Figure 4.202. Signal shaping is performed in the front-end with two

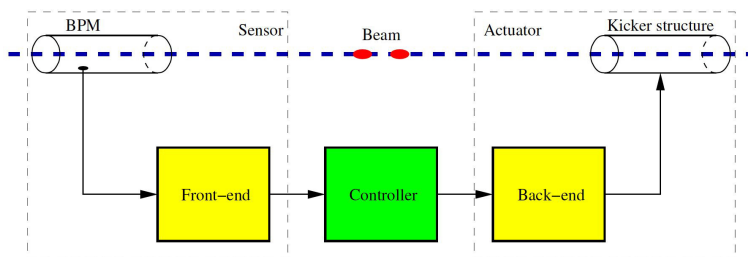


Figure 4.202. Block diagram of the longitudinal feedback system.

(competing) objectives: obtaining flat pulse top and minimizing bunch to bunch coupling. Flat pulse top is needed to reduce system sensitivity to sampling clock jitter and long term clock phase drifts. The beam signal is phase-compared with the RF master oscillator or its harmonic. Higher frequency detection provides more phase sensitivity but has lower bunch phase acceptance range. The system should operate below the TM beam-pipe cutoff frequency to avoid spurious signals due to propagating modes, which is fairly easily achieved at APS-U due to the small vacuum chamber aperture.

The baseband signal processor digitizes the processed beam phase, calculates a correction signal, and generates a baseband analog correction signal. The controller is typically implemented as a digital signal processor (DSP) running at the bunch repetition rate. Samples of individual bunches from multiple turns are used to calculate the correction signal. Finite impulse response (FIR) filtering is most commonly used for such a calculation. The output of such a filter is a convolution of the past inputs with the filter coefficients. The main requirement for the feedback controller is to generate a net 90° phase shift at the dipole oscillation frequency, since the system senses phase and acts

on energy. In addition, the feedback controller generates a bandpass response around the bunch oscillation frequency to reduce spending amplifier power on the out-of-band signals. Most critical of these is the direct current (DC) component due to physical or electronic offsets.

One difficulty for such a system is that the synchrotron tune is not well defined when the BLS is tuned for optimum lifetime, which makes design of the FIR filter problematic. For this reason, tracking simulations—see section 4-2.9.5—used a different methodology. A possible approach to this problem is described below.

The back end modulates the baseband correction signal to the operation frequency of the kicker. For APS-U, a frequency of 1.025 GHz is chosen which is suitable for all anticipated operating modes (48 bunches, 324 bunches, and 432 bunches would be possible as well). Preliminary particle tracking studies indicated that the form factor (0.8 – 0.9) and variation in kick along the bunch for long bunches ($\Delta t \approx 250ps$) does not have a significant negative impact on system effectiveness. The signal is then fed to power amplifiers to drive the feedback kickers. For APS-U, two 500-W amplifiers per kicker are anticipated.

4-3.8.8.2 Longitudinal Feedback Kicker The feedback kicker imposes an energy kick on each bunch, thus counteracting the instability motion. Its bandwidth needs to cover the same 60 MHz range as the processing unit, but shifted up in frequency. Fundamentally such kickers can be realized either as a drift-tube kicker[16] or as a strongly damped cavity kicker[17]. For APS-U, two cavity kickers are chosen as they tend to have higher shunt impedance (which means more kicker voltage for the same amplifier power) and the extreme bandwidth of the drift-tube kicker is not needed. Damped-cavity kickers have been in operation at several facilities (see e.g. [18, 19, 20]) in a frequency range similar to APS-U. A 4-port design is presently being pursued, with two ports being driven by the power amplifiers and two ports terminated by suitable high-power loads. Figure 4.203 shows a rendering of an electro-magnetic design for the APS-U kicker. The shunt impedance of the

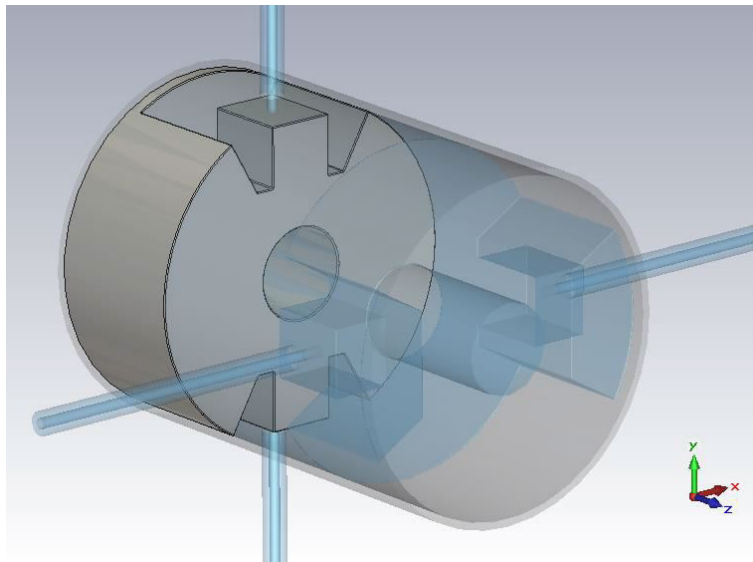


Figure 4.203. 3-d rendering of a conceptual design for the APS-U longitudinal-feedback kicker. Length of this model is 30 cm. Two of these kickers will be used in the APS-U storage ring.

kicker is a trade-off against the beam-pipe aperture, with smaller apertures providing a higher shunt impedance. At the same time, reducing the vacuum conductance through the aperture lowers the effective pumping speed achievable and potentially causes unacceptable pressure rise. A preliminary estimate indicates that the standard APS-U aperture of 22 mm provides sufficient aperture to maintain 5 nTorr average pressure on the beam axis in the kickers under conservative assumptions. Vacuum pumps will be located both upstream and downstream of the kicker pair but not in between. With this aperture, the shunt impedance reaches 4.35 k Ω , and two 500-W amplifiers per kicker can produce 2.95 kV per kicker on the beam axis, for a total of 5.9 kV and providing some redundancy in case of failure of one of the channels. Also, should more kicker voltage be required, operationally it is possible to add two more amplifiers to each kicker, thus doubling the power and increasing the voltage by a factor of $\sqrt{2}$ to 8.3kV. Table 4.81 gives the parameters of the kicker design.

Table 4.81. APS-U storage ring longitudinal-feedback kicker parameters

Parameter	Value	Unit
Frequency	1027	GHz
R/Q	125	Ω
Q_{ext}	17.4	
Q_0	14000	
R_s	4.35	k Ω
peak Voltage	2.95	kV at 1kW power
Rf Power	2×500	W
Beam pipe diameter	22	mm
No. of ports	4	(2 driven, 2 terminated)

4-3.8.8.3 Advanced feedback topology The low synchrotron frequency of APS-U—especially with the bunch-lengthening system fully engaged—presents a challenge to the longitudinal feedback system as the 90° phase rotation in the filter takes 1/4 of a synchrotron period. A conceptually promising option to enable longitudinal feedback at very low synchrotron frequency and a wide synchrotron frequency spread is direct energy-oscillation sensing. Such a system is assumed in tracking studies of multibunch instabilities, as reported in section 4-2.9.5. For the horizontal difference signal of a pickup it can be shown that, for sinusoidal oscillations, the signal is given by[15]

$$x(t) = 2g(n)i_b \left(x_0 + \eta \frac{\epsilon_0}{E_0} \cos(\omega_s t) \right) \sin \left(n\omega_{rf} t + n\omega_{rf} \frac{\alpha\epsilon_0}{E_0\omega_s} \sin(\omega_s t) \right), \quad (4.49)$$

where $g(n)$ is the pick-up gain as function of frequency, i_b , the bunch current, x_0 , the orbit offset at the pickup; η is the dispersion, and ω_s and ω_{rf} are the synchrotron and the rf frequency, respectively. Detection should be performed at the lowest possible harmonic of the rf frequency; a stripline pickup of sufficient length might be needed to provide sufficient signal-to-noise ratio, especially as the maximum dispersion in the APS-U storage ring is only about 0.08 m. It is necessary to separate the amplitude modulation from the phase modulation which will also be present; this can be done with a modified front-end and by rotating the samples from Cartesian to polar coordinates in the FPGA. The feasibility of this approach could be studied in the present APS.

References

- [1] Robert Lill Xiang Sun and Benjamin Stillwell. *Simulation Comparison between the Baseline and the Vendor Designs of the MBA BPM Button*. Tech. rep. AOP-TN-2016-006. APS, Sept. 2016 (cit. on p. 236).
- [2] Instrumentation Technologies. *Libera Brilliance+*. <http://www.i-tech.si/accelerators-instrumentation/libera-brilliance-plus/> (cit. on p. 237).
- [3] G. Rehm. “Recent Development of Diagnostics on 3rd Generation Light Sources.” In: *Proc. of EPAC 1908*. 2008, pp. 1016–1020 (cit. on p. 237).
- [4] R. Lill A. Brill H. Bui and N. Sereno. *Libera Brilliance+ Noise Measurements in Sector 27*. Tech. rep. AOP-TN-2015-018. APS, Nov. 2015 (cit. on p. 237).
- [5] B.X. Yang et al. “Advanced X-ray Beam Position Monitor System Design at the APS.” In: *Proc. of PAC 2013*. 2013, pp. 1079–1081 (cit. on p. 238).
- [6] H. Bui et al. “Performance of FPGA-Based Data Acquisition for the APS Broadband Beam Position Monitor System.” In: *Proc. of BIW 2008*. 2001, pp. 80–84 (cit. on p. 239).
- [7] S.H. Lee B. Yang J. Morgan and H. Shang. “High-Energy X-Ray Pinhole Camera for High-Resolution Electron Beam Size Measurements.” In: *Proc. of International Beam Instrumentation Conference (IBIC16), Barcelona, Spain*. 2016 (cit. on pp. 241, 244).
- [8] R. Lill et al. “Studies of APS storage Ring Vacuum Chamber Thermal Mechanical Effects and their Impact on Beam Stability.” In: *Proc. of BIW 2010*. 2010, p. 1500 (cit. on p. 244).
- [9] V. Shiltsev and J. Lach. “VLHC/NLC Slow Ground Motion Studies in Illinois.” In: *Proc. of PAC 2001*. 2001, pp. 1470–1472 (cit. on p. 244).
- [10] E. Trakhtenberg, P.K. Den Hartog, and G.E. Wiemerslage. “Extruded Aluminum Vacuum Chambers for Insertion Devices.” In: *Proc. of PAC 2011*. 2011, p. 2093 (cit. on p. 244).
- [11] Micro-Epsilon. *Micro-Epsilon CapaNCDDT 6200*. http://www.micro-epsilon.com/displacement-position-sensors/capacitive-sensor/capaNCDDT_6200/index.html (cit. on p. 245).
- [12] J Volk et al. “Hydrostatic level sensors as high precision ground motion instrumentation for Tevatron and other energy frontier accelerators.” In: *Journal of Instrumentation* 7 (2012) (cit. on p. 245).
- [13] Hamamatsu Corporation. *Univeral Streak Camera*. C10910 Series. 2013 (cit. on p. 247).
- [14] B. X. Yang et al. “Bunch-by-bunch diagnostics at the APS using time-correlated single-photon counting techniques.” In: *Proc. of BIW 2010*. 2010, p. 238 (cit. on p. 247).
- [15] D. Teytelman and J.M. Byrd. *APS-U Longitudinal Feedback Design Study*. Tech. rep. San Jose, California: Dimtel, Inc., Mar. 2017 (cit. on pp. 248, 249, 252).
- [16] J.N. Corlett and et al. “Longitudinal and Transverse Feedback Kickers for the ALS.” In: *Proc. European Part. Accel. Conf.* European Physical Society. London, GB, June 1994 (cit. on p. 251).
- [17] R. Boni and et al. “A waveguide Overloaded Cavity as a Longitudinal Kicker for the DAΦNE Bunch-by-Bunch Feedack System.” In: *Part. Accel.* 52 (1996), pp. 95–113 (cit. on p. 251).
- [18] P. McIntosh et al. “AN OVER-DAMPED CAVITY LONGITUDINAL KICKER FOR THE PEP-II LER.” In: *Proc. Part. Accel. Conf.* Portlans, Oregon: IEEE, May 2003 (cit. on p. 251).

- [19] W.Z. Wu et al. “Development of a bunch-by-bunch longitudinal feedback system with a wide dynamic range for the HIGS facility.” In: *Nucl. Instrum. Methods A* 632 (Dec. 2010), pp. 32–42 (cit. on p. 251).
- [20] X. Wei et al. “Design and optimization of a longitudinal feedback kicker cavity for the HLS-II storage ring.” In: *Chinese Physics C*. Vol. 37. 3. IOP Publishing, Ltd., 2013, p. 037003 (cit. on p. 251).

4-3.9 Accelerator Control System

4-3.9.1 Overview

The present APS control system is EPICS-based and consists of over 450 Input Output Controllers (IOCs), around ten thousand components, and over a half-million process variables (PV's). At the functional level, requirements for the APS-U accelerator control system are largely already met by the existing control system, and the APS-U design retains a large fraction of the present controls core infrastructure and high-level applications. This includes EPICS core software and extensions, physical infrastructure of network switches and VME crates distributed around the ring, Main Control Room (MCR) scripts, GUI screens, and high-level applications; largely built using SDDS and tcl/tk toolkits.

Specific enhancements are necessary, however, to meet the requirements of the state-of-the-art technical systems which are a part of the APS-U accelerator. Several of these challenges and the design approach to address them are listed in Table 4.82. Significant consideration must be given to the short amount of time allocated to system integration and machine commissioning. This places additional demands on the control system tools to facilitate efficient testing, troubleshooting, ad-hoc generation of scripts, and deployment of modified software in an effective manner. Such capabilities must be part of the control system design from the beginning.

Table 4.82. MBA Control System Challenges and Associated Design Goals

Control System Challenge	Design Goal
Ubiquitous embedded IOCs, FPGA-based controller, network appliances	Network infrastructure design which separates classes of traffic
Substantial increase in number of network ports	Accommodate in network infrastructure design
Substantial increase in network traffic and throughput requirements	Separate Data Acquisition (DAQ) System specifically for fast time-correlated data
All accelerator components on-site before installation begins	Deploy Component Database early
Short commissioning time	Early deployment of "virtual subsystems" for test script development
Expectation of high availability soon after commissioning	Built-in diagnostics and exhaustive first fault identification

Figure 4.204 illustrates the overall scope for the control system effort for the APS-U storage ring.

The items on a yellow background represent components of the control system and can be grouped into the following initiatives:

- Control System Infrastructure (including Timing)
- Control System Applications and Services
- Interfaces to Technical System

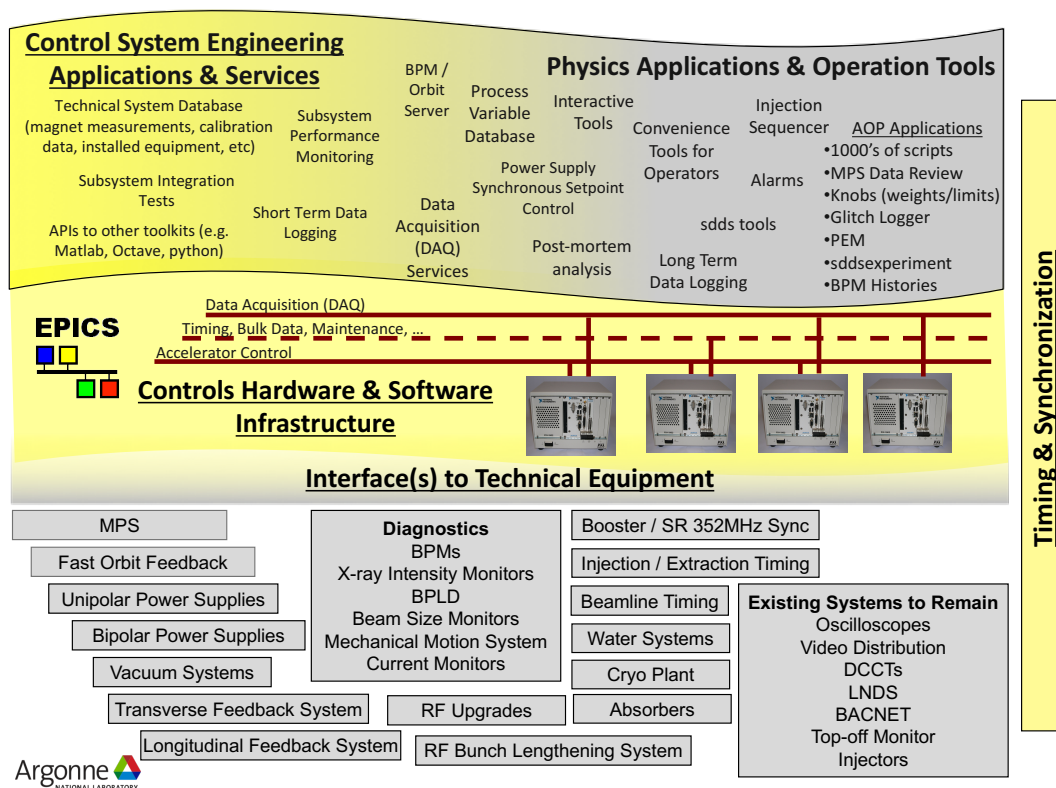


Figure 4.204. Controls Scope (yellow background).

4-3.9.2 Control System Infrastructure

The control system infrastructure provides the primary communication and synchronization between the software tools and the technical system components. It is comprised of the network switches, timing and event hardware, distributed VME and microTCA crates, and several linux clusters supporting soft IOCs and other services. It is this infrastructure that allows the diverse technical systems to be integrated and controlled as a single MBA accelerator.

4-3.9.2.1 Hardware Infrastructure - Timing and Event System The existing APS Event System has been functioning from the beginning of the APS. It is capable of generating events with 0.1 microsecond resolution and EPICS timestamps with a resolution of 1 microsecond. There are over 160 installed components that utilize this event system across the APS complex. For many applications, this system still provides sufficient capability and it will continue to be used as long as the custom hardware can be supported.

A more modern event system used throughout the global accelerator community is from MicroResearch Finland (MRF). This event system (or a higher performance equivalent) will be deployed in parallel to the original APS Event System to support requirements of more precise event timing and higher resolution timestamps (e.g. timestamping of turn-by-turn data). Deploying this “de facto

standard” MRF event system allows us to take advantage of work at other labs (e.g. event receiver FPGA IP) and capabilities within commercial equipment (e.g. the I-Tech Libera Brilliance+ BPM processor has a built-in MRF receiver that can be used for synchronization across many units).

As part of the Data Acquisition and orbit feedback R&D, events from the APS Event System were also distributed on the MRF event system, effectively integrating and synchronizing the two systems. This allowed correlation of timestamps from the existing RTFB and storage ring RF systems (which use the APS system) with timestamps from the APS-U prototype feedback controller (which uses the MRF system). This demonstrates the capability required for the APS-U which will need to accommodate both systems.

4-3.9.2.2 Infrastructure - Double-sector Configuration As a base controls infrastructure for the MBA storage ring, the following hardware will be installed at each double-sector to provide distribution and interface points for controls provided functions:

- Two Tier 3 network switches, each providing 48 ports
- A VME-based IOC
A VME chassis at every double-sector will allow us to utilize the plethora of custom VME modules developed for APS; delay modules, fiber fanouts, fiber-to-electrical converters, etc. The MBA Machine Protection System is currently envisioned to be an evolution of the existing VME-based MPS, which provides an additional requirement for this chassis.
- MPS Input Modules (provides interface points for technical systems that must trip the MPS)
- A VXI chassis
The VXI-based APS BSP100 BPM processor will continue to be used for a subset of RF BPMs, requiring a chassis in every double-sector.
- An APS Event Receiver and/or an APS Event Fanout module
These modules are required to distribute the APS Event Link to the APS BSP100 BPM processors.
- An MRF Event Receiver and/or an MRF Event Fanout module
These modules are required to distribute the MRF Event Link to instruments in every double-sector.
- A bank of Ethernet-to-serial devices for interfacing to technical system hardware
- A μ TCA chassis
A μ TCA chassis will be in every double-sector to house the fast orbit feedback processors and other diagnostic equipment. Although this chassis is provided by the Diagnostic Group, it may also house modules for the DAQ front-ends.

4-3.9.2.3 Infrastructure - EPICS IOC Software & Development Environment EPICS IOCs and services developed for the APS-U will use the standard EPICS build environment to build the IOC and related software programs, based on the IT Group's standard Red Hat Enterprise Linux platform wherever possible. However, these standards still leave many design choices to be considered, for example:

- Version control standards for the software source code
- Use of build automation (Continuous Integration servers)
- Software deployment and roll-back protocols for production
- Specify the on-disk layout to be used for production software
- Standards for IOC/service status reporting and monitoring
- Recommended tools and methods for doing IOC database design

In addition to the familiar EPICS V3 (currently EPICS 3.15) capabilities, some IOCs will utilize EPICS V4 features to provide the necessary functionality. For example, the Data Acquisition (DAQ) system requires EPICS V4 pvAccess to pass the structured data with timestamps to the services running on the host. The combination of EPICS V3 and V4 is often referred to as EPICS V7.

4-3.9.2.4 Infrastructure - Data Acquisition (DAQ) System A new component of the controls infrastructure is the DAQ, which provides time-correlated data acquisition from diverse technical systems. The DAQ is a powerful diagnostic that will allow fast correlation of events that disturb the beam. Each DAQ IOC must obtain fast sampled data from the technical system along with an accurate timestamp of when each sample was taken. The DAQ IOCs can take short snapshots of this data or it can be streamed continuously to a service that will either process the data or save it to disk (or both). Five DAQ systems have been prototyped during the R&D phase on several different platforms; VME, microTCA, embedded ARM CPUs, and DSPs. Figure 4.205 shows time correlated data captured during R&D from three of these systems, one of the systems being on the new MRF event/timing system.

DAQ IOCs will be attached to a separate VLAN to ensure the high data demand does not impact routine machine control. The DAQ is intended to be parasitic to normal machine operation, thereby allowing live changes and enhancements to be implemented quickly. It is anticipated that any subsystem that can influence the beam (e.g. RF, feedback, magnet power supplies, kickers) will have a DAQ IOC, thereby allowing fast determination of beam anomalies. The DAQ will also be a valuable asset in post-mortem diagnostics.

Table 4.83 shows the technical systems currently identified as requiring this DAQ capability.

4-3.9.2.5 Infrastructure - Network A significant requirement for the MBA control system is the need to accommodate ubiquitous IOCs and numerous FPGA-based controllers embedded within the technical systems. This puts a demand on the network infrastructure in terms of number of ports and the increased bandwidth for high data rates and large volumes of data. Figure 4.206 illustrates a network topology that will provide for these demands as well as allowing scaling of the network as additional requirements are understood.

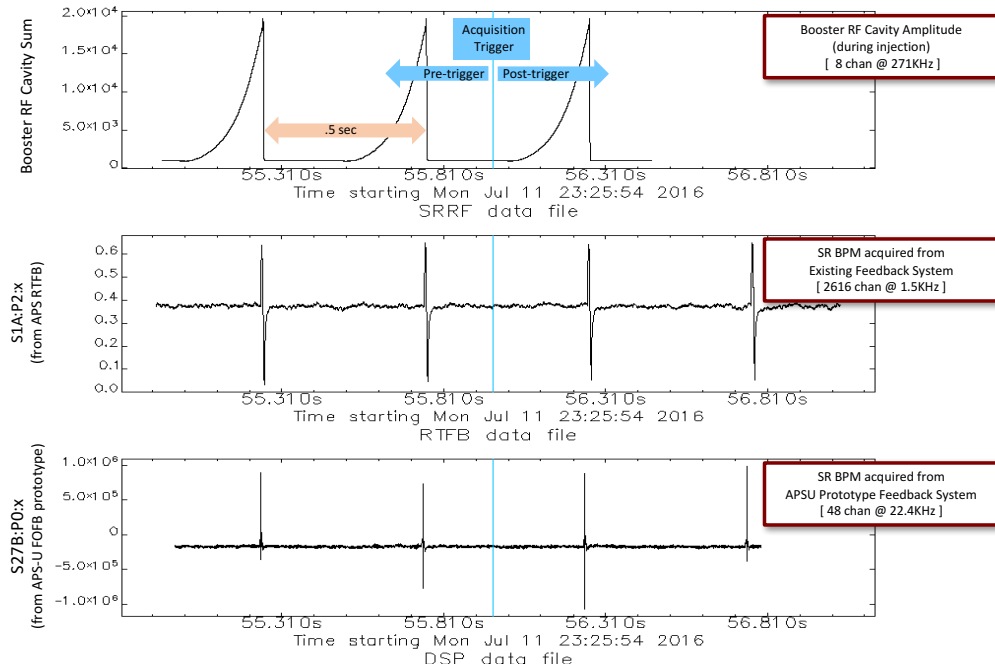


Figure 4.205. R&D DAQ use-case: simultaneous capture and time-correlation of waveforms from multiple sources during storage ring injection.

The key aspects of the illustrated network infrastructure are:

- Redundant connections from the Tier-1 switches to Tier 2
- Redundant connections from the Tier-2 switches to Tier 3
- 1/10Gbps ports at all Tier-3 switches (a Tier-3 switch every double sector)
- Each Tier-3 switch provides 48 ports. These switches can be “stacked” to provide additional ports when required.

The use of VLANs (Virtual LANs) will assist in the separation of network traffic to ensure consistent and reliable operation. Routine control and monitoring will be isolated from the fast DAQ data and bulk data transfers. Additional VLANs will be used for maintenance activities, untrusted network

Table 4.83. Technical Systems with DAQ Interfaces

Technical System	# of Nodes	Signals per Node	Sample Rate	Data Rate per Node
RF BPMs (Turn-by-turn)	20	30 BPMs x 2 planes	271KHz	65MB/s
X-Ray BPMs	20	5 BPMs x 2 planes	10KHz	0.4MB/s
Fast Orbit Feedback	20	100 signals	22.6KHz	9MB/s
Power Supplies (all types)	20	140 supplies x 3 values	22.6KHz	38MB/s
Injection/Extraction Systems	1	8 waveforms	4GHz	3.2KB/s
SR/Booster RF	3	12 cavities x 3 values	271KHz	39MB/s
Bunch Lengthening System	1	5 values	271KHz	5.4MB/s

devices, and I/O subnet devices.

It is assumed that APS-U is responsible for some of the scope shown in Figure 4.206, with the remainder being part of the facility infrastructure. It will be determined later exactly what is in-scope for the APS-U.

4-3.9.3 High-Level Engineering and Database Applications

This subsection identifies high-level software applications required for the design, installation, testing, and startup of the MBA accelerator.

4-3.9.3.1 Database Applications - Component Database (CDB) The Project requires a Components Database and electronic traveler system for tracking of all components during procurement, fabrication, inspection/test, and installation.

The component database (CDB) will contain an ‘MBA Component Catalog’ where each component type is identified and linked to drawings, documentation, vendors, and the component’s unique properties. Each fabricated or procured component will have a unique identification number encoded on a QR code attached to the component. Scanning this QR code will readily access all relevant information about this component, such as inspection history, test results, intended machine location, and more.

Based on experience with the existing APS, the number of process variables for the MBA will likely exceed 500,000. An application that automatically defines EPICS records from data in the Component Database (and other sources) will greatly minimize the number of errors compared to a manual database definition process and will be pursued. Additional capability to request or discover the appropriate PVs associated with certain machine components by technical system, component families, or by using wildcards will allow efficient development of other applications.

Recognizing the necessity of having the CDB available early in the design process, substantial progress has been achieved in the R&D and Preliminary Design phase. A screen shot of a component catalog entry is shown in Figure 4.207.

4-3.9.3.2 Control System Engineering Applications Due to the short installation, integration, testing, and commissioning time of the MBA, the technical system engineers require mature and flexible tools to quickly bring up their systems to full capability and reliable operation. Such software tools and applications will be used by APS-U staff to interact with the control system and the technical system components for control, monitoring, data acquisition, and data processing. Necessary tools include the Data Acquisition System (DAQ) services, management of calibration/characterization data, PV finder, high performance archiver, interactive debugging tools (strip chart, arbitrary PV table, camonitor, etc.), and an infrastructure monitoring system (for an early indication of a potentially hidden problem). Additionally, tools for subsystem integration testing, pre-operational testing, and integration with AOP commissioning tools will be required.

A vast library of custom high-level applications, controls GUIs, and scripts have been developed over

the past 20 years and are in routine use in the Main Control Room (MCR). These have been largely developed by the physics and operations groups using SDDS and tcl/tk. These tools will continue to be used as they are very familiar to the operations group. In addition, the suite of high-level tools will be expanded to include utilities and libraries that are more familiar and more accessible to the engineering groups for rapid development of ad-hoc engineering applications. Open-source equivalents to Matlab/Simulink, such as Octave and Scilab, are favored candidates. EPICS V4 has a mature API for python, making a vast number of open source projects available to the engineers. Availability of hooks into SDDS tools and use of SDDS data formats will be an explicit requirement.

4-3.9.4 Controls for Technical Systems

4-3.9.4.1 Technical Systems Interfaces A substantial fraction of the APS-U controls work will be reconfiguring the control system and controls applications to switch from the existing to the new technical equipment. Associated IOC databases, controls applications, and accelerator/operations high-level applications must point to the new equipment. This effort involves changing physical interfaces to several thousand technical components and several hundred-thousand EPICS process variables (PVs). A listing of the technical systems to be addressed is in Table 4.84 and Table 4.85. All the work to integrate the new systems and maintain the functionality of the existing systems through the installation year is part of the APS-U effort.

Table 4.84. Technical Systems with predominantly new hardware

Technical System	Primary Interface	Timing Req'd	DAQ Interface
Fast Orbit Feedback	Ethernet	Yes	Yes
Machine Protection System	Backplane	TBD	No
Libera BPMs	Ethernet	Yes	Yes
BSP100 BPMs	Ethernet	Yes	Yes
X-Ray BPMs	Ethernet	Yes	Yes
X-Ray Intensity Monitor	TBD	Yes	TBD
Beam Position Limit Detectors	Backplane	No	No
Beam Size Monitors	TBD	No	TBD
Mechanical Motion Systems	Ethernet	No	No
Current Monitors	Backplane	Yes	TBD
Transverse Feedback System	Ethernet	Yes	TBD
Injection/Extraction Systems	Ethernet	Yes	Yes
Booster/SR Synchronization	TBD	Yes	No
Longitudinal Feedback System	Ethernet	Yes	TBD
SR RF Upgrade	Backplane	Yes	Yes
RF Bunch Lengthening System	Ethernet	TBD	TBD
Bipolar Power Supplies	Ethernet	No	Yes
Unipolar Power Supplies	Ethernet	No	Yes
Vacuum Valves and Monitoring	Ethernet	No	No
Water Systems	Ethernet	No	No
Cryo Plant	Ethernet	No	No
Beamline Timing and RT Data Distribution	Ethernet	Yes	No

Table 4.85. *Technical Systems where hardware is predominantly unchanged*

Technical System	Primary Interface	Timing Req'd
SR Oscilloscopes	Ethernet	Yes
DCCT	GPIB	Yes
Video Distribution	Ethernet	Yes
Liquid Nitrogen Distribution System	Ethernet	No
Plant Systems (BacNet)	Ethernet	No
Top-off Monitor	Backplane	Yes
Timing Signals to Injectors	Backplane	Yes

4-3.9.4.2 Simulation of Technical Systems Because of the short installation and startup period, application development must occur well before there is a real machine against which to test. Therefore, simulation of many subsystems will be required to allow adequate testing time of the applications prior to the Integration Tests described below. An important part of this simulation will be to have all EPICS process variables present and responding as a real machine (as best as this can be simulated).

4-3.9.4.3 Integration Tests and Startup Tools/Applications After installation, the technical groups will do functional testing and checkouts of their individual subsystems. Prior to turning the machine over for startup, top-down integration testing (i.e. testing multiple subsystems through the control system) will be required. The exact tests to be used will need to be defined, implemented, and tested well before the actual startup phase.

4-3.9.5 Pre-Installation Phase

To the extent possible, EPICS databases, control screens, and other equipment will be rebuilt and debugged offline during the pre-installation phase. Similarly, during the pre-installation phase, physical/functional interfaces to new storage-ring technical equipment will be developed and debugged using the actual equipment. The 40-fold symmetry of the storage-ring means that much of the process of instantiation can be automated once databases for a single sector have been configured and debugged. A streamlined process for rebuilding and debugging the control system during the pre-installation phase will be fundamental to keeping the deployment and debugging time to a minimum during the APS-U test and commissioning phase. Module Assembly and Testing, discussed in Section 4-3.14, give additional opportunities to debug the control system interfaces prior to installation and commissioning.

An important scheduling issue is that a large fraction of the control-system activities need to occur earlier than the corresponding activities for other technical systems. In particular, every technical group relies on the control system for testing and operating their equipment, and hence relevant Controls infrastructure (hardware, IOCs, applications, etc.) must be ready and tested in order at the point when the other technical groups begin their testing.

4-3.9.6 Controls Support for Machine Testing and Commissioning

In typical accelerator construction projects, tools to support high-availability operation, such as exhaustive diagnostic information and post-mortem analysis, evolve during the operational period of the facility. Due to the short turn-on time of the MBA after installation, such tools must be available at the initial testing phase to provide quick determination of failures or performance problems. Thorough fault monitoring, time correlated data from diverse technical systems, first turn, and injection diagnostics are examples of capabilities that will provide an efficient environment for commissioning. The “virtual accelerator systems” mentioned earlier will be used to develop and debug these tools prior to the installation of the machine.

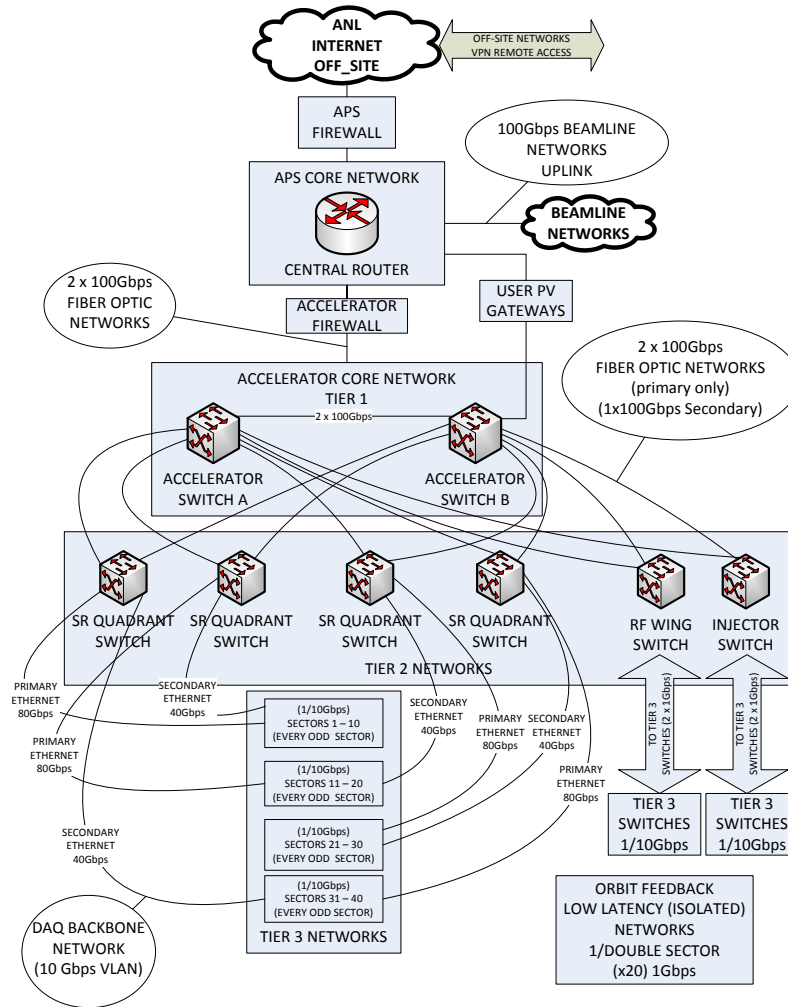


Figure 4.206. Controls networks topology.

Argonne
NATIONAL LABORATORY

Component Database Portal

Username: Not Logged In
Role: User
View: Default
Project: All

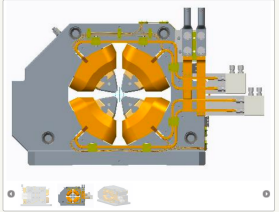
Browse Catalog Inventory Search Login About

Catalog Item Details

Name: DMM QUADRUPOLE UZZ1020202-111100
Model Number: UZZ1020202-111100
Alternate Name: -
Project: APS-U
Description: QUADRUPOLE ASSEMBLY, STEEL POLES
Technical System: Magnets
Function: Quadrupole

More Info Return

Gallery



Log Entries

Properties

Type	Tag	Value	Units	Dynamic	Actions
Traveler Template (Electronic)		APS-U Rigging Daily Lift Checklist			⊖
Traveler Instance (Electronic)		314 to EAA			⊖ ⊕
PDMLink Drawing	FRONT VIEW	UZZ1020202-111100_ASM			⊖ ⊕
Image					⊖
Image	UPSTREAM VIEW				⊖
Image	ISO VIEW				⊖
Traveler Template (CMS)		APS_1682422			⊖

Elements

Element Name	Contained Item	Model Number	Required	Owner	Group	Actions
⊖ Coil	DMM QUADRUPOLE COIL ASM	UZZ1020202-104000	Yes	djarosz	SSG	⊖ ⊕
⊖ Yoke	YOKE: DMM QUADRUPOLE UZZ1020202-111100-A001	UZZ1020202-111000	Yes	djarosz	SSG	⊖ ⊕

Sources

Inventory

More Info	Primary Image	Inventory Item	Tag	Grid	Serial Number	Description	Location	Actions
⊖		DMM QUADRUPOLE UZZ1020202-111100 - [DMM-QUADRUPOLE-AB01]	DMM-QUADRUPOLE-A001	000 000 107			314	⊖

Item Membership

Part Of	Description	Owner	Group
DMM MAGNET ASSEMBLY	CONCEPTUAL DESIGN & DEVELOPMENT (R&D); ACCELERATOR CONCEPTUAL DESIGN AND R&D; ACCELERATOR R&D/MAGNETS R&D; MULTIPLLET R&D; DMM MAGNET ASSEMBLY	jellu	MED

Figure 4.207. CDB catalog item.

4-3.10 Main Ring Rf System

The 41 pm lattice of the MBA ring has an energy loss per turn of 2.74 MeV at 6 GeV beam energy. Adding 1.33 MeV for a maximum of IDs closed and 50 keV energy lost to the vacuum system results in a total energy loss of up to 4.15 MeV. At 200 mA beam current, 830 kW need to be delivered to the beam.

Beam lifetime in APS-U is relatively short, less than 3 hours in 48-bunch mode. Therefore the possibility of a new rf system operating at a much lower frequency (117 MHz being the most-studied alternative) was revisited. The benefit sought is primarily longer bunches, which lower the peak current and thus increase the Touschek beam lifetime; about a factor of 2.5 can be gained by using a 117 MHz rf frequency. A side effect would be the possibility of higher efficiency in case the rf cavities would be superconducting, especially if the superconducting cavities were to be driven by solid-state power amplifiers (which are readily available commercially in the 100 MHz frequency band). After an in-depth review of the options, however, it became apparent that the benefits of a new 117 MHz rf system would not outweigh the risks inherent in such an approach, and in particular the resulting increase in bunch length would negatively affect the timing experiments. The results of the study are available in a report[1]. The Project therefore reaffirmed the decision to utilize the existing 352 MHz rf system. Four 1-MW continuous wave (CW) rf stations (RF1-RF4) power 12 single-cell copper cavities installed in groups of four in Sectors 36, 37 and 40. A fifth 1-MW rf system (RF5) is dedicated to supplying rf power to the booster rf cavities. Four rf cavities will be removed from the sector 38 straight section in order to make space available for the extraction kicker and the harmonic rf cavity of the bunch-lengthening system.

4-3.10.1 High-Level Rf System

Due to the lower electron-beam energy of APS-U, power and voltage requirements are less than at the present APS, and the MBA ring can be operated with 12 rf cavities and sufficient overhead to allow for full beam parameters even if one or two cavities have to be taken off-line for any reason. Table 4.86 shows the parameters for the system, with 8, 10, and 12 cavities. These parameters are maximum values assuming a large number of IDs are closed, and provide 5.5% momentum acceptance to maximize beam lifetime. Operationally the system will often run at lower power and voltage.

A single-line block diagram of the rf power system is shown in Figure 4.208. A system of motorized WR2300 waveguide components, including four waveguide switches, four 45° phase shifters, and two waveguide shutters are utilized to quickly select one of eight modes of operation. This system provides operational redundancy for both the booster and the storage ring to minimize downtime in the event of an rf station failure. These operating modes provide the ability to drive the sector 36 and 37 rf cavities with either RF2 or RF3 or both at an output power of up to 1.4 MW combined, thus meeting the requirement for full beam current and full rf voltage with 8 cavities in the event that Sector 40 becomes inoperable for any reason. The Sector-40 rf cavities may be powered by either RF1 or RF4 at an output power of up to 800 kW in case of reduced power or voltage from Sectors 36 and 37 and assuming each cavity can operationally handle up to 200 kW (see section below). The ability of RF1 to provide rf power for the 350-MHz rf test stand and RF3 to substitute for RF5 in powering the booster rf cavities is preserved. Waveguide safety shutters are used in the path between RF3 and RF5 to isolate the two accelerators for personnel safety. The

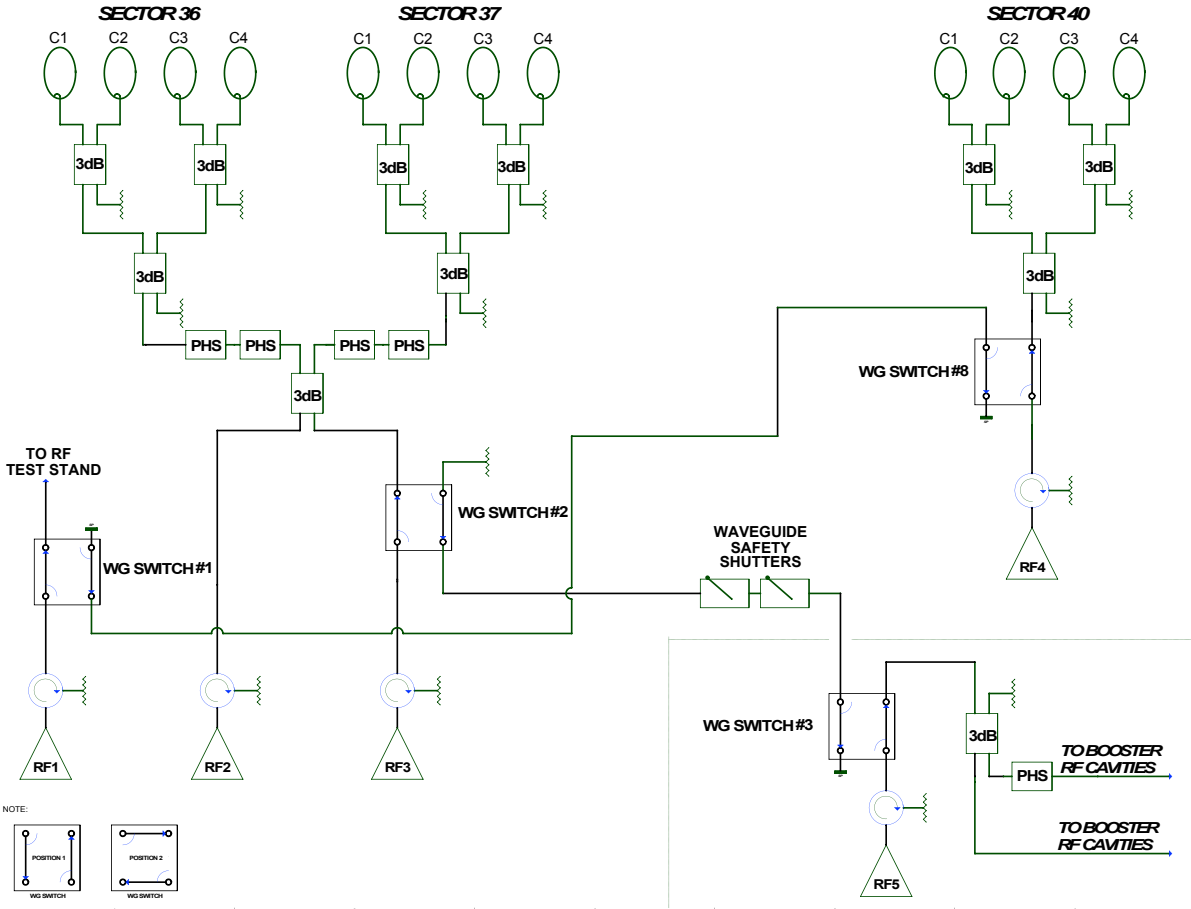


Figure 4.208. 352-MHz HLRF system configuration for MBA upgrade.

Table 4.86. 352MHz + 1408MHz rf system requirements for 1.33 MeV energy loss in the IDs and 50 keV energy loss to the vacuum system, at 200 mA beam current and 5.5% energy acceptance

	352 MHz			1408 MHz
	Fundamental			Harmonic
Voltage	6.585 MV			1.25 MV
# of Cavities	8	10	12	1
V_{cav} [kV]	823	658	549	1250
$Q_{ext} \times 10^3$	17.3	14.9	13.1	500
$Q_L \times 10^3$	12.7	11.4	10.3	500
3dB $\frac{1}{2}$ BW [kHz]	13.9	15.5	17.1	1.4
Δf [kHz]	-7.2	-9.0	-10.8	11.0
P_{cav} [kW]	61.9	39.6	27.5	0.072
P_{beam}/cav [kW]	110.2	88.2	73.5	-29.0
P_{rev}/cav [kW]	0	0	0	29
P_{gen}/cav [kW]	172	128	101	0
Total Installed RF [kW]	1377	1278	1212	0

motorized waveguide components are directed and monitored by a central control system, which also reconfigures the LLRF system, interlock, and control signals to and from the appropriate hardware, depending on the specific operating mode selected.

4-3.10.1.1 High-Power Coupler In order to fully utilize the redundancy built into the rf system, it is required to be able to handle power in excess of the present 100 kW per cavity. A 300 kW power coupler has been developed previously in collaboration with CERN[2]; ANL is now working towards building a new prototype addressing some issues uncovered in the development, with a goal of testing a new prototype first in the existing test cavity and, if successful, installing this coupler in a cavity in the APS storage ring. Figure 4.209 shows an exploded model of the coupler. The new coupler will be a 1-to-1 replacement of the existing one with minimal modifications necessary to the waveguide system. In addition, this coupler may provide a path towards improving the rf power handling in the Booster.

4-3.10.1.2 HOM Damping The APS-U will have a very low synchrotron tune and have higher multi-bunch instability growth rates, as seen in section 4-2.5 of this report. Since the modes in most cavities are not damped, they are narrow and temperature control of the cavities allows “parking” of the cavity HOMs, i.e. tuning them to fall in between revolution harmonics of the beam thereby minimizing coupling of the beam-current to the particular mode. This technique is already in use for the rf in each sector at the present APS storage ring; for APS-U it is anticipated that each cavity will be temperature-controlled to allow individual tuning. The required modifications to the cooling circuits are both moderate in scope and straightforward. An additional benefit will be the possibility of using the actual cavity temperature in a feedback loop, making the cavity temperature independent of the rf voltage.

There is a known cavity mode near 537 MHz that drives an instability near spatial beam mode 30. This mode can be damped with a dedicated HOM damper already installed in 4 out of the 12 cavities

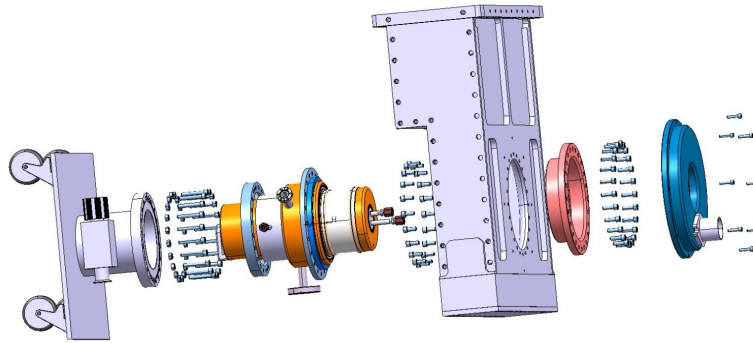


Figure 4.209. Exploded view of the CERN-ANL high-power rf coupler. The structure on the left side is a mounting car and not part of the coupler structure. (Figure courtesy of E. Montesinos, CERN.)

presently in the APS. Figure 4.210 shows a picture of the existing HOM damper. The damper in its present form damps the 537 MHz mode by about a factor of 9, with a smaller damping effect on the 920-MHz cavity mode. It is planned to review the design of this damper for possible improvements and provide such dampers in all cavities in the APS-U storage ring. Possible improvements of the extant design not only would enhance damping and affect a wider spectrum in frequency but may also improve the diagnostic information to be gained from the dampers e.g. by taking a monitoring signal off the element. Damping a mode decreases its shunt impedance but increases its width and thus reduces the effectiveness of the HOM tuning by the temperature described above. The balance of these effects is being studied and a final decision about the optimal degree of the damping will be taken after these investigations have come to a close.

4-3.10.2 Low Level Rf System

The low synchrotron tune will also make the beam more sensitive to rf noise and phase transients. At present, there is about 1 degree of phase noise (predominantly line noise at 360 Hz and 60 Hz) detectable on the rf voltage to the cavities, which is also impressed on the beam. With a synchrotron frequency of about 2 kHz, this noise is below the beam response and therefore not resonantly enhanced. In the APS-U storage ring, with a synchrotron frequency near 100 Hz when the bunch-lengthening system is active, stronger response of the beam to the noise is expected. In addition, operation of the beam with gaps in the fill pattern is anticipated for at least some operating scenarios to mitigate ion trapping; such gaps lead to phase transients that can be compensated to first order by tailoring the intensity of the bunches' neighboring the gaps, but residual phase excursions will remain.

A residual phase noise of 0.25° or less will be aimed for in order to prevent dipole oscillations of the bunches and to prevent excessive amplifier-power demands from the longitudinal feedback system which will detect such oscillation and try to reduce it. While some filtering is possible to reduce the



Figure 4.210. The APS HOM damper. Four of these dampers are installed in the Sec. 36 cavities.

signal at the low frequency (predominantly mode 0), tracking studies indicate a need for significant feedback gain even at very low frequency which would lead to amplification of the noise signals.

Mitigation of rf noise is done in a cost-effective way in the low-level rf system by a combination of feed-forward techniques—compensating, such as the ac ripple from the high-voltage power supplies that is very difficult to reduce at the source—and fast feedback techniques that suppress noise by the loop gain and reduce phase transients by stabilizing the rf voltage on a fast time scale. If found to be beneficial, a signal from the longitudinal feedback system can be fed into the low-level rf, using the main cavities as a low-bandwidth, high-voltage kicker. A digital implementation of the low-level rf allows the operational flexibility necessary to address the various needs. At the same time, such systems can incorporate sophisticated diagnostic capabilities that allow extensive time and frequency domain analysis, indispensable tools in tuning the rf system, and provide the ability to track down transients and root causes of rf-induced beam aborts through post-mortem analysis of history buffers.

Improvement of the 352-MHz low-level rf system will take maximum advantage of the work anticipated for the Booster low-level rf, as seen in section 4-3.13.5. A high degree of commonality between the LLRF systems across the complex is desirable not only to reduce effort and cost but also to reduce the inventory of spare modules needed to keep operational availability high.

4-3.11 Bunch Lengthening System

4-3.11.1 High Harmonic Cavity and Cryomodule

A higher-harmonic cavity (HHC) system in an upgraded APS x-ray source will provide a practical benefit to the majority of APS users by increasing the beam lifetime and availability in the storage ring. As discussed in Section 4-2.9, the lifetime in the upgraded APS storage ring will be limited by the so-called Touschek effect, a result of Coulomb scattering between electrons within the beam bunch, leading to beam loss from the longitudinal bucket. From a practical standpoint, the beam lifetime after the upgrade will be significantly shorter than the present 6-8 hours and may require injection into the storage ring more frequently than the present once per minute.

A single superconducting cavity can provide the necessary voltage in a compact footprint, $l \leq 2.5$ meters, needed to lengthen the beam bunch and increase the Touschek lifetime by 3-5 times. There are only two examples of bunch-lengthening superconducting rf (SRF) cavities used in storage rings [1] which achieve about a factor of two increase. Experimental data from these two facilities indicate that, with a well-designed system, additional lengthening may be possible. Furthermore, it is expected that the cavity and all of the subsystems will be designed and built based on technology that does not require major advances in the state-of-the-art and will not require years of development effort.

Regardless of the operating temperature, a superconducting harmonic cavity will have an intrinsic quality factor that is 3-5 orders of magnitude higher than the loaded Q required for the APS-U, which is of the order 10^5 . The choice of operating temperature is therefore determined based on issues of cryogenic costs, efficiency, and margin for operations for the cavity and the helium refrigerator. Microphonics induced from helium boiling would not be expected to be an issue for any cavity operating temperature.

4-3.11.2 High-level System Parameters

The bunch lengthening system cavity is excited by the circulating electron beam in the APS-U storage ring. The beam loss power, 32 kW maximum, is extracted from the circulating 200 mA beam through a pair of fundamental power couplers located next to the harmonic cavity accelerating cell. This extracted power, together with the offset frequency of +10 kHz, as adjusted with a mechanical slow tuner, determines values for the cavity voltage and phase (detuning angle) listed in Table 4.87. We note that these are nominal values from simple analytical formulae, and that actual operating values for coupling strength and detuning frequency will likely differ somewhat from these nominal values. Intrinsic properties of the cavity geometry and peak surface and electric fields are those for a cavity with the so-called TESLA shape developed in the early 1990s for the International Linear Collider[2]. The harmonic cavity surface fields required here are modest by today's standards, so the incentive to improve performance (by perhaps 10%) through development of a more advanced shape is not strong. The TESLA shape also avoids severe multipacting, which was problematic for early cavity geometries.

Table 4.87. Nominal harmonic cavity parameters for $I_{beam} = 200$ mA with fundamental rf power couplers

Parameter	Value	Unit
Operating temperature	2.1	K
R_{SH}/Q	104	Ω
Cavity Q factor	6×10^9	
External Q factor	6×10^5	
Cavity resonant frequency	1408	MHz
Cavity loaded bandwidth	2.4	kHz
Detuning frequency	10	kHz
Beam-induced voltage	1.25	MV
Detuning angle	85	degrees
Beam loss power	25	kW
Cavity wall losses	1.5	W
Cavity peak surface electric field	24	MV/m
Cavity peak surface magnetic field	49	mT

4-3.11.3 Cavity Design, Fabrication, and Testing

In the conceptual design phase of this work, a maximum working voltage of 1 MV was established as the system requirement. At 1 MV, the cavity heat load into a 4 K system was expected to be approximately 40 watts. This heat load has since been experimentally verified with a cavity, as will be presented. However, a more recent analysis including all possible sources of beam energy loss has shown that a harmonic cavity voltage as high as 1.25 MV will be required to satisfy energy acceptance and insertion device power requirements. Above 1 MV, the heat load into liquid helium rises rapidly at 4 K. This has significant consequences for the cavity and refrigerator requirements.

Shown in Figure 4.211 is the 1.4 GHz higher-harmonic cavity developed during APS-U R&D. The cavity is production-ready with all fabrication of the helium-jacketed niobium cavity and surface processing complete. The cavity subcomponents were die-formed from high-purity 3 mm thick niobium and then electron beam welded together to form the assembly shown in the left frame. Each cavity has five niobium-to-stainless steel ports furnace brazed together using high-purity copper at the interface. The middle panel shows the first complete 1.4 GHz superconducting higher-harmonic cavity inside of an integral stainless steel helium vessel. Visible is the ASME pressure vessel stamp (U-stamp) certifying that the vessel was designed and fabricated according the ASME Boiler and Pressure Vessel code for cryogenic pressure vessels. Alignment fiducials will be on four horizontal pads (two are visible) and referenced with an accuracy of 50 microns to the measured beam axis of the cavity. The right panel shows the view looking into one of the two cavity beam ports.

Shown in Figure 4.212 is the cavity electropolishing configuration. The cavity was electropolished heavily on the interior (RF) surface in order to remove the so-called surface-damage layer that results from normal fabrication processes. The top view shows the horizontally oriented cavity mounted inside of the rotating ANL electropolishing system as modified for the harmonic cavity. Also visible is the water cooling ‘shower’ that is used to precisely maintain the cavity temperature at 30 °C during the approximately 8-hour long procedure. A total of 114 microns of material was removed from the interior niobium surface as measured directly using an ultrasonic thickness probe. The cavity received a high temperature heat treatment at 600 °C for 10 hours in the FRIB vacuum furnace at Michigan State University in order to drive out the accumulated hydrogen.



Figure 4.211. 1.4 GHz higher-harmonic cavity. Left: bare cavity weldment. Center: Cavity encapsulated within helium vessel. Right: View along cavity bore.

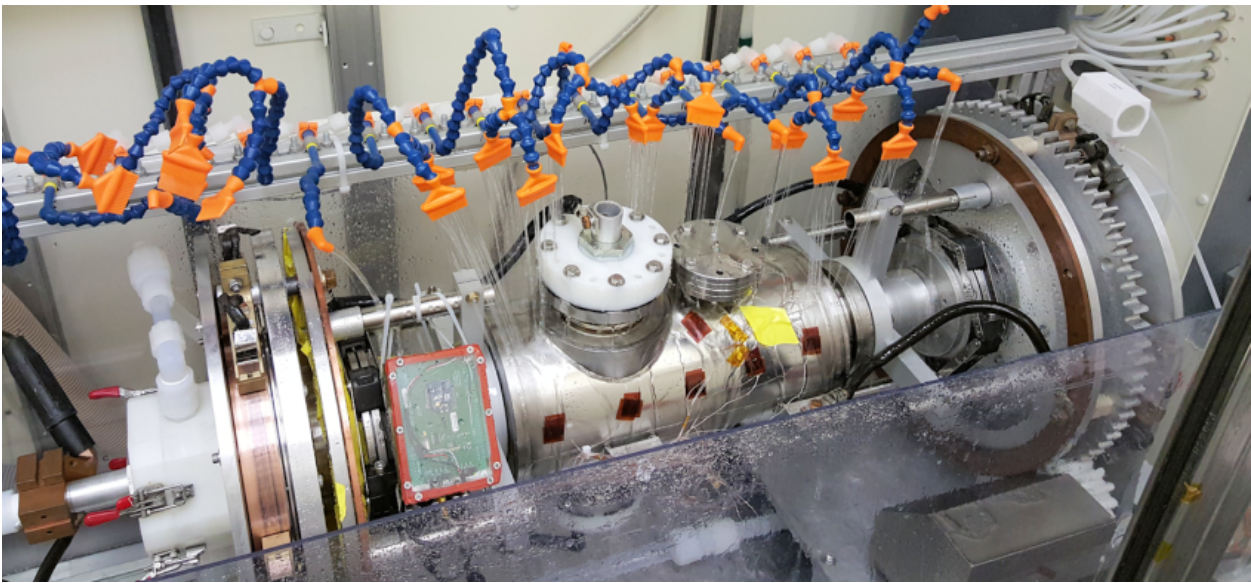


Figure 4.212. APS-U higher-harmonic cavity assembly during electropolishing.

Assembly with subsystems such as an RF coupler, pickup probe, and vacuum pump has been performed in the joint ANL/FNAL cavity processing facility at ANL in preparation for the initial cavity testing. The RF coupler was used as a drive probe with an antenna length chosen specifically for initial testing, such that the coupler can be critically coupled to the cavity at both 2 K and 4.5 K (Q_{ext} adjustable between 1×10^8 and 2×10^{10}).

Shown in Figure 4.213 is the assembly configuration for cold tests of the harmonic cavity, and in Figure 4.214 are the measurement results of cavity performance at 2 K and 4.5 K. The measured quality factor is within a few percent of the nominal design goal at 4.5 K and exceeds the nominal design goal at 2 K. In the case of 4.5 K operation, the cavity fields were turned up to an equivalent accelerating voltage of 1.1 MV over the course of several minutes and with essentially no conditioning activity apparent on either the RF pickup signal or the test cryostat radiation monitoring system. The maximum voltage at this temperature was limited only by the available 80 Watt 1.4 GHz RF source. For 2 K operation, the cavity field was turned up to 2.1 MV, also with no conditioning. At 2.1 MV, the onset of what is believed to be a multipacting barrier was observed. During these tests,

the explicit choice was made not to try to condition the barrier, since the voltage is already nearly a factor of two above the nominal design value and this type of conditioning is well known to be a possible cause of Q degradation in SRF cavities. The cavity field performance at either 2 K or 4.5 K appears to be suitable for the production bunch lengthening system cryomodule for a voltage of 1.25 MV with no further development. There are, however, important trade-offs between the two cases. The use of accelerating voltages substantially higher than 1 MV have been proposed more recently, for example, $V=1.25$ MV with the 41 pm lattice taking into account the energy losses in the storage ring insertion devices. At this voltage, the heat load at 4.5 K approaches 100 Watts so that 4.5 K operation becomes increasingly inefficient and less attractive. The current plan is to operate the cavity at 2.1 K.

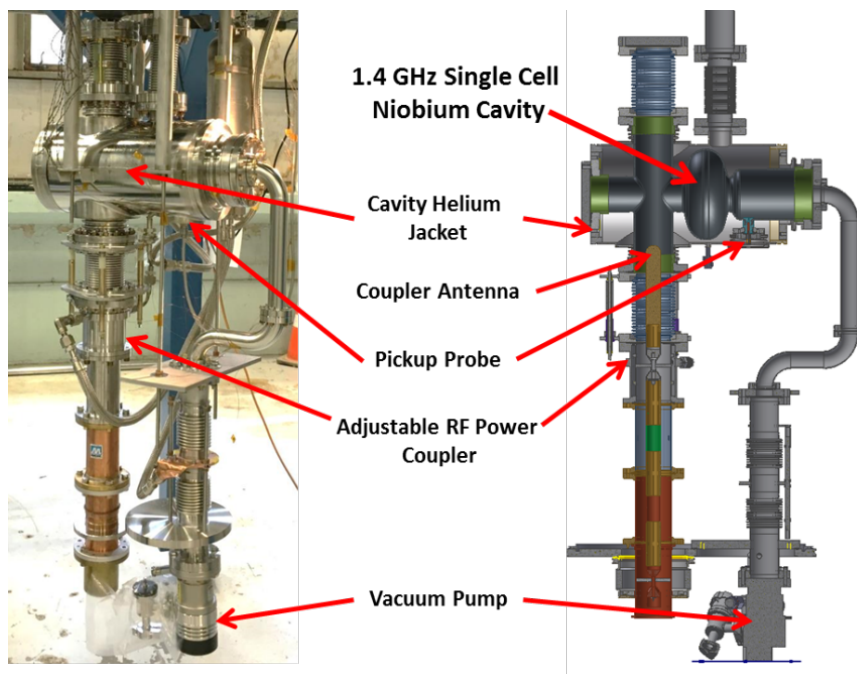


Figure 4.213. Cavity cold test configuration.

4-3.11.4 Fundamental RF power couplers

A pair of fundamental rf power couplers will be used to extract up to 32 kW of rf power in order to maintain the 1.25 MV harmonic cavity voltage for a range of beam currents and to avoid the Robinson instability. Each coupler will nominally extract half of the power and transport that power out of the cryomodule into a water cooled load. The coupler design is based on a pair of simple, rugged disc-shaped rf windows. The 50Ω line impedance is maintained by tapering the center conductor, as modelled in Figure 4.215. The lower image shows the anticipated temperature profile under the condition of 20 kW of rf power (per coupler) in the travelling wave mode. The rf windows are not coated with a low-SEC film. Multipacting was not predicted to be a problem and this conclusion has been supported by the experimental testing. The region between the two windows is common with the cryogenic vacuum. The space is pumped via narrow slots in the coupler outer conductor 80 K-to-300 K thermal transition.

A pair of prototypes has been built and tested as part of the APS-Upgrade R&D. It is planned

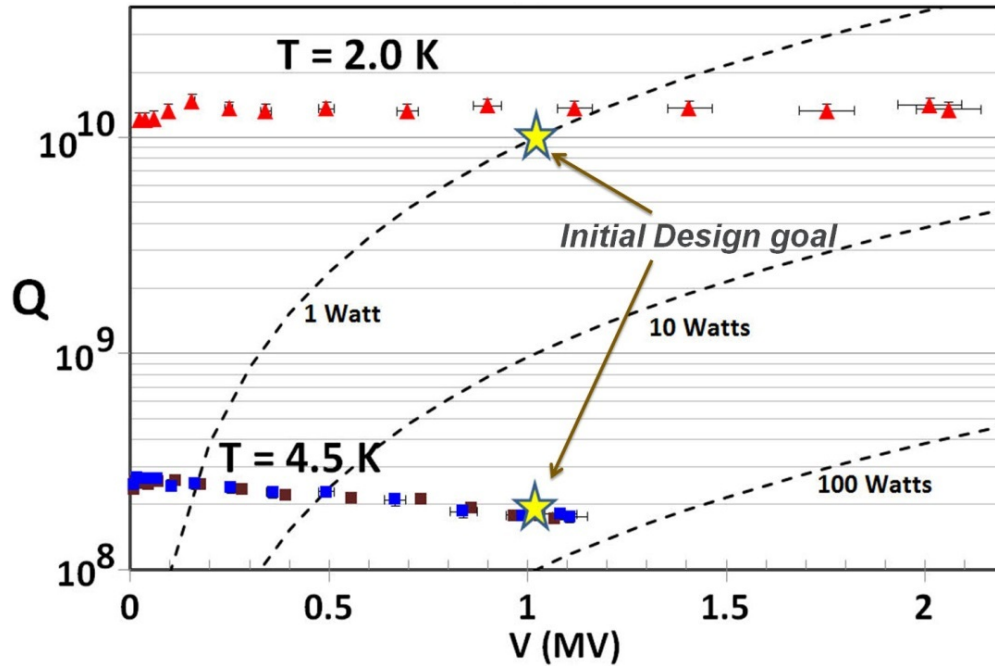


Figure 4.214. Cavity cold test configuration.

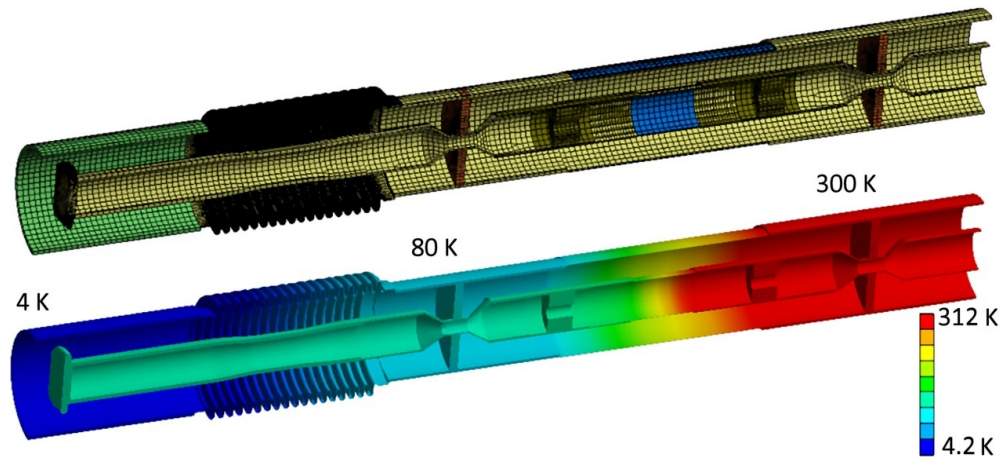


Figure 4.215. ANSYS mechanical model (top) and thermal simulation (bottom) showing the equilibrium temperature distribution for 20 kW cw operation of the fundamental power coupler in travelling wave mode.

that these will be used in the final bunch lengthening system assembly. The 79-mm outer diameter windows are fabricated from high purity (>97%) alumina, brazed together with OFHC copper inner and outer conductors. The geometry, and therefore thermal stresses due to differential contraction of copper and ceramic, are the same as for 40 mm and 50 mm couplers built by Argonne for ATLAS and Fermilab. The two-window approach has several benefits. First, the central conductor can be directly cooled by conduction through the ceramic disc, which has good thermal conductivity from room temperature down to 80 K. Second, the portion of the central conductor that projects in toward the beam is located only a few centimeters from the SRF cavity cell and will operate

at cryogenic temperatures under all conditions due to the high thermal conductivity of copper. Third, cavity clean room assembly can be simplified, since most of the coupler components are assembled outside of the clean room and without breaking cavity vacuum. This facilitates both cavity cleanliness and ease of installation into a cryomodule.

The coupler is adjustable by stretching or compressing the bellows, visible in Figure 4.215. The resulting movement of the center conductor by up to 4 cm relative to the cell of the cavity, in turn, changes the Q_{EXT} (per coupler) within the range of 1×10^6 to 1×10^8 . The thin-walled copper plated bellows also serves as the thermal break between the nitrogen cooled coupler window and the helium cooled cavity.

The components of the coupler are shown in Figure 4.216 and are the warm rf window (A), the room temperature to 80 K transition (B), the cold rf window (C), and the bellows (D). Note that in this assembly the bellows is held fixed at the neutral (midpoint) position. The heating in the coupler was measured in full transmission using the available 18 kW of rf power at 1.3 GHz for 3 hours. Heating was measured using a series of thermometers located both on the outside and inside of the transmission line and results are shown in Figure 4.217. Thermal time constants are of the order ~ 1 hour and indicate that operation is stable at this power level. Similar measurements were performed for several lower levels of rf power with no apparent problematic multipacting, conditioning, or heating. By modest extrapolation to 20 kW and 1.4 GHz, it is anticipated that the coupler will be suitable to meeting the full APS-U design requirements, however, additional high-power testing at 1.4 GHz would clearly be desirable.

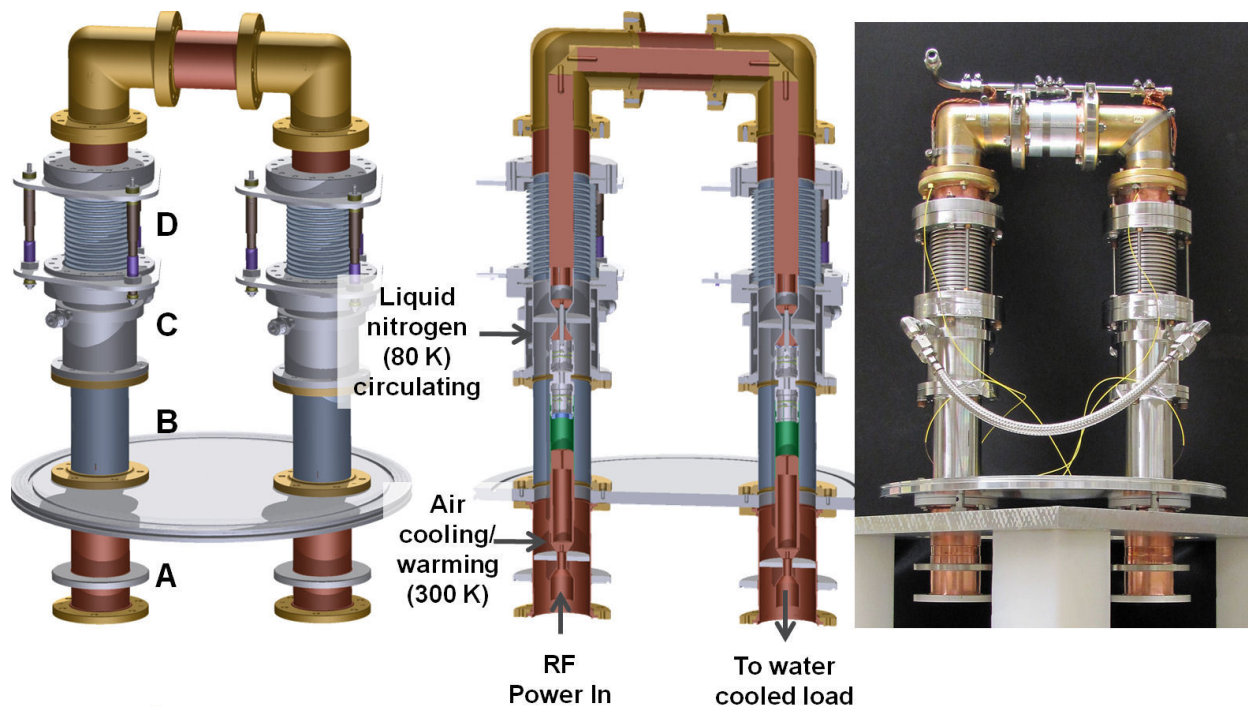


Figure 4.216. RF power coupler R&D test assembly.

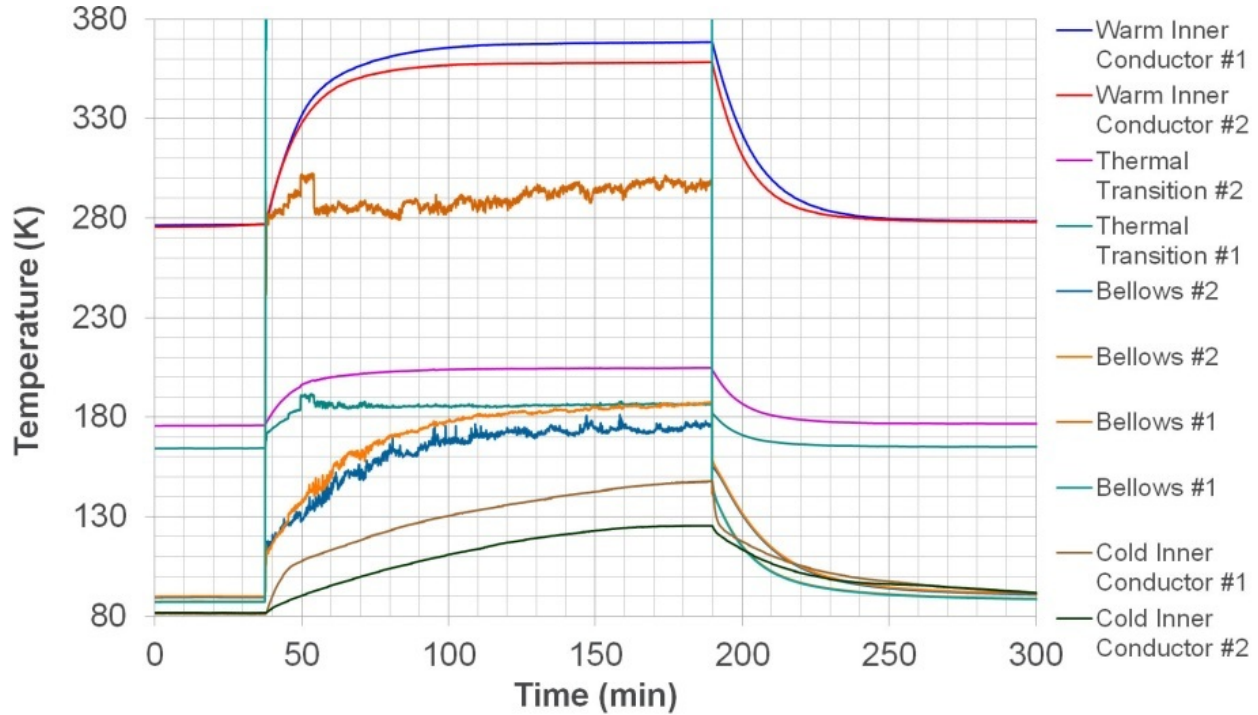


Figure 4.217. Measured rf heating in the power coupler for 18 kW of transmitted power at 1.3 GHz.

4-3.11.5 Higher Order Mode Dampers

The wakefields excited by the beam can be resonantly excited if the beam current spectrum drives one or more of the higher order modes (HOMs) in the harmonic cavity. These beam-induced HOMs must be damped because otherwise these may cause excessive cryogenic loads due to RF heating and/or will induce multi-bunch instabilities which will limit the practical single bunch charge. A pair of RF absorbers located just outside the ends of the cryomodule, so-called beam pipe HOM absorbers, is employed to damp HOMs. This method requires that HOMs excited in the cavity be extracted through beam pipes. One of the cavity beam pipes is flared to a 10 cm diameter such that the first cavity dipole mode, the TE₁₁ mode, can propagate along the beam pipe. The strategy for HOM damping in the bunch lengthening system is to damp all possible HOMs with the conservative assumption that they are excited on resonance with the beam. This strategy implies that we do not control the HOM resonant frequencies with respect to the beam harmonics.

The HOM absorber is essentially a lossy ceramic tube whose inner diameter is matched to the envelope of the beam pipe vacuum space. As a lossy RF material, the graphite-direct-sintered silicon carbide, Coorstek SC-35, has been chosen based on experience in the Cornell ERL Injector Cryomodule [3]. Dielectric properties of this material, which give the strength of HOM damping, have been experimentally characterized. Scattering parameters measured in a coaxial transmission line assembled with the SiC tube show that nominal dielectric constant ϵ is 45 and loss tangent $\tan \delta$ is 0.45 [4]. The SiC tube inserted into the beam is itself a resonator with a broad bandwidth due to the high loss tangent. The dimensions of the SiC tubes, which determine the frequency range of the broadband resonance, were chosen such that the resonance of the pair of different-size SiC tubes

occurs for frequencies between 2 and 4 GHz. Therefore, high r/Q modes in the harmonic cavity are strongly damped. The inner diameters are 104 mm for the larger damper and 70 mm for the smaller, and are the same as the cavity beam pipe inner diameters. The length and thickness are the same for both absorbers and are 135 mm and 5 mm, respectively.

Beam impedances in the bunch lengthening system were simulated with a simplified RF model that includes the cavity, a pair of the HOM absorbers, the beam pipe conical transitions, and a pair of identical couplers with shortened coaxial lines, as shown in Figure 4.218 (a). These simulation results show all HOMs excited in the cavity and/or couplers are well damped so that the HOM impedances have more than one order of magnitude of margin with respect to the calculated multi-bunch instability threshold limit. The couplers also contribute to HOM damping for HOMs associated with the couplers themselves. The monopole mode at 1.6 GHz is excited in the beam pipe space surrounded by the coupler antenna. This mode can propagate only along the coupler coaxial line and a specially shaped coupler antenna was designed for this purpose. As a result, the coupled mode at 1.6 GHz is strongly damped, as shown in Figure 4.218 (b) [4]. HOM damping across a broad spectrum was measured at room temperature using a finished niobium harmonic cavity assembled together with the finished SiC HOM absorber assemblies and a mockup of the other beam pipe components. The measured quality factors of the HOMs are consistent with those predicted in the simulations with the SiC HOM absorbers [4]. Beam-loss power estimated from the real part of the longitudinal impedance is 1.7 kW; approximately 1 kW will be dissipated in the larger SiC HOM absorber and the rest will be dissipated in the smaller.

SiC HOM absorbers operating at room temperature can easily handle the ~ 1 kW heat-load by water cooling. Figure 4.219 (a) shows the mechanical model of the SiC HOM absorber assembly for the larger one. The SiC tube is surrounded by a copper cooling jacket with 0.1 mm interference in diameter for the larger of the two, and 0.075 mm for the smaller. The interference in diameter was chosen such that the stress on the SiC tube is much smaller than the compressive strength of the SiC as shown in Figure 4.219 (b) and at the same time, the pressure on the contact surface between the SiC and copper is sufficient for good thermal contact. Figure 4.219 (c) shows the finished large HOM absorber assembly. The SiC tube is inserted into copper cooling jacket in a ‘shrink fit’ manner: first, the copper cooling jacket with the stainless steel housing was heated up in a furnace and, next, the SiC tube, at room temperature, was inserted into the housing. Once cooled, the thermal contact resistance was measured using a halogen bulb as a radiative heat source. The measured temperature rise was 2 degrees-C per 1 kW of heat load [5].

4-3.11.6 Cavity Slow Mechanical Tuner

During operation, the superconducting cavity resonant frequency should be set 13.5 kHz above the 4th harmonic of 352 MHz in order to achieve the nominal bunch lengthening parameters. Furthermore, the cavity fundamental mode should be detuned from the beam harmonics in the event of a failure in the cryomodule or cryogenics. The frequency shift for this ‘parking’ mode was chosen to be one and a half revolution harmonics (407 kHz) below the 4th harmonic frequency. The cavity slow frequency tuning system was designed to meet this criterion with additional margin. The designed frequency range is 600 kHz for the cold cavity.

The tuner, installed on the left-hand side of the cavity shown in Figure 4.220(b), is based on a pneumatic bellows which is actuated using helium gas up to an internal pressure of about 3 bar.

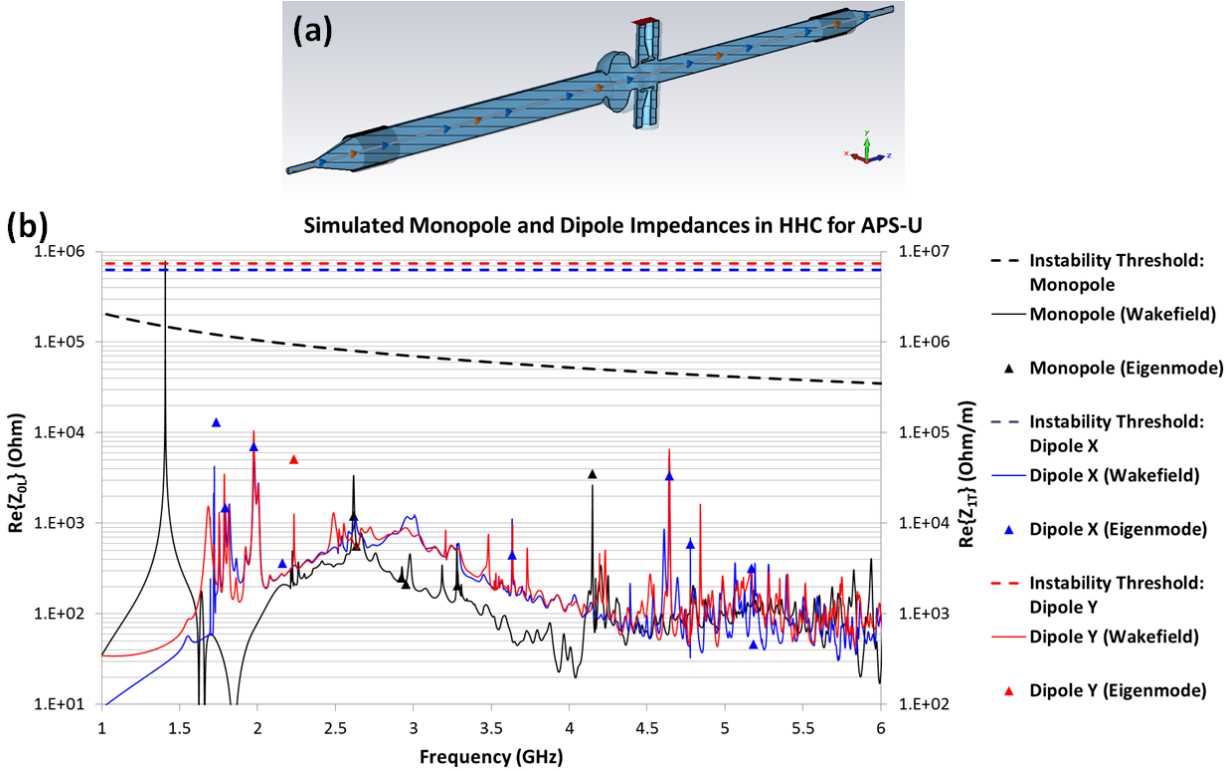


Figure 4.218. (a) RF model for impedance simulations and (b) simulation results by CST Wakefield and Eigenmode Solvers. Z_{0L} represents the longitudinal impedance of the monopole modes and Z_{1T} represents the transverse impedances of the dipole modes. Resolution in three impedance spectra calculated by the Wakefield Solver is 200 kHz and it is fine enough to resolve every high impedance peak.

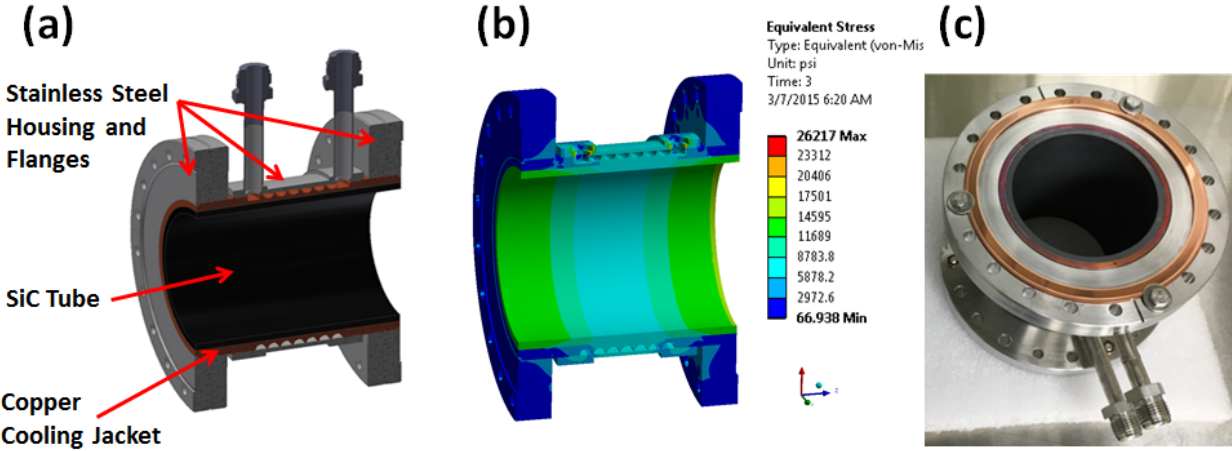


Figure 4.219. Details of the large HOM absorber assembly. (a): mechanical model, (b): von-Mises stress due to interference in diameter simulated by ANSYS, (c): finished assembly of the large HOM absorber.

In simple terms, the pneumatic bellows is captured between two large fixed plates (labeled 1 and 2 in Figure 4.110(b).) When the bellows is pressurized, the cavity beam port flange (labelled 7) is pushed inward, in turn exerting a compressive force across the cavity cell. Additional details are in the figure caption. Similar ANL-developed technology is used on slow tuners in the ATLAS superconducting heavy-ion accelerator and for approximately 200 new cavities in the FRIB driver linac at MSU. When expanded (as shown), the bellows exerts a longitudinal force of up to 26 kN across the cell of the niobium cavity in order to provide a full tuning range of 600 kHz for the 1.4 GHz cavity fundamental frequency. The tuner system assembled with the cavity was tested at cryogenic temperatures in the ANL vertical testing cryostat. Figure 4.220(a) shows a photograph of the assembly. Measured test data in Figure 4.221 show no plastic deformation or hysteresis.

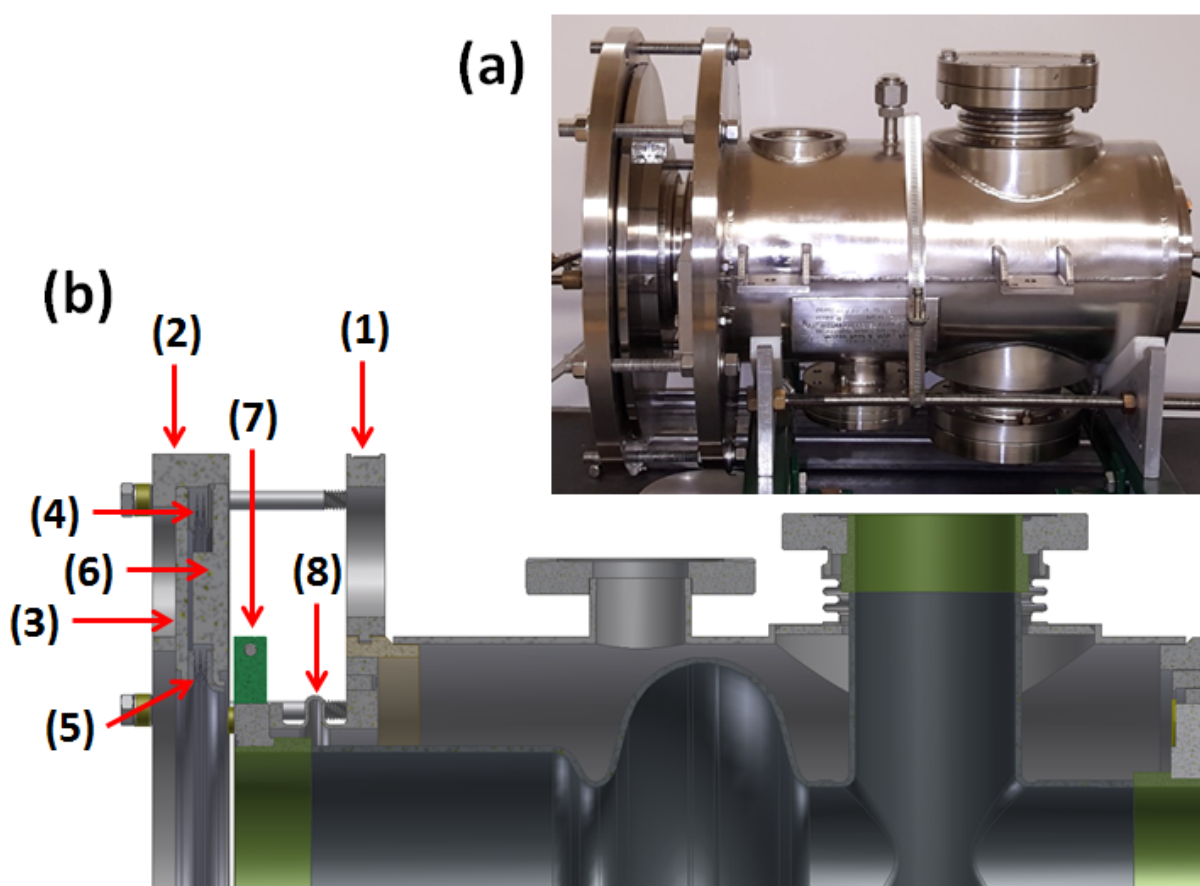


Figure 4.220. Mechanical model of the slow frequency tuner (a) and the prototype tuner assembled with the cavity (b). Detailed slow frequency tuner parts are as follows; (1), (2): cold (2 K) and warm (80 K) retaining rings, (3), (6): pressure plates, (4), (5) outer and inner bellows for the pressure plates, (7): cavity beam port flange clamp ring, (8): single-convolution bellow in helium jacket. On pressurizing the bellows (4,5), the pressure plate (6) and the clamp ring (7) move right relative to the cylindrical part of the helium jacket and this leads to longitudinal compression of the niobium cavity.

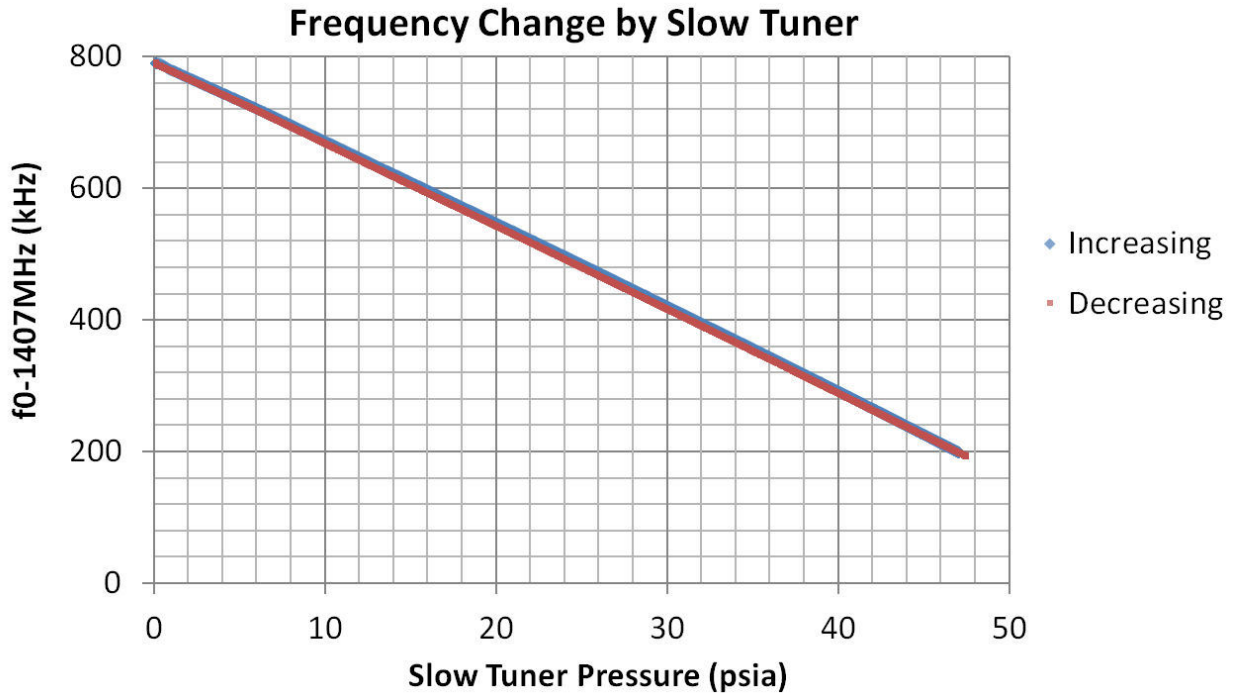


Figure 4.221. Measured cavity resonant frequency change with slow tuner helium gas pressure. Red dots were measured when the pressure was increasing, blue dots (partially obscured by the red dots) were measured when the pressure was decreasing.

4-3.11.7 Bunch Lengthening System Cryomodule

The harmonic cavity cryomodule shown in Figure 4.222 houses a single SRF accelerating cavity cooled by 2 K liquid helium inside an integral cavity helium vessel. The cryomodule outer vacuum vessel will be fabricated from 304 series stainless steel. Inside of the lower vessel (A) will be a room temperature magnetic shield (B), an 80 K aluminum heat shield (C), 80 K coolant distribution lines, thermal attachments to the heat shield, and multi-layer insulation (MLI) on both sides of the aluminum heat shield. The shields are shown at the left in Figure 4.222. Other components that are also attached to or suspended from the top lid, but are not shown in the figure include:

1. Helium feed and return
2. Helium storage vessel
3. Nitrogen feed and phase separator vessel
4. Heat exchanger and J-T valve for 2K operation
5. Upper rf power coupler
6. Cavity rf pickup
7. Slow tuner supply gas
8. Thermometers and heaters

The bunch lengthening cavity will require alignment (± 0.5 mm transverse) with respect to the APS-U vacuum chamber. For this purpose, the cavity will be equipped with 4 open wire targets all of which will be viewable through ports located on the end-walls of the cryomodule. The cryomodule

will have all metal rf gate valves attached to the ends as shown in Figure 4.222. The design allows the complete hermetically sealed superconducting cavity assembly to drop into the cryomodule vacuum vessel while the cavity remains under vacuum. The cryomodule, in turn, will be installed under vacuum into the APS- U storage ring.

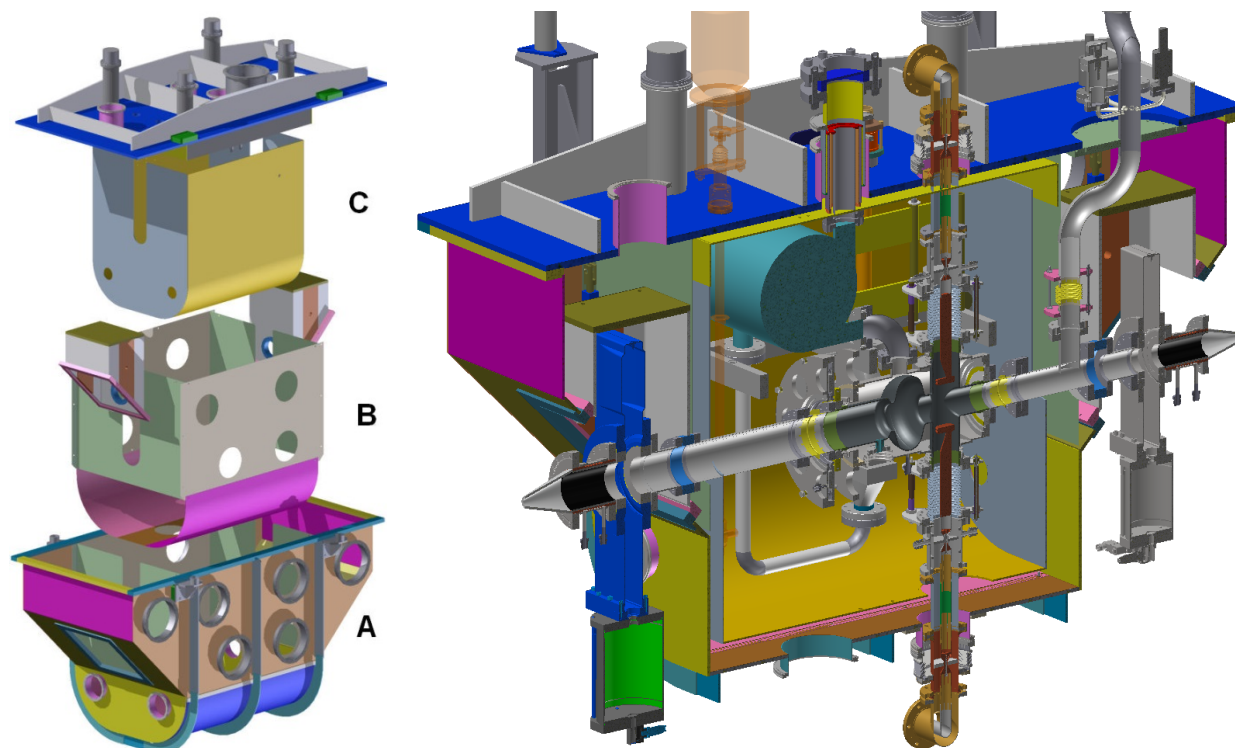


Figure 4.222. Vacuum vessel, thermal and magnetic shields (left) and half section of the full cryomodule (right).

4-3.11.8 Cryogenic Plant

A new 4-K liquid helium refrigerator and distribution system will be purchased to provide saturated liquid helium via a low-heat-leak distribution system to the cavity and cryomodule. A schematic of the helium flow is shown in Figure 4.223. A JT-valve and heat exchanger inside the cryomodule will provide up to 50 Watts of 2.1 K helium to the cavity. For the 4 K refrigerator cold box, commercially available models near the rated capacity are available from major international manufacturers. The anticipated lead time should be less than two years for standard models. The capacity accommodates the static heat loads presented by the cryomodule and distribution system, as well as the dynamic load imposed by cavity operation in order to maintain a stable temperature under all operating conditions. A 400-W liquid nitrogen capacity is required for thermal intercepts and thermal shielding inside the cryomodule and distribution system. The liquid nitrogen will be supplied from the APS nitrogen distribution system, either directly or indirectly via a storage tank. Liquid nitrogen is chosen for cooling the shields for several reasons: it is readily available at the APS; ANL has mature designs using this approach; and the ODH issues from the 5.5 g/s flow rate do not appear to be severe. The preliminary design assumes that the cryoplant is located close to Zone-F, in the Early Assembly Area (EAA) space. Elements that inform the design of a cryogenic system for the SRF cavity include:

- System margin: Some amount of overcapacity will be designed into the system to mitigate the risks associated with uncertain cavity dynamic heat load and the possibility that the completed plant underperforms. The latter can also be mitigated with an incentive-based procurement contract tied to actual measured capacity during commissioning.
- Safety (pressure, cryogenics, oxygen deficiency hazard, system venting, etc.): Safety analyses are a fundamental aspect of cryoplant design. Vendors will be held to applicable codes and standards with regard to pressure system safety. Oxygen deficiency hazard analyses will be conducted for all cryoplant enclosures, as well as the regions of the APS tunnel containing cryomodules and distribution system components.
- System reliability: The cryoplant availability must meet overall APS requirements. This may be achieved via on-line spares, modular design, and system margin. A robust control system is an integral part of this aspect of performance.

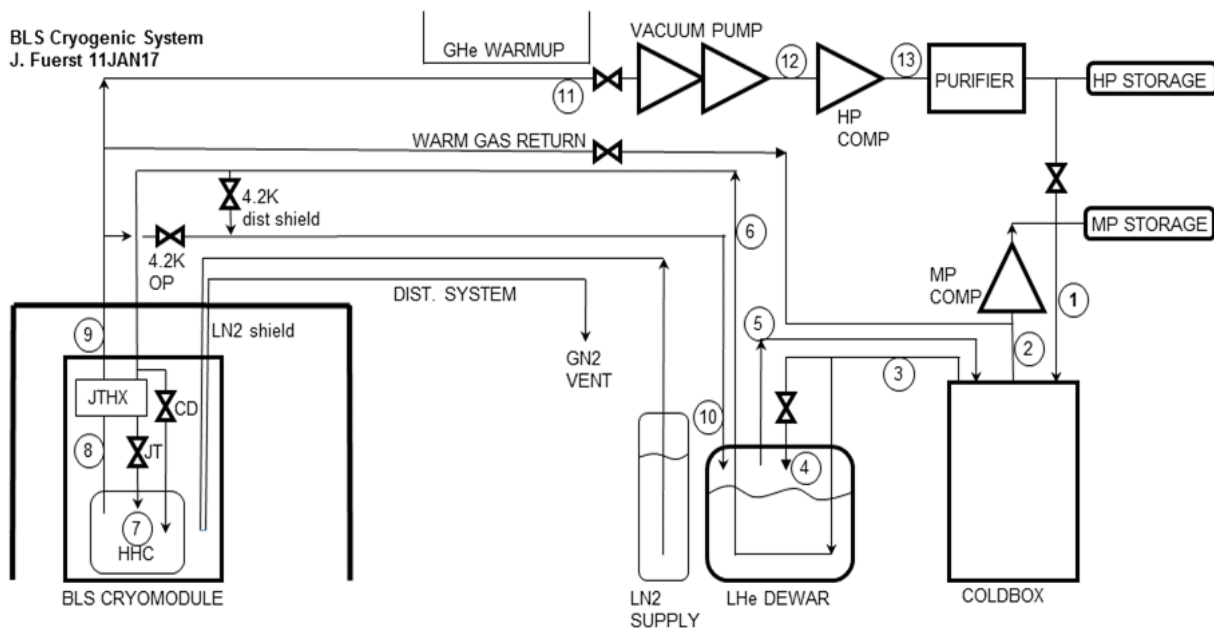


Figure 4.223. Schematic of the BLS cryogenic system.

4-3.11.9 Bunch-Lengthening RF System

A block diagram of the bunch-lengthening rf system is shown in Figure 4.224. The superconducting rf cavity is fitted with two output couplers utilizing $3 \frac{1}{8}$ -inch EIA coaxial flanges, each of which will be terminated with a dual coaxial directional coupler and a 50-kW broadband rf load to dissipate the rf power extracted from the beam. The directional couplers will be used to monitor the forward and reverse rf power at each load. The rf loads will be cooled with deionized water and will be monitored and protected by an interlock system to prevent over-dissipation, over-heating, or operation with insufficient water flow. Since the beam is the only source of power to the cavity, the primary mechanism for protecting the cavity will be to dump stored beam via the machine protection system (MPS).

The LLRF system will monitor and regulate the cavity field. Since the harmonic cavity is completely

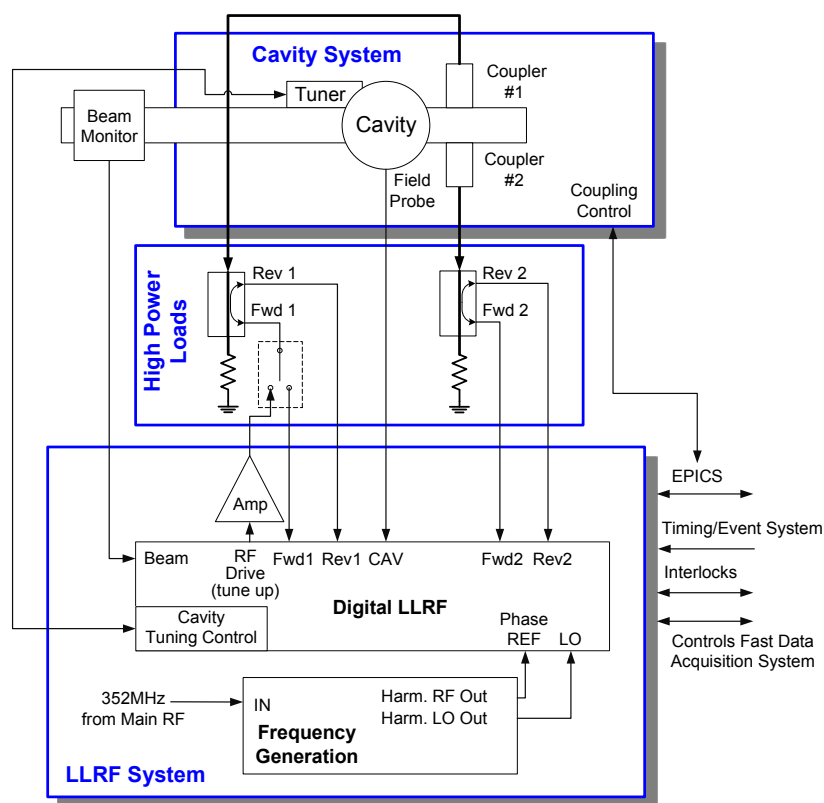


Figure 4.224. Block diagram for the bunch lengthening rf system.

driven by the beam, the cavity field is determined by the beam current, the cavity detuning, and the loaded Q . As discussed in section 4-2.9, the loaded Q will be held fixed. Thus the cavity amplitude will be controlled via the cavity tuner.

An rf drive signal will be made available by the LLRF system to aid with initial system setup without beam. The drive signal can be switched into a directional coupler for one of the input couplers to excite the cavity. The resonant frequency can then be found and adjusted before the cavity sees beam. Initial balancing of the input couplers can also be determined during ring down after shutting the rf drive off. The rf drive can then be switched out of the system in preparation for beam.

The LLRF system will interface to EPICS, the interlock system, and the Timing/Event system for time-stamping the data sent to the controls' fast data acquisition system (DAQ). A frequency generation unit will provide a phase reference signal as well as the local oscillator (LO) signal to translate the rf signals to an intermediate frequency for digital sampling. A channel will be reserved for a beam monitor which can be used to monitor the phase of the beam relative to the cavity field.

References

- [1] M. Pedrozzi et al. “First Operational Results of the 3rd Harmonic Superconducting Cavities in SLS and ELETTRA.” In: *Proc. PAC 2003*. 2003, p. 878 (cit. on p. 271).
- [2] E. Haebel et. al. “Cavity Shape Optimization for a Superconducting Linear Collider.” In: *Proc. of High-energy Accelerator Conference, Hamburg, Germany*. 1992 (cit. on p. 271).
- [3] R. Eichhorn et al. “Cornell’s HOM Beamline Absorbers.” In: *IPAC2013*. 2013 (cit. on p. 277).
- [4] S.H. Kim et al. “Higher Order Mode Damping in a Higher Harmonic Cavity for the Advanced Photon Source Upgrade.” In: *SRF2015*. 2015 (cit. on pp. 277, 278).
- [5] S.H. Kim. “HOM Damping in Superconducting 1.4 GHz Harmonic Cavity for APS Upgrade.” In: *ICFA Mini Workshop on High Order Modes in Superconducting Cavities (HOMSC16)*. 2016 (cit. on p. 278).

4-3.12 Engineered Safety Systems

The “Advanced Photon Source Safety Assessment Document” [1] describes the engineered safety systems used by the present APS. These systems, with appropriate modifications, are expected to be sufficient for the upgraded APS facility described in this document. The storage ring accelerator safety envelope value of 9280 joules of stored-beam energy is not envisioned to need to change, nor will the safety envelope injected beam power of 308 W. The beam lifetime is expected to be significantly lower than the 10 hour value used for the present APS, which directly impacts ambient radiation levels seen outside of the accelerator enclosure.

The injector machines will operate with higher charge per pulse, but will remain within the existing 154 W operating envelope beam power. More frequent injection into the storage ring will be needed to compensate for reduced beam lifetime. Safety considerations regarding full bunch replacement swap-out operation are quite similar to those encountered when top-up operation was instituted at the APS. Permanent magnets will be added to the beamline front ends as an additional safety measure to assure that injected beams cannot be transported out to x-ray experimental hutches. This will be done in addition to present top-up safeguards, including top-up stored beam monitors that inhibit injection with x-ray shutters open unless a sufficient amount of stored beam is already circulating.

Extensive simulations have been conducted to quantify radiation levels associated with high injector charge, stored beam lifetime-related losses, bremsstrahlung, swap-out single-bunch loss, and total beam loss. Operation at lower beam energy (6 GeV vs. 7 GeV) is expected to offset, to some extent, the higher stored beam current (200 mA vs. 100 mA) and higher injected single-bunch charge (~ 16 nC vs. ~ 2 nC).

A short summary of the APS Engineered Safety Systems is provided here, and the reader is referred to Ref. [1] for further details.

4-3.12.1 Access Control and Interlock System

The APS access control and interlock system (ACIS) is an engineered safety system for integrating access control and monitoring devices for the accelerator enclosures, including the linac, particle accumulator ring (PAR), booster synchrotron, linac extension area (LEA), and storage ring. The ACIS provides protection by ensuring that no one may occupy or enter an area where prompt radiation may be present. The system also inhibits beam generation when established radiation limits are exceeded, or when equipment failure is detected or improper access is gained. The plan is to use this system for the APS Upgrade. Modifications to the inputs/outputs/logic will be required due to the different operational modes for the APS Upgrade and choice of swap-out versus top-up for injection.

The APS facility is designed to allow the major systems, i.e., linac/PAR, booster synchrotron, LEA, and storage ring, to run independently of one another under specific conditions. This is accomplished by the partitioning of areas with concrete shielding, beam stops, and other safeguards. Five complete and independent ACIS implementations are provided, one for the linac-PAR tunnel area, one for the synchrotron tunnel area, one for the LEA tunnel area, one for the rf area of the storage ring (zone F), and one for the remainder of the storage ring (zones A through E). Each system is designed

using the applicable DOE orders and industrial safety standards. The APS/AES staff is responsible for the modification, verification, annual validation, and maintenance of the system. See Ref. [1] for further details.

4-3.12.2 Personnel Safety System

The APS has the potential of operating with up to 70 beamlines. Each beamline includes multiple shielded enclosures containing optics and experimental equipment. Personnel access into these enclosures is controlled during beamline operation by the personnel safety system (PSS). The PSS is an engineered safety system for each beamline for controlling access into the enclosures. It ensures that access is allowed only under safe conditions (i.e., x-ray beam is off in the enclosure) and disables storage ring operation if improper access is gained or a PSS system fault is detected that could potentially endanger personnel.

The PSS for each beamline interfaces directly with the accelerator's ACIS for disabling storage ring operation. Each PSS is totally isolated from the PSS of any other beamline to prevent a fault from one beamline affecting the operation of other beamlines.

Each PSS is designed to meet the requirements of the beamline after review and concurrence by the Beamline Safety Design Review Steering Committee. Each system is designed using the applicable DOE orders and industrial safety standards. The APS staff is also responsible for the installation, verification, annual validation, and maintenance of the system. Although beamline designs require some flexibility in possible modes of operation, types of devices to be interlocked, and other operational requirements, the basic configuration and control aspects remain the same. The system documentation, test procedures, and training include all basic as well as specialized equipment and operating modes. The beamline efforts in the APS Upgrade will use these same systems and processes.

4-3.12.3 Radiation and Shielding Assessment

4-3.12.3.1 Introduction The primary purpose of the APS is to use electrons to produce high-quality synchrotron radiation for use in x-ray experiments. Personnel must be shielded against direct exposure to these x-rays. As the electron beam circulates in the storage ring, a small fraction of the beam is lost because of orbital excursions, interactions among beam particles, and collisions with gas molecules, which also produce radiation. Finally, as the storage ring is filled during injector operations, beam losses in collimators, beam stops, septum magnets, and other accelerator components lead to the production of prompt radiation fields. These radiation fields consist mainly of photons (bremsstrahlung x-rays and gamma rays) and neutrons. In addition to the prompt radiation exposure, interaction of these radiations leads to potential activation of accelerator components, which could create delayed radiation exposure hazards. The APS radiation safety policy protects workers, users, and the general public from hazards associated with these radiation fields.

Table 4.88 summarizes some of the operating parameters for the present APS and the APS-Upgrade. The circulating current in the storage ring will be a factor of two higher in the Upgrade, at slightly lower electron energy, so that the energy stored in the storage ring will be nearly twice that at present. Two operating modes will be used, with the brightness mode being similar to present APS operations in terms of charge per bunch and beam lifetime in the storage ring. In the timing mode,

however, the higher bunch charge means that the beam lifetime will be shorter, requiring more frequent injection and thus a higher average injected beam power.

Table 4.88. Operating parameters for the present APS and the APS-Upgrade

Quantity	Present APS	APS-Upgrade	
		Timing Mode	Brightness Mode
Electron energy (GeV)	7	6	6
Beam Current (mA)	100	200	200
Number of bunches	24	48	324
Charge per bunch (nC)	15.3	15.3	2.3
Beam lifetime (h)*	8	2.91	5.96
Injection mode	top-up	swap-out	swap-out
Stored energy (J)	2576	4420	4420
Average injection power (W)	0.089	4.0	1.95

* 10th percentile lifetime

Perhaps the most significant change is the use of swap-out injection, in which circulating bunches will be replaced after their charge falls to approximately 90% of the initial value. This mode of operation, combined with the increased electron loss rate from the storage ring and higher stored current, means that the Upgrade must inject about sixty times more electrons into the storage ring than present operations at the APS.

These changes in operation may pose some challenges to the APS radiation safety program. A comprehensive analysis of radiation physics issues throughout the facility is underway to make sure the dose and dose rate goals stated below will be met. Because operation is similar in many ways to present APS operations, we do not anticipate any new radiation source terms. However, five areas have been identified for the APS-Upgrade that will require detailed investigation to assess their potential for increases in radiation source terms and the need for supplemental shielding. These are (1) losses throughout the injector chain due to high-bunch-charge acceleration (2) increased losses of injected beam around the injection septum and other localized loss points due to the more-frequent injection (3) greater stored beam losses due to higher circulating current and shorter beam lifetime (4) increased gas bremsstrahlung production in the straight sections and directed down x-ray beamlines due to changes in pressure and composition of residual gas in the storage ring and (5) dose due to a dedicated beam dump that will receive the charge in the swapped-out beam bunches.

4-3.12.3.2 APS-U Limits for Annual Dose Limits for annual dose due to operation of the APS-Upgrade are based on applicable DOE and ANL regulations and experience at other US-based light sources. The primary document that governs radiation protection at DOE facilities is 10 CFR 835, Occupational Radiation Protection [2]. In addition, accelerator-specific standards are set forth in DOE Order 420.2c, Safety of Accelerator Facilities [3, 4]. Argonne's Radiological Safety Program Description [5] provides details on the local implementation of radiation protection standards. Finally, the APS has adopted its own dose guidelines. Table 4.89 shows the annual dose limits for APS-U, which are the same as for the present APS.

The maximum annual exposure to radiation workers is specified in 10 CFR 835.202 as 5000 mrem

(50 mSv) effective dose.⁶ The 10 CFR 835 design objective for external exposure is 1000 mrem (10 mSv) for new or modified facilities, in areas of continuous occupancy (2000 h/y) [see 10 CFR 835.1002(b)]. Argonne also has an Administrative Control Level of 1000 mrem/y (10 mSv/y) for individual occupational exposure, and a design objective for new or modified facilities of 500 mrem/y (5 mSv/y). The general shielding requirement for the APS is that the maximum individual (radiation) worker dose will be ALARA and less than 500 mrem/y (5 mSv/y). APS shielding policy also stipulates that the average rad worker dose will be below 200 mrem/y (2 mSv/y). Dosimeter readings acquired since commencement of APS operations have demonstrated that the actual average radiation worker dose for present APS operations is much less than 100 mrem/y (1 mSv/y).

The annual dose limit in 10 CFR 835 for non-radiation workers in a controlled area is 100 mrem (1 mSv), the same as for members of the general public. This category includes APS users. The Argonne and APS policies for on-site non-radiation workers in the vicinity of the APS facilities require that the average non-radiation worker dose be below 100 mrem/y (1 mSv/y). In addition, the dose at the site boundary from all pathways is required to be below 10 mrem/y (0.1 mSv/y). Present estimates of the annual doses for these two categories of exposure indicate that these requirements are being met.

Table 4.89. Proposed annual dose limits for the APS-Upgrade

Category	present APS	proposed for APS-U
Radiation workers	500 mrem	500 mrem
Non-radiation workers	100 mrem	100 mrem
General public (off-site)	10 mrem	10 mrem

4-3.12.3.3 APS-U Shielding Policy Shielding at the APS-Upgrade must be sufficient to meet the dose goals presented in Table 4.89. Table 4.90 shows the proposed shielding criteria for the APS-Upgrade facility, which set dose rate limits in the various locations around the facility. The consequences of normal operations will include the effects of stored beam losses, losses during beam acceleration and injection, and some number of full beam dumps per year, which are usually initiated for machine protection purposes. Separate dose rate limits apply to cases of off-normal operation, which are typically events such as beam mis-steering or loss of vacuum, RF, or magnetic field. These events can be self-limiting (e.g. an RF trip causes loss of the stored beam in the storage ring, but no more is injected), ended due to automatic interruption (a high radiation level causes a beam trip), or ended by operator intervention in response to an alarm. Another situation considered is the dose rate when the storage ring is being filled from zero, since in this case the injector runs continuously for some period of time. Finally, the shielding design should also limit the dose rate due to the maximum credible incident (MCI) so that the APS-U facility will maintain the low hazard designation of the present APS.

Table 4.91 shows the operating modes of the present APS and of the APS-U, along with some of the relevant parameters for each operating mode. Calculations of annual dose due to normal and

⁶Note: 10 CFR 835 and Argonne's Radiological Safety Program Description use special units — Roentgen, rem, Curie, etc. — for designating radiological quantities, and that convention is followed here. SI units are indicated parenthetically.

Table 4.90. Shielding design criteria for the APS-Upgrade (based on 100% occupancy). See text for explanation of locations.

	Location	proposed for APS-U
Normal ops	experimental hall floor storage ring mezzanine utility corridor	0.05 mrem/h
	accelerator areas (linac/PAR/booster/LEA/RF)	0.05 mrem/h
	off-site	0.00125 mrem/h*
Normal injection (fill from zero)	experimental hall floor storage ring mezzanine	2 mrem/h
	utility corridor accelerator areas	5 mrem/h
Off-normal events	experimental hall floor storage ring mezzanine	200 mrem/h
	utility corridor accelerator areas	500 mrem/h
MCI		10 rem/h

* based on 8000 h/y

off-normal operations will assume that APS operates at the design performance goal (the right-most column in Table 4.91). This is the practice at other US-based light sources [6, 7, 8, 9], since this represents the conditions under which the facility is expected to run. Some facilities refer to this performance level as an operating envelope, although the term is used differently at APS. For calculation of dose due to normal operations, occupancy factors will also be considered, as many locations are not continuously occupied. These will be the actual occupancy of selected areas determined from occupancy data, or derived from values tabulated by the NCRP for photon radiotherapy facilities [10]. As an example, the occupancy of an x-ray beamline first optics enclosure can be determined by recording the amount of time the door to the area is open while beam is present in the storage ring. Calculation of consequences of the Maximum Credible Incident (MCI) will assume operations at the conditions of the Accelerator Safety Envelope, shown in the second column in Table 4.91, for each part of the facility. This is done to limit the maximum dose delivered in any accident that may be expected to occur during the lifetime of the facility.

The goal for annual dose on the experiment hall floor and storage ring mezzanine (the roof of the storage ring enclosure) is a maximum of 100 mrem (1 mSv) effective dose. This would be an average dose rate of 0.05 mrem/h (0.5 μ Sv/h) for 2000 h/y (full occupancy). If this is the maximum dose rate outside the shielding, the maximally-exposed individual should receive less than the dose limit since people do not spend all their time in the location that has the highest dose rate. The utility corridor along the inboard wall of the storage ring can be accessed from the storage ring mezzanine, but this location is not continuously occupied (typical occupancy is less than 0.1), so that somewhat higher dose rates can be tolerated there. The beamline first optics enclosures and experimental stations are also not continuously occupied, and data are being acquired to determine occupancy in those areas. Currently, all of these areas can be entered by anyone who has access to

Table 4.91. Selected Parameters for the APS Accelerator Safety Envelope and Operating Envelope [1]

Area (operational mode)	Safety Envelope	Operating Envelope	Design Performance APS	Goal APS-U
Booster/HET				
Beam Power (W)	308	154	84	120
Beam Energy (GeV)		7.7	7	6
Charge per cycle (nC)		10	6	20
Storage Ring Injection (closed shutters)				
Beam Power (W)	308	154	84	102
Maximum Beam Energy (GeV)		7.7	7	6
Charge per cycle (nC)		10	6	17
Storage Ring Injection (top-up)				
Beam Power (W)	308	154	0.17	swap-out 6.5
Minimum Beam Energy (GeV)	6	6.5	7	5.5
Maximum Beam Energy (GeV)	7.7	7.7	7	6
Charge per cycle (nC)		10	3	16.1
Minimum stored current (mA)	1	3	3	3
Storage Ring (stored beam)				
Maximum Stored Energy (J)	9280	7728	2576	4420
Maximum Beam Energy (GeV)		7.7	7	6

the storage ring experiment hall. It is anticipated that users and beamline scientists would spend most of their time on the experiment hall floor, and a small fraction of their time would be spent in an experimental hutch, on the storage ring mezzanine, or the roof of an experimental hutch. They will not need to be in the utility corridor, which is only accessed for maintenance activities that principally occur during shutdown periods when the beam is off.

Some areas outside the accelerator shielding can only be entered by those having cardkey access and the appropriate training. These areas include, but are not limited to, the RF building (420), indoor areas around the linac (411), PAR (Particle Accumulator Ring, 412), LEA (Linac Extension Area, 413), and booster (415), and outdoor areas inside of the fence surrounding the booster. However, many of these personnel are not radiation workers since they include maintenance and custodial staff and computer support personnel. In these areas, shielding will also be designed to 0.05 mrem/h based on full occupancy. This will keep the dose to non-radiation workers below the 100 mrem/y limit. Radiation workers will also receive dose when they enter the accelerator enclosures during periods when the beam is off. Keeping the dose rate outside the shielding in the accelerator areas below 0.05 mrem/h ensures that their entire dose budget is not consumed outside the shielding. Occupancy factors are being determined for each area and will be used in calculations for annual dose. If the calculated dose rate is above 0.05 mrem/h in any area when normalized to 2000 h/y, we will first try to reduce the dose rate through the use of local shielding. If this is not successful, access restrictions to certain areas may be needed. Results of calculations will be benchmarked by measurements made during commissioning and the use of radiation monitors and area dosimeters during operations.

It is also desirable to limit the dose rate during periods when the storage ring is being filled. In the

accelerator areas and in the utility corridor, the limit will be 5 mrem/h (0.05 mSv/h), which is the threshold for a radiation area. DOE does not have a dose rate limit for non-radiation workers, only the 100 mrem limit on annual dose. The dose rate on the experiment hall floor and the storage ring mezzanine during injection will be 2 mrem/h (0.02 mSv/h), which is also the NRC limit for members of the general public in unrestricted areas (see 10 CFR 20.1301 [11]).

10 CFR 835 also does not specify limits for exposure due to off-normal operations or due to MCI conditions. In such cases we have based our limits on those adopted by other US light sources. Since these events are generally not self-limiting, it is more appropriate to give a limit for dose rate than for total dose. For off-normal operations, such as beam mis-steering incidents, the maximum dose rate will be 500 mrem/h (5 mSv/h) in accelerator areas and the utility corridor, and 200 mrem/h (2 mSv/h) in the experiment hall and the storage ring mezzanine. Local shielding will be installed if required to reduce dose rates below these values.

For the Maximum Credible Incident, the maximum dose rate will be 10 rem/h (100 mSv/h), evaluated at the conditions of the Accelerator Safety Envelope. Table 4.91 shows the numerical values of the parameters for the Accelerator Safety Envelope and the Operating Envelope for the present APS facility. New values have not been fully defined for the APS-Upgrade, but the values of beam parameters for accelerator tunnels, beamlines, and experiment stations that were used to design the existing shielding exceed the maximum operating parameters that will result from the APS Upgrade project (6 GeV and 200 mA). While the accelerator systems' performance characteristics will be modified as a result of the Upgrade, the radiation hazards they pose are expected to be within the range of applicability for existing APS shielding and safety systems. Eventual operations, once the APS Upgrade scope is completed, will remain within the current APS safety envelope. The Operating Envelope will be increased for certain parts of the facility (e.g., stored energy in the storage ring) to reflect the new operating conditions.

Radiation monitors and accelerator diagnostics (e.g., for beam loss) will be used to limit the duration of off-normal and maximum credible incidents and thus limit the total dose delivered. Area radiation monitors will be installed in locations of expected beam loss in order to shut down the beam if high radiation levels are detected. Area radiation monitors have been in place around the storage ring since the early days of APS operations. These monitors shut down the beam in the event of excessive beam loss on insertion devices or other small apertures. Additional monitors are in place outside the bulk shielding of the PAR and the booster injection and extraction areas to detect high radiation levels that could lead to dose rates greater than 5 mrem in any one-hour period. Another protective measure is to monitor the beam loss in parts of the facility so that operators can take action in case the beam loss exceeds some set value (this can be done for reasons of both dose minimization to personnel and machine protection).

Since the upgrade will essentially be a new facility, dosimeters may initially be required for personnel working in some areas outside of the bulk shielding. Worker dose monitoring by dosimeters will still be required for unrestricted access to the accelerator system enclosures and for work with radioactive material. In addition, area dosimeters will continue to be used throughout the facility to integrate dose in selected areas. The results will be analyzed for higher-than-expected doses and trends of increased doses; in areas where such observations are made, shielding would be reevaluated and improved as appropriate.

The shielding requirements will be satisfied by using standard and high-density concrete for bulk shielding of the accelerator to ensure adequate attenuation of the photon and neutron components of the secondary radiation. This bulk shielding is already in place, and was designed for the present APS using conservative assumptions. In addition, earth berms, steel, lead, dense polyethylene, and castable shielding materials will be used in the accelerator to supplement the bulk shielding at locations of high beam loss.

Shielding of the experimental beamlines consists primarily of lead panels which are used to protect against the synchrotron radiation and bremsstrahlung produced in the storage ring and entering the first-optics enclosures and experimental hutches. Guidelines for the design of x-ray beamline components are specified in Ref. [12]. Beamline and experiment-station shielding was designed for the synchrotron radiation produced by either a bending magnet or an insertion device, and for bremsstrahlung radiation produced both by electron scattering from residual gas in the storage ring and by electron scattering from storage ring components. Typically one of the two sources dominates while the other is negligible, so that the shielding requirement is determined by the dominant source.

For bremsstrahlung radiation calculations for the present facility [12], the storage ring was assumed to operate at 7.0 GeV and 300 mA. The shielding recommendations for bremsstrahlung were scaled for 7.7 GeV and 327 mA. For synchrotron radiation calculations [1], the storage ring was assumed to operate at 7.5 GeV and 200 mA, above the normal APS operating current of 100 mA. In addition, the recommended shielding thicknesses for synchrotron radiation include an additional tenth-value layer (the thickness of shielding needed to reduce the dose rate by a factor of ten) of the shielding material. The existing shielding will be analyzed to make sure that any potential increase in radiation source terms (e.g., gas bremsstrahlung) will not lead to dose rates in excess of the shielding design criterion of 0.05 mrem/h (0.5 μ Sv/h) as stated above.

The dose rate at any location inside the APS-Upgrade facility is expected to be dominated by radiation penetrating either the accelerator bulk shielding or the x-ray beamline shielding, but not both. To determine the annual dose to personnel it should be sufficient to consider the two sources individually. For any location identified where the two sources contribute significantly to the dose rate, the sum of the dose rate from the two sources will be limited by the values in Table 4.90.

4-3.12.3.4 Tracking Simulations As input to the design and simulation of the radiation shielding, *elegant* tracking simulations are used to predict the loss distribution, i.e., the rate of particle loss around the circumference, for both injected and stored electron beams.

Studies of injected beam losses in section 4-2.10 indicate that losses should be low, with injection losses generally at or below 2% for nominal conditions. Injection losses have been found to occur predominantly at the small aperture insertion device chambers. For stored beam, losses occur because of lifetime-limiting phenomena such as Touschek and gas scattering, as described in section 4-2.11. These losses occur at the small aperture insertion device chambers, the injection septum, and collimator / beam dump apertures. Electrons hitting such features are lost, but not necessarily lost immediately. Instead, they are scattered and lost some distance away, which has been accounted for in the radiation physics analysis described below.

4-3.12.3.5 Radiation Physics Analysis New radiological consequence analyses will be performed to calculate dose rates outside the shielding due to anticipated electron beam losses and to ensure that the dose and dose rate goals outlined above will be met. Calculations of radiation dose due to beam losses will be performed with modern radiation transport computer codes such as MCNP [13]. A full set of normal and off-normal losses will be analyzed to determine the total dose due to all anticipated and potential losses around the facility.

Accelerator physics simulations are used to determine where electron losses can be expected to occur. For example, the vast majority of losses in the storage ring are expected to occur at collimators in sectors 37 through 01 and at the small-horizontal-aperture insertion devices (currently intended for sectors 04 and 33). Additional losses may occur at the other IDs and at the high-dispersion points in the storage ring, which will be in different locations for the new lattice than in the existing lattice. In general, the loss patterns for injected beam, stored beam, and dumped beam in the storage ring will each be different. Each of these have been modeled and the separate contributions must be added together to determine the dose consequences of potential beam losses at any location. Dose due to losses in other parts of the facility (the injector chain) will also be calculated to determine where supplemental shielding might be needed to bring dose rates in each area below the shielding criteria stated above.

As an example, consider beam losses at the storage ring insertion devices. Simulations show that, for complete loss of the stored beam (Section 4-2.11.4), electrons will primarily be incident on collimators in Zone F, so these events will not lead to significant losses at other locations around the storage ring. Simulations of injected beam losses (Section 4-2.10.3) show that the total loss will likely be quite small, under 2%, and that the losses will occur primarily at the two small-aperture IDs and at the collimators. The distribution of stored beam losses (Section 4-2.11.1) has also been calculated.⁷ The results from these three simulations are combined to calculate the electron beam energy lost at each location around the storage ring. Radiation shielding studies were performed using simulation results for an earlier version of the storage ring lattice, which provide good estimates of the electron losses and loss distributions and allow an assessment of the adequacy of the existing bulk shielding. MCNP simulations for electrons incident on the upstream transition piece of an insertion device show that, for loss rates less than 4 mW at a single insertion device, the dose rate at any location outside the shielding will be less than 0.05 mrem/h. Losses at all but the two small-horizontal-aperture insertion devices will be much smaller than this, with a maximum of about 0.5 mW. The energy loss rates at the two small-horizontal-aperture IDs will be larger than 4 mW, leading to dose rates around those locations that would be higher than the shielding design criteria. Local shielding can be added near the small-horizontal-aperture IDs to reduce the dose rate in those locations.

Consequences of the Maximum Credible Incident (MCI) will be calculated for the conditions of the Accelerator Safety Envelope in each part of the facility (linac, PAR, LEA, booster, storage ring). According to DOE Order 420.2c, the MCI is a “credible accident scenario with the maximum or worst-case consequences” which is not necessarily an incident involving the highest-energy beam. In this instance, “credible” means that the accident has the potential to occur within the lifetime of the facility [3]. In the case of the PAR or storage ring, the MCI would involve the continuous loss of injected beam from the linac or booster since that would create a higher power loss than repeated

⁷The distribution of gas-scattering losses has yet to be computed. These are assumed for now to follow the pattern for Touschek-scattered particles.

loss of stored beam after refilling. To determine the MCI, the dose rate due to loss of injected beam will be calculated at a number of locations, and the case which results in the highest dose rate will be defined as the MCI. In the storage ring, for example, the loss scenarios to be considered include:

- loss at a single high-dispersion point
- loss along a curved FODO section (this location is nearest to the outboard shield wall)
- loss at the quad doublets
- loss at the upstream transition piece of an insertion device
- loss at the injection septum
- loss at a single collimator
- loss of the full injected beam to the swap-out dump
- loss of RF during injection
- short of a dipole magnet during injection
- loss of vacuum during injection, and
- injected beam mis-steered into a beamline front end

The same cases will be considered for loss of stored beam as part of the calculation of dose due to normal losses.

Following installation of the Multi-Bend Achromat (MBA) lattice storage ring and modification of other accelerator systems, there will be a period of accelerator systems commissioning. During this time, the beam current will be kept low to reduce losses around the facility. It may become necessary to exclude personnel from portions of the experiment hall floor during off-shift times to expedite the conditioning of the storage ring vacuum chambers. Confirmatory radiological surveys of specific loss points will be performed. If persistent excessive dose rates are found at any locations, these can be addressed by changes to accelerator operations if possible or by the addition of local shielding.

4-3.12.3.6 Beam Lifetime Requirements The minimum requirements on beam lifetime and injection efficiency can be determined by considering a simplified model that relates the electron losses to radiation dose for a point around the storage ring. We will assume one spatial distribution for stored beam losses and one for injected beam losses which result from the beam physics simulations of Touschek scattering losses (section 4-2.11) and injection losses (section 4-2.10). We can then write the dose at some point outside the shielding as

$$\left[\frac{E_{stored}}{\tau} \cdot f_{st} + 10 \cdot \frac{E_{stored}}{\tau} \cdot (1 - \varepsilon_{inj}) \cdot f_{inj} \right] \cdot D \left(\frac{mrem}{J} \right) \cdot 2000h = 100mrem$$

where E_{stored} is the energy stored in the circulating beam = 4420 J for 200 mA at 6 GeV, τ is the beam lifetime, f_{st} is the fraction of stored beam losses occurring at the subject location, ε_{inj} is the injection efficiency, f_{inj} is the fraction of injected beam losses occurring at the subject location, D is a normalized dose that gives the dose outside the shield for a given beam loss inside the shield, and we assume full occupancy of 2000 h/y and an annual dose limit of 100 mrem. The factor 10 in front of the injection-related term accounts for the fact that a bunch is replaced when its intensity falls by 1/10th of the initial intensity. This equation can be simplified to

$$\tau = \frac{E_{stored} \cdot D \cdot 2000}{100} \cdot [f_{st} + 10 \cdot (1 - \varepsilon_{inj}) \cdot f_{inj}]$$

which gives the beam lifetime as a simple linear function of the injection efficiency. This equation can be applied to selected locations around the storage ring to impose a series of constraints on combinations of beam lifetime and injection efficiency. While the present analysis considers the beam lifetime and injection efficiency to be independent parameters, in practice the conditions that lead to shorter beam lifetime will probably also lead to reduced injection efficiency.

Figure 4.225 shows the combinations of beam lifetime and injection efficiency that lead to annual dose of no greater than 100 mrem/y at three locations around the APS-U storage ring: a standard ID with 16x6 mm aperture (for a dose point inside the adjacent first optics enclosure), a small-horizontal-aperture ID (dose point outside the adjacent first optics enclosure), and the horizontal collimator in sector 38 (dose point outside the outboard shield wall). These locations were chosen because they have the largest beam losses or provide bounding values over a set of similar locations. The curves in the figure should be interpreted as “for a given injection efficiency, the beam lifetime must be this long or longer”. Thus the allowable space is that which lies above all the curves. As we have already seen, the limit comes from beam incident on the small-horizontal-aperture IDs. The shielding factor assumed for the location outside 33-ID is easily achieved using a six-inch thick supplemental shield of borated polyethylene on the outside of the concrete bulk shield.

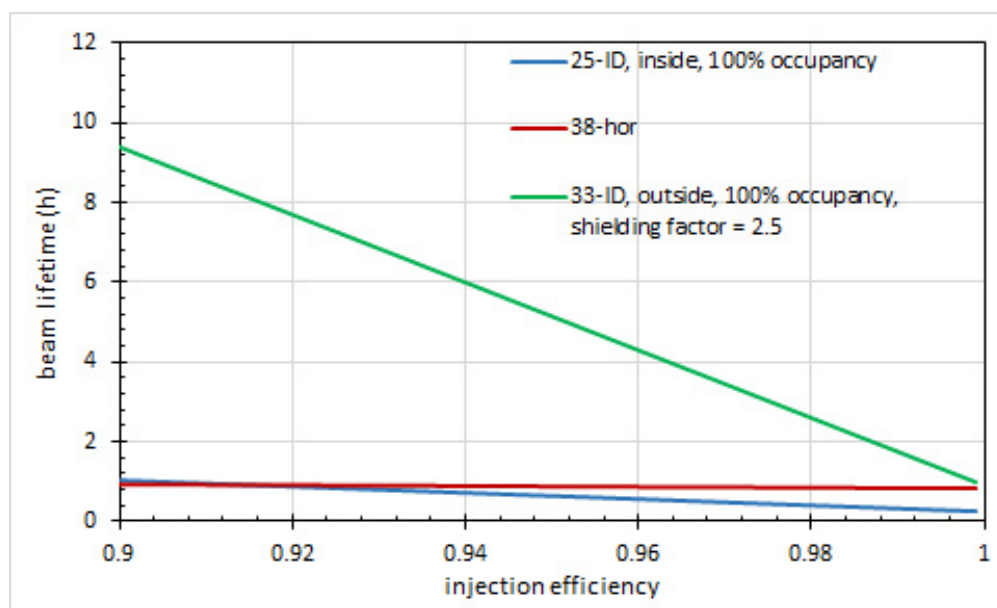


Figure 4.225. Minimum beam lifetime and injection efficiency for an annual dose of 100 mrem outside the APS-U storage ring bulk shielding.

In the 324-bunch mode, with 10th-percentile lifetime of about 6 hours, these criteria are satisfied for injection efficiency greater than about 95%. For the 48-bunch mode with 10th-percentile lifetime of about 2.9 hours, an injection efficiency of at least 98% would be needed to satisfy these criteria. If a larger shielding factor can be achieved using local shielding, the minimum injection efficiency would be reduced. Other mitigating steps are also possible, such as restricting access to areas with higher dose rates; because of the expected distribution of losses, these are expected to be few in number.

4-3.12.3.7 Results of Beam Loss Studies Several beam loss studies have been conducted in the PAR and booster synchrotron to test the effectiveness of the existing bulk and local shielding. In the PAR, well-defined scenarios were studied in which the entire beam coming into the PAR was intentionally lost by steering beam into the wall at selected locations around the ring. These measurements showed that, for continuous loss of the entire beam entering the PAR, the dose rate outside the PAR is less than 5 mrem/h when the current lost in the PAR is limited to 10 nA. One exception is a location in the storage cage at the southeast corner of the PAR, at which the dose rate is 5 mrem/h for a current loss of 6 nA in one of the scenarios. Dose rates on the PAR mezzanine are below 5 mrem/h for average lost current below 16 nA. However, beam losses in the PAR are expected to be much less than these values during operations. Active radiation monitoring is installed that shuts off the electron gun if dose rates are above 5 mrem/h.

Studies have also been performed for beam losses in the booster, again in well-defined scenarios. For beam lost at injection into the booster, the maximum dose rates outside the shielding near the injection septum scale to 1.2 mrem/h for 20 nA lost current (the measured value was about 0.6 mR/h for a loss of 5 nC at 2 pps). When beam in the booster is accelerated to 7 GeV but not extracted, the beam is lost in the booster at the end of the RF cycle. In this case, lost beam is distributed around the synchrotron. Dose rates were measured approximately every 15 feet on top of the shielding berm above the synchrotron tunnel. The highest readings, about 0.4 mR/h for operation at 3.5 nC and 2 pps, were measured above the end of the extraction straight section. This would scale to about 1.1 mrem/h for operation at 20 nA. Dose rates about half that value were measured above the end of the injection straight section. Measurements above the rest of the booster were at background. Thus any beam lost in the booster should be fairly localized and lead to small dose rates outside the shielding. The area above the booster is inside a fenced area which is generally not accessible to APS users or non-radiation workers.

During APS commissioning, local shielding was placed in the PAR, booster, and storage ring based on dose rate measurements taken outside the bulk shielding. It is anticipated that a similar procedure would be followed during commissioning of the APS-U. Furthermore, measurements were taken of specific scenarios that attempted to replicate conditions of maximum credible incidents and these have been documented in APS technical reports [14, 15, 16]. A similar process could be used during APS-U commissioning to benchmark the shielding calculations and verify the effectiveness of the installed shielding.

4-3.12.3.8 Activated Materials Radiation interactions with accelerator and beamline components can potentially induce small amounts of radioactivity. When removed, the existing storage ring will include slightly activated components. Radiological surveys performed after accelerator systems are de-energized at the start of each scheduled maintenance period provide records of any above-background radiation fields and their locations. Prior to removal, every component in the storage ring enclosure will be surveyed by health physics personnel, who will identify and tag any radioactive components. Worker doses will be monitored via dosimeters as needed when activated components must be handled. All activated materials and equipment will be inventoried, segregated from non-activated components, and stored in designated and posted controlled radioactive material areas. Except for the various septum magnets in the injector system and a few known locations where electron beam scraping or losses have occurred, it is anticipated that most components will be essentially free of radioactivity. Material and components removed from the APS will be han-

dled according to ANL-RS-TBD-003 [17], which is Argonne's implementation of the DOE standard DOE-STD-6004-2016 [18] for removal and disposal of activated components.

Since the operating parameters of the Upgrade injector and storage ring will be much like those of the present APS, we expect that any activation induced in the Upgrade will be much like that in the present machine. The locations of some losses will change, for example due to the use of collimators to localize losses in the Upgrade. Due to the use of swap-out injection (as opposed to the top-up injection used in APS), significantly more electrons will be injected into the storage ring, but 90% of those will end up at a dedicated swap-out beam dump. Thus the total level of activation around the storage ring should be roughly similar to that in the present APS. The beam dump for swapped-out bunches will be well shielded and any activation products would be distributed throughout the volume of the material. The expected radionuclide inventories in the swap-out dump will be calculated as part of the design process. Beam losses may also be higher in the linac, PAR, and booster synchrotron than for the present APS since more charge will be accelerated through the injector system. Experience shows that most of the booster losses are at injection (at relatively low energy) which will reduce neutron production and hence material activation. Finally, there may be increased potential for activation of shielding materials, soil, groundwater, and air. Estimates of these quantities will also be made as part of the overall radiation physics analysis.

4-3.12.4 Machine Protection Systems

The existing machine protection system (MPS) protects the APS storage ring vacuum system from x-ray beam heating, loss of water cooling, and elevated vacuum levels. Many hundreds of sensors are monitored and networked through the MPS system. An overall description of the MPS is given in Ref. [19].

Insertion devices generate x-ray beams with power up to 21 kW and power density as high as 600 kW/mrad², posing a danger to downstream vacuum components if misdirected. Mis-steering is monitored with beam position monitors at the upstream and downstream ends of the insertion device (ID) straight sections, which are used as inputs to the MPS to trigger a fast beam abort. This is the beam position limit detector (BPLD) system. Flow rates for the vacuum system cooling water are monitored by the MPS for loss of flow, which trips the beam. Vacuum gate valves are closed in the event of a significant elevated vacuum event to isolate the leak from adjacent vacuum chambers. To prevent damage to a valve if closed on a hot x-ray beam, closure of an interlocked gate valve triggers a fast MPS beam abort. If a fast beam abort event trigger occurs, the beam is intentionally dumped by removing the low-level rf drive to the main rf systems. In the present APS, the beam then spirals inward and is lost in about 300 microseconds. All fault conditions are latched and time stamped.

This system will also be used for the APS Upgrade with relatively modest modifications. The BPLD system will be generalized to allow interlocking on source angle vs. the present limit on individual BPM readbacks, for example. For the APS upgrade, the system will be configurable to allow interlocking on any individual BPM readback, not just those near insertion device source points as is done presently. The BPLD system interlocking insertion device source points are enabled when insertion device gaps are closed below some level, typically 50 mm for a standard planar hybrid permanent magnet undulator. In addition, there will be the capability to force the interlock to be activated independent of insertion device gap for testing and validation purposes; this is referred to

as the bpld force-enable bit.

The impact of a total beam loss on vacuum system components is an active area of development, and a collimation scheme is proposed in the beam physics section of this document. Other sensitive equipment, such as superconducting undulators, may need special measures to prevent damage or nuisance quenches.

A significant change since the Conceptual Design Report is the introduction of an injection/extraction pre-kicker to inflate the volume of the bunch before it is dumped (Section 4-2.10.2). Because inflating the volume of the bunch before swapping out is essential to prevent damage to the swap-out dump, firing of the swap-out kickers will be gated on the waveform from the pre-kicker. In this way, if the pre-kicker does not fire, or does not fire with sufficient amplitude or correct timing, swap-out will not occur.

References

- [1] *Advanced Photon Source Safety Assessment Document*. Tech. rep. APS-3.1.2.1.0, Rev. 4. APS, June 2012 (cit. on pp. 286, 287, 291, 293).
- [2] United States Nuclear Regulatory Commission. *Occupational Radiation Protection*. Jan. 2016. URL: <https://energy.gov/ehss/occupational-radiation-protection-program-10-cfr-835> (cit. on p. 288).
- [3] US Department of Energy. *Safety of Accelerator Facilities*. July 2011. URL: <https://www.directives.doe.gov/directives-documents/400-series/0420.2-BOrder-c/> (cit. on pp. 288, 294).
- [4] US Department of Energy. *Accelerator Facility Safety Implementation Guide for DOE O 420.4C, Safety of Accelerator Facilities*. Aug. 2014 (cit. on p. 288).
- [5] D. Q. McCormick. *Argonne National Laboratory Radiological Safety Program Description*. Jan. 2017 (cit. on p. 288).
- [6] J. C. Liu et al. *Radiation Safety Design for SPEAR3 Ring and Synchrotron Radiation Beamlines*. Tech. rep. SLAC Radiation Physics Note RP-05-33. SLAC, Dec. 2005 (cit. on p. 290).
- [7] J. C. Liu, S. H. Rokni, and V. Vylet. “Operational radiation protection in synchrotron light and free electron laser facilities.” In: *Radiation protection dosimetry* 137 (Oct. 2009), pp. 18–34 (cit. on p. 290).
- [8] P. K. Job and W. R. Casey. “Radiological considerations for bulk shielding calculations of national synchrotron light source-II.” In: *Nucl. Instr. Meth.* A660 (2011), pp. 1–6. DOI: 10.1016/j.nima.2011.08.015 (cit. on p. 290).
- [9] P. K. Job and W. R. Casey. “Shielding calculations for the National Synchrotron Light Source-II experimental beamlines.” In: *Nucl. Instr. Meth.* A698 (2013), pp. 196–201. DOI: 10.1016/j.nima.2012.08.043 (cit. on p. 290).
- [10] *Structural shielding design and evaluation for megavoltage x-and gamma-ray radiotherapy facilities*. Tech. rep. NCRP-151. NCRP, 2005 (cit. on p. 290).
- [11] United States Nuclear Regulatory Commission. *Standards for Protection Against Radiation*. <https://www.nrc.gov/reading-rm/doc-collections/cfr/part020/>. Jan. 2008 (cit. on p. 292).

- [12] P. Fernandez and S. Davey. *Guidelines for Beamline and Front-End Radiation Shielding Design at the Advanced Photon Source*. Dec. 2015 (cit. on p. 293).
- [13] D. Pelowitz et al. *MCNP6 User Manual, Version 1.0*. Tech. rep. LA-CP-13-00634. May 2013 (cit. on p. 294).
- [14] M. Pisharody et al. *Measurement of Gas-Bremsstrahlung from the Insertion Device Beamlines of the Advanced Photon Source*. Tech. rep. APS note LS-260. Argonne National Laboratory, 1997 (cit. on p. 297).
- [15] G. Decker et al. *Maximum Credible Incident Simulation Studies at the Storage Ring of the APS*. Tech. rep. APS note LS-262. 1997 (cit. on p. 297).
- [16] M. Pisharody, E. Semones, and P. K. Job. *Dose Measurements of Bremsstrahlung-Produced Neutrons at the Advanced Photon Source*. Tech. rep. APS note LS-269. 1998 (cit. on p. 297).
- [17] H. Hall. *Material Release Program Technical Basis Document*. Tech. rep. RS-TBD-003. Argonne National Laboratory, 2017 (cit. on p. 298).
- [18] US Department of Energy. *Clearance and Release of Personal Property From Accelerator Facilities*. <https://energy.gov/ehss/downloads/doe-std-6004-2016> (cit. on p. 298).
- [19] R. Fuja et al. “The APS machine protection system (MPS).” In: *Proc. of the Seventh Beam Instrumentation Workshop*. AIP Conf. Proc. 390, 1997, pp. 454–459 (cit. on p. 298).

4-3.13 Injector Modifications

The injectors need to reliably produce enough single-bunch charge to perform complete bunch replacement for the anticipated APS-U fill patterns. The present injectors can deliver the required charge for the 324-bunch mode, including the double-charge (5.6 nC) bunches needed for gap compensation bunches (see 4-2.6). The existing injectors can deliver more than half the charge required for the most-demanding 48-bunch mode. An R&D program was carried out to identify limitations to injector high-charge operation, and to develop a scope of work for production-phase upgrade activities. Steady progress was made on characterization of injector high-charge performance and comparison of data with simulations. Several improvements were carried out from 2013 to 2017, and are summarized in this section. The path to APS-U operations is also described.

Figure 4.226 shows the present APS injector complex. The 375-MeV (nominal energy) electron linac supplies 1 nC per 30-Hz pulse delivered by a thermionic rf gun (RG1 or RG2). (The schematic also shows the location of the photoinjector rf gun (PCG), which is not used for operations.) Up to 6 linac pulses are captured in the Particle Accumulator Ring (PAR) in a 1st harmonic rf system (RF1, 9.77 MHz). A 12th harmonic rf system (RF12, 117 MHz) compresses the damped single bunch for injection into the 7-GeV Booster [1] (planned to be operated at 6 GeV for APS-U). A bunch cleaning system in PAR drives out the beam in satellite bunches to provide bunch purity at the level of 10^{-7} in the APS storage ring [2].

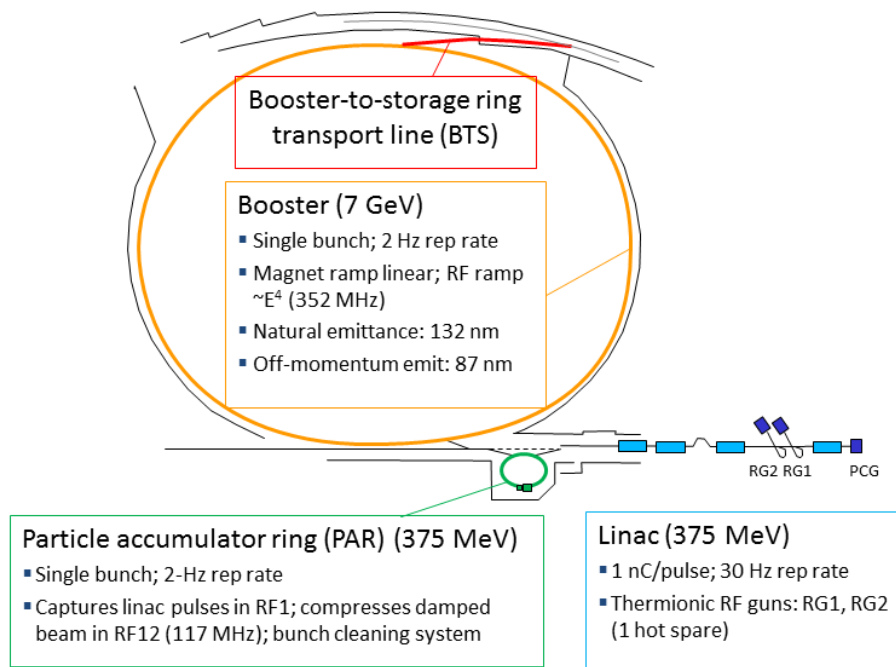


Figure 4.226. Present APS Injector Complex.

In present APS operations, the injectors deliver 2-3 nC single bunch to the storage ring at a 2-Hz rate. The plan is to meet the APS-U injection requirements through upgrades of the injector complex, while keeping the basic structure. Addition of a 1-Hz timing mode enables accumulation

of up to 20 linac pulses to meet the higher-charge requirement.

Swap-out injection places significant demands on the injector for the 48-bunch mode in particular. Table 4.92 gives the injector performance requirements. The calculation of the required charge assumes that the Booster injection efficiency is 85% and the storage ring injection efficiency is 95% (see 4-2.10.3). The 16-nC storage ring bunch charge includes a deliberate 5% overfill. The target shot-to-shot injected bunch charge variation is 5%; if distributed uniformly over 48 bunches, this results in a 1% variation in the average stored charge in the storage ring [3]. The present injector is capable of supporting 200 mA in the APS-U storage ring in 72-324 bunches; a maximum charge of 11 nC was achieved from Booster (although reproducibility and stability issues need to be addressed). PAR and Booster performance and improvements are discussed in Sections 4-3.13.2 through 4-3.13.5. Injector timing modifications will be described first.

Table 4.92. Injector Maximum Performance Requirements

	Machine	Single bunch charge nC	ϵ_x nm-rad	Ratio ϵ_y/ϵ_x	Charge stability ^a rms
Required	Storage ring (inject)	16	–	–	1%
	Booster/BTS (extract)	17	60	16/60=0.27 ^b	5% ^b
	PAR (extract)	20			
Achieved	Booster	11 ^c	^d	0.05–0.5	~10%
	PAR	15 ^e			

^a Total charge in storage ring, otherwise bunch charge [3].

^b Target numbers – minimum requirements are under evaluation.

^c In 132-nm lattice. Achieved 5.5 nC in 92-nm lattice, in use for operations 2012-2016.

^d For historical reasons, the Booster is operated off-momentum. In 132-nm lattice, computed natural emittance scaled to 6 GeV is 53 nm, assuming $\Delta p/p = -1\%$ [4]. Present operation is $\Delta p/p = -0.6\%$.

^e Normal operation. Achieved 24 nC in stored mode.

4-3.13.1 Injector Timing

There are two major courses of action related to injector timing for APS-U. First, as mentioned, to meet the higher-charge requirement, the PAR accumulation cycle needed to be extended from the nominal 0.5 s (2-Hz repetition rate) to 1 s (1-Hz repetition rate). To this end, a new 1-Hz timing system was developed and is presently used to study higher charge performance. Second, a new synchronization scheme between the Booster and ring is needed that allows operation of the injector complex using a separate master oscillator. This has several benefits, including the option to inject on-momentum in Booster and ramp to a chosen off-momentum condition before extraction. Timing system jitter requirements are under evaluation as this scheme is developed. The measured timing system jitter is in the range of 200-500 ps (peak-to-peak). PAR and Booster operation in 1-Hz mode is described first, followed by a description of a new synchronization scheme.

4-3.13.1.1 1-Hz Timing Operation Originally designed to capture and damp positron beams, the PAR now accumulates and compresses the electron beam for the Booster. Table 4.93 gives the relevant PAR parameters. Figure 4.227 shows PAR and linac timing in a 1-second cycle. During the first 633 ms, up to 20 linac pulses are accumulated in the fundamental rf bucket. The 12th harmonic rf is powered on at 750 ms. The beam is captured in the 12th harmonic bucket and compressed.

Bunch cleaning is turned on for 20 ms, 120 ms prior to beam extraction. The bunch lengths in the table are design (zero current) values. As described later in section 4-3.13.2, bunch lengthening at higher charge in PAR is a major issue that needs to be addressed for APS-U.

Table 4.93. PAR Parameters

Parameter	Value	Unit
Beam energy	375	MeV
Circumference	30.666	m
Emittance	233	nm-rad
Revolution frequency	9.776	MHz
Harmonic numbers	1 and 12	
Rad. damping time, horiz.	36	ms
Rad. damping time, vert.	45	ms
Rad. damping time, long.	26	ms
Momentum compaction (α_c)	0.224	
Equilib. bunch length (zero current), 1 st harm. only	0.9	ns
Equilib. bunch length (zero current), 1 st and 12 th harm.	0.3	ns
Equil. energy spread (zero current)	0.034	%

In 1-Hz timing mode, the Booster magnet current ramps are presently kept short in length, as in 2-Hz operation. For 7-GeV operation, the acceleration cycle length is 224 ms, and for 6 GeV, it is 191 ms. In the future, the ramp lengths may be extended. The ramp length will be chosen on the basis of what provides better overall Booster performance for APS-U. Figure 4.228 shows a schematic of the Booster dipole ramp in 1-Hz timing.

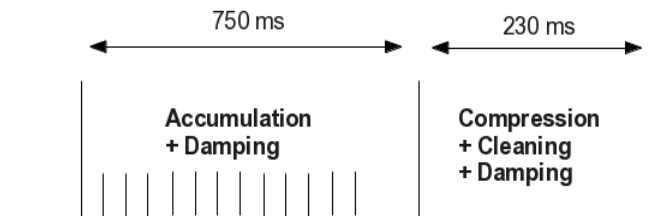


Figure 4.227. PAR accumulation cycle in 1-Hz timing.

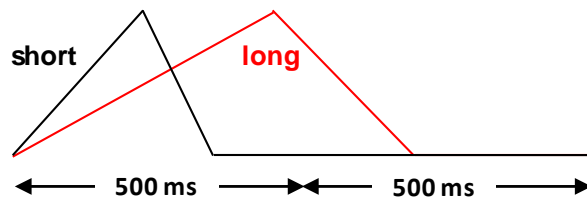


Figure 4.228. Booster dipole current ramp in 1-Hz timing. The short ramp is the default.

4-3.13.1.2 Booster-Storage Ring Synchronization The APS-U storage ring has a slightly smaller orbit length than the present APS storage ring, 1103.608 m instead of the present 1103.98 m.

This leads to its rf frequency being about 120 kHz higher than used at present. Unless the Booster circumference is reduced accordingly, its rf frequency will be different from that of the APS-U storage ring. At the same time, the ongoing high-charge injector studies indicate that acceptance of the Booster during the first few 1000 turns after injection is critical in maintaining high throughput at charges as high as 17 nC per bunch. It is therefore desirable to inject into the Booster as close to on-momentum as possible. At extraction, however, in order to keep the extracted transverse beam emittance from the Booster as small as possible, it is necessary to move the Booster beam to a negative momentum offset, thus manipulating the damping partition functions. Doing this is essential for low-loss injection into the APS-U storage ring.

For these reasons there is a plan to ramp the Booster momentum offset by programming the rf frequency accordingly[5]. As the beam is accelerated its size shrinks, providing extra room as shown in Figure 4.229. At extraction, an offset of -0.6% in momentum is achieved by a change in rf frequency during the Booster cycle of about $+21$ kHz. The basic rf parameters related to synchronization are given in Table 4.94.

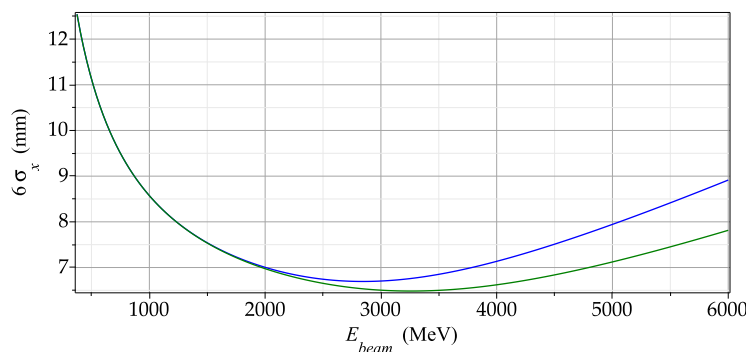


Figure 4.229. Evolution of the beam size during the acceleration cycle of the Booster. The $6\text{-}\sigma$ values shown are meant to give an indication of the aperture required. The blue curve is for on-momentum operation, the green curve, for -0.6% momentum offset.

The frequency program for the Booster will be designed to achieve three objectives:

- Set the momentum offset at injection (nominally $\delta p/p = 0$);
- Set the momentum offset at extraction (nominally $\delta p/p = -0.6\%$, optionally more negative);
- Ensure the total time taken for the Booster bunch being accelerated is just the correct amount (on a picosecond level) to inject into the chosen rf bucket in the storage ring. This bucket will change for each cycle, in a more-or-less random fashion.

These functions should be achieved with a minimum of parameters to be set and kept track of, ideally one parameter specifying the final momentum offset and a second one specifying the total path length. This is done by adding a second ramp to the Booster rf program to change the path length without changing the start or end points in frequency. The frequency ramps will use cosine-like functions to minimize high-frequency content in the variation. The number of turns in the Booster is adjusted according to the storage-ring bucket number to limit the path-length adjustment needed. The Booster rf frequency program is shown for the extreme cases of path-length correction in Figure 4.230. A time span of 25 ms is provided at the end of the momentum ramp before Booster extraction to allow any transients to damp.

Table 4.94. Parameters for Booster-storage-ring synchronization

Parameter	Machine	Value	Unit
Circumference	Booster	368.016	m
	APS-U Ring	1103.608	m
Revolution frequency	Booster	814618.00	s ⁻¹
	APS-U Ring	271648.11	s ⁻¹
Harmonic number	Booster	432	
	APS-U Ring	1296	
Rf frequency	Booster	351.9149761	MHz
	APS-U Ring	352.05598518	MHz
momentum compaction (α_c) ⁽¹⁾	Booster	0.0097	
Injection energy	Booster	375	MeV
	APS-U Ring	6000	MeV
Injection momentum offset	Booster	0	%
Extraction momentum offset ⁽²⁾	Booster	-0.6	%
Acceleration time (t_c)	Booster	225	ms
Frequency-ramp time (t_1)	Booster	200	ms

¹ On-momentum value.

² Nominal value; more negative values desirable.

Storage-ring values are for the 42-pm lattice V0. Booster values are on-momentum and from measurements (length) or the Booster lattice file (α_c , X11.75-Y9.80.e1e).

Three direct digital synthesizers will be used as the rf sources: one for the storage ring, one for the Booster, and one for the PAR. A Master Clock will serve as a common reference to achieve deterministic phase and frequency between the sources. The storage-ring source will be adjustable for orbit corrections. The Booster source will be offset by about -140 kHz from the storage ring and programmed as outlined above. The PAR source will be used to derive the signals for the PAR 1st harmonic and the 12th harmonic systems. The linac is free-running as it is in the present APS injector system.

The proposed architecture allows the PAR to maintain fixed frequency operation while the Booster is ramping. The Booster and PAR will be resynchronized each cycle so there is a fixed relationship at the moment of beam transfer from the PAR to the Booster. The phase relationship between

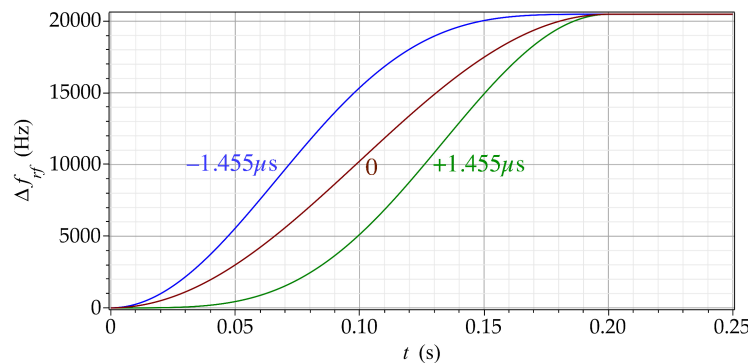


Figure 4.230. Booster rf program for injection into storage-ring, for the uncorrected ramp and two extreme corrections of ramp time (negative=faster). The uncorrected ramp is $7.275 \mu\text{s}$ faster than the unramped $\Delta f_{rf} = 0$ case.

Booster at extraction and the storage ring is critical for efficient injection; an accuracy of about 5° or 50 ps is aimed for.

Timing signals are generated by a system controller. Input to this controller are the turn clocks for storage ring and Booster as well as a “cycle start” signal which can be, for example, the “Last Bunch” signal from the present LIST module[6]. Turn clocks together with a synchronization method to define Bunch 0 in the APS storage ring are already provided in the APS injector timing system. Presently, the whole timing sequence is phase-synchronized to the 60 Hz mains frequency—this feature is essential for stable operation of the injector chain and will be retained. The rf signals are used to enable precise timing for the kickers with less than 100 ps jitter.

4-3.13.2 PAR Performance

The highest charge achieved in PAR is ~ 15 nC in 1-Hz operations (24 nC were achieved in stored beam mode). Transmission efficiency is typically close to 100% up to high charge. Attempts to accumulate higher charge often result in an RF1 trip. The trips are believed to be caused by beam loading (including HOMs) presented to the non-isolated triode tube and/or system transients. At high charge, the beam properties deviate from the design values, negatively impacting Booster performance. The high-charge PAR beam properties are described first. This is followed by the plan for improvements to address the tripping issue as well as controlling the beam properties.

Bunch length blowup: The most serious higher-charge issue in PAR is significant bunch length growth above ~ 8 nC. Figure 4.231 shows the rms bunch length near extraction (1-Hz cycle) as a function of charge. There appear to be two processes involved. First, there is a linear trend to longer bunch lengths as the charge increases. Second, above 8 nC, there is significant shot-to-shot variation, with some cycles exhibiting extreme bunch lengths. The bunch length data were acquired using a new fast photodiode diagnostic [7] developed to complement the existing streak camera diagnostic [8].

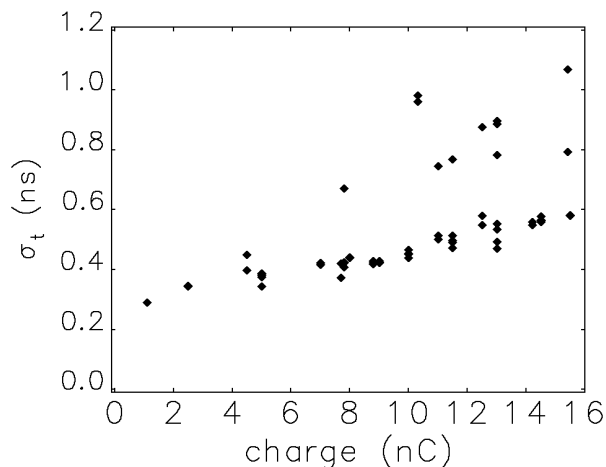


Figure 4.231. PAR bunch length as a function of charge, measured near extraction.

Early physics results using four prototype turn-by-turn (TBT) BPMs have yielded additional insights. Analyses of the data show development and evolution of multiple synchrotron frequency

sidebands over the cycle, especially at high charge, and indicate that only longitudinal motion is present.

The most likely cause of the extreme bunch lengthening is an HOM-type Robinson instability, though the broadband impedance cannot be ruled out. Nonlinear charge dependence of beam-driven HOM signals in the fundamental cavity suggest a causal relationship. Furthermore, the TBT and photodiode data both show that the instability begins before the bunch length is fully damped, which suggest that the instability depends on average charge, not peak charge. A HOM-type Robinson instability was predicted in an early design study [9, 10], but it has not caused operational issues at lower charge.

The linear bunch length increase may be due to beam loading in the fundamental rf. Evidence of beam loading or potential well distortion is supported by measurements of the shift in the bunch phase up to high charge. Earlier studies indicated beam loading issues at lower charge; these were compensated through rf system tuning [11].

At 15 nC, the bunch length is often longer than 0.8 ns; this is approaching three times the design value of 0.3 ns. The Booster capture efficiency is very sensitive to the injected bunch length (among other things). The bunch lengthening must be addressed before higher charge can be achieved in Booster.

Transverse beam size blowup: The transverse beam size was measured using a flag in the PAR-to-Booster (PTB) transport line. The beam size variation with charge up to 15 nC is shown in Figure 4.232.

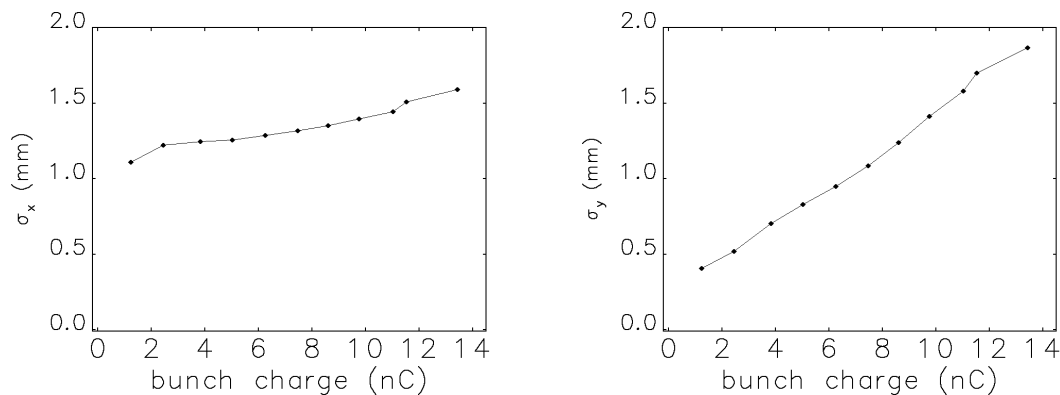


Figure 4.232. PAR charge-dependent horizontal (left) and vertical (right) rms beam size after extraction.

The horizontal beam size exhibits a 50% increase over the charge range that may be due at least in part to an energy spread growth resulting from the longitudinal instability (there is non-zero dispersion at the location of the flag). The non-dispersive beam size is not available for comparison, although there is no evidence of a horizontal instability in the TBT BPM data. Simulations are planned for comparison with the measurements and to distinguish between beam size and energy spread growth. In addition, emittance measurements are planned in the PTB using a quadrupole scan diagnostic developed for APS-U.

There is strong evidence of ion trapping in PAR, primarily in the vertical plane. The betatron tune slopes are positive, showing both time and charge dependence. There is excellent agreement between measurements and simulations of the tune slope when pressure variation, vertical beam size blowup, multiple ionization, and tune drive are taken into account [12]. No ion instability is predicted up to 20 nC or observed up to 15 nC. These simulations treat the ions dynamically and the bunch as a macroparticle. The code is discussed in more detail in section 4-2.6.

Ions are suspected to be the cause of the 3-fold vertical beam size growth observed between 1 and 15 nC. To confirm this, simulations that include bunch dynamics are planned.

Charge stability and reproducibility: PAR efficiency is typically 100%, even at high charge, but occasionally there are issues. Systematic studies will be carried out to identify the parameters that contribute the most to cycle-to-cycle charge stability and week-to-week reproducibility.

4-3.13.3 PAR Improvements

Fundamental rf trips: A new high-power filter in the fundamental rf amplifier output circuit is a possible solution to the trips observed at high charge. The filter currently installed in the system is transparent to certain beam-driven HOM frequencies that couple out of the cavity and then pass through to the amplifier. As HOM energy reflects back to the tube, the impedance seen by the tube changes drastically from its design value. The gain, efficiency, and power output drop, and in trying to compensate, the AGC loop may be overdriving the amplifier causing it to draw excessive plate current, leading to an interlock trip. The new filter, which will be installed after the existing filter, has better high-frequency rejection compared to the existing filter. It is also absorptive in design, so it will absorb rather than reflect the out-of-band energy and dissipate it in a suitable load.

Furthermore, tunability in the fundamental system amplifier output circuit would allow compensating for changes and achieving maximum operating efficiency under varied loading conditions, which would be of practical benefit for delivering from 2.5 nC to 20 nC. In the past, the output network was modified to fixed tuning when the original variable capacitors were damaged in the first few years of operation—HOM power generated by the beam was suspected at the time to be the cause. Heavily de-rated vacuum-variable capacitors could be installed for this purpose.

Beam loading: Beam loading is presently compensated using analog-based rf amplitude and phase feedback. A cavity tuning loop adjusts the bias of the ferrite tuners in the conventional way so as to minimize required generator power. Steady-state rf power requirements at 4 nC and 20 nC are shown in Table 4.95 using parameters measured in [13]. The harmonic cavity ideally should not deliver nor extract any power to the beam if it is phased correctly for bunch shortening. Its unloaded Q is a strong function of cavity detuning due to the ferrite tuners. The table lists the Q values obtained from [13] for the calculated ideal Δf .

The fundamental and harmonic amplifiers are rated at ~ 4 kW and ~ 3 kW respectively. It is not yet clear whether these amplifiers will suffice. Table 4.95 does not include beam losses to cavity HOMs which would require more power from the rf. Furthermore, the table refers to steady-state conditions. Additional headroom is required for transients such as those from the 30 Hz injection rate, the dynamics of turning on the harmonic cavity after accumulation, mis-phasing of the fundamental and harmonic cavities, and mis-tunings of the cavity during the transients due to

Table 4.95. PAR steady-state rf power estimates for 4 nC and 20 nC

Parameter		4 nC		20 nC	
		Fundamental	Harmonic	Fundamental	Harmonic
V_{cav}	kV	25	21	25	21
$(R/Q)_a$ ^a	Ω	73.3	215.7	73.3	215.7
Δf	kHz	-0.6	-24	-2.8	-117.6
$Q_o @ \Delta f$	$\times 10^3$	5.1	1.8	5.1	0.9
Q_{ext}	$\times 10^3$	5.3 ^b	1.9 ^c	5.3 ^b	1.9 ^c
Q_L	$\times 10^3$	2.6	0.92	2.6	0.61
3dB $\frac{1}{2}$ BW	kHz	1.9	64	1.9	96
P_{cav}	kW	1.7	2.22	1.7	2.2
P_{beam}	kW	0.07	0	0.33	0
P_{rev}	kW	0.01	0.33	0.03	0.32
P_{gen}	kW	1.8	2.6	2.1	2.5

^a $R_a \equiv V^2/P$

^b Presently measured Q_{ext} using a 50 Ω source. In reality a triode tube without a circulator drives the cavity and may alter this value.

^c Presently measured Q_{ext} . The harmonic cavity does have a circulator between the amplifier and cavity.

the response time of the cavity ferrites. Additional potential limitations include tuner loop response and maximum gap voltage in both rf systems. Evaluation of these issues and whether the amplifiers will be adequate is ongoing.

The present PAR rf diagnostics make it difficult to study the rf system transients and general behavior during high charge studies. The present sample rate of various baseband signals is only 1 kHz with a record length of 320 ms. On-hand digital low-level rf receivers will be modified for use as a rf diagnostic to aid PAR studies. One receiver will be installed for each of the fundamental and the harmonic systems. This will give four channels of rf signal monitoring for each system. The data can be sampled at 272 kHz, has nearly unlimited record length, and supports synchronized data acquisition. A stripline BPM signal will also be monitored and can be used to measure beam-to-rf phase to help understand beam-loading effects. Additionally, while rf phase tuning has been optimized by observing the bunch longitudinal position and bunch length using a streak camera [11], the new rf diagnostics will allow routine shot-to-shot phase measurements.

Finally the present analog rf control systems will be upgraded to digital LLRF control. It is anticipated that this will provide better stability and more precise control of the coordinated gymnastics between the fundamental and harmonic systems.

Beam size effects: Simulations suggest that ion effects and vertical beam-size blowup do not contribute significantly to the reduction in booster efficiency, up to 16 nC. However, the simulations do show that once the bunch length blowup and beam loading issues at 20 nC are solved, there will be small (~ 1 nC) losses on the vertical aperture caused by the blown-up vertical beam size. Mitigation options include reduced vacuum pressure and clearing electrodes in the PAR. Reducing the pressure by a factor of two is predicted to be very effective in reducing the ion trapping. This reduction is expected to be achieved through ion pump upgrades (completed), beam scrubbing

(ongoing), and if needed, NEG-coating the chamber or adding pumps to the flag ports. Clearing electrode designs are under investigation.

The existing BPM electronics will be upgraded to provide turn-by-turn capability and will be compatible with a large charge dynamic range. The upgrade will allow analysis of transverse and longitudinal beam stability as well as average beam position readbacks for orbit correction.

Bunch length blowup mitigation: Solving the bunch length blowup issue requires ongoing physics and engineering effort in order to develop a favored mitigation strategy. Measurements, calculations, simulations, and successful cures implemented elsewhere guide the study. In particular, measurements that distinguish between HOMs and broadband impedance are being developed. The PAR impedance model is being developed, and beam-loading simulations are underway. Longitudinal instabilities have been observed in numerous rings, caused either by HOMs or by the broadband impedance. High-charge bunch length oscillations and synchrotron spectra observed in PAR are qualitatively similar to observations in SURF [14, 15]. In SURF, the instability was cured by damping HOMs coupled out of the cavity and by tuning the rf phase. Nonlinear Robinson instabilities were observed at both ALS [16] and Aladdin [17] with passive harmonic cavities. Cures at ALS and Aladdin involved optimally tuning the rf parameters.

Strategies under investigation to mitigate the instability in PAR, in preference order, include:

- Optimize RF1 and RF12 parameters for high charge (e.g., voltage, phase, timing, detuning)
- Improve rf feedback
- Damp the HOMs and/or reduce the broadband impedance
- Operate at higher beam energy
- Damp the beam with a feedback system

4-3.13.4 Booster Performance

An historical rf frequency evolution (< 10 kHz) in the storage ring due to implementation of the Decker distortion (1999-2005) [18] resulted in off-momentum operation in the Booster. The negative momentum offset reduces the emittance due to the well-known effect on the damping partition functions. Lower Booster emittance is beneficial in reducing injection losses in the present storage ring, and will be similarly beneficial in APS-U (see 4-2.10.3). The accompanying increased energy spread is also beneficial in suppressing collective instabilities at injection into the ring (see 4-2.4.2).

The 92-nm “low-emittance” lattice⁸, operational from 2012 to 2016, was motivated by improving the storage ring injection efficiency. Early high-charge efforts were focused on the 92-nm lattice, but charge transport was limited to less than 6 nC, which is believed to be due to synchro-betatron coupling resulting from non-zero dispersion at the rf cavities [19]. It turns out that the original design, 132-nm “high emittance” lattice can also meet the APS-U injection emittance requirement. This is very promising, since the Booster delivers higher charge in the 132-nm lattice (notably, this lattice has zero dispersion at the rf cavities). Presently operating at -0.6% momentum offset, the zero-current natural emittance becomes 64 nm at 6 GeV [4]. If the Booster were operating at -1% momentum offset, the emittance becomes 53 nm (stated in Table 4.92, footnote (d)). The emittance reduction is due to a change in damping partitions and comes at a slight increase in energy

⁸The emittances quoted for the lattices are the natural emittances at 7 GeV. The emittance at 6 GeV is lower.

spread, which is 0.09% on-momentum and increases to 0.117% at -1% momentum offset, expressed as 1σ values. Increasing the vertical-to-horizontal emittance ratio decreases the horizontal emittance further, and gives a tuning knob for optimal APS-U injection. Therefore, the 132-nm lattice is the baseline for APS-U, and all the data and discussion in this section refer to that lattice.

Preserving the high-charge emittance is essential for low injection losses in the APS-U storage ring. Chromaticity correction to 7 units is expected to be sufficient to mitigate transverse beam instabilities at high charge. The focusing sextupole (SF) magnet power supply can provide the needed current, but the defocusing sextupole (SD) magnet power supply is close to its output current limit.

Figure 4.233 shows the best measured charge transport, averaging 11 nC, over the Booster cycle. The shot-to-shot variation is ± 0.6 nC, or $\sim 10\%$. For these data, the beam was extracted at 7 GeV. The efficiency for 10 nC was $\sim 70\%$. The efficiency is expressed as the charge at the end of the cycle divided by the injected charge.

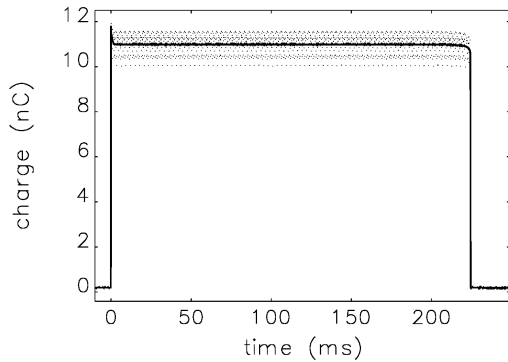


Figure 4.233. Best measured charge performance in Booster.

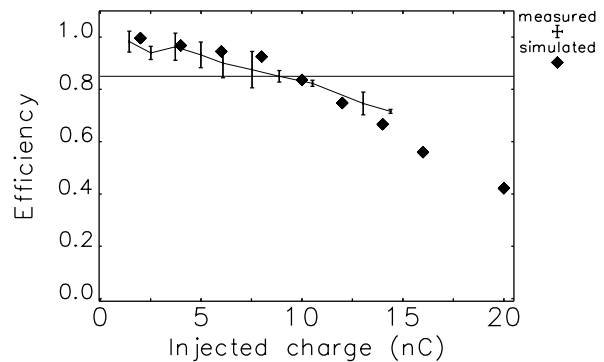


Figure 4.234. Booster charge-dependent efficiency compared to simulation. The 85% goal is marked.

Presently, the 85% efficiency goal is satisfied for injected charge up to ~ 8 nC, as shown in Figure 4.234. The measured efficiency agrees well with `elegant` [20] simulations, also shown in the figure. The simulations tracked 50,000 macroparticles for the first 3,000 booster turns (when the majority of losses occur). They include a model of the booster impedance [21], as well as beam loading in the RF cavities. The injected beam parameters include the measured blowup of the bunch length and transverse beam size with charge (Figs. 4.231 and 4.232), and injection trajectory and energy errors. The energy error is caused by variation in the bending magnet current at injection, which leads to an energy mismatch between the incoming beam and the booster. The resulting energy oscillations cause losses on the horizontal aperture at high dispersion locations.

The booster impedance model was developed using the same technique as the storage ring model (section 4-2.4). As shown in Figure 4.235, the model gives a predicted tune shift with charge that is very close to the measured value near extraction, and within $\sim 50\%$ in the middle of the ramp, i.e., 3-5 GeV. The measured data were too noisy to make a good comparison early in the ramp, i.e., < 3 GeV.

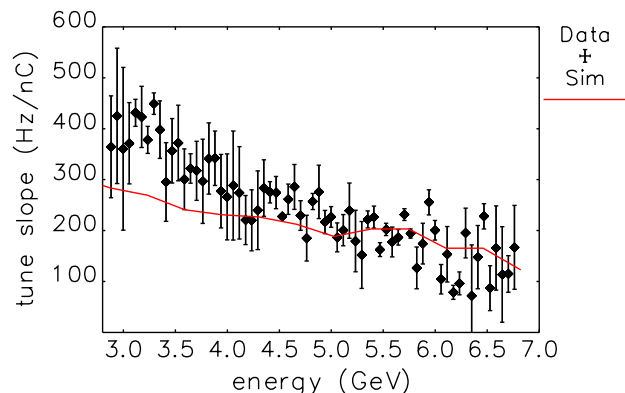


Figure 4.235. Comparison of measured and simulated booster vertical tune shift with charge.

A “zero-current” simulation study (i.e. ignoring the impedance and beam loading in the Booster, but including the errors) demonstrates how sensitive the efficiency is to the injected bunch length (Fig. 4.236). The efficiency is 100% for a 330-ps-long (rms) bunch, and drops to 90% for a 600-ps-long bunch and to 70% for a 1000-ps-long bunch. It is essential that the bunch length blowup in PAR is addressed.

Capture losses can be reduced by operating the Booster closer to on-momentum at injection. This effect is illustrated in simulations in Figure 4.237, where it is assumed that the 20-nC PAR bunch length is preserved to be 330 ps (rms); i.e., close to the design value. Under these conditions, the efficiency increases from 60% with -0.6% momentum offset to 85% with no momentum offset.

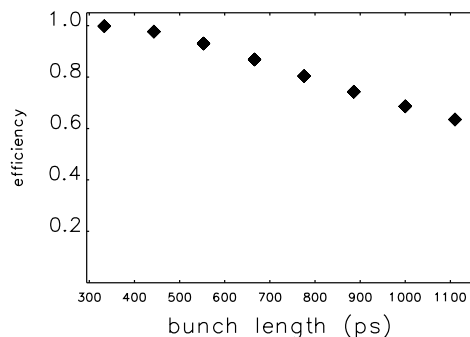


Figure 4.236. Simulated booster injection efficiency at 20 nC vs bunch length, ignoring collective effects.

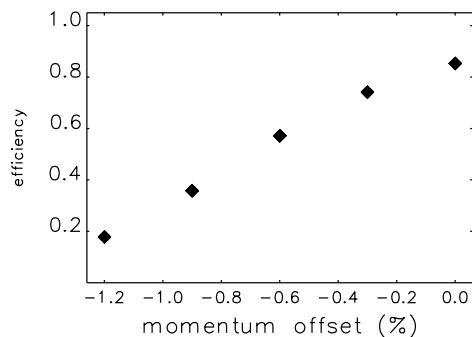


Figure 4.237. Simulated booster injection efficiency at 20 nC vs momentum offset, for fixed 330 ps PAR bunch length.

These simulation results show the benefit of both curing the PAR bunch lengthening and injecting the beam on-momentum in Booster. Improvements are needed in both PAR and Booster to reach the 85% efficiency goal at higher charge.

BPM upgrade: A new booster BPM system was installed that uses components with the same design as the APS storage ring BPM upgrade. Upgraded corrector ramp control hardware provides

a ramp update time of ~ 1 s. The new system provides average beam orbits and correction for up to 10 time slots along the acceleration cycle. Turn-by-turn histories are also available for such tasks as injection trajectory correction, beam stability analysis, and more.

The new BPM system has been used to correct the orbit along the booster ramp, using a response matrix technique. Figures 4.238 and 4.239 compare the orbit before and after correction in one time region of the ramp. The RMS orbit error was significantly reduced by the correction.

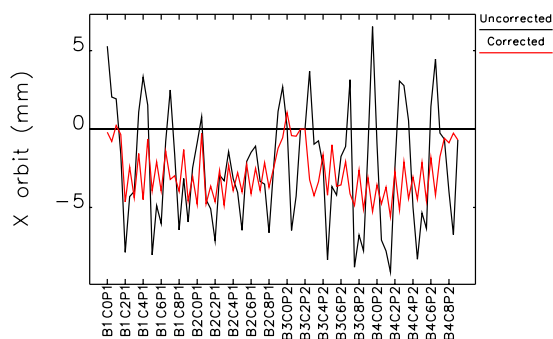


Figure 4.238. Horizontal booster orbit before and after correction. Note that the corrected orbit follows the dispersion function, since the booster is run off-momentum.

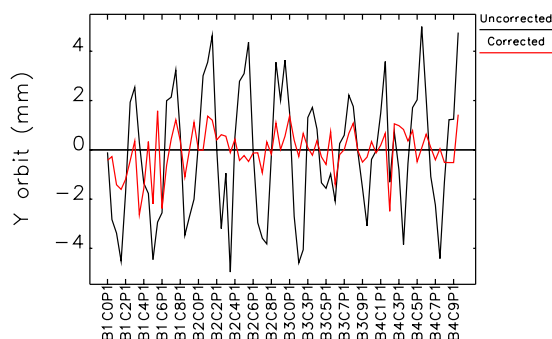


Figure 4.239. Vertical booster orbit before and after correction.

Beam loading: Another issue for Booster performance is heavy beam-loading. The Booster cavities are LEP-style 5-cell cavities made to ESRF specifications [22]. The cavity parameters are given in Table 4.96 [23, 24]. The large shunt impedance presents many challenges for beam-loading. At 20 nC, the corresponding 16 mA of beam current can drive the cavities to a total of ~ 1.4 MV at resonance (assuming a bunch form-factor of 0.75.) For comparison, the desired injection voltage is ~ 600 kV. The beam-induced voltage builds up quickly since the cavity time constant is $18 \mu\text{s}$, or 15 Booster turns, and which is $\sim 1/2$ of the synchrotron period. This presents difficulties with large transients at injection. The large R/Q also presents a loss factor of 3.1 kV/nC or $\sim 47 \text{ kV}$ (form-factor=0.75) seen on the first turn.

Table 4.96. Nominal Booster cavity parameters

	Single Cavity	Total 4 Cav.
$(R/Q)_a$	1400 Ω	5600 Ω
Q_o	38,500	38,500
Present Q_L	$\sim 20,000$	$\sim 20,000$
Loaded R_a^*	28 $M\Omega$	112 $M\Omega$

$$* R_a \equiv V^2/P$$

The deleterious effects of beam-loading are illustrated in Figure 4.240 which compares losses near injection with and without cavity beam-loading included in particle tracking simulations. The initial rapid loss is evidence of large transient beam-loading.

Another consideration is the well-known high-intensity Robinson stability limit [25]. Figure 4.241

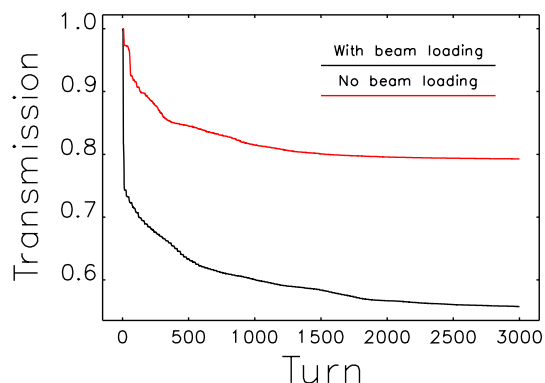


Figure 4.240. Simulated booster transmission at 20 nC with and without beam-loading.

shows the Robinson stability limit in Booster as a function of detuning at a nominal injection voltage of 600 kV. The beam loading factor, Y , is the ratio of the voltage that the beam can induce at resonance, V_{br} , to the cavity voltage V_{cav} . The blue line depicts the optimal detuning vs Y , and the dashed line represents the value of Y for 20 nC. The stability margin lies below the stability curve and above the higher of the dashed line or the blue line. While the stability margin increases at small detuning, the beam-induced voltage increases and Robinson damping decreases. This is not desirable since there is little radiation damping near injection. Therefore, stability requires large detuning at injection.

Figure 4.242 shows the stability limit for optimal detuning across a Booster cycle starting at 600 kV and ending at 5 MV. If the system were to be tuned optimally, the system should be below the theoretical stability limit across the entire cycle. More realistic limits, including various compensation schemes, are being investigated through particle tracking simulations (see Ref. [26]). Beam-loading studies with charge >10 nC on the real machine are presently limited, in large part by the PAR bunch length blowup.

Charge stability and reproducibility: Booster efficiency depends on many parameters, even at low charge. Once the high-charge issues are identified and mitigated, systematic studies will be carried out to identify the parameters that contribute the most to cycle-to-cycle charge stability and week-to-week reproducibility.

4-3.13.5 Booster Improvements

High-efficiency, high-charge transport in Booster is contingent mainly on minimizing the injected bunch length from PAR, sufficient chromatic correction to overcome transverse beam instabilities, and a beam-loading compensation strategy that is compatible with the synchronization scheme described in Section 4-3.13.1.2.

In this section, the PAR bunch length blowup at high charge is not included in the simulations. The possibility that the PAR bunch lengthening cannot be eliminated will be considered in future Booster injection simulations. If mitigation (discussed in 4-3.13.3) is not sufficient, a subharmonic cavity could be installed in Booster. The original Booster design (prior to adding PAR) included

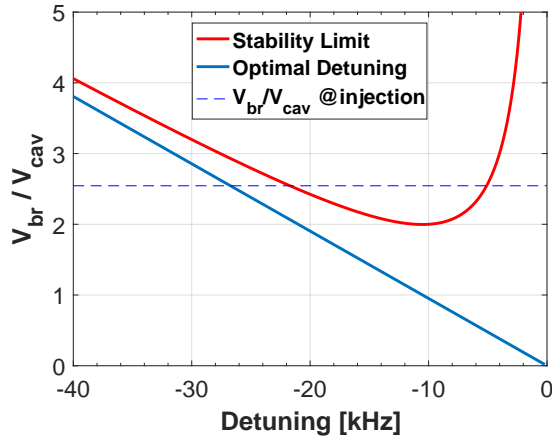


Figure 4.241. High intensity Robinson stability limit at injection voltage of 600kV as a function of detuning.

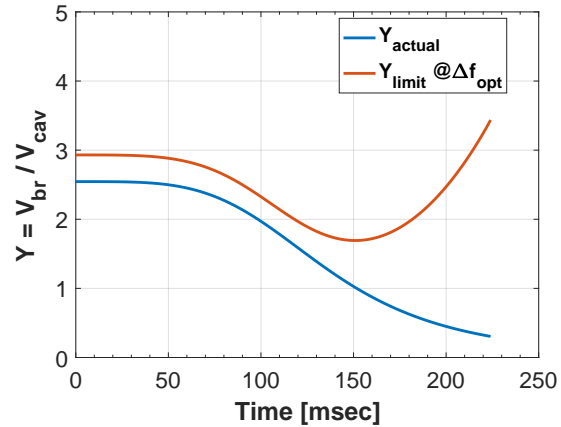


Figure 4.242. High intensity Robinson stability limit across the Booster ramp. The actual beam-loading factor is the blue curve.

a 39-MHz capture cavity [27]. Subharmonic capture simulation studies were performed later as well, assuming various frequencies [28]. These studies were motivated by exploring the possibility of direct injection from the linac. Implementing a dual harmonic system in Booster would require detailed design and trade-off studies before it would be considered for APS-U.

Power supply upgrade: In order to provide more chromatic correction, the SD supply was upgraded to supply a maximum current of 200 A. Field and thermal test of a sextupole magnet showed that it does not saturate or overheat up to 200 A. Simulation of the 92-nm lattice showed that maximum currents of 140 A and 200 A for the focusing sextupole (SF) and SD magnets, respectively, are sufficient to bring both chromaticities to -7 (results are expected to be similar in the 132-nm lattice).

Diagnostics upgrades: Ongoing characterization of the charge-dependent beam size in the Booster is performed using an existing synchrotron light monitor (SLM), which is also used as a visual aid in verifying good orbit correction through the cycle. The bunch length is measured using a streak camera. Both diagnostics use the same transport optics, whose in-vacuum mirror suffers from thermal motion. Upgrades include a remote control mirror to compensate the motion and remote intensity control to accommodate the beam charge dynamic range.

The existing emittance measurement diagnostic station in the Booster-to-storage ring (BTS) transport line is inadequate for measuring the beam properties at high charge and with sufficient resolution for the vertical plane. This will be upgraded to provide the needed charge dynamic range and the resolution for evaluating emittance at high charge, varying momentum offset, and varying y/x coupling [29].

Beam loading compensation: As described above, beam-loading in the booster is a significant issue for high bunch charge. Methods to counteract heavy transient and static beam-loading include [30]:

- rf feed-forward

- rf feedback
- detuning the cavity, especially at injection

RF Feed-Forward and Feedback: One way to counteract the beam-loading is to manipulate the rf drive using rf feed-forward. Ideally, the injection transient can be eliminated if the rf generator cancels the beam current at injection time. The generator current must be changed immediately from its vector value $\hat{I}_g = \frac{\hat{V}_{cav}}{\hat{Z}_{cav}}$ before injection to $\hat{I}'_g = \hat{I}_g - \hat{I}_B$ where \hat{I}_B is the beam-loading current. In general this requires a fast change in both magnitude and phase of the generator, although judicious cavity detuning for \hat{Z}_{cav} , such as half-detuning, may require only a phase change.

Injection transients can also be reduced using fast rf feedback, but very large gains are required. Practical limitations are imposed by the differential delay between the injection side and extraction side cavities which are driven together by a single klystron located on the extraction side of the Booster (the possibility of using fewer cavities is under investigation, as discussed below). While fast rf feedback reduces the effective impedance seen by the beam to reduce the beam-loading effect, that reduction in impedance also results in a reduction in Robinson damping. This is an undesirable effect since there is little radiation damping at injection time.

Preliminary particle tracking simulations in **elegant** indicate that both rf feed-forward and feedback perform worse than large cavity detuning (described below). However, more work is needed to fully evaluate these options, for example in combination with detuning.

Although fast rf feedback may present issues, at a minimum, slow rf feedback will be needed to regulate the amplitude and phase of the rf voltage across the Booster cycle. The present rf control system uses only slow rf feed-forward without any rf feedback. This makes the system susceptible to changes in beam-loading, cavity detuning, and klystron gain. At a minimum, slow rf feedback will be designed into the Booster llrf system. Provisions will also be made for rf feed-forward as well as cavity tuning control per the cavity detuning strategy to be chosen from below.

Cavity Detuning: Table 4.97 shows three possible strategies, depending on whether the booster is operated at fixed momentum offset over the cycle or using a momentum offset ramp as discussed in 4-3.13.1.2. Detuning the cavity is beneficial in all cases. The first option, dynamic tuning with momentum ramp, is the preferred choice as it minimizes overall performance risk. It would add technical complexity to the cavities through the addition of new ferrite-based tuners. The second and third options use only the present static tuners and incur both performance and technical risk. The second option relies upon comb-filter feedback [31], while the third option would require new high-power input couplers similar to those discussed in Section 4-3.10.

Table 4.97. Beam loading compensation strategies

Parameters	Preferred scheme	Alternate scheme	Highest performance risk
Momentum offset	ramp	ramp	fixed
Tuning type	dynamic	static	static
Simulated efficiency (20 nC injected)	>90%	<90%	~85%
Maximum detuning needed	60 kHz	20 kHz	30 kHz
Highest technical risk	dynamic tuners	comb filter	high-power rf coupler

Descriptions and the performance of the various beam loading compensation options is discussed in more detail in Ref [26]. A ferrite-based tuner concept is also discussed therein.

Fewer or alternate cavities: As discussed earlier, the large shunt impedance of the Booster cavities presents challenges for beam-loading compensation. The effect of beam loading could be reduced by using either fewer Booster cavities, or by replacing them with lower shunt impedance cavities, such as the storage ring cavities. Fewer cavities, installed, say, only on the extraction side of the Booster, also has the advantage of eliminating the differential delay and associated complications for the low-level rf control. The lower rf gap voltage required for 6 GeV (5–6 MV vs. 8–9 MV for 7 GeV) suggests that possibly two Booster cavities would be sufficient [26]. However, the per-cavity power requirement would likely be prohibitive for fixed detuning with two cavities, even with high-power couplers. On the other hand, the two-cavity option may be attractive with dynamic detuning or the comb filter approach. When the APS is decommissioned, four rf cavities will be removed. It may be possible to deliver the required Booster voltage with 5 or 6 single-cell storage ring cavities (i.e., the four that are removed plus spares). These alternate schemes are under active investigation.

Overall strategy: We plan to continue investigations of a ferrite-based dynamic tuner as well as particle tracking simulations with various rf control strategies. The existing analog low-level rf system will be upgraded to digital and will provide rf control as guided by the simulations. It will also include provisions for controlling a dynamic tuner. Detuning the cavity is beneficial in all cases, and adding ferrite-based dynamic tuners would minimize overall performance risk. This is, therefore, the preferred approach, albeit adding technical complexity to the cavities. Maintaining static detuning with a momentum ramp can be accommodated using comb-filter feedback; this is the alternate approach. The predicted performance with the comb filter appears to meet the efficiency goal, although more work is needed. Maintaining static detuning with no momentum ramp significantly increases both the performance and technical risk, as the efficiency goal is barely met (in simulations) and high-power couplers would be required. The possibility of using fewer Booster cavities, or replacing them with storage ring cavities, has a number of advantages from a beam-loading and rf control point of view, and these schemes are under active evaluation.

References

- [1] Y.W. Kang et al. “Rf Cavities for the Positron Accumulator Ring (PAR) of the Advanced Photon Source (APS).” In: *Proc. of 2016 Part. Accel. Conf.* 1996, p. 1693 (cit. on p. 301).
- [2] C.Y. Yao et al. “Results of Preliminary Tests of PAR Bunch Cleaning.” In: *Proc. of 2005 Part. Accel. Conf.* 2005, p. 3307 (cit. on p. 301).
- [3] M. Borland. “Simulations of swap-out for the APS MBA lattice.” private communication. Oct. 2013 (cit. on p. 302).
- [4] M. Borland. “Off-momentum parameters of the 132-nm lattice at 6 GeV.” private communication. May 2016 (cit. on pp. 302, 310).
- [5] U. Wienands. “Booster-APS-U MBA Synchronization.” priv. comm. Mar. 2017 (cit. on p. 304).
- [6] F. Lenkszus. “The APS Injection Timing System.” priv. comm. May 2003 (cit. on p. 306).
- [7] C-Y. Yao J.C. Dooling B.-X. Yang. “PAR Bunch Length Monitor Analysis.” private communication. Nov. 2016 (cit. on p. 306).

- [8] B.X. Yang et al. “Characterization of beam dynamics in the APS injector rings using time-resolved imaging techniques.” In: *1997 Particle Accelerator Conference*. 1997 (cit. on p. 306).
- [9] L. Emery. “Investigation of Robinson-type Instabilities in the PAR.” private communication. May 1992 (cit. on p. 307).
- [10] L. Emery. “More on Robinson-type Instabilities in the PAR.” private communication. May 1992 (cit. on p. 307).
- [11] C.Y. Yao et al. “Beam loading measurements and its applications to the harmonic rf control of the APS PAR.” In: *2006 European Particle Accelerator Conference*. 2006 (cit. on pp. 307, 309).
- [12] J. Calvey. “Ion effects in the APS injector and storage ring.” In: *2nd Topical Workshop on Instabilities, Impedance, and Collective Effects (TWIICE2)*. 2016 (cit. on p. 308).
- [13] T. Berenc and A. Goel. *PAR RF Cavity Parameters under Static and Pulsed Tuner Current*. Tech. rep. RF-TN-2015-004. APS, Nov. 2015 (cit. on p. 308).
- [14] U. Alp et al. “Spontaneous coherent microwave emission and sawtooth instability in a compact storage ring.” In: *Phys. Rev. ST Accel. Beams* 4 (2001), p. 054401 (cit. on p. 310).
- [15] K. Harkay et al. “Simulation investigations of the longitudinal sawtooth instability at SURF.” In: *2001 Part. Accel. Conf.* 2001 (cit. on p. 310).
- [16] J.M. Byrd and M. Georgsson. “Lifetime increase using passive harmonic cavities in synchrotron light sources.” In: *Phys. Rev. ST Accel. Beams* 4 (2001), p. 030701 (cit. on p. 310).
- [17] R.A. Bosch, K.L. Kleman, and J.J. Bisognano. “Robinson instabilities with a higher-harmonic cavity.” In: *Phys. Rev. ST Accel. Beams* 4 (2001), p. 074401 (cit. on p. 310).
- [18] G. Decker. *APS-U Beam Stability Physics Requirements Document*. Tech. rep. APS, 2012. URL: https://icmsdocs.aps.anl.gov/docs/groups/aps/@apsshare/@acceleratoroperationsphysics/documents/specification/aps%5C_1427507.pdf (cit. on p. 310).
- [19] J. Calvey et al. “Simulations of Booster Injection Efficiency for the APS-Upgrade.” In: *NA-PAC16*. WEA1CO03. 2016 (cit. on p. 310).
- [20] M. Borland. *elegant: A Flexible SDDS-Compliant Code for Accelerator Simulation*. Tech. rep. ANL/APS LS-287. Advanced Photon Source, Sept. 2000. URL: <http://www.aps.anl.gov/Science/Publications/lnotes/ls287.pdf> (cit. on p. 311).
- [21] J. Calvey. “Booster Modeling, APS-U Injector Beam Physics Preliminary Design Review.” private communication. May 2016 (cit. on p. 311).
- [22] “RF System.” In: *Advanced Photon Source Design Handbook*. Section 1.2.2.4. 1995 (cit. on p. 313).
- [23] J. Jacob. *Measurement of the Higher Order Mode Impedances of the LEP Cavities*. Tech. rep. ESRF, Jan. 1988 (cit. on p. 313).
- [24] J. Jacob and C. David. “352.2 MHz RF System for the ESRF.” In: *Proc. of EPAC 1988*. 1988, pp. 1169–1171 (cit. on p. 313).
- [25] K.W. Robinson. *Radiofrequency Acceleration II*. Tech. rep. CEA-11. Cambridge Electron Accelerator, Sept. 1956 (cit. on p. 313).
- [26] Berenc T et al. “Investigations of Booster beam loading compensation at high charge for APS-U.” private communication. May 2017 (cit. on pp. 314, 317).

- [27] *7-GeV Advanced Photon Source Conceptual Design Report*. Tech. rep. ANL-87-15. ANL-APS, 1987 (cit. on p. 315).
- [28] N. Sereno. *Booster suharmonic rf capture design*. Tech. rep. ANL/APS/LS-297. July 2002 (cit. on p. 315).
- [29] Lumpkin A. “Assessment of the BTS:FS3 electron-beam diagnostic for APS-U R&D.” private communication. Jan. 2017 (cit. on p. 315).
- [30] D. Boussard. “Control of Cavities with High Beam Loading.” In: *IEEE Transactions on Nuclear Science*. Vol. NS-32 No.5. Oct. 1985, pp. 1852–1856 (cit. on p. 315).
- [31] D. Boussard and G. Lambert. “Reduction of the Apparent Impedance of Wide Band Accelerating Cavities by RF Feedback.” In: *IEEE Transactions on Nuclear Science*. Vol. NS-30 No.4. Aug. 1983, pp. 2239–2241 (cit. on p. 316).
- [32] Jacobs Engineering Group. “Upgrade Project; Facility Space Requirements and Logistics Draft Document.” APS Upgrade Interactive Work Session, March 5-6, 2014. Apr. 2014 (cit. on p. 324).

4-3.14 Magnet Module Assembly and Testing

The previous parts of Section 4-3 described the various systems that make up the accelerator effort of the APS Upgrade. This section describes the integrated assembly into modules, and subsequent testing of these modules, prior to installation. All modules will be fully tested before installation starts. Components and sub-assemblies will be delivered to the integrated assembly area with a traveler, signifying that they have passed the required specifications for that system. The main components and sub-assemblies arriving for assembly are as follows:

- Magnets: integrated magnet sub-assemblies and individual magnet sub-assemblies with diagnostics, such as thermocouples and klixons.
- Mechanical support structures: support structures, plinths, and leveling hardware.
- Vacuum system sub-assemblies: sealed vacuum chambers on a strongback with BPMs, ion pumps, vacuum chamber supports, gauges, valves, flanges, etc.
- Instrumentation: cables, connectors, and components.
- Infrastructure connections.

The workflow of activities from receipt of materials to assembly and testing is shown in Figure 4.243. Ideally, all these activities would take place in one location.

4-3.14.1 Module Assembly

The magnet module sub-assemblies consist of individual magnets on a common support. The magnet module sub-assembly types are as follows:

- Quadrupole Doublet - L-bend - Multiplet (DLM) assemblies consisting of two quadrupoles, an L-bend, four quadrupoles, three sextupoles, and one fast corrector on a common support; 80 assemblies required.
- L-bend magnets with a base support; 80 assemblies required.
- FODO magnet assemblies consisting of four quadrupole magnets, three quadrupole bending magnets, and one 3PW on a common support; 40 assemblies required.

As described in previous sections and shown in Figure 4.243, the magnet module components will be received and QA tested before being released to assembly.

- Magnets will be received, QA tested for field quality, and their reference surfaces surveyed by the magnet group.
- Support plates and plinths will be received, QA tested dimensionally and for aperture placement, and assembled by the magnet support group, including painting of the concrete plinths.
- Vacuum strings will be delivered to the assembly group assembled, sealed, and fully tested.

The assembly and testing of the magnet modules will follow the delivery schedule of the individual components: magnets, plinths, and vacuum strings. The preliminary procurement delivery driven assembly schedule is shown in Figure 4.244.

Once the pre-tested components and sub-assemblies arrive at the assembly area, with the magnet support structure mounted and aligned on the plinth, the magnet subassemblies are mounted on the

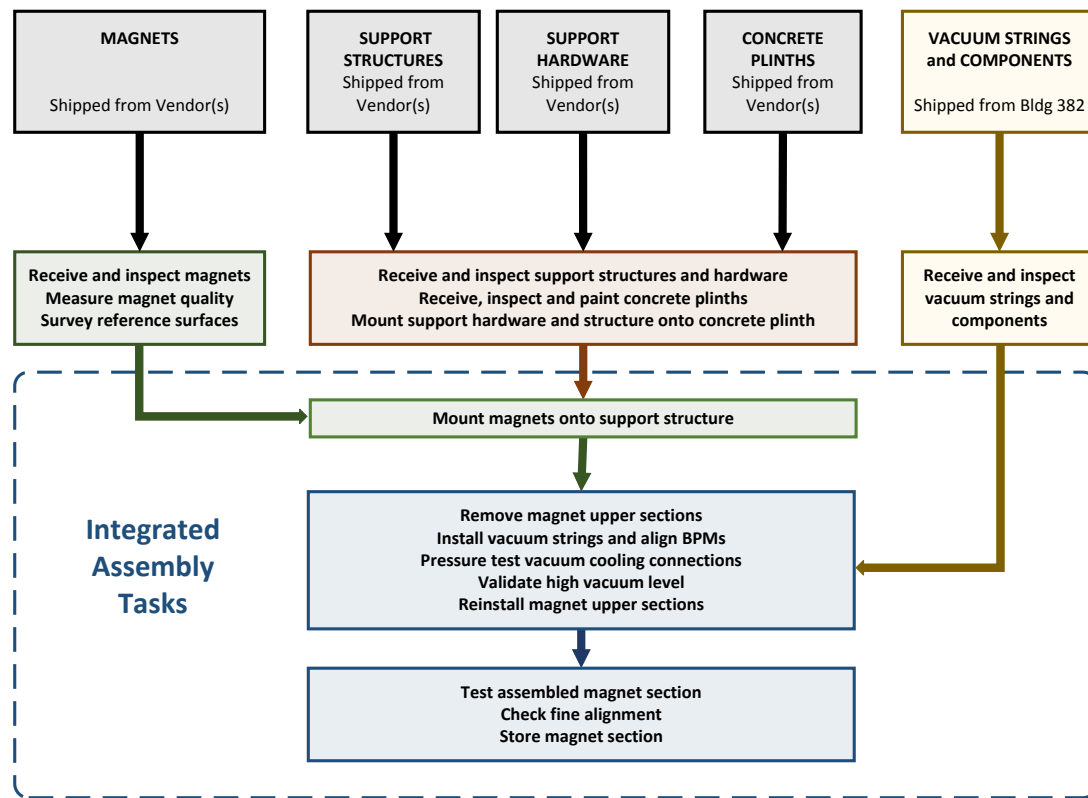


Figure 4.243. Integrated Assembly and Test Workflow.

support structure. Next, the top halves of the magnets in the assembly are removed, the vacuum chamber and components are installed, and the top halves of the magnets are replaced on the structure. An exploded view of the FODO magnet module assembly is shown in Figure 4.245.

A slightly more detailed description of the process includes the following steps:

1. Mount the magnets on the support structure and remove the top portions of the magnets. At this point, fiducialize the bottom half and rough align it to the plinth. Then, attach the vacuum supports to the magnet assemblies (for the L-bend, attach them to the subframe).
2. Insert the vacuum chamber with BPMs, assemble ion pumps (as needed), and connect pig tails (water lines, BPM electrical lines). Then, align the BPMs and absorbers to the fiducials and connect the BPM to the signal conditioning box.
3. Connect the water to the water manifold and the instrumentation to connector panels/terminal blocks for ease of installation.
4. Replace the tops of the magnets and verify the fiducials for the top and bottom of the magnets.
5. Perform the required QA checks of the work (for example, a hipot test, water line pressure test, etc.) before moving the assembled module to the module testing area.

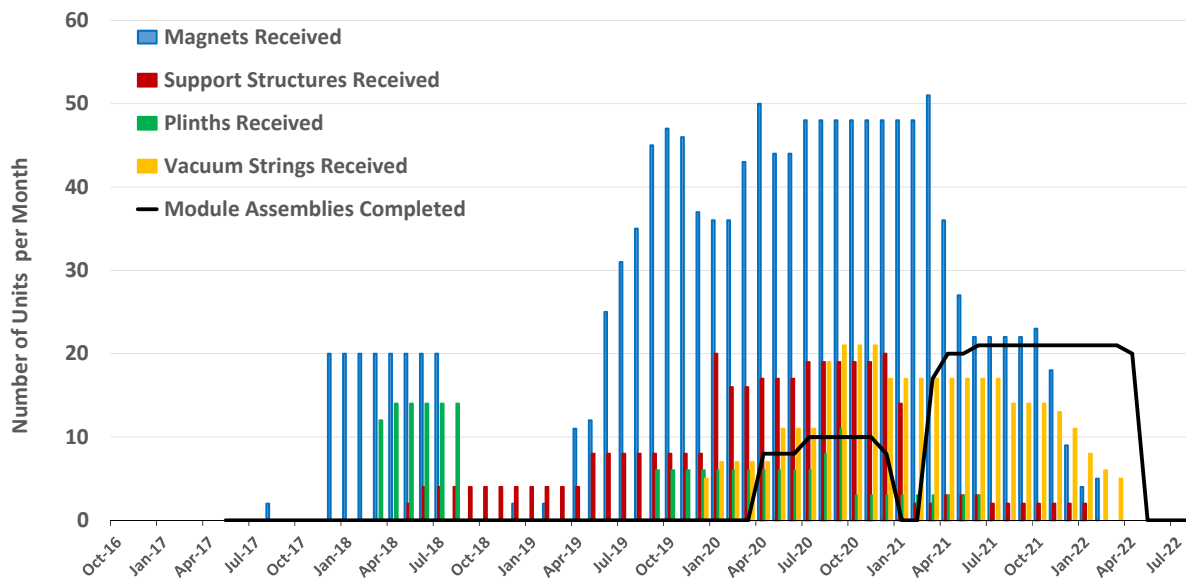


Figure 4.244. Component delivery driven magnet module assembly schedule.

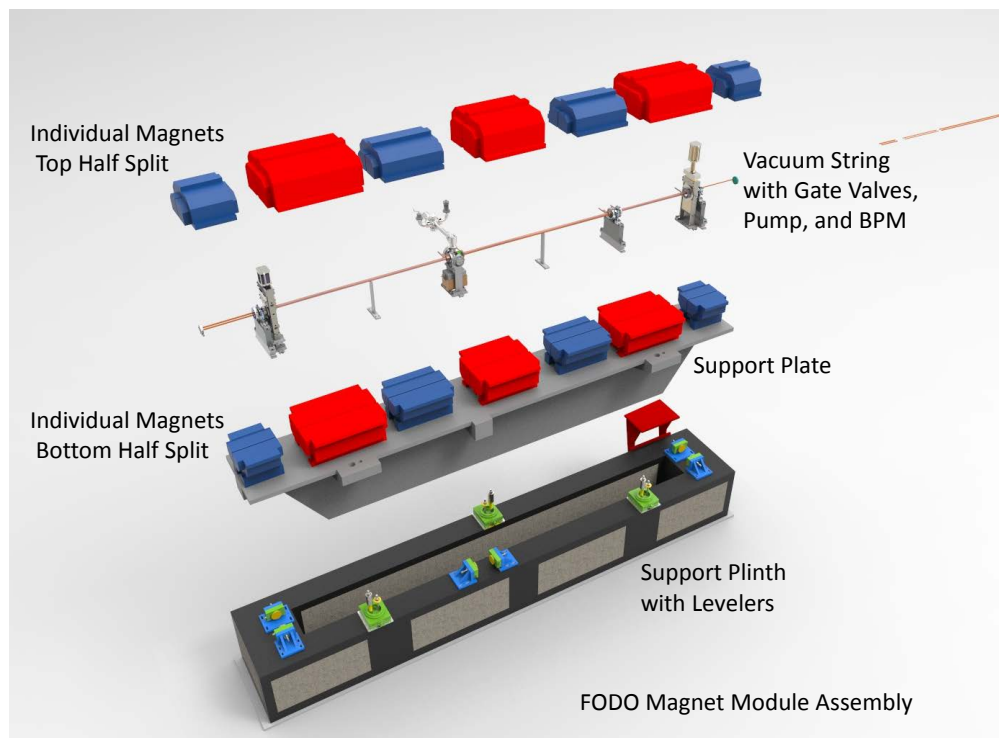


Figure 4.245. Exploded view of FODO magnet module assembly.

The FODO and DLM support plinths are moved on six air casters, with a combined capacity of 48 tons. A full description of the magnet and plinth transport system is given in section 4-3.4.2.

The assembly of the DLM magnet module follows a similar procedure to that of the FODO. A preliminary design of a completed DLM magnet module is shown in Figure 4.136.

The individual L-bend assembly, which spans two mechanical supports between the FODO and DLM in the tunnel, is moved into the tunnel on the subframe that it is assembled on without a plinth, and with the vacuum chamber installed. The subframe and plinth that the magnets are mounted on is the support that will be installed in the tunnel. A preliminary design of the L-bend magnet module assembly is shown in Figure 4.246.

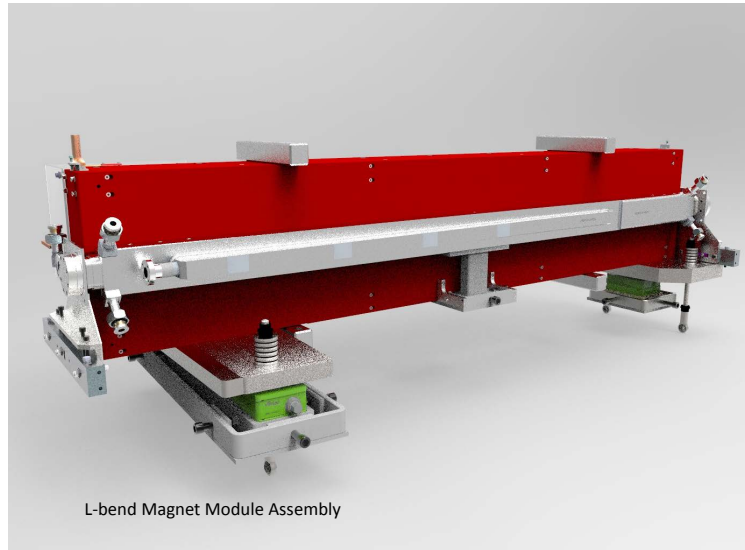


Figure 4.246. Preliminary design of M2 L-bend magnet module assembly.

4-3.14.2 Module Testing

After the magnet module is fully assembled and the alignment checked, the completed assembly will be moved to the integrated testing area. The infrastructure in the module testing area will allow for complete testing of all aspects of the assembled module to ensure that minimal issues arise once the module is installed in the tunnel, including hipot testing. Thus, all electrical, water, and vacuum connections would be made as they would be for the actual installation, and all components would be checked for readback and leaks (vacuum and water). Once the module passes all tests, it will be transported to storage, awaiting installation. The integrated testing area will be further utilized later on in training. Installation crews with specific tasks related to each installation will also be assigned to train on the full sector mockup.

4-3.14.3 Facilities to Support Module Assembly and Testing

Preparation, storage, and work spaces are required to support the module assembly and testing. Space needs for the project have been estimated. These are categorized into four areas:

1. Insertion Device (ID) Processing
2. Magnet Receiving Assembly and Staging

3. Component Receiving, Assembly, Test, and Staging
4. Vacuum Processing and Test Area

The vacuum processing and test area will utilize parts of Building 382 and Building 378. Vacuum cleaning and test facilities currently exist in Building 382. These areas should be sufficient for the project's vacuum processing and test needs. The remaining three areas are still being identified. A three day workshop with Jacobs Engineering led to an estimate of space requirements considering productivity, safety, and logistics [32]. Technical group leaders provided square footage requirements. The space requirements for these three areas, along with other technical areas in need of space for pre-installation activities, are given in Table 4.98.

Table 4.98. Space requirements based on technical lead input

Assembly and Testing Activity	Space [SF]
Magnet, magnet support, and vacuum loading dock, receiving and staging area	6,000
Magnet, support plate, and plinth inspection	3,300
Magnet, support plate, plinth, and vacuum assembly	4,400
Vacuum parts and chambers storage	4,200
Received plinth and completed magnet module assembly storage and staging area	32,700
Full sector mockup	6,000
Magnetic measurement and alignment	5,100
General electrical testing and parts storage	3,500
Power supply testing (including elevated temperature test room)	3,500
Diagnostics test and qualification	1,000
Insertion device and front end loading dock, receiving and staging area	6,300
Front end parts storage and cleanroom	2,800
Front end assembly and fabrication	2,900
Insertion device processing and magnetic measurement	5,100
Insertion device rework, assembly, storage, and staging area	12,700
Office space and restrooms	5,000
Total Space Required	104,500

The ID processing building will need about 17,500 square feet of space for building, modifying, and staging insertion devices. Some of this work is currently being done in Building 314. The APS Upgrade plans to continue to use Building 314 for insertion device work. This space will need to be supplemented with about 8,000 square feet for staging insertion devices and ID components. The location of this space has yet to be determined, but several local warehouse facilities have been visited for suitability. A typical layout of such a building to accommodate the requirements for magnet module assembly and testing, along with other technical areas, is shown in Figure 4.247. Support utilities such as compressed air, cooling water, and additional electrical power along with some infrastructure would be installed prior to occupation.

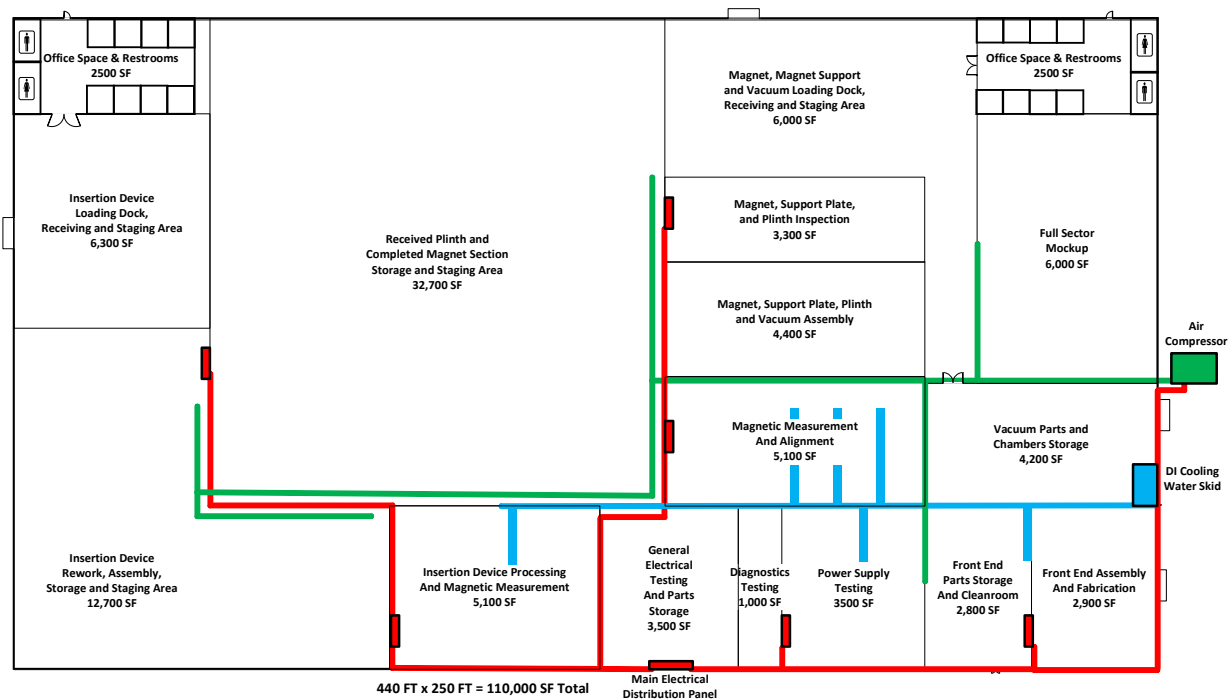


Figure 4.247. Preliminary layout of typical assembly and testing building.

References

- [1] Y.W. Kang et al. "Rf Cavities for the Positron Accumulator Ring (PAR) of the Advanced Photon Source (APS)." In: *Proc. of 2016 Part. Accel. Conf.* 1996, p. 1693 (cit. on p. 301).
- [2] C.Y. Yao et al. "Results of Preliminary Tests of PAR Bunch Cleaning." In: *Proc. of 2005 Part. Accel. Conf.* 2005, p. 3307 (cit. on p. 301).
- [3] M. Borland. "Simulations of swap-out for the APS MBA lattice." private communication. Oct. 2013 (cit. on p. 302).
- [4] M. Borland. "Off-momentum parameters of the 132-nm lattice at 6 GeV." private communication. May 2016 (cit. on pp. 302, 310).
- [5] U. Wienands. "Booster-APS-U MBA Synchronization." priv. comm. Mar. 2017 (cit. on p. 304).
- [6] F. Lenkszus. "The APS Injection Timing System." priv. comm. May 2003 (cit. on p. 306).
- [7] C-Y. Yao J.C. Dooling B.-X. Yang. "PAR Bunch Length Monitor Analysis." private communication. Nov. 2016 (cit. on p. 306).
- [8] B.X. Yang et al. "Characterization of beam dynamics in the APS injector rings using time-resolved imaging techniques." In: *1997 Particle Accelerator Conference.* 1997 (cit. on p. 306).

- [9] L. Emery. “Investigation of Robinson-type Instabilities in the PAR.” private communication. May 1992 (cit. on p. 307).
- [10] L. Emery. “More on Robinson-type Instabilities in the PAR.” private communication. May 1992 (cit. on p. 307).
- [11] C.Y. Yao et al. “Beam loading measurements and its applications to the harmonic rf control of the APS PAR.” In: *2006 European Particle Accelerator Conference*. 2006 (cit. on pp. 307, 309).
- [12] J. Calvey. “Ion effects in the APS injector and storage ring.” In: *2nd Topical Workshop on Instabilities, Impedance, and Collective Effects (TWIICE2)*. 2016 (cit. on p. 308).
- [13] T. Berenc and A. Goel. *PAR RF Cavity Parameters under Static and Pulsed Tuner Current*. Tech. rep. RF-TN-2015-004. APS, Nov. 2015 (cit. on p. 308).
- [14] U. Alp et al. “Spontaneous coherent microwave emission and sawtooth instability in a compact storage ring.” In: *Phys. Rev. ST Accel. Beams* 4 (2001), p. 054401 (cit. on p. 310).
- [15] K. Harkay et al. “Simulation investigations of the longitudinal sawtooth instability at SURF.” In: *2001 Part. Accel. Conf.* 2001 (cit. on p. 310).
- [16] J.M. Byrd and M. Georgsson. “Lifetime increase using passive harmonic cavities in synchrotron light sources.” In: *Phys. Rev. ST Accel. Beams* 4 (2001), p. 030701 (cit. on p. 310).
- [17] R.A. Bosch, K.L. Kleman, and J.J. Bisognano. “Robinson instabilities with a higher-harmonic cavity.” In: *Phys. Rev. ST Accel. Beams* 4 (2001), p. 074401 (cit. on p. 310).
- [18] G. Decker. *APS-U Beam Stability Physics Requirements Document*. Tech. rep. APS, 2012. URL: https://icmsdocs.aps.anl.gov/docs/groups/aps/@apsshare/@acceleratoroperationsphysics/documents/specification/aps%5C_1427507.pdf (cit. on p. 310).
- [19] J. Calvey et al. “Simulations of Booster Injection Efficiency for the APS-Upgrade.” In: *NA-PAC16*. WEA1CO03. 2016 (cit. on p. 310).
- [20] M. Borland. *elegant: A Flexible SDDS-Compliant Code for Accelerator Simulation*. Tech. rep. ANL/APS LS-287. Advanced Photon Source, Sept. 2000. URL: <http://www.aps.anl.gov/Science/Publications/lnotes/ls287.pdf> (cit. on p. 311).
- [21] J. Calvey. “Booster Modeling, APS-U Injector Beam Physics Preliminary Design Review.” private communication. May 2016 (cit. on p. 311).
- [22] “RF System.” In: *Advanced Photon Source Design Handbook*. Section 1.2.2.4. 1995 (cit. on p. 313).
- [23] J. Jacob. *Measurement of the Higher Order Mode Impedances of the LEP Cavities*. Tech. rep. ESRF, Jan. 1988 (cit. on p. 313).
- [24] J. Jacob and C. David. “352.2 MHz RF System for the ESRF.” In: *Proc. of EPAC 1988*. 1988, pp. 1169–1171 (cit. on p. 313).
- [25] K.W. Robinson. *Radiofrequency Acceleration II*. Tech. rep. CEA-11. Cambridge Electron Accelerator, Sept. 1956 (cit. on p. 313).
- [26] Berenc T et al. “Investigations of Booster beam loading compensation at high charge for APS-U.” private communication. May 2017 (cit. on pp. 314, 317).
- [27] *7-GeV Advanced Photon Source Conceptual Design Report*. Tech. rep. ANL-87-15. ANL-APS, 1987 (cit. on p. 315).

- [28] N. Sereno. *Booster suharmonic rf capture design*. Tech. rep. ANL/APS/LS-297. July 2002 (cit. on p. 315).
- [29] Lumpkin A. “Assessment of the BTS:FS3 electron-beam diagnostic for APS-U R&D.” private communication. Jan. 2017 (cit. on p. 315).
- [30] D. Boussard. “Control of Cavities with High Beam Loading.” In: *IEEE Transactions on Nuclear Science*. Vol. NS-32 No.5. Oct. 1985, pp. 1852–1856 (cit. on p. 315).
- [31] D. Boussard and G. Lambert. “Reduction of the Apparent Impedance of Wide Band Accelerating Cavities by RF Feedback.” In: *IEEE Transactions on Nuclear Science*. Vol. NS-30 No.4. Aug. 1983, pp. 2239–2241 (cit. on p. 316).
- [32] Jacobs Engineering Group. “Upgrade Project; Facility Space Requirements and Logistics Draft Document.” APS Upgrade Interactive Work Session, March 5-6, 2014. Apr. 2014 (cit. on p. 324).